

HARVARD  
Kenneth C. Griffin



GRADUATE SCHOOL  
OF ARTS AND SCIENCES

DISSERTATION ACCEPTANCE CERTIFICATE

The undersigned, appointed by the  
Department of Physics  
have examined a dissertation entitled

Fractionalization and disorder in strongly correlated systems

presented by Henry J. Shackleton

candidate for the degree of Doctor of Philosophy and hereby  
certify that it is worthy of acceptance.

Signature

A handwritten signature in blue ink that reads "Subir Sachdev".

Typed name: Prof. Subir Sachdev

Signature

A handwritten signature in blue ink that reads "Phillip Kim".

Typed name: Prof. Phillip Kim

Signature

A handwritten signature in blue ink that reads "Daniel Jafferis".

Typed name: Prof. Daniel Jafferis

Date: May 2, 2024

# Fractionalization and disorder in strongly correlated systems

A DISSERTATION PRESENTED  
BY  
HENRY SHACKLETON  
TO  
THE DEPARTMENT OF PHYSICS

IN PARTIAL FULFILLMENT OF THE REQUIREMENTS  
FOR THE DEGREE OF  
DOCTOR OF PHILOSOPHY  
IN THE SUBJECT OF  
PHYSICS

HARVARD UNIVERSITY  
CAMBRIDGE, MASSACHUSETTS  
MAY 2024

© 2024 - HENRY SHACKLETON  
ALL RIGHTS RESERVED.

## Fractionalization and disorder in strongly correlated systems

### ABSTRACT

Emergence in systems of many electrons can lead to macroscopic demonstrations of quantum mechanics which are intrinsically many-body. A primary focus of this dissertation is the phenomena of fractionalization, where the effective quasiparticles which emerge at long distances exhibit fractional quantum numbers of the microscopic degrees of freedom. The interplay between these emergent degrees of freedom and the microscopic symmetries can lead to a number of exotic properties including competing orders and unconventional phase transitions. I explore this phenomena in a number of platforms. This includes quantum antiferromagnets which can give rise to *quantum spin liquids*, where we predict critical properties of phase transitions between spin liquids and conventionally-ordered phases - due to the fractionalized excitations, such critical theories deviate from traditional Landau-Ginzburg predictions. I also study the interplay between fractionalized spin and charge excitations, as well as fractionalization in non-equilibrium contexts.

The second goal of this dissertation is to investigate the properties of disordered, strongly interacting, zero dimensional systems which exemplify many notable properties of higher-dimensional systems, such as doping-induced quantum criticality and non-Fermi liquid transport. The effects of disorder play an essential role in these models, leading to phenomena such as spin glass phases and conductance fluctuations which we investigate through both numerical and analytical methods.

## Contents

ABSTRACT	iii
CITATIONS TO PREVIOUSLY PUBLISHED WORK	viii
DEDICATION	ix
ACKNOWLEDGMENTS	xi
1 INTRODUCTION	1
1.1 Phases of matter and quasiparticles . . . . .	1
1.2 Fractionalization and quantum spin liquids . . . . .	5
1.3 Dynamics of open quantum systems . . . . .	15
1.4 Disorder in quantum systems . . . . .	18
1.5 Numerical methods for many-body systems . . . . .	24
2 DECONFINED CRITICALITY AND A GAPLESS $\mathbb{Z}_2$ SPIN LIQUID IN THE SQUARE LATTICE ANTIFERROMAGNET	34
2.1 Introduction . . . . .	34
2.2 Gapless $\mathbb{Z}_2$ spin liquid . . . . .	39
2.3 Continuum theory for Higgs transition from SU(2) to $\mathbb{Z}_2$ . . . . .	44
2.4 Renormalized perturbation expansion for the critical SU(2) gauge theory . . . . .	54
2.5 Transition from U(1) staggered flux to gapless $\mathbb{Z}_2$ spin liquid . . . . .	65
2.6 Renormalization group analysis . . . . .	69
2.7 Monopoles . . . . .	76
2.8 Conclusions . . . . .	78
3 SIGN-PROBLEM-FREE EFFECTIVE MODELS OF TRIANGULAR LATTICE ANTIFERROMAGNETISM	82
3.1 Introduction . . . . .	82
3.2 Connection between effective model and quantum magnetism . . . . .	84
3.3 Sign-problem-free mapping . . . . .	87
3.4 Results from Monte Carlo simulations . . . . .	96
3.5 Outlook . . . . .	105

4	PROTECTION OF PARITY-TIME SYMMETRY IN TOPOLOGICAL MANY-BODY SYSTEMS: NON-HERMITIAN TORIC CODE AND FRACTON MODELS	<b>107</b>
4.1	Introduction . . . . .	107
4.2	Pseudo-Hermitian Perturbations . . . . .	110
4.3	Non-Hermitian Toric Codes . . . . .	114
4.4	Non-Hermitian Fracton Models . . . . .	123
4.5	Non-Hermitian Quantum Fractal Liquids . . . . .	127
4.6	Summary and Conclusions . . . . .	131
5	AN EXACTLY SOLVABLE DISSIPATIVE SPIN LIQUID	<b>134</b>
5.1	Introduction . . . . .	134
5.2	Model . . . . .	136
5.3	Spectrum of the Lindbladian . . . . .	143
5.4	Perturbations away from exact solvability . . . . .	156
5.5	Summary and discussion . . . . .	158
6	DECONFINED QUANTUM CRITICALITY OF NODAL D-WAVE SUPERCONDUCTIVITY, NÉEL ORDER AND CHARGE ORDER ON THE SQUARE LATTICE AT HALF-FILLING	<b>161</b>
6.1	Introduction . . . . .	161
6.2	SU(2) square lattice gauge theory . . . . .	168
6.3	Quantum field theory and order parameters . . . . .	172
6.4	Fermion-boson interactions and spin gaps . . . . .	178
6.5	Honeycomb lattice . . . . .	180
6.6	Discussion . . . . .	182
7	QUANTUM PHASE TRANSITION AT NON-ZERO DOPING IN A RANDOM T-J MODEL	<b>185</b>
7.1	Random $t$ - $J$ model . . . . .	186
7.2	Dynamical Spin Response at $T = 0$ . . . . .	187
7.3	Thermodynamics and Entanglement . . . . .	189
7.4	Luttinger's theorem . . . . .	191
7.5	Discussion and Conclusion . . . . .	193
8	CONDUCTANCE AND THERMOPOWER FLUCTUATIONS IN INTERACTING QUANTUM DOTS	<b>195</b>
8.1	Introduction . . . . .	195
8.2	Setup . . . . .	199
8.3	Free fermion analysis . . . . .	204
8.4	Pure SYK analysis . . . . .	210
8.5	Interplay between hoppings and interactions . . . . .	215
8.6	Conclusion . . . . .	223

<b>APPENDICES</b>	<b>226</b>
<b>A APPENDIX TO CHAPTER 2</b>	<b>227</b>
A.1 Projective symmetry analysis . . . . .	227
A.2 Renormalization group analysis of the SU(2) gauge theory . . . . .	232
A.3 Isolation of logarithm-squared divergences in one-loop corrections . . . . .	235
A.4 Alternate computation of $z$ in the SU(2) gauge theory . . . . .	238
A.5 Higgs field renormalization in the SU(2) gauge theory . . . . .	239
A.6 Evaluation of two-loop SO(5) order parameter corrections . . . . .	240
A.7 Derivation of one-loop renormalization group equations . . . . .	242
A.8 Anisotropic correlation functions in real space . . . . .	244
A.9 Perturbative corrections to monopole scaling dimension . . . . .	246
<b>B APPENDIX TO CHAPTER 3</b>	<b>252</b>
B.1 Derivation of effective model . . . . .	252
B.2 Details of numerical simulations . . . . .	256
B.3 Surface worm algorithm . . . . .	256
B.4 Cluster algorithm for dual Ising model . . . . .	258
<b>C APPENDIX TO CHAPTER 5</b>	<b>259</b>
C.1 Perturbative derivation of the condition for reality of eigenvalues . . . . .	259
C.2 Interplay between X-Cube foliation and metric operators . . . . .	263
C.3 Haah's Cubic Codes . . . . .	264
<b>D APPENDIX TO CHAPTER 6</b>	<b>272</b>
D.1 Construction of Gamma matrices . . . . .	272
D.2 Non-vanishing steady-state expectation values . . . . .	273
D.3 Diagonalization of the free fermion Lindbladian . . . . .	273
D.4 Identification of single-site operators with flux configurations . . . . .	274
<b>E APPENDIX TO CHAPTER 1</b>	<b>277</b>
E.1 Spin Glass Analysis . . . . .	277
E.2 Thermal Pure Quantum states . . . . .	278
E.3 Temperature dependence of the thermal entropy . . . . .	280
E.4 Self-averaging, Electron distributions, and the Luttinger theorem . . . . .	281
<b>F APPENDIX TO CHAPTER 4</b>	<b>288</b>
F.1 Path integral calculation of fluctuations . . . . .	288
F.2 Replica off-diagonal fluctuations in the $(G, \Sigma)$ action . . . . .	290
F.3 Statistics of ratio distributions . . . . .	295
F.4 Conductance fluctuations for single-lead coupling . . . . .	297



## Citations to Previously Published Work

Much of the material in this thesis has been published in print. Details for particular chapters are given below.

- **Chapter 2:** H. Shackleton, A. Thomson, and S. Sachdev, Deconfined Criticality and a Gapless  $\mathbb{Z}_2$  Spin Liquid in the Square-Lattice Antiferromagnet, *Phys. Rev. B* 104, 045110 (2021). H. Shackleton and S. Sachdev, Anisotropic Deconfined Criticality in Dirac Spin Liquids, *Journal of High Energy Physics* 2022, 141 (2022).
- **Chapter 3:** H. Shackleton and S. Sachdev, Sign-problem-free effective models of triangular lattice quantum antiferromagnets, arXiv:2311.01572 (2023).
- **Chapter 4:** H. Shackleton and M. S. Scheurer, Protection of Parity-Time Symmetry in Topological Many-Body Systems: Non-Hermitian Toric Code and Fracton Models, *Phys. Rev. Research* 2, 033022 (2020).
- **Chapter 5:** H. Shackleton and M. S. Scheurer, An exactly solvable dissipative spin liquid, *Phys. Rev. B* 109, 085115 (2024).
- **Chapter 6:** M. Christos, H. Shackleton, S. Sachdev, and Z.-X. Luo, Deconfined quantum criticality of nodal d-wave superconductivity, Néel order and charge order on the square lattice at half-filling, arXiv:2402.09502 (2024).
- **Chapter 7:** H. Shackleton, A. Wietek, A. Georges, and S. Sachdev, Quantum Phase Transition at Nonzero Doping in a Random t-J Model, *Phys. Rev. Lett.* 126, 136602 (2021).
- **Chapter 8:** H. Shackleton, L. E. Anderson, P. Kim, and S. Sachdev, Conductance and thermopower fluctuations in interacting quantum dots, arXiv:2309.05741 (2023).

DEDICATED TO JACK FLOREY.

## Acknowledgments

In the past six years, I have grown immensely, from an incoming graduate student who had never taken a class in condensed matter physics to someone who, well, is still confused about many aspects of physics, but who is now knowledgeable enough to be awarded a degree. This would not have been possible without the support of many of the people in my life.

I would first like to thank my advisor, Subir Sachdev, for six years of invaluable support. Subir has provided numerous insights and substantial guidance in my research, and gave me many opportunities to develop as a researcher throughout my time in graduate school. Undoubtedly, I would not be a fraction of the physicist I am today without his support.

The rest of my committee, Professors Philip Kim and Daniel Jafferis, have also given tremendous insight into my research. Their wide breadth of expertise has helped contextualize my work in the broader field of physics. I would especially like to thank Philip Kim for allowing me to help teach his electromagnetism course over two semesters. Being able to do essentially any problem out of Griffith's Electrodynamics ad the drop of the hat is a party trick that I did not anticipate developing, but one that I consider myself lucky to have.

During my PhD, I had the opportunity to work extensively with two other professors - Shiwei Zhang and Matthias Scheurer. Having this breadth was essential to my development as a physicist, and their patience and guidance have allowed me to become a more effective collaborator.

I was fortunate enough to be exposed to physics research as an undergraduate and thank Salvatore Vitale, Liang Fu, and Mehran Kardar for educating me. I would especially like to thank Mehran Kardar for his support as my undergraduate research advisor, as well as his numerous insights both through research and through his statistical mechanics courses. I

have him to thank for understanding the renormalization group as well as I do now, although I suspect there will always be something more to learn.

Physics is inherently a collaborative process. In addition to the people already mentioned, I have benefited substantially from collaborations with Alex Wietek, Alex Thomson, Maine Christos, Zhu-Xi Luo, Antoine Georges, Laurel Anderson, and Nvedita. Being able to hold long discussions about physics with people with a diverse range of knowledge is a skill that is important and beneficial to develop, and these collaborations have aided in this substantially. Broader discussions about physics with the rest of the Harvard CMT department, including Maria, Haoyu, Chenyuan, Yanting, Alex, Rhine, Patrick, Ophelia, Rahul, Junkai, and many others have made me the physicist I am today.

I want to express my appreciation and gratitude to my family - my parents Karen and Scott, my brother John, and grandparents Evelyn, Liz, and Al, for their many decades of support and encouragement for me to pursue my passions.

Outside of physics, my housemates have been an invaluable source of comfort, especially during the height of the coronavirus pandemic. Adin, Amelia, Kai, Seth, Iliana, Dom, Yanisa, Hansa, Joaquin, Kendra, Andy, Sarah, and especially my current housemates, Elliott, Phoophie, Crystal, and Phoebe, have given me immeasurable support during my time as a graduate student. I am incredibly grateful to have such a large support network of friends, both in Boston and (unfortunately) far away. I would especially like to thank Caitlin and Milo for their unwavering support throughout my graduate program and for everything they have done for me.

*And so it goes, on and on, amidst a great deal of excitement.*

*And also of confusion.*

*In brief, business as usual.*

Abraham Pais

# 1

## Introduction

### 1.1 PHASES OF MATTER AND QUASIPARTICLES

A multitude of scientific breakthroughs in the early 20th century dramatically shifted our understanding of our universe, with the advent of quantum mechanics playing a central role in this paradigm shift. Quantum mechanical phenomena such as entanglement, superposition, and uncertainty gave a picture of reality that was jarringly different from ordinary human experience. Nevertheless, numerous experiments confirmed that quantum mechanics does indeed give an accurate description of physics on atomic scales. While many physicists dove deeper, probing smaller and smaller length scales to determine the fundamental building blocks of nature, other researchers took the equally profound route of understanding the full implications that a quantum mechanical theory, applied to complicated systems of atoms and electrons, can have on our universe. Just as it took many centuries between the establishment of classical Newtonian mechanics and the invention of the airplane, the consequences that the quantum mechanical nature of reality can have on our real world is a far from trivial corollary of the governing principles of quantum mechanics.

An essential conceptual ingredient in ascertaining the full consequences of quantum mechanics is the notion of emergence of new physics at different length scales in many-body

systems. While the full implications of quantum mechanics are unknown, the behavior of a single electron in isolation is in fact extremely well-understood and whose properties can be relatively easily predicted from the quantum mechanical single-particle Dirac equation, provided one does not probe sufficiently small length scales to see the subatomic nature of the electron. In contrast, the behavior of a macroscopic number of atoms interacting in a crystalline solid is not at all obvious, despite its long-distance properties being accurately captured by the many-particle Schrödinger equation. The behavior of these systems can lead to quantum phenomena which is intrinsically many-body and could not be predicted from the behavior of a single atom. Even more striking, this often leads to macroscopically observable consequences of the quantum nature of reality.

A direct attack of the many-body Schrödinger equation is infeasibly complex. Two indispensable conceptual developments in understanding these many-body systems were the notion of *quasiparticles* and *phases of matter*. While the microscopic degrees of freedom in a material may be made up of electrons, Coulomb interactions between these particles and periodic potentials imposed by the crystalline lattice leads to behavior at long distances that is distinct from that of free electrons, but nevertheless often has features that can be captured in a theory of weakly-interacting emergent *quasiparticles*. In the simplest case, these quasiparticles largely resemble the microscopic electrons, with the effect of interactions being to “renormalize” the mass of these electron-like quasiparticles. This is an essential ingredient in the Landau-Fermi liquid theory of metals [266]. However, the complexity of many-body quantum mechanical systems affords many more exotic possibilities. A central theme of this dissertation is the phenomena of *fractionalization*. Fractionalization arises when the effective low-energy degrees of freedom of a many-body system have quantum numbers, such as charge and spin, that are fractions of those of the microscopic degrees of freedom. This is indicative of the many-body nature of the problem; it means that the emergent degrees of freedom cannot be constructed in a simple picture of non-interacting microscopic particles, as this would at most yield integer multiples of the primitive quantum numbers. Fractionalization will be discussed in more detail in Section 1.2.

A complementary organizing principle in understanding the behavior of many-body systems, which also plays an essential role in this dissertation, is that of categorizing phenomena

in terms of *phases of matter* and phase transitions between them. Many distinct physical systems display qualitatively similar behavior at long distances. A useful way of organizing this behavior is to refer to similar materials as belonging to the same *phase of matter*, which captures the universal long-distance properties.

An early understanding of classifying phases of matter was put forward by Landau [265]. The governing equations of a system of electrons in a crystal obey some set of symmetries  $\mathcal{G}$ , often consisting of a combination of lattice symmetries, charge conservation, rotation of the internal spin of the electron, and time reversal symmetry. However, the quantum state that the system chooses may break these symmetries down to a subset  $\mathcal{H}$  - a ferromagnet, for example, breaks spin rotation and time reversal symmetry. This picture also has close connections to quasiparticles - for systems with spontaneously broken continuous symmetries, quasiparticles known as *Goldstone modes* emerge [161, 336] which correspond to slow rotations of this order parameter. More generally, defects of an order parameter in a symmetry-broken phase give rise to (potentially gapped) quasiparticles.

This symmetry-based classification is ultimately inadequate for capturing all intuitively-distinct phases of matter, at least in the simplest formulation. For example, a ferromagnet may have either insulating or metallic properties which are seemingly not distinguished through a symmetry-based criteria. The interpretation of superconductivity as spontaneous breaking charge conservation poses issues when the electromagnetic gauge field is properly taken into account and the symmetry at hand is demoted to a fictitious gauge symmetry. Finally, there exist “topological” phases of matter known as quantum spin liquids which break no symmetries of the underlying lattice but cannot be continuously deformed into a trivially disordered state. Substantial progress has been made in attempting to unify these phases using a sufficiently generalized notion of “symmetry,” [310] but this will not be the focus of this dissertation.

A more pervasive theme will be the focus on universal properties of transitions between phases of matter. In a conventional symmetry-based description, phase transitions are described by a Landau-Ginzburg theory, which is a generic field theory that captures long-distance fluctuations of the order parameter of a phase. The only input into this theory is the full symmetry of the system, the symmetry that is being broken, and the dimension of the system. The remarkable renormalization-group theory of criticality justifies this picture

and predicts universal properties of phase transitions which are only dependent on this input. However, there exist many exotic phase transitions that fall outside the Landau-Ginzberg paradigm, several of which are studied in this dissertation. For example, the presence of gapless metallic degrees of freedom - either on one side of the transition or across the transition - is not captured in a Landau-Ginzburg description. An early theory of Hertz-Millis criticality [188, 317] argued for a minimal description in terms of a symmetry order parameter coupled to a Fermi surface. An example of a phase transition with gapless fermionic degrees of freedom is studied in Chapter 7. Transitions into topologically-ordered states, which lack a local order parameter, do not naturally admit a Landau-Ginzburg description. Phase transitions of these types are studied in Chapter 2, where a Landau-like theory can be developed in terms of fractionalized quasiparticles. Finally, there is the possibility of a continuous phase transition between distinct symmetry-broken phases with residual subgroups  $\mathcal{H}$  and  $\mathcal{H}'$ , where neither is a subgroup of the other. The final possibility, known as *deconfined criticality*, can occur when the two phases of matter are “intertwined” in such a way that defects of one phase carry quantum numbers of the other. Models of deconfined criticality are studied in Chapters 3 and 6.

Several chapters of this dissertation focus on aspects of quantum systems which were historically regarded as antithetical to realizing exotic quantum behavior, but have since been understood to bring about intrinsically new physics. These are the phenomena of *decoherence* and *disorder*, which are reviewed in Sections 1.3 and 1.4, respectively. Both of these aspects are ubiquitous in realistic systems. Quantum materials can never be perfectly isolated from their environments, and interactions between these systems can cause the material to lose coherence. Similarly, materials rarely form perfect crystalline solids, and defects in these materials lead to deviations from idealized clean models. The understanding of these effects have revealed novel ways in which quantum mechanics can manifest itself on a macroscopic scale.

The dramatic rise in computing power over the last several decades, as well as an improved theoretical understanding of quantum many-body systems, has led to massive successes in the field of computational many-body physics. Chapters and explicitly involve applications of these methods, and essentially all chapters lean on developments in computational physics

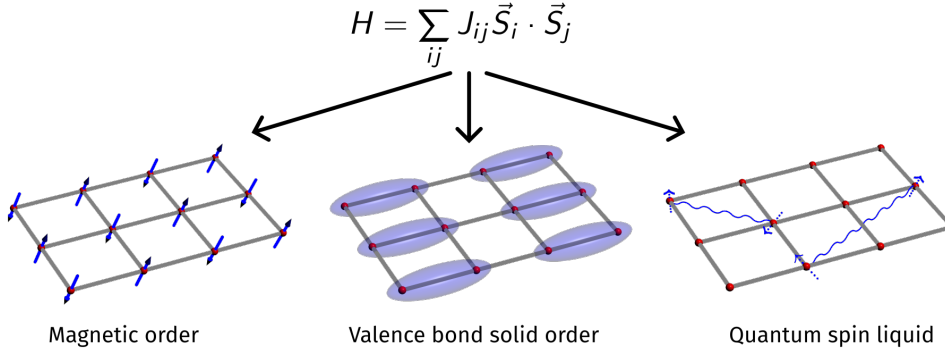


Figure 1.1: A quantum antiferromagnetic Heisenberg model can lead to a wealth of phases at zero temperature. In this dissertation, we will primarily be focused on three types of phases. In magnetically ordered states, each spin aligns in a definite direction in a manner which leads to long-range order, although the strength of this order is generally reduced due to quantum fluctuations. Valence bond solid order occurs when neighboring spins form a regular tiling of spin singlet states, breaking lattice symmetries. Quantum spin liquids break no symmetries of the lattice and possess fractionalized spin-1/2 spinon excitations.

in some way. In Section 1.5, we provide a brief overview of the various numerical tools of relevance to this dissertation.

## 1.2 FRACTIONALIZATION AND QUANTUM SPIN LIQUIDS

Fractionalization arises when the effective low-energy degrees of freedom of a many-body system have quantum numbers that are fractions of those of the microscopic degrees of freedom. This is indicative of the many-body nature of the problem; it means that the emergent degrees of freedom cannot be constructed in a simple picture of non-interacting microscopic particles, as this would at most yield integer multiples of the primitive quantum numbers. The most well-confirmed experimental demonstration of fractionalization is the fractional quantum Hall effect [20, 160, 176, 522], where the physical electron fractionalizes into composite fermions with fractional charge.

Quantum spin liquids (QSLs) provide an especially rich platform to study symmetry fractionalization. QSLs arise in quantum magnets when a combination of geometric frustration and quantum fluctuations preclude the existence of conventional order at zero temperature. Note that beyond conventional magnetic order, such as ferromagnetism and antiferromagnetism which have clear classical analogies, the quantum nature of the underlying spins al-

lows for additional paramagnetic phases known as *valence bond solid* (VBS) phases, shown in Fig. 1.1, where neighboring spins pair up in a regular fashion to form spin singlet pairs. These phases break translational symmetry and have a local order parameter, neither of which is the case for a QSL. A simple picture of a QSL was proposed by Anderson [17] as a “resonating valence bond” (RVB) state, where the QSL is constructed by taking a macroscopic superposition of different valence bond tilings of the lattice in a way which restores translational symmetry. More modern understandings of QSLs are formulated in terms of parton constructions, which is summarized in Section 1.2.1, or more abstractly in the language of topological and conformal field theories.

A hallmark feature of QSLs is the existence of charge-neutral spin-1/2 spinon excitations. This may superficially not appear to be a case of fractionalization, as the physical electron also has spin-1/2; however, recall that the electron also has electric charge, and forming a charge-neutral object requires an even number of electron-hole pairs and will therefore naturally have an integer spin. Indeed, conventional spin wave excitations in magnetically ordered phase have integer spin. A QSL can be thought of as a limiting case of spin-charge fractionalization, where an electron fractionalizes into a spinless charge  $e$  holon and a charge-neutral spin-1/2 spinon; the QSL arises when the holons are gapped and play no role in the low-energy description. In Anderson’s RVB picture, these spinons can be obtained by breaking a valence bond singlet; this creates an excitation with integer spin, but supported on two sites. Due to the superposition of different VBS configurations, these sites can be moved arbitrarily far away from each other without disrupting the overall RVB state, which constitutes a pair of spin-1/2 spinon excitations. Spin liquids also possess exotic spin 0 excitations, although the nature of these excitations is non-universal; for example, they may take the form of gapped “vison” excitations or gapless “photon” excitations. The nature of these additional excitations is related to the structure of a fluctuating gauge field that the spinons must be coupled to, and is elaborated in more detail in Section 1.2.1.

A recurring theme in this dissertation is symmetry fractionalization beyond spin-charge fractionalization. Frustrated spin systems generically possess a large number of symmetries beyond just spin rotation symmetry; for example, lattice symmetries such as translation and rotation, as well as time-reversal symmetry. The ways in which spinons as well as additional

excitations like visons realize these symmetries has important implications for the stability of spin liquid phases. Natural routes to proximate ordered phases may be obtained by condensing bosonic excitations of the spin liquid with non-trivial quantum numbers of the microscopic symmetries. For example, in Chapter 3, we demonstrate that one can obtain VBS order by condensing a spin 0 vison with a non-trivial fractionalized representation of the lattice symmetries. Understanding the multitude of ways in which the microscopic symmetries can act on fractionalized excitations also allows one to construct effective Landau-Ginzburg actions for such transitions, as is the focus of Chapter 2 and 6.

In the following section, we give a review of symmetry fractionalization through the language of parton constructions. It is important to note that the types of symmetry fractionalization realized in parton constructions only constitute a subset of the possible fractionalization patterns that can emerge in frustrated magnets. A full classification is easiest to see for *gapped* quantum spin liquids with  $\mathbb{Z}_2$  topological order. In this case, the low-energy theory can be described in terms of three anyons,  $e$ ,  $m$ , and  $\epsilon$ , along with their symmetry transformations. Because of the  $\mathbb{Z}_2$  gauge redundancy, the different symmetry representations are given by the  $\mathbb{Z}_2$  central extension of the lattice symmetry group. A mean-field description of partons focuses primarily on the symmetry fractionalization of *one* of these anyons corresponding to the spinon, with different projective symmetry representations of the vison not considered. Group cohomology methods [131] have been used to classify all possible projective symmetry representations, and found a large number (2,098,176) of possible gapped  $\mathbb{Z}_2$  spin liquids, significantly larger than the number of  $\mathbb{Z}_2$  spin liquids predicted by a fermionic parton construction (272). Moving beyond a parton theory of symmetry fractionalization for *gapless* spin liquids falls under a general theory of *symmetry-enriched quantum criticality* [491, 548], which is an emerging field of research.

### 1.2.1 FRACTIONALIZATION IN PARTON CONSTRUCTIONS

Much of the early work in understanding fractionalization in the language of projective symmetry groups was put forth in [511]. In this approach, one analyzes Heisenberg models of the form  $H = \sum_{ij} J_{ij} \mathbf{S}_i \cdot \mathbf{S}_j$  by rewriting the spin operator in terms of Abrikosov fermions, which

we refer to as *spinons*,

$$\mathbf{S}_i \equiv \frac{1}{2} f_{i\alpha}^\dagger \sigma_{\alpha\beta} f_{i\beta} . \quad (1.1)$$

Note that an alternative approach is to perform a decomposition in terms of bosonic operators. This rewriting introduces an SU(2) redundancy in our description; an equivalent way of stating the problem is that our Hilbert space has been enlarged to include the unphysical states  $|0\rangle$  and  $f_{i\uparrow}^\dagger f_{i\downarrow}^\dagger |0\rangle$ . One must enforce the constraints

$$f_{i\alpha}^\dagger f_{i\alpha} = 1 , \quad f_{i\alpha} f_{i\beta} \epsilon_{\alpha\beta} = 0 . \quad (1.2)$$

These constraints can be made more transparent by introducing the doublet

$$\psi = \begin{pmatrix} f_\uparrow \\ f_\downarrow^\dagger \end{pmatrix} \quad (1.3)$$

where the constraints take the form

$$\psi_i^\dagger \tau^l \psi_i = 0 \quad (1.4)$$

with Pauli matrices  $\tau^l$ . With this, we see that a full theory necessitates the addition of SU(2) gauge fields that couple to the current in Eq. 1.4, which converts our SU(2) redundancy into an appropriately-unphysical SU(2) gauge ambiguity.

The quantum Heisenberg Hamiltonian is quartic in the fermionic spinon operators. By performing a mean-field decoupling and treating the gauge fields as static, one can obtain quadratic spinon Hamiltonians which provide a mean-field description of our spin liquid state and schematically takes the general form

$$H = \sum_{ij} J_{ij} \psi_i^\dagger U_{ij} \psi_j . \quad (1.5)$$

$U_{ij}$  is required by spin rotation invariance to take the form  $U_{ij} = i\rho_{ij} W_{ij}$ , where  $\rho_{ij}$  is a real number and  $W_{ij}$  is an element of SU(2).

An important observation is that the spinon mean-field Hamiltonian is *not* gauge-invariant.

Under an SU(2) gauge transformation  $W_i$ , we have the transformation

$$\begin{aligned}\psi_i &\rightarrow W_i \psi_i \\ U_{ij} &\rightarrow W_i U_{ij} W_j^\dagger\end{aligned}\tag{1.6}$$

This observation has two consequences. First, the mean-field Hamiltonian may not be invariant under a generic global SU(2) rotation. If not, it may be invariant under a U(1) subgroup, or at worst the  $\mathbb{Z}_2$  center  $W_i = -1$ . Depending on these options, the relevant gauge fluctuations are also broken down to U(1) or  $\mathbb{Z}_2$ . This qualitatively affects the nature of the spin liquid phase; U(1) gauge fields support gapless photon excitations which may destabilize the spin liquid at low energies, whereas  $\mathbb{Z}_2$  gauge fields only have gapped vison excitations.

A second consequence of this is that the hoppings  $U_{ij}$  are permitted to break the lattice symmetries of the Hamiltonian, provided that the symmetry-transformed version of Hamiltonian is gauge-equivalent to the original one. When this is the case, one says that the spinons realize the lattice symmetries *projectively*. An example which appears frequently in this dissertation is the  $\pi$ -flux spin liquid, where the hoppings take the form

$$\begin{aligned}U_{i,i+\hat{x}} &= -U_{i+\hat{x},i} = i, \\ U_{i,i+\hat{y}} &= -U_{i+\hat{y},i} = i(-1)^{i_x}.\end{aligned}\tag{1.7}$$

These hoppings are invariant under global SU(2) gauge transformations. These hoppings seemingly break translational symmetry in the  $x$ -direction; however, symmetry can be restored by supplementing the symmetry with the gauge transformation  $W_i = (-1)^{i_y}$ . Similar transformations can be constructed for other naively-broken lattice symmetries such as rotation and reflection.

Classifying the distinct ways in which a mean-field fermionic spinon Hamiltonian can projectively realize the symmetries of the square lattice was one of the contributions of [511]. From this, numerous follow-up works analyzed the possible projective symmetry representations on other lattice geometries, including triangular [502, 573] and kagome [295, 502].

The connection between projective symmetry representations and symmetry fractionalization requires some elaboration. Fractionalization of the spin quantum number is immediately

apparent in our parton construction, and while projective representations of lattice symmetries clearly indicate that something atypical is going on, it is not clear in what sense these lattice symmetries are “fractional.” To elaborate this, we focus on the projective representation of translation symmetry, encoded in the identity  $T_x T_y T_x^{-1} T_y^{-1} = -1$ . For a gapped  $\mathbb{Z}_2$  spin liquid of half-integer spins, the vison excitations always have this projective symmetry, since this symmetry transformation causes the vison to encircle an odd number of spinons. Spinons may or may not realize these projective symmetries depending on the spin liquid. The  $\pi$ -flux spin liquid is an example of spin liquid with such a projective symmetry relation. With this projective symmetry, all irreducible representations are, up to similarity transformation [132],

$$T_x = e^{i\kappa_x} \tau^x \quad T_y = e^{i\kappa_y} \tau^z. \quad (1.8)$$

We refer to  $\kappa_{x,y}$  as “fractional momentum” as they are only defined modulo  $\pi$  rather than  $2\pi$ , since the sign of  $T_x, T_y$  can be changed by a unitary transformation. This halving of the momenta can be used as a dynamical signature of symmetry fractionalization and can be probed through response functions [471].

### 1.2.2 WHERE ARE THE SPIN LIQUIDS?

On a theoretical level, there are many powerful tools for classifying and characterizing possible spin liquid phases. However, as is often the case for many of the exotic states of matter proposed by theorists, a challenging but important step is to find realistic models that support these phases. For quantum spin liquids, the rough recipe for finding these phases is to maximize the frustration in a quantum spin system, such that a simple magnetically-ordered phase becomes energetically unfavorable and gives rise to more exotic paramagnetic phases. Note that this procedure may still give rise to non-topologically-ordered paramagnetic phases such as valence bond solids. Searching for candidate spin liquids can be carried out either experimentally in real materials with support localized magnetic moments and strong frustration, or numerically in simplified but realistic models of antiferromagnetism. To limit the scope of this section to topics most directly connected to later chapters, we focus primarily on the latter.

Before reviewing the evidence for spin liquid phases in realistic spin models, we first ask the question: how does one detect a spin liquid? This is a difficult question - especially in actual experiments where one has limited access to observables - due to the lack of a local order parameter to identify the state. A common method is simply by process of elimination - measures of magnetic order and lattice symmetry-breaking order are performed, and if such symmetries appear unbroken, then victory is claimed. This is not as bad of an argument as it might seem. This is because of the Lieb-Schultz-Mattis theorem [282] and its higher-dimensional generalizations [178, 349], which place non-perturbative constraints on the ground state wavefunction of Hamiltonians possessing spin rotation and lattice translation symmetry. Applied to our spin systems, it prevents the existence of a trivial (non-topologically-ordered), gapped, and symmetric ground state. As such, ruling out the existence of conventional symmetry-breaking means that the state must be topologically-ordered or gapless. The latter option is satisfied by spin liquid states with either gapless spinon or gauge excitations. A “boring” way out of this theorem would be to have a sufficiently ordinary gapless state whose excitations are non-fractionalized. However, to our knowledge, no such states have ever been proposed, although the non-triviality in constructing such an example perhaps makes such states interesting in their own right. Note that gaplessness by itself is not sufficient to be an allowed state - in more precise language, there is a mixed t’Hooft anomaly that must be matched by the low-energy effective theory in order to be a valid state. Putting aside this possibility, the lack of any detectable symmetry breaking provides strong evidence for a spin liquid ground state with fractionalized excitations. This comes with the caveat that candidate spin liquid phases often only appear in narrow parameter windows in between ordered phases, so demonstrating the existence of a stable symmetric phase rather than a direct transition between ordered phases requires careful finite size analysis and is often not without controversy.

A less rigorous approach is to explicitly construct spin liquid variational wavefunctions, optimize them for the spin system of interest, and compare the variational energies to more unbiased methods such as DMRG. If the two are in good agreement, then this gives good evidence for such a spin liquid phase, and moreover can give a great deal of insight into the nature of the spin liquid phase. This approach has a number of drawbacks. There is the obvious concern of how “good” of an energy must one get in order to be confident that the

variational ansatz provides an accurate description of the ground state. In terms of symmetry fractionalization, there exist a large number of spin liquid states, only a small fraction of which can be easily accessed by conventional parton constructions. A priori, there is no reason to expect this subset of fractionalization patterns to be the ones that emerge in physical spin models.

Several proposals have been made for detecting the symmetry fractionalization of spin liquid quasiparticles. These proposals have focused primarily on gapped  $\mathbb{Z}_2$  quantum spin liquids, as the gapped quasiparticle excitations and well-defined topological contribution to the ground state entanglement entropy allows for more controlled methods. An early proposal was the use of minimally entangled states (MES) [223], which argued that DMRG algorithm naturally picked out a preferred basis in the topologically degenerate ground state subspace, which can then be used for controlled extraction of the topological entanglement entropy. This idea was further developed by noting that fractionalization of lattice symmetries should be reflected by the quantum numbers of the MES with varying boundary conditions [373, 554]. The accuracy of these symmetry fractionalization methods are somewhat ambiguous. For example, these methods were applied to candidate spin liquids of triangular lattice Heisenberg models to obtain seemingly convincing evidence of symmetry fractionalization. Nevertheless, subsequent DMRG studies [193] gave strong evidence for a gapless Dirac spin liquid, consistent with variational Monte Carlo studies. MES studies gave evidence for gapped  $\mathbb{Z}_2$  spin liquids for both square and kagome antiferromagnets [223, 224], but both interpretations have fallen out of favor and are believed to host gapless spinon excitations. A better understanding the limits of these methods is an important research direction.

Extensive numerical simulations have been performed on a variety of magnetically frustrated systems. Below, we review some of the most recent numerical results on these lattices. To fix convention, we will use the variable  $J_n$  to refer to antiferromagnetic couplings between  $n$ -th nearest neighbor sites.

### 1.2.3 SQUARE LATTICES

The square lattice Heisenberg model with nearest-neighbor antiferromagnetic interactions, is an quantum antiferromagnet. This is not too surprising due to the lack of geometric frustration

in the square lattice, although the quantum nature of the spins means that the actual form of the ground state is modified substantially from a classical Néel state (as the latter is not an eigenstate of the Hamiltonian), and the magnitude of the antiferromagnetic order parameter is reduced by quantum fluctuations. By adding in a second-nearest-neighbor interaction  $J_2$ , frustration is maximized classically at  $J_2/J_1 = 0.5$ , and the presence of a non-magnetic phase in the quantum model has been well-established numerically. A more controversial question is the nature of this non-magnetic region - is it VBS order, a spin liquid, or are there two distinct VBS and spin liquid phases existing in this region? This is a challenging question due to the small size of the non-magnetic region, which only exists around  $0.5 \leq J_2/J_1 \leq 0.6$ . Nevertheless, the existence of long-range VBS order has been established for at least part of the non-magnetic region by careful finite-size analysis of VBS correlation functions. The inclusion of a third-nearest-neighbor coupling  $J_3$  has been shown to enlarge the region of VBS order [291], leading to an even more unambiguous demonstration of the VBS order.

Having clearly established the VBS order, the question is whether there is a direct transition between the VBS and Néel order, or if a narrow spin liquid phase appears in between the two. For methods such as DMRG, PEPS, and NQS, a direct finite size extrapolation of the Néel and VBS order parameters often indicates a stable spin liquid phase. A more subtle approach is to use *level spectroscopy* methods. Note that recent results using new DMRG techniques argue that improved level spectroscopy on larger system sizes indicate a direct Néel/VBS transition and no intermediate spin liquid phase [375], although this study did not investigate the Néel and VBS order parameters directly. The most direct insight into the nature of the spin liquid comes from variational Monte Carlo studies [140] that explicitly use a Gutzwiller-projected fermionic spinon trial wavefunction with a particular projective symmetry representation classified as Z2Azz13 using Wen's [511] projective symmetry notation. The gapless nature of this spin liquid is consistent with other numerical studies [290, 342, 505], although the details of the particular symmetry fractionalization have not been confirmed through independent methods. Nevertheless, we will assume this particular spin liquid when we analyze the nature of the phase transitions into proximate Néel and VBS phases in Chapter 2.

### 1.2.4 TRIANGULAR LATTICES

The triangular lattice Heisenberg model with nearest-neighbor antiferromagnetic interaction, while possessing more geometric frustration than a square lattice, is ultimately a magnetic phase with coplanar magnetic order illustrated in Fig. [42, 69, 200]. However, the strength of the order is extremely strongly suppressed by quantum fluctuations, and a very small next-nearest neighbor antiferromagnetic interaction  $J_2$  is sufficient to destroy the magnetic order [195, 207, 232, 345, 407, 517, 575]. The nature of this spin liquid has been debated over the years; early DMRG studies detected signatures of fractionalization consistent with a gapped  $\mathbb{Z}_2$  spin liquid [195, 575], contradicting VMC studies which indicated a gapless U(1) Dirac spin liquid [207]. Subsequent DMRG studies [193] found evidence for a gapless spin liquid, consistent with VMC results. Of note is a remarkable recent work [517] which carefully studied the low-lying energy eigenstates of the triangular lattice Heisenberg model in the putative spin liquid region and found a striking correspondance between them and excitations of a Dirac spin liquid, including spinon bilinear excitations as well as U(1) monopole excitations.

A second type of spin liquid on the triangular lattice has recently been proposed, which comes from reducing the strength of the repulsive interactions of the underlying electronic system that reduces to a Heisenberg model in the limit of strong interactions. In a parameter region between an antiferromagnetic insulator and a metal, a new phase appears to emerge which is both paramagnetic and has a charge gap [473]. DMRG studies have indicated that the spin liquid is chiral, and an analysis of effective spin interactions generated by virtual electron processes support this chiral spin liquid [93].

The existence of such a spin liquid phase near a metal-insulator transition motivates the development of variational wavefunctions, analogous to Gutzwiller-projected parton constructions, that can faithfully capture both the topological order of the spin liquid as well as the gapped charge excitations. A naive approach of softening the Gutzwiller projection is inadequate; as the parton mean-field ansatz may only realize certain lattice symmetries projectively, softening a Gutzwiller projection causes these projective symmetries to become broken. Some work was made in this direction [485] by replacing the Gutzwiller projection with singular Jastrow factors; however, this still leads to symmetry-broken phases. One of the goals of

Chapter 6 is to develop variational wavefunctions suitable for parameter regimes such as these.

### 1.2.5 KAGOME LATTICES

The kagome lattice Heisenberg antiferromagnet with nearest neighbor interactions is a strong candidate for a QSL, as it exhibits large geometric frustration and the classical antiferromagnet has extensive degeneracy. Upon promotion to a quantum model, this system is believed to support a quantum spin liquid without the need for additional longer-range Heisenberg interactions. Early DMRG works suggested a gapped  $\mathbb{Z}_2$  spin liquid [108, 223, 540]; however, subsequent DMRG simulations found signatures of gapless Dirac cones [183], which is consistent with variational parton studies [205, 206, 208, 209, 382].

## 1.3 DYNAMICS OF OPEN QUANTUM SYSTEMS

Theoretical models of quantum systems are generally taken to be closed - i.e, one defines a Hamiltonian for a system of interest which then evolves through unitary time evolution. However, quantum systems generically have some amount of coupling to their environment - for example, a cold atom system coupled to a reservoir. While the entire quantum system including the environment obeys the conventional unitary time evolution of quantum mechanics, one is often only interested in the physics of a subset of the total degrees of freedom. An effective description of only these degrees of freedom often goes by the name of *quantum master equations*. These describe the time evolution of the reduced density matrix  $\rho$  obtained by tracing out the environmental degrees of freedom. As  $\rho$  contains both quantum and classical superpositions of different states, interactions between a system and its environment is generically thought to lead to *decoherence*, where delicate quantum superpositions are obfuscated by classical correlations. Nevertheless, engineering these open system dynamics has turned out to be a prosperous field, with new applications such as the preparation of quantum states [31, 109, 259, 267, 509] including topologically-protected edge modes [110]. Chapters in this dissertation involve the study of such open systems, and we review some of the general principles below.

A generic operator  $\rho$  must satisfy several physical properties in order to be a legitimate density matrix of a quantum system. These conditions are

- Hermiticity,  $\rho^\dagger = \rho$
- $\text{Tr} [\rho] = 1$
- Positivity,  $\langle \phi | \rho | \phi \rangle$  for any state  $|\phi\rangle$

The most generic time evolution operator of a density matrix  $U_t : \rho(0) \rightarrow \rho(t)$  must take a valid density matrix  $\rho(0)$  to another valid density matrix  $\rho(t)$ . This implies that  $U_t$  must satisfy the mathematical properties of a *completely positive trace-preserving* (CPTP) map.

Generic CPTP maps are not required to be Markovian, i.e. they may not be expressible in the form of a local-in-time differential equation. Non-Markovian dynamics are a subject of intense study and can lead to many remarkable properties [105]. These include memory effects, where information about a quantum system can leak out into the environment but return back at a later time. However, the focus on decoherence in this dissertation will generally involve Markovian dynamics, where the relevant timescales of the environmental dynamics are sufficiently small relative to the timescales of our system, such that to a good approximation one can regard the environment at time  $t + dt$  as having “forgotten” about the state of the system at time  $t$ . The most general Markovian generator of CPTP maps is given by the Gorini–Kossakowski–Sudarshan–Lindblad equation [166, 288], or the Lindbladian,

$$\frac{d\rho}{dt} = -\frac{i}{\hbar}[H, \rho] + \sum_i \gamma_i \left( L_i \rho L_i^\dagger - \frac{1}{2} \{ L_i^\dagger L_i, \rho \} \right) \quad (1.9)$$

where  $L_i$  are a set of “quantum jump operators” describing the dissipative part of the dynamics and  $\gamma_i \geq 0$  govern the strength of the quantum jumps. The Lindbladian can be derived starting from the full unitary time evolution of a system and its environment and making approximations based on a hierarchy of relevant timescales in the system [71], but on very general grounds describes Markovian dynamics of CPTP maps.

In recent decades, there has been emerging interest in studying many-body quantum systems in a Lindblad framework. Analyses of the Lindbladian superoperator has revealed rich

symmetry-based classifications [237, 286, 405] and anomaly constraints on steady-state solutions [241].

A physically insightful interpretation of the Lindblad equation can be obtained through the quantum trajectory approach [116, 117]. The most agnostic statement way of framing this method is the observation of the mathematical equivalence between the Lindbladian time evolution defined in Eq. 1.9 on an initial state  $\rho_0 = |\psi\rangle\langle\psi|$  and stochastic time evolution governed by the following rules:

- An initial pure state  $|\psi\rangle$  is evolved in time according to an effective non-Hermitian Hamiltonian  $H_{\text{eff}} \equiv H - \frac{i}{2} \sum_i \gamma_i L_i^\dagger L_i$ .
- By choosing a uniformly-distributed random number  $0 \leq r \leq 1$ , a quantum jump occurs when  $|\langle\psi(t)|\psi(t)\rangle| = r$ . A jump operator  $L_i$  is selected according to the probability distribution  $p_i \sim \gamma_i \langle\psi(t)|L_i^\dagger L_i|\psi(t)\rangle$  and the operation  $|\psi\rangle \rightarrow L_i |\psi\rangle$  is performed. The state is renormalized after to have a magnitude of unity.
- Observables are calculated by averaging over all possible “quantum trajectories” obtained in this manner.

Practically this approach can be beneficial from the point of view of numerically simulating Lindbladian dynamics, as the full density matrix does not need to be manipulated. However, an interesting observation is that if such an interpretation had physical meaning, and if by performing many identical experiments one could “post-select” on a particular realization where no quantum jumps occur, then one would effectively generate non-unitary dynamics governed by the non-Hermitian Hamiltonian  $H_{\text{eff}}$ . There is substantial motivation for this - the study of non-Hermitian Hamiltonians has grown extensively over the past several decades, and many exotic phenomena have been found such as exceptional points [56, 184, 233], non-Hermitian topology [163, 240, 278, 284, 294, 444, 553, 569], and non-Hermitian skin effects [50, 129, 196, 239, 264, 274, 423, 530, 547]. Chapter studies the effects of exceptional points on topologically-ordered phases of matter. However, beyond the obvious desire to realize these properties in physical systems, even basic theoretical questions on how to interpret things like complex energy spectra and non-orthogonal eigenstates requires a grounding in some physical model, which a post-selection protocol such as this could provide.

Indeed, a physical interpretation of these quantum trajectories is possible. This interpretation requires knowledge of the full system, as generically the quantum jump operators  $L_i$  are not unique. An explicit derivation of the Lindblad equation starting from the full Hamiltonian of the system and environment can be followed to identify the modes of the environment that the quantum jump operators couple to, which can then be measured in an experiment [101]. This interpretation is especially clear in two-level systems coupled to a photonic cavity, where quantum jumps correspond to spontaneous emission events which can be detected by measuring the bath [101, 113, 117]. Note that sometimes measuring the environment is not necessary to perform this post-selection process; if quantum jumps correspond to irreversible particle loss, then one can post-select on the trajectory with no quantum jumps by simply measuring the total number of particles in the system at the end of the experiment.

## 1.4 DISORDER IN QUANTUM SYSTEMS

Disorder is a ubiquitous property in physical materials. In low dimensions, the interplay between disorder and quantum fluctuations can lead to new phenomena not present in clean systems. Several chapters in this dissertation are devoted to the study of such disordered systems. In this section, we review a few of the general concepts relevant to these works, including the replica trick, universal conductance fluctuations, spin glasses, and SYK models.

### 1.4.1 THE REPLICA METHOD

A central obstacle in the study of disordered systems is an accurate treatment of static, or *quenched*, disorder. In these scenarios, disorder is not a dynamical degree of freedom that can respond to electronic fluctuations in order to lower the energy of the system - it is a fixed background configuration. Calculating properties of individual disorder realizations is infeasible, and one must find a way to calculate disorder-averaged expectation values of observables while respecting their privileged position above the other degrees of freedom in the model. A number of techniques have been developed for this, including the Keldysh path integral, supersymmetric methods, and the replica trick, the latter of which will be employed in this dissertation and we review below.

The central dilemma of disorder is that observables are given by a ratio of path integrals,

$$\langle \mathcal{O}(x) \rangle_h = \frac{\int \mathcal{D}\phi \mathcal{O}(x) e^{iS[\phi,h]}}{\int \mathcal{D}\phi e^{iS[\phi,h]}} = \frac{\partial}{\partial J(x)} \ln Z[h, J] \Big|_{J=0} \quad (1.10)$$

where  $\mathcal{O}(x)$  is some function of the fields  $\phi$ ,  $h$  represents some disorder potential, and in the final line we have re-expressed the observable as a derivative of the path integral with  $\mathcal{O}$  coupled to some source field  $J$ . Naively integrating over  $h$  by adding it to the path integral, while computationally straightforward, is incorrect as both the numerator and denominator in the middle expression must correspond to the *same* disorder realization. In order to faithfully treat the disorder, we use the identity

$$\ln Z = \lim_{n \rightarrow 0} \frac{Z^n - 1}{n}. \quad (1.11)$$

The quantity  $Z^n$  consists of  $n$  “replicated” copies of the fields. In this replicated space, the disorder can be integrated out - doing this integral will generally couple different replicas. Observables are calculated as a function of  $n$  and the limit  $n \rightarrow 0$  is taken at the end of the calculation. While formally correct, analytically continuing to non-integer values of  $n$  and taking the  $n \rightarrow 0$  can be a delicate process.

#### 1.4.2 DISORDER IN WEAKLY-INTERACTING SYSTEMS

Some of the earliest progress in understanding the effects of disorder was in the context of weakly-interacting metallic systems, and in particular the implications of disorder on transport properties. An early breakthrough was the phenomena of Anderson localization [16], where it was observed that electronic wavefunctions in non-interacting systems are highly susceptible to localization in the presence of disorder, which leads to insulating behavior. This led to a scaling theory of localization [1], which demonstrated ... Interference between random quantum trajectories leads to diffusive particle-hole excitations known as diffusons as well as weak localization corrections to conductance [2, 18, 167].

A striking observation, which will be of relevance to Chapter 4, is the phenomenon of *universal conductance fluctuations* [10, 12, 272, 273]. Disordered metallic samples will display

random fluctuations in their measured conductance between different samples, or as a function of tuning a parameter such as chemical potential or applied magnetic field. Remarkably, the magnitude of these fluctuations are found to be  $\mathcal{O}(1)$  in units of the conductance quanta  $e^2/h$  and insensitive to microscopic details such as disorder strength; the coefficient only depends on a small number of details, such as the dimensionality of the sample and the number of channels. An intuitive picture of this phenomena as a function of magnetic field can be seen by noting that the Aharonov-Bohm effect leads to periodic oscillations in conductance due to quantum interference effects; the periodicity of these oscillations are dependent on the magnetic flux, and one may roughly think of an electron travelling diffusively through a conductor as forming many such loops with random areas. Indeed, the phenomena of universal conductance fluctuations is fundamentally a quantum interference effect, which suggests its independence on disorder strength. Early microscopic derivations [10, 12, 272, 273] eventually gave way to a statistical random matrix theory of quantum transport[29, 216]. The latter theory took a symmetry-based approach of modeling the scattering matrices of a conductor as random matrices, with the overall structure only determined by the symmetries of the system and the number of channels - the probability distribution of these matrices falls under the class of ensembles known as *circular ensembles*. This philosophy closely mirrors the original introduction of random matrix theory to physics by Wigner [521], who argued that the energy levels of complex nuclei can accurately be modeled by random Hamiltonians whose ensemble only contains information about the symmetry of the system. Remarkably, the magnitude of the fluctuations of quantities in these ensembles are universal and correctly reproduce expected results for universal conductance fluctuations. As these conductance fluctuations are indicative of coherent quasiparticle excitations, a motivating question of Chapter 6 is to understand conductance fluctuations in non-Fermi liquids where no well-defined quasiparticles exist.

#### 1.4.3 SPIN GLASSES

When strong interactions localize electrons, the residual degrees of freedom are encoded in the spin-1/2 moments of the electron, leading to models of quantum magnetism like the ones discussed in the context of spin liquids in Section. The presence of strong disorder in

the spin interactions can prevent the formation of conventional magnetic order, much like geometric frustration for spin liquids. In contrast to spin liquids, disordered interactions breaks translational symmetry, so LSM theorems do not constrain the possible ground states of these models. A possible phase unique to disordered systems is a *spin glass* phase, which is studied in more detail in Chapter 7. Roughly, one may think of a spin glass as a state where each individual spin points in a random direction, but not in an arbitrary manner - each spin is pinned by the disordered interactions in an attempt to satisfy all the competing random interactions. The large amount of randomness and frustration means that the low-energy landscape will consist of many distinct such configurations, each of which doing an approximately equally mediocre job at satisfying every interaction.

Spin glasses lead to ergodicity breaking; the complex energy landscape, with many local minima not related to each other by simple transformations, means that a particular realization of the system will get stuck in one minima and not explore the full range of states. Note that ergodicity breaking is a generic property of symmetry-breaking states; an Ising ferromagnet, for example, will break ergodicity by getting stuck in one of two possible ordered states. The unique property of spin glasses is to break ergodicity *without* developing any detectable form of long-range order. This can be quantified by the order parameters

$$m = \frac{1}{N} \left| \sum_i \overline{\langle \vec{S}_i \rangle} \right| \quad q = \frac{1}{N} \sum_i \overline{\langle \vec{S}_i \rangle \cdot \langle \vec{S}_i \rangle} \quad (1.12)$$

The quantity  $m$  measures ferromagnetic order, and is easily generalized to include other forms of magnetism such as antiferromagnetism. The quantity  $q$  is non-zero for a ferromagnetic phase, but is also non-vanishing for a spin glass phase, where each site picks out a definite random orientation. Calculation of these quantities within the replica formalism requires careful analysis of replica-off-diagonal saddle points, of which the Parisi solution [354] is the most well-known.

Both classical and quantum spin glasses have been extensively studied over the last several decades. Classical spin glasses probe static equilibrium properties of a classical partition function. Zero-temperature quantum spin glasses with quenched disorder, however, have properties distinct from their classical counterparts. One can immediately see from the respective

partition functions that a  $d$ -dimensional disordered quantum model differs dramatically from its  $d + 1$  classical analogy; the disorder in the former case is *static* in the temporal direction. Moreover, one can probe dynamical quantities in the quantum theory; with this perspective, one can naturally define an alternate probe of spin glass order in terms of the autocorrelation of a spin

$$\bar{q} = \lim_{\tau \rightarrow \infty} \frac{1}{N} \sum_i \overline{\langle \vec{S}_i(\tau) \cdot \vec{S}_i(0) \rangle}. \quad (1.13)$$

A non-zero  $\bar{q}$  indicates slow, glassy behavior - individual spins are frozen in time and retain memory of their initial state. Assuming factorization of the correlation function, one finds that the two definitions of spin glass order are equivalent, i.e.  $\bar{q} = q$  [388]. The presence of a non-zero  $\bar{q}$  implies a delta function peak in the dynamical structure factor,

$$S(\omega) \equiv \frac{1}{N} \sum_i \int d\tau \overline{\langle \vec{S}_i(\tau) \cdot \vec{S}_i(0) \rangle} = \bar{q}\delta(\omega) + \dots. \quad (1.14)$$

Measuring this delta function peak is the method used to detect spin glass order in Chapter 7.

#### 1.4.4 SYK MODELS AND DISORDER

A recent application of disorder over the last several decades has been to systematically construct classes of strongly-interacting models which retain exact solvability in the thermodynamic limit. The essential ingredients in these models tend to involve fully-disordered Hamiltonians with a large number of species of particles. Strong self-averaging leads to a reduction to a single species of fermion interacting self-consistently with a bath. For zero-dimensional systems with all-to-all interactions, this effective reduction to a single-site problem can be understood as a limit where dynamical mean-field theory (DMFT) becomes exact, although this analogy is less clear for finite-dimensional systems. The number of fermion flavors gives a large parameter which allows for a mean-field solution that is exact as the number of flavors goes to infinity.

A simple demonstration of this simplification is in the SYK model with Majorana fermions

[246, 303, 420]. The Hamiltonian of this model is

$$H = -\frac{1}{4!} \sum_{jklm} J_{jklm} \chi_j \chi_k \chi_l \chi_m \quad (1.15)$$

where  $\chi_j$ ,  $j = 1 \dots N$  are Majorana fermions and  $J_{jklm}$  is a real random variable with zero mean and variance  $\frac{3!J^2}{N^3}$ . Introducing  $M$  replicas and taking the disorder average, we obtain

$$\overline{Z^M} = \int \mathcal{D}\chi \exp \left[ -\frac{1}{2} \sum_{\alpha,j} \int d\tau \chi_j^\alpha \partial_\tau \chi_j^\alpha + \frac{NJ^2}{8} \sum_{\alpha,\beta} \int \int d\tau d\tau' \left( \frac{1}{N} \sum_j \chi_j^\alpha(\tau) \chi_j^\beta(\tau') \right)^4 \right]. \quad (1.16)$$

Here, we see a massive simplification, as the term in parenthesis is a local quantity. Introducing the field  $G_{\alpha\beta}(\tau, \tau') \equiv \frac{1}{N} \sum_j \chi_j^\alpha(\tau) \chi_j^\beta(\tau')$  and a Lagrange multiplier  $\Sigma_{\alpha\beta}(\tau, \tau')$  to enforce the equality, we can integrate out the fermions and obtain the action

$$\begin{aligned} \overline{Z^M} &= \int \mathcal{D}\Sigma \mathcal{D}G \exp(-I[\Sigma, G]) \\ I[\Sigma, G] &= N \left( -\ln \text{Pf}(-\partial_\tau - \Sigma) + \frac{1}{2} \sum_{\alpha,\beta} \int d\tau d\tau' \left( \Sigma_{\alpha\beta}(\tau, \tau') G_{\alpha\beta}(\tau, \tau') - \frac{J^2}{4} G_{\alpha\beta}(\tau, \tau')^4 \right) \right) \end{aligned} \quad (1.17)$$

Due to the explicit factor of  $N$  in the action, the saddle-point of the action as a function of  $(\Sigma, G)$  is exact in the large- $N$  limit. Assuming a replica-diagonal ansatz, i.e.  $G_{\alpha\beta} = \Sigma_{\alpha\beta} = 0$  for  $\alpha \neq \beta$  and  $G_{\alpha\alpha} \equiv G$ ,  $\Sigma_{\alpha\alpha} \equiv \Sigma$ , the saddle-point solutions can be solved numerically, although many of the remarkable properties of this model are obtainable analytically by working in the conformal limit ( $\beta J \gg 1$ ), where the  $\partial_\tau$  term can be neglected to leading order.

This method of using self-averaging properties of disorder to obtain an exact large- $N$  saddle point is quite robust, and has been used to great effect in studies of non-Fermi liquids [85] and strange metals [356]. However, note that oftentimes in these models, the disorder is only a means to an end and does not play any role beyond generating a set of exact Schwinger-Dyson equations. This is related to the observation that SYK models are often strongly self-averaging, where properties of individual disorder realizations quickly approach the ensemble average in the thermodynamic limit. In fact, disorder-free SYK models exist [523] which bear

close resemblance to tensor models [47] and can be used to recover replica-diagonal actions of the form in Eq. 1.17. However, there are situations where the random nature of the model plays an essential role. Detecting spin glass instabilities in these disordered models requires careful consideration of replica-off-diagonal fluctuations [86, 484]. Localization effects due to randomness can have important consequences for transport in SYK-like theories of strange metals [357]. Finally, which is the main focus of Chapter 4, statistical fluctuations of observables in SYK models display distinctive behavior as compared to weakly-interacting disordered systems. These fluctuations require consideration of replica-off-diagonal fluctuations, albeit starting from a replica-diagonal saddle point.

## 1.5 NUMERICAL METHODS FOR MANY-BODY SYSTEMS

A natural application of the rapid growth in computational power and resources is to analyze these many-body states. However, brute-force applications of these tools - for example, by evaluating a path integral via numerical integration, or by directly diagonalizing the many-body Hamiltonian when the Hilbert space is finite - are plagued by the *curse of dimensionality*, where the computational cost of these problems grows exponentially with the number of particles. For a system of particles which each have a finite Hilbert space of dimension  $D$ , this scaling can be seen explicitly in virtue of the many-body Hilbert space of  $N$  particles being a tensor product of  $N$  single-particle Hilbert spaces and whose resulting dimension is  $N^d$ .

As a consequence, computational many-body physics has grown into an extremely rich field. Dozens of distinct approaches to tackling the many-body problem have been developed, each with their own set of approximations and strengths. Several chapters in this dissertation focus on such computational methods. Here, we provide a broad but non-exhaustive overview of some of the modern numerical methods which are either used explicitly in this dissertation or whose results by other researchers play a central role in parts of this dissertation.

It is important to note that numerical methods will look quite different depending on the level of abstraction (or to be more quantitative, on the energy scale) that one is working with. Despite a shared goal of predicting the properties of complex quantum systems, ab

initio methods of deriving the band structure of a complex crystal differ substantially from quantum chemistry modeling of molecule binding energies, with both being distinct from the more abstracted problem of finding the ground state of a model many-body Hamiltonian. Of course, each of these methods can benefit substantially from advances in neighboring fields, and accurate predictions at all energy scales is essential for the broader goal of accurately studying strongly-interacting materials.

### 1.5.1 EXACT DIAGONALIZATION

Exact diagonalization is the most straightforward method of studying a many-body system with a finite Hilbert space. The many-body Hamiltonian is represented by a matrix exponentially large in the number of particles, and this matrix is diagonalized using standard numerical linear algebra routines. The performance of this method can be improved primarily through two methods. The first is through *symmetry* - if a Hamiltonian possesses some symmetry, it will be block diagonal in a symmetric basis of states. Diagonalizing the Hamiltonian only within a given symmetry sector reduces the size of the matrices to be diagonalized, although generically the size will often still scale exponentially in the number of particles. The second technique, which is appropriate if one only cares about properties of eigenvectors near the edge of the spectrum, is to use iterative method such as the Lanczos algorithm to extract low-lying eigenvalues. These iterative methods have the advantage that the full Hamiltonian does not need to be initialized in memory - one only needs to be able to perform matrix-vector multiplication with the Hamiltonian, which can be accomplished by memory-efficient functions  $f : \vec{x} \rightarrow \vec{y}$  which mimic these multiplications.

Despite its inefficiency, exact diagonalization is an essential technique in many-body physics. Practically, it is quite simple, with essentially the only nuances in interpreting the results coming from finite-size effects. It provides a benchmark for small system sizes with which approximate methods can compare to. Although it is rare to face a problem where obtaining the full spectrum explicitly is necessary, such cases do exist, such as statistical properties of the many-body spectrum in disordered systems [173] as well as recent applications of “fuzzy sphere” regularization [568, 574] where the full spectrum can give insight into the operator content of a conformal field theory.

Two recent algorithmic developments are worth mentioning, as they appear prominently in Chapter 7. The first involves the evaluation of finite-temperature quantities using the Lanczos algorithm, where the notion of *thermal pure quantum states* [469, 470] is employed. A more detailed analysis of this is provided in Appendix E. The second development pertains to efficient parallelization of the Lanczos algorithm across distributed computing clusters, as developed in [519]. Modern supercomputing clusters consist of large numbers of “nodes,” each with its own CPU and memory, with moderately fast communication between the nodes. As a result, the computation tasks that make the most use of these resources are not “embarrassingly parallelizable” tasks where computation consists of independent code running on many CPUs in parallel - for example, Monte Carlo simulations with different random seeds - with the results combined at the end with a minor post-processing step. Nor are tasks with a high amount of communication between different nodes appropriate, as memory transfer between nodes is still orders of magnitude slower than intra-node communication and can easily become a bottleneck. The best algorithms for these clusters make moderate use of communication between nodes and appropriately “balances” the CPU usage between cores. To implement matrix-vector multiplication for the Lanczos algorithm across multiple nodes, each node stores some component of the vector. Matrix multiplication is split up into two steps - multiplication within a node that does not require communication between nodes, and multiplication that does require communication. Organizing principles such as locality of the Hamiltonian can be employed such that an optimal basis is chosen that minimizes communication between nodes; however, some portion of the basis set is kept randomized in order to ensure that the computational load is evenly distributed.

### 1.5.2 TENSOR NETWORK METHODS

A class of numerical methods for studying many-body Hamiltonians take a variational approach. Given a Hamiltonian, one constructs a class of variational wavefunctions parameterized by a set of parameters, and the energy of the wavefunction is minimized within this class of variational wavefunctions. The essence of the problem is to construct adequately expressible variational wavefunctions which both have a small number of parameters and for which observables can be efficiently calculated.

Matrix product states [253] (MPSs), and tensor networks more broadly, have established themselves as highly versatile and efficient wavefunctions. The simplest example is the wavefunction of an  $N$ -site chain of spin-1/2 qubits, for which the coefficients of the MPS wavefunction are given as

$$\langle s_1, s_2, \dots, s_N | \psi \rangle \equiv \text{Tr} [A^{s_1} A^{s_2} \dots A^{s_N}] \quad (1.18)$$

where  $s_i \in \{0, 1\}$  is the local basis of states. The wavefunction is determined by  $N d \times \chi \times \chi$  tensors  $A^{s_i}$ , where  $d = 2$  is the local Hilbert space dimension and  $\chi$  is referred to as the bond dimension of the MPS. Any arbitrary state can be represented for sufficiently large bond dimension; however, the power of MPS is that many states can be described to good accuracy with computationally-tractable bond dimension size. This ties in closely with the concept of entanglement; it has been shown that the ground state of any gapped 1D Hamiltonian can be accurately represented by an MPS with finite bond dimension [493], which is connected to the fact that both exhibit area law entanglement entropy. Correlation functions of MPS states are therefore generically exponentially decaying, although algebraic decay can be approximated by taking a large enough bond dimension.

MPSs are highly efficient to work with - evaluating the expectation value of operators can be performed using matrix product operators (MPOs) and without the need for Monte Carlo sampling like many other variational methods. Moreover, the density matrix renormalization group [514] (DMRG) is a highly efficient algorithm for optimizing an MPS for a given Hamiltonian.

MPSs fall into a broader class of *tensor network* states, which can be used as variational wavefunctions for a wide class of quantum systems. The practical usage of any given tensor network depends on the efficiency with which one can evaluate (or “contract”) the tensor network. MPS states are very powerful in this regard, as the evaluation of observables can be done with a complexity that is polynomial in  $d$ ,  $N$ , and  $\chi$  (the precise details of the complexity are dependent on the problem at hand). For higher-dimensional generalizations, performing efficient contractions is the primary bottleneck in implementing tensor network states.

While MPS states are able to capture gapped 1D states to extremely high accuracy, the ability to describe both gapless and higher-dimensional states are more non-trivial. 1D gapless

states pose less of a difficulty, as careful extrapolation of observables as a function of bond dimension allows for the extraction of power law correlation functions. For higher-dimensional systems - in particular, the 2D frustrated antiferromagnets, which are a focus of much of this thesis - there are two main approaches. The first is to adapt a “quasi-1D” geometry, where an MPS is wrapped around a cylinder of radius  $N_x$  and length  $N_y$ , with  $N_y \gg N_x$ . The second is to use a non-MPS tensor network, with projected entangled pair states [492] (PEPs) being the most common tensor network for 2D systems. Both these approaches are used in studies of frustrated magnetism in two dimensions, and results from these studies on square lattices is leveraged in Chapter 2 where we study phase transitions of a putative spin liquid phase appearing in the square lattice antiferromagnet.

### 1.5.3 DYNAMICAL MEAN-FIELD THEORY

Dynamical mean-field theory (DMFT) [154] provides complimentary results to the models of study in Chapter 7. Formally, DMFT can be viewed as an improvement on the starting point of free electrons by including an arbitrary, but *local*, electron self-energy. Assuming all interactions in the problem are on-site, the problem is effectively reduced down to a single site model with all the interactions of the original model, but coupled to a free bath of electrons. This closely mirrors the philosophy of standard mean-field theory calculations, where a single site problem is solved in the presence of an effective potential generated by all the other sites. An important self-consistency loop is imposed by insuring that the local Green’s function of the lattice - which contains information about the band structure and dispersion - agrees with the Green’s function of the single site impurity model. The coupling of the local impurity to the bath is tuned until this self-consistence is reached.

Due to the retarded interactions with the bath, numerically solving the impurity model is still a non-trivial quantum problem. However, the fact that many distinct systems reduce down to solving this impurity problem in the DMFT approximation has motivated substantial development of numerical methods for tackling this problem. Methods range from exact diagonalization, functional renormalization group, quantum Monte Carlo, and tensor network methods. The fact that the impurity model must be solved not just once, but repeatedly until convergence is reached, makes the problem highly non-trivial.

A noteworthy example of when a many-body problem often reduces down exactly to an effective impurity model is when interactions between electrons are disordered and all-to-all. A demonstration of this simplification was already shown in the discussion of SYK models in Section 1.4.4. A relevant example of work where impurity solvers are used extensively is in [73, 118], which focused on a model of spinful electrons

$$H = \sum_{ij} t_{ij} c_{i\sigma}^\dagger c_{j\sigma} + U \sum_i n_{i\uparrow} n_{i\downarrow} + \sum_{ij} J_{ij} \mathbf{S}_i \cdot \mathbf{S}_j \quad (1.19)$$

where the hoppings  $t_{ij}$  and Heisenberg interactions  $J_{ij}$  are random and all-to-all. By employing the replica formalism to integrate out the disorder and assuming a replica-diagonal ansatz, the model reduces to an effective single-site problem whose action is

$$S = -\beta \sum_{n,\sigma} c_\sigma^\dagger (i\omega_n + \mu - \Delta(i\omega_n)) c_\sigma + U \int_0^\beta d\tau n_{\uparrow} n_{\downarrow} - \frac{J^2}{2} \int_0^\beta d\tau d\tau' Q(\tau - \tau') \mathbf{S}(\tau) \cdot \mathbf{S}(\tau') \quad (1.20)$$

where the hybridization function  $\Delta$  and spin-spin retarded interaction  $Q$  are determined self-consistently by

$$\Delta(\tau) = -t^2 \langle T c_\sigma(\tau) c_\sigma^\dagger(0) \rangle, \quad Q(\tau - \tau') = \frac{1}{3} \langle \mathbf{S}(\tau) \cdot \mathbf{S}(\tau') \rangle. \quad (1.21)$$

which can be solved using the CT-INT algorithm [401]. In certain scenarios, as shown in Section 1.4.4, the resulting impurity model simplifies dramatically can be solved through self-consistently solving a set of coupled Schwinger-Dyson equations for the impurity. Obtaining such a justified “classical” limit requires a large parameter, such as the system size, to appear as a coefficient in front of the impurity action. This simplification tends to happen for Sachdev-Ye-Kitaev models [168]. A version of this model for complex spinless fermions, of relevance to Chapter 6, is given by the Hamiltonian

$$H = \sum_{ij} t_{ij} c_i^\dagger c_j + \sum_{ijkl} J_{ijkl} c_i^\dagger c_j^\dagger c_k c_l. \quad (1.22)$$

For Eq. 1.19, this simplification does not happen due to the random Heisenberg interaction; however, generalizing the SU(2) spin interactions to SU( $M$ ) admits a large- $N, M$  expansion.

It is worth noting that beyond lattice models, DMFT has found considerable application in *ab initio* electronic structure calculations by supplementing density functional theory in order to account for strong electronic correlations and capture phenomena such as metal-insulator transitions [257].

#### 1.5.4 VARIATIONAL MONTE CARLO

The term “variational Monte Carlo” (VMC) is quite vague; by definition, it refers to a general class of variational wavefunctions whose properties can only be inferred through some sort of stochastic Monte Carlo sampling. This can encompass quite sophisticated wavefunctions such as neural quantum states, discussed in the following subsection. Here, we will outline the general principles and discuss some simple examples of VMC.

A general input to a VMC calculation is a variational wavefunction  $|\psi_\alpha\rangle$  which depends on a set of parameters  $\alpha$ . We assume that the state  $|\psi_\alpha\rangle$  is too complex to work with directly, but importantly, is simple enough that the quantities  $\langle a|\psi_\alpha\rangle$  can be computed for a complete set of many-body states  $\langle a|$ , which we will generally take to be in a real space basis. If this is true, then the expectation value of an observable  $\mathcal{O}$  can be written in the form

$$\frac{\langle\psi_\alpha|\mathcal{O}|\psi_\alpha\rangle}{\langle\psi_\alpha|\psi_\alpha\rangle} = \frac{\sum_a |\langle\psi_\alpha|a\rangle|^2 \frac{\langle a|\mathcal{O}|\psi_\alpha\rangle}{\langle a|\psi_\alpha\rangle}}{\sum_a |\langle\psi_\alpha|a\rangle|^2} \equiv \frac{\sum_a p(a)\mathcal{O}(a)}{\sum_a p(a)}. \quad (1.23)$$

Hence, evaluation of the observable  $\mathcal{O}$  over the exponentially-large many-body Hilbert space can be performed efficiently using Monte Carlo sampling of the local expectation value  $\mathcal{O}(a)$  guided by the positive-definite probability distribution  $p(a)$ . Computation of the local observable  $\mathcal{O}(a)$  is possible when  $\langle a|\mathcal{O} = \sum_b \langle b|\mathcal{O}_{ab}$  for a relatively small (polynomial in the system size) number of new many-body states  $\langle b|$ .

The most relevant VMC calculations to this dissertation are for quantum spin liquid states, where the variational wavefunctions  $|\psi_\alpha\rangle$  are Gutzwiller-projected fermionic spinon wavefunctions. To be more precise, one constructs a mean-field ansatz of fermionic spinons using the techniques outlined in Section 1.2.1. Starting from this state  $|\psi_0\rangle$ , one applies a Gutzwiller projection  $\mathcal{P}_G \equiv \prod_i (1 - n_{i\uparrow}n_{i\downarrow})$ , which removes all doubly-occupied sites and projects the wavefunction in the enlarged Hilbert space of fermionic spinons to the physical space of spin-

1/2 moments. Mathematically, this Gutzwiller projection is equivalent to integrating over the gauge field in the limit where there is no action for the gauge field. This final wavefunction,  $|\psi\rangle = \mathcal{P}_G |\psi_0\rangle$ , is amenable to VMC calculations, as we have the simple rule

$$\langle a|\psi\rangle = \begin{cases} \langle a|\psi_0\rangle & \text{no double occupancy in } a \\ 0 & \text{otherwise} \end{cases} \quad (1.24)$$

The overlap  $\langle a|\psi_0\rangle$  can be computed efficiently because they are both non-interacting states with the overlap determined by a determinant calculation with polynomial complexity.

### 1.5.5 NEURAL QUANTUM STATES

The advent of machine learning and neural networks has had wide-ranging impacts in theoretical physics. Neural quantum states [70] (NQSSs) are one such application, which comes from a remarkably simple application of a neural network. The simplest way of thinking about a neural network, which is sure to offend any computer scientist, is that it is nothing more than a highly-expressible and efficiently-trainable function of many variables. Given our previous discussion of variational methods, it is easy to see how such functions can be extremely powerful.

NQSSs have found much application in the study of frustrated quantum spin models. The bosonic degrees of freedom with a small local Hilbert space dimension make NQSSs well-equipped to describe wavefunctions of such models. Abstractly, the NQS is simply a function  $f : \{0, 1\}^N \rightarrow \mathbb{C}$ , which for a configuration of  $N$  spins  $\{\sigma_i\}$  returns the wavefunction  $\psi(\{\sigma_i\})$ . The performance of this function is heavily dependent on the choice of neural network architecture. A wide variety of networks have been studied, including restricted Boltzmann machines [70], feed forward neural networks [64], convolutional neural networks [281], and transformer networks [496]. Physics-informed considerations in neural network design have led to convolutional techniques which respect lattice translational symmetries [64], and improved architectures which explicitly respect all lattice symmetries [398]. NQS wavefunctions have obtained the lowest energies to date on frustrated square lattices [395] and triangular lattices [398], although it should be stressed that the energy difference between competing

methods such as DMRG is extremely small - for the frustrated square lattice, the relative error on DMRG as compared to NQS is less than 1%. Broader considerations regarding the applicability of NQS wavefunctions include the scalability to larger systems as well as the difficulty in optimization; unlike DMRG, estimating the energy of a NQS involves relatively slow Monte Carlo sampling, and the number of variational parameters can approach  $10^6$ .

A major obstacle with neural quantum states is the representation of fermionic wavefunctions, as the antisymmetry of the fermionic wavefunction must be respected. Substantial progress on this has been made in recent years through a number of methods. These methods often take the approach of using an explicitly antisymmetric parameterization of a fermionic wavefunction, such as a Slater determinant state, and enhancing its expressivity through neural network modifications built on top of this wavefunction, such as using a neural network to parameterize backflow corrections [297], or by projecting a Slater determinant in an enlarged Hilbert space [150, 397].

### 1.5.6 STOCHASTIC SERIES EXPANSION

The stochastic series expansion (SSE) differs from the previous numerical methods described, in that this method is primarily applicable to bosonic models with finite local Hilbert space dimension. This includes quantum spin models - a central theme of this dissertation - as well as models of hardcore bosons. This method involves Monte Carlo sampling and hence may exhibit a sign problem; however, for models where a sign problem is absent, this method is often the most powerful option as it avoids the Trotterization errors present in alternate stochastic formulations of the path integral.

The approach of SSE consists of a stochastic evaluation of the partition function through a high-temperature expansion. The quantum partition function,  $Z = \text{Tr}[e^{-\beta H}]$ , can be expanded in powers of  $\beta$  to obtain the expression

$$Z = \sum_{n=0}^{\infty} \frac{\beta^n}{n!} \text{Tr}[H^n] \tag{1.25}$$

Two additional steps are required in order to put the partition function in a form adequate for SSE. First, the trace is replaced by a sum over a complete set of states  $|\alpha\rangle$ . Second,

the Hamiltonian must be decomposed in a fashion  $H = \sum_b H_b$  such that generic expressions of the form  $\langle \alpha | H_{b_1} H_{b_2} \dots H_{b_n} | \alpha \rangle$  can be efficiently evaluated. A common way of satisfying this is to ensure  $H_b |\alpha\rangle \propto |\alpha'\rangle$ , i.e. each basis state gets mapped to a single new basis state, such that  $\langle \alpha | H_{b_1} H_{b_2} \dots H_{b_n} | \alpha \rangle$  is only non-zero if the successive applications of  $H_{b_i}$  map  $|\alpha\rangle$  back onto itself. Provided these quantities are real and positive, the partition function can be represented as a stochastic sum over configurations  $\{n, \alpha, b_1, b_2 \dots b_n\}$ .

The nature of the sign problem in SSE is less readily apparent than in DQMC, the absence of which in the latter can often be tied to a particular symmetry. For quantum spin systems, an important factor is *frustration*. The difference between a ferromagnetic and an antiferromagnetic Heisenberg model with nearest-neighbor interactions is just the overall sign of the Hamiltonian. As it is powers of this Hamiltonian that appear in the SSE, one can show that a ferromagnetic Heisenberg model does not have a sign problem with SSE, whereas an antiferromagnetic one generically does. This is not the full story, however. For *bipartite* lattices, one can show that negative signs always appear in pairs for non-vanishing values of  $\langle \alpha | H_{b_1} H_{b_2} \dots H_{b_n} | \alpha \rangle$ , and hence sign-problem-free SSE simulations are permitted. It is possible to add in non-trivial interactions on top of nearest-neighbor antiferromagnetic couplings which preserve the positivity of the weights - in particular, a class of models known as  $J - Q$  models on the square lattice support transitions between Néel antiferromagnetism and valence bond solid order. The lack of large-scale sign-problem-free Monte Carlo simulations for antiferromagnets on non-bipartite lattices such as the triangular lattice is a motivation for the results in Chapter 3, where an effective sign-problem-free model is constructed with partons (sign-problem-free models on non-bipartite lattices have, however, been studied for integer spin systems where the  $SU(N)$  spin rotation symmetry is replaced with  $SO(N)$  [234]).

*Zeus, the ruler of the Olympian gods, often conceals his identity by changing himself into different forms. Strongly interacting conformal field theories (CFTs), which underlie many different states of matter, can sometimes also be described by Lagrangians with very different forms.*

Cenke Xu

# 2

## Deconfined criticality and a gapless $\mathbb{Z}_2$ spin liquid in the square lattice antiferromagnet

### 2.1 INTRODUCTION

Antiferromagnetism on the square lattice became a topic of intense study soon after the discovery of high temperature superconductivity in the cuprates, and it continues to be a wellspring of interesting experimental and theoretical physics. It was established early on that the insulating antiferromagnet with  $S = 1/2$  spins on each site, and only nearest neighbor antiferromagnetic exchange interactions ( $J_1$ ) has long-range Néel order in its ground state *i.e.* global SU(2) spin rotation symmetry was broken with the spin expectation value  $\langle \mathbf{S}_i \rangle = \eta_i \mathbf{N}_0$  where  $\mathbf{S}_i$  is the spin operator on site  $i$ ,  $\eta_i = \pm 1$  on the two checkerboard sublattices, and  $\mathbf{N}_0$  is the antiferromagnetic moment. Much attention has since been lavished on the insulating  $J_1$ - $J_2$  antiferromagnet [75, 98, 153, 204, 391, 416], which also has a second-neighbor antiferromagnetic exchange interaction  $J_2$ . The key questions are the nature of the quantum phases of the model, and of the quantum phase transitions between them, as a function of increasing  $J_2/J_1$  after the Néel order vanishes at a critical value of  $J_2/J_1$ . These questions are also the focus of our attention here.

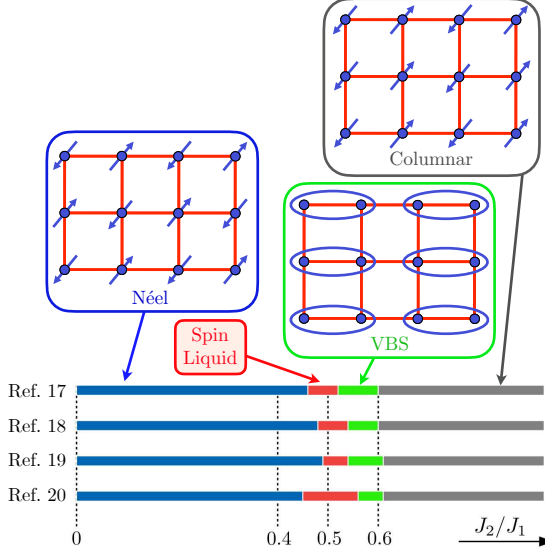


Figure 2.1: Phases of the  $S = 1/2$   $J_1$ - $J_2$  antiferromagnet on the square lattice, from the numerical results of Refs. [140, 290, 342, 505], all of which agree that the spin liquid is gapless. Each ellipse in the valence bond solid (VBS) represents a singlet pair of electrons. Lower part of figure adapted from Ref. [32].

An early proposal [389–391, 416] was that there was a direct transition from the Néel state to a valence bond solid (VBS) (see Fig. 2.1) which restores spin rotation symmetry but breaks lattice symmetries (followed by a first order transition at larger  $J_2/J_1$  to a ‘columnar’ state which breaks spin rotation symmetry, and which we do not address in the present paper). A theory of ‘deconfined criticality’ was developed [328, 434, 439] showing that a continuous Néel-VBS transition was possible, even though it was not allowed in the Landau-Ginzburg-Wilson framework because distinct symmetries were broken in the two phases. Evidence has since accumulated for the presence of a VBS phase in the  $J_1$ - $J_2$  model, but the nature of the Néel-VBS transition in this model has remained a question of significant debate. However, in the past year, a consensus appears to have emerged [32] among the groups investigating this question by different numerical methods [140, 290, 342, 505], and is summarized in Fig. 2.1: there is a narrow window with a gapless spin liquid phase between the Néel and VBS states. This gapless phase has been identified [68, 139, 140, 194, 212] as a  $\mathbb{Z}_2$  spin liquid [244, 391, 416, 510] with gapless, fermionic,  $S = 1/2$  spinon excitations with a Dirac-like dispersion [212, 245, 435, 437, 511], labeled Z2Azz13 in Wen’s classification [511].

The starting point of our analysis is the fermionic spinon dual [459, 462, 480, 500] of the

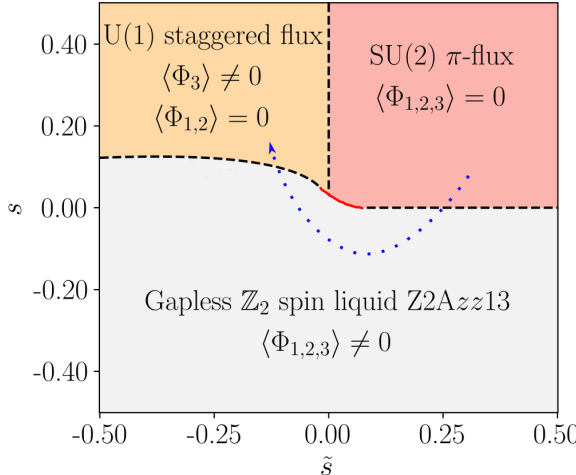


Figure 2.2: Mean field phase diagram of our low energy theory obtained by minimization of the Higgs potential in Eq. (2.39). Dashed (solid red) lines indicate second (first) order transitions in mean field theory. We assume the  $SU(2)$   $\pi$ -flux gauge theory confines to a Néel state, the  $U(1)$  staggered flux gauge theory confines to a VBS state, except at their deconfined critical boundaries to Wen’s stable, gapless  $\mathbb{Z}_2$  spin liquid  $Z2Azz13$ . The dotted blue line indicates a possible trajectory of the square lattice antiferromagnet with increasing  $J_2/J_1$ . However, we cannot rule out interchanging the assignments of the confining states between the  $SU(2)$  and  $U(1)$  spin liquids. The mean-field analysis was performed with  $w = u = 1$ ,  $v = -1$ ,  $\tilde{u} = 0.75$ , and  $v_4 = 0.5$  in Eq. (2.39). We use the ansatz  $\Phi_1^a = c_1 \delta_{ax}$ ,  $\Phi_2^a = c_1 \delta_{ay}$ , and  $\Phi_3^a = c_2 \delta_{az}$ , so the terms in  $V(\Phi)$  proportional to  $v_1, v_3$  are automatically zero.

bosonic spinon  $CP^1$  model used earlier [389, 390, 434, 439] to describe the Néel-VBS transition. This fermionic dual is a relativistic  $SU(2)$  gauge theory of 2 flavors of 2-component, massless Dirac fermions carrying fundamental gauge charges: this formulation is preferred over the bosonic spinons because the massless Dirac fermions connect naturally to the gapless fermionic spinons in the  $\mathbb{Z}_2$  spin liquid. Recent studies [182, 301, 332, 506] have indicated that the 2 fermion flavor  $SU(2)$  gauge theory does not ultimately describe a conformal field theory needed for Néel-VBS criticality, but exhibits a ‘pseudocriticality’ associated with a proximate fixed point at complex coupling [164, 165, 299, 500]. Ref. [480] used connections to bosonic spinon theories to argue that the 2 fermion flavor  $SU(2)$  gauge theory was ultimately unstable to confinement and symmetry breaking leading to the appearance of Néel order. We assume this is the case, and we can then describe the transition to the  $\mathbb{Z}_2$  spin liquid by the condensation of Higgs fields which break the  $SU(2)$  gauge symmetry down to  $\mathbb{Z}_2$ : see Fig. 2.2. The Néel- $\mathbb{Z}_2$  spin liquid transition is a confinement-Higgs transition, and the critical theory is proposed

to be a 2-flavor SU(2) gauge theory with critical Higgs fields [480]. We note that a similar critical theory was proposed in Ref. [151] for a continuous transition from the Néel state to a different gapless state with a  $\mathbb{Z}_2$  gauge field (the ‘orthogonal semi-metal’), and this scenario was supported there by quantum Monte Carlo simulations. Evidently, it is possible that critical Higgs fields can stabilize a scale-invariant critical point of the 2-flavor SU(2) gauge theory at the boundary of a Higgs phase where the SU(2) gauge symmetry is broken down to  $\mathbb{Z}_2$ .

As we will see below, an important difference between our critical Higgs SU(2) gauge theory and that of Ref. [151] is that our theory does not preserve Lorentz invariance. The Lorentz symmetry is broken by the Yukawa couplings between the Higgs fields and fermions. The Yukawa couplings also do not preserve the SO(5) flavor symmetry of the SU(2) gauge theory with only fermionic matter; this symmetry rotates between the Néel and VBS states. Both these features have important consequences for the Néel- $\mathbb{Z}_2$  spin liquid critical point, and lead to predictions described below which can be tested by numerical studies.

In earlier work, Ran and Wen [381, 384] had considered the 2-flavor SU(2) gauge theory as the description of an extended gapless phase on the square lattice—also called the  $\pi$ -flux phase [3]. They proposed a theory for a transition from the  $\pi$ -flux phase to the Z2Azz13 spin liquid by the condensation of a pair of adjoint Higgs fields, which we denote  $\vec{\Phi}_{1,2}$  (the vector symbol implies gauge SU(2) adjoint index). In light of our arguments above on the confining instability of the  $\pi$ -flux phase to the Néel state, the critical Higgs theory of Ran and Wen [381, 384] can serve as the deconfined critical theory for the Néel to Z2Azz13 spin liquid transition. However, as we shall see in Section 2.4, additional ‘dangerously irrelevant’ terms are needed to fully define the critical theory in a  $1/N_f$  expansion, and these contribute a logarithm-squared renormalization.

The mean-field phase diagram of the SU(2) gauge theory with adjoint Higgs fields describing the  $\pi$ -flux to Z2Azz13 transition turns out to naturally acquire an additional phase, as explained in Section 2.3.4—this is the U(1) staggered flux spin liquid [3]. We show that the adjoint Higgs field

$$\vec{\Phi}_3 \sim \vec{\Phi}_1 \times \vec{\Phi}_2 \quad (2.1)$$

(see Eq. (2.43)) is precisely that required to go from the  $SU(2)$   $\pi$ -flux phase to the  $U(1)$  staggered flux phase. Specifically, starting from the  $\pi$ -flux phase, if both  $\vec{\Phi}_{1,2}$  condense with  $\langle \vec{\Phi}_1 \rangle \times \langle \vec{\Phi}_2 \rangle \neq 0$ , we obtain the gapless  $\mathbb{Z}_2$  spin liquid (the simultaneous condensation of  $\vec{\Phi}_1$  and  $\vec{\Phi}_2$  does not require fine tuning because of symmetry constraints that we will describe). On the other hand, Eq. (2.1) implies that if only the composite field  $\vec{\Phi}_1 \times \vec{\Phi}_2$  condenses, but the individual fields  $\vec{\Phi}_{1,2}$  do not, then the  $\pi$ -flux phase turns into the  $U(1)$  staggered flux phase. Speaking imprecisely, starting from the parent  $\pi$ -flux phase, the Higgs condensate for the gapless  $\mathbb{Z}_2$  spin liquid is the ‘square root’ of the Higgs condensate for the staggered flux phase. (Let us also note that Song *et al.* [459] proposed that a trivial monopole would drive the staggered flux state into the  $\pi$ -flux state: so the Higgs field  $\vec{\Phi}_3$  can be viewed as a ‘dual’ description of the trivial monopole, and induces a transition in the opposite direction. Four-fermion terms have also been proposed as a route to reducing the emergent symmetry of the staggered flux state to that of the  $\pi$ -flux state [531].) The phase diagram of the Higgs fields  $\vec{\Phi}_{1,2,3}$  is computed in Section 2.3.4 and shown in Fig. 2.2. We propose here that the transition from the gapless  $\mathbb{Z}_2$  spin liquid to the VBS state is described by the deconfined critical theory appearing at the onset of the  $U(1)$  spin liquid. Other works [437, 459, 462] have discussed the possible instability of this  $U(1)$  spin liquid to either Néel or VBS order via monopole proliferation. The critical  $U(1)$  gauge theory is described briefly in Section 2.5, where we show that it does *not* contain the dangerously irrelevant terms found in the critical  $SU(2)$  theory.

We will review the derivation of the Ran-Wen theory, and discuss its symmetry properties in some detail in Section 2.2 and Appendix A.1. A continuum  $SU(2)$  gauge theory coupled to 3 adjoint Higgs fields and gapless Majorana fermions will be obtained in Section 2.3. The critical  $SU(2)$  gauge theory for the onset of the gapless  $\mathbb{Z}_2$  spin liquid phase from the  $\pi$ -flux phase will be presented in Section 2.4, along with an analysis of its properties in a  $1/N_f$  expansion. The critical  $U(1)$  gauge theory for the onset of the same gapless  $\mathbb{Z}_2$  spin liquid from the staggered flux phase appears in Section 2.5.

## 2.2 GAPLESS $\mathbb{Z}_2$ SPIN LIQUID

The fermionic spinon theory of  $\mathbb{Z}_2$  spin liquids proceeds by re-expressing the spin operators in terms of spinons  $f_{i\alpha}$ ,  $\alpha = \uparrow, \downarrow$  at site  $\mathbf{i} = (i_x, i_y)$  of the square lattice using

$$\mathbf{S}_{\mathbf{i}} = \frac{1}{2} \sum_{\alpha, \beta} f_{i\alpha}^\dagger \boldsymbol{\sigma}_{\alpha\beta} f_{i\beta}. \quad (2.2)$$

We write down a Bogoliubov Hamiltonian for the  $f_{i\alpha}$  to obtain a  $\mathbb{Z}_2$  spin liquid. Following Wen's notation [511], we introduce the Nambu spinor

$$\psi_{\mathbf{i}} = \begin{pmatrix} f_{i\uparrow} \\ f_{i\downarrow}^\dagger \end{pmatrix}, \quad (2.3)$$

resulting in the Bogoliubov Hamiltonian

$$H = - \sum_{ij} \psi_{\mathbf{i}}^\dagger u_{ij} \psi_j. \quad (2.4)$$

Here,

$$u_{ij} = i u_{ij}^0 + u_{ij}^x \tau^x + u_{ij}^y \tau^y + u_{ij}^z \tau^z, \quad (2.5)$$

with  $\tau^a$  Pauli matrices acting on the Nambu indices of  $\psi_{\mathbf{i}}$ . Invariance under global  $SU(2)_s$  spin rotation requires that the  $u_{ij}^\mu$  are all real numbers obeying

$$u_{ji}^0 = -u_{ij}^0, \quad u_{ji}^x = u_{ij}^x, \quad u_{ji}^y = u_{ij}^y, \quad u_{ji}^z = u_{ij}^z. \quad (2.6)$$

This fermionic spinon representation has a  $SU(2)_g$  gauge symmetry, under which

$$SU(2)_g : \psi_{\mathbf{i}} \rightarrow U_{g,\mathbf{i}} \psi_{\mathbf{i}}. \quad (2.7)$$

and a corresponding transformation for  $u_{ij}$ .

We will provide 3 different ansatzes for the  $u_{ij}$  in the Z2Azz13 spin liquid, each suited for different purposes. The 3 ansatzes are, of course, related to each other by  $SU(2)_g$  gauge

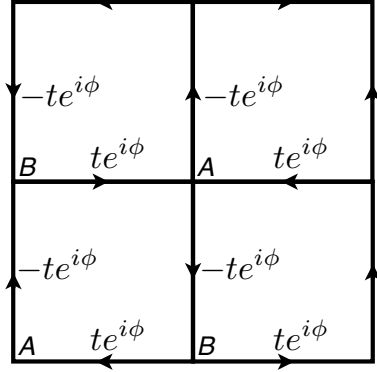


Figure 2.3: Nearest-neighbor fermionic spinon hopping showing the  $A$  ( $i_x + i_y$  even) and  $B$  ( $i_x + i_y$  odd) sublattices.

transformations. Wen's ansatz for the Z2Azz13 spin liquid is given in Appendix A.1, where the continuum Lagrangian describing the different spin liquid phases is deduced from symmetry fractionalization considerations. In the main text, we obtain the continuum theory directly from the lattice model, for which the ansatz given in Eq. (2.12) will be most useful. To derive this ansatz, we first describe the Z2Azz13 spin liquid by starting from the familiar staggered flux phase with U(1) gauge symmetry [3], and perturbing it with  $d_{xy}$  pairing. Explicitly, the

ansatz is

$$\begin{aligned}
 \tilde{u}_{\mathbf{i},\mathbf{i}+\hat{x}} &= \begin{pmatrix} te^{-i\phi} & 0 \\ 0 & -te^{i\phi} \end{pmatrix}, \quad i_x + i_y \text{ even} \\
 \tilde{u}_{\mathbf{i},\mathbf{i}+\hat{x}} &= \begin{pmatrix} te^{i\phi} & 0 \\ 0 & -te^{-i\phi} \end{pmatrix}, \quad i_x + i_y \text{ odd} \\
 \tilde{u}_{\mathbf{i},\mathbf{i}+\hat{y}} &= \begin{pmatrix} -te^{i\phi} & 0 \\ 0 & te^{-i\phi} \end{pmatrix}, \quad i_x + i_y \text{ even} \\
 \tilde{u}_{\mathbf{i},\mathbf{i}+\hat{y}} &= \begin{pmatrix} -te^{-i\phi} & 0 \\ 0 & te^{i\phi} \end{pmatrix}, \quad i_x + i_y \text{ odd} \\
 \tilde{u}_{\mathbf{i},\mathbf{i}+\hat{x}+\hat{y}} &= \begin{pmatrix} 0 & -(\gamma_1 - i\gamma_2) \\ -(\gamma_1 + i\gamma_2) & 0 \end{pmatrix} \\
 \tilde{u}_{\mathbf{i},\mathbf{i}-\hat{x}+\hat{y}} &= \begin{pmatrix} 0 & (\gamma_1 - i\gamma_2) \\ (\gamma_1 + i\gamma_2) & 0 \end{pmatrix}.
 \end{aligned} \tag{2.8}$$

The first four terms in (2.8) represent the fermion hopping, which is sketched in Fig. 2.3, and the last 2 terms are the  $d_{xy}$  pairing. With this ansatz, three distinct spin liquids may be described depending on the choice of parameters. These spin liquids are shown in Fig. 2.2, and we list them below:

- The  $\pi$ -flux phase with SU(2) gauge symmetry corresponds to  $\phi = \pi/4$ , and no fermion pairing  $\gamma_{1,2} = 0$ .
- The ‘staggered flux’ U(1) spin liquid is obtained for general  $\phi$ , and no fermion pairing  $\gamma_{1,2} = 0$ . The U(1) gauge field corresponds to a nearly spatially uniform modulation in the phases of the fermion hopping terms.
- The Z2Azz13 spin liquid is obtained when the  $d_{xy}$  pairing  $\gamma_1 + i\gamma_2$  is present, and breaks the U(1) down to  $\mathbb{Z}_2$ .

Note that we have  $d_{xy}$  pairing in the  $\mathbb{Z}_2$  spin liquid only, with opposite signs on the two sublattices.

In momentum space, we choose the  $A$  and  $B$  checkerboard sublattices as the basis sites (shown in Fig. 2.3), and the Hamiltonian acting on  $(f_{A,\mathbf{k}\uparrow}, f_{B,\mathbf{k}\uparrow}, f_{A,-\mathbf{k},\downarrow}^\dagger, f_{B,-\mathbf{k},\downarrow}^\dagger)^T$  in the gauge of Eq. (2.8) is

$$H = \begin{pmatrix} 0 & C_{\mathbf{k}} & D_{\mathbf{k}} & 0 \\ C_{\mathbf{k}}^* & 0 & 0 & D_{\mathbf{k}} \\ D_{\mathbf{k}}^* & 0 & 0 & -C_{\mathbf{k}}^* \\ 0 & D_{\mathbf{k}}^* & -C_{\mathbf{k}} & 0 \end{pmatrix} \quad (2.9)$$

where

$$C_{\mathbf{k}} = -2t(e^{-i\phi} \cos(k_x) - e^{i\phi} \cos(k_y)) \quad , \quad D_{\mathbf{k}} = 4(\gamma_1 - i\gamma_2) \sin(k_x) \sin(k_y). \quad (2.10)$$

The eigenvalues of (2.9) are

$$\varepsilon_{\mathbf{k}} = \pm \left( [\text{Re}(C_{\mathbf{k}})]^2 + [\text{Im}(C_{\mathbf{k}}) \pm |D_{\mathbf{k}}|]^2 \right)^{1/2} \quad (2.11)$$

and these co-incide with those obtained in Wen's gauge in (6.23). Note that the dispersion depends only on  $|\gamma_1 + i\gamma_2|$ , and not on  $\gamma_{1,2}$  separately. This is natural in the staggered flux gauge, where U(1) the gauge transformation acts simply as  $f_{i\alpha} \rightarrow f_{i\alpha} e^{i\phi_i}$ , and so the  $d_{xy}$  pairing acts like a charge 2 Higgs field: a simple identification of the charge 2 Higgs field is the advantage of the present gauge. This dispersion is plotted in Fig. (2.4). The staggered flux phase has Dirac nodal points at  $(\pm\pi/2, \pm\pi/2)$ . Introducing  $d_{xy}$  pairing does not gap these nodal points, but moves them away from these high symmetry points. Although the dispersion does not have full square lattice symmetry, all gauge-invariant observables do, and this is verified by the analysis in Appendix A.1.

### 2.2.1 MAJORANA GAUGE

For the remainder of the analysis in the body of the paper we map (2.8) onto the gauge used by Wang *et al.* [500] for the  $\pi$ -flux phase, which is convenient for eventual representation in Majorana fermions and making the gauge and spin rotation symmetries manifest. In this

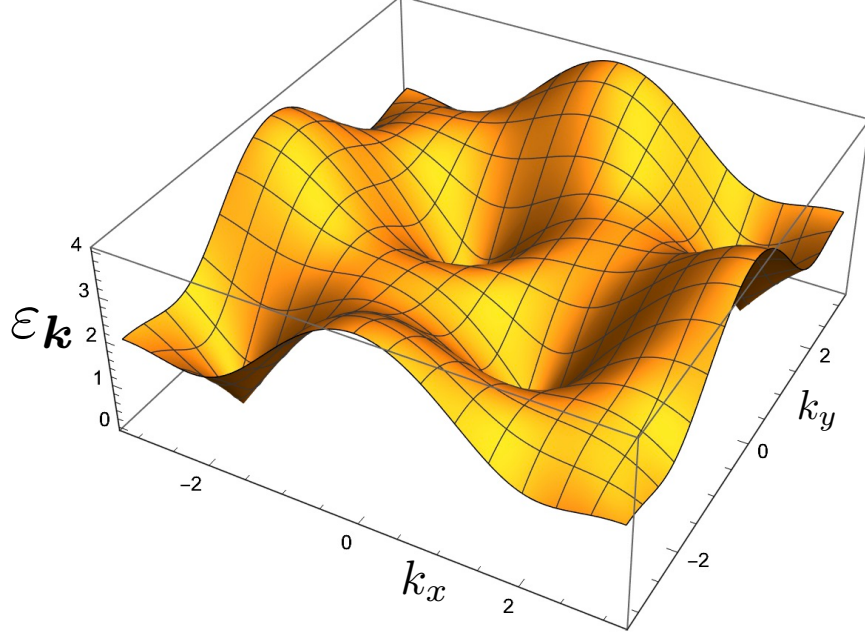


Figure 2.4: Plot of the dispersion,  $\varepsilon_{\mathbf{k}}$ , of the fermionic spinons of the  $\mathbb{Z}_2$  spin liquid Z2Azz13. The eigenvalues of the spinon Hamiltonian are  $\pm \varepsilon_{\mathbf{k}}$ . All gauge invariant observables are invariant under the square lattice space group, although the spinon dispersion is not. The plot is of Eq. (2.11) for  $t = 1.118$ ,  $\phi = 0.464$ ,  $\gamma_1 = 0.5$ ,  $\gamma_2 = 0$ .

gauge, the ansatz of the Z2Azz13 spin liquid (which is gauge equivalent to Eq. (2.8)) is

$$\begin{aligned}
 \bar{u}_{\mathbf{i}, \mathbf{i} + \hat{\mathbf{x}}} &= \begin{pmatrix} ite^{-4i\phi} & 0 \\ 0 & ite^{4i\phi} \end{pmatrix}, \quad i_x + i_y \text{ even} \\
 \bar{u}_{\mathbf{i}, \mathbf{i} + \hat{\mathbf{x}}} &= \begin{pmatrix} ite^{4i\phi} & 0 \\ 0 & ite^{-4i\phi} \end{pmatrix}, \quad i_x + i_y \text{ odd} \\
 \bar{u}_{\mathbf{i}, \mathbf{i} + \hat{\mathbf{y}}} &= (-1)^{i_x} \begin{pmatrix} te^{2i\phi} & 0 \\ 0 & -te^{-2i\phi} \end{pmatrix}, \quad i_x + i_y \text{ odd} \\
 \bar{u}_{\mathbf{i}, \mathbf{i} + \hat{\mathbf{y}}} &= (-1)^{i_x} \begin{pmatrix} -te^{-2i\phi} & 0 \\ 0 & te^{2i\phi} \end{pmatrix}, \quad i_x + i_y \text{ even} \\
 \bar{u}_{\mathbf{i}, \mathbf{i} + \hat{\mathbf{x}} + \hat{\mathbf{y}}} = \bar{u}_{\mathbf{i}, \mathbf{i} - \hat{\mathbf{x}} + \hat{\mathbf{y}}} &= \begin{pmatrix} 0 & (\gamma_1 - i\gamma_2)e^{-2i\phi} \\ (\gamma_1 + i\gamma_2)e^{2i\phi} & 0 \end{pmatrix}, \quad i_x + i_y \text{ even} \\
 \bar{u}_{\mathbf{i}, \mathbf{i} + \hat{\mathbf{x}} + \hat{\mathbf{y}}} = \bar{u}_{\mathbf{i}, \mathbf{i} - \hat{\mathbf{x}} + \hat{\mathbf{y}}} &= \begin{pmatrix} 0 & (-\gamma_1 + i\gamma_2)e^{4i\phi} \\ (-\gamma_1 - i\gamma_2)e^{-4i\phi} & 0 \end{pmatrix}, \quad i_x + i_y \text{ odd}
 \end{aligned} \tag{2.12}$$

As in the previous gauge, the  $\pi$ -flux phase is obtained when  $\phi = \pi/4$  while the staggered-flux phase corresponds to general  $\phi$ .

## 2.3 CONTINUUM THEORY FOR HIGGS TRANSITION FROM SU(2) TO $\mathbb{Z}_2$ .

### 2.3.1 $\pi$ -FLUX STATE WITH SO(5) SYMMETRY

We begin by working out the continuum SU(2) gauge theory with the 2-flavor massless Dirac fermion from the mean-field ansatz for the  $\pi$ -flux phase, using the Majorana gauge given in Eq. (2.12).

In this gauge, we replace the Nambu spinor in Eq. (2.3) by the matrix operator

$$\mathcal{X}_i = \begin{pmatrix} f_{i\uparrow} & -f_{i\downarrow}^\dagger \\ f_{i\downarrow} & f_{i\uparrow}^\dagger \end{pmatrix} \quad (2.13)$$

The spinon SU(2) gauge symmetry of Eq. (2.7) now acts on  $\mathcal{X}_i$  as

$$\text{SU}(2)_g : \mathcal{X}_i \rightarrow \mathcal{X}_i U_{g,i}^\dagger. \quad (2.14)$$

The physical spin symmetry acts on  $\mathcal{X}_i$  on the left:

$$\text{SU}(2)_s : \mathcal{X}_i \rightarrow U_s \mathcal{X}_i. \quad (2.15)$$

We write the Bogoliubov Hamiltonian Eq. (2.4) as

$$H_{MF} = \sum_{\langle ij \rangle} \left[ i\alpha_{ij} \text{Tr} (\mathcal{X}_i^\dagger \mathcal{X}_j) + \beta_{ij}^a \text{Tr} (\sigma^a \mathcal{X}_i^\dagger \mathcal{X}_j) + i\gamma_{ij} \text{Tr} (\sigma^a \mathcal{X}_i^\dagger \sigma^a \mathcal{X}_j) \right]. \quad (2.16)$$

The correspondence with the notation in Eq. (2.4) is

$$u_{ij} = i\alpha_{ij}\tau^0 + \beta_{ij}^a\tau^a. \quad (2.17)$$

The additional  $\gamma_{ij}$  hoppings involve projective realizations of the spin rotation symmetry, and will not be relevant. The degrees of freedom in this Hamiltonian can be represented by four

Majorana fermions,

$$\chi_i = \frac{1}{\sqrt{2}} (\chi_0 + i\chi_a \sigma^a). \quad (2.18)$$

The SU(2)-invariant  $\pi$ -flux state comes from the hoppings  $\beta^a = 0$  and

$$\alpha_{ij} = -\alpha_{ji} \quad \alpha_{i+\hat{x},i} = 2t \quad \alpha_{i+\hat{y},i} = (-1)^{i_x} 2t. \quad (2.19)$$

The low-energy behavior of this mean-field ansatz is described by an SU(2) gauge theory with an emergent SO(5) symmetry. To work out the dispersion relation of this Hamiltonian, we increase our unit cell by one lattice site in the  $x$  direction and so  $\chi$  acquires an additional sublattice index  $m = A, B$ . Note that this unit cell differs slightly from the one used in the staggered flux gauge. In momentum space, we then have

$$H = \sum_k \chi_{-k}^T H(k) \chi_k, \quad (2.20)$$

$$H(k) = -2t [\sin(k_y) \rho^z + \sin(k_x) \rho^x].$$

$\rho^i$  are Pauli operators acting on the sublattice space,  $m = A, B$ . This Hamiltonian is diagonal in the  $0, a$  indices in Eq. (2.18), and the gauge was chosen to have this feature. The Hamiltonian in Eq. (2.20) has Dirac points at  $k_y = 0, \pi, k_x = 0$ . Labelling these Dirac points by another index  $v = 1, 2$ , and expanding around these two points, we decompose our Majorana operator as

$$\chi_{m,i} \sim \rho^x \chi_{m,v=1}(x) + (-1)^{i_y} \chi_{m,v=2}(x). \quad (2.21)$$

With this, the Hamiltonian reduces to

$$H \approx 2it \sum_{v=1,2} \chi_v^T (\rho^x \partial_x - \rho^z \partial_y) \chi_v, \quad (2.22)$$

with the sublattice and  $0, a$  indices implicit. This gives the continuum Lagrangian

$$\mathcal{L}_{MF} = 2it \bar{\chi}_v \gamma^\mu \partial_\mu \chi_v \quad (2.23)$$

where  $\gamma^0 = \rho^y$ ,  $\gamma^x = i\rho^z$ ,  $\gamma^y = i\rho^x$ , and  $\bar{\chi} \equiv \chi^T \gamma^0$ . Here we have chosen to express  $\mathcal{L}_{MF}$  in the

Minkowski metric  $(+, -, -)$ ; we ultimately move to the Euclidean metric below to perform calculations.

We now define the  $4 \times 2$  matrix operator

$$X_{\alpha,v;\beta} = \frac{1}{\sqrt{2}} (\chi_{0,v} \delta_{\alpha\beta} + i \chi_{a,v} \sigma_{\alpha\beta}^a) \quad (2.24)$$

and  $\bar{X} = X^\dagger \gamma^0$ , where the sublattice/Dirac index  $m$  is left implicit. This lets us write our Lagrangian as

$$\mathcal{L}_{MF} = i \text{Tr} (\bar{X} \gamma^\mu \partial_\mu X) , \quad (2.25)$$

where we set  $t = 1/2$  from now on. In this form, the Hamiltonian describes 8 massless Majorana fermions (these are 2-component ‘relativistic’ Majorana fermions with an additional sublattice index). The  $SU(2)$  gauge symmetry acts on the right index ( $\beta$  in Eq. (2.24)) of  $X$ , and the gradient in  $\mathcal{L}_{MF}$  must be replaced by the appropriate covariant gradient when the gauge field is included. Global spin rotations act of the left index ( $\alpha$  in Eq. (2.24)) of  $X$ , and global valley rotations act of the  $v$  index. These global rotations combine to yield an emergent, low energy  $\text{Sp}(4)/\mathbb{Z}_2 \equiv \text{SO}(5)$  global symmetry in the  $\pi$ -flux phase [384, 500].

In the following subsections, we derive the continuum form of the perturbations given in Eq. (2.12), which break the  $\pi$ -flux state down to either the staggered flux state or the Z2Azz13 spin liquid. We do so by rewriting these perturbations in terms of the low-energy modes given in Eq. (2.21) and keeping only the lowest order gradient terms. These perturbations are coupled to adjoint Higgs fields, and the transition of the  $\pi$ -flux state to either the staggered flux state or Z2Azz13 spin liquid is obtained by condensing the corresponding Higgs fields. An alternative derivation of these continuum perturbations based on symmetry fractionalization is provided in Appendix A.1, and agrees with the following analysis.

### 2.3.2 FROM $\pi$ -FLUX TO STAGGERED FLUX

We obtain the continuum version of the perturbations to the staggered flux phase by expanding the mean field parameters  $\bar{u}_{ij}$  defined in Eq. (2.12) in powers of  $\phi = \pi/4 + \delta\phi$ . We subsequently employ Eq. (2.17), which in turn yields additional hopping parameters to the Hamiltonian of

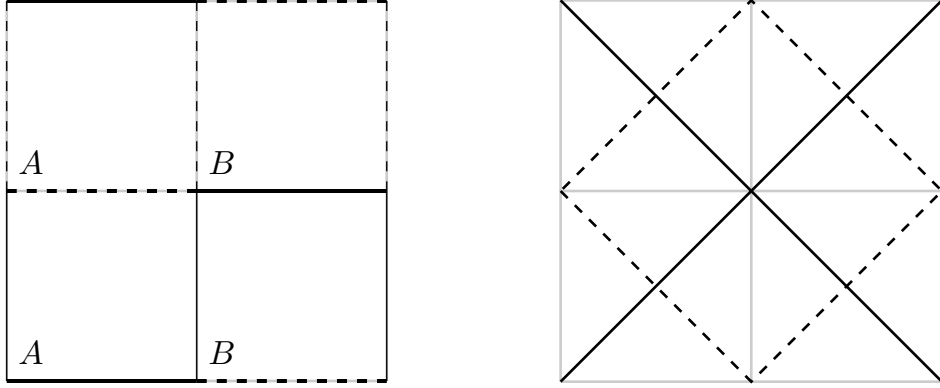


Figure 2.5: Shown are the leading-order perturbations that away from the  $SU(2)$   $\pi$ -flux state, in the Majorana gauge given by Eq. 2.12. Note that the unit cell, with sublattice sites  $A$  and  $B$ , differs from the gauge illustrated in Fig. 2.3. (Left) The perturbation that shifts the  $\pi$ -flux state to the staggered flux state, with hoppings proportional to  $\tau^z$ . Thickness of the line denotes strength (weaker in the  $y$ -direction) and solid/dashed indicates positive/negative sign. (Right) The  $d_{xy}$  pairing that breaks the  $U(1)$  gauge symmetry to  $\mathbb{Z}_2$ , with pairing  $\gamma_1 \tau^y - \gamma_2 \tau^x$  on solid lines and  $\gamma_1 \tau^x + \gamma_2 \tau^y$  on dashed lines.

the form

$$\beta_{\mathbf{i}, \mathbf{i}+\hat{\mathbf{x}}}^z = -4\delta\phi(-1)^{i_x+i_y}, \quad \beta_{\mathbf{i}, \mathbf{i}+\hat{\mathbf{y}}}^z = 2\delta\phi(-1)^{i_y}. \quad (2.26)$$

These terms are illustrated in Fig. 2.5. If we look at the components of the Majorana fermions (as defined in Eq. (2.18), with  $(0, a)$ ,  $a = x, y, z$ ), we see that these new terms introduce hopping between the  $0 \leftrightarrow z$  and  $x \leftrightarrow y$  Majorana fermions. For simplicity, we focus on the  $0 \leftrightarrow z$  hoppings, as the  $x \leftrightarrow y$  hoppings will be identical. We start with the hoppings in the  $x$ -direction, expand our Majorana operators in terms of low-energy modes, and keep only the lowest-order gradient terms. As in Eq. (2.24), the two indices on  $\chi$  correspond to  $(0, x, y, z)$

and valley, respectively, with the sublattice index implicit.

$$\begin{aligned}
 \delta H = & -4\delta\phi \sum_{\mathbf{i}} \left[ \chi_{0,1}^T(x_{\mathbf{i}}) \rho^x + (-1)^{i_y} \chi_{0,2}^T(x_{\mathbf{i}}) \right] (-1)^{i_y} \rho^x \left[ \rho^x \chi_{z,1}(x_{\mathbf{i}}) + (-1)^{i_y} \chi_{z,2}(x_{\mathbf{i}}) \right] \\
 & + 2\delta\phi \sum_{\mathbf{i}} \left[ \chi_{0,1}^T(x_{\mathbf{i}}) \rho^x + (-1)^{i_y} \chi_{0,2}^T(x_{\mathbf{i}}) \right] (-1)^{i_y} (\rho^x - i\rho^y) \\
 & \times \left[ \rho^x \chi_{z,1}(x_{\mathbf{i}+\hat{\mathbf{x}}}) + (-1)^{i_y} \chi_{z,2}(x_{\mathbf{i}+\hat{\mathbf{x}}}) \right] \\
 & + 2\delta\phi \sum_{\mathbf{i}} \left[ \chi_{0,1}^T(x_{\mathbf{i}}) \rho^x + (-1)^{i_y} \chi_{0,2}^T(x_{\mathbf{i}}) \right] (-1)^{i_y} (\rho^x + i\rho^y) \\
 & \times \left[ \rho^x \chi_{z,1}(x_{\mathbf{i}-\hat{\mathbf{x}}}) + (-1)^{i_y} \chi_{z,2}(x_{\mathbf{i}-\hat{\mathbf{x}}}) \right] \\
 \approx & 2\delta\phi \int d^2x \left[ \chi_{0,1}^T \rho^z \partial_x \chi_{z,2} - \chi_{0,2}^T \rho^z \partial_x \chi_{z,1} \right] \\
 \Rightarrow \delta\mathcal{L} = & -2i\delta\phi \text{Tr}(\sigma^z \bar{X} \mu^y \gamma^y \partial_x X)
 \end{aligned} \tag{2.27}$$

In our final term, we have reintroduced the  $x \leftrightarrow y$  hoppings. For the hoppings in the  $y$ -direction,

$$\begin{aligned}
 \delta H = & 2\delta\phi \sum_{\mathbf{i}} \left[ \chi_{0,1}^T(x_{\mathbf{i}}) \rho^x + (-1)^{i_y} \chi_{0,2}^T(x_{\mathbf{i}}) \right] (-1)^{i_y} \left[ \rho^x \chi_{z,1}(x_{\mathbf{i}+\hat{\mathbf{y}}}) - (-1)^{i_y} \chi_{z,2}(x_{\mathbf{i}+\hat{\mathbf{y}}}) \right] \\
 & - 2\delta\phi \sum_{\mathbf{i}} \left[ \chi_{0,1}^T(x_{\mathbf{i}}) \rho^x + (-1)^{i_y} \chi_{0,2}^T(x_{\mathbf{i}}) \right] (-1)^{i_y} \left[ \rho^x \chi_{z,1}(x_{\mathbf{i}-\hat{\mathbf{y}}}) - (-1)^{i_y} \chi_{z,2}(x_{\mathbf{i}-\hat{\mathbf{y}}}) \right] \\
 \approx & -2\delta\phi \int d^2x \left[ \chi_{0,1}^T \rho^x \partial_y \chi_{z,2} - \chi_{0,2}^T \rho^x \partial_y \chi_{z,1} \right] \\
 \Rightarrow \delta\mathcal{L} = & -2i\delta\phi \text{Tr}(\sigma^z \bar{X} \mu^y \gamma^x \partial_y X)
 \end{aligned} \tag{2.28}$$

Note that here and in Eq. (2.27) the Pauli matrix  $\sigma^z$  is acted on by the SU(2) gauge symmetry of the  $\pi$ -flux phase. Gauge invariance requires there exist nearly identical continuum model bilinears containing instead  $\sigma^x$  and  $\sigma^y$  Pauli matrices. It is therefore useful to express the perturbation in a gauge independent fashion using an adjoint Higgs field  $\Phi_3^a$ , where  $a = x, y, z$  is a SU(2) gauge index:

$$\delta\mathcal{L} = \Phi_3^a \text{Tr} \left[ \sigma^a \bar{X} \mu^y (\gamma^y i\partial_x + \gamma^x i\partial_y) X \right]. \tag{2.29}$$

(Our choice of subscript “3” will be clear shortly.) This Higgs field mediates the onset of the staggered flux phase, and in this present gauge we have the identification

$$\Phi_3^z \sim \delta\phi. \quad (2.30)$$

Condensing the Higgs field with  $\langle \Phi_3^a \rangle$  leads to a transition from the SU(2)  $\pi$ -flux state to the U(1) staggered flux state. For concreteness, we continue to work in the gauge where  $\Phi_3^a$  condenses in the  $z$  direction, as implied by Eqs. (2.27) and (2.28).

### 2.3.3 FROM $\pi$ -FLUX TO Z2Azz13

We now evaluate the effects of a non-zero  $\gamma_{1,2}$  in the  $\pi$ -flux phase, using the Majorana gauge as given in Eq. (2.12). We first consider turning on the perturbation

$$\bar{u}_{\mathbf{i},\mathbf{i}+\hat{\mathbf{x}}+\hat{\mathbf{y}}} = \bar{u}_{\mathbf{i},\mathbf{i}-\hat{\mathbf{x}}+\hat{\mathbf{y}}} = \gamma_1 \tau^y - \gamma_2 \tau^x, \quad i_x + i_y \text{ even}. \quad (2.31)$$

Recall that in the Majorana basis, terms proportional to  $\tau^x$  ( $\tau^y$ ) correspond to hoppings between the  $0 \leftrightarrow x(y)$  and  $z \leftrightarrow y(x)$  Majorana fermions. Focusing on the  $\gamma_1$  term, we expand in low-energy modes

$$\begin{aligned} \delta H &= \gamma_1 \sum_{\mathbf{i}} \left[ \chi_{0,1}^T(\mathbf{x}_{\mathbf{i}}) \rho^x + (-1)^{i_y} \chi_{0,2}^T(\mathbf{x}_{\mathbf{i}}) \right] \left[ \rho^x + (-1)^{i_y} \rho^y \right] \\ &\quad \times \left[ \rho^x \chi_{y,1}(\mathbf{x}_{\mathbf{i}+\hat{\mathbf{x}}+\hat{\mathbf{y}}}) - (-1)^{i_y} \chi_{y,2}(\mathbf{x}_{\mathbf{i}+\hat{\mathbf{x}}+\hat{\mathbf{y}}}) \right] \\ &\approx \gamma_1 \sum_{\mathbf{i}} \chi_{0,1}^T(\mathbf{x}_{\mathbf{i}}) \rho^x \chi_{y,1}(\mathbf{x}_{\mathbf{i}}) - \chi_{0,2}^T(\mathbf{x}_{\mathbf{i}}) \rho^x \chi_{y,2}(\mathbf{x}_{\mathbf{i}}) \\ &\quad + \chi_{0,1}^T(\mathbf{x}_{\mathbf{i}}) \rho^z \chi_{y,2}(\mathbf{x}_{\mathbf{i}}) + \chi_{0,2}^T(\mathbf{x}_{\mathbf{i}}) \rho^z \chi_{y,1}(\mathbf{x}_{\mathbf{i}}) \\ &\Rightarrow \delta \mathcal{L} = \gamma_1 \text{Tr} [\sigma^y \bar{X} (\mu^z \gamma^x + \mu^x \gamma^y) X] \end{aligned} \quad (2.32)$$

The perturbation is identical for the  $\gamma_2$  term, but with  $\sigma^y \Rightarrow -\sigma^x$ .

As in the previous section, the addition of the hopping parameters of Eq. (2.31) can be formulated in a gauge-invariant fashion by coupling the bilinear above to an adjoint Higgs

field  $\Phi_{\bar{1}}^a$ ,  $a = x, y, z$  (the bar on the “1” will be apparent below). In particular, when the term

$$\Phi_{\bar{1}}^a \text{Tr} [\sigma^a \bar{X} (\mu^z \gamma^x + \mu^x \gamma^y) X] \quad (2.33)$$

is added to the Lagrangian, we reproduce the continuum version of Eq. (2.31) we just derived when  $\Phi_{\bar{1}}^a$  condenses as

$$\langle \Phi_{\bar{1}}^x \rangle \sim \gamma_2 \quad , \quad \langle \Phi_{\bar{1}}^y \rangle \sim \gamma_1 . \quad (2.34)$$

We perform the same analysis for the second term proportional to  $\gamma_{1,2}$ :

$$u_{i,i+\hat{x}+\hat{y}} = u_{i,i-\hat{x}+\hat{y}} = \gamma_1 \tau^x + \gamma_2 \tau^y , \quad i_x + i_y \text{ odd} . \quad (2.35)$$

The continuum derivation of this is essentially identical to as before, yielding

$$\delta \mathcal{L} = \text{Tr} [(\gamma_1 \sigma^x + \gamma_2 \sigma^y) \bar{X} (\mu^z \gamma^x - \mu^x \gamma^y) X] , \quad (2.36)$$

prompting use to introduce  $\Phi_{\bar{2}}^a \text{Tr} [\sigma^a \bar{X} (\mu^z \gamma^x - \mu^x \gamma^y) X]$ . The continuum version of Eq. (2.31) is obtained through the condensation  $\Phi_{\bar{2}}^a$  such that  $\langle \Phi_{\bar{2}}^a \rangle = \gamma_1 \delta_{ax} + \gamma_2 \delta_{ay}$ .

### 2.3.4 MAJORANA-HIGGS LAGRANGIAN

We now combine the results of Sections 2.3.1, 2.3.2, and 2.3.3 to obtain the low energy Lagrangian for the Majorana field  $X$ , and 3 real, adjoint Higgs scalars, which we now identify as  $\Phi_1^a$ ,  $\Phi_2^a$ ,  $\Phi_3^a$  ( $\Phi_{1,2}^a$  are rotations of  $\Phi_{\bar{1},\bar{2}}^a$  in the 1,2 plane). We do not explicitly write out the coupling to the SU(2) gauge field in this subsection, which can be included by the usual requirements of minimal coupling.

The Lagrangian is

$$\begin{aligned} \mathcal{L} = & i \text{Tr} (\bar{X} \gamma^\mu \partial_\mu X) + \Phi_1^a \text{Tr} (\sigma^a \bar{X} \mu^z \gamma^x X) + \Phi_2^a \text{Tr} (\sigma^a \bar{X} \mu^x \gamma^y X) \\ & + \Phi_3^a \text{Tr} (\sigma^a \bar{X} \mu^y (\gamma^y i \partial_x + \gamma^x i \partial_y) X) + V(\Phi) . \end{aligned} \quad (2.37)$$

The staggered flux state is obtained when  $\langle \Phi_3 \rangle \propto (0, 0, \delta\phi)$ . The Z2Azz13 state follows from  $\langle \Phi_1 \rangle \propto (\gamma_1 - \gamma_2, \gamma_1 + \gamma_2, 0)$  and  $\langle \Phi_2 \rangle \propto (-\gamma_1 - \gamma_2, \gamma_1 - \gamma_2, 0)$ .

The Higgs potential  $V(\Phi)$  arises from integrating out the high energy spinon degrees of freedom. We deduce its form by carefully considering the symmetry properties of the theory, which are described in some detail in Appendix A.1. Here, we note that the theory should respect time reversal and the lattice symmetries,

$$\begin{aligned} T_x : (i_x, i_y) &\mapsto (i_x + 1, i_y), & T_y : (i_x, i_y) &\mapsto (i_x, i_y + 1), \\ P_x : (i_x, i_y) &\mapsto (-i_x, i_y), & P_y : (i_x, i_y) &\mapsto (i_x, -i_y), \\ R_{\pi/2} : (i_x, i_y) &\mapsto (-i_y, i_x), \end{aligned} \tag{2.38}$$

and we summarize the transformations of the Higgs fields here:

	$T_x$	$T_y$	$P_x$	$P_y$	$\mathcal{T}$	$R_{\pi/2}$
$\Phi_1^a$	–	+	–	–	–	$-\Phi_2^a$
$\Phi_2^a$	+	–	–	–	–	$-\Phi_1^a$
$\Phi_3^a$	–	–	+	+	+	–

From this, we can deduce that the following gauge-invariant terms are allowed to quartic order in the Higgs potential

$$\begin{aligned} V(\Phi) = & s (\Phi_1^a \Phi_1^a + \Phi_2^a \Phi_2^a) + \tilde{s} \Phi_3^a \Phi_3^a + w \epsilon_{abc} \Phi_1^a \Phi_2^b \Phi_3^c \\ & + u (\Phi_1^a \Phi_1^a + \Phi_2^a \Phi_2^a)^2 + \tilde{u} (\Phi_3^a \Phi_3^a)^2 + v_1 (\Phi_1^a \Phi_2^a)^2 + v_2 (\Phi_1^a \Phi_1^a) (\Phi_2^b \Phi_2^b) \\ & + v_3 [(\Phi_1^a \Phi_3^a)^2 + (\Phi_2^a \Phi_3^a)^2] + v_4 (\Phi_1^a \Phi_1^a + \Phi_2^a \Phi_2^a) (\Phi_3^b \Phi_3^b). \end{aligned} \tag{2.39}$$

where  $\epsilon_{abc}$  is the antisymmetric unit tensor.

An important feature of  $V(\Phi)$  is the cubic term proportional to  $w$ . This term implies that if any two of the Higgs fields are condensed, then so must the third. It also shows that even if we were only considering the transition from the SU(2)  $\pi$ -flux phase to the gapless  $\mathbb{Z}_2$  spin liquid by the condensation of  $\Phi_{1,2}^a$ , we would be forced to include  $\Phi_3^a$  in our theory, and hence the additional possibility of a U(1) staggered flux phase. The symmetry transformations show that  $\Phi_3^a$  is the unique adjoint Higgs field that can be made from the tensor product of the Higgs fields needed to describe the gapless  $\mathbb{Z}_2$  spin liquid,  $\Phi_1^a$  and  $\Phi_2^a$ : so the staggered flux phase is a natural partner of this gapless  $\mathbb{Z}_2$  spin liquid and the  $\pi$ -flux phase.

We can perform a mean-field minimization of Eq. (2.39), and typical results are shown in Fig. 2.2. There are 3 phases as a function of the tuning parameters  $s$  and  $\tilde{s}$ , which correspond to exactly those obtained in the lattice mean-field theory described in Section 2.2. The presence of the  $w$  term implies that there is a first order transition line near the point where the 3 phases meet [414], as shown in Fig. 2.2. We summarize and re-express the lattice theory results in terms of the continuum model parameters below.

### SU(2) $\pi$ FLUX PHASE

Here, there is no Higgs condensate  $\langle \Phi_{1,2}^a \rangle = 0$ ,  $\langle \Phi_3^a \rangle = 0$ , and the system lies in the red region on the top right of Fig. 2.2: the SU(2)  $\pi$ -flux phase. The continuum model possesses an SU(2) gauge symmetry, along with the corresponding gauge bosons. The theory is believed to confine to the Néel or VBS phase—as discussed in Section 2.1 and 2.8, we view the Néel phase to be more likely.

### U(1) STAGGERED FLUX PHASE

This state has  $\langle \Phi_3^a \rangle$  non-zero, while  $\langle \Phi_{1,2}^a \rangle = 0$ , resulting in the U(1) staggered flux phase represented on the top left of Fig. 2.2. Making contact with the lattice ansatz, we have

$$\langle \Phi_3^a \rangle \propto (0, 0, \phi - \pi/4) \neq 0. \quad (2.40)$$

Again, the theory has a continuous unbroken gauge degree of freedom, now with only a U(1) symmetry. There is a single gauge boson, which we nevertheless assume triggers confinement. As argued, the most likely fate of the theory is the VBS state, but we cannot preclude the Néel phase.

### $\mathbb{Z}_2$ SPIN LIQUID Z2Azz13

The  $\mathbb{Z}_2$  spin liquid Z2Azz13 corresponds to a Higgs condensate satisfying  $\langle \Phi_{1,2}^a \rangle \neq 0$ ; it is shown in the lower half of the phase diagram of Fig. 2.2. The symmetry transformations imply that  $\Phi_1^a$  and  $\Phi_2^a$  have the same mass, so only a single tuning parameter,  $s$ , is required to make them condense from the SU(2)  $\pi$ -flux phase. From the symmetry transformations,

we also see that the absence of a broken symmetry requires that the gauge-invariant bilinears obey

$$\langle \Phi_1^a \Phi_1^a \rangle = \langle \Phi_2^a \Phi_2^a \rangle > 0, \quad , \quad \langle \Phi_1^a \Phi_2^a \rangle = 0. \quad (2.41)$$

Such saddle points are obtained from the Higgs potential for a range of  $v_1$  positive and  $v_2$  negative. Moreover, such a saddle point is indeed present in the lattice ansatz of the previous section where

$$\langle \Phi_{1a} \rangle \propto (-\gamma_1 - \gamma_2, \gamma_1 - \gamma_2, 0) \quad , \quad \langle \Phi_{2a} \rangle \propto (\gamma_1 - \gamma_2, \gamma_1 + \gamma_2, 0). \quad (2.42)$$

We note that this implies  $\langle \Phi_1 \rangle \perp \langle \Phi_2 \rangle$  and  $|\langle \Phi_1 \rangle| = |\langle \Phi_2 \rangle|$ , where we use a vector shorthand for the indices  $a = x, y, z$  of the Higgs fields. By minimizing the potential  $V(\Phi)$  in Eq. (2.39), we see that this  $\mathbb{Z}_2$  spin liquid also implies the condensation of the remaining Higgs field:

$$\langle \Phi_3^a \rangle \propto w \epsilon_{abc} \langle \Phi_1^b \rangle \langle \Phi_2^c \rangle \quad (2.43)$$

It follows that  $\tilde{s}$  can change sign within this phase without any phase transition.

### 2.3.5 VISIONS

The  $\mathbb{Z}_2$  spin liquid is obtained from the theory in Eq. (2.37) + SU(2) gauge fields (which is Eq. (2.45) below) by condensing  $\Phi_{1,2}^a$ . This spin liquid has gapless fermionic spinon excitations, whose low energy dispersion can also be determined from the continuum theory. However, as in all  $\mathbb{Z}_2$  spin liquids, there must also be vison excitations, which are mutual semions with respect to the spinons. In the theory in Eq. (2.45), the vison is a finite energy excitation associated with vortex-like saddle point in which the Higgs fields  $\Phi_{1,2}^a$  undergo a topologically non-trivial SO(3) rotation, associated with  $\pi_1(\text{SO}(3)) = \mathbb{Z}_2$ , around the core of the vortex: see Ref. [418] for an explicit solution in a theory without the fermionic spinons. Given that the vison appears in a lattice model with a background spinon density of one spinon per site, we expect the vison transforms projectively under translational symmetries with  $T_x T_y = -T_y T_x$ , where  $T_\alpha$  is translation by one lattice spacing in the  $\alpha$  direction [197, 217, 411, 419, 435]. For the case of gapped spinons, this fact now has a modern interpretation in the theory of symmetry

fractionalization in topological phases [46, 80, 127, 315, 555]. We expect that a similar result applies in the present gapless spinon case, but this has not been explicitly established. For the case of gapped spinons, the vison projective transformation can be derived from a parent U(1) gauge theory (which is Higgsed down to  $\mathbb{Z}_2$ ) in which the monopoles carry Berry phases [217, 411, 419]. Such monopole Berry phases are in-turn related to a SO(5) Wess-Zumino-Witten term in an effective theory the Néel and VBS order parameters [436, 477]. Notably, this SO(5) WZW term is also linked to an anomaly of the Majorana theory in Eq. (2.45) [500]. It would therefore be interesting to establish  $T_x T_y = -T_y T_x$  for gapped visons in the presence of gapless spinons starting directly from Eq. (2.45) and condensing the Higgs fields: we leave such an analysis for future work.

## 2.4 RENORMALIZED PERTURBATION EXPANSION FOR THE CRITICAL SU(2) GAUGE THEORY

This section will present an analysis of the transition obtained by tuning the Higgs ‘mass’  $s$  in Eq. (2.39) across a quantum critical point at  $s = s_c$ , for  $\tilde{s} > 0$  in Fig. 2.2, between the SU(2) and  $\mathbb{Z}_2$  spin liquids. We have  $\langle \Phi_{1,2,3}^a \rangle = 0$  for  $s > s_c$ , yielding the  $\pi$ -flux spin liquid. For  $s < s_c$ , we have  $\langle \Phi_{1,2}^a \rangle \neq 0$  yielding the  $\mathbb{Z}_2$  spin liquid Z2Azz13. As we noted below Eq. (2.42),  $\langle \Phi_3^a \rangle$  will also be non-zero once both  $\langle \Phi_{1,2}^a \rangle$  are non-zero. However, as  $\langle \Phi_3^a \rangle$  is quadratic in  $\langle \Phi_{1,2}^a \rangle$  (see Eq. (2.43)), it is not a primary order parameter for the transition. So we can entirely neglect  $\Phi_3^a$  in the analysis of the criticality in the present section.

It is also convenient to write the theory in terms of 2 flavors of complex Dirac fermions which also carry a fundamental SU(2) gauge charge,  $\psi_{\alpha,v}$ ; Here  $\alpha$  is the SU(2) gauge index,  $v = 1, 2$  is the valley index, and the Dirac/sublattice index is suppressed. The global SU(2) spin symmetry is not manifest in this formalism, unlike in the earlier Majorana formalism. Since the Lagrangian in Eq. 2.37 does not contain terms that act on the physical SU(2) spin, our Lagrangian nevertheless has a simple form in terms of these Dirac fermions, although a more careful analysis will be required to calculate the behavior of the Néel order parameter, which does involve the physical SU(2) spin. Explicitly, the relationship between the Dirac

and Majorana fermions is

$$\psi_{\alpha,v} = i\sigma_{\alpha,\beta}^y X_{1,v;\beta}. \quad (2.44)$$

Applying this change of variables to Eq. (2.37), and including the SU(2) gauge field  $A_\mu^a$ , we obtain the Lagrangian for  $\psi$  and the  $\Phi_{1,2}^a$  Higgs fields

$$\begin{aligned} \mathcal{L} &= \mathcal{L}_\psi + \mathcal{L}_\Phi + \mathcal{L}_{\Phi\psi} \\ \mathcal{L}_\psi &= i \sum_v \bar{\psi}_v \gamma^\mu (\partial_\mu - i A_\mu^a \sigma^a) \psi_v. \\ \frac{\mathcal{L}_\Phi}{N_f} &= \frac{K}{2} \left[ (\partial_x \Phi_1^a - 2\epsilon_{abc} A_x^b \Phi_1^c)^2 + (\partial_y \Phi_2^a - 2\epsilon_{abc} A_y^b \Phi_2^c)^2 \right] + \frac{s}{2} (\Phi_1^a \Phi_1^a + \Phi_2^a \Phi_2^a) \\ &\quad + u (\Phi_1^a \Phi_1^a + \Phi_2^a \Phi_2^a)^2 + v_1 (\Phi_1^a \Phi_2^a)^2 + v_2 (\Phi_1^a \Phi_2^a) (\Phi_2^b \Phi_2^b) \\ \mathcal{L}_{\Phi\psi} &= \lambda (\Phi_1^a \bar{\psi} \mu^z \gamma^x \sigma^a \psi + \Phi_2^a \bar{\psi} \mu^x \gamma^y \sigma^a \psi) \end{aligned} \quad (2.45)$$

We will henceforth work in Euclidean signature, with  $(\gamma^\mu)^2 = 1$  for all  $\mu$ . This Lagrangian includes an important new term not present in Eq. (2.37): a bare spatial gradient term for the Higgs field proportional to the coupling  $K$  (we will define  $N_f$  shortly). This coupling is allowed by symmetry, and will turn out to be ‘dangerously irrelevant’ *i.e.* under renormalization,  $K$  flows to zero, but it cannot be set to zero at the outset because of some singular effects that we will describe below. In contrast, the quartic couplings  $u, v_{1,2}$  are genuinely irrelevant at the critical point, and will not be considered further.

The theory  $\mathcal{L}$  is invariant under SU(2) gauge, SU(2) spin rotation, time-reversal, and space group transformations, as it must be, because these are symmetries of the underlying Hamiltonian and its parton representation. However, the Yukawa coupling  $\lambda$  breaks both the emergent Lorentz and SO(5) symmetries of the fermion kinetic term. As we will show below,  $\lambda$  is not an irrelevant perturbation, and so the absence of these emergent symmetries will be apparent in the critical correlation functions.

We will analyze the critical properties of Eq. (2.45) by the  $1/N_f$  expansion used in earlier treatments of Dirac fermions coupled to scalar fields by Yukawa couplings which break relativistic invariance [199]. For this purpose, we will endow the fermions with an additional flavor index (not shown explicitly) which ranges over  $N_f$  values. Combined with the  $v$  index, there are a total of  $2N_f$  flavors and 2 colors of 2-component Dirac fermions. The physical

case of interest to us is  $N_f = 1$ .

As in Ref. [199], we will compute the renormalization constants of the theory  $\mathcal{L}$  in a  $1/N_f$  expansion. The most important of these will be the renormalization of the Fermi velocity, which has been implicitly set to unity above: this is non-zero because of the lack of the Lorentz invariance in the Yukawa coupling. The renormalization of the Fermi velocity in turn defines a dynamic critical exponent  $z$ : we will compute  $z$  to order  $1/N_f$  and find it to be a universal number at this order. Next, we shall examine the renormalization of the field scales. As in the Ref. [199], a convenient choice, as we explain below, is to renormalize the boson field scale  $\Phi$  so that the Yukawa coupling  $\lambda = 1$ ; we will assume  $\lambda = 1$  below. As usual, the renormalization of the fermion field,  $Z_\psi$ , is determined from the fermion self energy, which then determines a fermion anomalous dimension  $\eta_\psi$ . Here we will find an unusual phenomenon, which is one of our main results: the value of  $\eta_\psi$  is not universal at order  $1/N_f$ , but has a logarithmic dependence upon the irrelevant coupling  $K$ . Finally, we will also compute the renormalization of the fermion bilinears associated with the Néel and VBS order parameters: these are not equal to each other because the  $\text{SO}(5)$  symmetry is explicitly broken.

#### 2.4.1 BOSON PROPAGATORS

The first step in the large  $N_f$  expansion is to integrate out the large number of fermions  $\psi$ , which allows us to determine the propagators of the bosons: the Higgs fields and the gauge fields. To leading order in  $1/N_f$ , we have to evaluate the diagrams in Fig. 2.6, and this leads to an effective quadratic action of the following form

$$\begin{aligned} \frac{S_b}{N_f} = & \int_k \frac{1}{2} (s + K k_x^2 + \Gamma_1(k)) \Phi_1^a(k) \Phi_1^a(-k) + \frac{1}{2} (s + K k_y^2 + \Gamma_2(k)) \Phi_2^a(k) \Phi_2^a(-k) \\ & + \frac{\Gamma_A(k)}{2} \left( \delta_{\mu\nu} - \frac{k_\mu k_\nu}{k^2} \right) A_\mu^a(k) A_\nu^a(-k). \end{aligned}$$

We work in the Euclidean time signature, and  $k$  is a 3-momentum.

We first calculate the one-loop corrections to the Higgs propagators. The correction to the

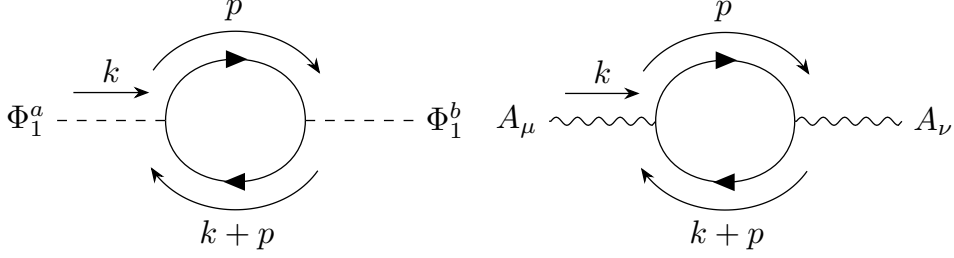


Figure 2.6: The leading order effective propagators for the Higgs (left) and gauge field (right) are generated by the one-loop contributions from  $N$  fermions.

$\Phi_1$  propagator is shown in the first diagram in Fig. 2.6, and is

$$\begin{aligned}\Gamma_1(k)\delta_{ab} &= \lambda^2 \text{Tr} \int \frac{d^3 p}{(2\pi)^3} [\mu^z \gamma^x \sigma^a] \left[ \frac{\not{p}}{p^2} \right] [\mu^z \gamma^x \sigma^b] \left[ \frac{\not{p} + \not{k}}{(k+p)^2} \right] \\ &= -8\lambda^2 \delta_{ab} \int \frac{d^3 p}{(2\pi)^3} \frac{p_0(p_0+k_0) - p_x(p_x+k_x) + p_y(p_y+k_y)}{p^2(k+p)^2} \\ &= \frac{\lambda^2 \delta_{ab}}{4} \frac{(k_0^2 + k_y^2)}{\sqrt{k^2}}.\end{aligned}\quad (2.46)$$

We have omitted a constant term, which will be tuned to zero at the critical point.

The correction to the  $\Phi_2$  propagator is identical to the  $\Phi_1$  correction, with  $k_x \leftrightarrow k_y$ .

$$\Gamma_2(k) = \frac{\lambda^2}{4} \frac{(k_0^2 + k_x^2)}{\sqrt{k^2}}. \quad (2.47)$$

The reader should now notice some key features. As in Ref. [199], the overall scaling in momentum is  $\Gamma_{1,2} \sim |k|$ . So, this fermion-induced contribution to the  $\Phi$  propagators is more important at low momenta than the  $k^2$  terms which would be present in the bare theory. In general, the bare boson  $k^2$  terms are irrelevant, and this is why we choose to set the field scale of  $\Phi$  with the renormalization condition  $\lambda = 1$ . However, unlike Ref. [199], we will see below in some detail that we cannot entirely ignore the bare  $k^2$  term. The expression for  $\Gamma_1$  ( $\Gamma_2$ ) is not an increasing function of  $k_x$  ( $k_y$ ) when it is larger than the other momentum components, and this will lead to infrared singularities at first order in  $1/N_f$ . Specifically, the integral over the propagator  $1/\Gamma_1$  ( $1/\Gamma_2$ ) has an infrared divergence in the  $k_0, k_y$  ( $k_0, k_x$ ) plane. Consequently, we do need to include the *dangerously* irrelevant  $Kk_x^2$  ( $Kk_y^2$ ) term in the bare action for  $\Phi_1^a$  ( $\Phi_2^a$ ), as we have anticipated in Eqs. (2.45) and (2.46).

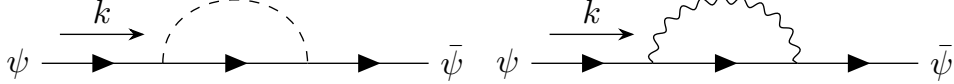


Figure 2.7: The two leading order contributions to the fermion self-energy, arising from Higgs (left) and gauge boson (right) couplings. To leading order in  $1/N_f$ , both the Higgs and gauge boson propagators are generated by the fermions.

The  $\mathcal{O}(N_f)$  propagator for the gauge field is obtained from

$$\begin{aligned}\Gamma_A(k)(k^2\delta^\mu\delta^\nu - k^\mu k^\nu) &= -\text{Tr} \int \frac{d^3p}{(2\pi)^3} \gamma^\mu \left[ \frac{\not{p}}{p^2} \right] \gamma^\nu \left[ \frac{(\not{k} + \not{p})}{(k + p)^2} \right] \\ &= \frac{1}{4\sqrt{k^2}} (k^2\delta^\mu\delta^\nu - k^\mu k^\nu) + \mathcal{O}(k^2).\end{aligned}\quad (2.48)$$

This is relativistically invariant, as expected.

#### 2.4.2 FERMION SELF-ENERGY

We first calculate the one-loop corrections to the fermion self-energy, which will determine the anomalous dimension of the fermion operators as well as the dynamical critical exponent  $z$ . Although the anomalous dimension of the fermion is not a gauge-invariant observable, it will be needed to calculate the critical behavior of the gauge-invariant  $\text{SO}(5)$  order parameter. The three contributions to the fermion self-energy, as shown in Fig. 2.7, come from the two Higgs bosons and the gauge field,  $\Sigma = \Sigma_1 + \Sigma_2 + \Sigma_A$ .

$$\Sigma_1(k) = \frac{3}{N_f} \int \frac{d^3p}{(2\pi)^3} \gamma^x \left[ \frac{\not{p} + \not{k}}{(p + k)^2} \right] \gamma^x \frac{1}{\Gamma_1(p) + Kp_x^2} \quad (2.49)$$

$$\Sigma_2(k) = \frac{3}{N_f} \int \frac{d^3p}{(2\pi)^3} \gamma^y \left[ \frac{\not{p} + \not{k}}{(p + k)^2} \right] \gamma^y \frac{1}{\Gamma_2(p) + Kp_y^2} \quad (2.50)$$

$$\Sigma_A(k) = \frac{3}{N_f} \int \frac{d^3p}{(2\pi)^3} \gamma^\mu \left[ \frac{\not{p} + \not{k}}{(p + k)^2} \right] \gamma^\nu \frac{\eta^{\mu\nu} - (1 - \xi) \frac{p^\mu p^\nu}{p^2}}{\Gamma_A(p)p^2}. \quad (2.51)$$

We have introduced  $\xi$  as a gauge-fixing parameter to obtain the gauge boson propagator.

Focusing on the Higgs corrections (Eqs. (2.49) and (2.50)), we analyze the behavior at small external momenta  $k_i$ . Note that the self-energy integrals are fully regulated by the presence of  $K$  and a non-zero external momenta. Since  $\Sigma_1$  ( $\Sigma_2$ ) is invariant under  $k_y \leftrightarrow k_0$  ( $k_x \leftrightarrow k_0$ ), and the two transform into each other under a 90 degree spatial rotation, there are two distinct

types of contributions for small external momenta. The first is proportional to  $k_x \gamma^x$  for  $\Sigma_1$ , and  $k_y \gamma^y$  for  $\Sigma_2$ . The second type includes all other possible choices of momenta, such as  $k_0 \gamma^0$ .

As we shall justify below and in Appendix A.2, we can focus on the regime  $|p_x| \gg |p_0|, |p_y|$  for graphs with a  $\Phi_1$  propagator. In this limit, we can approximate the  $\Phi_1$  propagator as

$$\frac{4|p_x|}{p_0^2 + p_y^2 + 4K|p_x|^3}. \quad (2.52)$$

At  $K = 0$ , this propagator has an infrared divergence when integrated over the  $p_{0,y}$  plane - so  $K$  is needed an infrared regulator. With this, we extract the  $\gamma^x$  correction to the self-energy from the  $\Phi_1$  propagator by considering the  $k_0 = k_y = 0$  limit:

$$\gamma^x \Sigma_1(k_x) = \frac{12}{N_f} \int^\Lambda \frac{d^3 p}{(2\pi)^3} \frac{(p_x + k_x)}{(p_x + k_x)^2 + p_0^2 + p_y^2} \frac{|p_x|}{p_0^2 + p_y^2 + 4K|p_x|^3}. \quad (2.53)$$

We have indicated a cutoff  $\Lambda$  to regulate the theory at large momenta, and this is needed in conformal gauge theories in 2+1 dimensions. However, with our inclusion of the irrelevant  $K$  to control the infrared singularity, we find that the integrand vanishes faster at large momenta. It is not difficult to see that for  $K \neq 0$  Eq. (2.53) is finite as  $\Lambda \rightarrow \infty$ , and we will take this limit in the present section. The theory with a finite  $\Lambda$  will be examined in Appendix A.2 in a renormalization group computation.

We will now show that Eq. (2.53) has a leading  $k_x \ln^2(k_x)$  contribution. One factor of  $\ln(k_x)$  is the usual one: it follows from the fact that at  $K = 0$  the integrand divided by  $k_x$  is a homogeneous function of momenta of dimension  $-3$ . The other comes from the infrared divergence regulated by  $K$  noted below Eq. (2.52).

Extracting the coefficient of the  $k_x \ln^2(k_x)$  contribution requires a number of approximations. To understand the values of  $p$  that dominate the integral in Eq. (2.53), it is useful to perform the integral over  $p_0$  and  $p_y$ :

$$\gamma^x \Sigma_1(k_x) = \frac{12}{N_f} \int \frac{dp_x}{8\pi^2} \frac{|p_x|(p_x + k_x) \ln[(p_x + k_x)^2 / (4K|p_x|^3)]}{(p_x + k_x)^2 - 4K|p_x|^3}. \quad (2.54)$$

By examining the form of the integrals in Eqs. (2.53) and (2.54), one can verify that the dom-

inant term at small  $k_x$  and  $K$  is proportional to  $k_x \ln^2(Kk_x)$ , and arises from the integration regime

$$\left[ K|p_x|^3 \right]^{1/2} \ll [p_0^2 + p_y^2]^{1/2} \ll |p_x| \ll \frac{1}{K}. \quad (2.55)$$

The scale  $K$  appears both as an ultraviolet cutoff and in defining the infrared bound. For future calculations, this integration regime will prove to be the relevant one in isolating similar  $\log^2$  contributions in other diagrams, although in principle one must still carry out an explicit calculation like in Eq. (2.54) to verify that no other integration regimes give comparable contributions. We provide these calculations in Appendix A.3 in addition to numerical evaluations of the one-loop integrals which confirm the validity of our approximations, and simply evaluate the one-loop integrals in the Eq. (2.55) limit in the main text.

We can extract the coefficient of this  $\log^2$  term by performing the integral in this regime,

$$\begin{aligned} \gamma^x \Sigma_1(k_x) &\approx \frac{12}{N_f} \int_{-1/K}^{1/K} \frac{dp_x}{2\pi} \frac{|p_x|}{(p_x + k_x)} \int_{(K|p_x|^3)^{1/2}}^{|p_x|} \frac{dp_y dp_0}{4\pi^2} \frac{1}{p_0^2 + p_y^2} \\ &\approx \frac{12}{N_f} \int_{-1/K}^{1/K} \frac{dp_x}{2\pi} \frac{|p_x|}{(p_x + k_x)} \frac{1}{4\pi} \ln(1/(K|p_x|)) \\ &\approx -\frac{12}{N_f} \frac{k_x}{8\pi^2} [\ln(Kk_x)]^2. \end{aligned} \quad (2.56)$$

Another discussion of the origin of the  $k_x \ln^2(k_x)$  is presented in Appendix A.2 using a renormalization group analysis.

We now calculate the form of the second type of corrections using the limits in Eq. (2.55), evaluating the  $\Phi_1$  contribution to the self-energy with external momentum  $k_0$  for concreteness.

$$\begin{aligned} \gamma^0 \Sigma_1(k_0) &\approx -\frac{12k_0}{N_f} \int_{-1/K}^{1/K} \frac{dp_x}{2\pi} \frac{1}{|p_x|} \int_{(K|p_x|^3)^{1/2}}^{|p_x|} \frac{dp_y dp_0}{(2\pi)^2} \frac{1}{p_0^2 + p_y^2} \\ &\approx -\frac{12k_0}{N_f} \int_{-1/K}^{1/K} \frac{dp_x}{2\pi} \frac{1}{|p_x|} \frac{1}{4\pi} \ln(1/(K|p_x|)) \approx -\frac{12}{N_f} \frac{k_0}{8\pi^2} [\ln(Kk_0)]^2. \end{aligned} \quad (2.57)$$

Combining the corrections from both Higgs propagators, we obtain the full expression for the self-energy for small external momenta at  $\log^2$  order,

$$\Sigma(k) \approx -\frac{3}{\pi^2 N_f} [k_0 \ln^2(Kk_0) \gamma^0 + k_x \ln^2(Kk_x) \gamma^x + k_y \ln^2(Kk_y) \gamma^y]. \quad (2.58)$$

In principle, the dependence on external momenta inside the logarithms could be more complicated for general  $k$ , i.e.  $\Sigma(k)\gamma^0 \sim k_0 \ln^2(Kf(k_0, k_x, k_y))$ , but since we have verified that  $f(k_0, 0, 0) = k_0$ , then corrections to this are subleading.

These divergent corrections are absorbed into the renormalization of the fermion field,  $\psi = \sqrt{Z_\psi} \psi_R$ , with

$$Z_\psi = 1 - \frac{3}{\pi^2 N_f} \ln^2(K\mu), \quad (2.59)$$

where we have renormalized the theory at some momentum scale  $\mu$ . This counterterm only cures the divergence at  $\log^2$  order, since the renormalized self-energy at some other momentum scale  $k$  will scale as

$$\ln^2(K\mu) - \ln^2(Kk) = \ln(\mu/k) \ln(K^2 k \mu). \quad (2.60)$$

This, along with the RG analysis in Appendix A.2, indicates that the subleading single-logarithm corrections will generically give non-universal behavior. However, these  $\log^2$  corrections to the self-energy are Lorentz invariant, and do not affect the renormalization of the dynamical critical exponent,  $z$ . Therefore, the subleading single-logarithm correction to the velocity anisotropy will lead to a universal correction to the dynamical critical exponent. To extract the subleading correction to  $z$  using  $K$  and the external momenta as a regulator, we start with the expression

$$\frac{\partial \Sigma}{\partial k_0} \gamma^0 - \frac{\partial \Sigma}{\partial k_x} \gamma^x = -\frac{12}{N_f} \int \frac{d^3 p}{(2\pi)^3} \frac{2(p_y + k_y)^2}{(p+k)^4} \frac{|p|}{4Kp_y^2|p| + p_0^2 + p_y^2}. \quad (2.61)$$

To leading order in  $k$ , we set  $k = 0$  inside the integrand and simply use it as an IR cutoff, which gives

$$\frac{\partial \Sigma}{\partial k_0} \gamma^0 - \frac{\partial \Sigma}{\partial k_x} \gamma^x \approx \frac{6}{N_f \pi^2} \ln(Kk). \quad (2.62)$$

This result can be obtained analytically by approximating the integration region  $k \leq |p_x| \leq 1/K$ , and can be verified by a numerical evaluation of Eq. 2.61. This implies a renormalization of the Fermi velocity,  $v_F = Z_v v_{F,R}$

$$Z_v = 1 + \frac{6}{\pi^2 N_f} \ln(K\mu) \quad (2.63)$$

The logarithmic derivative with respect to  $1/K$  determines the renormalization of the dynamical critical exponent,

$$z = 1 + \frac{6}{\pi^2 N_f}. \quad (2.64)$$

The one-loop calculation defined in Eq. (2.61) is actually well-defined when  $K = 0$  and can be regulated via more standard approaches, such as dimensional regularization, as shown in Appendix A.4. The same value of  $z$  is also obtained in a renormalization group computation in Appendix A.2.

### 2.4.3 SO(5) ORDER PARAMETER

In the absence of the Higgs fields, our theory possesses an emergent SO(5) symmetry corresponding to rotations between Néel and VBS order parameters. This SO(5) symmetry is broken by the critical Higgs fields, and as a result, the scaling behavior of Néel and VBS order parameters will differ. In terms of Dirac fermions, the fermion bilinears corresponding to the two-component VBS order parameter - determined by the action of the square lattice symmetries on the bilinears - may be written as

$$V^i = \bar{\psi} \Gamma^i \psi, \quad \Gamma^i = \{\mu^x, \mu^z\}. \quad (2.65)$$

The three-component Néel order parameter has a less concise expression in terms of Dirac fermions - this is due to the fact that the Dirac fermion representation obfuscates the action of the physical SU(2) spin rotation symmetry. In terms of the Majorana field  $X$ , the order parameter is  $\text{Tr}(\bar{X} \mu^y \sigma^a X)$ ,  $a = x, y, z$ . In order to calculate corrections to the Néel order parameter, we focus on the  $\sigma^z$  component, which happens to be simply expressible in terms of a Dirac fermion bilinear:

$$N^z = \bar{\psi} \mu^y \psi. \quad (2.66)$$

Because the Higgs couplings preserve the physical SU(2) spin rotation symmetry, the other components must have the same corrections, and this has been confirmed by an explicit calculation in terms of the Majorana fermions. To compute the corrections to the scaling dimensions of these composite operators, we couple the fermion bilinear  $n^i = \bar{\psi} \mu^i \psi$  to a source

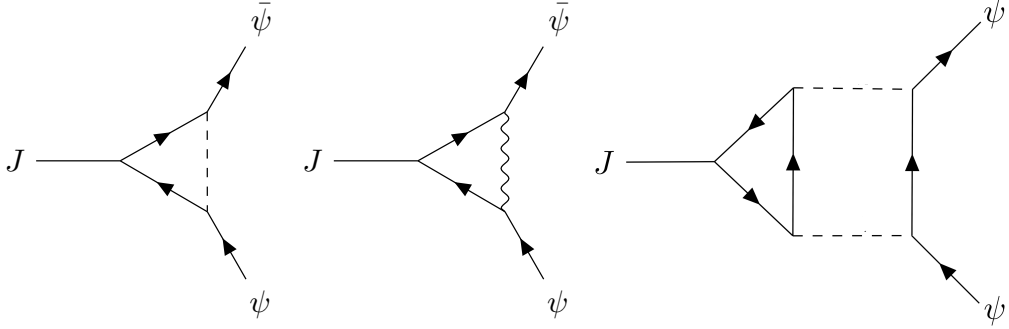


Figure 2.8: The  $\mathcal{O}(N_f^{-1})$  vertex corrections which contribute to the renormalization of the SO(5) order parameter. The order parameter receives corrections at one-loop order from the Higgs fields (left) and the gauge boson (center), although only the former gives a  $\log^2$  correction. An additional two-loop  $\mathcal{O}(N_f^{-1})$  contribution (right) is possible - we show in Appendix A.6 that it does not contain any  $\log^2$  divergences.

field  $J_i$ , and compute the  $\mathcal{O}(N_f^{-1})$  vertex corrections in Fig. 2.8. Aside from the corrections coming from the renormalization of the fermion self-energy, the  $\mathcal{O}(N_f^{-1})$  corrections that we will be interested in come from one-loop corrections of the Higgs fields with external momenta

$k_{1,2}$

$$\begin{aligned} & \frac{\mu^z \sigma^a \mu^i \sigma^a \mu^z}{N_f} \int \frac{d^3 p}{(2\pi)^3} \gamma^x \frac{\not{p} - \not{k}_1}{(p - k_1)^2} \frac{\not{p} - \not{k}_2}{(p - k_2)^2} \gamma^x \frac{1}{\Gamma_1(p) + K p_x^2} \\ & + \frac{\mu^x \sigma^a \mu^i \sigma^a \mu^x}{N_f} \int \frac{d^3 p}{(2\pi)^3} \gamma^y \frac{\not{p} - \not{k}_1}{(p - k_1)^2} \frac{\not{p} - \not{k}_2}{(p - k_2)^2} \gamma^y \frac{1}{\Gamma_2(p) + K p_y^2}, \end{aligned} \quad (2.67)$$

where the first and second terms arise from interactions with  $\Phi_1^a$  and  $\Phi_2^a$ , respectively. The gauge field correction does not break SO(5) symmetry and does not contribute to the renormalization at  $\log^2$  order, so we will focus on the Higgs corrections. Additionally, there is a possible two-loop diagram shown in Fig. 2.8 that contributes at  $\mathcal{O}(N_f^{-1})$ , but we show explicitly in Appendix A.6 that these corrections also do not contribute to the renormalization at  $\log^2$  order. At zero external momenta, the  $\log^2$  Higgs corrections to the VBS order parameter ( $\mu^i = \mu^x, \mu^z$ ) drops out entirely, leaving only Higgs corrections coming from the fermion renormalization.

We focus on vertex corrections to the Néel order parameter ( $\mu^i = \mu^y$ ). As is the case in the fermion self-energy, the spatial anisotropy in the Higgs propagators gives rise to  $\log^2$  divergences in their corrections to the SO(5) vertex. We isolate  $\log^2$  divergences in the Higgs correction to the SO(5) order parameter by including an external momenta  $2k_x$  to the order

parameter, which is distributed symmetrically between the two fermion fields. We calculate this for the  $\Phi_1$  propagator—approximating the Higgs propagator as  $4|p_x|/(p_0^2 + p_y^2 + 4K|p_x|^3)$  as in the previous section and taking the limit in Eq. (2.55), the one-loop correction is

$$\begin{aligned} & \frac{\mu^z \sigma^a \mu^y \sigma^a \mu^z}{N_f} \int \frac{d^3 p}{(2\pi)^3} \frac{p_x^2 - k_x^2 + p_y^2 + p_0^2}{[(p_x + k_x)^2 + p_y^2 + p_0^2] [(p_x - k_x)^2 + p_y^2 + p_0^2]} \frac{4|p_x|}{p_0^2 + p_y^2 + 4K|p_x|^3} \\ & \approx -\frac{12\mu^y}{N_f} \int_{-1/K}^{1/K} \frac{dp_x}{2\pi} \frac{(p_x^2 - k_x^2)|p_x|}{(p_x + k_x)^2(p_x - k_x)^2} \int_{(K|p_x|^3)^{1/2}}^{|p_x|} \frac{dp_y dp_0}{4\pi^2} \frac{1}{p_0^2 + p_y^2} \\ & \approx -\frac{12\mu^y}{N_f} \int_{1/K}^{1/K} \frac{dp_x}{8\pi^2} \frac{(p_x^2 - k_x^2)|p_x|}{(p_x + k_x)^2(p_x - k_x)^2} \ln(1/(K|p_x|)) \approx -\frac{3\mu^y}{2N_f\pi^2} \ln^2(Kk_x) \end{aligned} \quad (2.68)$$

The  $\Phi_2$  propagator gives an identical correction. Since the external momenta only play the role of an IR cutoff to leading order, we generalize this result to an arbitrary external momentum and obtain the composite operator renormalizations [576]

$$\begin{aligned} Z_{\text{VBS}} &= 1 \\ Z_{\text{Néel}} &= 1 + \frac{3}{N_f\pi^2} \ln^2(K\mu). \end{aligned} \quad (2.69)$$

We can state these results in terms of the perturbative corrections to the two-point correlator of the order parameters,  $\langle \bar{\psi} \Gamma^i \psi(k) \bar{\psi} \Gamma^j \psi(-k) \rangle$ , *i.e.* the corresponding susceptibilities  $\chi_{\text{VBS}}$  and  $\chi_{\text{Néel}}$ ; these combine the consequences of the composite operator renormalizations in Eq. (2.69), and  $Z_\psi$  in Eq. (2.59), to yield

$$\begin{aligned} \chi_{\text{VBS}}(k) &\sim -|k| \left( \frac{Z_\psi}{Z_{\text{VBS}}} \right)^2 = -|k| \left[ 1 - \frac{6}{N_f\pi^2} \ln^2(K|k|) \right] \\ \chi_{\text{Néel}}(k) &\sim -|k| \left( \frac{Z_\psi}{Z_{\text{Néel}}} \right)^2 = -|k| \left[ 1 - \frac{12}{N_f\pi^2} \ln^2(K|k|) \right]. \end{aligned} \quad (2.70)$$

After a Fourier transform to real space, these correlators are

$$\begin{aligned} \chi_{\text{VBS}}(r) &\sim \frac{1}{|r|^4} \left[ 1 - \frac{6}{N_f\pi^2} \ln^2(|r|/K) \right] \\ \chi_{\text{Néel}}(r) &\sim \frac{1}{|r|^4} \left[ 1 - \frac{12}{N_f\pi^2} \ln^2(|r|/K) \right]. \end{aligned} \quad (2.71)$$

The renormalization group analysis in Appendix A.2 shows how the above results may be

renormalized to large  $r$ ; we find

$$\begin{aligned}\chi_{\text{VBS}}(r) &\sim \frac{1}{|r|^a} \exp\left(-\frac{6}{N_f \pi^2} \ln^2(|r|/K)\right) \\ \chi_{\text{Néel}}(r) &\sim \frac{1}{|r|^b} \exp\left(-\frac{12}{N_f \pi^2} \ln^2(|r|/K)\right).\end{aligned}\tag{2.72}$$

where the exponents of the prefactors,  $a$  and  $b$ , are *non-universal* numbers.

Leading logarithm-squared corrections have appeared earlier in a few other problems in quantum many-body theory. They appear in the theory of weakly disordered two-dimensional metals with Coulomb interactions [11, 141, 271]. More recently,  $\log^2$  terms have also been found in computations of the density of states of clean bilayer graphene with Coulomb interactions [30, 337]. Renormalization group analyses of these cases [141, 337] also yield an exponentiation similar to that in Eq. (2.72).

As an aside, we note that the one-loop vertex corrections to the bilinear  $\bar{\psi}\psi$ , whose symmetry properties identify it as the scalar spin chirality [187], have the same magnitude and opposite sign as the Néel order parameter. Because of this, the  $\log^2$  divergence is in fact cancelled by the fermion self-energy. As shown in Appendix A.6, the two-loop corrections coming from the Higgs fields vanish, meaning that correlations of the scalar spin chirality should have power law decay at  $\mathcal{O}(N_f^{-1})$ . Since this power law decay is slower than the Néel and VBS correlations, this may indicate proximity to a chiral spin liquid.

## 2.5 TRANSITION FROM U(1) STAGGERED FLUX TO GAPLESS $\mathbb{Z}_2$ SPIN LIQUID

This section discusses the critical U(1) gauge theory for the transition between the U(1) staggered flux spin liquid and the gapless  $\mathbb{Z}_2$  spin liquid Z2Azz13 in Fig. 2.2. A similar theory has been considered earlier [437] for the Néel- $\mathbb{Z}_2$  spin liquid transition.

Both phases have the Higgs field  $\langle\Phi_3^a\rangle \neq 0$ . So let us fix  $\Phi_3^a = \delta_{az}\Phi$ , with  $\Phi$  a non-zero constant, which will turn into a coupling constant in the low energy theory below. In this situation, the SU(2) gauge symmetry is broken down to U(1), and we need only consider a U(1) gauge theory with the U(1) gauge field  $A_\mu \equiv A_\mu^z$ . Also important is the consequence of

the  $w$  term in the Higgs potential Eq. (2.39):

$$V(\Phi) = \dots + w \Phi (\Phi_1^x \Phi_2^y - \Phi_1^y \Phi_2^x) + \dots . \quad (2.73)$$

Choosing a gauge with  $w\Phi < 0$ , and diagonalizing the quadratic form of the Higgs potential for  $\Phi_{1,2}^{x,y}$ , we deduce that we need only focus on a single low energy complex Higgs field near the critical point

$$\mathcal{H} = \frac{1}{2} (\Phi_1^x + \Phi_2^y + i(\Phi_1^y - \Phi_2^x)) . \quad (2.74)$$

It can now be checked that  $\mathcal{H}$  transforms as a charge 2 Higgs field under the unbroken U(1) gauge symmetry. Other linear combinations of  $\Phi_{1,2}^{x,y}$  can be ignored for the critical theory.

We can now obtain the critical theory for the fermions  $\psi$ , the complex Higgs field  $\mathcal{H}$ , and the U(1) gauge field  $A_\mu$  from Eq. (2.37):

$$\begin{aligned} \mathcal{L}_{\text{sf}} &= \mathcal{L}_\psi + \mathcal{L}_\mathcal{H} + \mathcal{L}_{\mathcal{H}\psi} \\ \mathcal{L}_\psi &= i \sum_v \bar{\psi}_v \gamma^\mu D_\mu \psi_v + \Phi \bar{\psi} \mu^y \sigma^z (\gamma^y D_x + \gamma^x D_y) \psi . \\ \frac{\mathcal{L}_\mathcal{H}}{N_f} &= s |\mathcal{H}|^2 + u |\mathcal{H}|^4 \\ \mathcal{L}_{\mathcal{H}\psi} &= \lambda (\mathcal{H} \bar{\psi} (\mu^z \gamma^x + i \mu^x \gamma^y) \sigma^- \psi + \mathcal{H}^* \bar{\psi} (\mu^z \gamma^x - i \mu^x \gamma^y) \sigma^+ \psi) . \end{aligned} \quad (2.75)$$

We define the covariant derivative  $D_\mu = \partial_\mu - i A_\mu \sigma^z$  and operators  $\sigma^\pm = (\sigma^x \pm i \sigma^y)/2$ . Note that  $\Phi$  is a marginal coupling constant here, not a fluctuating field. A crucial feature of  $\mathcal{L}_{\text{sf}}$  is that it does not contain the  $K$  gradient terms: these terms are now truly irrelevant. This can be seen in the large  $N_f$  expansion: upon integrating the fermions, we obtain, in place of Eq. (2.46),

$$\frac{S_b}{N_f} = \int_k \left( s + \frac{\Gamma_1(k) + \Gamma_2(k)}{2} \right) |\mathcal{H}(k)|^2 + \frac{\Gamma_A(k)}{2} \left( \delta_{\mu\nu} - \frac{k_\mu k_\nu}{k^2} \right) A_\mu(k) A_\nu(-k) . \quad (2.76)$$

where  $\Gamma_{1,2}(k)$  are specified in Eqs. (2.46, 2.47) for  $\Phi = 0$ . In general, the sum  $\Gamma_1(k) + \Gamma_2(k)$  has the rotational symmetry of the square lattice, and its inverse does not contain the infrared singularities we encountered earlier. Consequently, there is no logarithmic violation of scaling by a dangerously irrelevant  $K$  here, and the  $1/N_f$  expansion of  $\mathcal{L}_{\text{sf}}$  should proceed along more

conventional lines.

The  $1/N_f$  expansion of the theory  $\mathcal{L}_\psi$  was presented in Refs. [187, 387]: they found a stable Lorentz invariant fixed point with  $\Phi = 0$  at the fixed point. In our case, for  $\mathcal{L}_{sf}$  we expect a critical theory with dynamic scaling with an exponent  $z \neq 1$ ,  $SO(5)$  symmetry broken by  $\mathcal{L}_{H\psi}$ , and a spatial anisotropy in the fermion velocities at the Dirac nodes determined by the fixed point value of  $\Phi$ . Note that even for  $\Phi = 0$  we do not expect Lorentz invariance with  $z = 1$ , because the relevant Yukawa couplings in  $\mathcal{L}_{H\psi}$  are not Lorentz invariant, and consequently  $\Gamma_1(k) + \Gamma_2(k)$  is not Lorentz invariant.

In order to study our critical theory, we proceed in a  $1/N_f$  expansion, with  $N_f$  the fermion number. Since our theory only makes sense when the number of fermions  $N$  is a multiple of 4, we define  $4N_f = N$ ; in other words, we take  $N_f = 1$  to correspond to our physical theory. At leading order in  $1/N_f$ , our effective bosonic action takes the form

$$\frac{S_b}{N_f} = \int_k [s + \Gamma(k)] \mathcal{H}^*(-k) \mathcal{H}(k) + \frac{1}{2} \Pi_{\mu\nu}(k) A_\mu(-k) A_\nu(k) \quad (2.77)$$

where the inverse propagators  $\Gamma, \Pi$  are generated by the one-loop fermion diagrams shown in

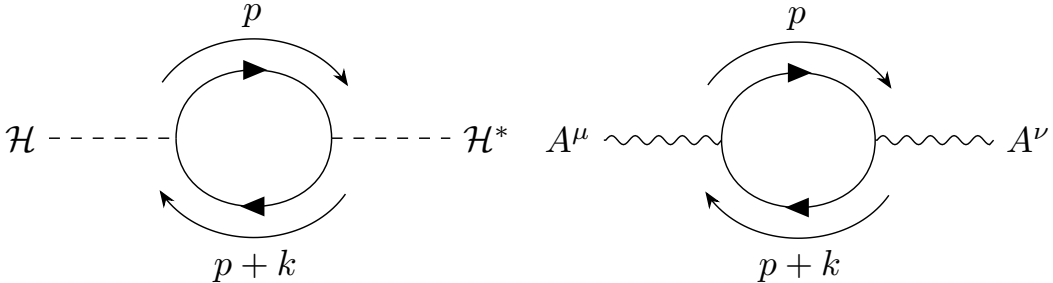


Figure 2.9: The effective action for the Higgs boson (left) and U(1) gauge field (right) are generated by the fermions at leading order in a  $1/N_f$  expansion.

Fig. 2.9. We have taken the bare Higgs mass to scale with  $N_f$ , although we will be interested in the critical theory where we tune the Higgs mass to zero.

To calculate the effective propagators, we need the fermion propagator, which receives corrections to its Lorentz-invariant value of  $1/\not{p}$  due to a non-zero  $\Phi$ . This may be treated perturbatively in  $\Phi$ , but the existence of a stable fixed point turns out to not be viewable at leading order, so we instead proceed with a non-perturbative treatment of  $\Phi$ . We include

further details of this calculation in Appendix A, and cite the results in the main text. Defining the variables

$$k_{x,\pm} \equiv k_x \pm \Phi k_y, \quad k_{y,\pm} \equiv k_y \pm \Phi k_x, \quad |k_{\pm}| \equiv \sqrt{k_0^2 + k_{x,\pm}^2 + k_{y,\pm}^2} \quad (2.78)$$

the effective inverse Higgs propagator (obtained from the  $\Phi$ -dependent fermion propagator) is

$$\Gamma(k) = \frac{1}{16N_f(1-\Phi^2)} \left[ \frac{k_+^2 + k_0^2 + 2k_{x,+}k_{y,+}}{|k_+|} + \frac{k_-^2 + k_0^2 - 2k_{x,-}k_{y,-}}{|k_-|} \right]. \quad (2.79)$$

Likewise, we need the general form of the effective gauge boson propagator. The presence of a non-zero  $\Phi$  modifies the gauge coupling, and hence non-Lorentz-invariant corrections arise both from  $\Phi$ -dependent modifications to the fermion propagator as well as  $\mathcal{O}(\Phi)$  vertices. We separate this calculation into three pieces. The first correction comes from using the  $\mathcal{O}(\Phi^0)$  vertices, but with the full fermion propagator. This one-loop term contributes

$$\Pi_{\mu\nu}^{(1)}(k) = \sum_{a=\pm} \frac{k_a^2}{8N_f(1-\Phi^2)|k_a|} \left( \delta_{\mu\nu} - \frac{k_{\mu a}k_{\nu a}}{k_a^2} \right). \quad (2.80)$$

The second correction comes from using one  $\mathcal{O}(\Phi)$  vertex, which gives the contribution

$$\begin{aligned} \Pi_{\mu x}^{(2)}(k) &= \Pi_{x\mu}^{(2)}(k) = \sum_{a=\pm} \frac{a\Phi k_a^2}{8N_f(1-\Phi^2)|k_a|} \left( \delta_{\mu y} - \frac{k_{\mu a}k_{ya}}{k_a^2} \right), \\ \Pi_{\mu y}^{(2)}(k) &= \Pi_{y\mu}^{(2)}(k) = \sum_{a=\pm} \frac{a\Phi k_a^2}{8N_f(1-\Phi^2)|k_a|} \left( \delta_{\mu x} - \frac{k_{\mu a}k_{xa}}{k_a^2} \right). \end{aligned} \quad (2.81)$$

There is also an extra factor of 2 in  $\Pi_{xx,yy}^{(2)}$  due to the two possible vertex orderings. Finally, the third correction comes from using two  $\mathcal{O}(\Phi)$  vertices,

$$\begin{aligned} \Pi_{xx}^{(3)}(k) &= \sum_{a=\pm} \frac{\Phi^2 k_a^2}{8N_f(1-\Phi^2)|k_a|} \left( 1 - \frac{k_{ya}^2}{k_a^2} \right), \\ \Pi_{yy}^{(3)}(k) &= \sum_{a=\pm} \frac{\Phi^2 k_a^2}{8N_f(1-\Phi^2)|k_a|} \left( 1 - \frac{k_{xa}^2}{k_a^2} \right), \\ \Pi_{yx}^{(3)}(k) &= \Pi_{xy}^{(3)}(k) = \sum_{a=\pm} -\frac{\Phi^2 k_{xa}k_{ya}}{8N_f(1-\Phi^2)|k_a|}. \end{aligned} \quad (2.82)$$

We verify that the combined inverse propagator  $\Pi_{\mu\nu}(k) = \sum_{i=1,2,3} \Pi_{\mu\nu}^{(i)}(k)$  annihilates the

vector  $(k_0, k_x, k_y)$ , as required by gauge invariance. Note that  $\Pi_{\mu\nu}$  requires a gauge fixing term in order to be invertable. Followin Ref. [187], we add the following non-local gauge fixing term to the Lagrangian

$$\frac{1}{4\xi|k|} A_\mu k^\mu k^\nu A_\nu. \quad (2.83)$$

All gauge-invariant observables have been checked to ensure they are independent of the choice of  $\xi$ .

## 2.6 RENORMALIZATION GROUP ANALYSIS

We perform a renormalization group (RG) analysis of the  $\mathcal{O}(1/N_f)$  effective theory. We are interested in studying the behavior of this theory under the rescaling

$$\begin{aligned} k &= k' e^{-\ell}, \\ \omega &= \omega' e^{-z\ell}. \end{aligned} \quad (2.84)$$

We also define a rescaling of the fermion fields

$$\psi(k, \omega) = \psi'(k', \omega') e^{\frac{\ell}{2}(2+2z-\eta_f)}. \quad (2.85)$$

The Higgs and gauge fields must also be suitably rescaled, although the anomalous dimensions of these fields will not be needed to calculate our observables of interest. In the absence of a standard boson kinetic term at leading order in  $1/N_f$ , we define the scaling of the boson field by performing our RG such that the Yukawa coupling remains fixed under RG.

### 2.6.1 FERMION SELF-ENERGY

We first evaluate the  $\mathcal{O}(1/N_f)$  contributions to the fermion self-energy, which come from both gauge and Higgs one-loop diagrams. The self-energy is UV divergent and requires a UV cutoff  $\Lambda$ . The logarithmic derivative of the fermion self-energy with respect to this cutoff takes the general form

$$\Lambda \frac{d}{d\Lambda} \Sigma(k) = C_0 k_0 \gamma^0 + C_1 (k_x \gamma^x + k_y \gamma^y) + C_2 \Phi \mu^y \sigma^z (k_x \gamma^y + k_y \gamma^x) \quad (2.86)$$

for constants  $C_{0,1,2}$ . One must verify that only these terms are generated at one-loop order, which we have done.

In order to calculate the constants  $C_i$ , we will use the momentum-shell RG approach outlined in Ref. [199]. The regularized one-loop contribution to the self-energy schematically takes the form

$$\Sigma(k) = \frac{1}{N_f} \int \frac{d^3 p}{(2\pi)^3} F(p+k) G(p) \mathcal{K}\left(\frac{p^2}{\Lambda^2}\right) \mathcal{K}\left(\frac{(k+p)^2}{\Lambda^2}\right) \quad (2.87)$$

where  $F$  and  $G$  are homogeneous functions of the three-momenta, and  $\mathcal{K}(y)$  serves as a UV cutoff with the property that  $\mathcal{K}(0) = 1$  and  $\mathcal{K}(y)$  falls off rapidly for large  $y$ . In our calculations, we take  $F$  to be the fermion propagator, and  $G$  to be the boson propagator (either Higgs or gauge), along with vertex coefficients. The fact that  $F$  and  $G$  are homogeneous functions allows us to remove the explicit dependence on  $\mathcal{K}$  upon taking the logarithmic derivative and integrating by parts. We refer to Appendix A.7 for an explicit derivation of this, and state the result here - the logarithmic derivative of the self-energy takes the form

$$\Lambda \frac{d}{d\Lambda} \Sigma(k) = \frac{k_\lambda}{8\pi^3 N_f} \int_0^{2\pi} d\phi \int_0^\pi \sin\theta d\theta \frac{\partial F(\hat{p})}{\partial p_\lambda} G(\hat{p}) . \quad (2.88)$$

where  $\hat{p} \equiv (\cos\theta, \sin\theta \sin\phi, \sin\theta \cos\phi)$ . The resulting integrals in Eq. (2.88) are fully convergent and may be evaluated numerically, from which we can extract the coefficients  $C_{0,1,2}$ .

### 2.6.2 FIXED POINTS

The RG equations for the velocity anisotropy  $\Phi$  are

$$\frac{d\Phi}{d\ell} = (C_1 - C_2)\Phi . \quad (2.89)$$

In the absence of the Higgs field,  $\Phi$  has a stable fixed point at  $\Phi = 0$ . The gauge field contribution to this equation has been calculated to leading order in  $\Phi$  [187], and we verify agreement with this result.

The evaluation of Eq. (2.89) is plotted in Fig. 2.10. A stable fixed point is found at

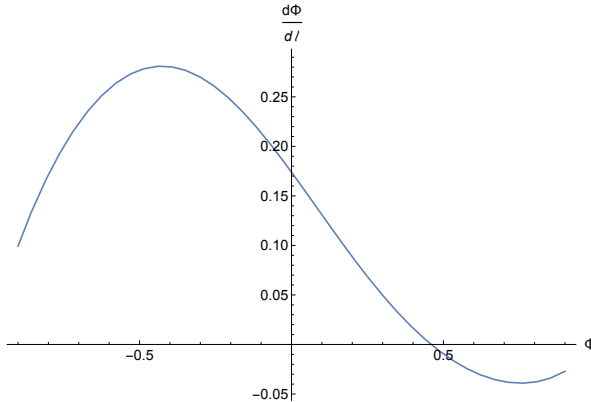


Figure 2.10: An evaluation of the RG flow of  $\Phi$ , showing a stable fixed point at  $\Phi_c \approx 0.46$ .

$\Phi_c \approx 0.45765$ . At this point, the dynamical critical exponent  $z$  is given by

$$z = 1 - C_0 + C_1 = 1 + \frac{0.225}{N_f^2} + \mathcal{O}(1/N_f^2). \quad (2.90)$$

Recall that when we derived this critical  $U(1) \rightarrow \mathbb{Z}_2$  theory as a component of a parent  $SU(2)$  theory, we made a gauge choice such that  $w\Phi < 0$ , where  $w$  is the coefficient of the symmetry-allowed cubic term,  $w\epsilon_{abc}\Phi_1^a\Phi_2^b\Phi_3^c$ . When  $\langle\Phi_3^a\rangle = \Phi\delta_{az}$ , we can diagonalize this term to yield a mass,  $w\Phi(\mathcal{H}^*\mathcal{H} - \mathcal{M}^*\mathcal{M})$ , where  $\mathcal{H}$  is the combination of  $\Phi_{1,2}^{x,y}$  given in Eq. 2.74 and  $\mathcal{M}$  is a charge-2 Higgs field of a similar form but with  $x \leftrightarrow y$ . If we assume  $w > 0$ ,  $\Phi < 0$ , then  $\mathcal{H}$  will become massless first, but the fixed-point value of  $\Phi$  gives a negative mass to  $\mathcal{M}$ , leading to a first-order transition driven by the condensation of  $\mathcal{M}$ . As a consequence, we must fix our parent  $SU(2)$  theory to have  $w < 0$  in order to yield a continuous transition. If we had made a gauge choice such that  $w\Phi > 0$ , then our theory would have been driven by the condensation of  $\mathcal{M}$  rather than  $\mathcal{H}$ ; this still leads to the gapless  $\mathbb{Z}_2$  spin liquid Z2Azz13, and all gauge-invariant observables at the critical point remain the same, although the sign of  $\Phi_c$  changes.

### 2.6.3 NÉEL AND VBS ORDER PARAMETER CORRECTIONS

We now calculate the vertex corrections to the Néel and VBS order parameters. These order parameters are given by fermion bilinears and can be identified based on the action of the microscopic square lattice symmetries on the fermions. The VBS order parameter is given

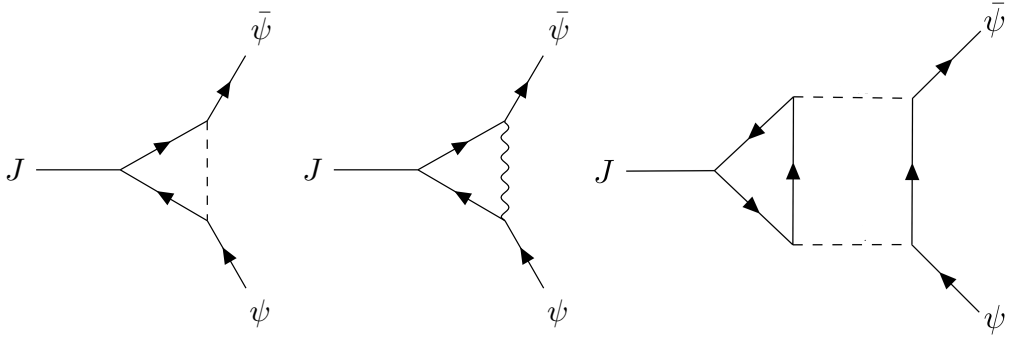


Figure 2.11: The  $\mathcal{O}(N_f^{-1})$  vertex corrections which contribute to the renormalization of the Néel and VBS order parameters. The order parameter receives corrections at one-loop order from the Higgs fields (left) and the gauge boson (center). An additional two-loop  $\mathcal{O}(N_f^{-1})$  contribution (right) is possible - the diagram shown involves two intermediate Higgs propagators, but additional diagrams with gauge propagators or mixed gauge/Higgs propagators are possible. These diagrams vanish exactly upon performing the trace over the internal fermion indices.

by the bilinears  $\bar{\psi}\mu^{z,x}\psi$ . As mentioned previously, our particular representation obfuscates the full SU(2) action of spin rotation symmetry; however, the U(1) subgroup generated by rotations around the  $z$ -axis is given by the global U(1) symmetry  $\psi \rightarrow e^{i\theta}\psi$  (recall that this is not the U(1) gauge symmetry, which acts as  $e^{i\theta\sigma^z}$ ). As a consequence, we focus on the  $z$ -component of the Néel order parameter, which is given by  $\bar{\psi}\mu^y\psi$ . The two-point correlation functions of these bilinears are obtained by coupling them to external sources  $J_{\text{VBS}}$ , Néel and calculating  $\mathcal{O}(N_f^{-1})$  vertex corrections, illustrated in Fig. 2.11. Of note are  $\mathcal{O}(N_f^{-1})$  two-loop corrections, the form of which were first found in Ref. [187]. These two-loop corrections to the Néel and VBS order parameters vanish in the pure staggered flux phase - this follows immediately from taking the trace over the internal fermion loop and noting that  $\text{Tr } \mu^i = 0$ . We verify that these diagrams remain zero upon the inclusion of both Higgs fields and velocity anisotropy, although this identity is less readily apparent.

We first outline the procedure from Ref. [199] for calculating the logarithmic corrections to the vertex functions. At zero external momenta, our one-loop vertex corrections schematically take the form

$$\Xi_i = \frac{1}{N_f} \int \frac{d^3 p}{(2\pi)^3} H_i(p) \mathcal{K}^3 \left( \frac{p^2}{\Lambda^2} \right) \quad (2.91)$$

where  $H_i(p)$ ,  $i = x, y, z$ , is a homogeneous function of  $p$  and illustrated in Fig. 2.11. The

index  $i$  indicates whether the  $J$  vertex includes a factor of  $\mu^{x,z}$  (VBS order parameter) or  $\mu^y$  (Néel order parameter). Once again, we can take the logarithmic derivative and remove the explicit cutoff dependence, leading to the equation

$$\Lambda \frac{d}{d\Lambda} \Xi_i = \frac{1}{8\pi^3 N_f} \int_0^{2\pi} d\phi \int_0^\pi \sin \theta d\theta H_i(\hat{p}) \equiv B_i \mu^i. \quad (2.92)$$

The  $B_i$ 's are not gauge-invariant by themselves, and must be combined with the self-energy to get a gauge-invariant quantity, which at the fixed-point value  $\Phi_c$  gives

$$\begin{aligned} \eta_{\text{VBS}} &= B_{x,z} + C_0 \approx 0.06468 N_f^{-1} + \mathcal{O}(N_f^{-2}), \\ \eta_{\text{Néel}} &= B_y + C_0 \approx -0.01634 N_f^{-1} + \mathcal{O}(N_f^{-2}). \end{aligned} \quad (2.93)$$

The Néel and VBS correlation functions in momentum space have the scaling form

$$\begin{aligned} G_{\text{Néel}}(k, \omega) &= G_{\text{Néel}}(ak, a^z \omega) a^{2\eta_{\text{Néel}} - 1}, \\ G_{\text{VBS}}(k, \omega) &= G_{\text{VBS}}(ak, a^z \omega) a^{2\eta_{\text{VBS}} - 1}. \end{aligned} \quad (2.94)$$

Making a Fourier transform to real space, the equal-time Néel and VBS correlators have the power law decay

$$\begin{aligned} G_{\text{Néel}}(r) &\sim \frac{1}{r^{3+z-2\eta_{\text{Néel}}}}, \\ G_{\text{VBS}}(r) &\sim \frac{1}{r^{3+z-2\eta_{\text{VBS}}}}. \end{aligned} \quad (2.95)$$

Note that both the anomalous dimensions for the Néel and VBS correlators are quite small. This is a rather surprising result and does not seem to be due to any particular small parameter. The magnitude of these anomalous dimensions do not decrease upon increasing the numerical precision of our integration, so we believe them to be small but not identically zero. We find that the gauge fluctuations generally enhance Néel and VBS correlations, whereas Higgs fluctuations suppress them - the combined result is the stated anomalous dimensions. As such, we cannot make a strong statement regarding which ordering the unstable U(1) phase will prefer, as neither the Néel nor VBS order parameter show exceptionally enhanced correlations. Higher-order corrections may show a clearer preference to either Néel or VBS

ordering.

#### 2.6.4 TREE-LEVEL EFFECT OF VELOCITY ANISOTROPY ON CORRELATION FUNCTIONS

As we have emphasized, one of the key features of this critical theory is that the emergent Lorentz invariance of the staggered flux phase is broken by the presence of critical Higgs fields, leading to a non-zero value of the symmetry-allowed velocity anisotropy term. This anisotropy term also has the effect of breaking the emergent  $SU(4)$  flavor symmetry. We refer to Ref. [187] for a more extensive study of the intertwining physical order parameters of the  $SU(4)$  theory and which relations hold in the presence of the velocity anisotropy - for our purposes, we note that the emergent  $SO(5) \subset SU(4)$  symmetry that relates the Néel and VBS order parameters is broken down to the microscopic  $SO(3) \times C_4$ . At tree-level, the scaling dimensions of the two order parameters are still the same, but the angular profile of their correlation functions are modified due to the velocity anisotropy. This lack of an emergent  $SO(2)$  spatial rotation symmetry in the Néel and VBS correlation functions may be useful as a numerical probe of the critical behavior, so we study the angular profile in more detail.

We analytically compute the spatial profile of the Néel order parameter at tree level. This calculation turns out to be feasible non-perturbatively in the velocity anisotropy  $\Phi$ . The VBS correlator is more difficult to study non-perturbatively in the velocity anisotropy, and we will later compute corrections to leading order in  $\Phi$ .

The two-point function in momentum space is given by, with  $Q(p)$  the fermion propagator,

$$\begin{aligned} G_{\text{Néel}}(k) &= - \int \frac{d^3 p}{(2\pi)^3} \text{Tr} [Q(p)\mu^y Q(p+k)\mu^y] \\ &= - \frac{2}{1-\Phi^2} \sum_{a=\pm} \int \frac{d^3 p}{(2\pi)^3} \frac{p_0(p_0+k_0) + ap_x(p_x+k_{x,a}) + ap_y(p_y+k_{y,a})}{p^2(p+k_\pm)^2} \\ &= \frac{1}{8(1-\Phi^2)} (|k_+| + |k_-|) . \end{aligned} \quad (2.96)$$

As before, we define  $k_\pm = (k_0, k_x \pm \Phi k_y, k_y \pm \Phi k_x)$ . The Fourier transform

$$\int \frac{d^3 k}{(2\pi)^3} e^{ik \cdot r} |k_\pm| \quad (2.97)$$

can be performed by a change of variables to give

$$G_{\text{N\'eel}}(r) \sim \sum_{a=\pm} f_a(\theta, \phi)^{-2} \frac{1}{r^4} \quad (2.98)$$

where we change to spherical coordinates,  $t = r \cos \theta$ ,  $x = r \sin \theta \sin \phi$ ,  $y = r \sin \theta \cos \phi$ , and

$$f_{\pm}(\theta, \phi) = 1 + \frac{\sin^2 \theta (\pm 2\Phi \sin 2\phi + 3\Phi^2 + \Phi^4)}{(1 - \Phi^2)^2}. \quad (2.99)$$

Therefore,

$$G_{\text{N\'eel}}(r) \sim g(\theta, \phi) \frac{1}{r^4} \quad (2.100)$$

where  $g(\theta, \phi) = 1/f_+(\theta, \phi)^2 + 1/f_-(\theta, \phi)^2$  is plotted in Fig. 2.12. We note the enhanced correlations of the N\'eel order parameter along the diagonals, which holds true for generic values of  $\Phi$ .

An analogous calculation of the VBS order parameter is less analytically tractable, as the one-loop integral cannot be made isotropic by a coordinate transformation. As such, we resort to a perturbative study of the velocity anisotropy. This gives

$$G_{\text{VBS}}(k) \sim |k| - \Phi^2 \left[ 2|k| + \frac{k_x^2 k_y^2 - k_0^2 k^2}{|k|^3} \right] + \mathcal{O}(\Phi^4) \quad (2.101)$$

in momentum space, or

$$G_{\text{VBS}}(r) \sim \frac{1}{r^4} [8 + \Phi^2 (\cos 2\theta (40 + 12 \cos 4\phi) + \cos 4\theta (6 - 3 \cos 4\phi) - 18 \cos 4\phi - 14)] \quad (2.102)$$

in real space. The equal-time VBS correlation function is plotted in Fig. 2.12, showing enhanced correlations along the cardinal directions. Note that the correlation function changes sign on the diagonals - this is an unusual feature, and would seemingly indicate lines in real space where the VBS correlator vanishes. This feature is also present in the  $\mathcal{O}(\Phi^2)$  corrections to the N\'eel correlator but ultimately vanishes in the non-perturbative result, so this result may only be an artifact of the perturbative expansion. Further details on this calculation can be found in Appendix A.8.

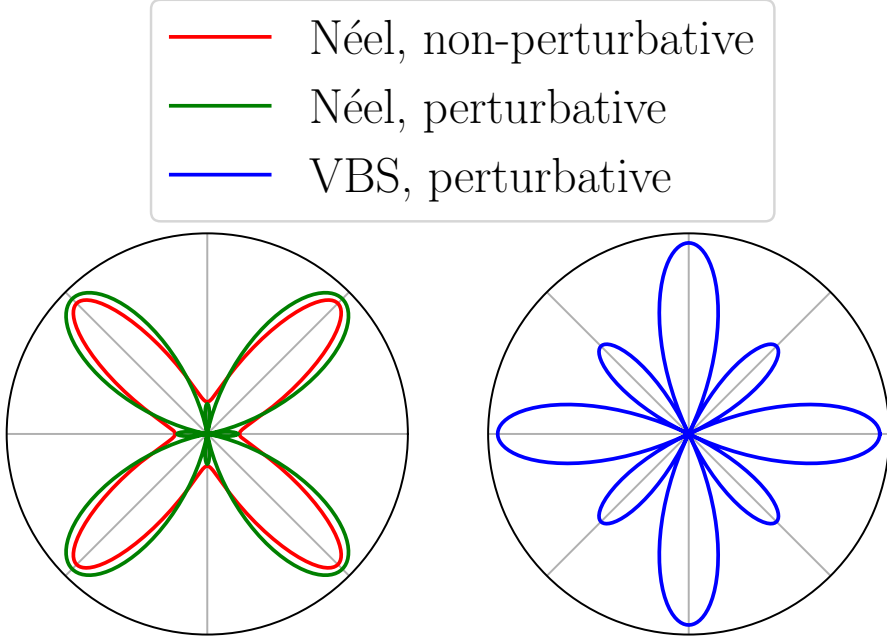


Figure 2.12: Plotted are the angular profiles of the equal-time Néel and VBS correlation functions in real space, at the fixed point value of velocity anisotropy  $\Phi_c$ . The Néel order parameter shows enhanced correlations along the diagonals, whereas the VBS correlations are more enhanced along the  $x$  and  $y$  directions. Note that we only plot the absolute value of the correlation function, and the signs of the perturbative Néel and VBS correlators flip when moving from the  $x$  and  $y$  axes to the diagonals. As this feature is not present in the non-perturbative Néel correlator, it is possible that this feature similarly vanishes at higher orders for the VBS correlator.

## 2.7 MONOPOLES

On the square lattice, there exists a monopole operator in the staggered flux phase - the *trivial monopole* - that is invariant under all microscopic symmetries, and hence is an allowed perturbation. To leading order, the scaling dimension of the monopole operator scales with the number of fermions and becomes irrelevant for  $N_f \geq 3$ . Hence, the staggered flux phase with  $N_f = 1$  by itself is unstable to monopole proliferation - this is the mechanism which we claim gives rise to ordered phases in the staggered flux phase, as condensation of the trivial monopole is conjectured to lead to a fermion chiral mass generation corresponding to either Néel or VBS order [459, 462]. Our calculations of the critical theory rely on the assumption that the presence of massless scalar fields screens monopoles and renders them irrelevant at the

critical point. Here, we draw attention to an additional contribution to the monopole scaling dimension, which is the non-zero anisotropy in the spinon dispersion. Prior calculations of monopole scaling dimensions in  $\text{QED}_3$  assume a Lorentz-invariant action for the fermions, which is natural in pure  $\text{QED}_3$  given that velocity anisotropy terms are irrelevant in a  $1/N_f$  expansion. However, as we have shown, the presence of critical Higgs fields can give rise to a non-zero velocity anisotropy at the critical point. An important question is whether this anisotropy increases or decreases the monopole scaling dimension. In contrast with the direct modification arising from the critical fields, which is  $\mathcal{O}(1)$ , the effect of the anisotropy on the monopole scaling dimension is  $\mathcal{O}(N_f)$ . Such a modification, if calculated perturbatively in  $\Phi$ , arises at  $\mathcal{O}(\Phi^2)$  - this is still an appreciable shift given the relatively large anisotropy  $\Phi_c \approx 0.46$ . Previous works have studied the effects of a spin Hall mass on the monopole scaling dimension [119, 120], although this perturbation is more tractable as the spin Hall mass is diagonal in the basis of spinor monopole harmonics. In Appendix A.9, we outline the structure of a perturbative calculation for calculating the  $\mathcal{O}(\Phi^2)$  corrections to the monopole scaling dimension. An important observation which makes this calculation tractable is that, while the saddle-point monopole gauge configuration will not take the form of the rotationally-invariant Dirac monopole, corrections to the scaling dimension arising from this difference only arise at higher orders in  $\Phi$ ; hence, to lowest non-trivial order, one can assume a Dirac monopole background. This calculation ultimately yields a divergent summation of terms involving Wigner 3- $j$  symbols; we leave for future work further study of how to properly regularize this calculation.

Additionally, we briefly comment on the relation between this velocity anisotropy and the monopole quantum numbers. Prior studies on the effects of a spin Hall mass [119, 120] have found that the presence of such a term induces a spin polarization on the monopoles. Each fermion flavor has a zero mode in the presence of a monopole, and half of these zero modes must be filled in order to maintain gauge neutrality of the monopole. The presence of a spin Hall mass polarizes these zero modes, which in turn causes a splitting in the scaling dimension of the monopoles, with the most-relevant monopole being spin polarized. One may wonder whether a similar valley polarization can arise due to our velocity anisotropy term due to the presence of a  $\mu^y$  in the anisotropy; however, we check that the first-order energy splitting

of the fermion zero modes due to the velocity anisotropy vanishes. Higher-order corrections including corrections from Higgs and gauge fluctuations will in general break the six-fold degeneracy of monopole scaling dimensions; in particular, the monopoles with Néel and VBS quantum numbers will have different scaling dimensions, which may cause a preference towards a particular type of symmetry-breaking in the staggered flux phase. Further study of the spectrum of monopoles at this critical point may be useful for determining the IR fate of the proximate staggered flux phase - for now, we simply note that this behavior is more complicated than a simple valley polarization of the monopoles.

## 2.8 CONCLUSIONS

Building upon the results of recent numerical studies [140, 290, 342, 505], we have proposed resolutions of long-standing controversies connected to theories of the cuprates: the phases of the frustrated square lattice spin  $S = 1/2$  antiferromagnets, and the nature of deconfined criticality in such models. Deconfined criticality expresses the low energy physics in terms of fractionalized degrees of freedom and emergent gauge fields, which can enter various confining states with possible broken symmetries on either or both sides of the critical point. Although there are several well-established examples, the transition between Néel and VBS states in square lattice antiferromagnets [389–391, 416] has been of particular interest. One formulation of this deconfined critical point is a version of QCD<sub>3</sub>, quantum chromodynamics in 2+1 dimensions: a SU(2) gauge theory with 2 flavors of 2-component massless Dirac fermions, each carrying a fundamental color charge. This theory is dual to a SO(5) non-linear sigma model with a Wess-Zumino-Witten term [436, 477, 500]. There is now significant numerical evidence that such a conformal field theory (CFT) does not exist, although there is likely a nearby ‘complex’ CFT [164, 165, 182, 299, 301, 332, 506]. This leaves open the fate of a physical model with a Hermitian Hamiltonian, such as the  $J_1$ - $J_2$  antiferromagnet on the square lattice, between the Néel and VBS states. Here we have presented a theory in which the putative QCD<sub>3</sub> CFT is resolved into an intermediate stable gapless phase with  $\mathbb{Z}_2$  topological order and gapless Dirac fermions [245, 435, 511]. The intermediate  $\mathbb{Z}_2$  spin liquid is flanked by two proposed deconfined critical points, neither of which is a CFT, or even invariant under

Lorentz transformations. The absence of Lorentz symmetry permits several novel phenomena, including the appearance of dangerously irrelevant couplings and logarithm-squared renormalizations, which can be tested in numerical studies. All of these phases and critical points are described by extending QCD<sub>3</sub> with 3 real adjoint Higgs fields. The couplings of these Higgs fields are tightly constrained by the transformations of QCD<sub>3</sub> under the symmetries of the underlying square lattice antiferromagnet, and an analysis of these symmetries occupy a significant portion of this paper.

Our main results can be summarized in the context of the mean-field phase diagram in Fig. 2.2 obtained from the SU(2) gauge theory with 3 adjoint Higgs field  $\Phi_{1,2,3}^a$  in Eq. (2.37). This mean field theory yields 3 spin liquids, with deconfined SU(2), U(1), and  $\mathbb{Z}_2$  gauge fields. We assume that the spin liquids with continuous gauge symmetries confine, except at possible deconfined critical transitions to the  $\mathbb{Z}_2$  spin liquid. This phase diagram maps onto the  $J_1$ - $J_2$  model along the trajectory of the dotted blue line, and our proposed deconfined critical theories are at the boundaries between the mean field SU(2) and  $\mathbb{Z}_2$  spin liquids, and the U(1) and  $\mathbb{Z}_2$  spin liquids.

The numerical evidence for the confinement of the SU(2)  $\pi$ -flux spin liquid was reviewed in Section 2.1. This confining state should have either Néel or VBS order [500], and Ref. [480] argued by comparing to bosonic spinon theories that it should be the Néel state. The structure of the critical theory from such a confining state to the gapless  $\mathbb{Z}_2$  spin liquid was presented in Section 2.4, and we found some unusual  $\log^2$  corrections to both the Néel and VBS critical correlators. From the geometry of the mean field phase diagrams in Fig. 2.2, and the numerical studies on the square lattice antiferromagnet noted in Fig. 2.1, it is then natural to propose that the U(1) staggered flux spin liquid confines to the VBS state. The critical U(1) gauge theory for the boundary between the U(1) and  $\mathbb{Z}_2$  spin liquid was presented in Section 2.5, and this has no  $\log^2$  terms. We also note that the  $\log^2$  correlators in Eqs. (2.71) and (2.72) show a faster decay of the Néel order than the VBS order, which might be evidence that the SU(2) critical theory is proximate to the VBS state rather than the Néel state, which would reverse the direction of the arrow in Fig. 2.2.

Irrespective of the assignment of the Néel or VBS confining states to the SU(2) or U(1) spin liquids in Fig. 2.2, we expect any direct phase boundary between the Néel and VBS states to

be a first order transition. This follows from the numerical studies [182, 301, 332] noted in Section 2.1.

Our critical SU(2) gauge theory for the  $S = 1/2$  square lattice antiferromagnet has massless 2-component Dirac fermions with 2 flavors and 2 colors, and real critical Higgs fields with 2 flavors and 3 colors, and is shown in Eq. (2.45). This derives from a theory for the  $\pi$ -flux to gapless  $\mathbb{Z}_2$  spin liquid transition proposed by Ran and Wen [381, 384], and includes an additional ‘dangerously irrelevant’ coupling  $K$ , which is the coefficient of a spatial gradient term in the Higgs fields. We analyzed this theory along the lines of the  $1/N_f$  expansion of Ref. [199] (the case of interest to us here is  $N_f = 1$ ). We found that the theory with  $K = 0$  has infrared divergencies that arise from the highly anisotropic spatial structure of the Higgs correlations, which is in turn a consequence of the non-Lorentz invariant Yukawa couplings between the Higgs fields and the fermions. So even though the coupling  $K$  is formally irrelevant, it must be included to understand the long-distance and long-time behavior of the theory *i.e.* the coupling  $K$  is dangerously irrelevant. We found that the coupling  $K$  leads to leading logarithm-squared corrections to various correlators, such as those in Eqs. (2.70) and (2.71) for the correlations of the Néel and VBS order parameters; Appendix A.2 showed how these corrections are exponentiated in a renormalization group analysis, lead to Eq. (2.72). We also note that the logarithm-squared term was absent in the contributions to the dynamic critical exponent,  $z$ , and we computed a non-Lorentz-invariant value for  $z$  in Eq. (2.64).

The critical U(1) gauge theory for the  $S = 1/2$  square lattice antiferromagnet was discussed in Section 2.5. It has massless 2-component Dirac fermions with 4 flavors and  $\pm 1$  U(1) gauge charges, and a single complex critical Higgs fields with  $\pm 2$  U(1) gauge charge. The fixed point of this theory yields a stable anisotropic dispersion for the fermionic spinons, which modifies the angular profile of both Néel and VBS correlation functions. This anisotropy also has non-trivial modifications to the scaling dimensions of the monopole operators of the critical theory, although we leave a full calculation of this shift to future work.

It would be useful to examine numerical studies of the square lattice antiferromagnet for logarithmic violations of scaling, Lorentz invariance, and SO(5) symmetry, and compare to our predictions. In particular, we note the violations of scaling observed in Ref. [443], although for a different square lattice antiferromagnet.

Finally, we note that gapless  $\mathbb{Z}_2$  spin liquid studied is an attractive candidate for the ancilla model of doped antiferromagnets [340, 561, 562], as it can realize a stable state in the second ancilla layer for the pseudogap state.

As we were completing this paper, we became aware of some related work:

- (i) Superconductivity has been observed [162, 220] in the doped  $J_1$ - $J_2$  model; doping the gapless  $\mathbb{Z}_2$  spin liquid is known to be a natural route to  $d$ -wave superconductivity [212, 437].
- (ii) Yang *et al.* [542] have detected a gapless spin liquid phase next to the Néel phase on the Shastry-Sutherland model, which is obtained from the  $J_1$ - $J_2$  model by removing 3/4 of the  $J_2$  bonds.

*Alright, fellow physicists, let's ditch the textbook magnets and plunge into the turbulent waters of quantum spin liquids (QSLs). Forget your neat lines of arrows - these guys are the anti-ferromagnetic free spirits, perpetually swirling in a quantum ballet of their own making.*

ChatGPT, when I asked it to write a talk on this

# 3

## Sign-problem-free effective models of triangular lattice antiferromagnetism

### 3.1 INTRODUCTION

*Quantum spin liquids* [413, 426] (QSLs) are exotic phases of matter which arise when strong frustration in a quantum spin system prevents the emergence of a conventional long-range ordered phase at zero temperature. Among the various platforms proposed to realize these unconventional phases, the geometric frustration present in triangular lattice Heisenberg antiferromagnets make them a natural candidate for QSL behavior. Experimental realizations in Yb-based compounds [48, 49, 99, 112, 279, 351, 385, 386, 429, 445, 534, 564, 565] as well as organic compounds [211, 448, 449, 539] have yielded promising results, including a lack of magnetic order and a continuum of low-energy spin excitations suggestive of fractionalized spinon degrees of freedom. Although the ground state of the spin  $S = 1/2$  Heisenberg antiferromagnet on the triangular lattice with only nearest-neighbor interactions is known to host conventional coplanar magnetic order [42, 69, 200], the strength is reduced substantially by quantum fluctuations, and only a small amount of additional frustration from next-nearest-neighbor interactions is necessary to destroy the magnetic order [195, 207, 232, 345, 407, 517, 575]. The

nature of the non-magnetic phase has been the source of much debate, both in these idealized lattice models and in aforementioned experimental realizations. In particular, there have been conflicting results on whether the fractionalized spinon excitations are gapped, have gapless Dirac nodes, or form a spinon Fermi surface.

Parton constructions provide a robust theoretical technique for describing a large class of phases of frustrated antiferromagnets, as well as phase transitions between them. The spin-1/2 operator  $\vec{S}_i$  can formally be expressed as a bilinear operator in terms of either bosonic or fermionic spinons, with the constraint of one spinon per site enforced by the introduction of gauge fields. When the gauge field is deconfined, the system is a quantum spin liquid with fractionalized spin-1/2 spinon excitations. Various ordered phases, such as antiferromagnetism and valence bond solid (VBS) ordering, can be understood as instabilities to this deconfined phase.

Using this parton construction as a starting point, effective lattice models for describing the possible phases of quantum antiferromagnets can be deduced by minimally coupling bosonic spinons to emergent gauge fields. These effective models have the advantage of being more amenable to numerical simulations, as demonstrated in [355], where an effective lattice model describing quantum antiferromagnets on the square lattice with easy-plane U(1) symmetry was simulated numerically using Monte Carlo techniques. Large-scale simulations of the non-compact  $\text{CP}^1$  model, conjectured to describe the deconfined quantum critical point separating Néel and VBS order on the square lattice, have also been studied [45, 79, 262, 335] through Monte Carlo sampling. Outside the context of quantum magnetism, much progress has been made in developing numerical methods for simulating bosonic matter coupled to gauge fields [106, 128].

Following this approach, we present the results of a Monte Carlo simulation of an effective model of SU(2) antiferromagnetism on the triangular lattice. This effective model is derived using a bosonic spinon representation of the spin-1/2 degrees of freedom, where a mean-field analysis [408] yields a gapped QSL phase with  $\mathbb{Z}_2$  gauge fluctuations and an emergent O(4) symmetry that rotates between the two low-energy bosonic spinon excitations. Our effective model which captures the QSL phase as well as ordered phases arising from either spinon condensation (coplanar magnetic order) or gauge confinement (non-magnetic VBS order) is

that of an O(4) vector field coupled to an *odd*  $\mathbb{Z}_2$  gauge field [143, 217, 419, 435]. The odd nature of this  $\mathbb{Z}_2$  gauge field is a consequence of the half-integer spin, and is essential in preventing the existence of a trivial disordered phase. The odd gauge field also leads to the appearance of a Berry phase in the action, which prohibits a direct Monte Carlo sampling of the partition function due to a sign problem. One of the primary contributions of this work is to present a sign-problem-free representation of this model, which is applicable to

The primary result of this work - the phase diagram as a function of boson hopping  $J$  and gauge action  $K_d$  (to be precisely defined later) - is given in Fig. 3.1. All three phases - QSL, magnetic order, and VBS order - are present, with the valence bond ordering being of the  $\sqrt{12} \times \sqrt{12}$  form, consistent with the pure gauge theory ( $J = 0$ ) limit, which has been studied extensively [92, 318, 320, 378, 379]. Of note is a direct transition between the VBS and magnetic phases, which has been argued [219, 458, 463, 517] to be described by an emergent quantum electrodynamics with  $N_f = 4$  flavors of massless Dirac fermions. Our numerical results give some evidence for a first-order transition, although for reasons we will describe later, accurate Monte Carlo simulations of this model pose a number of challenges and we do not believe a continuous transition can be definitively ruled out.

The structure of this paper is as follows. In Section 3.2, we make explicit the connection between our effective model and the microscopic spin degrees of freedom. In Section 3.3, we describe the duality transformations that render the effective model sign-problem-free. Although these techniques are of general interest, we stress to the reader that the results of the Monte Carlo simulations, presented in 3.4, may be understood independent of the duality transformations.

### 3.2 CONNECTION BETWEEN EFFECTIVE MODEL AND QUANTUM MAGNETISM

We first outline a derivation of the effective model to be studied, and analyze its possible phases. Our starting point is the spin-1/2 Heisenberg antiferromagnet on the triangular lattice,

$$H = \sum_{ij} J_{ij} \vec{S}_i \cdot \vec{S}_j, \quad (3.1)$$

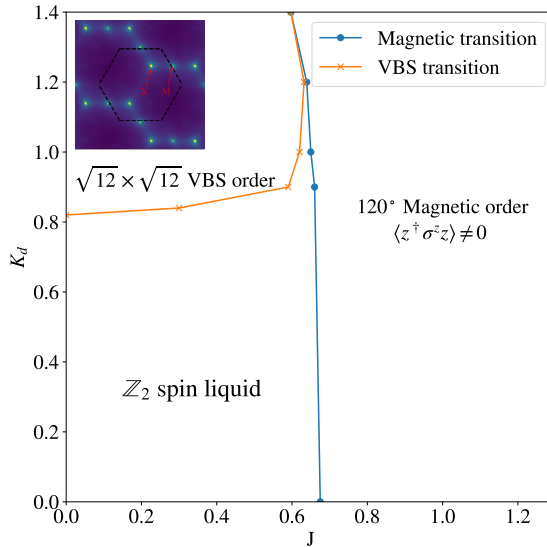


Figure 3.1: We plot the phase diagram of an  $O(4)$  vector model coupled to an odd  $\mathbb{Z}_2$  gauge field on a triangular lattice, as determined through classical Monte Carlo simulations. The model exhibits three phases, which correspond to a quantum spin liquid,  $\sqrt{12} \times \sqrt{12}$  VBS, and coplanar antimagnetic order when regarded as an effective model of spin-1/2 Heisenberg antiferromagnetism on the triangular lattice. Algorithmic limitations discussed later prevent clear establishment of the location of the magnetic phase transition.

with  $J_{ij}$  short-ranged antiferromagnetic interactions. The relation between the  $SU(2)$  triangular lattice antiferromagnet and a theory of bosonic spinons coupled to a  $\mathbb{Z}_2$  gauge field was first derived in [408] - by generalizing the  $SU(2)$  theory to  $USp(2M)$  and proceeding via a combined large- $M$  and large- $S$  expansion, the model becomes analytically tractable. For completeness, we provide a derivation of this in Appendix B.1, and summarize the main points here:

- The bosonic spinon representation introduces a dynamical  $U(1)$  gauge field. The gapless photon excitations arising from these gauge fluctuations can present an obstacle for realizing a stable spin liquid phase. However, the saddle-point solutions for the gauge field - justified in a large- $M, S$  expansion - spontaneously break the  $U(1)$  fluctuations down to  $\mathbb{Z}_2$ , where the gauge excitations (visons) are gapped.
- The bosonic spinon dispersion in the presence of this saddle-point solution has two minima at non-zero momenta. Writing an effective action in terms of these low-energy spinons, the lowest-order quartic interaction terms allowed by symmetry preserves an

$O(4)$  symmetry that rotates between the two complex bosons, which contains both the  $SO(3)$  spin rotation and  $120^\circ$  lattice rotation symmetry.

From these points, can write down an effective model for triangular lattice antiferromagnetism, which we will show can support magnetic order, VBS order, and spin liquids. This model consists of an  $O(4)$  vector on each site of the triangular lattice, which parameterizes the bosonic spinon fluctuations. These degrees of freedom are minimally coupled to a  $\mathbb{Z}_2$  gauge field. Importantly, this is an *odd*  $\mathbb{Z}_2$  gauge field, which arises from a background spinon density of one spinon per site. The odd nature of this gauge theory prevents the confining phase from being a trivial gapped phase, in agreement with LSM theorems that prohibits such a phase for half-integer spins.

This model supports three types of phases. When the  $O(4)$  spinons are uncondensed and the gauge field is deconfined, the system is a gapped  $\mathbb{Z}_2$  spin liquid with topological order. Condensing the bosons spontaneously breaks the  $O(4)$  symmetry, which in turn breaks both the  $SO(3)$  spin rotation symmetry and  $120^\circ$  lattice rotation symmetry. Because of the  $\mathbb{Z}_2$  gauge redundancy, the ground state manifold (GSM) for this order is  $S^3/\mathbb{Z}_2 = SO(3)$  - in agreement with the  $SO(3)$  GSM of the  $120^\circ$  magnetic order. The confining phase of the  $\mathbb{Z}_2$  gauge field preserves spin rotation symmetry, but due to the odd nature, breaks lattice symmetries rather than being trivial - it is a valence bond solid phase. The pattern of lattice symmetry breaking is known in the pure gauge theory limit with nearest-neighbor interactions to be a  $\sqrt{12} \times \sqrt{12}$  order [320], with a 12-site unit cell, although effective longer-range interactions generated by the spinons can lead to different symmetry breaking patterns [455].

We study this model using Monte Carlo techniques. The partition function for this two-dimensional quantum model on the triangular lattice can be mapped to an equivalent classical model on a three-dimensional stacked triangular lattice,

$$\begin{aligned} \mathcal{Z} &= \sum_{s_{j,j+\hat{\mu}}=\pm 1} \prod_j \int dz_{j\alpha} \delta \left( \sum_\alpha |z_{j\alpha}^2| - 1 \right) \left[ \prod_j s_{j,j+\tau} \right] \exp(-H[z_\alpha, s]) \\ H[z_\alpha, s] &= -\frac{J}{2} \sum_{\langle j, \mu \rangle} s_{j,j+\hat{\mu}} (z_{j,\alpha}^* z_{j+\hat{\mu},\alpha} + \text{c.c}) - K \sum_{\triangle \square} \prod_{\triangle \square} s_{j,j+\hat{\mu}}, \end{aligned} \quad (3.2)$$

The two bosonic spinons  $z_{j\alpha}$ ,  $\alpha = 1, 2$  are minimally coupled to a classical  $\mathbb{Z}_2$  gauge field

$s_{j,j+\hat{\mu}}$  living on the links of the stacked triangular lattice. The odd nature of the gauge field is captured by the Berry phase term  $\prod_j s_{j,j+\tau}$ . Note that this Berry phase takes on values  $\pm 1$ , and hence the partition function as written in Eq. 3.2 is not amenable to Monte Carlo simulations. As such, we must perform a series of transformations to obtain a sign-problem-free representation, where the partition function is expressed as a sum over purely positive weights.

### 3.3 SIGN-PROBLEM-FREE MAPPING

In this section, we describe the mapping from the partition function in the previous section to one consisting only of positive weights. This is a very general mapping, valid for any  $O(2n)$  vector model with integer  $n$  on a large class of lattices, including the stacked triangular lattice relevant to our study of quantum antiferromagnetism on the 2D triangular lattice. However, the general approach does not differ substantially from the simplest case, which is an  $O(2)$  model on the 3D cubic lattice. As the notation required to state the mapping in its most general form is rather complex, we find it most clear to first describe the sign-free mapping of an  $O(2)$  model coupled to an odd  $\mathbb{Z}_2$  gauge field on a 3D cubic lattice, and then subsequently describe the modifications necessary for alternate lattices or for general  $O(2n)$  models. The mapping in this simpler limit was first carried out in [355, 415], but using a different approach that does not as easily generalize to  $O(2n)$  models. We outline a more generalizable mapping which also more carefully treats subtleties involving periodic boundary conditions. The initial steps of this mapping follow along the same lines as well-known particle-vortex dualities [103, 227, 363], which map an  $O(2)$  model to a dual  $O(2)$  model coupled to an emergent  $U(1)$  gauge field. In this language, our  $\mathbb{Z}_2$  gauge field couples to the emergent  $U(1)$  gauge field via a mutual Chern-Simons term - we demonstrate that this allows for the  $\mathbb{Z}_2$  gauge field to be integrated out, yielding a sign-problem-free representation.

### 3.3.1 O(2) MODEL

Our model is described by the partition function

$$\begin{aligned} \mathcal{Z} = & \sum_{\{s_{j,j+\hat{\mu}}=\pm 1\}} \int \prod_j d\theta_j \exp \left( K \sum_{\square} \prod_{\square} s_{j,j+\hat{\mu}} \right. \\ & \left. + \frac{4}{g} \sum_{j,\hat{\mu}} s_{j,j+\hat{\mu}} \cos \left( \frac{\Delta_\mu \theta_j}{2} \right) - i \frac{\pi}{2} \sum_j (1 - s_{j,j+\hat{\mu}}) \right), \end{aligned} \quad (3.3)$$

with, as in the previous section,  $\Delta_\mu$  denoting the discrete lattice derivative, and  $\prod_{\square}$  denoting the product of spins around a plaquette. This is an XY model whose degrees of freedom are angular variables  $\theta_j$ , coupled to an odd  $\mathbb{Z}_2$  gauge field. The final term, corresponding to the Berry phase of the background boson filling, gives negative weights to the summation, thereby preventing sampling through Monte Carlo techniques.

Our first step is to rewrite the action for  $\theta_j$  using the identity

$$e^{sA \cos \theta} \propto \sum_{p=-\infty}^{\infty} e^{ip(\theta + \pi \frac{1-s}{2})} I_p(A) \quad (3.4)$$

where  $A > 0$ ,  $s = \pm 1$ , and  $I_p(A)$  is the modified Bessel function of the first kind. The asymptotic behavior of  $I_p(A)$  as  $A \rightarrow \infty$  contains the more standard action for  $p$  when the Villain approximation is used,

$$I_p(A \gg 1) \propto \exp \left[ -\frac{p^2}{2A} \right]. \quad (3.5)$$

For the O(2) model, this approximation does not alter the phase diagram, so we will use this for notational simplicity and to connect to prior work. However, the following mapping can be carried out while keeping the full Bessel function explicit, which will be necessary for general O( $2n$ ) models as an analogous approximation breaks the O( $2n$ ) symmetry down to O(2) $^{\otimes n}$ .

We apply this identity to each instance of  $s_{j,j+\hat{\mu}} \cos \left( \frac{\Delta_\mu \theta_j}{2} \right)$ , thereby introducing an integer-valued field  $p_\mu$  on each of the links. This allows  $\theta_j$  to be integrated out at the cost of imposing a divergence-free constraint  $\Delta_\mu p_\mu = 0$ . This divergence-free constraint implies that  $p_\mu$  must form closed integer-valued “current loops.” This requirement can be made explicit by writing

$p_\mu$  as the curl of a height field,  $h_{\bar{j}\mu}$  living on the links of the dual lattice. This allows for the creation of local current loops - for periodic boundary conditions, one must also include the possibility of non-contractible loops that cannot be expressed as the curl of a height field. Assuming we have periodic boundary conditions in all three directions, it is sufficient to pick a representative non-contractible current loop in each direction,  $(w_{j\mu}^x, w_{j\mu}^y, w_{j\mu}^\tau)$  and express

$$p_{j\mu} \equiv \epsilon_{\mu\nu\lambda} \Delta_\nu h_{\bar{j}\lambda} + \vec{n} \cdot \vec{w}_{j\mu} \quad (3.6)$$

where  $\vec{n} \equiv (n_x, n_y, n_\tau)$  is an integer-valued vector specifying the winding number of the current in each of the three dimensions. This representation introduces additional degrees of freedom, as one may always shift  $h_{\bar{j}\mu}$  by the divergence of a scalar field without changing the current configuration. In the language of particle-vortex dualities, this reflects the emergent U(1) gauge redundancy. These additional degrees of freedom are crucial to our sign-free mapping. Our partition function at this point is

$$\begin{aligned} \mathcal{Z} = & \sum_{\{s_{j,j+\hat{\mu}}=\pm 1\}} \sum_{h_{\bar{j}\mu}=-\infty}^{\infty} \sum_{n_i=-\infty}^{\infty} \exp \left( K \sum_{\square} \prod_{\square} s_{j,j+\hat{\mu}} \right. \\ & \left. - \frac{g}{8} \sum_{j,\hat{\mu}} p_{j\mu}^2 + i \frac{\pi}{2} \sum_{j,\hat{\mu}} p_{j\mu} (1 - s_{j,j+\hat{\mu}}) - i \frac{\pi}{2} \sum_j (1 - s_{j,j+\hat{\tau}}) \right). \end{aligned} \quad (3.7)$$

In this form, the Berry phase term can be absorbed by a shift  $h_{\bar{j}\mu} \rightarrow h_{\bar{j}\mu} + h_{\bar{j}\mu}^0$ , where  $\epsilon_{\mu\nu\lambda} \Delta_\nu h_{\bar{j}\lambda}^0 = \delta_{\mu,\tau}$ .

We now address the coupling between the current  $p_{j\mu}$  and the gauge field, which corresponds to a mutual Chern-Simons term in the vortex representation. For the local current loops expressible in terms of the height field, we use the identity

$$\exp \left[ i\pi \sum_{j,\hat{\mu}} \epsilon_{\mu\nu\lambda} \Delta_\nu h_{\bar{j}\lambda} \frac{1 - s_{j,j+\hat{\mu}}}{2} \right] = \exp \left[ i\pi \sum_{j,\hat{\mu}} h_{\bar{j}\mu} \frac{1 - \prod_{\square} s_{j,j+\hat{\mu}}}{2} \right], \quad (3.8)$$

which can be verified by expanding out the curl and collecting terms proportional to  $h_{\bar{j}\mu}$ . To address the coupling to non-contractible current loops, we first note that after performing the transformation in Eq. 3.8, the coupling to the non-contractible current loops is the only place

where the gauge field appears explicitly - all other terms in the partition function only depend on the plaquette flux  $\prod_{\square} s_{j,j+\hat{\mu}}$ . We argue that if any component of  $\vec{n}$  is odd, the contribution to the partition function vanishes. This is because for an arbitrary configuration and for a choice of direction  $\hat{\nu}$ , one can make a “large” gauge transformation consisting of flipping all  $s_{j,j+\hat{\nu}}$  spins that intersect a plane tangent to  $\hat{\nu}$ . This keeps all the plaquette fluxes invariant but flips the sign of a single  $s_{j,j+\hat{\nu}}$  that intersects the non-contractible current loop in the  $\hat{\nu}$  direction. If the winding number in this direction is odd, the new configuration contributes to the partition function with the same magnitude but opposite sign as the original one, leading to an exact cancellation. We therefore restrict our sum over  $n_i$  to be even, in which case the coupling to the gauge field drops out entirely as it always contributes a factor of 1. If one interprets the current loops as bosonic worldlines, this constraint is simply the statement that bosons must be created in pairs and sectors with odd numbers of bosons are unphysical.

We now integrate out the gauge field. Note that only the plaquette flux  $\frac{1-\prod_{\square} s_{j,j+\hat{\mu}}}{2} \equiv \Phi_{\bar{j},\mu}$  appears in the partition function (the dual link  $\bar{j},\mu$  uniquely labels a plaquette). Although normally incorrect, we claim that it is valid to perform an independent summation over all possible plaquette flux values  $\Phi_{\bar{j},\mu} = 0, 1$  on each plaquette. This is not true in general, as there is a non-trivial constraint on the possible values of flux - starting from the flux-free configuration with  $s_{j,j+\hat{\mu}} = 1$ ,  $\Phi_{\bar{j},\mu} = 0$ , gauge fluctuations can only change the divergence of  $\Phi$  at any dual site by multiples of two, i.e.,

$$\nabla_{\mu} \Phi_{\bar{j},\mu} = 0 \bmod 2. \quad (3.9)$$

The key observation is that the redundant degrees of freedom introduced in the height field representation for  $p_{j,\mu}$  serve as Lagrange multipliers to dynamically enforce Eq. 3.9. As a consequence, one can directly perform the summation over all gauge field configurations. To see how this constraint is enforced, let us make the redundant degrees of freedom explicit by writing  $h_{\bar{j},\mu} = \tilde{h}_{\bar{j},\mu} + \Delta_{\mu} f_{\bar{j}}$ , where we perform the summation over both distinct current loop configurations  $\tilde{h}$  and the redundant degrees of freedom  $f$ . The coupling of  $f$  to the gauge

field is

$$\exp \left[ i\pi \sum_{j\mu} \Delta_\mu f_{\bar{j}} \Phi_{\bar{j},\mu} \right] = \exp \left[ -i\pi \sum_{j\mu} f_{\bar{j}} \Delta_\mu \Phi_{\bar{j}\mu} \right]. \quad (3.10)$$

Performing a summation over  $f_{\bar{j}}$  will impose the constraint Eq. 3.9.

Integrating out the gauge field gives the final sign-free representation of our partition function,

$$\mathcal{Z} = \sum_{h_{\bar{j}\mu}=-\infty}^{\infty} \sum_{n_i=-\infty}^{\infty} \exp \left( -\frac{g}{8} \sum_{j,\mu} p_{j\mu}^2 + K_d \sum_{j,\mu} \varepsilon_{\bar{j},\bar{j}+\mu} \sigma_{\bar{j},\bar{j}+\mu} \right) \quad (3.11)$$

where

$$\begin{aligned} \tanh K_d &= e^{-2K}, \\ \sigma_{\bar{j},\bar{j}+\mu} &= 1 - 2(h_{\bar{j}\mu} \bmod 2), \end{aligned} \quad (3.12)$$

$p_{j\mu}$  is defined in terms of  $h_{\bar{j}\mu}$  and  $\vec{n}$  as in Eq. 3.6, and  $\varepsilon$  is a *fixed* field taking values  $\pm 1$ , with the constraint that the product of  $\varepsilon$  around any temporal (spatial) plaquette is  $+1$  ( $-1$ ). The factor of  $\varepsilon$  arises because of the background height field  $h^0$ , which in turn is a consequence of the Berry phase. Because of this, the model in the limit  $g \rightarrow \infty$  (i.e. when the O(2) coupling drops out and we recover a pure  $\mathbb{Z}_2$  gauge field) reduces down to a 3D Ising model with frustration on the xy-planes, which is dual to an odd  $\mathbb{Z}_2$  gauge theory, rather than a frustration-free Ising model dual to an even  $\mathbb{Z}_2$  gauge theory.

This theory has a simple interpretation, illustrated in Fig. 3.2. One can interpret the field  $\sigma_{\bar{j},\bar{j}+\mu}$  as a  $\mathbb{Z}_2$  flux variable living on the plaquettes of the lattice, and the relationship between  $p$  and  $\sigma$  translates into the constraint that any odd current loop must form the perimeter of an open “surface” of flux. Closed surfaces correspond to height field configurations with vanishing curl. For an *even*  $\mathbb{Z}_2$  gauge theory, the coupling constant  $K_d$  has the simple interpretation of a surface tension, with an energy cost proportional to the surface area. When only closed surfaces are allowed, these surfaces also have the interpretation of domain walls of the dual Ising model. For an odd  $\mathbb{Z}_2$  gauge theory, the background field  $\varepsilon$  introduces frustration - plaquette fluxes cost positive or negative energy depending on the location, and it is no longer possible to energetically satisfy all plaquettes using only closed surfaces.

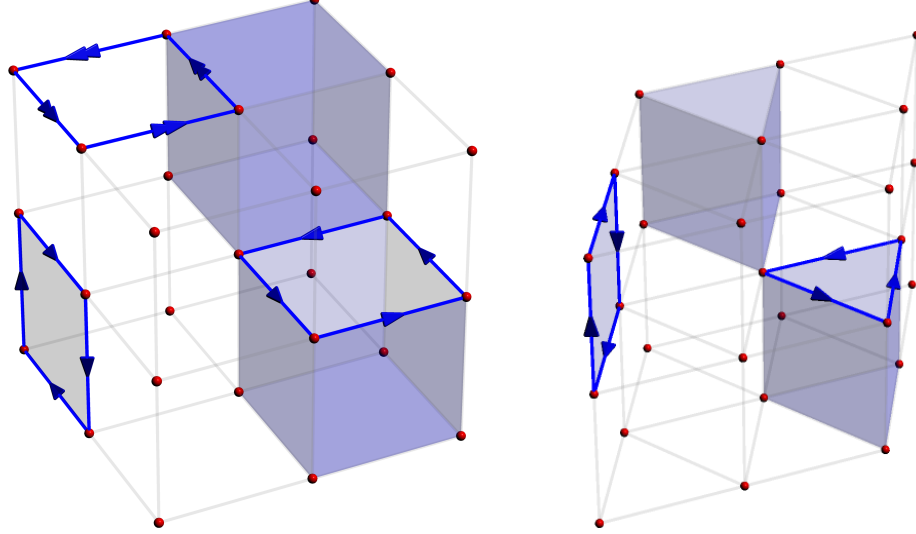


Figure 3.2: The dual representation of an  $O(2)$  model coupled to  $\mathbb{Z}_2$  gauge field can be expressed in terms of integer-valued current loops and  $\mathbb{Z}_2$  membranes of flux, with the constraint that odd-valued current loops must form the boundary of an open  $\mathbb{Z}_2$  surface. The effect of a Berry phase is to introduce frustration in the surface action. This dual mapping is suitable for both the square lattice (left) as well as the triangular lattice (right).

### 3.3.2 GENERALIZATION TO $O(2n)$ MODELS

We now show how this sign-free mapping lifts to a model where our degrees of freedom consist of  $O(2n)$  spins, with  $n \geq 1$ . While particle-vortex dualities do not have a generalization to non-Abelian  $O(2n)$  models, one may think of this mapping as a sort of particle-vortex duality applied to an Abelian  $O(2)^{\otimes n}$  subgroup. The full non-Abelian  $O(2n)$  symmetry is preserved in virtue of working with an explicit lattice action and restricting oneself to exact transformations that necessarily keep the partition function invariant.

An  $n$ -component complex vector  $z_{j\alpha}$ ,  $1 \leq \alpha \leq n$ , lives on each site, with the constraint that  $\sum_\alpha |z_{j\alpha}|^2 = 1$ . Our partition function is

$$\begin{aligned} \mathcal{Z} = & \sum_{\{s_{j,j+\hat{\mu}}=\pm 1\}} \int \prod_{j,\alpha} dz_{j\alpha} \delta(\sum_\alpha |z_{j\alpha}|^2 - 1) \exp \left( K \sum_{\square} \prod_{\square} s_{j,j+\hat{\mu}} \right. \\ & \left. + J \sum_{j,\hat{\mu},\alpha} s_{j,j+\hat{\mu}} (z_{j\alpha}^* z_{j+\mu,\alpha} + \text{c.c}) - i \frac{\pi}{2} \sum_j (1 - s_{j,j+\hat{\tau}}) \right), \end{aligned} \quad (3.13)$$

Our starting point is a representation  $z_j$  that makes connection to our previous mapping,  $z_{j\alpha} \equiv r_{j\alpha} e^{i\theta_{j\alpha}}$ . Note that in this representation, the magnitude fields  $r_{j\alpha}$  are gauge-neutral,

and only the phase variables  $\theta_{j\alpha}$  are affected by gauge transformations. In terms of these variables,

$$\begin{aligned} \mathcal{Z} = & \sum_{\{s_{j,j+\hat{\mu}}=\pm 1\}} \prod_{j,\alpha} \int_0^{2\pi} d\theta_{j\alpha} \int_0^1 r_{j\alpha} dr_{j\alpha} \delta\left(\sum_{\alpha} |r_{j\alpha}|^2 - 1\right) \exp\left(K \sum_{\square} \prod_{\square} s_{j,j+\hat{\mu}} \right. \\ & \left. + J \sum_{j,\hat{\mu},\alpha} s_{j,j+\hat{\mu}} r_{j,\alpha} r_{j+\mu,\alpha} \cos(\Delta_{\mu} \theta_{j\alpha}) - i \frac{\pi}{2} \sum_j (1 - s_{j,j+\hat{\mu}})\right), \end{aligned} \quad (3.14)$$

As before, we use the identity Eq. 3.4, except we introduce  $n$  different integer-valued fields  $p_{j\mu\alpha}$  on each link. Making the Villain approximation is no longer appropriate in this case - doing so breaks the full  $O(2n)$  symmetry down to  $n$  copies of  $O(2)$ , as the coefficient in front of the cosine term is no longer just a coupling constant but rather the dynamical field  $r_{j,\alpha} r_{j+\mu,\alpha}$ . As such, we keep the Bessel functions  $I_{p_{j,\alpha,\mu}}(J r_{j,\alpha} r_{j+\mu,\alpha})$  explicit in our rewriting. Such an approach has previously been used to study  $O(2n)$  models at finite density [128] - this current loop representation also serves to cure the sign problem present when one introduces a non-zero chemical potential. This representation obfuscates the full  $O(2n)$  symmetry, but retains an  $S_n$  subset coming from permutations of the  $\alpha$  indices.

The rest of the mapping proceeds in a similar manner. We introduce  $n$  height field representations  $h_{\bar{j}\mu\alpha}$ , with the plaquette flux  $\Phi_{\bar{j}\mu}$  coupling to the *total* height field  $\sum_{\alpha} h_{\bar{j}\mu\alpha}$ . The Berry phase term can be absorbed by a shift in any of the  $n$  height fields - the choice is arbitrary and does not change the final representation.

Integrating out the gauge field gives the final form of our partition function,

$$\begin{aligned} \mathcal{Z} = & \sum_{h_{\bar{j},\alpha,\mu}=-\infty}^{\infty} \prod_{j\alpha} \int_0^1 r_{j,\alpha} dr_{j,\alpha} \delta\left(\sum_{\alpha} r_{j,\alpha}^2 - 1\right) \exp(-H[r_{\alpha}, h_{\alpha}]) \\ H[r_{\alpha}, h_{\alpha}] = & \sum_{\langle j,\mu \rangle} \left[ -\ln I_{p_{j,\alpha,\mu}}(J r_{j,\alpha} r_{j+\hat{\mu},\alpha}) + K_d \varepsilon_{\bar{j},\mu} \sigma_{\bar{j},\mu} \right]. \end{aligned} \quad (3.15)$$

where

$$\sigma_{\bar{j},\mu} = 1 - 2 \left( \sum_{\alpha} h_{\bar{j},\alpha,\mu} \right) \bmod 2 \quad (3.16)$$

$$e^{-2K_d} = \tanh K$$

and  $\varepsilon$  is a static field taking values  $\pm 1$ , such that the product of  $\varepsilon$  around each spatial

(temporal) dual plaquette is  $-1$  ( $+1$ ).

### 3.3.3 GENERALIZATION TO ALTERNATE GEOMETRIES

In our previous sections, we described this sign-free mapping on a cubic lattice, primarily for the simplicity in notation that the lattice provides. However, we emphasize that this mapping holds for more general lattices, including the stacked triangular lattice relevant to our current interest, as well as a stacked kagomé lattice. This mapping is easiest on lattices with even coordination, where integrating out the  $\theta$  fields yields a familiar divergence-free constraint on  $p$ . In Fig. 3.3, we show this for a stacked triangular lattice, where the constraint is  $\Delta_\mu p_{j\mu} = 0$ ,  $\mu = \hat{e}_1, \hat{e}_2, \hat{e}_3, \hat{\tau}$ . and can again be satisfied by a height field representation. These height fields couple to the  $\mathbb{Z}_2$  gauge flux in an identical manner, and inclusion of the Berry phase term manifests itself as a constant field  $\varepsilon_{\bar{j},\bar{j}+\mu}$  living on the dual lattice (stacked hexagonal lattice), with the constraint that the product around any spatial (temporal) plaquette is  $-1$  ( $+1$ ). An example configuration is shown in Fig. 3.3. While the dual lattice has odd coordination and a dual bond cannot technically be specified by the indices  $(\bar{j}, \mu)$ , we will continue to use the notation  $h_{\bar{j}\mu}$  for simplicity as this subtlety will not be relevant.

The lack of a bipartite lattice raises an important point in our duality mapping. Because our original lattice is not bipartite, the dual lattice does not have a natural definition of divergence - this can be seen from the stacked hexagonal lattice, dual to the triangular lattice, which has odd coordination so no symmetric definition of “ingoing” and “outgoing” bonds can be made. As a consequence, one must make sense of the use of dual lattice divergences in our derivation, which is employed in Eq. 3.9. Important to this is the  $\mathbb{Z}_2$  nature of our gauge field - as a consequence, all divergences appear in equations that are only sensitive to whether the resulting expression is even or odd. Hence, the sign structure of the divergence operator on the dual lattice is irrelevant, as a different sign structure only changes the divergence by an even amount.

We may also verify our method of integrating out the  $\mathbb{Z}_2$  gauge field without making any reference to a divergence. Our “naive” procedure of integrating out the  $\mathbb{Z}_2$  gauge field by independently summing over all possible plaquette flux values  $\Phi_{\bar{j},\mu} = 0, 1$  is valid so long

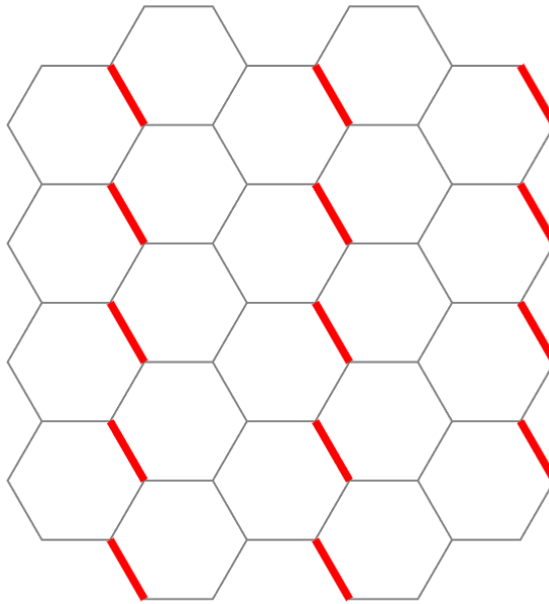


Figure 3.3: The presence of a Berry phase gives rise to frustration in the effective Ising model on the dual lattice. For our theory defined on a triangular lattice, we show one possible tiling of the dual (hexagonal lattice) lattice, where the field  $\varepsilon_{\bar{j},\bar{j}+\mu} = -1$  on red links, and 1 otherwise. This is chosen so that the product around any spatial plaquette gives  $-1$ .

as unphysical flux configurations are dynamically cancelled out by the redundant degrees of freedom introduced by introducing a height field representation. The key feature we need is some notion of a “gauge” transformation  $h_{\bar{j}\mu} \rightarrow h_{\bar{j}\mu} + \Delta_\mu f_{\bar{j}}$  that can leave the  $p_{j\mu}$  current configuration invariant but change the parity of  $h_{\bar{j}\mu}$  along an arbitrary closed surface. Unphysical flux configurations correspond to having an odd total flux along some closed surface, and for these configurations, performing a gauge transformation flips the sign of its contribution to the partition function and hence cancels out the unphysical configuration. For a triangular lattice, defining such a transformation in terms of the divergence of a scalar field on the dual lattice is not straightforward - however, one can easily verify that such a transformation is still possible by creating a current loop on each plaquette of the closed surface, with the orientations chosen in such away that all currents cancel out. The smallest such surface involves five plaquettes, and as such, there is no symmetric way of distributing the shifts  $h_{\bar{j}\mu} \rightarrow h_{\bar{j}\mu} \pm 1$ . Crucially, the  $\mathbb{Z}_2$  gauge field only sees the *parity* of  $h_{\bar{j}\mu}$ , so this subtlety is not an issue.

For lattices with odd coordination, such as the hexagonal lattice, one must take extra care with dealing with the divergence-free constraint on the original lattice. While we believe that

our duality mapping will likely be applicable to these models as well, we defer a more thorough analysis for future work.

### 3.4 RESULTS FROM MONTE CARLO SIMULATIONS

We now present numerical results of the simulation of an O(4) vector model coupled to an odd  $\mathbb{Z}_2$  gauge field on the triangular lattice. The Hamiltonian is defined in Eq. 3.15 for two species of current loops. This model has several simple limits:

- $K_d = 0$ : in this limit, the gauge field becomes static and our model reduces to that of an O(4) model, albeit in an unconventional current loop representation. The presence of a  $\mathbb{Z}_2$  gauge field still has the effect of restricting our observables to be gauge-invariant, and hence the critical theory for the boson condensation is given by O(4)\*, which possesses the same critical exponents as the O(4) universality class but for which differences can be found in terms of the excitation spectrum for a finite-size system [515]. This difference is reflected in our dual theory by the topological constraint that the winding number of current loops must be even.
- $K_d = \infty$ : in this limit, confinement of the gauge field prevents individual bosonic excitations. The relevant degrees of freedom are the gauge-invariant SO(3) order parameters  $z_i^\dagger \vec{\sigma} z_i$ . For an even  $\mathbb{Z}_2$  gauge field, this limit would be described by a non-linear  $\sigma$  model, and would support an ordered and disordered phases. This trivial disordered phase is ruled out in our case from the LSM theorem, and the simple non-linear  $\sigma$  model picture is modified for an odd  $\mathbb{Z}_2$  gauge field by the influence of a Berry phase on vortices of the SO(3) order parameter. We expect that this limit will always give an ordered phase, which we will verify in future numerical studies.
- $J = 0$ : in this limit, we expect to recover an odd  $\mathbb{Z}_2$  gauge theory. In our dual formulation, current loop excitations cost infinite energy and our state space is restricted to configurations with  $p_{j\mu\alpha} = 0$ . Within this space, we have a single  $\mathbb{Z}_2$  degree of freedom residing on each dual site ( $\bar{j}$ ), the flipping of which at site  $\bar{k}$  corresponds to the shift  $h_{\bar{j}\mu\alpha} \rightarrow h_{\bar{j}\mu\alpha} + \Delta_\mu f_{\bar{j}\alpha}$ , with  $f_{\bar{j}\alpha} = \delta_{\bar{j}\bar{k}}$  (performed on a random choice of  $\alpha$ ). Since

the action is only sensitive to the parity of  $\sum_{\alpha} h_{\bar{j}\mu\alpha}$ , this is effectively a  $\mathbb{Z}_2$  degree of freedom. Our model then reduces down to a frustrated Ising model defined on the dual lattice - dual to the odd  $\mathbb{Z}_2$  gauge theory - which displays a transition at a critical value of  $K_d$  from a disordered to an ordered phase. In terms of the original spin degrees of freedom, this is a transition from the gapped  $\mathbb{Z}_2$  spin liquid to a VBS phase. Semiclassical analyses [320] predict that this transition is in the O(4) universality class, and this prediction is supported by quantum dimer model simulations [541].

We analyze the Hamiltonian in Eq. 3.15, for  $n = 2$  and defined on an  $L \times L \times L$  stacked triangular lattice, by sampling configurations  $\{r_{j\alpha}, h_{\bar{j}\mu\alpha}\}$ . Simulations are done for  $L = 12, 24$ , and  $36$  - keeping the linear system size a multiple of 12 is necessary to accommodate the large unit cell of the  $\sqrt{12} \times \sqrt{12}$  VBS order. Movement through the configuration space is accomplished by four types of local moves, which are accepted with a probability determined by the Metropolis algorithm::

- Updates of the radial variables  $r_{\alpha}$  on a random site.
- Shifts of one of the two random height fields.  $h_{\bar{j}\mu\alpha} \rightarrow h_{\bar{j}\mu\alpha} \pm 1$  on a random dual bond
- Shifts of the random height fields on two neighboring temporal dual bonds. This is done to assist in thermalization, as it removes intermediate energy barriers required to annihilate certain current loop configurations. The utility of this move is a consequence of the triangular lattice geometry.
- On a random dual site, shifts of all the neighboring height fields by  $\pm 1$ , chosen in a way such that the current loops  $p_{j\mu\alpha}$  remain invariant. This effectively constitutes a single-site spin flip of the Ising model that resides on the dual lattice.

We also use several global updates, which we will describe in the subsequent sections.

To measure the breaking of the O(4) symmetry (corresponding to coplanar antiferromagnetism), we define the order parameter  $s = \sum_j (r_{j1}^2 - r_{j2}^2)$ . This transforms under the adjoint representation of the O(4) symmetry - in terms of the original complex spinons  $\vec{z}_j$ , this is the quantity  $\sum_j \vec{z}_j^\dagger \sigma^z \vec{z}_j$  - although it is only this element that remains local under our set of duality transformations described in the previous section. This is a simplification of O( $2n$ ) models

for  $n > 1$ ; for an O(2) model in this representation, no such local order parameter exists, and symmetry breaking must be measured through the winding number of non-contractible loops.

We use the Binder cumulant

$$U_s \equiv 1 - \frac{\langle s^4 \rangle}{3\langle s^2 \rangle^2} \quad (3.17)$$

to identify the location of the magnetic phase transition. This quantity approaches unity in the ordered phase (when  $\langle s^2 \rangle^2 = \langle s^4 \rangle$ ) and zero in the disordered phase (when  $s$  is a random Gaussian variable with mean zero,  $\langle s^4 \rangle = 3\langle s^2 \rangle^2$ ). Within the framework of our classical model, the mechanism for the symmetry breaking of  $s$  for large  $J$  is as follows. As is the case for an O(2) model, we have an entropic proliferation of current loops at large  $J$ . Here, we have two flavors of current loops. A current loop of flavor  $\alpha = 1$  induces a polarization of the  $r_j$  variables along that current loop such that it is energetically preferable to have  $r_{j1} > r_{j2}$ , and analogously for an  $\alpha = 2$  current loop. Frustration results from current loops of different flavors intersecting on the same site, and hence it becomes energetically favorable for a single flavor of current loop to coherently proliferate. As we will demonstrate, the complexity of this multi-step mechanism for symmetry breaking leads to large autocorrelation time for  $s$  in the ordered phase, as it becomes difficult for  $s$  to switch sign once current loops have proliferated.

Non-magnetic order resulting from gauge field confinement is reflected by lattice symmetry breaking of the gauge-invariant bond frustration,  $\varepsilon_{\bar{j},\mu} \sigma_{\bar{j},\mu}$ . To make connection with prior work studying triangular lattice VBS order [234], we associate an unsatisfied dual bond ( $\epsilon_{\bar{j},\mu} \sigma_{\bar{j},\mu} = 1$ ) with the presence of a valence bond  $P_{j,\mu} = 1$  on the spatial bond below  $(\bar{j}, \mu)$ . With this identification, we can calculate the momentum-dependent susceptibility

$$\chi_{\text{VBS}}(\mathbf{k}) = \frac{1}{L^3} \sum_{ij} e^{i\mathbf{k} \cdot (\mathbf{r}_i - \mathbf{r}_j)} \langle P_{i,\hat{e}_1} P_{j,\hat{e}_1} \rangle \quad (3.18)$$

where we choose to probe the bond structure on the  $\hat{e}_1$  bond. Note that  $\mathbf{k}$  and  $\mathbf{r}_{i,j}$  are two-dimensional vectors specifying only the spatial index. The presence of  $\sqrt{12} \times \sqrt{12}$  VBS order is reflected in sharp peaks at the  $X$  and  $M$  points in the Brillouin zone. We define the quantity  $R_{\text{VBS}}^M = 1 - \frac{\chi_{\text{VBS}}(M + a2\pi/L)}{\chi_{\text{VBS}}(M)}$ , which approaches unity in the VBS ordered phase where the Bragg peak becomes infinitely sharp as  $L \rightarrow \infty$ , but goes to zero in a phase when

the height and width of the Bragg peak saturate with system size. The crossing of  $R_{\text{VBS}}^M$  for different system sizes is universal and serves as a probe of the location of the VBS phase transition. We also present results for an analogous quantity  $R_{\text{VBS}}^X$  which measures the height of the Bragg peak at the X point.

### 3.4.1 PURE O(4) MODEL LIMIT

We first present results for the pure O(4) model limit ( $K_d = 0$ ). In this limit, we can compare our numerical results to a classical Monte Carlo simulation of an O(4) nonlinear  $\sigma$  model. Note that while gauge fluctuations drop out entirely, there is still a non-trivial gauge constraint in our Hilbert space, such that only gauge-invariant observables such as spinon bilinears are non-zero. The critical theory of the phase transition is hence O(4)\*, which possesses the same critical exponents as the O(4) universality class but for which differences can be found in terms of the excitation spectrum for a finite-size system [515]. This difference is reflected in our dual theory by the topological constraint that the winding number of current loops must be even.

Recall that for the simpler case of an O(2) model, where are dual theory consists only of a single type of integer-valued current loops, classical Monte Carlo simulations which only involve local moves are insufficient for measuring the order parameter for the O(2) transition given by a non-zero average winding number of the current loops. These non-contractible loops cannot be obtained from local deformations and must either be generated through a large global update proposal - acceptance of which becomes exponentially unlikely as the system size increases - or through the use of worm algorithms [370, 371], where current loops are generated by starting with an “open” current string and letting the ends move with suitably-defined probabilities until the two ends meet and form a closed loop. Our generalization to an O(4) model naively avoids the need for worm algorithms, as our dual theory retains access to a local order parameter  $s$  in addition to the winding number. However, we find that the autocorrelation time of  $s$  becomes intractably large, on the order of  $10^5$  global sweeps for  $L = 24$ , near the critical point and into the ordered phase when only local updates are used. This is because, even if one is restricted to the zero winding number sector, large fluctuations

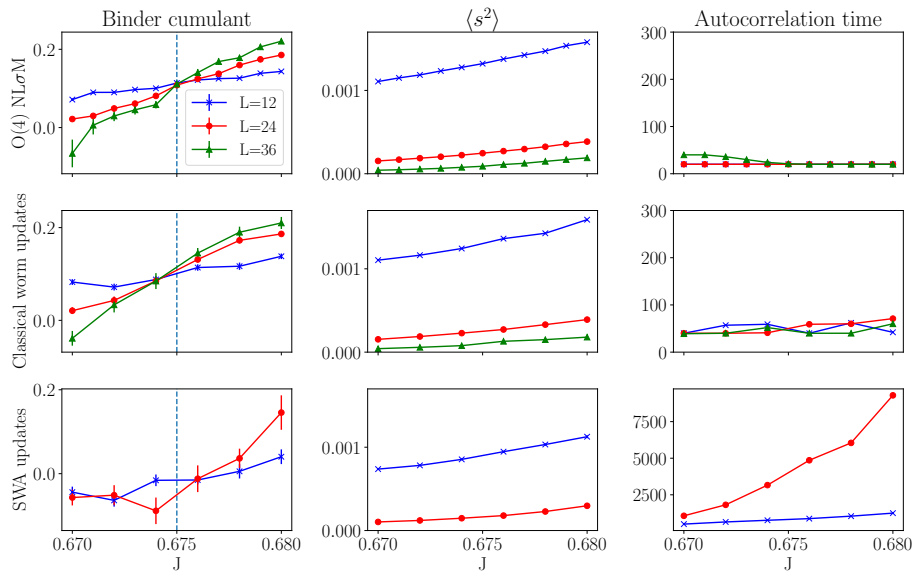


Figure 3.4: We compare results of numerically simulating the bosonic  $O(4)^*$  transition while neglecting gauge fluctuations ( $K_d = 0$ ). Direct simulation of an  $O(4)$  non-linear  $\sigma$  model (top row) accurately determines the critical point  $J_c \approx 0.675$  while retaining a small autocorrelation time due to global Wolff updates. A dual current loop representation with classical worm updates (middle row) has comparable performance. After restricting to “surface worm” updates (bottom row), which are the updates that can be generalized to include gauge fluctuations, we observe a diverging autocorrelation time as we enter the ordered phase and a decrease in accuracy of the Binder cumulant, although an estimate of the location of the critical point can still be inferred.

in the total current are necessary to induce fluctuations in  $s$ . The acceptance rate for the creation of local current loops is quite small, on the order of 1-2% near criticality. Combined with the geometric inefficiency of local current loop updates - creation and annihilation of large current loops require a number of local moves proportional to its area, despite the energy only scaling with the perimeter - leads to this diverging autocorrelation time. Generalizing the classical worm algorithm to account for gauge fluctuations is non-trivial, as one has the constraint that odd current loops must form the boundaries of surfaces of gauge flux. While it is straightforward to apply a classical worm algorithm to a gauge-invariant *pair* of current loops, we find that this, along with an implementation of a “surface worm algorithm” (SWA) proposed in [106] and summarized in Appendix B.3, are insufficient for reducing the autocorrelation time to a tractable magnitude. This is because the propagation of a *pair* of current loops is much more energetically costly than a single current. An appropriate worm algorithm in the limit of weak gauge fluctuations would be to propagate a worm as normal, calculate the energy cost of an enclosed surface (ideally the minimal surface) once the worm has terminated, and accept the worm with a probability determined by the energy cost of the surface. However, implementing this algorithm is challenging as it requires an efficient way of finding a candidate surface once the worm has been grown. We leave further development of this approach to future work.

In Fig. 3.4, we present the Binder cumulant, the order parameter  $\langle s^2 \rangle$ , and the autocorrelation time from direct simulations of an O(4) NL $\sigma$ M as compared to simulations in the dual theory, using either a classical worm algorithm (only appropriate in the  $K_d = 0$  limit) or a SWA. While our simulation with a SWA is able to identify the location of the critical point  $J_c \approx 0.675$  with reasonable accuracy, the large autocorrelation time prevents us from both going to larger system sizes and obtaining high precision results for the Binder cumulant.

### 3.4.2 PURE GAUGE THEORY LIMIT

We also consider the pure gauge theory limit ( $J \rightarrow 0$ ), which is dual to an Ising model with spatial frustration. In this limit, all current loops cost infinite energy, and our state space is restricted to configurations with  $p_{j\mu\alpha} = 0$ . Within this space, we have a single  $\mathbb{Z}_2$  degree of freedom residing on each dual site ( $\bar{j}$ ), the flipping of which at site  $\bar{k}$  corresponds to the shift

$h_{\bar{j}\mu\alpha} \rightarrow h_{\bar{j}\mu\alpha} + \Delta_\mu f_{\bar{j}\alpha}$ , with  $f_{\bar{j}\alpha} = \delta_{\bar{j}\bar{k}}$  (performed on a random choice of  $\alpha$ ). Since the action is only sensitive to the parity of  $\sum_\alpha h_{\bar{j}\mu\alpha}$ , this is effectively a  $\mathbb{Z}_2$  degree of freedom. Our model then reduces down to a frustrated Ising model defined on the dual (hexagonal) lattice, the simulation of which is carried out using local spin flips and a global cluster update similar to the one described in [320]. We define our cluster update explicitly in Appendix B.4. Note that in contrast to the pure O(4) model limit where we provided a numerical comparison with results from an O(4) NL $\sigma$ M simulation, we do not provide an analogous comparison here as the degrees of freedom in our model explicitly corresponds to that of a frustrated Ising model.

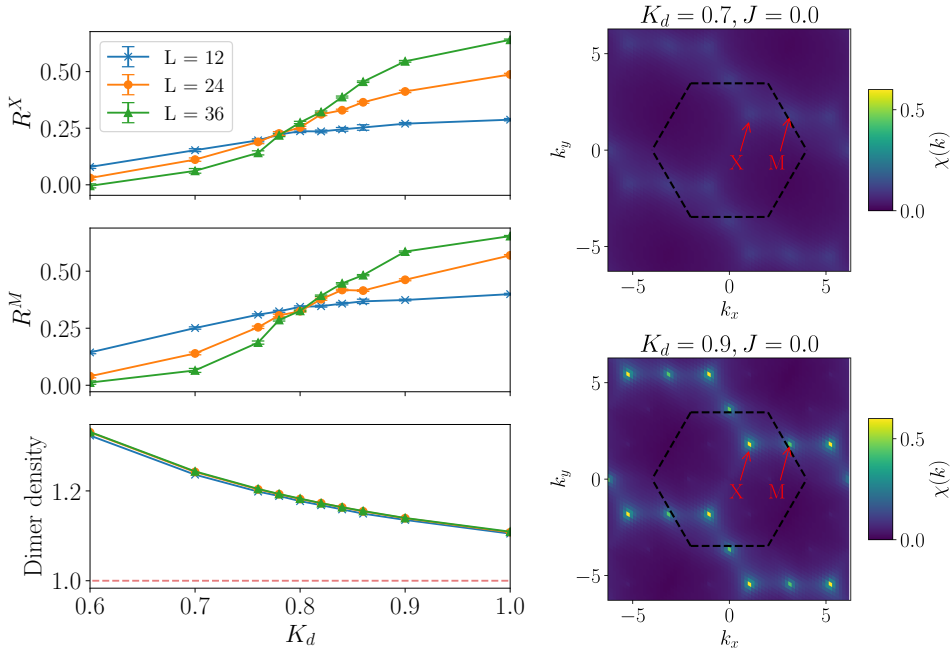


Figure 3.5: We present results of simulating an odd  $\mathbb{Z}_2$  gauge theory on a triangular lattice, which displays a transition from a deconfined phase for  $K_d < K_d^c$  and a VBS phase with  $\sqrt{12} \times \sqrt{12}$  order for  $K_d > K_d^c$ , with  $K_c \approx 0.82$ . The equal-time dimer correlation function, plotted here for  $L = 36$ , displays sharp peaks at the  $M$  and  $X$  points in the ordered phase.

The phase diagram of the fully frustrated quantum Ising model on the hexagonal lattice has been analyzed theoretically [92, 319], although no numerical studies have been conducted to our knowledge aside from results at a single point in the ordered phase in [320]. In the limit of small transverse field, this is equivalent to a triangular lattice quantum dimer model with interaction strength  $V$  and hopping  $t$  at the point  $V/t = 0$ . These models have been studied much more extensively [378, 379] and the existence of a  $\sqrt{12} \times \sqrt{12}$  phase has been

well-established. We note that path integral Monte Carlo simulations of this two dimensional quantum Ising model in terms of a three dimensional classical model pose much more challenges due to the inherent discretization errors not present in dimer model simulations. In particular, we find that an isotropic scaling of the spatial and temporal couplings  $K_d^s, K_d^\tau$  leads to very weak ordering. This is because for a system size finite in the temporal direction, increasing  $K_d^\tau$  simultaneously increases the antiferromagnetic interaction strength as well as the effective temperature of the quantum model. In order to obtain a clear signature of the phase transition, we parameterize the couplings as

$$\begin{aligned} K_d^s &= K_d \\ K_d^\tau &= \min \left\{ K_d, \frac{\ln 2}{2} \right\} \end{aligned} \tag{3.19}$$

in order to prevent  $K_d^\tau$  from getting too large; the particular value of  $\frac{\ln 2}{2}$  is chosen such that the quantum temperature (in units of the transverse field) is equal to the inverse length of the system size in the temporal direction.

We present numerical results in Fig. 3.5. We identify a transition into a  $\sqrt{12} \times \sqrt{12}$  ordered phase at  $K_d \approx 0.82$ , in surprisingly good agreement with semiclassical analyses [319] of the quantum Ising model which predict  $K_d = \frac{2}{\sqrt{6}} \approx 0.816$ . We also plot the “dimer density,” defined as the number of unsatisfied spatial bonds per site. This should approach the minimum value of one and hence reduce to the  $V/t = 0$  quantum dimer model in the  $K_d \rightarrow \infty$  limit, which agrees with our numerical results.

### 3.4.3 ANTIFERROMAGNET TO VBS TRANSITION

Having established the validity of our sign-problem-free model in the limit where either the spinons or visons are static, we now analyze the transition from VBS to antiferromagnetic order, obtained by starting in the VBS phase and increasing  $J$  until the proliferation of current loops destroys the effective dual Ising model. This is plotted across two slices,  $K_d = 1.4$  in Fig. 3.6 and  $K_d = 1.2$  in Fig. 3.7. We find that the loss of VBS order closely coincides with growing antiferromagnetic order, indicating a direct transition. However, we emphasize that the difficulties present in establishing the antiferromagnetic transition for  $K_d = 0$  also

persist for  $K_d > 0$  - the autocorrelation time for the antiferromagnetic order parameter  $s$  quickly diverges as we approach the magnetically ordered phase, which prohibits us from reaching larger system sizes. As a consequence, while we observe some signatures of a first-order transition - including the Binder cumulant dipping below zero near the phase transition, along with a sharper upturn in  $s^2$  which may evolve into a discontinuous jump for larger system sizes - our numerical results currently cannot definitely establish the nature of this transition.

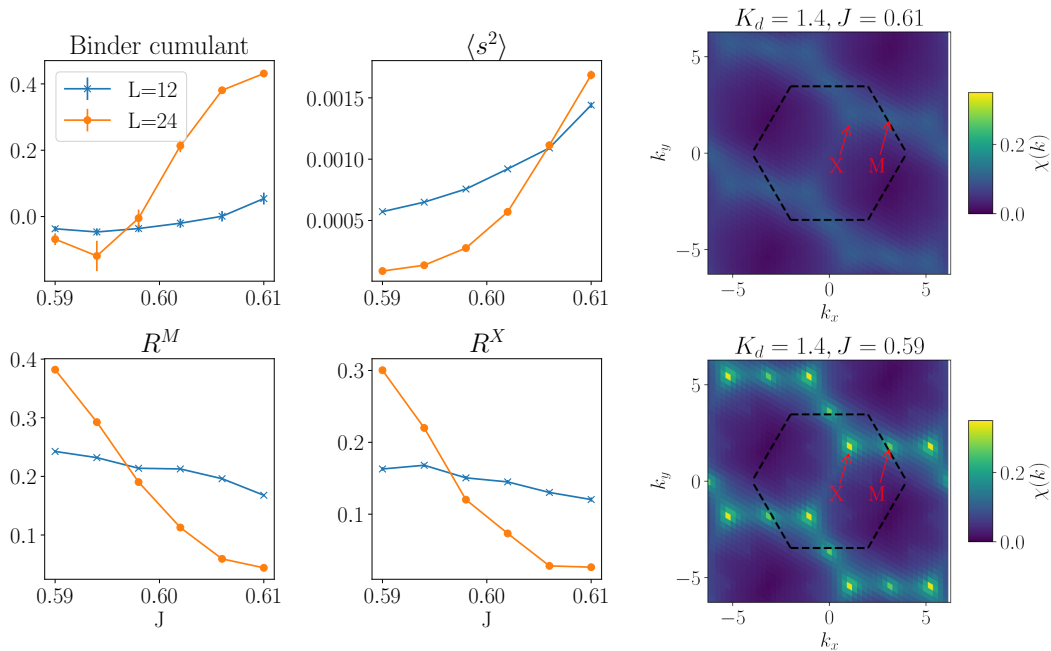


Figure 3.6: We present measurements of the antiferromagnetic order parameter  $s$  and its Binder cumulant, along with measures of the VBS order at the  $X$  and  $M$  points in the Brillouin zone, at fixed gauge coupling  $K_d = 1.4$  as a function of  $J$ . The crossing of the Binder cumulant at  $J_c \approx 0.6$  closely coincides with the loss of VBS order, suggesting a direct transition between the two phases. On the right, we plot the equal-time dimer correlation function  $\chi(k)$ , demonstrating the loss of order at the  $M$  and  $X$  points for  $J > 0.6$ .

For even larger  $K_d$ , we expect for current loops to proliferate at smaller values of  $J$ , as the  $\mathcal{O}(K_d)$  energy penalty incurred by unsatisfied bonds in the dual Ising model can be alleviated through the presence of current loops. In particular, as  $K_d \rightarrow \infty$ , we expect the antiferromagnetic phase to persist for any non-zero value of  $J$ . This behavior was found in an analogous simulation of an O(2) model on a square lattice [355], where the current loop

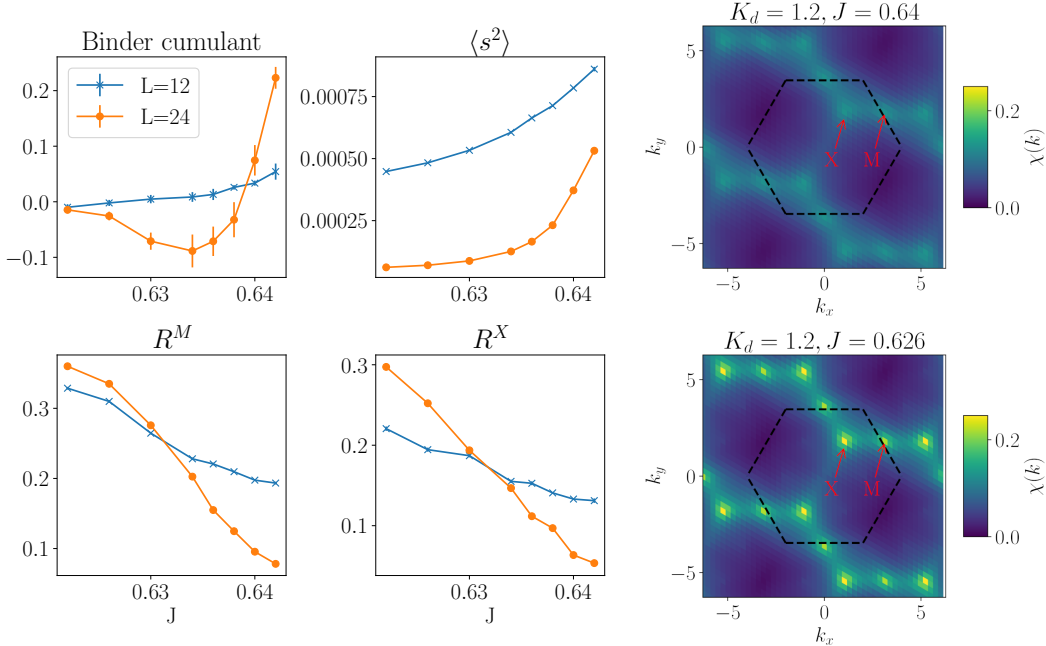


Figure 3.7: We plot the same data as in Fig. 3.6, but for weaker gauge fluctuations,  $K_d = 1.2$ . We note a larger gap between the vanishing of the VBS order and the appearance of antiferromagnetic order, suggesting that the  $\mathbb{Z}_2$  spin liquid phase might persist in this region; however, larger system sizes may yield a direct transition.

proliferation at  $K_d \rightarrow \infty$  is a consequence of the superfluid instability of the Bose-Hubbard model at half-integer filling to arbitrarily weak hopping. We intend to investigate this limit further in future work, as specialized updates become necessary for large  $K_d$ .

### 3.5 OUTLOOK

In this work, we present an effective model of quantum antiferromagnetism on the triangular lattice and demonstrate that it can be mapped to a classical sign-problem-free partition function. This extends known duality mappings [106, 128, 355] and yields sign-problem-free models for a broad class of systems, of which our effective model is only one example of. Additional models are of interest for future research. In particular, our effective model may be defined on a kagomé lattice, where a similar effective description of  $O(4)$ -symmetric bosons coupled to an odd  $\mathbb{Z}_2$  gauge field exists [408]. Numerical studies of extended Heisenberg models on the kagomé lattice [520] have given evidence for a ‘‘diamond’’ VBS order - it would be fruitful to study whether such a VBS pattern can naturally emerge from  $\mathbb{Z}_2$  gauge

field confinement with a background Berry phase. As our mapping also applies to bosons at *generic* fillings - not just a fixed background of one boson per site - it is also of interest to study the effects that a  $\mathbb{Z}_2$  gauge field has on the phase diagram of the Bose-Hubbard model. Recent experimental proposals [191] for realizing such models in quantum simulators make this question of timely importance.

Additionally, there is much room for algorithmic improvements in Monte Carlo simulations of these models. With the current system sizes accessible to us, we are able to establish the existence of spin liquid, VBS, and antiferromagnetic phases. However, the nature of the VBS to antiferromagnet transition is unclear; our results support a first-order transition, but the small number of system sizes accessible to us along with a diverging autocorrelation time leaves open the possibility of a continuous transition. Broadly-applicable techniques such as parallel tempering and reweighting may somewhat improve numerical results, but our classical model presents a fundamental complexity arising from the competition between multiple types of degrees of freedom. We have implemented several global updates to improve sampling, but we expect that more sophisticated sampling methods would have more success in clearly resolving the putative DQCP. It would also be useful to consider formulations in terms of alternate degrees of freedom. One of the difficulties that prevent robust global updates is the geometric complexity in the model, where degrees of freedom effectively live on sites, bonds, dual sites, and dual bonds. This is in contrast to J-current formulations used for simulating NCCP<sup>1</sup> models [262], where all the degrees of freedom live on bonds and good worm algorithms exist. We expect that a continuous-time generalization of this classical model would also improve performance as well as remove Trotterization errors and connect more directly to the underlying quantum model.

*I have no idea where this will lead us, but I have a definite feeling it will be a place both wonderful and strange.*

Dale Cooper

# 4

## Protection of parity-time symmetry in topological many-body systems: Non-Hermitian toric code and fracton models

### 4.1 INTRODUCTION

Isolated systems are governed by Hermitian Hamiltonians, with real energy eigenvalues and unitary time evolution. Nonetheless, non-Hermitian Hamiltonians [23, 34, 35, 37, 400], for which eigenvalues may generally be complex, are also physically relevant as effective descriptions of a large variety of different systems. For instance, they have been studied in the context of biological [13, 330, 339], mechanical [36], and photonic [53, 76, 84, 137, 138, 148, 169, 190, 226, 252, 287, 331, 359–361, 380, 393, 403, 472, 508, 526, 532, 566] systems, electrical circuits [40, 185, 430], cavities [44, 83, 111, 276], optical lattices [275], superconductors [179, 180], and open quantum systems [72, 110, 285, 331, 347, 400, 423]. In the latter case, the emergence of complex eigenvalues can be interpreted as arising due to dissipation. On top of a complex spectrum, non-orthogonal eigenstates and exceptional points are unique features of non-Hermitian Hamiltonians, with crucial physical consequences [56, 184, 233]. In the past few years, there has been growing interest in the condensed matter community in studying non-Hermitian generalizations of quantum many-body systems. Most of these recent efforts

were motivated by the question of how to generalize topological band theory to non-Hermitian systems [41, 551], uncovering a modified bulk-boundary correspondence [50, 129, 196, 239, 264, 274, 423, 530, 547] and topological classification [163, 240, 278, 284, 294, 444, 553, 569], as well as exceptional nodal phases [61, 258, 322, 346, 402, 570]. Furthermore, there has also been research on disordered systems [238, 307, 557, 559] and studies of non-Hermitian physics where many-body correlations play a crucial role, such as non-Hermitian fractional quantum Hall phases [550], Kondo physics [333], critical points [22, 177], and many more [170, 171, 210, 289, 296, 308, 329, 536, 537, 556].

Among these models, a particularly important and commonly studied class of non-Hermitian Hamiltonians is provided by  $\mathcal{PT}$ -symmetric Hamiltonians which are invariant under a combination of parity and time-reversal. Despite being non-Hermitian, these Hamiltonians can exhibit real spectra [34, 35, 37–39]. Intuitively, this may be attributed to a balance of gain and loss between the system and its environment. Mathematically, the protection is related to the fact that  $\mathcal{PT}$  symmetry implies that eigenvalues come in complex-conjugate pairs such that isolated real eigenvalues cannot become complex immediately. When they “meet” with another eigenvalue, they can either stay on the real axis or form complex-conjugate partners; when the latter happens,  $\mathcal{PT}$  is said to be broken. Therefore, the analysis of  $\mathcal{PT}$ -symmetry breaking is particularly subtle in systems with (approximate) degeneracies.

For symmetry-imposed degeneracies, the reality of the eigenvalues can be simply protected by the symmetry itself and the fact that eigenvalues must come in complex conjugate partners. *A priori*, this is different for degeneracies related to intrinsic topological order [412, 529]: for instance, the toric code model [244] has four ground states on a torus, that are guaranteed to be (exponentially) close in energy, even if all unitary symmetries are broken; similar statements apply to other spin-liquid phases. An even more dramatic ground-state degeneracy (GSD), that scales exponentially with linear system size, is realized in fracton models—novel quantum states of matter that are characterized by excitations with restricted mobility [338, 368]. Similar to spin-liquids, the GSD of fracton phases is topological in the sense that the different ground states are locally indistinguishable. One might be tempted to conclude that turning on a non-Hermitian,  $\mathcal{PT}$ -symmetric perturbation in such systems will immediately lead to complex ground-state energies. Contrary to these expectations, we demonstrate in this paper

that the reality of the ground-state eigenvalues in these phases can be surprisingly robust against a large class of such perturbations, even if all unitary symmetries are broken and in the presence of exponentially many degenerate states.

More specifically, we study under which conditions the eigenvalues of a given (almost degenerate) subspace of a Hermitian quantum system will stay real upon adiabatically turning on a non-Hermitian perturbation such that the total Hamiltonian commutes with a generalized  $\mathcal{PT}$  symmetry. Here, “adiabatically” refers to keeping the gap to all other states finite and “generalized  $\mathcal{PT}$ ” indicates that  $\mathcal{P}$  does not have to be spatial inversion, but might be any unitary operator. We first discuss a general mathematical condition for the eigenvalues to stay real and, hence,  $\mathcal{PT}$  symmetry to be protected. We then demonstrate that this condition has strong implications for the protection of  $\mathcal{PT}$  symmetry in the ground-state manifold of systems with topological GSDs, taking the toric code [244], the X-cube model [495], the checkerboard models [494, 495], Haah’s 17 CSS cubic codes [174], and the large class of quantum fractal liquids of Ref. [549] as examples. It is found that  $\mathcal{PT}$  symmetry will be preserved on systems with even linear system sizes,  $L_j$ , (in some Haah codes, divisibility by 4 is required) for a large class of perturbations, while it is generically fragile in systems with odd  $L_j$ .

We emphasize that understanding the preservation or breaking of  $\mathcal{PT}$  symmetry is not only one of the central theoretical questions of  $\mathcal{PT}$ -symmetric quantum mechanics, but also of practical relevance for experimental realizations and potential applications of effectively non-Hermitian systems. We hope that our framework for predicting the stability of the reality of eigenvalues and the presence or absence of exceptional points will provide greater control over the effects of non-Hermitian perturbations, which is, e.g., important for the observation of power-law oscillations [7, 393, 476, 528] and the potential applications as topological lasers [26, 27, 466] and sensing devices [293, 516].

The remainder of the paper is organized as follows. In Sec. 4.2, we define the type of non-Hermitian Hamiltonians we are interested in,  $\mathcal{PT}$  symmetry, and the more general condition of pseudo-Hermiticity. We also discuss the general, mathematical condition for colliding eigenvalues to stay real. It is first applied to the toric code, in Sec. 4.3, to the X-cube, checkerboard models, and Haah’s codes in Sec. 4.4, and finally to the fractal liquids of Ref. [549] in Sec. 4.5.

A summary of our findings is provided in Sec. 4.6.

## 4.2 PSEUDO-HERMITIAN PERTURBATIONS

We start with a general explanation of the class of non-Hermitian perturbations under consideration. To this end, let us first assume that our non-Hermitian Hamiltonian  $H$  admits a complete biorthonormal eigenbasis  $\{|\psi\rangle, |\phi\rangle\}$  [56], which means that

$$\begin{aligned} H|\psi_n\rangle &= E_n|\psi_n\rangle, \\ H^\dagger|\phi_n\rangle &= E_n^*|\phi_n\rangle, \\ \langle\phi_n|\psi_m\rangle &= \delta_{mn}. \end{aligned} \tag{4.1}$$

This is equivalent to the statement that  $H$  is diagonalizable, which is a very natural assumption for a generic (non-Hermitian) Hamiltonian of a physical system. Note, however, that it can be violated, most importantly at exceptional points [184, 233], which we will discuss separately below.

In the study of non-Hermitian perturbations to quantum systems, it is common to further assume that these Hamiltonians are  $\mathcal{PT}$ -symmetric [34, 35, 37–39], i.e.,  $[H, \mathcal{PT}] = 0$ , where  $\mathcal{P}$  can be abstractly defined as any unitary operator that squares to  $\mathbb{1}$ , and  $\mathcal{T}$  is complex conjugation in a certain basis. Doing so imposes additional restrictions on the spectrum of  $H$ . Eigenvalues must come in complex conjugate pairs, as  $H(\mathcal{PT})|\psi_n\rangle = E_n^*(\mathcal{PT})|\psi_n\rangle$ . Importantly, this means that if one starts with a Hermitian,  $\mathcal{PT}$ -symmetric Hamiltonian and applies a  $\mathcal{PT}$ -symmetric non-Hermitian perturbation, isolated eigenvalues cannot become complex on their own—they must merge with another eigenvalue on the real axis before becoming complex. This feature leads to the reality of energy spectra generally being robust to sufficiently small  $\mathcal{PT}$ -symmetric perturbations, although degenerate subspaces are not necessarily protected from becoming complex. When  $\mathcal{PT}|\psi_n\rangle \propto |\psi_n\rangle$ ,  $\mathcal{PT}$  symmetry is said to be “unbroken” and the associated eigenvalues are real. Once eigenvalues meet and become complex,  $\mathcal{PT}$  symmetry is “broken” and  $|\psi_n\rangle$  is not an eigenstate of  $\mathcal{PT}$  any more.

In this work, however, we do not restrict ourselves to  $\mathcal{PT}$  symmetry, and instead impose a closely related but more general condition of *pseudo-Hermiticity* [325–327]. A Hamiltonian

$H$  is pseudo-Hermitian if there exists a linear operator  $\eta$ , which we will refer to as the *metric operator*, such that

$$\eta H \eta^{-1} = H^\dagger. \quad (4.2a)$$

In this paper, we take  $H$  to consist of a Hermitian component,  $H_0$ , and a non-Hermitian perturbation,  $\epsilon V$ , with magnitude that we control with  $\epsilon \in \mathbb{R}$ :

$$H = H_0 + \epsilon V, \quad H_0^\dagger = H_0. \quad (4.2b)$$

For the Hermitian part  $H_0$ , Eq. (4.2a) implies  $[\eta, H_0] = 0$ , i.e.,  $\eta$  is a symmetry of the unperturbed Hamiltonian. We also take  $\eta$  to be unitary, so that Eq. (4.2a) is equivalent to  $\eta H \eta^\dagger = H^\dagger$ . The purpose of this work is to derive and discuss general conditions under which (certain physically relevant parts of) the spectrum of  $H$  in Eq. (4.2b) can stay real upon adiabatically turning on  $\epsilon$ .

This condition of pseudo-Hermiticity (4.2a) is manifestly identical to  $\mathcal{PT}$  symmetry with  $\mathcal{P} \equiv \eta^{-1}$  provided  $H$  is symmetric,  $H = H^T$ . In fact, it was shown [560] that any  $\mathcal{PT}$  symmetric, finite-dimensional Hamiltonian is also pseudo-Hermitian. For this reason and since it does not involve any anti-linear operators and, thus, does not require a choice of basis, we focus on pseudo-Hermiticity in this work. Moreover, pseudo-Hermiticity gives a more systematic way of constructing non-Hermitian perturbations  $\epsilon V$  to Hermitian models: one can immediately obtain all the possible choices of  $\eta$  as it has to be a symmetry of the unperturbed, Hermitian part,  $H_0$ , of the model, which then specifies the suitable non-Hermitian perturbations.

#### 4.2.1 PROTECTION OF REALITY OF ENERGIES

If  $H$  is pseudo-Hermitian, complex eigenvalues also must come in conjugate pairs, since the combination of Eqs. (4.1) and (4.2a) implies  $H\eta^{-1}|\phi_n\rangle = E_n^*\eta^{-1}|\phi_n\rangle$ . As is the case with  $\mathcal{PT}$ -symmetric perturbations, this means that if a non-Hermitian perturbation is applied, the reality of isolated eigenvalues is stable to small pseudo-Hermitian perturbations. If a group of eigenvalues are degenerate (or almost degenerate) under  $H_0$ —as is common in models involving symmetries or topological superselection sectors—they are generally not stable to pseudo-Hermitian perturbations. In these cases, we identify two main mechanisms by which

these degenerate eigenvalues can stay real under pseudo-Hermitian perturbations:

(I) The first method of ensuring degenerate eigenvalues stay real is simply to preserve the degeneracy under pseudo-Hermitian perturbations. Pseudo-Hermiticity implies that if degenerate eigenstates are going to become complex, they must acquire imaginary parts with opposite signs. If one forces the (in general complex) eigenvalues to remain degenerate, this can never be satisfied for a non-zero imaginary component, unless the eigenvalues meet with another set of symmetry-unrelated eigenvalues. The latter, however, requires a sufficiently large value of  $\epsilon$ , as symmetry-unrelated states are generically not degenerate for  $\epsilon = 0$ . The symmetries enforcing the degeneracy can be unitary symmetries, fermionic time-reversal symmetry [239], or even bosonic time-reversal symmetries unique to pseudo-Hermitian systems [424].

(II) The second mechanism is more subtle and our main focus in this work. If a pseudo-Hermitian term breaks all symmetries protecting the degeneracy, the eigenvalue splitting will generally be nonzero. This splitting can be either real or imaginary. However, one can show that *if all the eigenstates of  $H_0$  of the degenerate (or almost degenerate) subspace of interest have the same eigenvalue under  $\eta$ , then this splitting will always be real*. This mathematical fact can be readily understood within the framework of  $G$ -Hamiltonian systems developed by Krein, Gel'fand and Lidskii [152, 260] in the 1950s for the case of Hermitian  $\eta$ . In Appendix C.1, we provide a simple and physically insightful proof to all orders of perturbation theory that works for  $\eta$  being Hermitian or unitary. Furthermore, our analysis shows that, *if the eigenvalues of  $\eta$  are identical, the projections of the associated eigenstates to the (almost) degenerate subspace of  $H_0$  will be orthogonal to first order in  $\epsilon$  and to zeroth order in the limit of a large gap to the rest of the spectrum*; it also follows that, as long as the energetic separation of the subspace of interest from the rest of the spectrum is sufficiently large, they will be approximately orthogonal in the entire Hilbert space, even though the Hamiltonian is not Hermitian any more. This is very different when the eigenvalues of  $\eta$  are not the same. In that case, there can be exceptional points [184, 233], where the Hamiltonian is defective, eigenstates coalesce and become identical, irrespective of how large the gap to the other states of the system is.

Intuitively, this is related to the fact that the Hamiltonian restricted to the degenerate subspace is Hermitian: denoting the degenerate eigenfunctions by  $|\psi_i\rangle$  and writing  $\eta|\psi_i\rangle =$

$e^{i\delta} |\psi_i\rangle$ , we have

$$\hat{H}_{ij} \equiv \langle \psi_i | H | \psi_j \rangle \stackrel{(4.2a)}{=} \langle \psi_i | \eta^{-1} H^\dagger \eta | \psi_j \rangle = \hat{H}_{ji}^*. \quad (4.3)$$

The complete argument of Appendix C.1 involves constructing a full effective Hamiltonian for the degenerate subspace, and showing that it is Hermitian via similar reasoning.

#### 4.2.2 REMARKS ON CONDITION FOR REALITY

Some comments should be made regarding the possibility of multiple degeneracies and multiple metric operators. In the case of a two-fold degeneracy, i.e., two eigenvalues being identical, there are only two possibilities for the eigenvalues of  $\eta$ —either they both have the same eigenvalue under  $\eta$ , or they are different. In the former case, the splitting is always real. In the latter case, the energy splitting can be real or complex depending on the magnitudes of the matrix elements in the effective Hamiltonian. When there are more than two degenerate eigenstates, the full criteria becomes more complicated, as some eigenvalues may become complex while others stay real. For a concrete system, it should always be possible to determine the nature of the splitting through perturbation theory, using the methods described in Appendix C.1. However, we note that it is *always* the case that if all the unperturbed eigenstates have the same eigenvalue under  $\eta$ , their energies will stay real.

One can also consider a case where there is a two-fold degeneracy, but multiple possible choices of metric operators. If there are two metric operators,  $\eta_1$  and  $\eta_2$ , such that both eigenstates have the same eigenvalue under  $\eta_1$  and different eigenvalues under  $\eta_2$ , the degeneracy can be protected as a consequence of the mechanism (I) above:  $S = \eta_1^{-1} \eta_2$  is, by construction, a symmetry of  $H$  and if  $S |\psi_1\rangle = |\psi_2\rangle$ , the eigenvalues will remain identical for  $\epsilon \neq 0$ . However, the pseudo-Hermiticity of  $H$  with respect to  $\eta_2$  can be broken without causing the eigenvalues to become complex.

In this paper, we focus on the protection mechanism (II) for the reality of the eigenvalues, i.e., on cases where pseudo-Hermitian perturbations break all the relevant symmetries, eigenvalue degeneracies are not preserved and hence the interplay between the metric operator and the unperturbed eigenstates are important in deducing whether the energies stay real. The general procedure for utilizing this phenomenon goes as follows. First, specify a subspace of

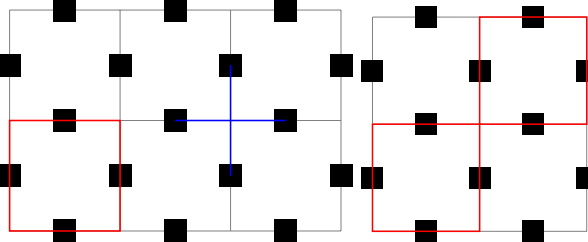


Figure 4.1: (Top) The toric code is defined on a cubic lattice, with Pauli spins on each edge. The Hamiltonian is a sum of stabilizers, consisting of either a product of  $X$  operators on a plaquette (red), or a product of  $Z$  operators adjacent to a vertex (blue). We here show the case  $L_x = 3$  and  $L_y = 2$ . (Bottom) On an even-by-even lattice (depicted here for a  $2 \times 2$  lattice), every site can be covered by a combination of non-overlapping plaquette operators (red). The four sites that are seemingly not covered by plaquette operators are redundant due to periodic boundary conditions. This covering is also possible with vertex operators. The coverings of larger lattices can be accomplished by sewing together copies of this  $2 \times 2$  covering—of course, this only works for even-by-even lattices.

interest, whose energies are separated from the rest of the spectrum. Next, identify the unitary symmetries under which the subspace has a definite eigenvalue under. These symmetries will yield a class of non-Hermitian perturbations—namely, those that are pseudo-Hermitian with the symmetry as a metric operator—for which the degenerate eigenvalues will stay real.

This notion of stability is useful in quantum systems when the subspace under consideration is well-separated from the rest of the spectrum. In the remainder of the paper we will be concerned with gapped many-body systems with several degenerate ground states and discuss under which conditions the ground-state energies can remain real, provided the perturbations do not close the gap between the ground and excited states.

### 4.3 NON-HERMITIAN TORIC CODES

We begin with a study of non-Hermitian perturbations to the two-dimensional toric code [244], focusing on the reality of the ground-state subspace. Non-Hermitian generalizations of the toric code [172, 308] or closely related models [170] have recently been studied; these works, however, have a different focus and a systematic understanding of the stability of  $\mathcal{PT}$  symmetry or, more generally, of the reality of the spectrum in the ground-state subspace remains unexplored.

The toric code is defined on a square lattice, with Pauli spins on every edge, see Fig. 4.1. We denote the number of sites along the  $x$  and  $y$  directions by  $L_x$  and  $L_y$  and focus on periodic boundary conditions. The Hamiltonian is

$$H^{TC} = -\alpha \sum_c A_c - \beta \sum_p B_p, \quad (4.4)$$

where we have introduced the vertex operators,  $A_c$ , which cover the four spins adjacent to a vertex  $c$ , and the plaquette operators,  $B_p$ , which cover the four spins on a plaquette  $p$ ,

$$A_c = \prod_{i \in c} Z_i, \quad B_p = \prod_{i \in p} X_i.$$

Unless stated otherwise, we will use  $\alpha = \beta = 1$ . In accordance with quantum code terminology, we refer to  $A_c$  and  $B_p$  collectively as ‘‘stabilizers.’’

Each term in Eq. (4.4) commutes with the rest of the Hamiltonian, so the ground states can be obtained by minimizing the energy of each operator independently. Any state  $|\psi\rangle$  in the ground-state subspace satisfies  $A_c |\psi\rangle = B_p |\psi\rangle = |\psi\rangle$ . If defined on a torus, one can define loops of  $Z$  or  $X$  operators that wind around either of the two cycles of the torus. These logical string operators, that cannot be deformed to the identity by applications of stabilizers, imply a fourfold degenerate ground state, with string operators acting irreducibly within that subspace.

#### 4.3.1 PSEUDO-HERMITIAN PERTURBATIONS

We are interested in pseudo-Hermitian perturbations to Eq. (4.4) and how they affect the degenerate ground states. To this end, let us first focus on three possible choices of  $\eta$ ,

$$\eta = \prod_i X_i, \prod_i Y_i, \prod_i Z_i, \quad (4.5)$$

where the product involves all sites of the system, and postpone the discussion of other options to Sec. 4.3.4 below. One can easily check that  $[H^{TC}, \eta] = 0$ .

In contrast with many other features of the toric code, which only depend on the topology of the manifold, the eigenvalues of the ground states under  $\eta$  in Eq. (4.5) are highly sensitive

to the system size. On an even-by-even lattice, the entire ground-state subspace has the same eigenvalue under  $\eta$ . This can most easily be seen by the fact that  $\eta$  can be written as a product of plaquette and vertex operators, and must give eigenvalue +1 in the ground-state subspace as a result, see Fig. 4.1. This cannot be accomplished on any other lattice size for the following reason: a straight line drawn along the  $x$  ( $y$ ) direction going through the centers of the plaquettes will intersect  $L_x$  ( $L_y$ ) sites. If we attempt to cover the full lattice with plaquette operators, the placement of an additional operator will always change the number of covered sites on the line by an even amount. The same holds true for vertex operators and lines drawn through the vertices. Therefore, if either  $L_x$  or  $L_y$  is odd, the full lattice can never be assembled solely from stabilizers. The fact that  $\eta$  cannot be written as a product of stabilizers is sufficient to show that not all ground states can have the same eigenvalue under  $\eta$ . To see this, suppose that all ground states have the same eigenvalue under  $\eta$ . If this holds, then we can add  $\eta$  to the group of stabilizers of the toric code without modifying the GSD. If  $\eta$  is independent from the rest of the stabilizers, we arrive at a contradiction, since increasing the number of independent stabilizers lowers the GSD.

The observation that all the ground states have the same sign under  $\eta$  can also be seen by noting that  $\eta$  commutes with all the logical string operators on an even-by-even lattice, which take the system between different ground states. On an odd-by-even or an odd-by-odd lattice,  $\eta$  anti-commutes with at least one of the logical string operators, which in both cases lead to two ground states having eigenvalue +1 and the other two having eigenvalue -1.

What sort of perturbations,  $\epsilon V$ , can we add to our Hamiltonian for which  $\eta V \eta^\dagger = V^\dagger$ ? Writing  $V = i\mathcal{O}$ , this requires

$$\eta\mathcal{O} = -\mathcal{O}^\dagger\eta, \quad (4.6)$$

which reduces to  $\{\eta, \mathcal{O}\} = 0$  for Hermitian  $\mathcal{O}$ . Taking  $\eta$  to be the product of  $Y$  operators for concreteness, this means that  $\mathcal{O}$  can be a sum,  $\mathcal{O} = \sum_t g_t \mathcal{O}_t$ ,  $g_t \in \mathbb{R}$ , over terms  $\mathcal{O}_t$  which are products of Pauli matrices, only constrained to contain an odd number of  $X_i$  and  $Z_i$ . This includes a large class of perturbations such as random, planar fields,  $V = i \sum_i (g_{i1} X_i + g_{i3} Z_i)$ ,  $g_{i1}, g_{i3} \in \mathbb{R}$ , and highly non-local terms, such as  $i \sum_{i < j < k} g_{ijk} X_i X_j X_k$ , or  $\sum_{i < j < k} g_{ijk} X_i Y_j Y_k$ ,  $g_{ijk} \in \mathbb{R}$ . Since each term satisfies Eq. (4.6) separately, there is no relation between the

prefactors of the different terms required and we can think of them as random, non-Hermitian disorder, that in general breaks all symmetries of the system (other than  $\mathcal{PT}$ ).

In combination with our results of Sec. 4.2, this implies that on an even-by-even lattice, the ground-state subspace of the toric code remains real under the large class of pseudo-Hermitian perturbations that satisfy Eq. (4.6) with  $\eta$  given by Eq. (4.5). As the eigenvalues must stay real for small perturbations, they never exhibit any square root singularities [184] and exceptional points are avoided in the ground-state subspace. This is verified by exact diagonalization (ED) of the toric code spectrum in Fig. 4.2(a,b), where it can be seen that the ground-state energies can only become complex when meeting with the excited states. As such, the  $\mathcal{PT}$  symmetry of the ground-state manifold is protected by the gap to the excited states.

In contrast, on a lattice that is not even-by-even, the ground states generically become complex immediately upon applying the same non-Hermitian perturbations. This sensitivity of the ground state to the system size can be thought of as representative of the highly entangled nature of the toric code ground states. Even if one was to consider arbitrarily large system sizes, the toric code ground states are still able to “detect” whether the system size is even or odd. A similar interpretation of this phenomenon is that even for local perturbations, the order in perturbation theory in which the ground state energy splitting will occur necessarily involves a non-local operator which winds around the torus and, as such, can be sensitive to (the parity of) the system size.

This sensitivity to system size may seem surprising, as the toric code is a paradigmatic example of topological order where physical features are only sensitive to the genus of the underlying manifold. To reconcile this, we emphasize that these non-Hermitian features assume the preservation of  $\mathcal{PT}$ -symmetry or pseudo-Hermiticity, which is a common assumption for non-Hermitian systems. Since the topological order of the Hermitian toric code would remain even if this symmetry was broken, the phenomenon we observe is not topological in a strict sense, even though it can be interpreted as arising due to the long-range entanglement intrinsic to topological order. In the following sections, we show that despite this, these features are a robust property of the topological phase rather than a fine-tuned consequence of the

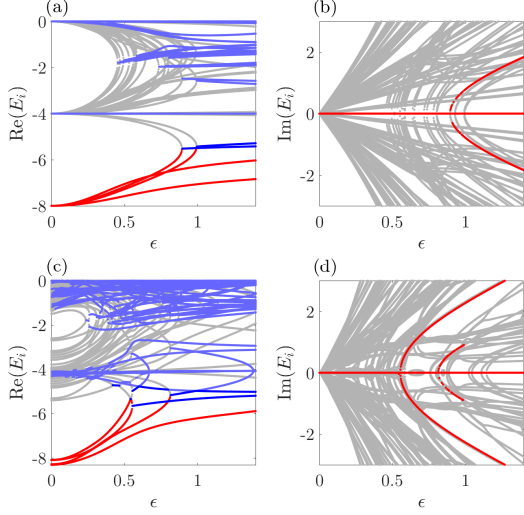


Figure 4.2: Spectrum of the toric with non-Hermitian random field perturbation,  $i\epsilon \sum_i g_i X_i$ , where  $g_i$  was initialized randomly according to a Gaussian distribution with mean and variance 1. In (a,b) and (c,d) we take the bare toric-code Hamiltonian (4.4) and the perturbed one, Eq. (4.7) with Gaussian distributed  $h_i$  (mean 0 and standard deviation 0.4), as starting point, respectively. In (a,c), the real part of the energy is shown with red and gray referring to real-valued ground and excited energy levels, whereas eigenvalues with a complex part (broken  $\mathcal{PT}$  symmetry) are indicated in blue. The corresponding imaginary parts can be found in (b,d) with red indicating the ground states, defined as those four states with the lowest  $\text{Re}(E_i)$ .

exact solvability of Eq. (4.4).

#### 4.3.2 STARTING WITH PERTURBED TORIC CODE

One might wonder whether the remarkable protection of  $\mathcal{PT}$  and reality of the ground-state energies is just a consequence of the highly fine-tuned and exactly solvable toric code Hamiltonian (4.4) or a more general property of the underlying topologically ordered phase. To investigate this, let us take as our base Hamiltonian the toric code with some small Hermitian perturbation, for example a field along the  $Z$ -direction with in general spatially varying amplitude,

$$H_0 = H^{TC} + \sum_i h_i Z_i, \quad h_i \in \mathbb{R}. \quad (4.7)$$

The perturbation in Eq. (4.7) forces us to choose  $\eta = \prod_i Z_i$  in Eq. (4.5), as it is the only one that commutes with the Hermitian Hamiltonian. Note that, of course, a completely random Hermitian field will break all symmetries and no  $\eta$  is possible; we are, however, not interested in this case as the Hamiltonian would break  $\mathcal{PT}$  *explicitly* and the question of whether it is

broken *spontaneously* would become ill defined.

With the additional perturbation in Eq. (4.7), we no longer have exactly degenerate ground states for  $\epsilon = 0$ , but a finite energy splitting that is exponentially suppressed by the system size. The four low-energy states will still all be even under  $\eta$  for an even-by-even lattice, since our perturbation respects the  $\eta$  symmetry. Consequently, the ground-state energies will stay real, even when they “meet” each other at finite  $\epsilon$ , as long as the gap to excited states stays finite. The protection of  $\mathcal{PT}$  symmetry is, thus, a more general property of the underlying phase with topological order. We also demonstrate this with a concrete example in Fig. 4.2(c,d).

#### 4.3.3 EXCEPTIONAL POINTS

A surprising observation is that, while these Hermitian perturbations do not change whether the ground states become complex, they do change the nature of *how* they become complex. Non-Hermitian Hamiltonians can exhibit exceptional points [184, 233]. Here, the eigenvalues coalesce, the matrix becomes defective, i.e., also the eigenvectors become degenerate, and the eigenvalues exhibit a square-root singularity in the tuning parameter, in our case  $\epsilon$ , in the sense that the difference of eigenvalues scales with  $\sqrt{\epsilon_0 - \epsilon}$ . This has crucial consequences, e.g., for the Green’s function that exhibits a pole of second order in addition to the conventional first-order pole [184]. For pseudo-Hermitian or  $\mathcal{PT}$ -symmetric Hamiltonians, exceptional points typically arise at the moment when two eigenvalues meet on the real line and become complex. If we start with an unperturbed toric code on an even-by-odd lattice and apply a non-Hermitian, pseudo-Hermitian perturbation  $\epsilon V$ , such as an imaginary transverse field, the degenerate ground states can immediately become complex. However, this degeneracy is not an exceptional point, since the degeneracy occurs in the Hermitian limit and must admit a complete basis of eigenvectors. In contrast, if one first applies a Hermitian perturbation, such as in Eq. (4.7), and then  $\epsilon V$ , we have verified by ED on a  $2 \times 3$  lattice that the ground states *will* form an exceptional point when they meet each other on the real line to become complex, and the corresponding eigenstates become identical. We emphasize that this is true for arbitrarily small Hermitian perturbations. This is in stark contrast to systems with even  $L_x, L_y$ ; here the ground-state energies must stay real for small perturbations, such that their

splitting does not exhibit the characteristic square-root behavior  $\propto \sqrt{\epsilon_0 - \epsilon}$ , and exceptional points do not occur.

To illustrate this subtle behavior of perturbed systems with odd system sizes, let us take a two-level system as an effective description of two ground states with opposite eigenvalue of  $\eta$  meeting to become complex. Denoting Pauli matrices acting in this subspace by  $\sigma_{x,y,z}$ , we have  $\eta = \sigma_z$  and the most general pseudo-Hermitian Hamiltonian has the form

$$h = E_0 \mathbb{1} + \Delta \sigma_z + i\epsilon (\cos \alpha \sigma_x + \sin \alpha \sigma_y), \quad (4.8)$$

with the real-valued parameters  $E_0$ ,  $\Delta$ ,  $\alpha$ , and  $\epsilon$ ; the latter parameterizes the strength of anti-Hermitian perturbations as before. Note that the model is  $\mathcal{PT}$  symmetric only if  $2\alpha/\pi \in \mathbb{Z}$ . The right eigenvalues and eigenvectors of  $h$  in Eq. (4.8) are given by  $E_{\pm} = E_0 \pm \sqrt{\Delta^2 - \epsilon^2}$  and  $\psi_{\pm} \propto (\Delta \pm \sqrt{\Delta^2 - \epsilon^2}, i\epsilon e^{i\alpha})^T$ . The eigenvalues meet when  $\epsilon = \pm\Delta$  and become complex for  $|\epsilon| > |\Delta|$ . When  $\Delta = 0$ , however, this is not an exceptional point as  $\psi_{\pm} \rightarrow (\pm 1, \text{sign}(\epsilon)e^{i\alpha})^T/\sqrt{2}$ , forming an orthonormal basis, and  $\Delta E = E_+ - E_- \rightarrow 2|\epsilon|$  scaling linearly with  $\epsilon$ , for  $\Delta \rightarrow 0$ . For  $\Delta \neq 0$ , instead, we get  $\psi_+ \rightarrow \psi_-$  when  $\epsilon \rightarrow \pm\Delta$ , showing that the matrix becomes defective, and the difference of eigenvalues scales as  $\Delta E \sim 2\sqrt{2\epsilon_0}\sqrt{\epsilon_0 - \epsilon}$ , for  $\epsilon$  near  $\epsilon_0 = \pm\Delta$ . It is also readily verified that the overlap,  $\langle \phi_{\pm} | \psi_{\pm} \rangle$ , with the corresponding left eigenvector is non-zero except for the exceptional points  $\epsilon = \pm\Delta \neq 0$ , where it vanishes; this “self-orthogonality” rules out the construction of a bi-orthogonal basis as in Eq. (4.1). In summary, we should think of the special case of vanishing splitting,  $\Delta = 0$  or of the unperturbed toric code, as a fine-tuned limit where two lines of exceptional points,  $\epsilon = \pm\Delta$ , meet and give rise to a non-defective Hamiltonian, as required by Hermiticity.

We finally point out that this behavior is also visible on an even-by-even lattice when taking into account the excited states: as can be seen in Fig. 4.2(b,d), the imaginary part of the excited states that become complex at infinitesimal  $\epsilon$  scales linearly in  $\epsilon$ , whereas the  $\mathcal{PT}$  symmetry breaking at finite  $\epsilon$  exhibits the aforementioned square-root singularity.

#### 4.3.4 OTHER METRIC OPERATORS

So far, we have focused on the three different choices of  $\eta$  in Eq. (4.5), but there are in principle many more possibilities for the bare toric code model (4.4), as it possesses many other symmetries. Here, we argue that our choices of  $\eta$  are unique provided we assume our anti-Hermitian perturbations can be disordered and are not required to have a specific spatial structure.

As a starting point, one might use spatial symmetries—lattice translations  $T_{x,y}$ , four-fold rotation  $C_4$ , and inversion  $I$  and combinations thereof. For instance,  $\eta = I$  with

$$I\mathcal{O}_iI^{-1} = \mathcal{O}_{-i}, \quad \mathcal{O}_i = X_i, Y_i, Z_i, \quad (4.9)$$

is clearly a symmetry,  $[H^{TC}, I] = 0$ , and it is easy to see that all ground states have the same eigenvalue under it for any system size (the same holds for  $T_{x,y}$  but not for  $C_4$ ). However, it is not a natural choice for a generic system with spatially varying Hermitian or non-Hermitian perturbations, such as those discussed above. For example, for an imaginary field,  $V = i \sum_i \sum_{\mu=1}^3 g_{i\mu} (X_i, Y_i, Z_i)_{\mu}$ , it would require  $g_{i\mu} = -g_{-i\mu}$  and, hence, fine-tuning between spatially distant sites. Not even a site-independent complex field is possible.

Having established that choosing an  $\eta$  which relates spatially distant sites requires fine tuning, we focus on  $\eta$  that commute with all stabilizers separately. This requirement can alternatively be thought of as a restriction to symmetries that are preserved in the presence of spatial disorder in the couplings of the bare toric code, i.e.,  $\alpha \rightarrow \alpha_c > 0$ ,  $\beta \rightarrow \beta_p > 0$  in Eq. (4.4). This leads to two distinct classes of possible  $\eta$ , schematically given by

$$\eta = \prod \text{(stabilizers)} \quad (4.10a)$$

or

$$\eta = \prod \text{(stabilizers)(logical strings)}, \quad (4.10b)$$

where “logical strings” stands for strings of  $X_i$  or  $Z_i$  operators along a non-contractible loop of the torus connecting the different ground states.

Clearly, the ground states will have the same eigenvalues under  $\eta$  in Eq. (4.10a) and, thus, stay real. For even system sizes,  $\eta$  in Eq. (4.5) are of this form and, as we have seen above, indeed admit a large class of non-Hermitian perturbations.

This is different for  $\eta$  of the form of Eq. (4.10b): the ground states will have different eigenvalues under  $\eta$  and  $\mathcal{PT}$  symmetry is in general fragile. However, since  $\eta$  in Eq. (4.5) can be written in the form (4.10a), it is clear that Eq. (4.10b) cannot be spatially homogeneous on an even-by-even lattice, but must be distinct on a non-contractible loop around the torus; the same must hold for the associated non-Hermitian perturbation, which requires, again, significant spatial fine-tuning. Let us illustrate this latter point using the concrete example of  $\eta = \prod_i X_i \prod_{j \in P} Z_j$ , where  $P$  is a non-contractible closed path through the centers of the plaquettes. In that case, an imaginary field,  $V = i \sum_i \sum_{\mu=1}^3 g_{i\mu} (X_i, Y_i, Z_i)_{\mu}$ , must satisfy  $g_{i1} = 0$  for  $i \notin P$  and  $g_{i2} = 0$ ,  $g_{i1} \neq 0$  for  $i \in P$  (note that  $g_{i1} \neq 0$  on  $P$  is required, as we otherwise can simply choose  $\eta = \prod_i X_i$ , which is of the form of Eq. (4.10a), and all eigenvalues stay real). In other words, the perturbation must have vanishing  $X$  components on all sites except for a non-contractible loop with non-zero  $X$  components; again, not even a spatially homogeneous perturbation is possible.

We conclude that, setting aside fine-tuned non-Hermitian perturbations with special spatial structure along non-contractible loops, suitable metric operators are of the form of Eq. (4.10a) for even-by-even lattices. As the ground states will always have eigenvalue +1 under any such  $\eta$ , the reality of their eigenvalues and, thus,  $\mathcal{PT}$  symmetry are protected.

#### 4.3.5 ARBITRARY SYSTEM SIZES

So far, we have focused our attention on even-by-even lattices since the homogeneous metric operators in Eq. (4.5) can be written as a product of stabilizers, while this is not possible on even-by-odd or odd-by-odd lattices; nevertheless, if one naively applies the covering shown in Fig. 4.1 on these lattices, one can obtain a modified metric operator  $\tilde{\eta}$ , defined as the product of Pauli operators,  $X_i$ ,  $Y_i$ , or  $Z_i$ , on all sites except for a single line (in the even-by-odd case) or two lines (in the odd-by-odd case) that wind around the odd lengths of the torus. In other words,  $\eta$  in Eq. (4.5) is necessarily of the form of Eq. (4.10b) on a lattice with at least one of  $L_x$ ,  $L_y$  odd. Based on our previous discussion, this implies that the reality of the ground-state

eigenvalues and  $\mathcal{PT}$  symmetry are generically fragile on even-by-odd and odd-by-odd lattices.

We finally mention, for completeness, one less general but potentially useful immediate consequence. As follows from using  $\tilde{\eta}$  as metric operator, any pseudo-Hermitian perturbation  $\epsilon V$  with anti-Hermitian part,  $\epsilon(V - V^\dagger)/2$ , that has support only in a subregion of the system that is contractible around the odd lengths of the torus, will leave the ground-state eigenvalues real.

#### 4.4 NON-HERMITIAN FRACTON MODELS

Our analysis of the toric code carries over to many well-known fracton models in three dimensions. Fracton models [54, 74, 174, 300, 338, 368, 450, 454, 494, 495, 549] constitute a unique phase of matter, characterized by excitations with restricted mobility, either by being immobile or only mobile in certain directions. These systems are typically gapped and have GSDs exponential in linear system size. In this section, we analyze various models with fracton order—namely, the X-cube model, checkerboard model, and Haah’s codes—and show that, like the toric code, the full ground-state subspaces are stable against a large class of non-Hermitian perturbations provided the linear system sizes along all directions are even. Unless stated otherwise, we take  $\eta$  to be defined in the same way as in Eq. (4.5), i.e., as a product of  $X$ ,  $Y$ , or  $Z$  operators over all qubits in the system; as motivated in Sec. 4.3 above in the context of the toric code, these  $\eta$  provide the largest class of allowed non-Hermitian perturbations by virtue of being spatially homogeneous.

##### 4.4.1 X-CUBE MODEL

The X-cube model [495] is defined on a cubic lattice, with qubits living on the edges of the lattice. It has a Hamiltonian composed of mutually commuting terms

$$H^X = - \sum_c A_c - \sum_{i=x,y,z} \sum_v B_v^i \quad (4.11)$$

where  $A_c = \prod_{j \in \partial c} X_j$  is the product of  $X$  operators on the 12 edges of the cube labelled by  $c$ , and  $B_v^i$  is a vertex operator, composed of four  $Z$  operators at vertex  $v$  in the plane perpendicular to the  $i$ 'th direction. On an even-by-even-by-even lattice, our  $\eta$  operators in

Eq. (4.5) can be assembled from these terms, thereby showing that the entire ground-state subspace has eigenvalue +1 under  $\eta$ , see Fig. 4.3. An identical argument as in the toric code case implies that  $\eta$  cannot be assembled from stabilizers on a lattice with any odd length. In combination with the fact that it commutes with all stabilizers  $A_c$ ,  $B_v^i$  separately, it must be of the form of Eq. (4.10b) for odd system lengths, with “logical strings” here referring to the logical string-like operators of the X-cube model.

By our analysis of the toric code, this immediately implies that the X-cube ground states on an even-by-even-by-even lattice stay real under the non-Hermitian perturbations permitted by  $\eta$ , which includes the application of imaginary transverse fields, non-local terms like the ones considered for the toric code, and many others. One can check that all other features of non-Hermitian toric code perturbations, such as their additional stability against real perturbations and the ability to add contractible perturbations on lattices with odd system sizes, also hold. However, these features are more striking for fracton models: instead of a four-dimensional code subspace being protected against these perturbations, fracton models have a GSD that grows exponentially with system size; for the X-cube model on a three-dimensional torus, the GSD obeys

$$\log_2 \text{GSD} = 2L_x + 2L_y + 2L_z - 3.$$

The reality of the code subspace in the presence of pseudo-Hermitian perturbations holds for the X-cube model defined on general three-dimensional manifolds [450], provided the full space can be covered by plaquette or star operators.

This sensitivity to system size may be surprising, since the X-cube model exhibits *foliated fracton order* [450]. This means that the length of any of the sides of the X-cube model can always be extended by attaching layers of toric code and applying a series of local unitary transformations. In Appendix C.2, we present a detailed study of how the metric operators  $\eta$  behave under foliations. The end result is that, while the ground states can be extended by this foliation procedure, the foliation acts non-trivially on  $\eta$ , meaning that the interplay between  $\eta$  and the X-cube ground states can change depending on the system size.

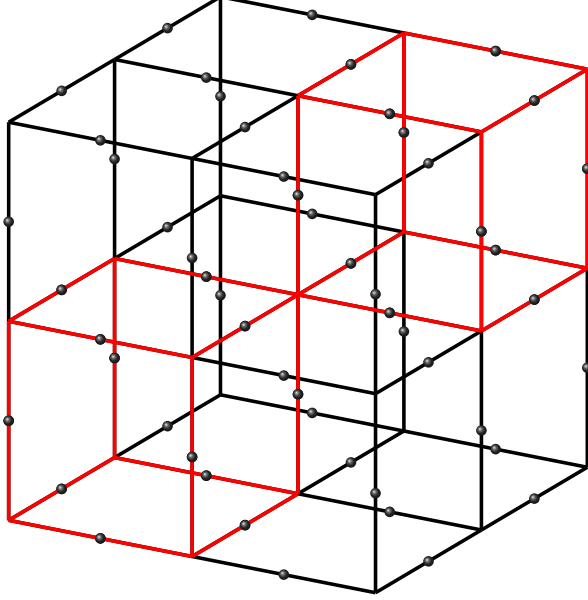


Figure 4.3: For the X-cube model defined on an even-by-even-by-even lattice (shown here for  $2 \times 2 \times 2$ ), the full lattice can be covered by non-overlapping plaquette operators (red). The lattice can also be covered by vertex operators. Although this is more difficult to visualize, it can be generated by covering each 2D layer in a definite plane by a toric code covering. The remaining sites on the edges connecting these 2D layers can then be covered by chains of vertex operators.

#### 4.4.2 CHECKERBOARD MODEL

The checkerboard model [495] is another example of a system with fracton excitations. This model has spins defined on the vertices of a three-dimensional cubic lattice, as opposed to the edges. By separating the cubes of the lattice with alternating labels  $A$  and  $B$ , each forming a three-dimensional checkerboard lattice, and denoting the cubic operators  $\prod_{i \in \partial c} Z_i$  and  $\prod_{i \in \partial c} X_i$  as  $Z_c$  and  $X_c$  respectively, the checkerboard model is given by the Hamiltonian

$$H^C = - \sum_{c \in A} Z_c - \sum_{c \in A} X_c. \quad (4.12)$$

The geometry of the checkerboard model requires it to be defined on an even-by-even-by-even lattice if periodic boundary conditions are imposed, since otherwise one cannot uniformly partition the cubes into  $A$  and  $B$  labels. On even-by-even-by-even lattices, the entire lattice can be covered by non-overlapping stabilizers, and therefore the ground-state subspace is even under any  $\eta$  in Eq. (4.5). Again, this implies that the ground-state energies of the

checkerboard model always remain real under non-Hermitian perturbations that are pseudo-Hermitian under  $\eta$ . Although only small system sizes are accessible via ED, we have checked these predictions numerically for the checkerboard model on a  $2 \times 2 \times 2$  lattice.

A Majorana version of the checkerboard model has also been studied [494], which simply replaces the Pauli spins with Majorana fermions  $\gamma_i$ , i.e., the model has one Majorana fermion per site  $i$  of the cubic lattice. By defining  $\prod_{i \in c} \gamma_i = \gamma_c$ , the Hamiltonian of the Majorana checkerboard model is

$$H = - \sum_{c \in A} \gamma_c. \quad (4.13)$$

Because the entire lattice can be covered with  $\gamma_{c \in A}$ , all ground states of the system are even under the operator

$$\eta = \prod_i \gamma_i,$$

which can be interpreted as the total fermion parity,  $\eta \propto \prod_\alpha (c_\alpha^\dagger c_\alpha - 1/2)$ , when combining pairs of Majorana fermions into auxiliary complex fermions  $c_\alpha$ . Therefore, the ground states remain real under perturbations of the form  $i\epsilon\mathcal{O}$ , where each term in  $\mathcal{O}$  contains an odd number of Majorana operators, i.e., changes the total occupation of auxiliary complex fermions by an odd amount.

#### 4.4.3 HAAH’S CODES

Finally, we consider Haah’s 17 CSS cubic codes [174], all of which are defined on a cubic lattice with two qubits per site  $i$ . Each cube has two stabilizers: one is built up of tensor products of  $Z$  and  $\mathbb{1}$  operators on each site  $i$ , such as  $Z_i \otimes \mathbb{1}_i$  or  $Z_i \otimes Z_i$ ; the other one involves tensor products of  $X$  and identity operators, e.g.,  $X_i \otimes \mathbb{1}_i$ . The exact form of the stabilizers differs from code to code, but all have a sub-extensive GSD. We defer a more detailed discussion of these codes to Appendix C.3—our conclusion is that, with the choice of  $\eta$  analogous to Eq. (4.5),

$$\eta = \prod_i X_i \otimes X_i, \prod_i Y_i \otimes Y_i, \prod_i Z_i \otimes Z_i, \quad (4.14)$$

the behavior of the code subspace under pseudo-Hermitian perturbations is sensitive not only to whether the system lengths are even or odd, but also whether the system lengths are

divisible by 4. Moreover, since not all cubic codes are symmetric under rotations, this behavior is dependent on which directions are even or odd, and which are divisible by 4. This admits eight different classes of codes, based on the relation between their code subspace stability under pseudo-Hermitian perturbations and their system sizes. These classes range from cubic code 7, whose code subspace stays real on all system sizes other than odd-by-odd-by-odd, and cubic code 17, where the code subspace only stays real if  $L_x, L_y$  are divisible by 4. We refer to Appendix C.3 for a complete characterization of this behavior.

## 4.5 NON-HERMITIAN QUANTUM FRACTAL LIQUIDS

In this section, we will generalize the previous analysis to also include another class of fracton models dubbed “quantum fractal liquids” [549] and reformulate the criterion of stability against non-Hermitian perturbations using a polynomial representation of Pauli operators. In this way, we will recover the criterion of stability of the toric code in an algebraic way and show that the reality of eigenvalues of the exponentially large number of ground states of quantum fractal liquids is protected against a wide range of non-Hermitian terms in the Hamiltonian.

### 4.5.1 POLYNOMIAL REPRESENTATION OF OPERATORS

To set up the notation, we will briefly introduce the polynomial representation of operators, a commonly used technique [302]. To this end, consider a polynomial of three variables,  $x, y, z$ ,

$$f = \sum_{j,k,\ell \in \mathbb{Z}} c_{jkl} x^j y^k z^\ell, \quad c_{jkl} = 0, 1,$$

over  $\mathbb{F}_2$ , meaning that all coefficients are to be understood modulo 2. This allows to define a corresponding Pauli operator whose components lie on the vertices of a cubic lattice in three dimensions in the following way

$$Z(f) := \prod_{jkl} Z_{jkl}^{c_{jkl}}, \quad X(f) := \prod_{jkl} X_{jkl}^{c_{jkl}}.$$

Here  $Z_{jkl}$  ( $X_{jkl}$ ) is the  $Z$  ( $X$ ) operator acting at vertex  $(j, k, \ell)$ . For example, a stabilizer of the checkerboard model, given by the product of Pauli matrices on the eight vertices of a cube, corresponds to the polynomial  $f = 1 + x + y + z + xy + yz + xz + xyz$ . On a finite lattice, periodic boundary conditions are specified by imposing  $x^{L_x} = y^{L_y} = z^{L_z} = 1$ . We denote the dual of  $f$ , obtained by taking  $x \rightarrow x^{-1}$ , and likewise for  $y$  and  $z$ , by  $\bar{f}$ .

Certain relations can be expressed more concisely with this polynomial representation. Translating an operator  $Z(f)$  one lattice site along the  $x$ -direction is simply given by  $Z(xf)$ , and likewise for translations in the  $y$  and  $z$ -direction. Additionally, the polynomials defined over  $\mathbb{F}_2$  naturally encode the commutation relations of the Pauli operators. To see this, consider the *commutation polynomial*, defined as  $f\bar{g}$  for two polynomials  $f$  and  $g$ . Writing  $f\bar{g}$  as

$$f\bar{g} = \sum_{ijk} d_{ijk} x^i y^j z^k,$$

$d_{ijk} = 1$  (0) implies that  $Z(f)$  and  $X(x^i y^j z^k g)$  anti-commute (commute).

Quantum fractal liquids are defined on a cubic lattice with two spins on every vertex. The form of their stabilizers is given by [549]

$$\begin{aligned} Z(\alpha, \beta), \quad X(\bar{\beta}, \bar{\alpha}), \\ \alpha = 1 - f(x)y, \quad \beta = 1 - g(x)z, \end{aligned} \tag{4.15}$$

and translations thereof, where the two arguments of  $Z$  and  $X$  denote operators on the two distinct spins per site. Different choices of polynomials  $f$  and  $g$  define different models. Clearly, all stabilizers commute, as follows from the associated commutation polynomial,  $\alpha\bar{\beta} + \beta\bar{\alpha} = 2\alpha\beta = 0$ .

For codes defined by stabilizers of this type, the logical operators take the form

$$\begin{aligned} \ell_i^{(Z)} &= Z(0, x^i \mathbf{f}(x, y)), \quad r_i^{(Z)} = Z(x^i \mathbf{g}(x, z), 0), \\ \ell_i^{(X)} &= X(x^i \bar{\mathbf{f}}(x, y), 0), \quad r_i^{(X)} = X(0, x^i \bar{\mathbf{g}}(x, z)), \end{aligned} \tag{4.16}$$

for integer  $i = 0, 1, \dots, L_x - 1$ , where we define

$$\mathbf{f} = \sum_{k=1}^{L_y} (fy)^{k-1}, \quad \mathbf{g} = \sum_{\ell=1}^{L_z} (gz)^{\ell-1}. \quad (4.17)$$

It is straightforward to verify that the operators in Eq. (4.16) commute with the stabilizers and constitute logical operators if

$$f^{L_y} = 1, \quad g^{L_z} = 1. \quad (4.18)$$

There are various ways to satisfy Eq. (4.18): the “trivial” solution, that works for any set,  $L_x$ ,  $L_y$ ,  $L_z$ , of system sizes, is  $f = g = 1$ . This corresponds to layers of toric code in the  $(\hat{y}, \hat{z})$  plane, upon noting that the bond variables of the toric code, see Fig. 4.1, can be seen as two qubits per vertex. In this case,  $\ell_i^{(Z,X)}$  and  $r_i^{(Z,X)}$  in Eq. (4.16) become Z-, X-type string operators in the  $i$ th layer along the  $\hat{y}$  and  $\hat{z}$  direction, respectively. Another way of satisfying Eq. (4.18) that works for arbitrary isotropic system sizes,  $L_x = L_y = L_z = L$ , is  $f = x^{n_f}$ ,  $g = x^{n_g}$ . However, the largest class of possible polynomials  $f$ ,  $g$  and, thus, possible models is allowed in the isotropic case with  $L = 2^{n_L}$ , since Eq. (4.18) will hold as long as  $f(1) = g(1) = 1$  [549]. Here, we refer to the latter set of models as “quantum fractal liquids,” which have been shown to exhibit exponential scaling of the GSD, obeying  $\log_2 \text{GSD}(2L) = 2 \log_2 \text{GSD}(L)$  [549]. Note, however, that the absence of string-like logical operators and mobile quasiparticles further requires that  $f$  and  $g$  are not algebraically related, i.e., that there are no integers  $n_1$  and  $n_2$  such that  $f^{n_1} = g^{n_2}$  (neglecting periodic boundary conditions). An example of a model free of string-like logical operators is provided by  $f = 1 + x + x^2$  and  $g = 1 + x + x^3$ .

#### 4.5.2 PSEUDO-HERMITIAN PERTURBATIONS

As before, we are interested in adding pseudo-Hermitian perturbations to this class of models that will leave the ground-state subspace real. We take  $\eta$  to be defined analogous to Eq. (4.14)

or, in polynomial representation,

$$\begin{aligned} \eta &= Z(h, h), X(h, h), iX(h, h)Z(h, h), \\ h &= \sum_{j=1}^{L_x} \sum_{k=1}^{L_y} \sum_{\ell=1}^{L_z} x^{j-1} y^{k-1} z^{\ell-1}. \end{aligned} \tag{4.19}$$

Any  $\eta$  in Eq. (4.19) will commute with all stabilizers (4.15). This readily follows from the associated commutation polynomial upon noting that  $h = \bar{h}$  is invariant under multiplication by any monomial, physically related to the translation invariance of  $\eta$ , and that the number of monomials in both  $f$  and  $g$  must be odd. The latter is a consequence of Eq. (4.18) and of the observation that the parity of the number of terms of a polynomial  $f$  over  $\mathbb{F}_2$  is the same as that of any of its powers,  $f^n$  with  $n > 0$ .

Based on our discussion of Sec. 4.2, we want to analyze under which conditions the ground-state subspace is even under these operators to guarantee that their eigenvalues stay real. Previously, we had verified this by attempting to assemble  $\eta$  via the stabilizers of the model. In the set of models introduced above, the polynomial representation makes it easier to instead verify whether  $\eta$  commutes with all the logical operators (4.16), which in turn implies that all ground states have the same eigenvalue of  $\eta$  [and that  $\eta$  is of the form of Eq. (4.10a) rather than Eq. (4.10b)].

The condition for  $\eta$  to commute with all the logical string operators is given by

$$hg = hf = 0, \tag{4.20}$$

for any of the three possible choices in Eq. (4.19). This simple expression arises from the fact that  $\bar{h} = h$  and that the logical operators come in exactly the form of operators relevant to the commutation polynomial, so one can verify that  $\eta$  commutes with all the string operators with one equation. It would technically suffice for  $hg$  and  $hf$  to be only a function of  $y$  and  $z$ , since one is only concerned with the commutations of operators like  $Z(h)$  and  $X(x^i f)$ , but not those with relative shift along the  $\hat{y}$  or  $\hat{z}$  directions. However, recalling that  $h$  is invariant under multiplication by any monomial, there is no way for  $g$  or  $f$  to conspire to cancel out only the terms independent of  $y$  and  $z$  in  $hg$  and  $hf$  without simply giving 0.

Another important consequence of  $h$  being invariant under the multiplication by any monomial is that Eq. (4.20) is satisfied if and only if  $\mathbf{f}$  and  $\mathbf{g}$  contain an even number of monomials. As argued above, Eq. (4.18) implies that  $f, g$  and, therefore, also  $f^n, g^n$  must contain an odd number of terms. Taken together, Eq. (4.20) is obeyed and, thus, *the reality of the eigenvalues of the ground states is protected against pseudo-Hermitian perturbation with  $\eta$  given in Eq. (4.19) if  $L_y$  and  $L_z$  are even*. Note that the  $x$ -direction is distinguished from the other two directions in this criterion, a reflection of the fact that the stabilizers given by Eq. (4.15) also distinguishes the  $x$ -direction.

Let us illustrate this for the different special cases of  $f$  and  $g$  noted above. Taking  $f = g = 1$  corresponds to  $L_x$  uncoupled layers of toric code and the above statement implies that the toric code is protected if and only if the number of sites in each in-plane direction is even, reproducing the result of Sec. 4.3. Our current formalism, however, captures many more cases. For instance, we immediately conclude that any model with  $f = x^{n_f}, g = x^{n_g}$  and  $L_x = L_y = L_z = L$  is protected only for even  $L$ . As the two polynomials are algebraically related, this two-parameter family of models is characterized by string-like logical operators and has excitations mobile along the direction  $n_g \hat{y} - n_f \hat{z}$  [549]. Finally, as already noted above, quantum fractal liquids with arbitrary  $f$  and  $g$ , only constrained by  $f(1) = g(1) = 1$ , are in general defined on lattices with an even number of sites and, as such, are always protected against pseudo-Hermitian perturbations with metric operator in Eq. (4.19).

## 4.6 SUMMARY AND CONCLUSIONS

In this work, we studied the behavior of the eigenvalues of quantum many-body Hamiltonians of the form of Eq. (4.2), i.e., starting from a Hermitian system,  $H_0$ , we turn on a non-Hermitian perturbation,  $\epsilon V$ , and demand that the entire Hamiltonian be pseudo-Hermitian. Using pseudo-Hermiticity rather than  $\mathcal{PT}$  symmetry is related to the fact that the former is more general than the latter [560]; we note, however, that all of the explicit examples considered here are both  $\mathcal{PT}$  symmetric and pseudo-Hermitian. We analyzed whether the energies,  $E_i$ , of a given subspace of interest of  $H_0$  will remain real as long as the gap to other states of the system is finite ( $\mathcal{PT}$  symmetry protected) or whether they can move into

the complex plane without closing the gap ( $\mathcal{PT}$  symmetry fragile). While symmetries can enforce degeneracies ( $E_i = E_{i'}$ ) and protect eigenvalues from becoming complex in conjunction with pseudo-Hermiticity ( $E_i = E_{i'}^*$ ), we discussed that this is also possible in the absence of symmetries: if the eigenvalues of the metric operator  $\eta$  are the same for all states in the subspace of interest,  $E_i$  are guaranteed to stay real and  $\mathcal{PT}$  symmetry is protected.

We demonstrated that this criterion can be readily applied to various paradigmatic many-body models with crucial implications. As a first example, we took the toric code model (4.4) as unperturbed Hamiltonian,  $H_0$ . On a torus, it exhibits four degenerate ground states and one would generically expect them to become complex when turning on  $\epsilon V$ . However, we have shown that  $\eta$  of the form given in Eq. (4.5) allows for a large class of non-Hermitian perturbations; these are shown to leave the ground-state energies real on an even-by-even lattice, even if all symmetries are broken. They can only become complex and  $\mathcal{PT}$  can only be broken in the ground-state subspace, when the gap to the excited states closes. In fact, we have argued that any sufficiently generic non-Hermitian perturbation (see Sec. 4.3.4) in a system with both linear system sizes even (at least one of them odd) will only allow for  $\eta$  of the form of Eq. (4.10a) [of the form of Eq. (4.10b)] and the ground-state eigenvalues are protected (not protected) from becoming complex. This sensitivity to system size reflects the highly entangled nature of the toric-code ground states.

We came to the same conclusions for the ground-state manifolds of the X-cube (4.11), the spin (4.12) and Majorana (4.13) checkerboard models, and for the fractal liquids of Ref. [549]. In these cases, the stability of  $\mathcal{PT}$  symmetry is even more surprising due to the enormous GSD that grows exponentially with system size. For Haah’s 17 codes, the stabilizers have a slightly more complicated form and the minimal requirement for stability differs from code to code, although we observe several groups of codes which all obey the same requirements. This classification of Haah’s codes based on stability of  $\mathcal{PT}$  symmetry approximately follows previous classifications based on entanglement renormalization [115].

On a more general level, our work illustrates that  $\mathcal{PT}$  symmetry and the reality of energies can be protected in the degenerate ground-state manifold of correlated many-body systems with different forms of topological order—even in the absence of any symmetries and although exceptional points are generically expected to be abundant [296]. By virtue of being exact

and simple, our framework can be readily applied to a large class of systems and provides a systematic method for constructing pseudo-Hermitian perturbations that ensures the reality of the resulting eigenvalues. This is not only relevant for experimental studies [7, 393, 476, 528] and potential applications [26, 27, 293, 466, 516], but might also help deepen our theoretical understanding of non-Hermitian systems hosting exotic phases of matter, e.g., by providing novel ways of classifying spin-liquid or fracton phases according to their sensitivity to such perturbations.

*It's about control or lack thereof*

*A twist of fate, a change, a reversal*

Sprain, The Lamb As Effigy

# 5

## An exactly solvable dissipative spin liquid

### 5.1 INTRODUCTION

Quantum spin liquids (QSLs) are exotic phases of matter characterized by emergent anyon excitations with non-trivial braiding statistics, in conjunction with the absence of any conventional long-range order [57, 251, 427]. Further interest in these states have grown due to their potential applications for use in fault-tolerant quantum computation [107, 479] through their non-local encoding of quantum information.

The interplay between QSLs and open quantum systems has been an active area of research for many years, with a primary focus on the robustness of their information storage and on approaches to detect their presence when perturbations generic to experimental realization are introduced, such as a non-zero temperature, decoherence, and more [6, 58, 229, 231, 343, 364, 432, 572]. Rather than taking this approach of considering generic forms of decoherence, we instead consider engineering a particular form of environmental coupling to a QSL in order to realize unique non-equilibrium physics. This general approach of leveraging dissipation has been shown to be efficient at preparing quantum states [31, 109, 259, 267, 509] including topologically-protected edge modes [110]. Recent applications of this idea to spin liquids [201, 543] have yielded new insights into the behavior of emergent anyon excitations in the presence

of dissipation.

We study a quantum spin-3/2 model on a two-dimensional square lattice, which is a particular limit of the QSL studied in [546], and subject it to a certain choice of Markovian open dynamics generated by the Lindblad equation. We show that in a particular limit, the Lindbladian becomes exactly solvable through a parton construction. As such, exact statements about its steady-state solutions as well as transient behavior can be made. Exactly solvable Lindbladians have been studied previously using techniques such as third quantization [372, 428, 468], Bethe ansätze [104, 311], operator-space fragmentation [133], and through parton constructions [447] similar to our own. From a practical perspective, this exact solvability is especially useful as the wealth of analytic tools developed to approximately study the low-energy behavior of Hermitian Hamiltonians do not immediately carry over to these non-Hermitian Lindbladians, although several methods for approximately studying the spectrum of Lindbladians have been developed [243, 394].

A particular property of our exact solution that we emphasize is the existence of distinct quasiparticle excitations of the Lindbladian when viewed as an effective non-Hermitian Hamiltonian acting on an enlarged Hilbert space. We advocate for this as a powerful tool for understanding the non-equilibrium behavior of a generic state or density matrix as it equilibrates to its steady-state solution. We show that the imaginary energy gap associated with a particular type of quasiparticle excitation in this enlarged Hilbert space can be associated with the equilibration timescale of the expectation value of a certain class of observables. These classes of observables turn out to have a close relation to excitations of the corresponding unitary spin liquid. An expert reader might immediately want to inspect Sec. 5.5 for a summary of the spectrum. Importantly, the different time scales of these classes of operators have different parametric dependence on the strength  $\gamma$  of the coupling to the environment, which can be found simply by diagonalizing a quadratic Hamiltonian numerically, or in some cases is derived exactly analytically. For instance, in the limit of small  $\gamma$ , a certain set of operators, that are not conserved by the unitary dynamics, decay rapidly on a scale set by the exchange coupling rather than  $\gamma$  itself. Fractionalized string-like operators that can be interpreted as pairs of emergent Majorana fermion excitations in the unitary system, however, survive up to a time-scale  $\propto 1/\gamma$ . After that, also the Majorana fermions heat up and

only gauge-invariant fluxes of the emergent gauge fields or Wilson-loop operators remain in their original configuration. In this sense, our model realizes a three-step and exactly solvable analogue of the “fractionalized pre-thermalization” discussed recently [225] for stroboscopic time-evolution in the Kitaev model.

The remainder of the paper is organized as follows. A mathematical definition of all the involved operators and of the dissipative model we study can be found in Sec. 5.2. We derive and interpret the spectrum of the Lindbladian in Sec. 5.3. A discussion of perturbations away from the exactly solvable point and a conclusion are provided in Sec. 5.4 and Sec. 5.5, respectively.

## 5.2 MODEL

The time evolution of a density matrix  $\rho$  can be described in its most general form by a completely-positive and trace preserving map  $\Phi(\rho) \rightarrow \rho'$ . The Lindblad equation [166, 288] is the most generic continuous Markovian map satisfying these properties,

$$\frac{d\rho}{dt} = \mathcal{L}[\rho] = -i[H, \rho] + \sum_j \left( L_j \rho L_j^\dagger - \frac{1}{2} \{ L_j^\dagger L_j, \rho \} \right), \quad (5.1)$$

where the quantum jump operators  $L_j$  parameterize the nature of the environmental coupling. One may express the superoperator  $\mathcal{L}$  as an operator in a “doubled” Hilbert space, namely the Hilbert space of all operators. For a choice of basis in the original Hilbert space,  $|\psi_i\rangle$ ,  $i = 1 \dots \mathcal{D}$ , we can represent any operator  $\mathcal{O} = \sum_i \mathcal{O}_{ij} |\psi_i\rangle \langle \psi_j|$  as a state  $\|\mathcal{O}\rangle \equiv \sum_{ij} \mathcal{O}_{ij} |\psi_i\rangle \otimes |\psi_j\rangle$  in this doubled Hilbert space, with inner product  $\langle\langle \mathcal{O}_1 \| \mathcal{O}_2 \rangle \rangle = \frac{1}{\mathcal{D}} \text{tr} (\mathcal{O}_1^\dagger \mathcal{O}_2)$ . Within this doubled Hilbert space, the action of the Lindbladian superoperator is

$$i\mathcal{L} = H_{\text{eff}} \otimes \mathbb{1} - \mathbb{1} \otimes H_{\text{eff}}^\dagger + \sum_j i\gamma L_j \otimes L_j^\dagger, \\ H_{\text{eff}} \equiv H - \frac{i\gamma}{2} \sum_j L_j^\dagger L_j. \quad (5.2)$$

We will take  $L_j$  to be unitary, such that  $H_{\text{eff}} = H$  up to an overall imaginary constant.

This doubled Hilbert space construction is a powerful tool for characterizing the behavior of mixed states; notably, it has seen recent use in diagnosing the stability of quantum information

stored in mixed states [28, 269]. For a quantum spin model in two dimensions, it is instructive to think of this doubled Hilbert space as corresponding to a bilayer system, where the first (second) layer corresponds to the bra (ket). In this scenario, the Lindbladian consists of two copies of the Hamiltonian  $\pm H$  acting on each of the two layers, with anti-Hermitian couplings  $i\gamma \sum_j L_j \otimes L_j^\dagger$  between the two layers. To better connect with intuition from unitary time evolution, we will focus on the eigenvalues of the matrix  $i\mathcal{L}$  rather than  $\mathcal{L}$  and refer to  $i\mathcal{L}$  as “the Lindbladian”; in this convention, the imaginary components of eigenvalues correspond to dissipation, and the non-existence of exponentially growing solutions requires the imaginary part to always be negative.

### 5.2.1 UNITARY TIME EVOLUTION

The Hermitian dynamics that we consider is a particular limit of an exactly solvable quantum spin-3/2 model on a square lattice first studied in [546]. We define this model here and review some properties of its solution, as our results are most clearly stated within this framework. Due to the four spin polarizations per site, we may express the spin-3/2 degrees of freedom in terms of anticommuting Gamma matrices  $\Gamma^a$ ,  $a = 1 \dots 5$ , which obey  $\{\Gamma^a, \Gamma^b\} = 2\delta^{ab}$ . In terms of the physical spin operators,

$$\begin{aligned}\Gamma^1 &= \frac{1}{\sqrt{3}}\{S^y, S^z\}, & \Gamma^2 &= \frac{1}{\sqrt{3}}\{S^z, S^x\}, \\ \Gamma^3 &= \frac{1}{\sqrt{3}}\{S^x, S^y\}, & \Gamma^4 &= \frac{1}{\sqrt{3}}[(S^x)^2 - (S^y)^2], \\ \Gamma^5 &= (S^z)^2 - \frac{5}{4}.\end{aligned}\tag{5.3}$$

We emphasize that the key property needed in our construction is the presence of five anti-commuting Gamma matrices. This can alternatively be accomplished by a pair of spin-1/2 operators (or qubits) on each site. In this approach, there are multiple ways of constructing anti-commuting Gamma matrices. One possible representation is

$$\begin{aligned}\Gamma^1 &= S^x \otimes S^x, & \Gamma^2 &= S^x \otimes S^y, \\ \Gamma^3 &= S^x \otimes S^z, & \Gamma^4 &= S^y \otimes \mathbb{1}, \\ \Gamma^5 &= S^z \otimes \mathbb{1}.\end{aligned}\tag{5.4}$$

The choice of representation will influence the physical interpretation of the dissipation, as will be discussed later. Additional choices are discussed in Appendix D.1.

The Hamiltonian is defined on a square lattice as

$$H = \sum_j \left[ J_x \Gamma_j^1 \Gamma_{j+\hat{x}}^2 + J_y \Gamma_j^3 \Gamma_{j+\hat{y}}^4 \right] + \sum_j \left[ J'_x \Gamma_j^{15} \Gamma_{j+\hat{x}}^{25} + J'_y \Gamma_j^{35} \Gamma_{j+\hat{y}}^{45} \right] - J_5 \sum_j \Gamma_j^5 \quad (5.5)$$

where  $\Gamma_j^{ab} \equiv [\Gamma_j^a, \Gamma_j^b]/2i$ . For simplicity, we will assume that the lattice has an even number of sites in both the  $\hat{x}$  and  $\hat{y}$  directions. The exact solvability of this model is a consequence of an extensive number of conserved fluxes,

$$W_j = \Gamma_j^{13} \Gamma_{j+\hat{x}}^{23} \Gamma_{j+\hat{y}}^{14} \Gamma_{j+\hat{x}+\hat{y}}^{24}, \quad (5.6)$$

and can be understood most conveniently by performing a Majorana decomposition of the  $\Gamma$  matrices; specifically, one employs the representation

$$\begin{aligned} \Gamma_j^\mu &= i c_j^\mu d_j, & \Gamma_j^{\mu 5} &= i c_j^\mu d'_j, & \mu &= 1, 2, 3, 4, \\ \Gamma_j^5 &= i d_j d'_j, \end{aligned} \quad (5.7)$$

with the constraint  $-ic_j^1 c_j^2 c_j^3 c_j^4 d_j d'_j = \Gamma_j^1 \Gamma_j^2 \Gamma_j^3 \Gamma_j^4 \Gamma_j^5 = -1$ . In this representation, the Hamiltonian can be rewritten in terms of static  $\mathbb{Z}_2$  gauge fields  $\hat{w}_{j,\alpha}$  living on the bonds of the lattice, which come from conserved bilinears of the  $c_j^\mu$  operators, coupled to two species of Majorana fermions,  $d_j$  and  $d'_j$ .

We will not give a detailed review of the various properties of this solution [546], as it will not be important for our analysis. However, we will emphasize the relation between these emergent degrees of freedom and physical observables, as the results of our dissipative model concisely fit into this picture. The  $\mathbb{Z}_2$  gauge fluxes - products of closed loops of  $\hat{w}_{j,\alpha}$  operators - correspond to the conserved fluxes  $W_j$ . Pairs of Majorana fermions coupled by a string of  $\mathbb{Z}_2$  gauge fields are given by strings of  $\Gamma$  matrices. For a pair of  $d$  excitations, the operator

can be generated by a string of bond operators:

$$V_{j,\alpha} = \begin{cases} \Gamma_j^1 \Gamma_{j+\hat{x}}^2 & \alpha = x, \\ \Gamma_j^3 \Gamma_{j+\hat{y}}^4 & \alpha = y. \end{cases} \quad (5.8)$$

A similar construction follows for a pair of  $d'$  fermions,

$$V'_{j,\alpha} = \begin{cases} \Gamma_j^{15} \Gamma_{j+\hat{x}}^{25} & \alpha = x, \\ \Gamma_j^{35} \Gamma_{j+\hat{y}}^{45} & \alpha = y, \end{cases} \quad (5.9)$$

as well as the combination of a  $d$  and  $d'$  fermion, a special case of which is  $\Gamma_j^5 = id_j d'_j$ .

Note that a closed loop of either the  $V_{j,\alpha}$  or  $V'_{j,\alpha}$  operators is equivalent to a product of the conserved fluxes contained inside the loop.

In order to retain the exact solvability upon the inclusion of dissipation, we take  $J'_x = J'_y = J_5 = 0$ , which causes the bond operators  $V'_{j,\alpha}$  to become conserved quantities. In the Majorana fermion language, this limit quenches the dispersion of the  $d'_j$  fermions and the ground state becomes highly degenerate as pairs of  $d'_j$  may be added in at no energy cost.

### 5.2.2 JUMP OPERATORS

We now introduce jump operators  $L_j = \Gamma_j^5$ . Note that our Lindbladian jump operators commute with the conserved flux,  $[L_j, W_k] = 0$ . This property implies that the flux operators  $W_j$  constitute *strong symmetries* of the system, as defined in [60], and means that an initial state with a definite flux configuration will remain in such a configuration. If we express our Hermitian model as free Majorana fermions coupled to a static  $\mathbb{Z}_2$  gauge field, the interpretation of this phenomenon is that the gauge fields will remain static under the Lindbladian time evolution while generically we expect the Majorana fermions to evolve to resemble a finite-temperature Gibbs state. One may think of this behavior as “fractionalized thermalization.” For a generic set of quantum jump operators that commute with  $W_j$ , we expect the steady-state solutions of the Lindbladian can be represented as the tensor product of a thermal Gibbs state of Majorana fermions with a pure state of  $\mathbb{Z}_2$  gauge fields. We note

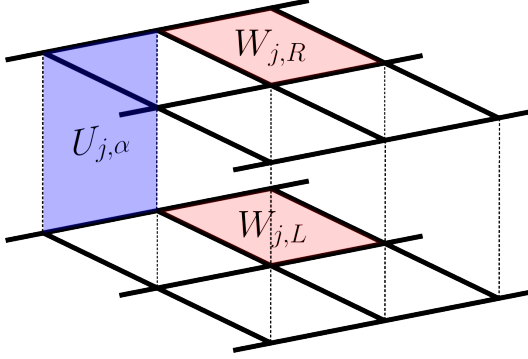


Figure 5.1: In the doubled Hilbert space representation, the Lindbladian super operator possesses two types of conserved fluxes. The first are intralayer fluxes  $W_{j,R}$ ,  $W_{j,L}$ , which correspond to physical conserved plaquette operators. The second,  $U_{j,\alpha}$ , have a purely superoperator interpretation, as explained in the main text.

related work studying the separation of thermalization timescales in fractionalized excitations on the Kitaev honeycomb model [225] under stroboscopic time evolution, as well as more directly analogous work studying the Kitaev honeycomb model coupled to jump operators that commute with the conserved fluxes [201]. Apart from fluxes being exactly conserved under dissipative dynamics, we also uncover below an additional, less apparent regime of fractionalized thermalization in our exactly solvable model, which occurs in the limit of small dissipation.

The above discussion follows for any jump operator that commutes with the conserved fluxes, and remains true even away from the limit  $J'_x = J'_y = J_5 = 0$ . However, our particular model admits additional conserved quantities which render the full dissipative dynamics exactly solvable. To see this, we use the doubled Hilbert space formalism, see Eq. (5.2), to express the Lindbladian superoperator as an operator acting on a bilayer spin-3/2 system, with Gamma matrices  $\Gamma_R^a, \Gamma_L^a$  for the two layers - the  $R, L$  subscript indicates that they correspond to the right and left action of the gamma matrices on the physical operator. The Lindbladian can be written as

$$i\mathcal{L} = H[\Gamma_R] - H[\Gamma_L] + i\gamma \sum_j \Gamma_{j,R}^5 \Gamma_{j,L}^5 - i\gamma N, \quad (5.10)$$

where  $N$  is the number of sites. This bilayer representation makes it clear that, in addition to the intralayer fluxes  $W_{j,R}, W_{j,L}$  which are defined in analogy to Eq. (5.6) and commute with

the Lindbladian separately, we have a new set of conserved interlayer fluxes  $U_{j,\alpha} \equiv V'_{j,\alpha,R} V'_{j,\alpha,L}$  defined on the plaquettes connecting the two layers, shown in Fig. 5.1. These conserved quantities are “weak” symmetries [60]. In contrast to the strong symmetries generated by the flux operators  $W_j$ , the operators  $V'_{j,\alpha}$  do not commute with the jump operators  $L_j$  individually, and it is exclusively the conserved *superoperator* consisting of the simultaneous right and left action of  $V'_{j,\alpha}$  that commutes with the Lindbladian.

We comment here on the physical interpretation of the jump operators  $\Gamma_j^5$  in terms of the microscopic degrees of freedom. If our Gamma matrices are built out of pairs of spin-1/2 operators,  $\Gamma^5 = S^z \otimes \mathbb{1}$  and our dissipation should be thought of as an *asymmetric* dephasing acting on only one of the two spin-1/2 degrees of freedom. For spin-3/2 operators,  $\Gamma^5 = (S^z)^2 - \frac{5}{4}$ , which acts as a dephasing term between the  $S^z = \pm\frac{1}{2}$  and the  $S^z = \pm\frac{3}{4}$  states.

### 5.2.3 PARTON CONSTRUCTION

To elucidate the exact solvability of this model, we represent the Gamma matrices in terms of six Majorana fermions,

$$\begin{aligned}\Gamma_{j,R}^\mu &= i c_{j,R}^\mu d_{j,R}, & \Gamma_{j,R}^{\mu 5} &= i c_{j,R}^\mu d'_{j,R}, & \mu &= 1, 2, 3, 4, \\ \Gamma_{j,R}^5 &= i d_{j,R} d'_{j,R},\end{aligned}\tag{5.11}$$

with an analogous representation for  $\Gamma_L^\mu$  in terms of  $c_{j,L}^\mu, d_{j,L}, d'_{j,L}$ . This enlarges our Hilbert space, which necessitates the constraint  $-ic_{j,R}^1 c_{j,R}^2 c_{j,R}^3 c_{j,R}^4 d_{j,R} d'_{j,R} = \Gamma_{j,R}^1 \Gamma_{j,R}^2 \Gamma_{j,R}^3 \Gamma_{j,R}^4 \Gamma_{j,R}^5 = -1$  on all physical states, and likewise for the  $\Gamma_L$  operators.

In this representation, the Hamiltonian  $H[\Gamma_R]$  becomes

$$H[\Gamma_R] = \sum_j J_x \hat{w}_{j,x,R} i d_{j,R} d_{j+\hat{x},R} + J_y \hat{w}_{j,y,R} i d_{j,R} d_{j+\hat{y},R}\tag{5.12}$$

where  $\hat{w}_{j,x,R} \equiv -ic_{j,R}^1 c_{j+\hat{x},R}^2$  and  $\hat{w}_{j,y,R} \equiv -ic_{j,R}^3 c_{j+\hat{y},R}^4$  are conserved quantities with eigenvalue  $\pm 1$ . An analogous rewriting follows for the Hamiltonian on the second layer. Observe that the Majorana fermions  $d'_{j,R}, d'_{j,L}$  drop out of the intralayer Hamiltonian entirely. As a

result, the interlayer coupling also becomes quadratic in the Majorana fermions,

$$\begin{aligned} i\gamma \sum_j \Gamma_{j,R}^5 \Gamma_{j,L}^5 &= -i \sum_j d_{j,R} d'_{j,R} d_{j,L} d'_{j,L} \\ &= -\gamma \sum_j \hat{v}_j d_{j,R} d_{j,L}, \end{aligned} \quad (5.13)$$

where  $\hat{v}_j \equiv -id'_{j,R} d'_{j,L}$  is a conserved quantity with eigenvalue  $\pm 1$ . With this rewriting, our model becomes one of free fermions  $d_{j,R}, d_{j,L}$  hopping on a bilayer square lattice in the presence of a background  $\mathbb{Z}_2$  gauge field  $\hat{w}_{j,\alpha,R}, \hat{w}_{j,\alpha,L}, \hat{v}_j$  living on the links. Written out explicitly,

$$i\mathcal{L} = \sum_{\ell=L,R} \sum_j s_\ell [J_x \hat{w}_{j,x,\ell} d_{j,\ell} d_{j+\hat{x},\ell} + J_y \hat{w}_{j,y,\ell} id_{j,\ell} d_{j+\hat{y},\ell}] - \gamma \sum_j \hat{v}_j d_{j,R} d_{j,L} - i\gamma N \quad (5.14)$$

where  $s_L = 1, s_R = -1$ . This Lindbladian possesses a local  $\mathbb{Z}_2$  gauge symmetry, given by the transformation  $d_{j,\ell} \rightarrow \Lambda_{j,\ell} d_{j,\ell}, \hat{w}_{j,\alpha,\ell} \rightarrow \Lambda_{j,\ell} \hat{w}_{j,\alpha,\ell} \Lambda_{j+\hat{\alpha},\ell}, \hat{v}_j \rightarrow \Lambda_{j,L} \hat{v}_j \Lambda_{j,R}$ , where  $\Lambda_{j,\ell} = \pm 1$ . The gauge-invariant fluxes around a single intralayer plaquette gives the conserved quantities  $-W_{j,R}, -W_{j,L}$ , and the fluxes around an interlayer plaquette gives the conserved superoperator  $-U_{j,\alpha}$ . Note the relative minus signs between the two quantities - as will be relevant later, working in a sector with  $U_{j,\alpha} = 1$ , which is the sector where steady-state solutions will belong to, requires us to pick a gauge configuration such as  $\hat{v}_j = (-1)^j$ .

In order to obtain physical states, we must project back to our physical (doubled) Hilbert space. This is obtained by the projection operator  $P = \prod_{j,\ell} \frac{1+D_{j,\ell}}{2}$ , where

$$D_{j,\ell} = -ic_{j,\ell}^1 c_{j,\ell}^2 c_{j,\ell}^3 c_{j,\ell}^4 d_{j,\ell} d'_{j,\ell}. \quad (5.15)$$

A careful analysis of this for a single-layer Hamiltonian was performed in [546] and our analysis proceeds along similar lines. We can write  $P = P'(1 + D)$ , where  $D \equiv \prod_{j,\ell} D_{j,\ell}$  and  $P'$  is a linear combination of all inequivalent gauge transformations. Since  $D^2 = 1, [D, \mathcal{L}] = 0$ , this means that we must restrict ourselves to eigenstates with  $D = 1$ . We write

$$D = \prod_{j,\alpha,\ell} \hat{w}_{j,\alpha,\ell} \prod_j \hat{v}_j \prod_j id_{j,L} d_{j,R}. \quad (5.16)$$

In order to more readily leverage the gauge constraint, we re-express the Majorana fermions  $d_{j,R}, d_{j,L}$  in terms of complex fermions. A representation that will prove to be useful for future analysis is

$$f_j = i^j (d_{j,L} + i(-1)^j d_{j,R}) / 2. \quad (5.17)$$

With this,  $2f_j^\dagger f_j - 1 = (-1)^j i d_{j,L} d_{j,R}$  and  $(-1)^{N_f} \equiv (-1)^{\sum_j f_j^\dagger f_j} = \prod_j i d_{j,L} d_{j,R}$ . Therefore, gauge invariance restricts the total fermion parity,  $(-1)^{N_f}$ , to equal the total “gauge parity,”  $\prod_{j,\alpha,\mu} \hat{w}_{j,\alpha,\mu} \prod_j \hat{v}_j$ .

### 5.3 SPECTRUM OF THE LINDBLADIAN

In the previous section, we have shown that our Lindbladian reduces down to one of free fermions coupled to a static  $\mathbb{Z}_2$  gauge field. As such, the full spectrum and eigenvectors can in principle be calculated - analytically for translationally-invariant gauge field configurations, and by diagonalizing a non-Hermitian single-particle Hamiltonian for more general gauge configurations. However, the interpretation of these properties must be done in terms of density matrices of our physical Hilbert space, rather than a more conventional analysis of Hermitian systems. We outline our general approach to understanding these properties below.

#### 5.3.1 GENERAL REMARKS

The most important eigenstates of the Lindbladian are those with eigenvalue zero, which correspond to steady-state solutions. Since the eigenvalues  $\lambda_i$  of the Lindbladian obey  $\text{Im}[\lambda_i] \leq 0$ , every initial density matrix will eventually evolve into some superposition of these steady-state solutions (for simplicity, we ignore the possibility of solutions with purely real eigenvalue, i.e. density matrices that do not decay but whose phase oscillates in time, as these are not present in our spectrum). Our first task will be to find these steady-state solutions and understand their properties.

Ascertaining the properties of these steady-state solutions is a non-trivial task within the doubled Hilbert space formalism. Given a density matrix  $\|\rho\|$ , the expectation value of a Hermitian operator  $A$  is given by  $\text{Tr}[A\rho] = \langle\langle A \|\rho\| \rangle\rangle$ . As such, standard intuition for calculating observables of pure states in ordinary Hilbert spaces,  $\langle\psi| A |\psi\rangle$ , is not applicable here. While

it is possible to develop the machinery to perform such calculations, we instead proceed with a more intuitive symmetry-based analysis. The exact solvability of our model provides an extensive number of superoperators that commute with the Lindbladian, and hence  $\langle\!\langle \rho \rangle\!\rangle$  will be an eigenstate of them. By decomposing our Hilbert space into subspaces with definite eigenvalue under these superoperators, we can conclude that  $\langle\!\langle A | \rho \rangle\!\rangle$  must vanish unless the two have the same eigenvalue. In general, this symmetry analysis only gives us limited information about  $\langle\!\langle \rho \rangle\!\rangle$ . However, the extensive number of conserved quantities makes this perspective especially powerful for our model, and we will find that only a small amount of additional analysis is required to fully characterize the steady-state solution.

After characterizing the steady-state solutions, we will analyze the dissipative solutions - operators with eigenvalue  $\lambda_i$  obeying  $\text{Im } \lambda_i < 0$ . We will be interested in eigenvalues whose imaginary components have the smallest magnitude, which defines the *Liouvillian gap*, and a corresponding timescale associated with the decay to the steady-state solution. As the spectrum of our Lindbladian has the interpretation of fermions coupled to a  $\mathbb{Z}_2$  gauge field, we find it insightful to define distinct types of Liouvillian gaps depending on the nature of the excitation. For example, one may inquire into the Liouvillian gap with respect to fermionic excitations, or with respect to gauge excitations (visons). This is not an arbitrary labeling, the motivation for which ties back to our symmetry-based analysis of steady-state solutions. Excitations within a given sector will have different eigenvalues under the symmetries of our Lindbladian, and hence can be characterized by distinct classes of observables that have a non-zero overlap with these excitations. The corresponding Liouvillian gap for these excitations specify a timescale which governs the rate at which the expectation values for these classes of observables asymptote to their steady-state solutions. We note that a similar hierarchy of timescales was recently studied in random local Liouvillians [504] and in fact observed in simulations on a quantum computer [457] - in this model, the separation of timescales was associated with differing spatial extents of operators. A symmetry-based analysis of the low-energy properties of the Lindbladian spectra has also been recently leveraged in Brownian circuits to construct an effective hydrodynamics description of the real-time dynamics [344].

To be more explicit with our perspective, consider a steady-state solution  $\langle\!\langle \rho_{ss} \rangle\!\rangle$  and a dissipative solution  $\langle\!\langle a \rangle\!\rangle$  which we interpret as a quasiparticle excitation of type  $a$ . A physical

density matrix can be constructed by  $\|\rho_d\| \equiv \|\rho_{ss}\| + c\|a\|$ , where  $c$  is some constant chosen to ensure  $\text{Tr}[\rho_d^2] < 1$ . This density matrix asymptotes to  $\|\rho_{ss}\|$  at late times but displays transient behavior dictated by  $\|a\|$  up to a timescale  $t_a = -\text{Im}[\lambda_a]^{-1}$ . It is useful to characterize this operator  $a$  in terms of observables  $\{\mathcal{O}_a\}$  such that  $\text{Tr}[\mathcal{O}_a a] \neq 0$ , in which case one can say that the expectation value of observables  $\mathcal{O}_a$  relax to their steady-state values with a timescale dictated by  $t_a$  for the density matrix  $\|\rho_d\|$ . Of course, a generic initial density matrix will be more complicated than  $\|\rho_d\|$ ; however, if  $\|a\|$  is the lowest-energy excitation that has a non-zero overlap with the observables  $\mathcal{O}_a$ , then  $t_a$  provides an upper bound on the equilibration timescale for the expectation value of these observables.

The utility of this picture is contingent on the operators  $\mathcal{O}_a$  having a sufficiently simple representation. As we will show, these different classes of observables are most conveniently stated in terms of fractionalized operators acting on the original Hilbert space, such as the bond operators in Eq. 5.8 and Eq. 5.9. In other words, we demonstrate a close connection between fractionalized excited states in the *doubled* Hilbert space formalism and fractionalized operators in the *physical* Hilbert space, with the imaginary energy of the former defining the equilibration timescale of expectation values of the latter.

We note an emerging body of work [175, 268, 323, 324] which take a conceptually related stance to our own, which is that the Liouvillian gap does not solely determine the relaxation time of a dissipative system to its steady-state solution. These works noted that an anomalously small overlap between left and right eigenmodes of the Lindbladian - induced, for example, through a non-Hermitian skin effect - can enhance the relaxation time of the system. While we have verified numerically in our model that no such small overlap is present, we note the similarity with our work in that the structure of the *eigenvectors*, rather than purely the energy gap, can qualitatively change the nature of the relaxation process. In our case, certain long-lived eigenmodes only have an effect on distinct classes of observables, which we identify by leveraging the extensive amount of symmetries present in our model.

### 5.3.2 STEADY-STATE SOLUTIONS

We now study the properties of the steady-state solutions. Recall that for isolated systems with similar Hamiltonians (free fermions coupled to static  $\mathbb{Z}_2$  gauge fields), there is a theorem

due to Lieb [283] for bipartite lattices that fixes the gauge flux sector in which the ground state resides in. In a similar spirit, we leverage general arguments given in [60] that allow us to deduce gauge flux sectors which support steady-state solutions.

A fact that we will use in this argument is that any dissipative eigenstate of the Lindbladian must have zero trace - if it had a non-zero trace, the dissipative nature implies that the trace would decay in time, contradicting the trace preservation of the Lindbladian time evolution. Hence, the search for steady-state solutions can be recast as a search for eigenstates with a non-zero trace. This comes with the caveat that we may miss steady-state solutions that happen to also have zero trace; however, we explicitly diagonalize the Lindbladian for a  $4 \times 4$  lattice in each gauge sector and have found no such solutions.

We first constrain the interlayer fluxes  $U_{j,\alpha}$ , which constitute weak symmetries. Recall that the superoperator  $U_{j,\alpha}$  acts on density matrices as  $U_{j,\alpha}[\rho] = V'_{j,\alpha}\rho V'_{j,\alpha}$ . An eigenstate of  $U_{j,\alpha}$  with non-zero trace must have eigenvalue 1, since unitarity and Hermiticity of  $V'_{j,\alpha}$  implies  $\text{Tr}[\rho] = \text{Tr}[V'_{j,\alpha}\rho V'_{j,\alpha}]$ . Hence, we will constrain ourselves to the  $U_{j,\alpha} = 1$  sector.

We now turn to the “strong” symmetries  $W_i$ . A similar argument as the last paragraph implies that we must constrain ourselves to sectors where  $W_j\rho W_j = \rho$ . However, recall that in the doubled Hilbert space formulation, the right and left fluxes ( $W_{j,R}$  and  $W_{j,L}$ ) are conserved separately. Hence, our analysis only constrains the eigenvalues of  $W_{j,R}$  and  $W_{j,L}$  to be the same. This is actually not a new constraint - the product of fluxes around any closed surface must be +1, so the constraint that all  $U_{j,\alpha} = +1$  automatically implies  $W_{j,R} = W_{j,L}$ . We will denote this choice of  $W_{j,R}, W_{j,L}$  eigenvalue as  $\bar{W}_j$  to distinguish from the operator  $W_j$ . One can prove, as in Appendix A of [60], that at least one steady-state solution exists for each choice of eigenvalue.

Translating the above statements to our gauge field representation, we fix our gauge sector to be  $\hat{w}_{j,\alpha,R} = \hat{w}_{j,\alpha,L} \equiv \hat{w}_{j,\alpha}$  and  $\hat{v}_j = (-1)^j$ . The complex fermion representation chosen in Eq. 5.17 makes the Lindbladian in the steady-state gauge sector especially simple, as

$$\begin{aligned} 2(f_j^\dagger f_{j+\hat{x}} + f_{j+\hat{x}}^\dagger f_j) &= id_{j,R}d_{j+\hat{x},R} - id_{j,L}d_{j+\hat{x},L}, \\ 2f_j^\dagger f_j &= 1 - (-1)^j id_{j,R}d_{j,L}, \end{aligned} \tag{5.18}$$

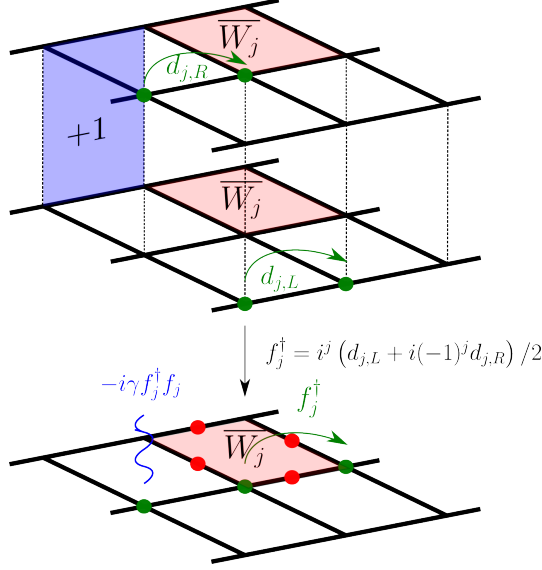


Figure 5.2: In the steady-state gauge sector, where all interlayer fluxes are set to +1 and intralayer fluxes are equal on the two layers, the bilayer Majorana Lindbladian can be directly mapped onto a model of complex fermions on a square lattice coupled to a  $\mathbb{Z}_2$  gauge field on the links and with an imaginary chemical potential.

where an identical relation as in the first line but for  $\hat{x} \leftrightarrow \hat{y}$  also holds. As a consequence, the Lindbladian takes the simple form

$$i\mathcal{L} = \sum_j \left( J_x \hat{w}_{j,\hat{x}} f_j^\dagger f_{j+\hat{x}} + J_y \hat{w}_{j,\hat{y}} f_j^\dagger f_{j+\hat{y}} + \text{h.c.} \right) - 2i\gamma \sum_j f_j^\dagger f_j, \quad (5.19)$$

see Fig. 5.2. The non-Hermiticity of  $i\mathcal{L}$  is manifest as simple imaginary chemical potential, and we can immediately identify the steady-state solution as the  $f_j^\dagger$  vacuum state. The real part of the dispersion is unaffected by the dissipation, and all excitations come with the same dissipative energy penalty  $2\gamma$ .

What are the expectation values of observables in these steady-state solutions? Recall that these solutions have eigenvalue 1 under the symmetries  $U_{j\alpha}$  and  $W_{jR}W_{jL}$ . Any observable with a non-zero expectation value with respect to this steady-state must have identical eigenvalues. Phrased in terms of operators on our original Hilbert space, the requirement is that observables must commute with the flux operators  $W_j$  and the bond operators  $V'_{j\alpha}$ . This is a strong

constraint - the only operators that satisfy this condition are precisely products of the  $V_{j\alpha}$  bond operators defined in Eq. 5.8. One can check explicitly that these operators satisfy the required constraints, and the claim that these are the only operators with such a property follows from dimension counting, worked out in Appendix D.2. Physically, these correspond to all operators that can be expressed in terms of pairs of  $d_j$  Majorana fermions connected by strings of  $\mathbb{Z}_2$  gauge fields  $\hat{w}_{j\alpha}$ .

We now argue that among these operators, only *closed loops* of  $V_{j\alpha}$  operators have a non-zero expectation value - recall that these correspond to products of flux operators  $W_j$ . This is a consequence of the steady-state solution being the vacuum state of the  $f_j^\dagger$  operators, which gives an additional set of constraints:  $(1 - 2f_j^\dagger f_j)\|\rho\rangle\!\rangle = \|\rho\rangle\!\rangle$ . We can turn this into a gauge-invariant statement by the following rewriting

$$\begin{aligned}\|\rho\rangle\!\rangle &= (-1)^j(1 - 2f_j^\dagger f_j)\hat{v}_j\|\rho\rangle\!\rangle \\ &= d_{j,R}d_{j,L}d'_{j,R}d'_{j,L}\|\rho\rangle\!\rangle \\ &= \Gamma_{j,R}^5\Gamma_{j,L}^5\|\rho\rangle\!\rangle.\end{aligned}\tag{5.20}$$

Hence, any non-zero observable must have eigenvalue 1 under the symmetry  $\Gamma_{j,R}^5\Gamma_{j,L}^5$  (i.e., they commute with  $\Gamma_j^5$ ), and these are precisely closed loops of  $V_{j,\alpha}$  operators. Using the fact that the steady-state solution obeys the relation  $W_{j,L}\|\rho\rangle\!\rangle = W_{j,R}\|\rho\rangle\!\rangle \equiv \bar{W}_j\|\rho\rangle\!\rangle$ , we can deduce that the expectation value of the flux operators in this steady state are given precisely by the intralayer gauge fluxes  $\bar{W}_j$ .

When our model is defined on a torus, the steady states of our Lindbladian exhibit a four-fold topological degeneracy arising from the possibility of flipping non-contractible loops of  $\hat{w}_{j,\alpha}$  operators, shown in Fig. 5.3. Physically, this implies four distinct steady-state density matrices  $\rho_{1-4}$  for each local flux configuration, which are distinguishable based on the expectation values of non-contractible strings of  $\Gamma$  matrices. We emphasize that, while this may be thought of as a topological degeneracy - and more generally,  $\mathbb{Z}_2$  topological order - within the doubled Hilbert space formalism, it does not constitute true mixed state topological order in the sense of being able to encode logical qubits in the steady-state solutions. What may appear to be a “quantum” superposition of different topological sectors  $\|\rho_1\rangle\!\rangle + \|\rho_2\rangle\!\rangle$  within

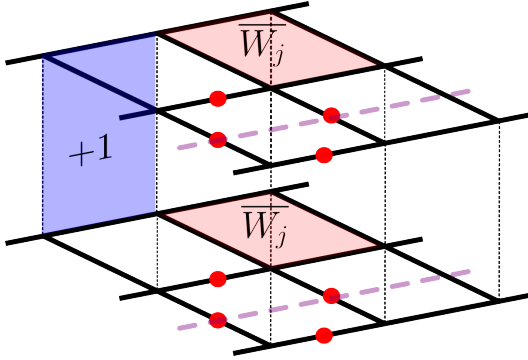


Figure 5.3: When our model is defined on a torus, one can flip non-contractible loops of intralayer gauge fields in order to obtain a set of four steady-state solutions with equal flux configurations.

the doubled Hilbert space formalism translates to a mere classical superposition of density matrices  $\rho_1 + \rho_2$  within our original Hilbert space (moreover, the relative phase between the superposition of the two steady-states is not freely tunable - it is fixed by the Hermiticity and positive semi-definite constraint on the physical density matrix).

### 5.3.3 LIOUVILLIAN GAPS

Moving beyond steady-state solutions, we can calculate the Liouvillian gap - the energy of the next-lowest state in imaginary energy. It is useful to draw a distinction between different types of Liouvillian gaps. The three types of degrees of freedom in our Lindbladian are complex fermions  $f_j$ , interlayer gauge fields  $\hat{v}_j$ , and intralayer gauge fields  $\hat{w}_{j,\alpha,R}$ ,  $\hat{w}_{j,\alpha,L}$ . Excitations with respect to any of these three variables may be considered. Recall from Eq. 5.16 that gauge invariance requires an even number of excitations.

- Within a gauge field configuration with a steady-state solution, we compute the *fermion gap*, which is the energy associated with a fermionic excitation. In accordance with the condition of gauge invariance discussed previously, any valid state must include a pair of these excitations.
- We also compute the effects of interlayer gauge excitations, which corresponds to the energy associated with flipping a single  $\hat{v}_j$  away from the “checkerboard” sector. We call this the *interlayer gauge gap*.

- Finally, we analyze intralayer gauge field excitations, which come from flipping a single  $\hat{w}_{j,L}$  operator. We choose left gauge fields for concreteness - an identical calculation follows for right gauge fields.

We will study each of these excitations in turn. In addition to calculating their Liouvillian gaps, we also identify operators whose equilibration timescales can be upper bounded by these gaps. We make this identification primarily through the symmetry-based analysis outlined previously in Section 5.3.1. To be precise, each of these excitations will be associated with a particular flux configuration, and the excitations can therefore only have a non-zero overlap with operators whose eigenvalues under the flux superoperators are identical. This analysis is robust and can be applied to any excitation; however, for interlayer gauge excitations, we will find that the nature of the fermionic degrees of freedom allows us to say more about the structure of the long-lived excitations.

#### FERMION GAP

We first study the Liouvillian gap associated with fermionic excitations within the steady-state gauge sector. As is clear from Eq. 5.19, the fermion gap is always  $2\gamma$ , and a pair of these excitations will cost energy  $4\gamma$ . As these excitations remain in the same gauge sector, they will still have eigenvalue 1 under the symmetries  $U_{j,\alpha}, W_{j,R}W_{j,L}$ . Recalling the relation between  $f_j$  and the Majorana fermions in Eq. 5.17, we see that this fermion gap of  $4\gamma$  defines the inverse timescale under which the expectation values of pairs of  $d_j$  fermions will asymptote to their steady-state value of zero. The fact that also the Hermitian part of  $i\mathcal{L}$ , the first line in Eq. 5.19, is quadratic means that the (in general  $\hat{w}_{j,\alpha}$  dependent) exact eigenstates of the Lindbladian in the steady-state gauge sector and the time-dependent phases they pick up are characterized by all possible occupation numbers of the  $N$  Bloch states of the  $f_j$  and their band structure; the associated decay rate is just given by  $2\gamma$  times the number of occupied Bloch states.

## INTERLAYER GAUGE EXCITATION

Creating an interlayer gauge excitation at site  $k$  gives us the free fermion Lindbladian

$$i\mathcal{L} = \sum_j \left( J_x \hat{w}_{j,\hat{x}} f_j^\dagger f_{j+\hat{x}} + J_y \hat{w}_{j,\hat{y}} f_j^\dagger f_{j+\hat{y}} + \text{h.c.} \right) \\ - 2i\gamma \sum_{j \neq k} f_j^\dagger f_j - 2i\gamma(1 - f_k^\dagger f_k). \quad (5.21)$$

The structure of the Lindbladian is the same for multiple interlayer gauge excitations - the chemical potential at each site is changed from  $f_k^\dagger f_k$  to  $(1 - f_k^\dagger f_k)$ . A single one of these flips is not gauge-invariant; one must either flip an additional gauge degree of freedom or add in an odd number of fermions in order to recover a physical excitation. The Liouvillian gap for these excitations must be computed numerically since, as opposed to Eq. 5.19, the Hermitian and anti-Hermitian part of  $i\mathcal{L}$  do not commute anymore. However, we can readily see analytically that this gap vanishes in the limit of strong dissipation,  $\gamma \rightarrow \infty$ . In this limit, we ignore the Hermitian terms in Eq. 5.21 and we can obtain steady-state solutions by simply placing fermions wherever the imaginary chemical potential is negative (this automatically satisfies the gauge constraint, as we place as many fermions as we flip  $\hat{v}_i$ 's).

For general  $\gamma$ , the gap of interlayer gauge with fermion excitations (i.e., flipping a single  $\hat{v}_k$  and introducing a single fermion to the vacuum) is plotted in Fig. 5.4. For this and all subsequent plots, the parameters used were  $J_x = J_y \equiv J = 1$ , and  $N = 1600$ . The gap depends on the background  $W_j$  flux configuration - we present results for zero flux,  $W_j = +1$ ,  $\pi$ -flux,  $W_j = -1$ , and a random flux configuration. Note that there are two distinct contributions to the Liouvillian gap in Eq. 5.21. The first is the overall shift of  $2i\gamma$ , and the second comes from the dissipative strength of the fermion excitation with the smallest imaginary energy. For small  $\gamma$ , the imaginary energy of this fermion excitation is positive - in other words, adding in the single fermion excitation to the vacuum is energetically unfavorable and causes the eigenstate to decay more rapidly, but one is nevertheless forced to include it by the constraint of gauge invariance. This fermion excitation energy eventually transitions from positive to negative, asymptotically approaching  $-2i\gamma$ .

Depending on the background flux configuration, the fermion spectrum may exhibit an

anti- $\mathcal{PT}$ -symmetry breaking transition at a critical value of  $\gamma$ , which causes a sharp kink in the gap. In this situation, the eigenvalues with the smallest imaginary part for small  $\gamma$  come in pairs, with the real parts opposite in sign - this symmetry is a consequence of the Lindbladian descending from a completely positive and trace-preserving quantum channel and can be expressed in terms of modular conjugation [237]. The anti- $\mathcal{PT}$ -symmetry breaking transition happens when the two eigenvalues meet on the imaginary axis and split off. We see that in Fig. 5.4, this happens for both the uniform flux as well as the particular random flux configuration plotted, but not for the  $\pi$ -flux scenario. A survey of generic random flux configurations suggest that this transition is common but not necessarily guaranteed. As this symmetry-breaking transition pertains to dissipative rather than steady-state solutions, the physical consequence of the transition are more subtle, although in principle it may be detected by longest-lived mode in this sector transitioning from having a real (oscillatory) component to being purely dissipative.

What is the physical interpretation of these interlayer gauge excitations? As was the case in the steady-state gauge sector, we can proceed with a symmetry analysis of the operators in this sector. In terms of gauge-invariant fluxes, the flip of a single  $\hat{v}_j$  away from its steady-state checkerboard configuration changes the fluxes of the four neighboring  $U_{j,\alpha}$  operators to be  $-1$ . Hence, operators that have a non-zero overlap with this excitation must have identical eigenvalues under these flux operators. Recall that in the steady-state sector, the operators that satisfied the flux constraint consisted of pairs of  $d_j$  fermion excitations connected by a string of gauge fields  $\hat{w}_{j,\alpha}$ . An interlayer gauge excitation at site  $k$  “pins” a  $d'_k$  fermion excitation to site  $k$ , and the allowed operators are gauge-invariant string-like operators that involve a  $d'_k$  fermion at site  $k$ . Therefore, the Liouvillian gap in Fig. 5.4 determines the equilibration timescale of operators given by a single  $d'$  fermion coupled to a  $d$  fermion by a  $\mathbb{Z}_2$  Wilson line.

The above argument applies to all operators in this gauge sector, regardless of their energy. In the limit  $\gamma \rightarrow \infty$ , we can also analytically understand the nature of the lowest-energy (i.e. the longest lived) operator in this sector. For an interlayer gauge excitation at site  $k$ , the steady-state solution obeys  $f_k^\dagger f_k |\psi\rangle\rangle = 1$  and  $f_j^\dagger f_j |\psi\rangle\rangle = 0$  elsewhere. By leveraging this

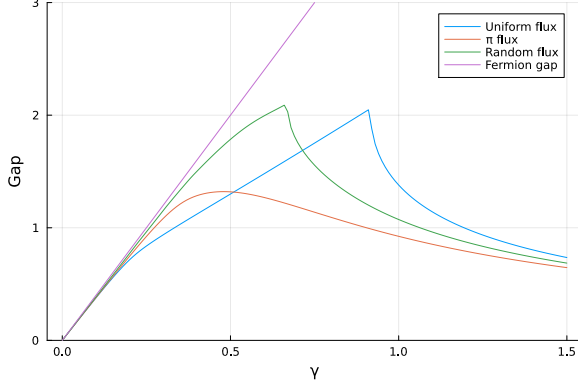


Figure 5.4: We plot the Liouvillian gap associated with the flipping of a single interlayer gauge degree of freedom  $\hat{v}_j$  for various different background flux configurations. All configurations have a quantum Zeno limit as  $\gamma \rightarrow \infty$ , where the Liouvillian gap vanishes and a new steady-state emerges. For comparison, we also plot the fermion gap of  $4\gamma$  and note that the interlayer gauge gap has an identical slope at small  $\gamma$ .

constraint using analogous manipulations as in Eq. 5.20, we find that this is only satisfied by the operator  $\Gamma_k^5$ , which can be interpreted as the bound state of a  $d$  and  $d'$  fermion localized on a single site [cf. Eq. 5.7]. Hence, in the limit  $\gamma \rightarrow \infty$ , we recover steady-state excitations with definite  $\Gamma^5$  eigenvalue. This is a consequence of the quantum Zeno effect; if we interpret the jump operators  $L_j = \Gamma_j^5$  as the environment performing measurements of  $\Gamma^5$  with frequency specified by  $\gamma$ , our state can become frozen in a  $\Gamma^5$  eigenstate for large  $\gamma$ .

The interpretation of the lowest-energy excitation as a  $\Gamma_k^5$  operator also holds approximately away from the  $\gamma \rightarrow \infty$  limit, which is a consequence of the localization of the corresponding single-particle eigenvector of Eq. 5.21 around site  $k$ . As shown in Fig. 5.5, the fermion with smallest imaginary eigenvalue is highly localized around site  $k$  even for small values of  $\gamma$ ; hence, the operator whose equilibration time is determined by Fig. 5.4 retains a large overlap with  $\Gamma_k^5$ . We leave a detailed analysis of the extent of eigenvector localization for future work, although we mention related work [486] of a similar single-particle system but with a fully disordered imaginary chemical potential, rather than our case of a chemical potential that is everywhere positive except for a single site. For their model, numerical simulations were consistent with a localization transition for arbitrarily weak disorder strength.

The above analysis has been for a single interlayer gauge field excitation. It is natural to consider multiple gauge excitations, which correspond to symmetry sectors with multiple  $\hat{v}_j$

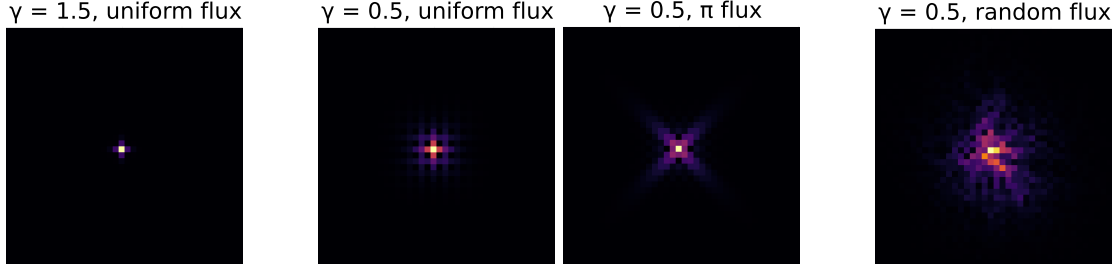


Figure 5.5: We plot the spatial distribution of the magnitude of the lowest-energy fermion excitation of the single-particle Lindbladian in Eq. 5.21, with the single interlayer gauge defect in the center of the lattice. For large  $\gamma$  (top left), the eigenstate is highly localized at the defect site, irrespective of the background flux configuration. For smaller  $\gamma$ , the eigenstate remains well-localized, and the spatial distribution around the defect site is dependent on the background flux.

gauge fields flipped away from their steady-state configuration. A physically relevant quantity to consider is the Liouvillian gap associated with the  $f$  vacuum in the sector with a pair of interlayer gauge field excitations at sites  $k$  and  $\ell$ . This determines the equilibration timescale of an operator given by a pair of  $d'$  fermions at sites  $k$  and  $\ell$ . This state is an exact eigenstate of the Lindbladian with imaginary energy  $4\gamma$  - note that for sufficiently large  $\gamma$ , this energy may be reduced further by including pairs of  $f$  fermions, with a quantum Zeno effect yielding a steady-state solution at  $\gamma \rightarrow \infty$  by adding a pair of fermions at sites  $k$  and  $\ell$ .

#### INTRALAYER GAUGE EXCITATIONS

The final types of excitation we will study are *intralayer* gauge excitations, when we flip a gauge field on one of the two layers such that  $\hat{w}_{k,\alpha,L} = -\hat{w}_{k,\alpha,R}$  for some bond  $(k, \alpha)$ . Operators associated with these excitations - i.e., operators consistent with this flux configuration - are single-site operators  $\Gamma_j^\mu$ ,  $\mu = 1, 2, 3, 4$ , on the two sites adjacent to the bond  $(k, \alpha)$ . A more precise identification of these operators, including the flux configurations corresponding to operators  $\Gamma_j^{\mu 5}$  and  $\Gamma_j^{\mu\nu}$ , are given in Appendix D.4.

In this gauge sector, the Lindbladian no longer has a simple expression in terms of complex fermions  $f_j^\dagger$ , as the intralayer gauge excitation induces pairing terms into the Lindbladian - explicitly,

$$2 \left( f_j^\dagger f_{j+\hat{x}}^\dagger + f_{j+\hat{x}} f_j \right) = -i(-1)^j (d_{j,L} d_{j+\hat{x},L} + d_{j,R} d_{j+\hat{x},R}) \quad (5.22)$$

The single-particle Lindbladian is quadratic and can thus still be easily diagonalized; we

provide more details of this procedure in Appendix D.3. However, the determination of whether the resulting ground state is physical - i.e, whether it has the odd fermion parity to not be annihilated by the projection to the physical subspace - is non-trivial due to the non-Hermiticity of the Lindbladian. We leave a full analysis of this problem as an open question and plot both the ground state energy and the energy of the first excited state in Fig. 5.6. The ground state energy gives a lower bound on the physical Liouvillian gap. However, one must be careful at large  $\gamma$ , since the  $\gamma \rightarrow \infty$  limit gives a fictitious quantum Zeno effect. In this limit, the ground state approaches the  $f_j$  vacuum state, which is a steady-state solution but unphysical as its fermion parity is even. As a consequence, we also plot the first excited state, which gives a more physical lower bound for large  $\gamma$ .

We comment on a surprising aspect of this Liouvillian gap, which is a sudden increase when an arbitrarily small  $\gamma$  is turned on, with a subsequent plateau at a gap of magnitude  $J$ . For finite  $N$ , the gap smoothly evolves as a function of  $\gamma$ , but the slope at small  $\gamma$  is proportional to  $N$ , as shown in the inset of Fig. 5.6. This indicates that in the thermodynamic limit, an infinitesimally small  $\gamma$  causes a discontinuous jump in the Liouvillian gap to  $J$ . A possible physical explanation of this fact is that, in contrast to the fractionalized operators considered earlier which have a correspondence with coherent excitations of the closed system, the operators  $\Gamma_j^{1,2,3,4}$  have no such association, and hence deconstructive interference generated by the unitary dynamics of the closed system also contributes to the decay of the expectation values of these observables. Intuition on this phenomenon can also be gained from the fermion representation - by examining the single-particle eigenstates of the Lindbladian at  $\gamma = 0$  expressed in the complex fermion representation, one can see that the act of exchanging a single hopping term with a pairing term causes strong hybridization between the delocalized particle-like and hole-like excitations, which in turn leads to an extensive  $\mathcal{O}(\gamma)$  shift in the Liouvillian gap when dissipation is turned on. This phenomenon of the decay rate approaching a non-zero value as  $\gamma \rightarrow 0$  in the thermodynamic limit has been found in the Lindbladian dynamics of Sachdev-Ye-Kitaev models [263, 404],

This observation demonstrates a striking feature of our model in the small- $\gamma$  limit. In this regime, the expectation values of string-like operators such as  $V_{j\alpha}$  as well as  $\Gamma_j^5$  have an  $\mathcal{O}(\gamma^{-1})$  upper bound on their equilibration timescale, in contrast to local single-site operators

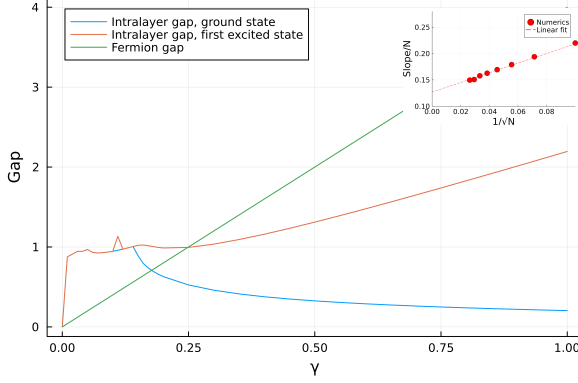


Figure 5.6: We plot the Liouvillian gap associated with flipping a single intralayer gauge field away from a uniform flux configuration. As it is non-trivial to ensure that the ground state configuration has the proper fermion parity necessary for gauge invariance, we plot both the lowest energy configuration as well as the energy of a state with a single fermionic excitation, with the latter giving a more physical lower bound in the  $\gamma \rightarrow \infty$  limit. The Liouvillian gap for small  $\gamma$  has a large slope, and a finite size analysis (inset) shows that this slope is extensive in the system size. We plot results for a uniform flux configuration, where the behavior of the gap in the thermodynamic limit appears to take a particularly simple form - an immediate jump up to a gap of magnitude exactly  $J$  and a plateau up to  $\gamma_c = J/4$ , after which the gap scales linearly in  $\gamma$ . For generic background flux configurations, we verify that the qualitative nature of the gap remains the same, although the precise coefficients are non-universal.

such as  $\Gamma_j^{1,2,3,4}$  whose timescales are bounded by  $\mathcal{O}(J^{-1})$ .

#### 5.4 PERTURBATIONS AWAY FROM EXACT SOLVABILITY

As the exact solvability of our Lindbladian requires a precise set of couplings, it is natural to consider perturbations away from this exactly solvable point. Here, we discuss different types of perturbations and their physical effects. Our Lindbladian possesses an extensive number of *strong* symmetries  $W_j$  and *weak* symmetries  $V_{j,\alpha}$ . The combination of the two gives us our exact solvability, and perturbations are conveniently classified in terms of their breaking of these symmetries.

The simplest perturbations retain both the strong and weak symmetries of our system. These terms are rather artificial - the most local terms consist of either explicitly adding in the flux terms  $W_j$  to the Hamiltonian, or adding a two-site jump operator  $L_{j,\alpha} = V_{j,\alpha}$ . Both these choices preserve the steady-state solutions as well as the structure of the quasiparticle excitations; however, details of the Liouvillian gaps will be modified.

Perturbations that break the weak symmetries but preserve the strong symmetries of our model include the  $J'_x$ ,  $J'_y$ , and  $J_5$  terms in the full Hamiltonian of Eq. 5.5. In this case, our quantum jump operators still commute with the fluxes  $W_j$ , and an initial state in a definite flux sector will remain in that sector for arbitrary time. However, while we can still make statements about the steady-state solutions of the Lindbladian, the full spectrum and consequently the Liouvillian gap is no longer analytically tractable in an exact way. For future work, it would be interesting to study whether coherent quasiparticle excitations still remain in this spectrum at low energies. Recall that in the exactly solvable limit, the existence of distinct types of quasiparticle excitations led to the interpretation of distinct Liouvillian gaps which give equilibration timescales for different observables - the manner in which this picture is modified away from the exactly solvable point is an important open question.

We may also consider perturbations that break the strong symmetries but conserve the weak ones. This is accomplished by a generic choice of quantum jump operator, such as  $\Gamma_j^{1,2,3,4}$ . In this scenario, we expect our system to asymptote to a unique steady-state,  $\rho \propto \mathbb{1}$ . The weak symmetries cause the Lindbladian spectrum to decompose into an extensive number of symmetry sectors, with the steady-state solution residing in a particular sector. This means that one still retains the ability to discuss Liouvillian gaps with respect to the steady-state sector versus gaps of different sectors, and a careful analysis of the sectors would allow one to identify the operators that live in these sectors. In passing, we note that particular choices of quantum jump operators such as  $\Gamma_j^{\mu\nu}$  with  $\mu, \nu \in \{1, 2, 3, 4\}$  will break the local strong symmetries  $W_j$  but preserve a global strong symmetry  $Q \equiv \prod_j \Gamma_j^5$  (this is not a “new” symmetry, as it can be re-expressed as a product of  $W_j$  operators). As such, in this case we expect a pair of steady-state solutions  $\rho_{\pm} \propto \mathbb{1} \pm Q$ .

Finally, a fully generic choice of perturbation that breaks all symmetries will give a single steady-state solution. We again stress an important open question of to what extent quasiparticle excitations of the Lindbladian are robust to these types of perturbations. With regards to the extensive number of steady-state solutions in the exactly solvable limit, one will expect that a small generic perturbation away from this point will cause all but one of these steady-states to persist for a long timescale given by the inverse strength of the perturbation. Developing an analogous theory for the excitations is a promising research direction, as it

emphasizes a physical interpretation of the Lindbladian spectrum that is already familiar in the study of closed systems.

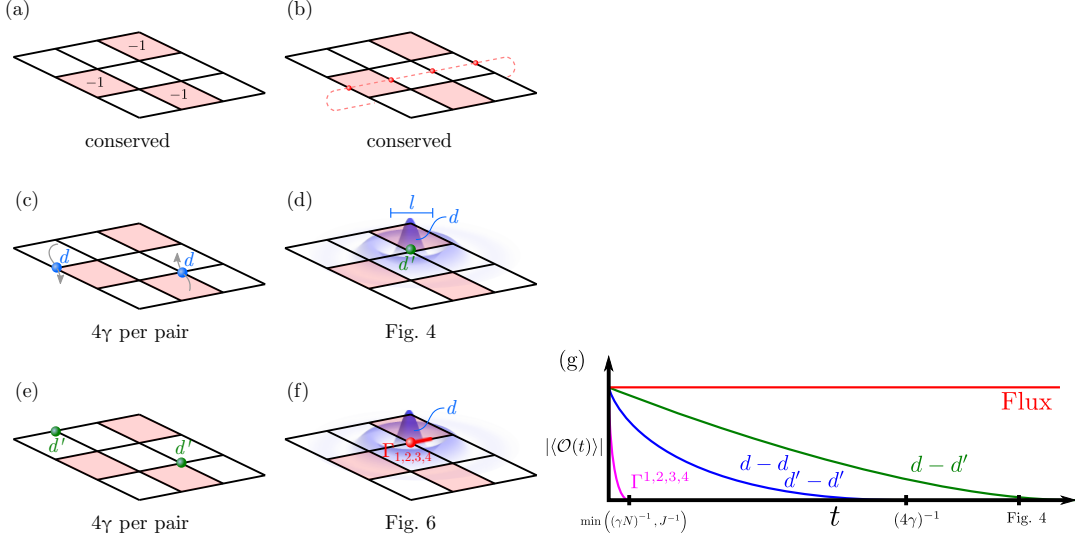


Figure 5.7: We illustrate the classes of observables considered in our work, as well as their corresponding Liouvillian gaps. a) flux operators  $W_j$ , which are conserved under Lindbladian time evolution. b) Non-local Wilson loop operators, which are also conserved - we emphasize that *quantum* superpositions of states with different Wilson loop eigenvalues are not steady-state solutions and eventually evolve into classical superpositions. c) A pair of  $d$  Majorana fermion excitations, connected by the Wilson line of a  $\mathbb{Z}_2$  gauge field (not shown). These have a Liouvillian gap of  $4\gamma$  and the arrows indicate that the eigenstates of  $i\mathcal{L}$  are delocalized Bloch-wave-like configurations. d) A  $d$  and  $d'$  Majorana fermion, connected by the Wilson line of a  $\mathbb{Z}_2$  gauge field. The Liouvillian gap is shown in Fig. 5.4, and we find that the wavefunction of the  $d$  fermion is highly localized around the  $d'$  site. The single-site operator  $\Gamma_j^5$  corresponds to the limit  $l \rightarrow 0$ . e) A pair of  $d'$  Majorana fermion excitations, connected by the Wilson line of a  $\mathbb{Z}_2$  gauge field. These have a Liouvillian gap of  $4\gamma$ . f) Generic single-site operators  $\Gamma^{1,2,3,4}$ , as well as multi-site operators obtained by including  $d$  fermion excitations. Lower bounds on this Liouvillian gap are given in Fig. 5.6. Part g) is a schematic of the resulting decay of the different classes of operators under dissipative time evolution.

## 5.5 SUMMARY AND DISCUSSION

In this work, we analyze the Lindbladian dynamics of a quantum spin-3/2 system which admits an exact solution in terms of Majorana fermions coupled to static  $\mathbb{Z}_2$  gauge fields. This allows us to characterize the steady-state solutions as well as identify distinct classes of Liouvillian gaps, with different gaps determining the equilibration timescale of different classes of observables, as summarized in Fig. 5.7. Crucially, these timescales fall into different

categories with distinct parametric dependencies on  $\gamma$ . While closed loops of  $V_{j\alpha}$  in Eq. (5.8)—i.e., the fluxes, Fig. 5.7(a), and on a torus also the non-local Wilson loops, see part (b)—do not decay at all in the exactly solvable limit, pairs of emergent Majorana fermions, Fig. 5.7(c-e), decay with rates that scale linearly with small  $\gamma$ ; depending on whether they exhibit a quantum Zeno effect, these rates decay to zero in the large- $\gamma$  limit. Finally, operators of the last category, like  $\Gamma^{1,2,3,4}$ , see Fig. 5.7(f), which are not conserved by the Hermitian dynamics, exhibit a decay rate that is singular for small  $\gamma$  in the thermodynamic limit; naturally, the entire dynamics is unitary at  $\gamma = 0$ , however, sending  $\gamma \rightarrow 0^+$  *after* taking the thermodynamic limit  $N \rightarrow \infty$ , the decay rates of these operators is of order of the exchange couplings  $J$  of the Hamiltonian (5.5). This leads to particularly non-trivial three-step fractionalized thermalization dynamics, see Fig. 5.7(g), in the thermodynamic limit: first, at times of the order of the inverse exchange couplings  $1/J$ , all operators of the third kind decay, which is parametrically separated from the time-scale  $\propto 1/\gamma$  where (gauge invariant pairs of) the Majorana fermions  $d$  and  $d'$  decay. Then only closed loops of  $V_{j\alpha}$  survive, which cannot decay unless perturbations beyond our solvable limit (cf. Sec. 5.4) are included.

We emphasize that our model, while fine-tuned to ensure exact solvability, demonstrates a novel and potentially generic feature - the presence of distinct quasiparticle excitations in the Lindbladian spectrum, when regarded as a non-Hermitian operator in a doubled Hilbert space, leads to a separation of timescales in the equilibration behavior of different classes of observables. The exact solvability of our model allows us to demonstrate these features explicitly, and can serve as a useful starting point for understanding the robustness of this phenomena in the presence of interactions between quasiparticles. Alternative methods such as the Keldysh formalism [452, 538] may prove to be useful in making perturbative treatments of these interactions tractable.

One promising direction for future research is the construction of additional exactly solvable Lindbladians through this fermionization technique. For closed systems, there exists a rich literature on generalizations of the Kitaev honeycomb model to other exactly solvable models [90, 305, 451, 525, 545]; in these cases, the exact solvability is often geometric in nature (i.e. arising from a particular choice of lattice connectivity and hopping structure) and is unaffected if a subset of couplings become non-Hermitian. One interesting phenomenon

that may arise in a certain parameter regime of these models is *gapless* fermionic excitations, in contrast to our model where fermion excitations have a constant gap  $4\gamma$ . This would imply algebraic, rather than exponential, decay of the expectation values of certain classes of operators [63]. Lindbladians with gapless excitations are not new [312, 334, 465, 577] - the intriguing new feature of this would be the ability to cleanly separate this spectrum of gapless excitations from gapped gauge excitations, implying distinct equilibration timescales of these operators.

Generalized Lindbladian constructions may also prove useful at developing a general relation between the exactly solvable open system and the underlying Hermitian dynamics. In our model, the Hermitian dynamics was given by a QSL with two species of Majorana fermions, with the dispersion of one of the fermions tuned to zero. In this limit, a particular choice of quantum jump operators admit quasiparticle excitations of the Lindbladian which display a close relation with the excitation spectrum of the closed system. It is intriguing to ask whether, in a generic system that is rendered exactly solvable through this technique, a similar relation exists between quasiparticle excitations in the doubled Hilbert space and quasiparticle operators of the physical Hilbert space. A more robust understanding of this relation, including potential violations in certain systems, is another promising direction for future research.

*Note added.* Just before posting our work, a related paper appeared on arXiv [100], studying exactly solvable BCS-Hubbard Lindbladians. Although the starting point of their analysis involves a distinct microscopic model of complex fermions with pairing terms, a transformation to Majorana fermions yields the same Lindbladian as ours within the  $\pi$ -flux sector. Due to the different microscopic models, our theory also has a non-trivial gauge invariance requirement, with non-trivial consequences. For instance, the Liouvillian gap in the  $\pi$ -flux sector in Fig. 5.4 is larger as an additional fermion has to be included. We also cite a related work [157] studying a quantum spin Lindbladian very similar to our own, which appeared on arXiv shortly after our posting. Our results are consistent with their analysis.

*The miracle of the appropriateness of the language of mathematics for the formulation of the laws of physics is a wonderful gift which we neither understand nor deserve. We should be grateful for it and hope that it will remain valid in future research and that it will extend, for better or for worse, to our pleasure, even though perhaps also to our bafflement, to wide branches of learning.*

Eugene Wigner

# 6

## Deconfined quantum criticality of nodal d-wave superconductivity, Néel order and charge order on the square lattice at half-filling

### 6.1 INTRODUCTION

The cuprate high temperature superconductors display a complex phase diagram involving low temperature ( $T$ ) phases with  $d$ -wave superconductivity, Néel antiferromagnetic order, and charge order, and the higher  $T$  pseudogap and strange metals [242]. The remarkable pseudogap metal phase is of central importance, and many of its properties can be described by a model of hole pocket Fermi surfaces [43, 87, 134, 235, 236, 313, 362, 374, 396, 409, 422, 453, 467, 497, 512, 513, 544, 563]. Such Fermi surfaces enclose an area distinct from the Luttinger volume, and this requires the presence of a background spin liquid, realizing a state that has been called a ‘fractionalized Fermi liquid’ (FL\*) [438, 440]. Recent works [87, 88] have proposed that the low  $T$  cuprate phase diagram can be understood from a theory of the confining instabilities of a FL\* state with a ‘ $\pi$ -flux’ critical spin liquid on the square lattice. The critical spin liquid emerges from a background into a central role in such confining transitions, and a detailed understanding of its role then becomes a central ingredient in unraveling the mysteries of the cuprate phase diagram.

An important feature of the FL\* theory is that its fractionalized excitations have the same basic structure as that in a Mott insulator at half-filling, even though the pseudogap state is at non-zero doping. The doping is accounted for by the hole pocket Fermi surfaces, which are coupled to the spin liquid. Given this relatively innocuous influence of non-zero doping, the present paper will investigate a simpler model which remains at half-filling, but has the same set of conventional symmetry-breaking phases without fractionalization at low temperatures, as at non-zero doping: a *d*-wave superconductor with 4 nodal points for Bogoliubov quasiparticles, and conventional states with Néel, valence-bond solid, charge, or staggered current orders. There are quantum phase transitions between these states which are very likely described by deconfined critical points, allowing a systematic study of associated critical spin liquids. Our simpler model should be amenable to numerical simulations by the well-developed methods of lattice gauge theory of relativistic systems [399], and shed light on the role of spin liquids in the phase diagram of the cuprates.

We begin by noting a few recent developments which relate to the FL\*-confinement proposal of Ref. [87]:

- Angle-dependent magnetoresistance measurements on the underdoped cuprates [136] are consistent with hole pocket Fermi surfaces [43, 87, 134, 235, 236, 313, 362, 374, 396, 409, 422, 453, 467, 497, 512, 513, 544, 563].
- A long-standing issue with the hole pocket model of the pseudogap metal is that the pairing of quasiparticles around the hole pocket leads to a *d*-wave superconductors with *eight* nodal points [321]. This problem can be resolved by *not* viewing the onset of superconductivity from the pseudogap normal state as a BCS-like pairing of electronic quasiparticles on Fermi surface. Instead, the spin liquid of the pseudogap already features a singlet pairing of electrons [350], and we should consider the onset of superconductivity as a confining transition of the  $\pi$ -flux spin liquid by the condensation of a fundamental Higgs scalar. (In both viewpoints, the non-zero temperature transition of the onset of superconductivity remains in the Kosterlitz-Thouless universality class.) Then the fermionic spinon nodal points of the spin liquid annihilate four of the nodal points descending from the hole pockets, and we obtain a *d*-wave superconductor with

*four* nodal points [77, 88], as is expected in a conventional BCS state. Moreover, the large velocity anisotropy of the nodal quasiparticles is easily obtained in this approach.

- Photoemission observations in the electron-doped cuprates [533] show a gap maximum at an intermediate wavevector away from the edge of the Brillouin zone, and not on the Fermi surface. This feature is also obtained as a consequence of the background spin liquid [88]. Indeed, even when the pseudogap metal has no Fermi surfaces intersecting the zone diagonals, the resulting *d*-wave superconductor still has 4 nodal points along the zone diagonals, and these are directly descended from the nodal spinons of the underlying spin liquid [88].
- Numerical fuzzy sphere and other studies have found evidence for  $\pi$ -flux spin liquid criticality, which ultimately gives way either to ‘pseudo-criticality’ [574] or nearby multicriticality [81, 475, 567]. In contrast, the commonly used ‘staggered flux’ spin liquid [270] is expected to be strongly unstable to a trivial monopole [5, 460].
- Numerical studies [140, 292, 342, 376, 505] of  $S = 1/2$  square lattice antiferromagnets with first- and second-neighbor exchange interactions (the  $J_1$ - $J_2$  antiferromagnet) display a transition from the Néel state to valence bond solid order [389, 392], across an intermediate spin-liquid regime which is likely described by the  $\pi$ -flux spin liquid [501]. A gapless  $\mathbb{Z}_2$  spin liquid has also been proposed for this intermediate regime, and this can be obtained naturally by condensing Higgs fields on the  $\pi$ -flux spin liquid [381, 384, 441, 442] (the model studied in the present paper can be easily extended to include these Higgs fields, but we will not present the extension here<sup>1</sup>). Doping this square lattice spin liquid has recently been shown [221, 222] to lead to robust *d*-wave superconductivity, and this establishes a close connection between the  $\pi$ -flux phase and *d*-wave superconductivity [213, 558].
- Nuclear magnetic resonance experiments on  $\text{YBa}_2\text{Cu}_3\text{O}_y$  [571] show the appearance of a secondary spin gap which is possibly connected to the appearance of charge order.

---

<sup>1</sup>The theory of Ref. [442] can exhibit a bicritical point where the Néel, VBS, and gapless  $\mathbb{Z}_2$  spin liquids meet. This bicritical point can realize SO(5)-symmetric bicritical point in the studies of Ref. [81, 475] if the Yukawa couplings between the Higgs fields and spinons are irrelevant at the bicritical point.

This can be associated with the gapping out of the spinon excitations upon a confining transition to charge order, as we study in a simplified model in this paper.

- Magnetotransport studies in  $\text{HgBa}_2\text{Ca}_2\text{Cu}_3\text{O}_{8+\delta}$  [348] indicate a direct transitions between magnetic and charge ordered states. Such direct transitions are possible across deconfined critical points considered here.

The ‘ $\pi$ -flux’ critical spin liquid is described by a theory of fermionic spinons with  $N_f = 2$  massless Dirac points in their dispersion coupled to a SU(2) gauge field [4]. This state also has a dual description [501] in terms of the critical  $\mathbb{CP}^1$  theory of the bosonic spinons [389]. These dual descriptions are important in understanding the low temperature states of the cuprate phase diagram as confinement/Higgs transitions of this spin liquid:

- (i) The onset of Néel order is described by the Higgs condensate of the bosonic spinons in the  $\mathbb{CP}^1$  theory [341], or equivalently, by the confinement of the SU(2) gauge field of the fermionic spinon theory.
- (ii) The onset of *d*-wave superconductivity with nodal Bogoliubov quasiparticles [77], along with the onset of charge order, is described by the Higgs condensation of a charge  $e$ , SU(2) fundamental boson  $B$  (introduced in Refs. [270, 512]) of the fermionic spinon theory.

As noted above, this paper will study a simpler limit of the theory of Ref. [87]. We will move from the system at non-zero doping, and instead consider only the half-filled square lattice with a particle-hole symmetric Hamiltonian. Rather than introducing superconductivity and charge-order by doping, we will explore the onset of such phases at half-filling as may be induced by reducing the Hubbard  $U$  [377], or by introducing additional short-range interactions including pair-hopping terms [24, 535].

At half-filling, there are no hole pocket Fermi surfaces, and this simplifies the treatment of charge fluctuations. The particle-hole symmetry leads to a Lorentz-invariant form for the dispersion of the excitations at low energies. We will study zero temperature quantum phase transitions between (A) the insulating Néel state, (B) a *d*-wave superconductor with 4 gapless nodal quasiparticles, and (C) a state with charge order; see Fig. 6.1 for the phase diagrams

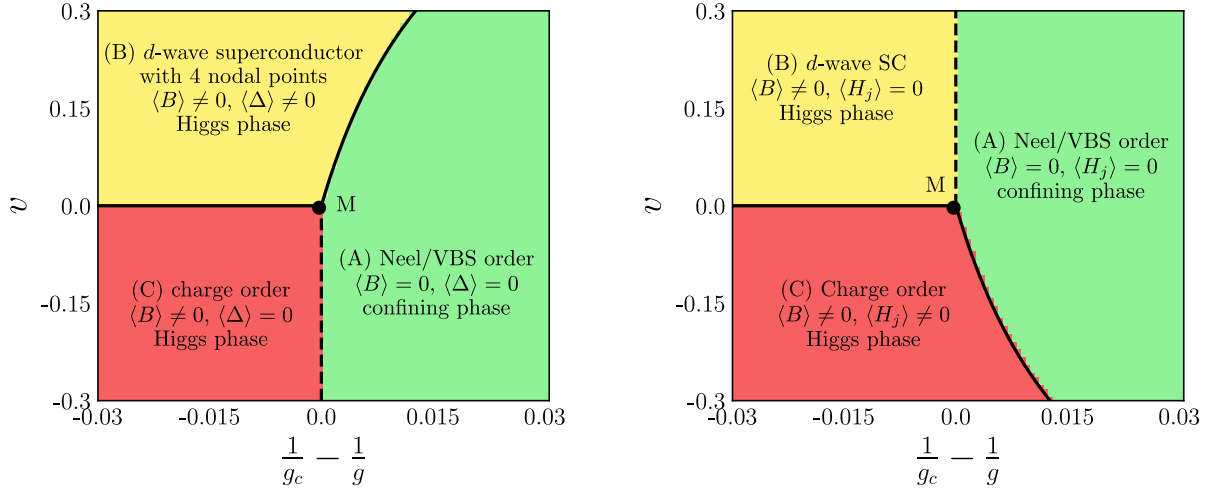


Figure 6.1: We are interested in a SU(2) gauge theory with  $N_f$  fundamental Dirac fermions, and  $N_b = 2$  fundamental complex scalars. We show phase diagrams of two distinct large  $N_f$  and  $N_b$  limits, with  $N_f/N_b$  fixed. First order phase transitions are denoted with a solid line while second order phase transitions are denoted with a dashed line. (a) Phase diagram of the theory  $\mathcal{L}_\psi + \mathcal{L}_B$  in (6.17) and (6.23). There is a  $\text{USp}(2N_f) \times \text{USp}(N_b) \times \text{U}(1)$  global symmetry for  $v \neq 0$ . (b) Phase diagram in an alternative large  $N_b$  limit discussed in [89] of the theory  $\mathcal{L}_\psi + \tilde{\mathcal{L}}_B$  in [89], with a  $\text{USp}(2N_f) \times \text{SU}(N_b) \times \text{U}(1)$  global symmetry for  $v \neq 0$ . The theories in (a) and (b) co-incide along the line  $v = 0$ , when they both have  $\text{USp}(2N_f) \times \text{USp}(2N_b)$  global symmetry. The two theories are also identical for the physically interesting case with  $N_f = N_b = 2$  for all  $v$ .

of the continuum field theories to be introduced in Section 6.3. This field theory is a SU(2) gauge theory  $N_b = 2$  relativistic scalars in addition to the  $N_f = 2$  massless Dirac fermions of the  $\pi$ -flux state.

We note an earlier work [383] which considered a continuous Néel/ $d$ -wave superconductor quantum transition, but without gapless nodal quasiparticles in the  $d$ -wave superconductors, and only easy-plane Néel order. Also, SU(2) gauge theories of the cuprates have been studied extensively earlier, as reviewed in Ref. [270], but in reference to a staggered-flux spin liquid which breaks the gauge symmetry to U(1)—we will not consider this spin liquid because it is expected to be unstable to a trivial monopole [5, 460].

In Section 6.5, we will consider the consequences of adding charge fluctuations to the Néel-VBS transition on the honeycomb lattice [146, 390] (VBS order is also known as ‘kekule’ order on the honeycomb lattice). Following the same procedure as for the square lattice, we find only a Dirac semi-metal phase with no broken symmetry, in contrast to the superconducting and

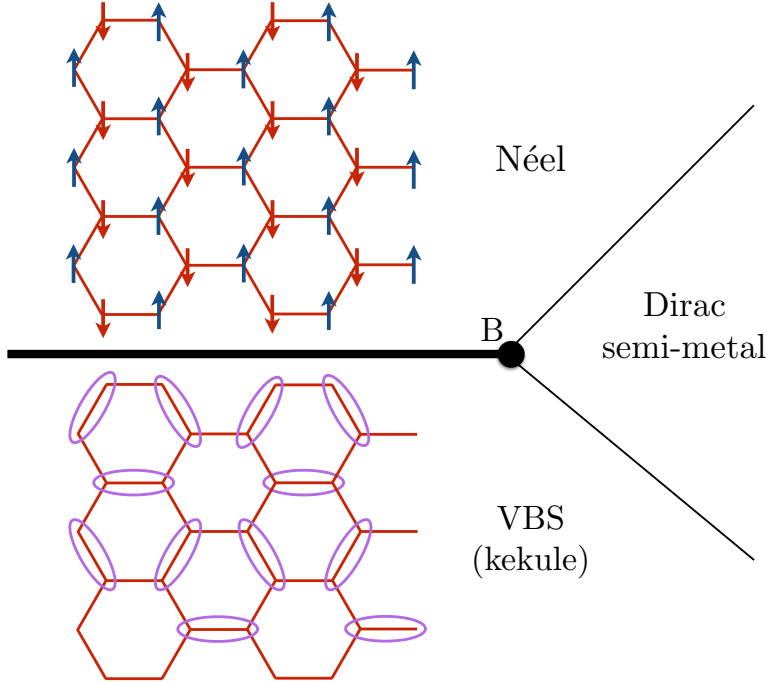


Figure 6.2: Schematic phase diagram for the  $SU(2)$  gauge theory of an extended Hubbard model on the honeycomb lattice. The bicritical point  $B$  [256] is described by the  $N_f = 2$ ,  $N_b = 1$   $SU(2)$  gauge field theory. The thick line indicates a first-order transition. The thin lines indicate second-order transitions out of the Dirac semi-metal phase which are presumed to be described by Gross-Neveu-Yukawa field theories [52] without gauge fields.

charge-ordered phases on the square lattice. As shown in Fig. 6.2, the Néel, VBS, and Dirac semi-metal phases of the honeycomb lattice are proposed to meet at a multicritical point, as in the numerical study of the Hubbard model on the honeycomb lattice in Ref. [280]. In our theory, the multicritical point is bicritical [256], and is described by the  $N_f = 2$ ,  $N_b = 1$  case of the  $SU(2)$  gauge field theory considered in the body of the paper. The same field theory was considered earlier by Hermele [186] for a different proposed transition on the honeycomb lattice.

Our main results here are obtained by two different large flavor expansions of our  $SU(2)$  gauge theory. The resulting phase diagrams in Fig. 6.1 contains first-order boundaries, a multi-critical point  $M$  where all three phases meet, and second-order transitions between Néel/VBS order, charge order, and nodal  $d$ -wave superconductivity. The multi-critical point  $M$  and the second-order transition are described by deconfined critical  $SU(2)$  gauge theories. We will determine the scaling dimensions of gauge-invariant Néel, valence bond solid (VBS),

d-wave superconductor, and charge order parameters in these critical theories.

Of particular interest is the scaling dimension of the gauge-invariant electron operator, which we also determine. This controls the manner in which gapless nodal quasiparticles emerge in the *d*-wave superconductor across the transition from an insulator with a non-zero gap to charged excitations. We summarize the results on scaling dimensions in [89]. Ref. [88] considered a mean-field theory of the corresponding transition in the electron-doped cuprates: in this case, the transition is to a pseudogap-metal, but the nodal region of the Brillouin zone can be gapped in the electron-doped pseudogap metal. Thus our theory has a remarkable feature not present in BCS theory: gapless nodal quasiparticles appear in a superconductor at a momentum which is gapped in the normal state. As we noted above, Ref. [88] pointed out connections of this feature to recent photoemission experiments in the electron-doped cuprates [533].

Section 6.2 introduces the square lattice SU(2) gauge theory of interest in this paper. This theory is defined in terms of fermionic spinons  $f_{i\alpha}$ ,  $\alpha = \uparrow, \downarrow$  and charge  $e$  bosons  $B_i$  on the sites  $i$  of the square lattice. Both the fermionic and bosonic matter fields transform as SU(2) gauge fundamentals, and there is also a dynamical SU(2) gauge field on the links of the lattice. We then consider the most general lattice gauge theory for these matter and gauge fields consistent with the projective symmetry transformations of the  $\pi$ -flux spin liquid, and with gauge-invariant observables having the same symmetry signatures as the Hubbard model with particle-hole symmetry. In the limit of strong gauge couplings, we can perform a strong-coupling expansion of our lattice gauge theory by integrating out the lattice gauge fields [399], and this will lead to the extended Hubbard model corresponding to our SU(2) lattice gauge theory. See Chapter 14 of Ref. [413] for a simpler example of a conventional theory of gauge-invariant degrees of freedom obtained from a lattice gauge theory of partons.

Note that our method is the converse of that usually followed in the condensed matter literature. We do not start from a lattice model of correlated electrons, and then obtain a gauge theory by fractionalizing the electrons. Instead, we start from a lattice gauge theory and match it to the electronic problem of interest by general arguments based on gauge invariance and global symmetry. This is a powerful method of incorporating non-perturbative knowledge of a fractionalized state (in our case, the  $\pi$ -flux spin liquid) in a very general setting.

Section 6.3 describes the continuum limit of the square lattice gauge theory of Section 6.2 along the lines of Ref. [87]. This leads to a quantum field theory of  $N_f = 2$  Dirac fermions and  $N_b = 2$  complex scalars, both transforming as SU(2) gauge fundamentals. We also discuss the generalizations of this theory to general  $N_{f,b}$ , and the operators corresponding to the gauge-invariant observables of the Hubbard model.

Section 6.4 examines the nature of fermion-boson couplings in the continuum field theory without any spatial and temporal gradients. We find that there are no allowed terms which are relevant in the large  $N_{f,b}$  expansion of critical theories. However, we do need to consider the higher-order formally irrelevant terms because they are important in determining the fate of the spin gap in the Higgs phases where the bosons are condensed.

Section 6.5 describes the extension of our results to the honeycomb lattice.

Analysis of the resulting continuum theory, including the  $N_b = \infty$  saddle points and  $1/N_{f,b}$  corrections to scaling dimensions, is performed in a separate work [89]. In particular, analysis of the  $N_b = \infty$  saddle points leads to the phase diagrams in Fig. 6.1, where *d*-wave superconductivity, charge order, and Néel/VBS order are all found.

## 6.2 SU(2) SQUARE LATTICE GAUGE THEORY

We begin by recalling the SU(2) square lattice gauge theory of Ref. [87] in the simpler setting of a half-filled square lattice, with no Fermi surfaces in any of the states studied. We also assume a particle-hole symmetry. This lattice gauge theory is likely free of a sign problem in quantum Monte Carlo.

We write the electron spin operators as

$$C_i = \begin{pmatrix} c_{i\uparrow} \\ c_{i\downarrow}^\dagger \end{pmatrix}, \quad (6.1)$$

on sites  $i$  of a square lattice. We fractionalize the electrons into fermionic spinons  $f_{i\alpha}$ ,  $\alpha = \uparrow, \downarrow$  and charge  $e$  bosons  $B_i$  via [512]

$$C_i = \mathcal{B}_i^\dagger \psi_i, \quad (6.2)$$

Symmetry	$c_\alpha$	$f_\alpha$	$B_a$
$T_x$	$c_\alpha$	$(-1)^y f_\alpha$	$(-1)^y B_a$
$T_y$	$c_\alpha$	$f_\alpha$	$B_a$
$P_x$	$c_\alpha$	$(-1)^x f_\alpha$	$(-1)^x B_a$
$P_y$	$c_\alpha$	$(-1)^y f_\alpha$	$(-1)^y B_a$
$P_{xy}$	$c_\alpha$	$(-1)^{xy} f_\alpha$	$(-1)^{xy} B_a$
$\mathcal{T}$	$\varepsilon_{\alpha\beta} c_\beta$	$(-1)^{x+y} \varepsilon_{\alpha\beta} f_\beta$	$(-1)^{x+y} B_a$
$\mathcal{C}$	$(-1)^{x+y} \varepsilon_{\alpha\beta} c_\beta^\dagger$	$\varepsilon_{\alpha\beta} f_\beta^\dagger$	$(-1)^{x+y} B_a^*$

Table 6.1: Projective transformations of the  $f_{i\alpha}$  spinons and  $B_i$  chargons on lattice sites  $\mathbf{i} = (x, y)$  under the symmetries  $T_x : (x, y) \rightarrow (x + 1, y)$ ;  $T_y : (x, y) \rightarrow (x, y + 1)$ ;  $P_x : (x, y) \rightarrow (-x, y)$ ;  $P_y : (x, y) \rightarrow (x, -y)$ ;  $P_{xy} : (x, y) \rightarrow (y, x)$ ; time-reversal  $\mathcal{T}$ , and particle-hole symmetry  $\mathcal{C}$ . The indices  $\alpha, \beta$  refer to global SU(2) spin, while the index  $a = 1, 2$  refers to gauge SU(2). Also shown are the (non-projective) transformations of the gauge-invariant electron  $c_\alpha$ .

where

$$\psi_{\mathbf{i}} \equiv \begin{pmatrix} f_{\mathbf{i}\uparrow} \\ f_{\mathbf{i}\downarrow}^\dagger \end{pmatrix}, \quad (6.3)$$

and

$$B_{\mathbf{i}} \equiv \begin{pmatrix} B_{1\mathbf{i}} \\ B_{2\mathbf{i}} \end{pmatrix}, \quad \mathcal{B}_{\mathbf{i}} \equiv \begin{pmatrix} B_{1\mathbf{i}} & -B_{2\mathbf{i}}^* \\ B_{2\mathbf{i}} & B_{1\mathbf{i}}^* \end{pmatrix}. \quad (6.4)$$

This fractionalization introduces a SU(2) gauge symmetry, where

$$\psi_{\mathbf{i}} \rightarrow U_{\mathbf{i}} \psi_{\mathbf{i}}, \quad B_{\mathbf{i}} \rightarrow U_{\mathbf{i}} B_{\mathbf{i}}, \quad (6.5)$$

under a SU(2) gauge transformation  $U_{\mathbf{i}}$ .

Remarkably, essentially all of the physics of the  $\pi$ -flux spin liquid phase, and its descendants, studied here are consequences of the SU(2) gauge symmetry, the spin rotation symmetry, and the action of other symmetries on the spinons as summarized in Table 6.1. The action of the latter symmetries on the  $B$  chargons follows from the decomposition (6.2), and these are also shown in Table 6.1. A key property of Table 6.1 is the relation

$$T_x T_y = -T_y T_x, \quad (6.6)$$

which ensures  $\pi$ -flux on both spinons and chargons, and at least two degenerate minima in

the dispersion the chargons.

The degrees of freedom of our square lattice gauge theory are one SU(2) fundamental fermion  $\psi_i$  on each lattice site, one SU(2) fundamental boson  $B_i$  on each lattice site, and a SU(2) link field  $U_{ij}$  on each nearest-neighbor link of the square lattice. We now describe the various terms in the Hamiltonian coupling these degrees of freedom.

The simplest fermion spinon imaginary time ( $\tau$ ) Lagrangian compatible with Table 6.1 is

$$\mathcal{L}(\psi) = \sum_i \psi_i^\dagger D_\tau \psi_i - iJ \sum_{\langle ij \rangle} [\psi_i^\dagger e_{ij} U_{ij} \psi_j + i \leftrightarrow j], \quad (6.7)$$

where  $D_\tau$  is a co-variant time derivative,  $i, j$  are nearest-neighbors,  $J$  is a real coupling constant of order the antiferromagnetic exchange,

$$e_{ji} = -e_{ij} \quad (6.8)$$

is a fixed element of the  $\mathbb{Z}_2$  center of the gauge SU(2) which ensures  $\pi$  flux per plaquette; we choose

$$e_{i,i+\hat{x}} = 1, \quad e_{i,i+\hat{y}} = (-1)^x, \quad (6.9)$$

where  $i = (x, y)$ ,  $\hat{x} = (1, 0)$ ,  $\hat{y} = (0, 1)$ . The link field  $U_{ij} = U_{ji}^\dagger$  is the fluctuating SU(2) lattice gauge field, and the mean-field saddle point of the  $\pi$ -flux phase is obtained by setting  $U_{ij} = 1$ . The hopping term in  $\mathcal{L}(\psi)$  has been chosen pure imaginary as that ensures a simple coupling to the SU(2) gauge field, along with SU(2) spin rotation invariance. The spin operator on each site  $S_i = (1/2) f_{i\alpha}^\dagger \sigma_{\alpha\beta} f_{i\beta}$  ( $\sigma$  are the Pauli matrices) can be expressed in terms of the  $\psi_i$  in the following SU(2) gauge-invariant combinations:

$$2S_{zi} = \psi_i^\dagger \psi_i - 1, \quad S_{xi} - iS_{yi} = -\varepsilon_{ab} \psi_{ai} \psi_{bi}, \quad (6.10)$$

where  $a, b = 1, 2$  are SU(2) gauge indices, and  $\varepsilon_{ab}$  is unit antisymmetric tensor. The nearest-neighbor bond energy operator can be identified with each individual term in  $\mathcal{L}(\psi)$

$$\text{bond energy: } \langle S_i \cdot S_j \rangle \sim Q_{f,ij} = Q_{f,ji} = -i [\psi_i^\dagger e_{ij} U_{ij} \psi_j + i \leftrightarrow j]. \quad (6.11)$$

In the cuprates, modulations of  $Q_{f,ij}$  would show up as modulations in the charge density on the sites (and similarly for modulations in  $Q_{b,ij}$  below).

Turning to the bosonic partons, and following Ref. [87], we can also write down the most general effective Lagrangian for the  $B_i$ , keeping only terms quadratic and quartic in the  $B_i$ , and with only on-site or nearest-neighbor couplings:

$$\mathcal{L}(B) = \sum_i |D_\tau B_i|^2 + r \sum_i B_i^\dagger B_i - iw_1 \sum_{\langle ij \rangle} \left[ B_i^\dagger e_{ij} U_{ij} B_j + i \leftrightarrow j \right] + \mathcal{V}(B). \quad (6.12)$$

A linear time derivative term is allowed only in the absence of particle hole symmetry, and so has been omitted. The couplings  $r, w_1$  are real Landau parameters, and the quartic terms are in  $\mathcal{V}(B)$ . These quartic terms are more conveniently expressed in terms of quadratic gauge invariant observables. By examining the transformations in Table 6.1, we can deduce the following correspondences between bilinears of the  $B$  with those of the bilinears of the gauge-neutral electrons:

$$\text{site charge density: } \langle c_{i\alpha}^\dagger c_{i\alpha} \rangle \sim \rho_i \equiv B_i^\dagger B_i$$

(the correspondence between  $\rho_i$  and site charge density holds

only in the absence of particle-hole symmetry; see Section 6.4),

$$\text{bond density: } \langle c_{i\alpha}^\dagger c_{j\alpha} + c_{j\alpha}^\dagger c_{i\alpha} \rangle \sim Q_{b,ij} = Q_{b,ji} \equiv \text{Im} \left( B_i^\dagger e_{ij} U_{ij} B_j \right),$$

$$\text{bond current: } i \langle c_{i\alpha}^\dagger c_{j\alpha} - c_{j\alpha}^\dagger c_{i\alpha} \rangle \sim J_{ij} = -J_{ji} \equiv \text{Re} \left( B_i^\dagger e_{ij} U_{ij} B_j \right),$$

$$\text{pairing: } \langle \varepsilon_{\alpha\beta} c_{i\alpha} c_{j\beta} \rangle \sim \Delta_{ij} = \Delta_{ji} \equiv \varepsilon_{ab} B_{ai} e_{ij} U_{ij} B_{bj}. \quad (6.13)$$

Note that the bond density observable  $Q_{b,ij}$  of bosons above has the same symmetry signature as the bond energy  $Q_{f,ij}$  of fermions in (6.11), and both are identical to the hopping terms in  $\mathcal{L}(B)$  and  $\mathcal{L}(\psi)$  respectively. Now we can write an expression for  $\mathcal{V}(B)$  by keeping all quartic terms which involve nearest-neighbor sites:

$$\begin{aligned} \mathcal{V}(B) &= \frac{u}{2} \sum_i \rho_i^2 + V_1 \sum_i \rho_i (\rho_{i+\hat{x}} + \rho_{i+\hat{y}}) + g \sum_{\langle ij \rangle} |\Delta_{ij}|^2 \\ &\quad + J_1 \sum_{\langle ij \rangle} Q_{b,ij}^2 + K_1 \sum_{\langle ij \rangle} J_{ij}^2. \end{aligned} \quad (6.14)$$

We also have the usual flux energy term of lattice gauge theory for the gauge field  $U_{ij}$

$$\mathcal{L}(U) = -\frac{1}{g} \sum_{i,j,k,l \in \square} \text{Tr} [U_{ij} U_{jk} U_{kl} U_{li}] + \text{c.c.}, \quad (6.15)$$

along with a gauge field kinetic energy [255].

Finally, we can consider quartic terms which couple the spinons and chargons directly. From the composite operators defined above we can write down the following terms involving only nearest-neighbor sites

$$\mathcal{L}(B\psi) = \sum_{\langle ij \rangle} \left[ \lambda_1 c_{i\alpha}^\dagger c_{j\alpha} + \lambda_1 c_{j\alpha}^\dagger c_{i\alpha} + \lambda_2 Q_{b,ij} Q_{f,ij} \right]. \quad (6.16)$$

Our aim is to determine the phase diagram of the above square lattice gauge theory as a function of the boson ‘mass’ tuning parameter  $r$ , and the various quartic boson couplings in (6.14). The general physics is that of a transition between Higgs and confining phases of the SU(2) gauge theory, with deconfined conformal gauge theories describing continuous transitions between the phases. When  $r$  is large and positive,  $B$  excitations are gapped, and we can work with the fermion-only theory in (6.7)—this theory is expected to confine into an insulator with either Néel or VBS order [474, 501, 574]. On the other hand, when  $r$  is negative,  $B$  condenses in Higgs phases, and fully quenches the SU(2) gauge field. The Higgs phases break one or more of the global symmetries, based upon the correspondence in (6.13).

### 6.3 QUANTUM FIELD THEORY AND ORDER PARAMETERS

Now we take the continuum limit of the square lattice gauge theory action in Section 6.2, and obtain the quantum field theory studied in the present paper. We will take the simplest case in which the boson hopping terms are only nearest-neighbor, as in (6.12), so there are only two valleys in the boson dispersion. This will lead to a SU(2) gauge theory with  $N_f = 2$  flavors of SU(2) fundamental Dirac fermions  $\psi$ , and  $N_b = 2$  flavors of SU(2) fundamental bosons  $B$ . As for the lattice gauge theory in Section 6.2, almost everything follows from the symmetry transformations of the fields: the continuum limits of the transformations in Table 6.1 are presented in Table 6.2.

For the continuum limit action of the fermionic spinons, we follow the notation of Ref. [441], which follows that of earlier related works [442, 481, 501], in obtaining from (6.7) the fermionic Lagrangian

$$\mathcal{L}_\psi = i\bar{\psi}\gamma^\mu (\partial_\mu - iA_\mu^\alpha \sigma^\alpha) \psi, \quad (6.17)$$

where  $\sigma^\alpha$  are the Pauli matrices,  $\alpha = x, y, z$ ,  $\gamma^\mu$  are  $2 \times 2$  Dirac matrices which act on the sublattice space,  $A_\mu^\alpha$  is the SU(2) gauge field, and the  $\psi$  have an additional  $N_f = 2$  valley ('flavor') index which is not shown. From the  $\psi$  bilinears, we can make a gauge-invariant 5-component real vector, which represents the  $3 + 2$  components of the Néel and VBS order parameters [381, 384, 501]; the Néel order is a staggered modulation of the spin in (6.10), while the VBS order is a modulation of the bond energy in (6.11). The properties of  $\mathcal{L}_\psi$  are invariant under global  $\text{SO}(5)_f$  rotations of this vector, and all our analysis below will preserve this  $\text{SO}(5)_f$  symmetry (the  $f$  subscript merely denotes that the symmetry acts on the fermions).

It is a simple matter to generalize (6.17) to arbitrary integer  $N_f$ : we allow the valley index to run over  $1 \dots N_f$ . After transforming to Majorana fermions, the free fermion Lagrangian has a  $\text{SO}(4N_f)$  symmetry, and modding out the gauge symmetry as in Ref. [501], we conclude that the Lagrangian  $\mathcal{L}_\psi$  has a  $\text{USp}(2N_f)/\mathbb{Z}_2$  global symmetry.

In the bosonic matter sector, we express the lattice  $B_i$  bosons in terms of complex bosons  $B_{as}$ , with  $a = 1, 2$  the SU(2) gauge index, and  $s = 1 \dots N_b = 2$  the valley ('flavor') index [87]:

$$B_a(\mathbf{r}) = \begin{cases} -B_{a1}e^{i\pi(x+y)/2} + B_{a2}(\sqrt{2} + 1)e^{i\pi(x-y)/2}, & x \text{ even} \\ B_{a1}(\sqrt{2} + 1)e^{i\pi(x+y)/2} - B_{a2}e^{i\pi(x-y)/2}, & x \text{ odd} \end{cases} \quad (6.18)$$

Under particle-hole symmetry  $\mathcal{C}$ , the transformations in Table 6.1 now imply that  $B_{as} \rightarrow B_{as}^*$ . Then (6.13) leads to the following gauge-invariant order parameters in the continuum limit

[87]

$$\begin{aligned}
 & d\text{-wave superconductor : } \varepsilon_{ab} B_{a1} B_{b2} \\
 & x\text{-CDW : } B_{a1}^* B_{a1} - B_{a2}^* B_{a2} \equiv B^\dagger \mu^z B \\
 & y\text{-CDW : } B_{a1}^* B_{a2} + B_{a2}^* B_{a1} \equiv B^\dagger \mu^x B \\
 & d\text{-density wave : } i(B_{a1}^* B_{a2} - B_{a2}^* B_{a1}) \equiv -B^\dagger \mu^y B
 \end{aligned} \tag{6.19}$$

where  $\mu$  acts on valley indices. In terms of the lattice order parameters in (6.13), the  $d$ -wave superconductor has  $\Delta_{i,i+\hat{x}} = -\Delta_{i,i+\hat{y}}$ , but is independent of  $i$ . The charge density waves (CDWs) have period 2 modulations of  $Q_{b,ij}$  and  $\rho_i$  (the modulations of  $\rho_i$  are absent when there is particle-hole symmetry, see Section 6.4), and are site-centered unlike the bond-centered modulations of  $Q_{f,ij}$  in the VBS state. The  $d$ -density wave order is odd under time-reversal, and has a staggered pattern of electrical currents  $J_{ij}$ . Note that the CDW and  $d$ -density wave orders can be written as a SO(3) vector  $B^\dagger \mu^i B$ ,  $i = x, y, z$ . In combination with the complex superconducting order, the order parameters in (6.19) form a SO(5)<sub>b</sub> vector, for reasons very similar to the fermions (again the  $b$  subscript denotes that this SO(5) acts on the bosons). Computing the magnitude of this SO(5)<sub>b</sub> vector, we obtain an important identity which is easily verified by explicit evaluation

$$(B^\dagger B)^2 = \left( B^\dagger \mu^i B \right)^2 + 4 |\varepsilon_{ab} B_{a1} B_{b2}|^2 . \tag{6.20}$$

The continuum limit of the Lagrangian (6.12) for the bosonic sector is

$$\begin{aligned}
 \mathcal{L}_B = & \left| (\partial_\mu - i A_\mu^\alpha \sigma^\alpha) B \right|^2 + r |B|^2 + \bar{u} |B|^4 \\
 & + v_1 \left( B^\dagger \mu^z B \right)^2 + v_1 \left( B^\dagger \mu^x B \right)^2 \\
 & + v_2 \left( B^\dagger \mu^y B \right)^2 + v_3 |\varepsilon_{ab} B_{a1} B_{b2}|^2 .
 \end{aligned} \tag{6.21}$$

The first three terms in  $\mathcal{L}_B$  have the SO(5)<sub>b</sub> global symmetry, for reasons essentially identical to those for  $\mathcal{L}_f$ . All the order parameters in (6.19) are degenerate in this limit. This degeneracy and the SO(5)<sub>b</sub> symmetry are broken by the  $v_{1,2,3}$  terms in (6.21), which are simply

squares of the order parameters in (6.19). The identity in (6.19) was overlooked in Ref. [87], and has the consequence that the 5 quartic terms in (6.21) are not all independent—this has no material consequence to the mean-field results of Ref. [87], apart from a redundant labeling of couplings. In the Higgs phase where  $B$  is condensed, one of the order parameters in (6.19) must be non-zero, and, in mean-field theory, the choice is determined by the relative values of  $v_{1,2,3}$  [87].

The generalization of the first three terms in (6.21) to arbitrary integer  $N_b \geq 2$ ,  $N_b$  even is straightforward, but the  $v_{1,2,3}$  terms in require further consideration. We limit ourselves to the case  $v_1 = v_2$ , so that the CDW orders and the  $d$ -density wave orders become degenerate. Then we can write (6.21) as

$$\begin{aligned} \mathcal{L}_B = & \left| (\partial_\mu - iA_\mu^\alpha \sigma^\alpha) B \right|^2 + r|B|^2 + \bar{u}|B|^4 \\ & + v_1 \left( B^\dagger \mu^i B \right)^2 + v_3 |\varepsilon_{ab} B_{a1} B_{b2}|^2 . \end{aligned} \quad (6.22)$$

Next, we use the redundancy implied by (6.20) to set  $v_1 = 0$  in (6.22). Then one extension of (6.22) to general  $N_b$  for the bosonic flavor indices is obtained by replacing  $\varepsilon_{st}$  in the  $v_3$  term by  $\mathcal{J}_{st}$  the  $U\text{Sp}(N_b)$  invariant tensor, consisting of  $N_b/2$  copies of  $\varepsilon_{st}$  along the diagonal. In this manner we obtain a Lagrangian valid for any  $N_b$  (following conventions in Ref. [366])

$$\mathcal{L}_B = \left| (\partial_\mu - iA_\mu^\alpha \sigma^\alpha) B \right|^2 + \frac{u}{2N_b} (|B_{as}|^2 - N_b/g)^2 - \frac{v}{N_b} |B^T \mathcal{J} \varepsilon B|^2 . \quad (6.23)$$

Recall that the indices  $a, b$  act on the  $SU(2)$  gauge indices, and not the flavor indices, and so do not need a large  $N_b$  generalization. For  $N_b = 2$ , the correspondence to the couplings in (6.21) is  $u = 2N_b \bar{u}$ ,  $g = -u/r$ ,  $v = -N_b v_3/4$ . For general  $N_b$ , the order parameters in (6.19) are replaced by the  $SU(2)$  gauge-invariant operators

$$\begin{aligned} d\text{-wave superconductor : } & \mathcal{J}_{st} \varepsilon_{ab} B_{as} B_{bt} \\ \text{charge order : } & B_{as}^* T_{st}^i B_{at} \end{aligned} \quad (6.24)$$

where  $T^i$  are generators of  $\mathrm{USp}(N_b)$  obeying

$$T^{i\dagger} = T^i \quad , \quad T^{iT} \mathcal{J} + \mathcal{J} T^i = 0 . \quad (6.25)$$

We refer to the combined and degenerate CDW and  $d$ -density orders simply as ‘charge order’.

We can now use standard methods to generate a large  $N_b$  expansion of (6.23) at fixed  $u$ ,  $g$ , and  $v$ . The coupling  $g$  will be used to tune across the transition, while  $v$  will determine the fate of Higgs phase where  $B$  is condensed. The theory in (6.23) has a global  $\mathrm{USp}(N_b) \times \mathrm{U}(1)$  symmetry, and the Higgs phase with  $B$  condensed either breaks the  $\mathrm{U}(1)$  symmetry leading to  $d$ -wave superconductivity, or breaks the  $\mathrm{USp}(N_b)$  symmetry leading to degenerate CDW/ $d$ -density wave orders.

At  $v = 0$ , the global symmetry of (6.23) is enhanced to  $\mathrm{USp}(2N_b)/\mathbb{Z}_2$  (as for the fermionic spinons [501]), and the superconducting and charge orders all become degenerate. The enhanced symmetry is evident in the matrix form of the bosonic fields in (6.4), which generalizes in the continuum to

$$\mathcal{B}_s = \begin{pmatrix} B_{1s} & -B_{2s}^* \\ B_{2s} & B_{1s}^* \end{pmatrix} , \quad (6.26)$$

obeying the reality condition

$$\mathcal{B}_s = \sigma^y \mathcal{B}_s^* \sigma^y . \quad (6.27)$$

The  $\mathrm{USp}(2N_b)$  global symmetry  $U_g$  then acts as right multiplication  $\mathcal{B} \rightarrow \mathcal{B} U_g$ , where  $U_g$  is a  $2N_b \times 2N_b$  matrix acting on both the  $s$  flavor index, and the right matrix index of (6.26).

The condition (6.27) leads to the defining conditions for  $\mathrm{USp}(2N_b)$ :

$$U_g^\dagger U_g = 1 \quad , \quad U_g^T \sigma^y U_g = \sigma^y . \quad (6.28)$$

Note, also, that the  $\mathrm{SU}(2)$  gauge symmetry in (6.5) acts a left multiplication  $\mathcal{B}_s \rightarrow U \mathcal{B}_s$ . As in the fermion case, the  $\mathrm{USp}(2N_b)$  and gauge  $\mathrm{SU}(2)$  share a common  $\mathbb{Z}_2$  center, and hence

Symmetry	$B_a$	$X_{ab}$
$T_x$	$-i\mu^x B_a$	$\mu^x X_{ab}$
$T_y$	$-i\mu^z B_a$	$\mu^z X_{ab}$
$P_x$	$B_a$	$-i\gamma^x \mu^z X_{ab}$
$R_{\pi/2}$	$-\frac{\mu^x + \mu^z}{\sqrt{2}} B_a$	$e^{i\pi\gamma^0/4} e^{-i\pi\mu^y/4} X_{ab}$
$\mathcal{T}$	$B$	$\gamma^0 \mu^y X^*$
$\mathcal{C}$	$B^*$	$X \sigma^y$
$U(1)_c$	$e^{i\theta} B_a$	$X_{ab}$
$SU(2)_g$	$U_g B$	$X U_g^\dagger$
$SU(2)_s$	$B$	$U_s X$

Table 6.2: We tabulate the action of the microscopic symmetries, along with the  $SU(2)$  gauge transformations, on the continuum fields. To concisely express the action of  $SU(2)$  spin rotation symmetry, we represent the spinon degrees of freedom in terms of a matrix of Majorana fermions  $X$ . The  $\gamma$  matrix  $\gamma^0$  is the labels the temporal component.

the global symmetry is  $USp(2N_b)/\mathbb{Z}_2$ .

The full action of the microscopic symmetries on the continuum fields is listed in Table 6.2. To retain a concise representation of the  $SU(2)$  spin rotation symmetry, we re-express our spinon degrees of freedom in terms of Majorana fermions. Following Ref [501], we introduce the  $4 \times 2$  matrix of Majorana fermions  $X_{a,s;b}$ . Here  $a, s, b$  are the spin, valley and gauge indices, respectively. The relation between  $X$  and the Dirac fermions is given by  $\psi_{a,s} = i\sigma_{a,b}^y X_{1,s,b}$ . The  $SU(2)$  gauge symmetry acts as  $X_{a,s;b} \rightarrow X_{a,s;c} U_{cb}^\dagger$  and  $SU(2)$  spin rotation symmetry acts as  $X_{a,s;b} \rightarrow U_{ac} X_{c,s;b}$ . The action of all the symmetries apart from spin rotation symmetry lifts directly to the complex fermions, although a  $U(1)$  subgroup corresponds to a uniform phase rotation  $\psi \rightarrow e^{i\theta}\psi$ . Both representations will be utilized here - the Majorana representation for when a complete symmetry analysis is required, and the Dirac representation for perturbative computations.

Along with the gauge-invariant fermion and boson bilinears noted above, we will also consider mixed gauge-invariant bilinears which lead to the electron operator measured in photoemission experiments. The quantum field theory yields the electron operator near the 4 nodal points  $\mathbf{k} = (\pm\pi/2, \pi/2)$ . The particular combination of low-energy spinons and chargons that correspond to these nodal excitations is rather complicated, as the spinor structure of the Dirac spinons must be unpacked, i.e we consider the fields  $\psi_{as\alpha}$  with gauge index  $a$ , valley index  $s$ , and spinor index  $\alpha$  (which microscopically corresponds to a sublattice index). Sup-

pressing the valley index and taking the Pauli matrices  $\mu^i$  to act on both chargon and spinon valley indices,  $B_a^* \mu^i \psi_{a\alpha} \equiv B_{as}^* \mu_{st}^i \psi_{at\alpha}$ , we have

$$\begin{aligned} C_{\mathbf{k}=(\pi/2,\pi/2)} &\propto \begin{pmatrix} B_a^* i \mu^y (\psi_{a1} + (\sqrt{2} + 1) \psi_{a2}), \\ \epsilon_{ab} B_a ((\sqrt{2} + 1) \psi_{a1} - \psi_{a2}) \end{pmatrix} \\ C_{\mathbf{k}=(-\pi/2,\pi/2)} &\propto \begin{pmatrix} -B_a^* i \mu^z ((\sqrt{2} + 1) \psi_{a1} + \psi_{a2}) \\ \epsilon_{ab} B_a \mu^x (-\psi_{a1} + (\sqrt{2} + 1) \psi_{a2}) \end{pmatrix} \end{aligned} \quad (6.29)$$

As we will show, generic operators of the form  $B_{as}^* \psi_{as'\alpha}$  and  $\epsilon_{ab} B_{as} \psi_{bs'\alpha}$  are all renormalized in the same way at criticality, so the details of Eq. 6.29 will not be relevant for computing the scaling dimension of the electron operator.

We will analyze the theory  $\mathcal{L}_\psi + \mathcal{L}_B$  in the limit of large  $N_f$  and  $N_b$ , with a fixed ratio  $N_f/N_b$ . We obtain the leading  $1/N_{f,b}$  corrections to the scaling dimensions of the gauge-invariant fermion and boson bilinear order parameters, and also the electron operators in (6.29). We will also obtain the corresponding properties in an alternative large  $N_b$  limit. Both of these calculations are contained in [89].

#### 6.4 FERMION-BOSON INTERACTIONS AND SPIN GAPS

In Section 6.3, we constructed a Lagrangian describing spinon and chargon fluctuations and their coupling to a shared SU(2) gauge field. Importantly, there exist three independent quartic chargon interactions which are relevant at tree-level and must be tuned in order to reach a continuous transition. In this section, we consider symmetry-allowed interactions between the spinons and chargons. The reason for this is twofold. First, quartic interactions involving two spinons and two chargons are marginal at tree-level, and corrections to their scaling dimension are important for the behavior of the critical theory. Second, condensation of the chargons can qualitatively modify the dispersion of the spinons in the charge-ordered phase, either by producing a gap or generating a Fermi surface. Note that upon condensation of the chargons, the spinon becomes associated with the electron, and these dispersion modifications are reflected in the electronic spectral function. We show that in fact *no* quartic

chargon-spinon interactions are allowed by the microscopic symmetries in the critical theory, provided we enforce particle-hole symmetry. Relaxing particle-hole symmetry admits two quartic interactions. In the charge ordered phase, these terms shift the Fermi energy of the Dirac spinons, thereby inducing a spinon Fermi surface.

In this section, we will use the Majorana representation of the fermionic spinons; the explicit action of spin rotation symmetry is essential in our symmetry analysis. In this language, a generic quartic interaction that respects both charge conservation and spin rotation invariance can be expressed in the form

$$\sum_{\alpha,\beta,j} A_{\alpha,\beta,j} \text{tr} \left[ B \mu^\alpha B^\dagger \bar{X} \gamma^j \mu^\beta X \right], \quad (6.30)$$

where  $\bar{X} \equiv X^\dagger \gamma^0$  and  $A$  is a coefficient tensor, not to be confused with the gauge field. The indices  $\alpha, \beta, j$  run over four variables, the three Pauli and  $\gamma$  matrices as well as an additional identity element. We perform a systematic search for symmetry-allowed quartic couplings by deducing the action of the microscopic symmetries on  $A_{\alpha,\beta,j}$ , which we regard as a  $4^3 = 64$ -dimensional vector. Symmetry-allowed quartic terms are given by choices of  $A$  which have eigenvalue 1 under all the symmetries, the existence of which can be checked numerically.

With this approach, we deduce two terms that are allowed by all the microscopic symmetries, but are odd under particle-hole symmetry which we assume to be emergent in the critical theory:

$$\begin{aligned} & \text{tr} \left[ BB^\dagger \bar{X} \gamma^0 X \right], \\ & \text{tr} \left[ B \mu^z B^\dagger \bar{X} \mu^z \gamma^x X \right] + \text{tr} \left[ B \mu^x B^\dagger \bar{X} \mu^x \gamma^y X \right]. \end{aligned} \quad (6.31)$$

One can also consider analogous quartic couplings of the form

$$\sum_{\alpha,\beta,j} C_{\alpha,\beta,j} \text{tr} \left[ B \mu^\alpha B^\dagger \right] \text{tr} \left[ \bar{X} \gamma^j \mu^\beta X \right]. \quad (6.32)$$

The tensor  $C$  transforms identically to  $A$ ; however, the two quartic couplings in this case vanish identically due to the anticommutation relations of the Majorana fermions. These results are consistent with taking the continuum limit of the quartic spinon-chargon interactions on the lattice given by (6.16), where we find that the leading order terms with no derivatives

vanish. Allowing for quartic interactions that break particle-hole symmetry, such as an on-site chemical potential or a second-neighbor electron hopping, generate the continuum interactions in (6.31). The first term acts as a chemical potential and, at each of the two gapless points in momentum space, induces an equal and opposite shift in the Fermi energy on the two species of spinons.

Quartic interactions do not generate a spin gap in the ordered phases. To find six-term interactions that can open up a spin gap in the CDW phase, we take the approach of considering the CDW order parameter,  $B^\dagger \mu^z B$  and  $B^\dagger \mu^x B$  for  $x$ -CDW and  $y$ -CDW respectively, and coupling them to a quartic chargon-spinon interaction that has the same symmetry transformations. Multiple six-term interactions can be obtained in this manner; however, only two are capable of producing a spin gap, which are

$$\begin{aligned} & B^\dagger \mu^z B \operatorname{tr} [B \mu^x B^\dagger \bar{X} \mu^y X] , \\ & B^\dagger \mu^x B \operatorname{tr} [B \mu^z B^\dagger \bar{X} \mu^y X] . \end{aligned} \tag{6.33}$$

Note that these terms vanish unless *both* the  $x$ -CDW and  $y$ -CDW terms are non-zero. This is consistent with the fact that, once we are in the CDW phase, one is allowed to add non-gauge-invariant terms to the spinon dispersion which break translational symmetry. The symmetry transformations of gauge singlet and triplet spinon bilinears were tabulated in Ref. [481]; from this analysis, one can conclude that the only possible mass term in the CDW phase,  $\operatorname{tr} [\sigma^a \bar{X} \mu^y X]$ , must be odd under translations in both the  $x$  and  $y$  directions. This term also breaks particle-hole symmetry; however, as it is proportional to four powers of the chargon condensate, it will generically be smaller than the previously-discussed perturbations which generate a spinon Fermi surface.

## 6.5 HONEYCOMB LATTICE

The ground state of the large- $U$  Hubbard model on the honeycomb lattice at half-filling has long-range Néel order, as for the square lattice. Also as for the square lattice, adding frustrating interactions leads to a phase with VBS (*i.e.* kekule) order [146, 280, 390]. But in contrast to the square lattice, at smaller  $U$  the honeycomb lattice features a semi-metal phase

with no broken symmetry, and an electronic dispersion with 2 massless Dirac fermion points in the Brillouin zone.

In this section we extend the SU(2) gauge theory analysis to the honeycomb lattice. We find just the three phases noted above, with no additional superconducting or charge-ordered phases. This difference from the square lattice case can be traced to the fact that the bosonic chargons,  $B$ , move in a background zero flux on the honeycomb lattice [186]. Consequently, the  $B$  dispersion has only a single minimum in the Brillouin zone, and the Higgs phase where  $B$  is condensed breaks no symmetries and realizes the Dirac semi-metal. We sketched a phase diagram for the honeycomb lattice SU(2) gauge theory in Fig. 6.2.

The details of such a theory have previously been worked out in Ref. [186], but with the interpretation of the deconfined phase as being stable - our interpretation is that this phase is ultimately unstable to either Néel or VBS order. The low energy theory consists of  $N_f = 2$  Dirac fermions with an emergent SO(5) symmetry rotating between Néel and kekule VBS order. As there is only a single minima of the chargon disperion at  $\mathbf{k} = (0, 0)$ , the spinons are coupled to  $N_b = 1$  bosonic chargons, with the full symmetry of the low-energy action being  $\text{SO}(5) \times \text{SU}(2)$ , with the SU(2) chargon symmetry corresponding to the pseudospin. An important point which is not explicitly discussed in Ref. [186] is the possibility of symmetry-allowed quartic interactions between the chargons and spinons, which would be marginal at tree level. However, this is rather simple to rule out due to the fact that the chargon minima is at  $\mathbf{k} = (0, 0)$ , and hence transforms trivially under all the lattice symmetries (an exception are transformations which exchange the  $A$  and  $B$  sublattice, where the sublattice structure of the chargon eigenvalue causes the chargon to acquire a minus sign - this has no effect on chargon bilinears). As a result, symmetry-allowed chargon/spinon quartic interactions demand that the spinon bilinear component is independently allowed by symmetry, and one can easily verify that no such term exists.

The large- $N_f, N_b$  expansion proceeds identically to the one discussed previously in the paper, with the exception that the chargon sector does not contain any quartic interactions aside from a  $B^4$  term (in other words, we take  $v = 0$ ). The results for the various scaling dimensions in [89] carry over to this scenario, although some of the chargon bilinears studied can only be defined for even  $N_b$ .

We note an interesting relation between the model of Ref. [425] and the  $SU(2)$  gauge field theory with  $N_f = 2$  and  $N_b = 1$ . The global symmetry of the quantum field theory of Section 6.3 is  $SO(5)_f$  in the fermionic sector for  $N_f = 2$ , and  $USp(2)/\mathbb{Z}_2$  in the bosonic sector for  $N_b = 1$ . Ref. [425] considered a honeycomb lattice model in which quantum spin Hall, superconducting, and Dirac semi-metal phases meet at a multicritical point, and proposed a  $SO(5)$  Gross-Neveu-Yukawa field theory for the multicriticality. The GNY field theory has no gauge fields, and hence there is an additional  $SO(3) \cong USp(2)/\mathbb{Z}_2$  global symmetry which acts on the Dirac fermions. So the global symmetries of our  $SU(2)$  gauge field theory at  $N_f = 2$  and  $N_b = 1$  are identical to those of the  $SO(5)$  GNY theory. It remains an interesting open question whether these two theories are the same conformal field theory.

## 6.6 DISCUSSION

The discovery of high temperature superconductivity in the cuprates sparked decades of theoretical work on quantum phases proximate to the familiar Néel ordered state of the  $S = 1/2$  square lattice antiferromagnet. Early work [389] argued that the proximate insulator has valence bond solid (VBS) order. The nature of the Néel-VBS quantum transition has also been extensively studied [434, 439, 501], and recent fuzzy sphere investigations [574] have concluded that it is described by a ‘pseudo-critical’ theory with an approximate conformal symmetry, and a nearly exact global  $SO(5)$  symmetry which rotates between the  $3 + 2$  components of the Néel and VBS orders. One formulation of the pseudo-critical theory has a  $SU(2)$  gauge field coupled to  $N_f = 2$  fundamental massless Dirac fermions: we have used the fuzzy sphere results to conclude that this gauge theory confines in the infrared with either Néel or VBS order, and the Néel-VBS transition is weakly first order. The ordering is selected by terms which are formally irrelevant in the continuum theory, and we assume here that Néel order is selected.

The present paper extends these investigations by allowing for charge fluctuations, while remaining at half-filling and preserving particle-hole symmetry. Following earlier work [87], we have shown that adding charge fluctuations to the  $SU(2)$  gauge theory leads naturally to a  $d$ -wave superconductor with nodal quasiparticles, and states with period-2 charge order. We can

then consider quantum transitions between the Néel state and the  $d$ -wave superconductor, or between the Néel state and charge order. Such transitions are described by a direct extension of the SU(2) gauge theory with  $N_f = 2$  fundamental massless Dirac fermions—there are additional fundamental  $N_b = 2$  massless complex scalars. Given the weakly broken conformal symmetry for  $N_f = 2$ ,  $N_b = 0$  [474, 567, 574], and the stability of conformal gauge theories at large  $N_{f,b}$ , it is very plausible that the  $N_f = 2$ ,  $N_b = 2$  case exhibits true deconfined criticality with an exact emergent conformal symmetry.

The  $N_f = 2$ ,  $N_b = 2$  quantum field theory studied in this paper is defined by the Lagrangian  $\mathcal{L}_\psi + \mathcal{L}_B$  in (6.17) and (6.21). Here  $r$  is the tuning parameter which takes the system from the Néel state (present when  $r$  is large and positive and  $B$  is not condensed) to the states allowed by charge fluctuations (with  $d$ -wave superconductivity or charge order). The coefficients of the quartic couplings  $v_{1,2,3}$  in (6.21) select among the latter states.

We studied two different large  $N_{f,b}$  generalizations of this theory, defined by the extensions in the bosonic sector, discussed further in [89]. The phase diagrams of these theories at  $N_b = \infty$  appear in Fig. 6.1. The  $1/N_{f,b}$  expansions of the second-order quantum phase transitions are described in [89]. We computed the scaling dimensions of the gauge-invariant order parameters, which are composites of two fermions or two bosons, and the electron operators at momenta  $(\pm\pi/2, \pm\pi/2)$ , which are the composites of one fermion and one boson in (6.29). Our results are summarized in [89]. The results are not expected to be accurate at  $N_f = N_b = 2$ , when the  $1/N_{f,b}$  corrections are quite large.

The scaling dimension of the electron operator determines a novel feature of the quantum transition out of the  $d$ -wave superconductor. The  $d$ -wave superconductor itself is conventional, and has 4 nodal points with gapless Bogoliubov quasiparticles. In BCS theory, such gapless quasiparticles are remnants of the Fermi surface of the parent metal, and so the electronic quasiparticle residue remains non-zero across the metal-superconducting transition. However, for the transition from the  $d$ -wave superconductor to the Néel state, there is no longer a simple relationship between the Bogoliubov quasiparticles and the Fermi surface excitations of a parent metal. Instead, the Bogoliubov quasiparticles of the superconductor are connected to the spinons of the deconfined quantum critical point. As there are no gapless electronic excitations in the Néel state, and the electronic quasiparticle residue vanishes at the transition

out of the  $d$ -waves superconductor with an exponent determined by the scaling dimension of the electron operator at the deconfined quantum critical point.

A recent paper [88] has shown that a similar phenomenon can also happen in the *electron* doped case in a situation where the normal state has no Fermi surface crossing the zone diagonals: nevertheless, gapless nodal quasiparticles do appear in the proximate  $d$ -wave superconductor, in a region of the Brillouin zone which is gapped in the normal state. Furthermore, there are connections of this remarkable phenomenon to the recent photoemission observations of Ref. [533] on the electron doped cuprates.

Along the same lines, we believe the  $d$ -wave superconductor found in the quasi-one-dimensional numerical study of Ref. [222], by doping the spin liquid of the  $J_1$ - $J_2$  antiferromagnet, will have 4 nodal points in the two-dimensional limit.

Finally, we note the analysis of Section 6.5, where we applied the same line of thought to the Néel-VBS transition on the honeycomb lattice [146, 390]. We found only a single additional phase upon including charge fluctuations: a Dirac semi-metal with no broken symmetries. All these phases (Néel, VBS (kekule), Dirac semi-metal) have been observed in experiments on monolayer graphene [91, 552]. It is interesting to speculate that the absence of a superconducting phase on the honeycomb lattice in our theory, in contrast to the square lattice, is the underlying reason for the low superconducting  $T_c$ 's observed in the graphene family of compounds.

*Find something that is relevant.*

Mehran Kardar

# 7

## Quantum phase transition at non-zero doping in a random t-J model

Two recent experiments [135, 142] have shed new light on the transformation in the metallic parent state of the cuprate superconductors near optimal doping, while also highlighting the central theoretical puzzles. Angle-dependent magnetoresistance measurements in  $\text{La}_{1.6-x}\text{Nd}_{0.4}\text{Sr}_x\text{CuO}_4$  [135] are compatible with a Luttinger volume ‘large’ Fermi surface only at a hole doping  $p > p_c \approx 0.23$ . Nuclear magnetic resonance and sound velocity measurements in  $\text{La}_{2-x}\text{Sr}_x\text{CuO}_4$  [142] in high magnetic fields have uncovered glassy antiferromagnetic order for  $p < p_c \approx 0.19$ . These, and other, observations show that the parent metallic state of the cuprates exhibits Fermi liquid behavior for  $p > p_c$ , and transforms to an enigmatic pseudogap metal with glassy magnetic order for  $p < p_c$ . Observations also indicate that the reshaping of the Fermi surface, and the onset of the pseudogap, for  $p < p_c$  cannot be explained by long-range antiferromagnetic order, which sets in at a doping smaller than  $p_c$ .

Here, we present exact diagonalization results on clusters of  $N$  sites of a  $t$ - $J$  model with random and all-to-all hopping and exchange interactions (see (7.1)). In the thermodynamic limit  $N \rightarrow \infty$ , the replica-diagonal saddle point of this model, and a related Hubbard model [73], are described by (extended) dynamic mean-field equations in which the disorder self-averages E. Moreover, closely related mean-field equations also appear in non-random models

in high spatial dimensions [181, 456], indicating that the self-averaging features of the random models properly capture generic aspects of strong correlation physics. A direct solution of the  $N = \infty$  replica-diagonal saddle point of the Hubbard model is presented in a separate paper [118], with complementary results which are consistent with our conclusions below.

The insulating model at  $p = 0$  has been studied previously by exact diagonalization [21], and a non-self-averaging spin glass ground state was found. We find similar results at  $p = 0$ , but with a reduced estimate for the magnitude of the spin glass Edwards-Anderson order parameter,  $q$ . At non-zero  $p$ , we find that  $q$  decreases monotonically, vanishing at a quantum phase transition  $p_c \approx 1/3$ . We present several results for thermodynamic, entanglement, and spectral properties across this transition. All our results are consistent with the presence of a self-averaging Fermi liquid state for  $p > p_c$ ; in particular, we find that the one-particle energy distribution function is consistent with a disordered analog of the Luttinger theorem E. The entropy, entanglement entropy and compressibility all have maxima near  $p_c$ . We find that the low frequency dynamic spin susceptibility matches that of the Sachdev-Ye-Kitaev (SYK) class of models [250, 420] over a significant range of frequencies near  $p_c$ ; this includes a subleading contribution which arises from a boundary graviton in dual models of two-dimensional quantum gravity [247, 304, 410, 482, 483]. Such spectral features are not present in theories that treat the transition at  $p = p_c$  in a Landau-Ginzburg-Hertz framework for the onset of spin glass order in a Fermi liquid [417, 433].

## 7.1 RANDOM $t$ - $J$ MODEL

We consider the Hamiltonian

$$H = \frac{1}{\sqrt{N}} \sum_{i \neq j=1}^N t_{ij} P c_{i\alpha}^\dagger c_{j\alpha} P + \frac{1}{\sqrt{N}} \sum_{i < j=1}^N J_{ij} \mathbf{S}_i \cdot \mathbf{S}_j \quad (7.1)$$

where  $P$  is the projection on non-doubly occupied sites,  $\mathbf{S}_i = (1/2) c_{i\alpha}^\dagger \sigma_{\alpha\beta} c_{i\beta}$  is the spin operator on site  $i$ . The hoppings  $t_{ij} = t_{ji}^*$  and real exchange interactions  $J_{ij}$  are independent random numbers with zero mean and variance  $t^2, J^2$ . Henceforth, we set  $t = J = 1$ . We work in the canonical ensemble, where our system has a fixed particle (hole) density,  $n$  ( $p = 1 - n$ ). At  $p = 0$ , hopping is prevented due to the double occupancy constraint, and the model

reduces to an infinite-range Heisenberg model with random couplings. The  $p = 0$  model has been studied analytically by generalizing the SU(2) symmetry to SU( $M$ ) and taking a large- $M$  limit [155, 156, 420], and numerically for the case of  $M = 2$  [21, 66]. For SU(2), a spin glass phase is found below a critical temperature  $T_c \approx 0.10J$ . When doping is present, Ref. [352] predicts a disordered Fermi liquid phase for all non-zero values of  $p$  in the large- $M$  limit. However, it was recently argued [228, 478] that for the case of SU(2), the spin glass phase should persist up to a critical finite value of doping,  $p_c$ , corresponding to a quantum critical point separating the spin glass phase from a disordered Fermi liquid. Near criticality, the model is predicted to exhibit SYK-like criticality with a non-zero extensive entropy and a linear-in-temperature resistivity [172]. In a weak-coupling renormalization group, this critical point emerges when the three fractionalized excitations in the  $t$ - $J$  model become degenerate in energy, leading to a zeroth order prediction of  $p_c = 1/3$ .

## 7.2 DYNAMICAL SPIN RESPONSE AT $T = 0$

We first present results on the nature of the spin correlations at  $T = 0$ , providing evidence that the spin glass phase shown to exist at  $p = 0$  is stable for small values of doping, up to a critical value of doping near  $p = 1/3$ . Using the Lanczos algorithm, we calculate the spectral function at  $T = 0$ ,

$$\begin{aligned}
 \chi''(\omega) &= \frac{1}{3} \sum_{\alpha} \frac{1}{N} \sum_i \sum_n |\langle \psi_n | S_i^{\alpha} | \psi_0 \rangle|^2 \\
 &\times [\delta(\omega - (E_n - E_0)) - \delta(\omega + (E_n - E_0))] ,
 \end{aligned} \tag{7.2}$$

where numerically the delta functions are replaced by Gaussians with a small variance. The signature of spin glass order,  $\lim_{t \rightarrow \infty} \frac{1}{N} \sum_i \langle \mathbf{S}_i(0) \mathbf{S}_i(t) \rangle = q \neq 0$ , is reflected by a  $q\delta(\omega)$  contribution to the dynamical structure factor  $S(\omega)$ , which is related to the spectral function at  $T = 0$  by  $\chi''(\omega) = S(\omega) - S(-\omega)$ . For a finite system size, the exact delta function in  $S(\omega)$  is replaced by a peak at low frequency, whose width approaches 0 in the thermodynamic limit and whose total spectral weight gives  $q$ . Therefore, the spin glass contribution to  $\chi''(\omega)$  for finite systems is given by a low frequency peak, and was analyzed for this model at  $p = 0$  in [21]. Above  $p_c$ , a disordered Fermi liquid is expected to have a low-frequency behavior of

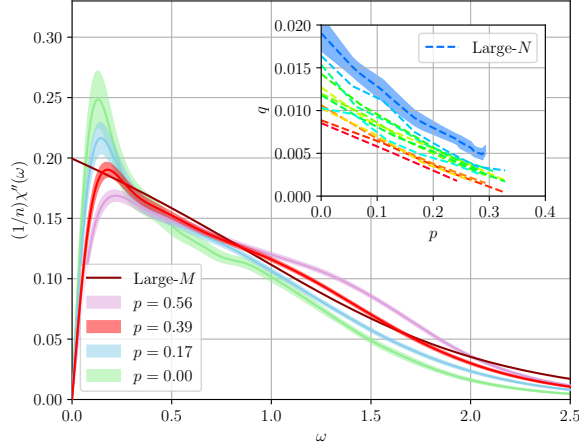


Figure 7.1: The spectral function  $\chi''(\omega)$  of the random  $t - J$  model, averaged over 100 disorder realizations on an 18-site cluster. At low dopings, a sharp peak at low-frequency at low doping is indicative of spin glass order. With increasing doping, the magnitude of this peak is reduced, and the low-frequency behavior closely resembles the rescaled spectral function of the large  $M$  SYK theory [420, 482, 483]. (Inset) After an extrapolation to the thermodynamic limit, the integrated weight of the low-frequency peak is non-zero, indicating spin glass order. This weight vanishes near  $p \approx 0.4$ . Plotted is the integrated weight for  $8 \leq N \leq 18$  (as a gradient from red to blue), and the large- $N$  extrapolation with error bars.

$$\chi''(\omega) \sim \omega.$$

The spectral function for the random  $t$ - $J$  model, calculated using the Lanczos algorithm on an 18-site cluster, is shown for several values of doping in Fig. 7.1. A prominent hump at low-frequency for dopings  $p \lesssim 0.4$  suggests the presence of spin glass order in this range of doping. However, a large- $N$  analysis of this hump must be performed in order to verify that the hump asymptotes to a delta function in the thermodynamic limit. To do this, we first subtract off a background contribution to account for the rest of the spectral weight. Anticipating SYK behavior near the critical point at low frequencies, we subtract a spectral weight obtained by rescaling the solution of the Schwinger-Dyson equations of the  $p = 0$  model in the large- $M$  limit [420, 482, 483] (we rescale  $J$ , while preserving total spectral weight). This SYK spectral weight has a leading term  $\chi''(\omega) \sim \text{sgn}(\omega)$  as  $|\omega| \rightarrow 0$  at  $T = 0$  (which generalizes to  $\tanh(\omega/2T)$  at low  $T$ ). The next-to-leading SYK term depends linearly in  $\omega$ , and arises from the boundary graviton in the holographic dual [482, 483]. It is important to note that the exponents of these two leading SYK contributions are universal and independent of  $M$ .

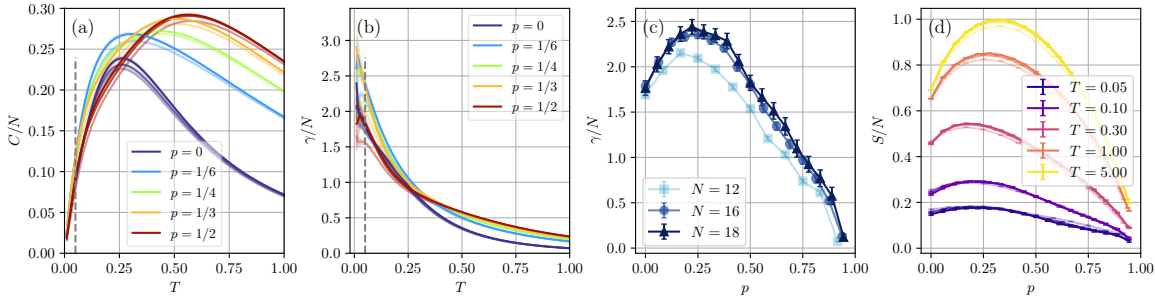


Figure 7.2: Thermodynamics of the random  $t$ - $J$  model for system sizes  $N = 12, 16, 18$ , indicated by increasing opacity. (a) The specific heat  $C$  as a function of temperature for various values of doping. (b) The linear-in- $T$  coefficient of specific heat,  $\gamma = C/T$ , for various dopings as a function of temperature, and (c) for  $T = 0.05$  as a function of doping. (d) The thermal entropy  $S$  as a function of doping for various temperatures.

Away from the critical point and in the spin glass phase, we find that the spectral function is described well by a combination of the SYK result and a low-frequency hump. A large- $N$  analysis of this low-frequency hump, described in more detail in the supplementary material, confirms that the variance of the hump vanishes in the thermodynamic limit, whereas the spectral weight, shown in Fig. 7.1, remains non-zero. Our analysis gives a large- $N$  estimate of  $q \sim 0.02$  at  $p = 0$ . For larger values of doping,  $q$  decreases from its value at  $p = 0$ , eventually vanishing at some critical value of doping  $p_c$ . By linearly extrapolating the large- $N$  prediction for  $q$  to higher dopings, we obtain an estimate of  $p_c = 0.420 \pm 0.007$ . Around this range of dopings, the spectral function shows good agreement with the large- $M$  critical prediction given in Fig. 7.1. At dopings well above  $p = 0.4$ , we find the spectral function to be largely independent of system size. No gap at low frequency is visible, and  $\chi''(\omega) \sim \omega$  behavior consistent with Fermi liquid predictions is clear. We will provide a more rigorous verification of the Fermi liquid phase at higher dopings via Luttinger's theorem later in the paper.

### 7.3 THERMODYNAMICS AND ENTANGLEMENT

We investigate the specific heat and thermal entropy given by,

$$C = \frac{\partial E}{\partial T}, \quad \text{and} \quad S = \log(\mathcal{Z}) + \frac{E}{T}, \quad (7.3)$$

where  $\mathcal{Z}$  denotes the canonical partition function, and  $E = \langle H \rangle$  the internal energy. Results for system sizes  $N = 12, 16, 18$  are shown in Fig. 7.2. To obtain the results on system sizes  $N = 16, 18$  we employed thermal pure quantum (TPQ) states [469, 470] as described in Refs. [192, 518, 519] similar to the finite-temperature Lanczos method [215, 367] (see E for details). For each set of random couplings we sampled  $R = 5$  TPQ states, cf. [518]. Error estimates have been obtained from 1000, (400, 100) random couplings for  $N = 12, (16, 18)$ .

The specific heat for  $p = 0$  exhibits in Fig. 7.2(a) exhibits a broad maximum at  $T \approx 0.25$ , in agreement with previous results [21]. At small values of doping  $p \lesssim 1/6$  this maximum remains at  $T \approx 0.25$  while we observe an increase of the specific heat at higher temperatures. The maximum is gradually shifted towards a higher value  $T \approx 0.50$  for dopings from  $p = 1/4$  to  $p = 1/2$ . At low temperatures we observe that the specific heat is approximately linear in temperature, with a maximal slope attained between dopings  $p = 0.20$  and  $p = 0.40$ . The linear-in- $T$  coefficient of the specific heat,  $\gamma = C/T$ , is shown in Fig. 7.2(b). We observe an increase of  $\gamma$  when lowering the temperature for all values of doping. We show  $\gamma$  at temperature  $T = 0.05$  as a function of doping in Fig. 7.2(c) for  $N = 12, 16, 18$ . At this temperature, the maximum is attained at  $p \approx 0.25$ . However, we find that this maximum is dependent on the temperature. At temperatures below  $T = 0.05$  sample fluctuations become too large for a reliable estimate of the maximum. We note that a divergence of the  $\gamma$  coefficient has been reported at the pseudogap quantum critical point in cuprate superconductors [316].

The thermal entropy for different temperatures and  $N = 12, 16, 18$  is shown in Fig. 7.2(d). Again we observe maxima at dopings between  $p = 0.20$  and  $p = 0.40$  depending on temperature. At  $T = 0.05$  the maximum is attained at

$$\tilde{p} \approx 0.296 \pm 0.025. \quad (7.4)$$

We refer to the supplement E for more discussion of the  $T$  dependence of the thermal entropy. To access the limit  $T \rightarrow 0$  we calculate the von-Neumann entanglement entropy of the ground state,

$$\mathcal{S}_{\text{vN}}(A) = -\text{Tr}[\rho_A \log \rho_A]. \quad (7.5)$$

Here,  $\rho_A = \text{Tr}_B(|\psi_0\rangle \langle \psi_0|)$  is the reduced density matrix of the ground state  $|\psi_0\rangle$  on a subsys-

tem  $A$ .  $B$  denotes the complement of  $A$ . Results for  $\mathcal{S}_{\text{vN}}(A)$  for subsystem sizes  $M = 1, 2, 3, 4$  and total system sizes  $N = 10, 12, 16$  are shown in Fig. 7.3. We find that the single-site ( $M = 1$ ) and two-site ( $M = 2$ ) entanglement entropy are well converged as a function of total system size  $N$ . For a  $N = 16$  site cluster and  $M = 4$  we estimate we estimate the maximum to be located at,

$$\tilde{p} \approx 0.285 \pm 0.024 \quad [\text{from } \mathcal{S}_{\text{vN}}(A)], \quad (7.6)$$

in agreement with our estimate obtained from the thermal entropy at  $T = 0.05$  in Eq. 7.4.

Finally, we investigate the charge susceptibility (compressibility),

$$\chi_c = \frac{\partial n}{\partial \mu} = \left( \frac{\partial^2 e}{\partial n^2} \right)^{-1} = \left( \frac{\partial^2 e}{\partial p^2} \right)^{-1}, \quad (7.7)$$

computed by taking the inverse of the second derivative of the internal state energy density  $e = E/N$  w.r.t. doping  $p$ . Here, the chemical potential is given by  $\mu = \partial e / \partial n$ . Results for different temperatures at  $N = 18$  are shown in Fig. 7.3(b). At temperatures  $T = 0$  and  $T = 0.1$  we detect a maximum at doping  $p = 1/3$ . We observe a shoulder-like feature at lower doping. At higher temperatures  $T = 0.3$  and  $T = 0.5$  this feature develops into a maximum at  $p \approx 0.2$ . We notice, that this shift matches the shift of  $\tilde{p}$  in the thermal entropy shown in Fig. 7.2(b,c). We note that the occurrence of a maximum in the compressibility, specific heat coefficient and local entanglement entropy has been recently discussed in cluster-DMFT studies of the Hubbard model without randomness in relation to the pseudogap and Mott critical points [145, 464, 498, 499].

## 7.4 LUTTINGER'S THEOREM

Having found strong signatures of a spin glass phase persisting from half filling up to  $p_c \approx 1/3$ , we now provide evidence of a Fermi liquid phase at higher values of doping, which vanishes at a critical value of doping near the onset of spin glass order. To verify the presence of a Fermi

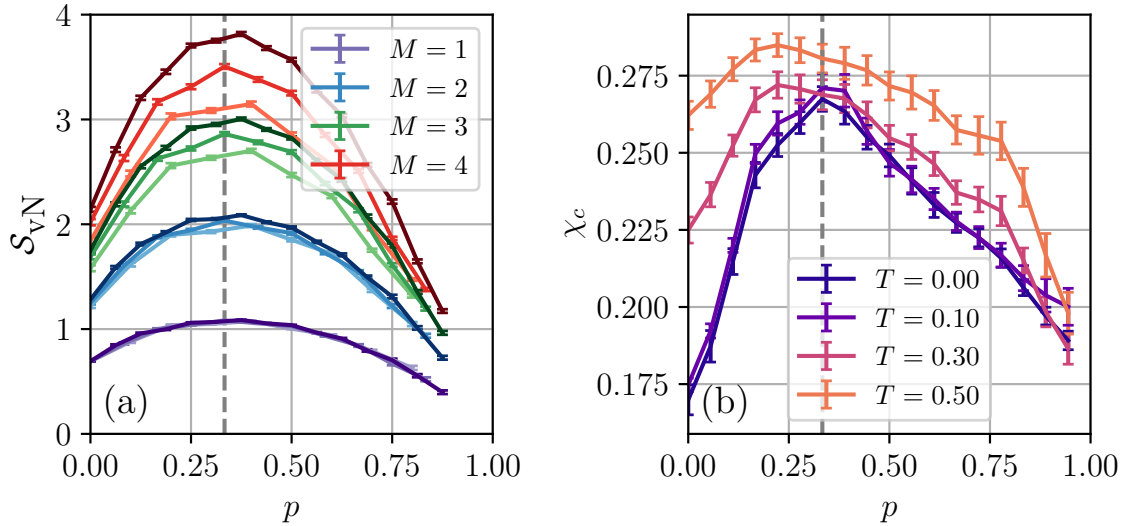


Figure 7.3: (a) The ground state entanglement entropy  $S_{VN}$  of subsystems of size  $M$ . Results are compared for total system size  $N = 10, 12, 16$ , shown as increasing opacity. The maxima are attained at values close to  $p = 1/3$ , indicated by the gray dashed line. (b) Charge susceptibility  $\chi_c$  for different temperatures at  $N = 18$ . The low-temperature maximum at doping  $p = 1/3$  is shifted towards a smaller doping  $p \approx 0.2$  at higher temperatures.

liquid phase, we introduce the *one-particle energy distribution function*,

$$\mathcal{N}(\epsilon) = \frac{1}{N} \sum_{\lambda} \delta(\epsilon - \epsilon_{\lambda}) \sum_{ij\sigma} \langle \lambda | i \rangle \langle c_{i\sigma}^{\dagger} c_{j\sigma} \rangle \langle j | \lambda \rangle \quad (7.8)$$

where  $|\lambda\rangle$  are the single-particle *non-interacting* eigenstates with energy  $\epsilon_{\lambda}$ , obtained by diagonalizing the hopping matrix  $t_{ij}$ . This quantity is analogous to the particle occupation number in momentum space,  $n(\mathbf{k})$ , commonly used in systems with translational invariance. For a non-interacting system with fixed particle number  $n$ , the averaged quantity  $\overline{\mathcal{N}(\epsilon)}$  converges to  $D(\epsilon)\theta(\epsilon - \epsilon_F)$ , where  $D(\epsilon)$  is the single-particle density of states and  $\epsilon_F$  is the Fermi energy, defined by:

$$D(\epsilon) = \frac{1}{N} \overline{\sum_{\lambda} \delta(\epsilon - \epsilon_{\lambda})}, \quad n = 2 \int_{-\infty}^{\epsilon_F} d\epsilon D(\epsilon). \quad (7.9)$$

For the interacting system, we show in the supplemental material E that, because the random couplings are all to all,  $\mathcal{N}(\epsilon)$  displays self-averaging properties in the thermodynamic limit  $N \rightarrow \infty$ . In this limit, the signature of Luttinger's theorem is a discontinuity of  $\overline{\mathcal{N}(\epsilon)}$  at the non-interacting value of  $\epsilon_F$  defined in Eq. (7.9).

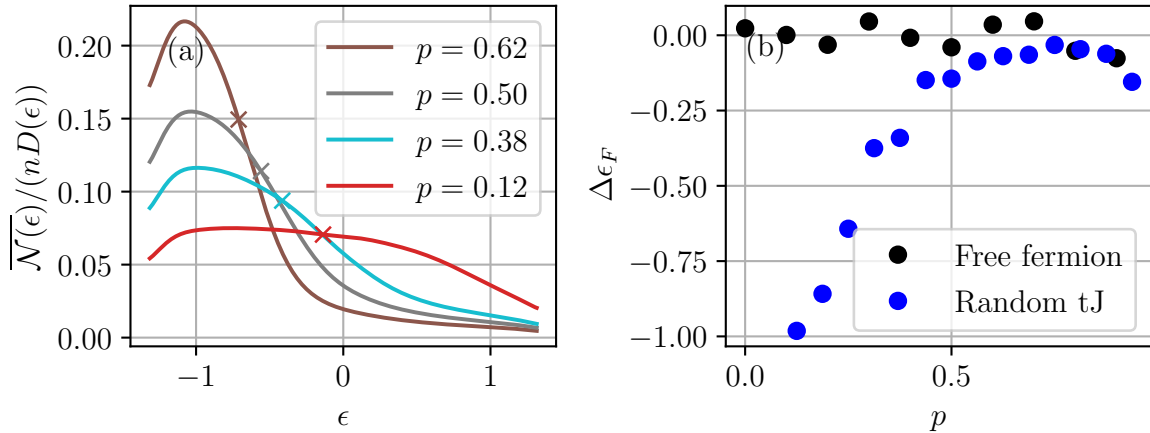


Figure 7.4: (a) At high values of doping, the one-particle energy distribution function drops sharply near the energy level predicted by Luttinger’s theorem (marked by crosses). At lower values of doping, this function becomes more broadened, suggesting a breakdown of Luttinger’s theorem. (b) A comparison of the Fermi energy given by Luttinger’s theorem and the numerically-computed value given by the inflection point of the one-particle energy distribution function. For a 16 site cluster, the two show good agreement up to a critical value between  $6/16 = 0.38$  and  $7/16 = 0.44$ , in contrast with the same quantity computed for free fermions which agree well for all values of doping.

In Fig. 7.4, we plot the quantity  $\overline{\mathcal{N}(\epsilon)}/D(\epsilon)$ , averaged over 1000 realizations on a 16-site cluster. The density of states  $D(\epsilon)$  is a semicircle distribution in the large- $N$  limit; however, in order to account for finite-size corrections to this distribution, we instead use the numerically calculated value of  $D(\epsilon)$  obtained from our data. Although the drop in particle occupation at the Fermi energy is substantially broadened due to interactions and finite-size effects, the location of the inflection point still reliably tracks the location of the Fermi energy predicted by Luttinger’s theorem at high values of doping as shown in Fig. 7.4. The effects of the infinite-strength Hubbard repulsion becomes stronger at lower values of doping, eventually causing a breakdown of Luttinger’s theorem at a critical doping  $0.38 < p_c < 0.44$ , which is also the location where spin glass order appears to emerge.

## 7.5 DISCUSSION AND CONCLUSION

Our numerical results demonstrate a transition in the random all-to-all  $t$ - $J$  model from a spin glass to a disordered Fermi liquid at a critical value of doping. The near-critical behavior has similarities to the criticality of SYK models, consistent with recent theoretical propos-

als [228] and numerical results on related systems [73]. We find a near-critical dynamic spin susceptibility which is consistent with the SYK behavior  $\chi''(\omega) \sim \text{sgn}(\omega) [1 - g|\omega| + \dots]$  over a significant frequency regime; the  $g$  term is a universal boundary “graviton” contribution. This is the first appearance of such features in a doped spin-1/2 SU(2) model. SYK criticality also predicts an extensive zero temperature entropy: we do find a maximum in the entropy near the critical point, but our finite-size data does not allow us to identify if there is an extensive contribution. However, we note that for  $SU(M = 2)$  models, SYK criticality is preempted at small enough  $T$  by a spin glass instability [118, 156], and so the extensive  $T = 0$  entropy is not ultimately expected. We also find a maximum in the entanglement entropy, specific heat coefficient, and compressibility near criticality.

An interesting observation is that the breakdown of Luttinger’s theorem coming from high doping, as well as the vanishing of spin glass order from low doping, occurs near  $p = 0.4$ , which differs from the maxima in the thermodynamic and entanglement entropy closer to  $p = 0.3$ . While the system sizes accessible to our methods are relatively small and only discrete values of doping are accessible, recent (E)DMFT calculations of the  $t$ - $J$  model with finite Hubbard repulsion [118] also give evidence of SYK criticality occurring at a lower value of doping than the spin glass/Fermi liquid transition. These observations are consistent with the spin glass instability of SYK criticality for finite  $M$  [156] noted above. Understanding the nature of this separation, and the very low  $T$  at which the spin glass instability of SYK criticality appears, remain open questions to be explored.

*All models are wrong, but some are useful.*

George E. P. Box

# 8

## Conductance and thermopower fluctuations in interacting quantum dots

### 8.1 INTRODUCTION

The Sachdev-Ye-Kitaev (SYK) model [246, 421] is a strongly interacting quantum many-body system without quasiparticle excitations, whose exact solvability in the large- $N$  limit - with  $N$  the number of sites - has led to significant interest in it both as a toy model for non-Fermi liquid behavior as well as an analytically tractable example of holographic duality [85, 248].

In contrast to its analytic solvability, experimental realizations of the SYK model have proved to be challenging. The SYK model is defined microscopically as a system of fermions with random all-to-all quartic interactions, and is unstable at low temperatures to single-particle hopping. As such, any experimental proposal must generate strongly-disordered interactions with a high degree of connectivity, while simultaneously quenching any single-particle hopping terms. Several promising proposals have been made to this extent, involving Majorana zero modes [82, 365], quantum processors [25, 149], ultracold gases [102, 487, 507] and disordered graphene flakes [59, 78]. Simulations of the SYK model have been achieved on quantum processors [214] and controllable nuclear-spin-chain simulators [298]. Our study here was motivated by experiments on disordered graphene flakes [14], results of which will be reported in a separate paper [15].

Each experimental realization of the SYK model will have a different set of observables that it is best suited to study. Our focus will be on proposals for realizing the SYK model with complex fermions in a disordered graphene flake, for which the measurable quantities are thermoelectric transport observables, such as conductance and thermopower. Theoretical predictions for the average values of these quantities have been calculated [261, 358] for realistic models that include both SYK terms and experimentally-relevant perturbations. The conclusion of this analysis is that thermoelectric quantities display a crossover from Fermi liquid-like behavior at temperatures below a coherence energy  $E_{\text{coh}} = t^2/J$ , where small single-particle hopping terms, with r.m.s. value  $t$ , produce coherent quasiparticle excitations, to SYK-like behavior at temperatures  $E_{\text{coh}} \ll T \ll J$ , where  $T$  is the temperature, and  $J$  is the r.m.s. value of the SYK interactions.

In experimental realizations of these mesoscopic systems, transport quantities such as the conductance and thermopower will display sample-to-sample fluctuations, or alternatively fluctuations as a function of tuning external parameters such as chemical potential or magnetic field. For weakly-interacting disordered quantum dots at zero temperature coupled to broad multi-channel leads, this results in the well-studied phenomenon of *universal conductance fluctuations* (UCF) at zero temperature, where the conductance displays  $\mathcal{O}(1)$  fluctuations (in units of the conductance quanta,  $e^2/h$ ) whose magnitude is independent of the disorder strength [10, 12, 272, 273]. An analogous treatment of disorder fluctuations in strongly-correlated quantum dots has not been explored previously. In this work, we analyze the fluctuations in transport properties in quantum dots with strong SYK interactions, and study the behavior of these fluctuations as their average values crossover from Fermi liquid-like for  $T \ll E_{\text{coh}}$  to SYK-like for  $T \gg E_{\text{coh}}$ . We contrast analysis of these properties in the SYK regime, which involve statistical fluctuations of the *single-particle* Green's function, with the large body of work analyzing statistical properties of the many-body spectrum [8, 95, 218, 406].

In this work, we analyze the conductance and thermopower fluctuations of a *closed* interacting quantum dot, with sufficiently high tunneling barriers such that transport quantities can be inferred via equilibrium properties of the isolated quantum dot. Within this framework, we find that variance of the conductance in the Fermi liquid regime displays a  $T^{-1}$  falloff at higher temperatures, consistent with prior studies of weakly-interacting disordered

quantum dots [125]. However, we find a surprising feature of these fluctuations for temperatures larger than the coherence energy. In contrast to the mean values of transport quantities, whose behavior for  $T \gg E_{\text{coh}}$  is well-described by a pure SYK model ( $t = 0$ ), the same is not true for the variance - at leading order in  $N^{-1}$ , the variance of the conductance for a pure SYK model is distinct from the variance in a model with SYK interactions and random hopping with r.m.s. value  $t$ , provided  $t > \sqrt{TJ}/N$ . The self-averaging properties of the pure SYK model are so strong that, to leading-order in  $N^{-1}$ , fluctuations of the physical transport properties remain driven by fluctuations of random hopping terms, even if their mean values are well-described by the pure SYK solution. Distinct predictions are still found for the two temperature regimes, arising from the different form of the average spectral function in the two limits, and we find a  $T^{-2}$  suppression of the conductance variance in the SYK regime in contrast with the  $T^{-1}$  Fermi liquid prediction.

These aspects of our results are illustrated by the following summary of our prediction for the mean ( $\bar{\sigma}$ ) and variance of the electrical conductance ( $\sigma$ ):

$$\bar{\sigma}_{FF} \propto \frac{\Gamma e^2}{\hbar} \frac{1}{t} , \quad \text{Var } \sigma_{FF} \propto \left( \frac{\Gamma e^2}{\hbar} \right)^2 \frac{1}{N t T} \quad (8.1)$$

$$\bar{\sigma}_{SYK} \propto \frac{\Gamma e^2}{\hbar} \frac{1}{\sqrt{JT}} , \quad \text{Var } \sigma_{SYK} \propto \left( \frac{\Gamma e^2}{\hbar} \right)^2 \frac{1}{N^3 JT} \quad (8.2)$$

$$\bar{\sigma}_{tSYK} \propto \frac{\Gamma e^2}{\hbar} \frac{1}{t} , \quad \text{Var } \sigma_{tSYK} \propto \left( \frac{\Gamma e^2}{\hbar} \right)^2 \frac{1}{N J T}, \quad T \ll E_{\text{coh}} \quad (8.3)$$

$$\bar{\sigma}_{tSYK} \propto \frac{\Gamma e^2}{\hbar} \frac{1}{\sqrt{JT}} , \quad \text{Var } \sigma_{tSYK} \propto \left( \frac{\Gamma e^2}{\hbar} \right)^2 \frac{\mathcal{E}^2 t^2}{N J^2 T^2}, \quad E_{\text{coh}} \ll T \ll J \quad (8.4)$$

Here (i)  $FF$  refers to the free-fermion results in Section 8.3.1 with  $\Gamma$  a measure of the coupling to the leads, and the various of  $\sigma_{FF}$  crosses over to the UCF value when  $T < \Gamma^2/Nt$ ; (ii) the pure SYK results are in Section 8.4.1; (iii)  $tSYK$  refers to the model with both hopping and interactions with  $t \ll J$ ,  $E_{\text{coh}} = t^2/J$ , the results for  $T \ll E_{\text{coh}}$  are in Section 8.5.1, and the results for  $E_{\text{coh}} \ll T \ll J$  are in Section 8.5.2 ( $\mathcal{E}$  is a measure of the particle-hole asymmetry). All these results are obtained for the case where the coupling to the leads,  $\Gamma$ , is the smallest energy scale, and to leading order in a  $1/N$  expansion.

Note that in all cases, the effect of the SYK interactions is to *reduce* the strength of the conductance fluctuations:

- (i) Eq. 8.2 is suppressed by a factor of  $1/N^3$  in contrast to  $1/N$  in all other cases,
- (ii) Eq. 8.3 is smaller than Eq. 8.1 by a factor of  $t/J$ , and
- (iii) Eq. 8.4 is smaller than Eq. 8.3 by a factor of  $E_{\text{coh}}/T$ .

The structure of this paper is as follows. In Section 8.2, we make explicit the setup of our theoretical model as well as the assumptions used in calculating thermoelectric quantities. In Section 8.3, we calculate the fluctuations of transport quantities in the non-interacting limit, where properties are governed by single-particle random matrix theory (RMT). We emphasize that this approach is distinct from more standard approaches of modeling UCF phenomena using RMT [33], where calculations are done at zero temperature and involve the statistical treatment of transmission eigenvalues. Our treatment is primarily done at non-zero temperature and in the limit of weak environmental coupling, although we show that it is possible to extend our results down to zero temperature and recover  $\mathcal{O}(1)$  universal fluctuations in an appropriate limit. In Section 8.4, we study transport fluctuations in the SYK regime, presenting results both for pure SYK as well as more realistic models with random single-particle hopping. In Section 8.5, we study a model with both SYK and random hopping terms and demonstrate that the transport fluctuations for  $T \gg E_{\text{coh}}$  are qualitatively different than that of a pure SYK model.

In each of these sections, we discuss the fluctuations of the thermopower in addition to the conductance. The statistical properties of the thermopower require more care; in our formalism, we find that the thermopower is determined by a ratio of two Gaussian random variables, and hence the variance is formally not well-defined. An approximation to normality is still appropriate in certain parameter regimes for small fluctuations around the mean, and hence we can formally define a variance within this approximation. We state results given this assumption and find qualitatively similar behavior as the conductance variance, which is that the presence of strong SYK interactions serves to reduce the fluctuations around the mean value.

## 8.2 SETUP

### 8.2.1 HAMILTONIAN AND TRANSPORT COEFFICIENTS

Our goal is to characterize fluctuations in transport properties of disordered quantum dots with random all-to-all interactions. We model this quantum dot by the Hamiltonian

$$H_{\text{dot}} = \frac{1}{(2N)^{3/2}} \sum_{ij;kl} J_{ij;kl} c_i^\dagger c_j^\dagger c_k c_l + \frac{1}{N^{1/2}} \sum_{ij} t_{ij} c_i^\dagger c_j - \mu \sum_i c_i^\dagger c_i \quad (8.5)$$

where  $J_{ij;kl}$  and  $t_{ij}$  are complex random numbers with zero mean and variances  $J^2$  and  $t^2$ , respectively. The complex SYK model is given by the first term, whereas the second term is a random single-particle hopping which leads to Fermi liquid behavior at low temperatures.

The quantum dot is coupled to two leads. Following the approach of [158], we model the leads by considering the Hamiltonian

$$H = H_{\text{dot}} + \sum_{\mathbf{q}} \epsilon_{\mathbf{q}} a_{\mathbf{q}}^\dagger a_{\mathbf{q}} + \sum_{i,\mathbf{q},\alpha} \left[ \lambda_{i\alpha} c_i^\dagger a_{\mathbf{q}\alpha} + \lambda_{i\alpha}^* a_{\mathbf{q}\alpha}^\dagger c_i \right]. \quad (8.6)$$

where  $\alpha = R, L$  labels the right and left leads. To parameterize the coupling to the leads, we define the matrices

$$\Gamma_{ij}^\alpha = \pi \rho_{\text{lead},\alpha} \lambda_{i\alpha} \lambda_{j\alpha}^*, \quad (8.7)$$

where  $\rho_{\text{lead},\alpha}$  is the density of states in lead  $\alpha$  near the Fermi level. We will assume  $\rho_{\text{lead},L} = \rho_{\text{lead},R} \equiv \rho_{\text{lead}}$ .

We will find that the nature of the conductance fluctuations depends sensitively on how we model the coupling to the leads,  $\lambda_{i\alpha}$ . This is in contrast to the mean values of transport quantities, which is not as sensitive. We first make the assumption that the two couplings are proportional to each other, i.e.  $\lambda_{iR} = \alpha \lambda_{iL}$  for some constant  $\alpha$ . With this constraint, it becomes possible to express transport properties solely in terms of the equilibrium Green's functions of the quantum dot. Using expressions derived in [94], we define

$$\mathcal{L}_{ab} = -\frac{i}{2\pi\hbar} \int_{-\infty}^{\infty} d\omega \omega^{a+b-2} f'(\omega) \text{Im Tr} [\mathbf{\Gamma} \mathbf{G}^R] , \quad (8.8)$$

with  $\mathbf{G}^{R,A}(\omega)$  the local retarded and advanced Green's function of  $H$ , both  $N \times N$  matrices,  $f(\omega)$  the Fermi function  $f(\omega) = 1/(e^{\omega/T} + 1)$ , and  $\mathbf{\Gamma} \equiv \mathbf{\Gamma}^L \mathbf{\Gamma}^R / (\mathbf{\Gamma}^L + \mathbf{\Gamma}^R)$ . For cases where the matrix  $\mathbf{\Gamma}^L + \mathbf{\Gamma}^R$  is non-invertable, this equation is modified by omitting the null subspace of the matrix. The Green's functions must be solved for the full Hamiltonian, including the coupling to the leads; however, we will primarily be focused on the parameter regime where  $\Gamma$  is the smallest energy scale and the Green's functions of the isolated system  $H_{\text{dot}}$  are used.

The electric conductance  $\sigma$ , thermal conductance  $\kappa$ , and thermopower  $\Theta$  are given by

$$\sigma = e^2 \mathcal{L}_{11}, \quad \kappa = \beta \left( \mathcal{L}_{22} - \frac{\mathcal{L}_{12}^2}{\mathcal{L}_{11}} \right), \quad \Theta = \frac{\beta}{e} \frac{\mathcal{L}_{12}}{\mathcal{L}_{11}}. \quad (8.9)$$

where  $\beta = 1/T$ .

Beyond this point, we must make further assumptions on the nature of the coupling to the leads. For notational simplicity, we will assume  $\lambda_{iR} = \lambda_{iL} \equiv \lambda_i$  - generalization to the case where the magnitude of the couplings are asymmetric does not qualitatively affect our results.

#### SINGLE SITE LEAD COUPLING

In this model, we take our two leads to be coupled to a single site, i.e.  $\lambda_i \equiv \delta_{i1}\lambda$ . Defining  $\Gamma \equiv \pi\rho_{\text{lead}}|\lambda|^2$ , we have

$$\overline{\mathcal{L}_{ab}} = \frac{2\Gamma}{\pi\hbar} \int_{-\infty}^{\infty} d\omega \omega^{a+b-2} f'(\omega) \overline{\text{Im } G_{11}^R(\omega)} \quad (8.10)$$

Recall that the Green's functions are dependent on the random variables  $J_{ij;kl}, t_{ij}$ . Averaging over disorder, we find that  $\overline{\text{Im } G_{11}^R(\omega)} = N^{-1} \sum_{ii} \overline{\text{Im } G_{ii}^R(\omega)} \equiv \overline{\text{Im } G^R(\omega)}$ . Note that this relation relies on neglecting corrections to  $\mathbf{G}^R$  arising from the couplings to the leads, as these corrections will be site-dependent.

Higher moments of these transport coefficients are given by

$$\overline{\mathcal{L}_{ab}\mathcal{L}_{ab}} - \overline{\mathcal{L}_{ab}} \overline{\mathcal{L}_{ab}} = \left( \frac{2\Gamma}{\pi\hbar} \right)^2 \int_{-\infty}^{\infty} d\omega d\epsilon \omega^{a+b-2} \epsilon^{a+b-2} f'(\omega) f'(\epsilon) \rho_d(\omega, \epsilon) \quad (8.11)$$

where we define

$$\rho_d(\omega, \epsilon) \equiv \frac{1}{N^2} \sum_{ij} \left[ \overline{\text{Im } G_{ii}^R(\omega)} \overline{\text{Im } G_{jj}^R(\epsilon)} - \overline{\text{Im } G_{ii}^R(\omega)} \overline{\text{Im } G_{jj}^R(\epsilon)} \right] \quad (8.12)$$

The subscript  $d$  indicates that this quantity describes the covariance of the *diagonal* component of the Green's function,  $G_{ii}^R$ .

#### ALL-TO-ALL COUPLINGS

Here, we take the leads to be coupled to all sites with equal hopping,  $\lambda_i \equiv \frac{\lambda}{\sqrt{N}}$ . This model is also appropriate for hoppings that are equal in magnitude but with site-dependent phases, as the overall phase can be absorbed by a unitary transformation on the quantum dot operators. Defining  $\Gamma \equiv \pi \rho_{\text{lead}} |\lambda|^2$  as before, we have

$$\overline{\mathcal{L}_{ab}} = \frac{1}{N} \sum_{ij} \frac{2\Gamma}{\pi\hbar} \int_{-\infty}^{\infty} d\omega \omega^{a+b-2} f'(\omega) \overline{\text{Im } G_{ij}^R(\omega)} = \frac{2\Gamma}{\pi\hbar} \int_{-\infty}^{\infty} d\omega \omega^{a+b-2} f'(\omega) \overline{\text{Im } G^R(\omega)}. \quad (8.13)$$

where we utilize the fact that  $\overline{G_{ij}^R(\omega)} = 0$  for  $i \neq j$ . The overall scaling of  $N^{-\frac{1}{2}}$  in  $\lambda_i$  was chosen such that the mean value of the conductance is consistent with the previous model.

The second moment is given by

$$\overline{\mathcal{L}_{ab}\mathcal{L}_{ab}} - \overline{\mathcal{L}_{ab}} \overline{\mathcal{L}_{ab}} = \frac{1}{N^2} \sum_{ij,kl} \left( \frac{2\Gamma}{\pi\hbar} \right)^2 \int_{-\infty}^{\infty} d\omega d\epsilon \omega^{a+b-2} \epsilon^{a+b-2} f'(\omega) f'(\epsilon) [\rho_d(\omega, \epsilon) + \rho_o(\omega, \epsilon)]. \quad (8.14)$$

where now we define the off-diagonal Green's function covariance,

$$\rho_o(\omega, \epsilon) \equiv \frac{1}{N^2} \sum_{ij} \left[ \overline{\text{Im } G_{ij}^R(\omega)} \overline{\text{Im } G_{ji}^R(\epsilon)} - \overline{\text{Im } G_{ij}^R(\omega)} \overline{\text{Im } G_{ji}^R(\epsilon)} \right]. \quad (8.15)$$

#### DISORDERED ALL-TO-ALL COUPLINGS

If our sites physically correspond to spatially random modes, as is the case in graphene realizations of strongly interacting quantum dots in the zeroth Landau level, then it may be appropriate to model the coupling to the leads as additional random variables. To analyze

this case, we treat  $\lambda_i$  as Gaussian random variables:

$$\begin{aligned}\overline{\lambda_i} &= 0, \\ \overline{\lambda_i^* \lambda_j} &= \delta_{ij} \frac{\lambda^2}{N},\end{aligned}\tag{8.16}$$

which in turn implies that  $\overline{\Gamma_{ij}^\alpha} = \delta_{ij} \frac{\pi \rho_{\text{lead}} \lambda^2}{N} \equiv \delta_{ij} \frac{\Gamma}{N}$ . Crucial to the calculation of fluctuations, we note the identity

$$\overline{\Gamma_{ij}^\alpha \Gamma_{kl}^\beta} = \left( \frac{\Gamma}{N} \right)^2 (\delta_{ij} \delta_{kl} + \delta_{il} \delta_{jk}).\tag{8.17}$$

The average values of the transport coefficients are the same as in the previous models. Using the relation

$$\overline{(\Gamma_{ij}^R + \Gamma_{ij}^L)(\Gamma_{kl}^R + \Gamma_{kl}^L)} = \left( \frac{2\Gamma}{N} \right)^2 (\delta_{ij} \delta_{kl} + \delta_{il} \delta_{jk}),\tag{8.18}$$

we can obtain higher moments of the transport coefficients. This leads to a result for the variance almost identical to the uniform all-to-all couplings in the previous section. The crucial difference is that in this case, the disconnected component of  $\rho_o(\omega, \epsilon)$ , defined in Eq. 8.15, is not subtracted off in the expression for the variance of  $\mathcal{L}_{ab}$ . The consequence of this is a trivial contribution to the variance of  $\mathcal{L}_{ab}$ , which is given by  $N^{-1} \overline{\mathcal{L}_{ab}}^2$  and can be thought of as being driven by the disorder in the leads in contrast to the intrinsic disorder in the quantum dot. While this is suppressed by a factor of  $N^{-1}$ , we will find that fluctuations generically only appear at the order or higher, so this contribution cannot be disregarded on these grounds.

We have shown that the variance of transport quantities, such as the conductance, are determined by the single-particle Green's function covariances  $\rho_d$ ,  $\rho_o$ . The primary focus of our paper will be an analysis of these functions, and their implications for conductance fluctuations. For concreteness, we will give our predictions for conductance fluctuations in a model with uniform all-to-all couplings, such that both  $\rho_o$  and  $\rho_d$  contribute, and so that there is no trivial contribution to the variance arising from disordered leads. We summarize results for single-mode couplings in Appendix F.4.

### 8.2.2 COMPARISON TO OTHER ANALYSES

Due to the extensive literature on conductance fluctuations in mesoscopic systems, we make precise here the connection between our setup and prior work.

The most well-established results for conductance fluctuations pertain to the  $T = 0$  conductance of a sufficiently weakly-interacting quantum dot such that a single-particle picture is appropriate. In this limit, conductance fluctuations can be understood most directly via a random matrix analysis of the scattering matrices, which take values in the circular ensemble [29, 216]. An alternative approach, suitable for studying the effects of non-zero temperature and weak magnetic fields, is to start with a microscopic single-particle Hamiltonian modeled as a random matrix, much like our Hamiltonian in the limit  $J = 0$ . In the non-interacting limit, the conductance for a generic set of lead couplings  $\lambda_{jL}, \lambda_{jR}$  is given by the Landauer formula for a single channel,

$$\sigma = \frac{e^2}{h} \int d\omega f'(\omega) t(\omega) t^*(\omega),$$
$$t(\omega) \equiv 2\pi\rho_{\text{lead}} \sum_{ij} \lambda_{iL}^* G_{ij}^R(\omega) \lambda_{jR}.$$
(8.19)

The conductance variance is thus related to the disorder average of four copies of  $G^R$ , solved in the presence of the leads. This becomes a tractable problem in the limit where the number of channels in the leads is large, and can be dealt with rigorously using supersymmetry techniques [125, 144, 202, 203, 489] to give results consistent with random matrix predictions. This formulation can also be generalized to non-zero temperature [125], where a  $T^{-1}$  falloff of the conductance variance is observed. However, these supersymmetry techniques cannot be generalized to accommodate strong interactions. Our results are most appropriately compared to the prior results on closed quantum dots, where the number of channels is small and are weakly coupled to the dot. These works have primarily focused on the  $T = 0$  conductance in either the weakly-interacting limit [309, 369], where non-Gaussian behavior of the conductance was found, or in the Coulomb blockade-dominated limit [216] which found a non-Gaussian distribution of the conductance peaks. To our knowledge, conductance fluctuations in the parameter regime of closed quantum dots with  $T \gg \Gamma$  and for negligible Coulomb blockade

effects has not been studied previously. This is the regime where we will conduct our analysis, as it is in this limit that the effects of strong SYK interactions becomes analytically tractable.

### 8.3 FREE FERMION ANALYSIS

#### 8.3.1 CONDUCTANCE STATISTICS

We begin with an analysis of conductance fluctuations in the non-interacting limit ( $J = 0$ ).

In this limit, the conductance is independent of temperature [261],

$$\bar{\sigma} = \frac{e^2}{\hbar} \frac{\Gamma \sqrt{4t^2 - \mu^2}}{\pi t^2}. \quad (8.20)$$

In order to understand the behavior of conductance fluctuations, we must calculate the single-particle covariances  $\rho_{d,o}(\omega, \epsilon)$ . This may be done diagrammatically, only keeping diagrams to leading order in  $N^{-1}$ . We do this by calculating the covariance of the Green's function in imaginary time and analytically continuing to the real axis. The calculation of  $\rho_d$  involves analytic continuation of the quantity  $\sum_{ij} G_{ii}(i\omega)G_{jj}(i\epsilon)$ , and for  $\rho_o$ ,  $\sum_{ij} G_{ij}(i\omega)G_{ji}(i\epsilon)$ .

Diagrams that contribute to the covariance of the Green's function consists of diagrams of pairs of Green's functions that are only connected along disorder lines. The structure of these diagrams is shown in Fig. 8.1. The diagrammatic structure of both the  $\rho_d$  and  $\rho_o$  fluctuations are similar - both involve an infinite summation over a set of ladder diagrams, given in the first figure in Fig. 8.1. The leading order contributions to  $\rho_o$  are just given by this set of diagrams. For  $\rho_d$ , two additional classes of diagrams must be considered and are shown in Fig. 8.1. The first class yields an  $n$ -fold degeneracy of ladders with  $n$  rungs, and the second class gives additional disorder averaging on either side of the ladder rungs.

Putting all this together, we obtain the final form for the Green's function covariances,

$$\begin{aligned} g_d(i\omega, i\epsilon) &\equiv \frac{1}{N^2} \sum_{ij} \left( \overline{G_{ii}(i\omega)G_{jj}(i\epsilon)} - \overline{G_{ii}(i\omega)} \times \overline{G_{jj}(i\epsilon)} \right) \\ &= \frac{1}{N^2} \frac{t^2 G(i\omega)^2 G(i\epsilon)^2}{[1 - t^2 G(i\omega)G(i\epsilon)]^2} \frac{1}{1 - t^2 G(i\omega)^2} \frac{1}{1 - t^2 G(i\epsilon)^2} \\ g_o(i\omega, i\epsilon) &\equiv \frac{1}{N^2} \sum_{ij} \left( \overline{G_{ij}(i\omega)G_{ji}(i\epsilon)} - \overline{G_{ij}(i\omega)} \times \overline{G_{ji}(i\epsilon)} \right) = \frac{1}{N} \frac{t^2 G(i\omega)^2 G(i\epsilon)^2}{1 - t^2 G(i\omega)G(i\epsilon)} \end{aligned} \quad (8.21)$$

where in the RHS, we use the average Green's function

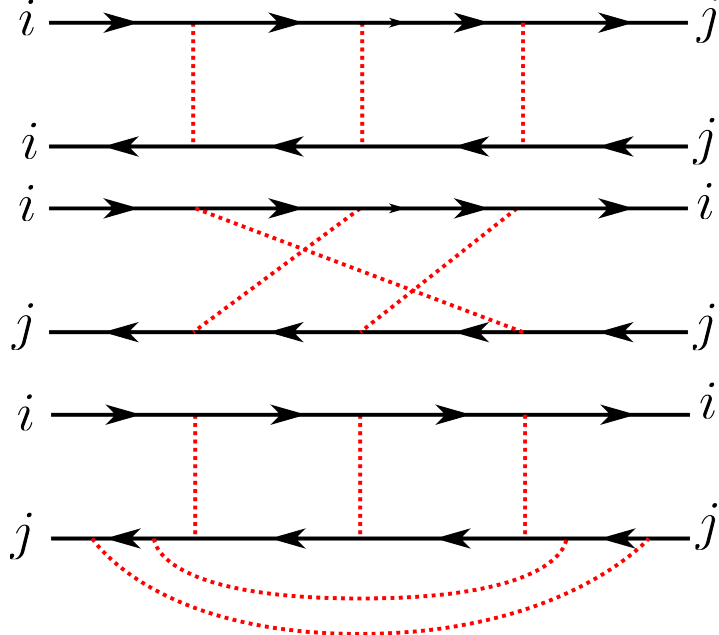


Figure 8.1: Ladder diagrams that contribute to the fluctuations of the single-particle spectral function. The first class of diagrams contributes to both the covariances  $\rho_d$  and  $\rho_o$ , with the contribution to  $\rho_d$  coming from the  $i = j$  case. The last two classes only contribute to  $\rho_d$ . Disorder-averaging of the single-particle hopping (SYK interactions) is represented in red (blue).

$$G_0(i\omega) = \frac{i\omega + \mu}{2t^2} - i \frac{\text{sgn}(\omega)}{2t^2} \sqrt{4t^2 + (\omega - i\mu)^2}. \quad (8.22)$$

To obtain expressions for  $\rho_{o,d}$ , we analytically continue these to the real axis,

$$\rho_\alpha = -\frac{1}{4} [g_\alpha(\omega^+, \epsilon^+) + g_\alpha(\omega^-, \epsilon^-) - g_\alpha(\omega^-, \epsilon^+) - g_\alpha(\omega^+, \epsilon^-)] \quad (8.23)$$

where  $\omega^\pm \equiv \omega \pm i\eta$ ,  $\eta \rightarrow 0$ . The expression for  $\rho_d$  has been derived before using a similar diagrammatic approach [55], although we are not aware of an analogous calculation for  $\rho_o$ .

From this analysis, we see that fluctuations arising from  $\rho_o$  are enhanced relative to the  $\rho_d$  fluctuations by a factor of  $N$ , and hence will be the main focus of our analysis. However, we will show that a more careful analysis of  $\rho_d$  will be necessary to recover UCF behavior at zero temperature.

Due to the form of the average Green's function, we find a singular behavior for the Green's

function covariances in Eq. 8.21 for  $|\omega - \epsilon| \rightarrow 0$ , as

$$\begin{aligned} 1 - t^2 G(\omega^+) G(\epsilon^-) &= \frac{1}{t} \left( -\eta + \frac{i}{2}(\omega - \epsilon) \right) + \mathcal{O}((\omega/t)^2, (\epsilon/t)^2), \\ \rho_d(\omega, \epsilon) &= -\frac{1}{8N^2} \operatorname{Re} \left[ \frac{1}{(i(\omega - \epsilon)/2 - \eta)^2} \right] \\ \rho_o(\omega, \epsilon) &= -\frac{1}{2Nt} \operatorname{Re} \left[ \frac{1}{i(\omega - \epsilon)/2 - \eta} \right] \end{aligned} \quad (8.24)$$

The above divergence holds for arbitrary chemical potential  $\mu$ . We see that the  $(\omega - \epsilon)^{-2}$  divergence in  $\rho_d(\omega, \epsilon)$  is *independent* of the energy scale  $t$ . The correlation function  $\rho_d$  determines fluctuations of the single-particle energy levels - for the non-interacting system, the distribution of single-particle energy levels is determined by the Gaussian Unitary Ensemble (GUE) in which fluctuations are known to take this universal form [55, 121, 122].

For  $T \neq 0$ , this divergence may be regulated by carefully taking the  $\eta \rightarrow 0$  limit in the analytic continuation to the real axis. We state the calculation in a general form, for use later. For real-valued functions  $A(\omega)$ ,  $B(\omega)$ , and  $\rho(\omega - \epsilon) = \rho(\epsilon - \omega)$ , we have the identity

$$\int d\omega d\epsilon A(\omega)B(\epsilon)\rho(\omega - \epsilon) = \sqrt{2\pi} \int dk \operatorname{Re} \left[ \tilde{A}(k)\tilde{B}^*(k) \right] \tilde{\rho}(k). \quad (8.25)$$

where we define the Fourier transform  $\tilde{A}(k) \equiv \frac{1}{\sqrt{2\pi}} \int e^{-ikx} A(x) dx$ .

The Fourier transform of the Green's function covariances are:

$$\begin{aligned} \tilde{\rho}_d(k) &= \frac{1}{8N^2} \sqrt{\frac{\pi}{2}} |k|, \\ \tilde{\rho}_o(k) &= \frac{\sqrt{2\pi}}{4Nt}. \end{aligned} \quad (8.26)$$

This analysis for  $\rho_d$  recovers the well-known Dyson-Mehta formula for the variances of linear statistics in RMT [121, 122], and the more general covariance formula for linear statistics [97]; however, these fluctuations are a factor of  $N^{-1}$  smaller than the contributions from  $\rho_o$  fluctuations.

This formula yields the result for the conductance variance,

$$\text{Var } \sigma = \left( \frac{\Gamma e^2}{\hbar} \right)^2 \frac{2}{3\pi tTN}, \quad (8.27)$$

which agrees well with a numerical simulation, shown in Fig. 8.2. This expression is valid for  $\Gamma^2 \ll NTt$ , as suggested by the  $T \rightarrow 0$  divergence. In order to obtain results for  $T = 0$ , a more careful treatment of the coupling to the leads is required.

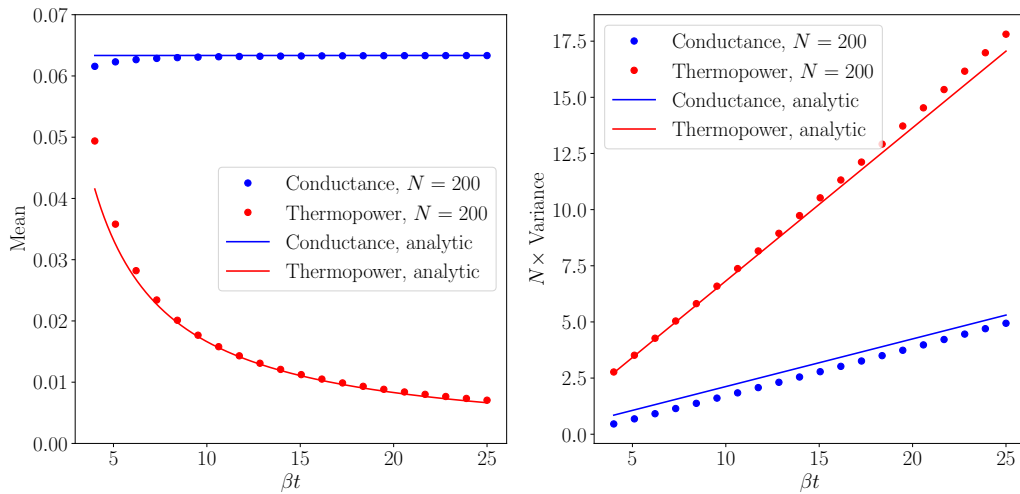


Figure 8.2: We plot the mean and variance of both the conductance and thermopower, calculated in the non-interacting ( $J = 0$ ) limit of our disordered quantum dot and using Eq. 8.8 averaged over 100000 realizations of the hoppings  $t_{ij}$ . We set the chemical potential  $\mu = 0.33$ . In this calculation, the Green's function of the quantum dot is solved independent of the leads. We set the strength of the leads coupling  $\Gamma = 0.1$  in order for the mean thermopower and conductance to have comparable magnitudes, although we emphasize that this value only appears as an overall coefficient in the conductance. These numerical results are compared with the analytic predictions given in Eq. 8.27 and Eq. 8.34, which show good agreement.

To obtain a  $T \rightarrow 0$  result, we must include the self-energy arising from the coupling to the leads. The form of this correction is dependent on the manner in which we choose the coupling. For uniform all-to-all couplings, we have

$$\Sigma_{ij}(i\omega) = 2 \int d\epsilon \frac{\rho(\epsilon)|\lambda|^2}{i\omega - \epsilon} \approx \frac{2i\Gamma}{N} \text{sgn}(\omega) \quad (8.28)$$

where  $\rho$  is the density of states in the leads, which we approximate by its value at the Fermi

level. To leading order in  $\Gamma$ ,

$$\overline{G_{ij}(i\omega)} = \delta_{ij}G_0(i\omega) + \frac{2i\Gamma G_0(i\omega)^2}{N} \text{sgn}(\omega) \quad (8.29)$$

Using this result for  $G$  in Eq. 8.21, we can directly evaluate the  $T = 0$  conductance fluctuations

$$\begin{aligned} \Gamma^2 \rho_d(0, 0) &= -\frac{1}{32} + \mathcal{O}(\Gamma/t), \\ \Gamma^2 \rho_o(0, 0) &= \mathcal{O}(\Gamma/t), \\ \text{Var } \sigma(T = 0) &= \left(\frac{e^2}{h}\right)^2 \left(\frac{1}{8} + \mathcal{O}(\Gamma/t)\right). \end{aligned} \quad (8.30)$$

Note that in this case,  $\rho_d$  and  $\rho_o$  contribute at the same order; the  $T = 0$  divergences are regulated by an  $\mathcal{O}(N^{-1})$  self-energy, and  $\rho_d$  is more singular at  $T = 0$ . We stress that this result is not rigorous - as evident from the above results, this manner of including the corrections from the leads is not done consistently in an  $N^{-1}$  expansion. A proper extrapolation down to  $T = 0$  necessitates, for example, the use of supersymmetric techniques [202].

### 8.3.2 THERMOPOWER STATISTICS

Although less well-studied than conductance fluctuations, thermopower fluctuations have been studied analytically for single-mode contacts at  $T = 0$  [488] and for broad contacts [130]. Experimental measurements [147, 159] have found good agreement with these predictions. Our analysis will fall in a distinct parameter regime to these results, where we consider a quantum dot weakly coupled to its environment, at temperatures much larger than the coupling strength.

In the free fermion limit, the mean thermopower vanishes linearly with temperature [261]

$$\overline{\Theta} = \frac{\pi^2 T}{3e} \frac{\mu}{4t^2 - \mu^2}. \quad (8.31)$$

The linear temperature dependence is a consequence of the linear temperature dependence of the entropy, and hence is generic for systems with quasiparticle excitations.

In our framework, the statistical properties of the thermopower is determined by the *ratio* of two random variables,  $\mathcal{L}_{12}$  and  $\mathcal{L}_{11}$ . As higher order moments are suppressed by addi-

tional factors of  $N^{-1}$ , our transport coefficients are Gaussian to leading order in  $N^{-1}$ . The thermopower distribution is then determined by the ratio of two Gaussian statistics, which in general is non-Gaussian. Nevertheless, an approximation to Gaussian is appropriate [189] for capturing small fluctuations around the mean value, so long as the width of the Gaussian distribution is small relative to the mean. We provide more details on this approximation in Appendix F.3. A similar approach was used to characterize fluctuations of the Fano factor in weakly-interacting quantum dots [96]. Such an approximation requires knowledge of the covariance of the two quantities  $\mathcal{L}_{12}$  and  $\mathcal{L}_{11}$ . This is given by

$$\text{Cov}(\mathcal{L}_{11}, \mathcal{L}_{12}) = - \left( \frac{\Gamma}{\pi \hbar} \right)^2 \int d\omega d\epsilon \omega f'(\omega) f'(\epsilon) [\rho_d(\omega, \epsilon) + \rho_o(\omega, \epsilon)] \quad (8.32)$$

which vanishes by an application of Eq. 8.25. Therefore to leading order in  $N^{-1}$ , the random variables  $\mathcal{L}_{11}$  and  $\mathcal{L}_{12}$  are both uncorrelated and have a bivariate normal distribution, so we treat them as independent. With this assumption, the typical fluctuations of  $\Theta$  around its mean value  $\frac{\beta}{e} \overline{\mathcal{L}_{12}}$  are Gaussian with variance

$$\frac{\text{Var } \Theta}{\Theta^2} = \frac{\text{Var } \mathcal{L}_{11}}{\mathcal{L}_{11}^2} + \frac{\text{Var } \mathcal{L}_{12}}{\mathcal{L}_{12}^2}, \quad (8.33)$$

with

$$\begin{aligned} \text{Var } \mathcal{L}_{11} &= \left( \frac{\Gamma}{\hbar} \right)^2 \frac{2}{3\pi NTt} \quad \overline{\mathcal{L}_{11}} = \frac{\Gamma}{\hbar} \frac{\sqrt{4t^2 - \mu^2}}{2\pi t^2} \\ \text{Var } \mathcal{L}_{12} &= \left( \frac{\Gamma}{\hbar} \right)^2 \frac{(\pi^2 - 6)T}{9\pi Nt} \quad \overline{\mathcal{L}_{12}} = -\frac{\Gamma}{\hbar} \frac{\pi\mu T^2}{6t^2 \sqrt{4t^2 - \mu^2}}. \end{aligned} \quad (8.34)$$

This analytic prediction agrees well with the numerically calculated variance, shown in Fig. 8.2. Similar to the conductance variance, the thermopower variance scales as  $T^{-1}$  at low temperature, although the fact that the mean value scales linearly with temperature means that, in contrast to the conductance, the variance normalized by the mean squared diverges as  $T^{-3}$ .

## 8.4 PURE SYK ANALYSIS

### 8.4.1 CONDUCTANCE STATISTICS

We now move to an analysis of conductance fluctuations for a pure SYK model ( $t = 0$ ), where the average value takes the form at half-filling

$$\overline{\sigma} = \frac{e^2}{\hbar} \frac{0.72\Gamma}{\sqrt{JT}} \quad (8.35)$$

(the exact value of the prefactor is  $2\sqrt{2}\pi^{-1/4}\Gamma(3/4)\Gamma(1/4) \approx 0.72$ ). Deviations away from half-filling only constitute a change in the numerical coefficient. For full generality, we present results for an  $\text{SYK}_q$  model with  $q$ -fermion interactions - the case  $q = 4$  is the one of experimental relevance. The diagrammatic prescription for calculating the Green's function covariances  $\rho_d$ ,  $\rho_o$  remain the same, and we consider pairs of Green's functions that are only connected via disordered lines. The  $N$  scaling of disorder-connected diagrams has been considered in SYK-like models previously [168, 248, 446, 503], although an explicit evaluation of such diagrams has only been carried out for the off-diagonal covariance,  $\rho_o$ , in the Majorana SYK model [503].

The simplest leading-order diagram, which contributes to both  $\rho_d$  and  $\rho_o$ , is shown on top in Fig. 8.3. This contributes to  $\rho_o$  with coefficient  $N^{1-q}$  and  $\rho_d$  with coefficient  $N^{-q}$ . The different coefficients arise because the  $\rho_d$  contribution appears with a factor of  $\delta_{ij}$ . We find that  $\rho_d$  contains additional “ladder” diagrams as shown in the bottom of Fig. 8.3 that also contribute at  $\mathcal{O}(N^{-q})$ .

Both these covariances can be evaluated analytically in the conformal limit, when  $\beta J \gg 1$ . To see this, we examine the first diagram, in the top of Fig. 8.3. In the conformal limit, the Green's functions take the following form:

$$g^R(\overline{\omega}, \overline{T}) = -ie^{-i\theta} \left( \frac{\pi}{\cos 2\theta} \right)^{1/4} \left( \frac{1}{2\pi\overline{T}} \right)^{1/2} \frac{\Gamma\left(\frac{1}{4} - \frac{i\overline{\omega}}{2\pi\overline{T}} + i\mathcal{E}\right)}{\Gamma\left(\frac{3}{4} - \frac{i\overline{\omega}}{2\pi\overline{T}} + i\mathcal{E}\right)} \quad (8.36)$$

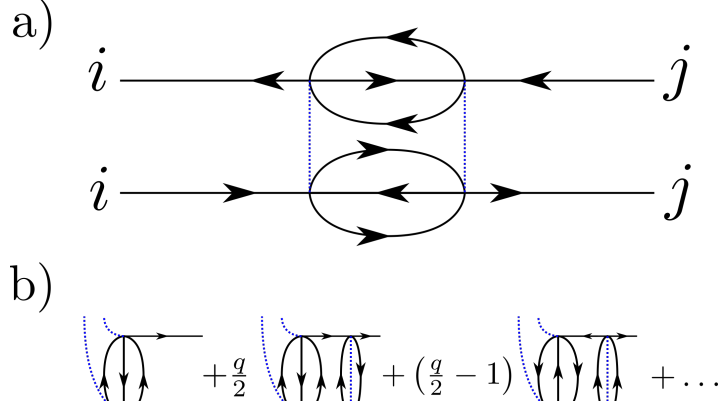


Figure 8.3: a) The leading-order diagram for a pure SYK model that contributes to the Green's function covariance. This contributes to  $\rho_o$  with a factor of  $N^{1-q}$ , and the specialized  $i = j$  case contributes to  $\rho_d$  with a factor of  $N^{-q}$ . b) For the diagonal covariance  $\rho_d$ , the diagram in a) is the first in an infinite series of diagrams, generated from the first by attaching ladder rungs to either the top or bottom diagram in the manner shown here. We have deformed the diagram from a) in order to more clearly illustrate the structure of the ladder rungs.

where  $\theta$  and  $\mathcal{E}$  characterize the spectral asymmetry and are related to the total charge  $\mathcal{Q}$  by

$$\begin{aligned}\mathcal{E} &= \frac{1}{2\pi} \ln \frac{\sin(\pi/4 + \theta)}{\sin(\pi/4 - \theta)}, \\ \mathcal{Q} &= \frac{1}{2} - \frac{\theta}{\pi} - \frac{\sin(2\theta)}{4}.\end{aligned}\tag{8.37}$$

We have the bounds  $-\frac{\pi}{4} \leq \theta \leq \frac{\pi}{4}$  which implies  $0 \leq \mathcal{Q} \leq 1$ , and the particle-hole symmetric point is  $\mathcal{Q} = \frac{1}{2}$ . Note that in contrast to the free fermion case, the SYK solution is most easily analyzed in the canonical ensemble with fixed charge  $\mathcal{Q}$ . These Green's functions satisfy the Schwinger-Dyson (SD) equation  $\Sigma(\omega)G(\omega) = -1$ ,  $\Sigma(\tau_1, \tau_2) = J^2 G(\tau_1, \tau_2)^{\frac{q}{2}} (-G(\tau_2, \tau_1))^{\frac{q}{2}-1}$ . We can evaluate the  $\tau$  integrals of the top and bottom part of the Feynman diagram independently. Making use of the conformal SD equations, we find that each of these parts evaluates to

$$\begin{aligned}J^2 \int d\tau_a d\tau_b G(\tau_1, \tau_a) G(\tau_a, \tau_b)^{\frac{q}{2}} (-G(\tau_b, \tau_a))^{\frac{q}{2}-1} G(\tau_b, \tau_2) \\ = \int d\tau_a d\tau_b G(\tau_1, \tau_a) \Sigma(\tau_a, \tau_b) G(\tau_b, \tau_2) = -G(\tau_1, \tau_2).\end{aligned}\tag{8.38}$$

A careful analysis of combinatoric factors from the disorder lines yields the result

$$\rho_o(\omega, \epsilon) \frac{(q/2)!(q/2-1)!}{N^{q-1}} \text{Im}[G^R(\omega)] \text{Im}[G^R(\epsilon)].\tag{8.39}$$

For calculating  $\rho_d$ , the summation of ladder diagrams in Fig. 8.3 must be carried out. These ladder diagrams are well-studied in the SYK literature; in particular, evaluation in the strict conformal limit often leads to a divergent summation, with the regularizing near-conformal corrections taking a universal form that reflect the underlying dual quantum gravity description. This divergent summation is a consequence of “resonant” eigenfunctions of the ladder kernel which have eigenvalue unity. Remarkably, there is no such effect in this class of ladder diagrams - because of the relation in Eq. 8.38, we find that the conformal Green’s function is an *exact* eigenfunction with eigenvalue  $q - 1$ , and therefore no resonance occurs. Because of this, the ladder diagrams may be evaluated via a geometric series to obtain the result

$$\rho_d(\omega, \epsilon) \frac{(q/2)!(q/2 - 1)!}{q^2 N^q} \text{Im}[G^R(\omega)] \text{Im}[G^R(\epsilon)]. \quad (8.40)$$

To leading order in  $N^{-1}$ , the conductance fluctuations are driven by  $\rho_o$ . The fact that  $\rho_o$  factorizes into two copies of the spectral function leads to the simple result,

$$\frac{\text{Var } \sigma}{\bar{\sigma}^2} = \frac{(q/2)!(q/2 - 1)!}{N^{q-1}}. \quad (8.41)$$

The statement that the variance divided by the mean squared takes the above form holds for any linear statistic  $A$  of the spectral function,  $A = \int_{-\infty}^{\infty} d\omega A(\omega) \text{Im} G^R(\omega)$ .

For the SYK model with four-fermion interactions, this gives

$$\text{Var } \sigma = \left( \frac{e^2}{\hbar} \right)^2 \frac{1.04\Gamma^2}{N^3 JT}. \quad (8.42)$$

We compare this result to numerical calculations of the conductivity variance using exact diagonalization, shown in Fig. 8.4. We also plot the mean values, which show decent agreement with their respective analytic predictions despite the relatively small system sizes. Recall that Eq. 8.41 is only valid in the conformal limit, where  $\beta J \gg 1$ . For finite size systems, we also require  $\beta J \ll N$  due to Schwarzian fluctuations setting in at lower temperatures [168, 249, 254, 303]. Exact diagonalization studies are restricted to small system sizes, with  $N = 12$  the maximum size studied here. This implies a rather narrow temperature window where

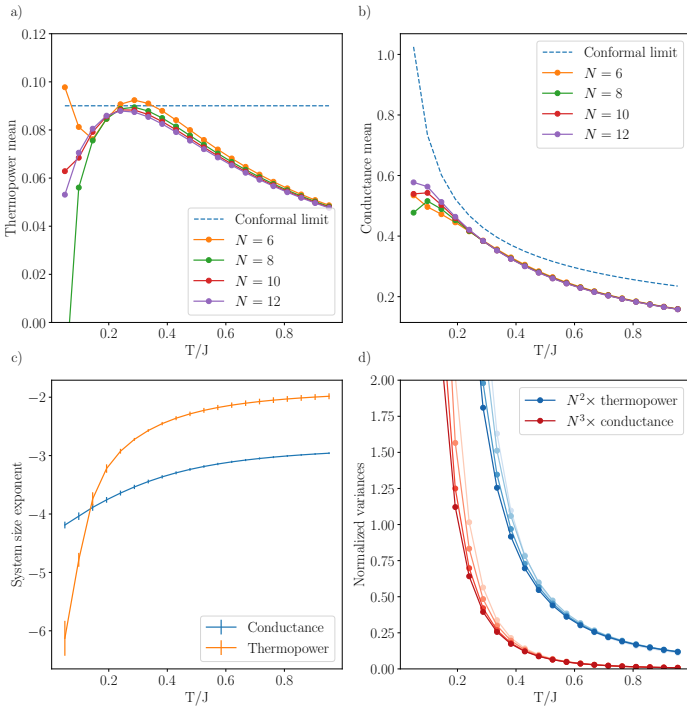


Figure 8.4: We present numerical results for the conductance and thermopower of a complex SYK model, for even system sizes  $6 \leq N \leq 12$ . All results are averaged over  $10^5$  realizations with  $J = 1$ ,  $\mu = 0.05$ . a) The average thermopower, and conformal prediction. b) The average conductance, and conformal prediction. c) The system size scaling of the conductance and thermopower variance, obtained by fitting the variance as a function of  $N$  to a power law at each temperature. d) Temperature dependence of the normalized conductance and thermopower variance for  $6 \leq N \leq 12$ , both rescaled by their appropriate system size -  $N^{-3}$  for conductance and  $N^{-2}$  for thermopower. Darker plots indicate larger system sizes.

conformal behavior could be expected. We are unable to establish the constant temperature dependence predicted by Eq. 8.41; however, the predicted  $N^{-3}$  scaling is expected to hold even at higher temperatures, away from the conformal limit, and this is validated by our numerical results.

#### 8.4.2 THERMOPOWER STATISTICS

We now analyze statistics of the thermopower, where the extensive entropy leads to a constant thermopower

$$\overline{\Theta} = \frac{4\pi}{3e} \mathcal{E}. \quad (8.43)$$

Recall that the thermopower is given by the ratio of two random variables, whose linear covariance vanished in the free fermion limit. Strikingly, the opposite behavior is true for an SYK model. To quantify this, we examine the Pearson correlation coefficient of the two random variables  $A$  and  $B$ ,

$$r_{A,B} \equiv \frac{\text{Cov}(A, B)}{\sqrt{\text{Var } A \times \text{Var } B}}. \quad (8.44)$$

$r_{A,B}$  lies between  $-1$  and  $+1$  and measures the degree of correlation between two random variables. For the SYK model, a particular property of  $\rho_o$  is that it factorizes into a product  $\alpha(\omega)\alpha(\epsilon)$  to leading order in  $N^{-1}$ . Therefore, in sharp contrast to the Fermi liquid regime where the variables  $\mathcal{L}_{11}$  and  $\mathcal{L}_{12}$  were uncorrelated, we generically expect  $r_{A,B} = 1 - \mathcal{O}(N^{-1})$ .

Despite this, we may still approximate our distribution as Gaussian. The approximation to normality of the distribution of two correlated Gaussian random variables follows along similar lines as the uncorrelated ratio [189], which we also discuss in more detail in Appendix F.3. Defining  $r$  as the correlation coefficient between  $\mathcal{L}_{11}$  and  $\mathcal{L}_{12}$ ,

$$\frac{\text{Var } \Theta}{\overline{\Theta}^2} = \frac{\text{Var } \mathcal{L}_{11}}{\mathcal{L}_{11}^{-2}} + \frac{\text{Var } \mathcal{L}_{12}}{\mathcal{L}_{12}^{-2}} - \frac{2r\sqrt{\text{Var } \mathcal{L}_{11} \times \text{Var } \mathcal{L}_{12}}}{\mathcal{L}_{11}\mathcal{L}_{12}}. \quad (8.45)$$

Both  $\mathcal{L}_{11}$  and  $\mathcal{L}_{12}$  are linear statistics, so the conformal prediction of  $\frac{\text{Var } \mathcal{L}_{11}}{\mathcal{L}_{11}^{-2}} = \frac{\text{Var } \mathcal{L}_{12}}{\mathcal{L}_{12}^{-2}}$  leads to a vanishing thermopower variance. The leading order non-zero result in the conformal limit is hence suppressed by an additional factor of  $N^{-1}$ . However, high-temperature non-conformal

corrections will still give an  $\mathcal{O}(N^{1-q})$  contribution. Additionally, corrections higher order in  $\Gamma$  arising from hybridization with the leads may also produce  $\mathcal{O}(N^{1-q})$  corrections, albeit strongly suppressed as  $\Gamma \rightarrow 0$ .

Surprisingly, we find strong disagreement between this prediction and the exact diagonalization in Fig. 8.4. The thermopower variance in the temperature regime  $\beta J \gg N^{-1}$  is well fit by a  $N^{-2}$  scaling, rather than the  $N^{-3}$  high-temperature contribution or the  $N^{-4}$  conformal contribution. This arises due to an anomalous  $N^{-2}$  scaling in the variance of the numerator,  $\mathcal{L}_{12}$ . As this quantity is proportional to the particle-hole asymmetry, we conjecture that this is related to additional fluctuations in the asymmetry not captured by our diagrammatic approach.

## 8.5 INTERPLAY BETWEEN HOPPINGS AND INTERACTIONS

In the previous sections, we have derived results for the conductance variance for both the limiting cases of non-interacting fermions with random hopping and a pure SYK model. In this section, we more carefully analyze the physically-relevant model with includes both random hopping and SYK terms.

Analysis of crossover behavior in these models has been performed previously [261, 353, 461] for the average values of observables. The conclusion of these analyses is that there exists a coherence energy scale  $E_{\text{coh}} \equiv \frac{t^2}{J}$  such that transport properties closely resemble the free fermion model for temperatures  $T \ll E_{\text{coh}}$ , with SYK behavior emerging for  $T \gg E_{\text{coh}}$  (throughout this analysis, we assume  $T \ll t, J$ ). The source of this behavior lies in the solution to the set of Schwinger-Dyson equations for the average value of the Green's function, which is exact in the large- $N$  limit:

$$\begin{aligned} G(i\omega_n)^{-1} &= -i\omega_n + \mu - t^2 G(i\omega_n) - \Sigma(i\omega_n), \\ \Sigma(\tau) &= -J^2 G^2(\tau) G(-\tau). \end{aligned} \tag{8.46}$$

It is this Green's function that displays a crossover at  $T \sim E_{\text{coh}}$  from the free fermion-like solution to an SYK-like solution, which in turn leads to a crossover of the average values of transport properties.

In contrast, we claim that the variance of transport quantities displays a qualitatively different type of crossover behavior. This is a consequence of the free fermion variance in Sec 8.3 and the SYK variance in Sec 8.4 containing different powers of  $N$ . Fluctuations driven by the randomness in SYK interactions are strongly suppressed relative to fluctuations driven by the random single-particle hopping. As a result, to leading order in  $N^{-1}$ , the free fermion Feynman diagrams in Fig. 8.1 - which exist for any arbitrarily small random hopping - are always the relevant ones for calculating fluctuation properties so long as the ratio  $\frac{t}{J}$  does not scale with some inverse power of  $N$ . The effect of SYK interactions is to renormalize the average Green's functions, such that the Green's function that appear in Eq. 8.21 are given by the solution to Eq. 8.46 rather than just the free fermion result. One can verify that to leading order in  $N^{-1}$ , the inclusion of SYK interactions does not modify the diagrammatic structure any further than this, with the exception of a class of diagrams illustrated in Fig. 8.5 - these diagrams only contribute to  $\rho_d$  and hence will not be relevant for our analysis.

The key difference that results in the average values of thermoelectric properties being described by pure SYK for  $T \gg E_{\text{coh}}$  and not their variances may be best understood conceptually within the framework of the  $(G, \Sigma)$  action, which is worked out explicitly in Appendix F.2. The intuition is as follows. For systems such as  $H_{\text{dot}}$  with random all-to-all couplings, the fermionic degrees of freedom may be integrated out and the problem reformulated as a path integral over bilocal fields  $G(\tau_1, \tau_2)$ ,  $\Sigma(\tau_1, \tau_2)$ , with an action that includes an explicit pre-factor of  $N$ ; hence, the large- $N$  solution is described by the saddle point value of this action, which is precisely Eq. 8.46. The disorder-averaged spectral function, and in turn the average values of thermoelectric quantities, depend solely on this saddle-point solution. This is not true for fluctuations, which are subleading in  $N^{-1}$  and is governed by replica off-diagonal fluctuations around the large- $N$  saddle point. The structure of the perturbation theory around the saddle point may be completely modified by the presence of a hopping term  $t$  - Feynman diagrams proportional to  $t$  may appear at lower orders in  $N^{-1}$ , and whose contributions will *a priori* be dominant even in a parameter regime where the saddle point is well-described by the  $t = 0$  solution.

Our approach to studying the behavior of transport fluctuations for an interacting quantum

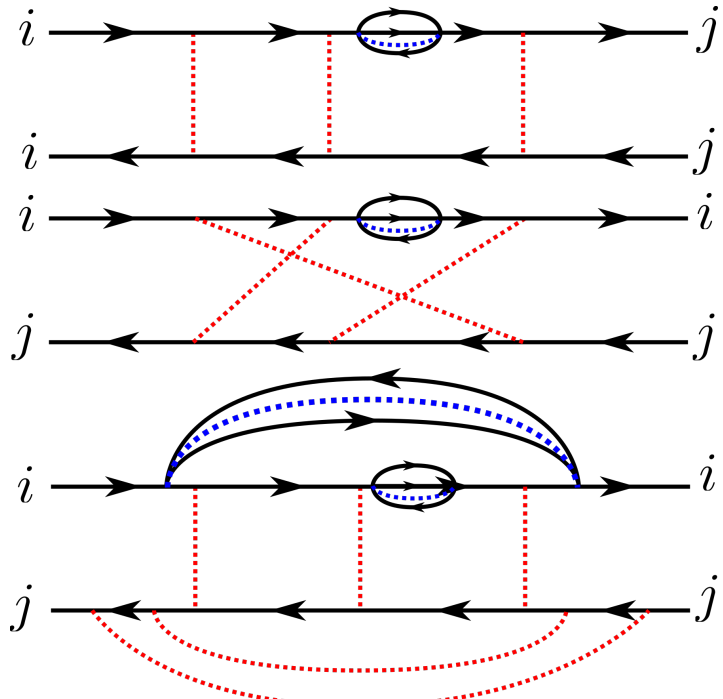


Figure 8.5: Ladder diagrams that contribute to the fluctuations of the single-particle spectral function to leading order in  $N^{-1}$ , for a model that includes both random single-particle hopping and SYK interactions. Disorder-averaging of the single-particle hopping (SYK interactions) is represented in red (blue). The structure of the diagrams are largely identical to the free fermion case illustrated in Fig. 8.1, with the SYK interactions having the effect of renormalizing the average Green's functions. An exception to this is the additional set of diagrams, illustrated in the last diagram, which are qualitatively distinct from the free fermion limit. These diagrams only contribute to the diagonal covariance  $\rho_d$  and hence will be neglected as they are suppressed by a factor of  $N^{-1}$  relative to the off-diagonal covariances.

dot will again involve calculating the single-particle covariance  $\rho_{d,o}(\omega, \epsilon)$ . We will work in the regime where  $\omega, T \ll t, J$ , and the average Green's function takes the universal form [353]

$$G(\omega, T) = \frac{1}{t} g\left(\frac{\omega}{E_{\text{coh}}}, \frac{T}{E_{\text{coh}}}\right) \equiv \frac{1}{t} g(\bar{\omega}, \bar{T}), \quad (8.47)$$

where we define the dimensionless quantities  $\bar{\omega} \equiv \omega/E_{\text{coh}}$ ,  $\bar{T} \equiv T/E_{\text{coh}}$ . We find that the system sizes accessible to exact diagonalization are inadequate for establishing even the approximate crossover of the average Green's function; due to the narrow temperature window  $N^{-1} \ll T \ll J, t$  where our analysis is valid, any crossover behavior is obscured by combination of high temperature or finite size effects. As a consequence, numerical results in this section will be restricted to self-consistent solutions of the Schwinger-Dyson equations given in Eq. 8.46.

### 8.5.1 FERMI LIQUID REGIME

For  $\bar{T}, \bar{\omega} \ll 1$ , it is known [353] that  $g^R(\bar{\omega}, \bar{T})$  has a Fermi liquid behavior. These properties can most simply stated at half filling ( $\mu = 0$ ), where the Fermi liquid nature implies

$$g^R(\bar{\omega} \ll 1, \bar{T} \ll 1) \approx -i. \quad (8.48)$$

This behavior is determined by Luttinger's theorem, which for a generic charge  $\mathcal{Q}$  says that

$$\mu(\mathcal{Q}) - \Sigma(i0^+) = \mu_0(\mathcal{Q}) \quad (8.49)$$

where  $\mu(\mathcal{Q})$  is the chemical potential necessary to tune to the charge  $\mathcal{Q}$ , and  $\mu_0(\mathcal{Q})$  is that same value for the non-interacting ( $J = 0$ ) system. This fixes  $G^R(\omega \rightarrow 0, T \rightarrow 0)$  to be that of the non-interacting Green's function, the latter of which we know has the property  $|g^R(\omega \rightarrow 0, T \rightarrow 0)|^2 = 1$  for generic filling. This property is sufficient for recovering the temperature-independent non-interacting prediction for the mean value of the conductance at low temperature, given in Eq. 8.20 and likewise properly recovers the small  $\omega, \epsilon$  divergence of  $\rho_{d,o}$  given in Eq. 8.24. Although an explicit calculation of the conductance variance requires knowledge of the small frequency and temperature behavior of  $g^R$ , which is not fixed by

Luttinger's theorem, the degree of the  $T \rightarrow 0$  divergence and the assumption that small frequency/temperature corrections appear at linear order in  $\bar{\omega}, \bar{T}$  imply from dimensional analysis that

$$\begin{aligned} \text{Var } \sigma(T \ll E_{\text{coh}}) &\propto \frac{1}{t^2 N \bar{T}} = \frac{1}{N J T}, \\ \frac{\text{Var } \sigma(T \ll E_{\text{coh}})}{\sigma(T \ll E_{\text{coh}})^2} &\propto \frac{1}{N \bar{T}}. \end{aligned} \quad (8.50)$$

This result is confirmed by calculating the conductance variance using the Green's function  $G^R$  obtained from numerically solving the large- $N$  Schwinger-Dyson equations, shown in Fig. 8.7.

### 8.5.2 SYK REGIME

We now analyze the conductance fluctuations for  $\bar{T} \gg 1$ , where the average Green's function approaches the conformal SYK result given in Eq. 8.36. The mean value of the conductance is then given by the pure SYK result in Eq. 8.35. Using this form of the Green's function, we find that the  $(\omega - \epsilon)^{-1}$  divergence of  $\rho_o(\omega, \epsilon)$  is no longer present. The infinite sum of ladder diagrams that yields  $\rho_o$  is convergent for large  $\bar{T}$ . Expanding in powers of  $\bar{T}^{-1}$ , we obtain the leading-order expression

$$\begin{aligned} \text{Var } \sigma(T \gg E_{\text{coh}}) &= \left( \frac{e^2}{\hbar} \frac{\Gamma}{t \bar{T}} \right)^2 \frac{1}{N \pi^5} \frac{1}{2 \cos(2\theta)} \left[ \int_{-\infty}^{\infty} dx \frac{e^x}{(1 + e^x)^2} \text{Im} [h(x)^2] \right]^2, \\ h(x) &\equiv e^{-i\theta} \frac{\Gamma \left( \frac{1}{4} - \frac{ix}{2\pi} + i\mathcal{E} \right)}{\Gamma \left( \frac{3}{4} - \frac{ix}{2\pi} + i\mathcal{E} \right)}. \end{aligned} \quad (8.51)$$

This integral must be done numerically; however, one can see that at the particle-hole symmetric point ( $\theta = \mathcal{E} = 0$ ,  $\mathcal{Q} = 1/2$ ), the integrand vanishes. We emphasize that this expression for the conductance variance is obtained by using the conformal SYK form of the Green's function *and* taking to leading order a large- $\bar{T}$  expansion of the integral for the conductance variance, the latter of which is not a homogeneous function of  $\bar{T}$ . In particular, Eq. 8.51 does not imply that the conductance variance vanishes exactly in the conformal limit when  $\mathcal{E} = 0$ . Rather, the variance for  $\mathcal{E} = 0$  is given by a subleading  $\bar{T}^{-3}$  term. For general  $\mathcal{Q}$ , we find that

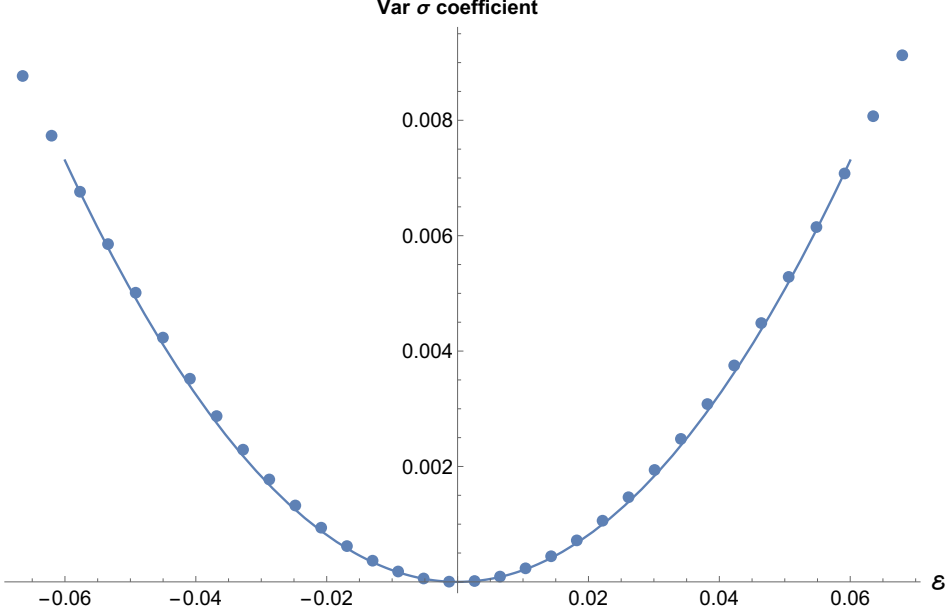


Figure 8.6: We plot the numerical coefficient of the leading-order conductance variance in the conformal SYK limit, obtained by a numerical evaluation of the integral in Eq. 8.51, along with a quadratic approximation  $4.05\mathcal{E}^2$ .

the resulting expression is well-fit, see Fig. 8.6 by the function

$$\begin{aligned}\text{Var } \sigma(T \gg E_{\text{coh}}) &\approx \left( \frac{e^2}{\hbar} \frac{\Gamma}{t \bar{T}} \right)^2 \times \frac{2.02\mathcal{E}^2}{N}, \\ \frac{\text{Var } \sigma(T \gg E_{\text{coh}})}{\sigma(T \gg E_{\text{coh}})^2} &\approx \frac{3.91\mathcal{E}^2}{N\bar{T}}.\end{aligned}\quad (8.52)$$

We see that the conductance variance normalized by the mean squared has a  $T^{-1}$  scaling, identical to the Fermi liquid regime. However, both quantities individually have distinct behavior, with the conductance variance scaling as  $T^{-2}$  for  $T \gg E_{\text{coh}}$  in contrast to the  $T^{-1}$  scaling for  $T \ll E_{\text{coh}}$ . As an aside, we state the generalization to an  $\text{SYK}_q$  model with  $q$ -fermion interactions; using the conformal Green's function gives a  $\bar{T}^{\frac{8}{q}-4}$  scaling of the conductance variance, and a  $\bar{T}^{\frac{4}{q}-2}$  scaling of the normalized conductance variance.

This crossover behavior is demonstrated in Fig. 8.7, where we solve for the conductance variance given the form of the Green's function covariance in Eq. 8.21, where we use the average Green's function  $G^R(\omega)$  obtained from a full self-consistent solution of the Schwinger-Dyson equations in real time. Details on the numerical implementation for solving the real-time Schwinger-Dyson equations can be found in [461]. We note a unique difficulty in calculating

the conductance variance not present in the average value, which comes from the denominator  $1 - t^2 G^R(\omega)G^A(\omega)$  in the Green's function covariance. As discussed previously, it is characteristic of a Fermi liquid that this denominator goes to zero as  $T \rightarrow 0$ . As a consequence, the accuracy with which one must numerically solve for  $G^R(\omega)$  diverges as  $T \rightarrow 0$ ; small errors at low temperatures can easily lead to an unphysical divergence in the conductance variance. Our self-consistent solution for  $G^R(\omega)$  utilizes a grid of  $2^{28}$  frequency points on the real axis, which gives a sufficiently accurate solution down to  $T/E_{\text{coh}} \approx 0.03$  and is enough to recover the predicted  $T^{-1}$  scaling at low temperatures.

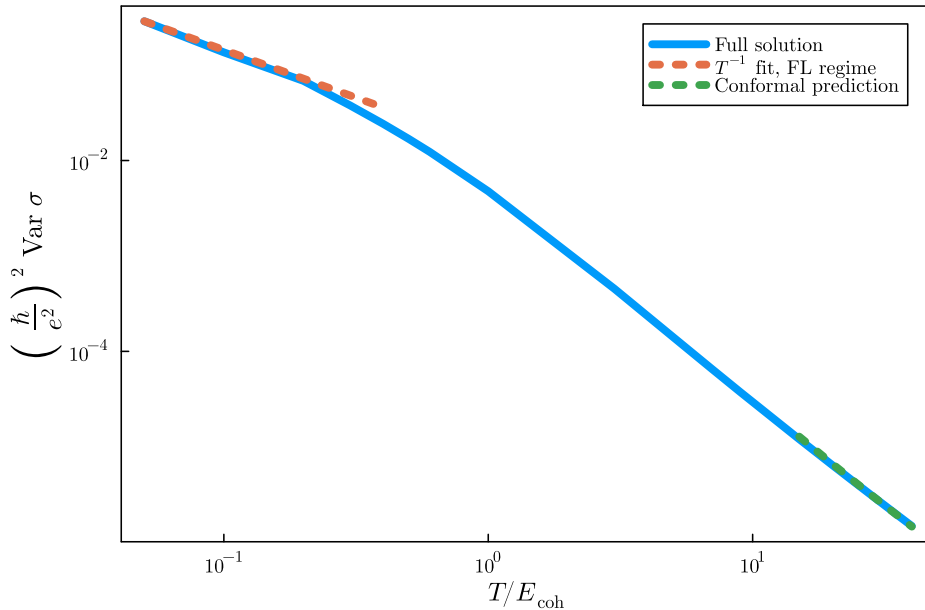


Figure 8.7: For parameters  $J = 10$ ,  $t = 0.1$ ,  $Q = 0.4$ ,  $N = 30$ , and  $\Gamma = 0.1$ , we numerically solve for the leading order contribution to the conductance variance in the large- $N$  limit by solving the Schwinger-Dyson equations for the average Green's function over a range of temperatures. We demonstrate a crossover from  $T^{-1}$  behavior at low temperatures, indicative of Fermi liquid behavior, to a more rapid  $T^{-2}$  falloff at higher temperatures which reflects the average Green's function approaching the conformal SYK form.

### 8.5.3 THERMOPOWER STATISTICS

The mean thermopower in a model with both random hopping and SYK interactions displays a crossover from the linear temperature scaling characteristic of a Fermi liquid for  $T \ll E_{\text{coh}}$  to the constant SYK value for  $T \gg E_{\text{coh}}$ . The coefficient of the mean thermopower in the

Fermi liquid regime receives a renormalization due to the presence of SYK interactions, from  $\bar{\Theta} \sim (et)^{-1}T$  in the free fermion model to  $\bar{\Theta} \sim (eE_{\text{coh}})^{-1}T$ . This is not true for the mean conductance, whose value for  $T \rightarrow 0$  is determined by the zero-frequency spectral density and is fixed by Luttinger's theorem, Eq. 8.48.

We now discuss the crossover behavior of the thermopower variance. For  $T \ll E_{\text{coh}}$ , the thermopower variance follows from the free fermion analysis in Section 8.3 and diverges as  $\bar{T}^{-1}$  for low temperatures, albeit with a renormalized coefficient. For  $T \gg E_{\text{coh}}$ , we find that the Pearson correlation coefficient  $r$  between  $\mathcal{L}_{11}$  and  $\mathcal{L}_{12}$  is 1 to leading order in  $\bar{T}$ . We apply Eq. 8.45, which gives the thermopower variance in terms of  $r$  and the statistics of  $\mathcal{L}_{11}$  and  $\mathcal{L}_{12}$ , where now we have

$$\begin{aligned}\text{Var } \mathcal{L}_{11} &= \left(\frac{\Gamma}{\hbar}\right)^2 \times \frac{2.02\mathcal{E}^2}{Nt^2\bar{T}^2}, \quad \overline{\mathcal{L}_{11}} = \frac{\Gamma}{\hbar} \frac{0.72}{t\sqrt{\bar{T}}}, \\ \text{Var } \mathcal{L}_{12} &= \left(\frac{\Gamma}{\hbar}\right)^2 \times \frac{0.07}{Nt^2}, \quad \overline{\mathcal{L}_{12}} = \frac{\Gamma}{\hbar} \frac{3.01\bar{T}^{1/2}\mathcal{E}}{t}.\end{aligned}\quad (8.53)$$

All of the terms in Eq. 8.45 decay as  $\bar{T}^{-1}$ , which implies that in the limit  $r = 1$ ,

$$\frac{\text{Var } \Theta}{\bar{\Theta}^2} = \frac{1}{N\bar{T}} \left( 1.97|\mathcal{E}| - 0.09|\mathcal{E}|^{-1} \right)^2. \quad (8.54)$$

The coefficient is rather striking, as it predicts a suppression of this leading-order variance at a critical value of the particle-hole asymmetry  $|\mathcal{E}_c| \approx 0.24$ . Recall that this leading-order suppression happens generically for a pure SYK model - this is a consequence of expanding around the limit of perfect correlation between  $\mathcal{L}_{11}$  and  $\mathcal{L}_{12}$ , along with the identity  $\frac{\text{Var } \mathcal{L}_{11}}{\overline{\mathcal{L}_{11}}^2} = \frac{\text{Var } \mathcal{L}_{12}}{\overline{\mathcal{L}_{12}}^2}$ . The latter identity is not true generically in this model, but only occurs at the aforementioned fine-tuned value  $\mathcal{E}_c$ . This value of  $\mathcal{E}$  corresponds to a rather large particle-hole asymmetry however,  $\mathcal{Q}_c \approx \frac{1}{2} \pm 0.41$ , and is hence not easily accessible.

## 8.6 CONCLUSION

We have analyzed the fluctuations of thermoelectric transport properties in strongly-correlated quantum dots. Despite the apparent simplicity of our microscopic model due to its exact large- $N$  solution, this saddle point only describes the mean value of transport quantities; higher-order statistical moments are controlled by replica off-diagonal fluctuations around this saddle point, and as such require a more unconventional analysis (we note that this is distinct from quantities such as the shot noise, which can be thought of as the second moment of the current and have saddle point contributions as discussed in [158]). We find distinct system size scalings for these fluctuations in a free fermion model ( $N^{-1}$ ) and an SYK model ( $N^{-3}$ ). The SYK prediction is qualitatively changed by the inclusion of a small random hopping, which we find is able to drive conductance fluctuations at the same order as the free fermion prediction. However, we still find distinct temperature scalings, with a  $T^{-2}$  suppression for temperatures above the coherence energy in contrast to the  $T^{-1}$  scaling at lower temperatures predicted by the free fermion result.

Our main analytic results for the conductance,  $\sigma$  were summarized in Section 8.1. We also computed the thermopower,  $\Theta$ . The mean thermopower vanishes linearly with  $T$  in the Fermi liquid regime (see Eq. 8.31), while the SYK regime has a  $T$ -independent thermopower (see Eq. 8.43). Furthermore, the finite  $N$  Schwarzian corrections are quite small for the mean thermopower in the SYK regime [261]. These features make the thermopower an ideal probe for detecting the SYK regime in experiments. However, analytic computations of the sample-to-sample fluctuations in the thermopower are not straightforward because the expression for the thermopower involves the ratio of electron Green's functions. We made partial analytic progress assuming small Gaussian fluctuations about the mean of both the numerator and the denominator, and also obtained numerical exact-diagonalization results for small values of  $N$ . Our main results are as follows. For a free fermion model, the thermopower variance scales as  $t(NT)^{-1}$ , in good agreement with numerical results. For a pure SYK model, we find surprisingly that the leading order  $N^{-3}$  contribution to the thermopower variance vanishes in the conformal limit ( $T \ll J$ ) due to perfect correlation between the numerator and denominator. Fluctuations in this regime are hence governed by a combination

of high-temperature and  $\mathcal{O}(N^{-4})$  corrections, although we are unable to verify this behavior numerically due to anomalous  $\mathcal{O}(N^{-2})$  fluctuations. For a model with both random hopping and SYK interactions, our predictions once again are qualitatively modified. The scaling of the variance in the low temperature Fermi liquid regime is suppressed from the free fermion result  $t(NT)^{-1}$  by an additional factor of  $t/J$ . In the SYK regime, the scaling is identical, albeit arising from distinct mechanisms. A noteworthy feature in the SYK regime is that this leading-order variance vanishes at a critical value of the particle-hole asymmetry  $\mathcal{E}_c$ , in which case the first non-zero contribution scales as  $N^{-1}(T/E_{\text{coh}})^{-2}$ .

The presence of a non-zero charging energy, as well as Schwarzian effects, have also been predicted to lead to distinct signatures in transport quantities for strongly interacting quantum dots [9, 261, 358], both within the weak tunnelling approximation as well as considering higher order processes. An important direction for future study is the analysis of transport fluctuations in this regime. As shown in our work, the central quantity that determines these fluctuations is the covariance of the equilibrium Green's function,  $\overline{G(\omega)G(\epsilon)}$ , as well as potentially higher order moments. As these quantities can be expressed in terms of the average Green's function, which is known to display Coulomb blockade (Schwarzian) effects at temperatures on the order of  $E_c$  ( $J/N$ ), we expect that their effects on transport fluctuations will set in at analogous temperature scales.

A more careful treatment of the effects of the coupling between the quantum dot and the leads may reveal richer physics. In this work, we restrict our parameter regime to a “closed” quantum dot, where the coupling to the leads is the smallest energy scale in the system and transport quantities follow from the properties of the isolated quantum dot. A more robust framework for treating the effects of the leads can be developed by treating both the single-particle hopping in the leads and the coupling to the quantum dot as random variables, for which an exact (in the large- $N$  limit) set of Schwinger-Dyson equations can be obtained for the non-equilibrium Green's functions [67]. The mean value of the conductance has been studied using this framework, although the effects of single-particle hopping within the quantum dot were not considered. In addition to treating conductance fluctuations within this framework, an analysis of the effects of inter-dot single-particle hopping, which was not considered in [67], may lead to new predictions even in the average value of transport properties. Corrections

due to leads in the SYK regime has also been considered in [158], and may also provide an appropriate framework for studying conductance fluctuations.

The nature of conductance fluctuations for a pure SYK model is also deserving of further analysis. The results we present are confined to the conformal regime. Deviations from this prediction at higher temperatures can be captured by an analysis of the large- $N$  numerical solution to the Schwinger-Dyson equations, and low-temperature deviations may be understood analytically through Schwarzian fluctuations. This analysis is also expected to give greater agreement with numerical results for small system sizes, where clear agreement with the conformal prediction is absent.

# Appendices

# A

## Appendix to Chapter 2

### A.1 PROJECTIVE SYMMETRY ANALYSIS

This appendix will present a detailed analysis of the projective symmetry group (PSG) of the Z2Azz13 spin liquid, and its neighboring phases. Here, we will employ the gauge used by Wen [511]. Wen described the Z2Azz13 spin liquid by the Bogoliubov Hamiltonian in Eq. (2.4) with the ansatz

$$\begin{aligned}
 u_{\mathbf{i},\mathbf{i}+\hat{x}} &= \chi \tau^x - \eta \tau^y \\
 u_{\mathbf{i},\mathbf{i}+\hat{y}} &= \chi \tau^x + \eta \tau^y \\
 u_{\mathbf{i},\mathbf{i}+\hat{x}+\hat{y}} &= -\gamma_1 \tau^x \\
 u_{\mathbf{i},\mathbf{i}-\hat{x}+\hat{y}} &= \gamma_1 \tau^x
 \end{aligned} \tag{A.1}$$

In terms of the spinons  $f_{i\alpha}$ , this can be written as

$$H = - \sum_{\mathbf{k}} [2\chi(\cos(k_x) + \cos(k_y)) - i2\eta(\cos(k_x) - \cos(k_y)) + 4\gamma_1 \sin(k_x) \sin(k_y)] f_{-\mathbf{k}\downarrow} f_{\mathbf{k},\uparrow} + \text{H.c.} \tag{A.2}$$

So in this gauge, the Z2Azz13 spin liquid has both  $d_{x^2-y^2}+is$  and  $d_{xy}$  pairing and no hopping, and the fermion dispersion relation is

$$\varepsilon_{\mathbf{k}}^2 = [2\chi(\cos(k_x) + \cos(k_y)) + 4\gamma_1 \sin(k_x) \sin(k_y)]^2 + [2\eta(\cos(k_x) - \cos(k_y))]^2 \quad (\text{A.3})$$

In the ansatz in Eq. (A.1), the 3 spin liquids are

- The  $\pi$ -flux phase with SU(2) gauge symmetry corresponds to  $\chi = \eta \neq 0$ ,  $\gamma_1 = 0$ .
- The ‘staggered flux’ U(1) spin liquid is obtained for  $\chi \neq 0$ ,  $\gamma_1 = 0$ ,  $\eta \neq 0$  with  $\chi \neq \eta$ .
- The Z2Azz13 spin liquid is obtained when the  $d_{xy}$  pairing  $\gamma_1$  breaks the U(1) down to  $\mathbb{Z}_2$ .

For our purposes, and in general, a complex Higgs field is needed to break U(1) down to  $\mathbb{Z}_2$ .

We have characterized the  $d_{xy}$  pairing above by a real parameter  $\gamma_1$ , and we need to generalize this to a complex parameter. From the analysis in Section 2.2, we deduce that this is obtained by taking a complex  $d_{xy}$  order parameter which has opposite phases on the two sublattices *i.e.*

$$\begin{aligned} u_{\mathbf{i}, \mathbf{i} + \hat{x} + \hat{y}} &= \begin{pmatrix} 0 & -(\gamma_1 - i\gamma_2) \\ -(\gamma_1 + i\gamma_2) & 0 \end{pmatrix}, \quad \mathbf{i}_x + \mathbf{i}_y \text{ even} \\ u_{\mathbf{i}, \mathbf{i} + \hat{x} + \hat{y}} &= \begin{pmatrix} 0 & -(\gamma_1 + i\gamma_2) \\ -(\gamma_1 - i\gamma_2) & 0 \end{pmatrix}, \quad \mathbf{i}_x + \mathbf{i}_y \text{ odd} \\ u_{\mathbf{i}, \mathbf{i} - \hat{x} + \hat{y}} &= \begin{pmatrix} 0 & (\gamma_1 - i\gamma_2) \\ (\gamma_1 + i\gamma_2) & 0 \end{pmatrix}, \quad \mathbf{i}_x + \mathbf{i}_y \text{ even} \\ u_{\mathbf{i}, \mathbf{i} - \hat{x} + \hat{y}} &= \begin{pmatrix} 0 & (\gamma_1 + i\gamma_2) \\ (\gamma_1 - i\gamma_2) & 0 \end{pmatrix}, \quad \mathbf{i}_x + \mathbf{i}_y \text{ odd}. \end{aligned} \quad (\text{A.4})$$

### A.1.1 LATTICE PSGs

We first recall the spin liquid classification scheme of Ref. [511]. If  $u_{ij}$  is the mean field ansatz for a spin liquid symmetric under the group action  $G$ , it transforms as

$$\mathcal{P}G : \quad u_{ij} \rightarrow W_g^\dagger(\mathbf{i}) u_{G(i), G(j)} W(\mathbf{j}) \quad (\text{A.5})$$

where  $W_G(\mathbf{i})$  is a gauge transform. In addition to the symmetries, these gauge transformations characterize the spin liquid, yielding the projective symmetry group (PSG) [511].

Using the notation from Ref. [511], the spin liquid Z2Azz13 is defined by the PSG

$$\begin{aligned} W_{tx}(\mathbf{i}) &= \tau^0, & W_{px}(\mathbf{i}) &= (-)^{i_x+i_y} i\tau^z, & W_{pxy}(\mathbf{i}) &= i\tau^x, \\ W_{ty}(\mathbf{i}) &= \tau^0, & W_{py}(\mathbf{i}) &= (-1)^{i_x+i_y} i\tau^z, & W_t(\mathbf{i}) &= i\tau^z \end{aligned} \quad (\text{A.6})$$

while the PSG of U1Cn01n (the staggered flux phase) is

$$\begin{aligned} W_{tx}(\mathbf{i}) &= g_3(\theta_x) i\tau^x, & W_{px}(\mathbf{i}) &= (-)^{i_x} g_3(\theta_x) i\tau^x, & W_{pxy}(\mathbf{i}) &= g_3(\theta_{pxy}) i\tau^x, \\ W_{ty}(\mathbf{i}) &= g_3(\theta_y) i\tau^x, & W_{py}(\mathbf{i}) &= (-)^{i_y} g_3(\theta_y), & W_t(\mathbf{i}) &= (-)^{i_x+i_y} g_3(\theta_t), \end{aligned} \quad (\text{A.7})$$

where  $g_3(\theta) = e^{i\theta\tau^z}$ . From these PSGs we can extract the symmetry fractionalization through the group relations given in the appendix of Ref. [480] (Eq. (B8)). These are provided in Table A.1. Note that instead of  $P_{xy} : (i_x, i_y) \rightarrow (i_y, i_x)$ , we consider the  $90^\circ$  rotation  $R_{\pi/2} = P_{xy}P_y$ . Similarly,  $P_x$  is related to the other symmetries through  $R_{\pi/2}P_yR_{\pi/2}^{-1}$ .

### A.1.2 IDENTIFICATION OF STAGGERED FLUX IN CONTINUUM MODEL

The staggered flux state (U1Cn01n) can be obtained by coupling a Higgs field to the bilinear

$$\mathcal{O}_3^a = \text{tr}(\sigma^a \bar{X} \mu^y (\gamma^x i\partial_y + \gamma^y i\partial_x) X) \quad (\text{A.8})$$

	Group relations	Z2Azz13	U1Cn01n lattice	U1Cn01n cont
1	$T_y^{-1}T_xT_yT_x^{-1}$	1	$e^{-2i(\theta_x-\theta_y)\tau^z}$	$-e^{-2i(\phi_x-\phi_y)\sigma^z}$
2	$P_y^{-1}T_xP_yT_x^{-1}$	-1	$e^{-2i\theta_{py}\tau^z}$	$e^{2i\phi_{py}\sigma^z}$
3	$P_y^{-1}T_yP_yT_y$	-1	$e^{-2i\theta_{py}\tau^z}$	$e^{2i\phi_{py}\sigma^z}$
4	$P_y^2$	-1	$e^{2i\theta_{py}\tau^z}$	$e^{-2i\phi_{py}\sigma^z}$
5	$P_y^{-1}R_{\pi/2}P_yR_{\pi/2}$	1	$-e^{-2i\theta_{py}\tau^z}$	$-e^{2i\phi_{py}\sigma^z}$
6	$R_{\pi/2}^4$	1	$\mathbb{1}$	$\mathbb{1}$
7	$R_{\pi/2}^{-1}T_xR_{\pi/2}T_y$	-1	$e^{i(2[\theta_{pxy}+\theta_{py}]-[\theta_x+\theta_y])\tau^z}$	$e^{i(2\phi_r-\phi_x-\phi_y)\sigma^z}$
8	$R_{\pi/2}^{-1}T_xR_{\pi/2}T_x^{-1}$	-1	$e^{i(2[\theta_{pxy}+\theta_{py}]-[\theta_x+\theta_y])\tau^z}$	$e^{i(2\phi_r-\phi_x-\phi_y)\sigma^z}$
9	$\mathcal{T}^{-1}R_{\pi/2}^{-1}\mathcal{T}R_{\pi/2}$	-1	$e^{-2i\theta_t\tau^z}$	$e^{-2i\phi_t\sigma^z}$
10	$\mathcal{T}^{-1}P_y^{-1}\mathcal{T}P_y$	1	$\mathbb{1}$	$\mathbb{1}$
11	$\mathcal{T}^{-1}T_x^{-1}\mathcal{T}T_x$	1	$-e^{-2i\theta_t\tau^z}$	$-e^{-2i\phi_t\sigma^z}$
12	$\mathcal{T}^{-1}T_y^{-1}\mathcal{T}T_y$	1	$-e^{-2i\theta_t\tau^z}$	$-e^{-2i\phi_t\sigma^z}$
13	$\mathcal{T}^2$	-1	$e^{2i\theta_t\sigma^z}$	$e^{2i\phi_t\sigma^z}$

Table A.1: Symmetry fractionalization. In keeping with the conventions of Ref. [480], the gauge is chosen such that group relation 7 is fixed to equal  $-1$  for the  $\mathbb{Z}_2$  spin liquid.

giving something like

$$\mathcal{L} = \text{tr}(\bar{X}\gamma^\mu i\partial_\mu X) + \Phi_3^a \text{tr}(\sigma^a \bar{X} M X). \quad (\text{A.9})$$

The U(1) spin liquid U1Cn01n is then obtained upon condensing one component of  $\Phi_3$ . This was determined by considering the symmetry fractionalization of the U(1) spin liquid obtained by condensing the  $z$ -component of  $\Phi_3$ :  $\langle \Phi_3^z \rangle \neq 0$ . Based on the symmetry transformations outlined in Table A.2, this condensate has a corresponding continuum PSG

$$\begin{aligned} V_{tx} &= g_3(\phi_x)i\sigma^x, & V_{px} &= g_3(\phi_{px}), & V_r &= g_3(\phi_r)i\sigma^x, \\ V_{ty} &= g_3(\phi_y)i\sigma^x, & V_{py} &= g_3(\phi_{py}), & V_t &= g_3(\phi_t), \end{aligned} \quad (\text{A.10})$$

where  $g_3(\phi) = e^{i\phi\sigma^z}$  is an arbitrary gauge transformation. Importantly, in the U(1) spin liquid, the phases  $\phi$  can take any value. When these phases are rewritten in terms of the U(1)

Operators	$\mathcal{T}$	$P_x$	$P_y$	$T_x$	$T_y$	$R_{\pi/2}$
$\mathcal{O}_1^a$	$\text{tr}(\sigma^a \overline{X} \mu^z \gamma^x X)$	—	—	—	+	$-\mathcal{O}_2^a$
$\mathcal{O}_2^a$	$\text{tr}(\sigma^a \overline{X} \mu^x \gamma^y X)$	—	—	+	—	$-\mathcal{O}_1^a$
$\mathcal{O}_3^a$	$\text{tr}(\sigma^a \overline{X} \mu^y (\gamma^x i \partial_y + \gamma^y i \partial_x) X)$	+	+	+	—	—

Table A.2: Symmetry transformations of the three fermion bilinears which must be coupled to SU(2) adjoint Higgs fields in order to realize the PSG of the  $\mathbb{Z}_2$  spin liquid Z2Azz13.

phases from Eq. (A.7),  $\theta_G$ , according to

$$(\phi_x, \phi_y, \phi_{py}, \phi_t, \phi_r) = \left( \theta_x + \frac{\pi}{4}, \theta_y - \frac{\pi}{4}, -\theta_y, \theta_t, \theta_{pxy} + \theta_{py} \right) \quad (\text{A.11})$$

the symmetry fractionalizations given in columns 4 and 5 of Table A.1 are identical. It is possible that two distinct spin liquids (as defined by having distinct PSGs) could nevertheless have identical symmetry fractionalization. This seems unlikely in this situation and is, moreover, proven false by the explicit derivation of the continuum action from the lattice model.

### A.1.3 IDENTIFICATION OF Z2Azz13 IN CONTINUUM MODEL

The spin liquid Z2Azz13 is proximate to U1Cn01n in that the PSG of Eq. (A.6) may be obtained through gauge transformations and judicious choices of the angles  $\theta_G$  in Eq. (A.7). It is, however, simpler to determine the U(1) transformations (*i.e.* the angles  $\phi_\mu$ ) that map the symmetry fractionalization of U1Cn01n to the symmetry fractionalization of Z2Azz13. That is, we find that the assignment

$$(\phi_x, \phi_y, \phi_{py}, \phi_t, \phi_r) = \quad (\text{A.12})$$

$$\left( \theta + \frac{\pi}{4}, \theta - \frac{\pi}{4} + n_y \pi, (2n_{py} + 1) \frac{\pi}{2}, (2n_t + 1) \frac{\pi}{2}, \theta + (2n_r + n_y + 1) \frac{\pi}{2} \right), n_\mu \in \mathbb{Z} \quad (\text{A.13})$$

transforms the 5th column of Table A.1 into a set of  $\pm 1$ s that match the third column. Inserting these  $\phi_\mu$ s into the PSG defined in Eq. (A.10) and selecting  $n_\mu = 0$ ,  $\mu = y, py, t, r$

and  $\theta = \pi/4$ , we obtain the  $\mathbb{Z}_2$  continuum PSG<sup>1</sup>

$$\begin{aligned} V_{tx} &= -i\sigma^y, & V_{px} &= \pm i\sigma^z & V_r &= -\frac{i}{\sqrt{2}}(\sigma^x - \sigma^y) \\ V_{ty} &= -i\sigma^x, & V_{py} &= -i\sigma^z, & V_t &= i\sigma^z. \end{aligned} \quad (\text{A.14})$$

We can now ask what form of operator needs to couple to a new Higgs field in order to realize this PSG and hence the  $\mathbb{Z}_2$  spin liquid Z2Azz13. Firstly, it's clear that the  $\sigma^x$  or  $\sigma^y$  components of the Higgs field must condense—condensing in the  $\sigma^z$  channel,  $\sim \langle \tilde{\Phi}^z \rangle \text{tr}(\sigma^z \bar{X} \widetilde{M} X)$ , would not break the U(1) symmetry. However, in considering condensates in  $x$  or  $y$ , we see that the gauge transformations corresponding to the translations  $T_x$  and  $T_y$  are different and, further, the rotation  $R_{\pi/2}$  exchanges  $\sigma^x$  and  $\sigma^y$ , meaning that both must be present in a symmetric spin liquid.

Based on the symmetry relations documented in Ref. [480], we find that the operators  $\mathcal{O}_{1,2}$ ,

$$\mathcal{O}_1^a = \text{tr}(\sigma^a \bar{X} \mu^z \gamma^x X), \quad \mathcal{O}_2^a = \text{tr}(\sigma^a \bar{X} \mu^x \gamma^y X), \quad (\text{A.15})$$

induce the PSG of Eq. (A.14) provided they couple to Higgs fields that condense in perpendicular directions. The symmetry transformation properties of  $\mathcal{O}_{1,2}^a$  are given in Table A.2. That is, given a Lagrangian:

$$\mathcal{L}' = \text{tr}(\bar{X} \gamma^\mu i \partial_\mu X) + \Phi_1^a \text{tr}(\sigma^a \bar{X} \mu^z \gamma^x X) + \Phi_2^a \text{tr}(\sigma^a \bar{X} \mu^x \gamma^y X) + \Phi_3^a \text{tr}(\sigma^a \bar{X} \mu^y (\gamma^x i \partial_y + \gamma^y i \partial_x) X), \quad (\text{A.16})$$

the PSG in Eq. (A.14) is obtained when  $\langle \Phi_1 \rangle = (\alpha, 0, 0)$ ,  $\langle \Phi_2 \rangle = (0, \alpha, 0)$ , and  $\langle \Phi_3 \rangle = (0, 0, \beta)$ , for  $\alpha, \beta \in \mathbb{R}$ . This agrees with conclusions reached in Section 2.3.4.

## A.2 RENORMALIZATION GROUP ANALYSIS OF THE SU(2) GAUGE THEORY

In this appendix, we describe the origin of the  $\log^2$  terms in the critical SU(2) gauge theory in a renormalization group (RG) framework. Integrating the RG equations will lead to an exponentiated prediction for the correlators.

---

<sup>1</sup>The symmetry  $P_x$  is related to the other symmetries through  $R_{\pi/2} P_y R_{\pi/2}^{-1}$ .

We start with the expression in Eq. (2.53), keep the full Higgs propagator as in Eq. (2.49), and perform a standard momentum shell RG in the window  $\Lambda - d\Lambda < (p_0^2 + p_x^2 + p_y^2)^{1/2} < \Lambda$

$$\delta\gamma^x\Sigma_1(k_x) = \frac{12}{N_f} \int_{\Lambda-d\Lambda}^{\Lambda} \frac{d^3p}{(2\pi)^3} \frac{(p_x + k_x)}{(p_x + k_x)^2 + p_0^2 + p_y^2} \frac{|p|}{p_0^2 + p_y^2 + 4K|p|p_x^2}. \quad (\text{A.17})$$

Expanding to linear order in  $k_x$ , using spherical co-ordinates with

$$(p_0, p_y, p_x) = \Lambda(\sin\theta\cos\phi, \sin\theta\sin\phi, \cos\theta), \quad (\text{A.18})$$

and setting  $\mu = \cos\theta$ , we obtain

$$\delta\gamma^x\Sigma_1(k_x) = \frac{6k_x}{N_f\pi^2} \frac{d\Lambda}{\Lambda} \int_0^1 d\mu (1 - 2\mu^2) \frac{1}{1 - \mu^2 + 4K\Lambda\mu^2}. \quad (\text{A.19})$$

Under normal circumstances, the  $\mu$  integral would be a finite numerical constant, and the co-efficient of  $d\Lambda/\Lambda$  would be the usual RG log which would then contribute (in this case) to the exponent  $\eta_\psi$ . However, that is not the case here, because of the logarithmic divergence of the  $\mu$  integral near  $\mu = 1$ . Evaluating the  $\mu$  integral, we obtain

$$\delta\gamma^x\Sigma_1(k_x) = -\frac{3k_x}{N_f\pi^2} \frac{d\Lambda}{\Lambda} \left[ \ln\left(\frac{1}{K\Lambda}\right) - 4 + \mathcal{O}(K\Lambda) \right]. \quad (\text{A.20})$$

In a similar manner, we obtain for the frequency dependence of the self energy

$$\delta\gamma^0\Sigma_1(k_0) = -\frac{12}{N_f} \int_{\Lambda-d\Lambda}^{\Lambda} \frac{d^3p}{(2\pi)^3} \frac{(p_0 + k_0)}{(p_0 + k_0)^2 + p_x^2 + p_y^2} \frac{|p|}{p_0^2 + p_y^2 + 4K|p|p_x^2}. \quad (\text{A.21})$$

In spherical co-ordinates this simplifies to

$$\begin{aligned} \delta\gamma^0\Sigma_1(k_0) &= -\frac{6k_0}{N_f\pi^2} \frac{d\Lambda}{\Lambda} \int_0^1 d\mu (1 - (1 - \mu^2)) \frac{1}{1 - \mu^2 + 4K\Lambda\mu^2} \\ &= -\frac{3k_0}{N_f\pi^2} \frac{d\Lambda}{\Lambda} \left[ \ln\left(\frac{1}{K\Lambda}\right) - 2 + \mathcal{O}(K\Lambda) \right]. \end{aligned} \quad (\text{A.22})$$

The expression for  $\delta\gamma^y\Sigma_1(k_y)$  is the same as  $\delta\gamma^0\Sigma_1(k_0)$ , after mapping  $k_0 \Rightarrow k_y$ .

We can also examine the vertex correction for the SO(5) order parameter in a similar manner. From Eq. (2.68) at zero external momentum, we note that the vertex correction

needs the integral

$$\begin{aligned}
 \delta V &= \frac{1}{N_f} \int_{\Lambda-d\Lambda}^{\Lambda} \frac{d^3 p}{(2\pi)^3} \frac{1}{p_x^2 + p_y^2 + p_0^2} \frac{4|p|}{p_0^2 + p_y^2 + 4K|p|p_x^2} \\
 &= \frac{1}{2N_f\pi^2} \frac{d\Lambda}{\Lambda} \int_0^1 d\mu \frac{4}{1 - \mu^2 + 4K\Lambda\mu^2} \\
 &= \frac{1}{N_f\pi^2} \frac{d\Lambda}{\Lambda} \left[ \ln\left(\frac{1}{K\Lambda}\right) + \mathcal{O}(K\Lambda) \right]. \tag{A.23}
 \end{aligned}$$

We now proceed as usual to obtain the RG equations from the momentum shell results under the rescaling

$$\begin{aligned}
 x' &= xe^{-\ell} \\
 y' &= ye^{-\ell}. \\
 \tau' &= \tau \exp\left(-\int_0^\ell d\ell' z(\ell')\right) \tag{A.24}
 \end{aligned}$$

Importantly, we note the flow of the irrelevant coupling  $K$  under this transformation

$$\frac{dK}{d\ell} = -K. \tag{A.25}$$

For the fermion field we define

$$\psi' = \psi \exp\left(\int_0^\ell d\ell' \frac{1 + z(\ell') + \eta_\psi(\ell')}{2}\right) \tag{A.26}$$

The field  $\psi$  is not gauge-invariant, and neither is its anomalous dimension  $\eta_\psi$ . However, the leading  $\log^2$  term we shall find shortly is gauge invariant. In the presence of the  $\log^2$  term, we will also see that the usual logarithm terms have a non-universal co-efficient. So we ignore the gauge field contributions here (the gauge field induced renormalizations have been computed in Refs. [381, 384]), because they only contribute logarithm terms which become part of overall terms which are non-universal.

Matching Eqs. (A.20,A.22) to Eqs. (A.24,A.26) we obtain

$$\begin{aligned}\eta(\ell) &= \frac{6}{N_f\pi^2} \left[ \ln \left( \frac{1}{K(\ell)\Lambda} \right) - 3 \right] \\ z(\ell) &= 1 + \frac{6}{N_f\pi^2}\end{aligned}\tag{A.27}$$

Assuming a bare value  $K(0) = K_0$ , integrating Eq. (A.25) to obtain  $K(\ell) = K_0 e^{-\ell}$ , and then integrating Eq. (A.27) we obtain

$$\int_0^\ell \eta(\ell') d\ell' = \frac{6}{N_f\pi^2} \left[ \frac{\ell^2}{2} - (\ln(K_0\Lambda) + 3)\ell \right]\tag{A.28}$$

We can now obtain the momentum dependence of physical observables by evaluating them at a scale  $\ell = \ell^* = \ln(\Lambda/|p|)$ . Note that the co-efficient of  $\ell^*$  involves the bare value of  $K_0$ , and hence the co-efficient of the logarithm term is non-universal, as claimed earlier. The leading term is  $\log^2$ , and its co-efficient is universal and agrees with that in Eq. (2.59); similarly, Eq. (A.23) agrees with Eq. (2.69). Inserting the integral Eq. (A.28) into Eq. (A.26), we obtain results of the form in Eq. (2.72).

### A.3 ISOLATION OF LOGARITHM-SQUARED DIVERGENCES IN ONE-LOOP CORRECTIONS

We state in the main text that logarithm-squared divergences in the critical SU(2) gauge theory arise in the one-loop diagrams in a certain parameter regime, given by Eq. (2.55). This is shown in the main text for the simplest one-loop calculation, which is the  $\Phi_1$  ( $\Phi_2$ ) contribution to the fermion self-energy with external momenta  $k_x$  ( $k_y$ ). Here, we provide more general calculations for other cases.

We first analyze the  $\Phi_1$  contribution to the fermion self-energy with external momenta  $k_0$ . This is equivalent to the  $k_y$  external momenta, as well as the  $\Phi_2$  contribution with external

momenta  $k_0, k_x$ .

$$\begin{aligned}
 \gamma^0 \Sigma(k_0) &\approx -\frac{12}{N_f} \int \frac{d^3 p}{(2\pi)^3} \frac{p_0 + k_0}{(p_0 + k_0)^2 + p_x^2 + p_y^2} \frac{|p_x|}{p_0^2 + p_y^2 + 4K|p_x|^3} \\
 &= -\frac{12}{N_f} \int \frac{dp_x}{8\pi^2} \frac{|p_x|(p_x^2 - 4K|p_x|^3 - k_0^2)}{k_0 \sqrt{-(4K)^2|p_x|^6 + 8K|p_x|^3(p_x^2 - k_0^2) - (p_x^2 + k_0^2)^2}} \\
 &\quad \left[ \tan^{-1} \left( \frac{-p_x^2 + 4K|p_x|^3 - k_0^2}{\sqrt{-(4K)^2|p_x|^6 + 8K|p_x|^3(p_x^2 - k_0^2) - (p_x^2 + k_0^2)^2}} \right) \right. \\
 &\quad \left. + \tan^{-1} \left( \frac{-p_x^2 + 4K|p_x|^3 + k_0^2}{\sqrt{-(4K)^2|p_x|^6 + 8K|p_x|^3(p_x^2 - k_0^2) - (p_x^2 + k_0^2)^2}} \right) \right] \\
 &\quad - \frac{12}{N_f} \int \frac{dp_x}{8\pi^2} \frac{|p_x|}{2k_0} \ln \left( \frac{p_x^2}{4K|p_x|^3} \right).
 \end{aligned} \tag{A.29}$$

We see that the dominant term is proportional to  $k_0 \log^2(Kk_0)$ , arising in the same limit as in Eq. 2.55. This  $\log^2$  dependence comes from the inverse tangents, since  $2\tan^{-1}(x) = i \log \left( \frac{1+ix}{1-ix} \right)$ . Assuming  $K|p_x|^3 \ll p_x^2$ , the expression in the denominator of the inverse tangent argument is  $\approx ip_x^2$ , so our integrand  $\approx i \tan^{-1}(i(1 + 4K|p_x|))$ . If we further assume  $K|p_x| \ll 1$ , we get an integrand that scales like  $k_0/p_x \ln(Kp_x)$ , and hence the full expression scales as  $k_0 \log^2(Kk_0)$ .

These  $\log^2$  contributions are verified by numerically evaluating Eq. 2.53 and Eq. A.29 and analyzing the behavior at small  $k$ , as shown in Fig. A.1.

For the Higgs vertex correction to the SO(5) order parameter, we can also isolate a  $\log^2$  divergence. Calculating the  $\Phi_1$  correction to the vertex, we regulate the integral by including an external momenta  $2k_x$  evenly distributed between the two outgoing fermions. The vertex

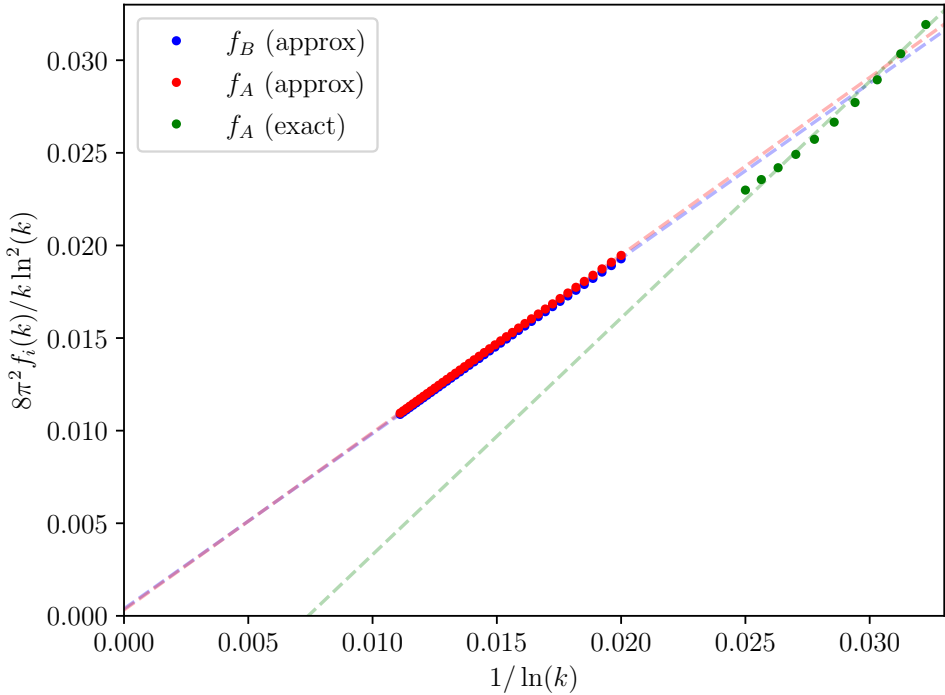


Figure A.1: Denoting the integrands of the two types of self-energy contributions in Eq. (2.53) and Eq. (A.29) with  $K = 1$  as  $f_A(k_x)$  and  $f_B(k_0)$ , we plot a numerical evaluation of  $8\pi^2 f_i(k)/(k \ln^3(k))$  vs  $1/(\ln(k))$ . The form of this expression is designed to isolate the  $\log^2$  contribution at small momenta, and agreement with our analytic predictions should give a straight line with a slope of 1. The approximation of the Higgs propagator as Eq. 2.52 allows for greater numerical precision, as the dimensionality of the integral can be reduced by performing portions of the integral analytically. These numerical evaluations give good agreement with analytic predictions as well as calculations using the full form of the Higgs propagator.

correction is

$$\begin{aligned}
 & \frac{\mu^z \sigma^a \Gamma^i \sigma^a \mu^z}{N_f} \int \frac{d^3 p}{(2\pi)^3} \frac{p_x^2 - k_x^2 + p_y^2 + p_0^2}{[(p_x + k_x)^2 + p_y^2 + p_0^2] [(p_x - k_x)^2 + p_y^2 + p_0^2]} \frac{4|p_x|}{p_0^2 + p_y^2 + 4K|p_x|^3} \\
 &= \frac{\mu^z \sigma^a \Gamma^i \sigma^a \mu^z}{N_f} \int \frac{r dr dp_x}{(2\pi)^2} \frac{p_x^2 - k_x^2 + r^2}{[(p_x + k_x)^2 + r^2] [(p_x - k_x)^2 + r^2]} \frac{4|p_x|}{r^2 + 4K|p_x|^2} \\
 &= \frac{\mu^z \sigma^a \Gamma^i \sigma^a \mu^z K}{N_f} \int \frac{dp_x}{4\pi^2} \frac{|p_x|}{k_x p_x \left[ (p_x - x_x)^2 - 4K|p_x|^2 \right] \left[ (p_x + k_x)^2 - 4K|p_x|^2 \right]} \\
 &\quad \times \left[ \left( (p_x^2 - k_x^2)|p_x|^2 + \frac{(p_x + k_x)^2(p_x - k_x)^2}{4K} \right) \ln \left( \frac{(p_x + k_x)^2}{(p_x - k_x)^2} \right) \right. \\
 &\quad + (p_x + k_x)^2 \left[ |p_x|^3 \ln \left( \frac{4K|p_x|^3}{(p_x + k_x)^2} \right) + \frac{(k_x^2 - p_x^2)}{4K} \ln \left( \frac{4K|p_x|^3}{(p_x - k_x)^2} \right) \right] \\
 &\quad \left. - (p_x - k_x)^2 \left[ |p_x|^3 \ln \left( \frac{4K|p_x|^3}{(p_x - k_x)^2} \right) + \frac{(k_x^2 - p_x^2)}{4K} \ln \left( \frac{4K|p_x|^3}{(p_x + k_x)^2} \right) \right] \right] \tag{A.30}
 \end{aligned}$$

We can obtain a  $\log^2$  from the second logarithm in the brackets in the limit given by Eq. (2.55).

#### A.4 ALTERNATE COMPUTATION OF $z$ IN THE SU(2) GAUGE THEORY

In the main text we emphasize that although irrelevant terms in the Higgs propagator turn out to strongly influence the renormalization of the critical theory, these effects cancel in the dynamical critical exponent, and its value can be computed through more standard methods. In this section, we compute  $z$  via dimensional regularization after explicitly setting the irrelevant Higgs terms to zero, and show that it gives the same answer for  $z$  as in the main text. For the calculation of  $z$ , we are interested in the counterterms generated by

$$\gamma^0 \frac{\partial \Sigma}{\partial k_0} \Big|_{k=0} - \gamma^x \frac{\partial \Sigma}{\partial k_x} \Big|_{k=0} = -\frac{6}{N_f} \int \frac{d^3 p}{(2\pi)^3} \left[ \frac{p_y^2}{p^4 \Gamma_1(p)} - \frac{p_0^2 - p_x^2}{p^4 \Gamma_2(p)} \right] \tag{A.31}$$

This integrand is well-behaved for  $p^2 \neq 0, \infty$ , and one can see that the second term in brackets vanishes, since the  $\Gamma_2$  propagator is invariant under  $p_x \leftrightarrow p_0$ .

The integrals over  $p_0, p_y$  can be performed exactly in radial coordinates, which gives

$$-\frac{3}{\pi^2 N_f} \int_{-\infty}^{\infty} dp_x \frac{1}{|p_x|} = -\frac{6}{\pi^2 N_f} \int_0^{\infty} \frac{dp_x}{p_x}. \tag{A.32}$$

Continuing the  $p_x$  integral to  $1 - \epsilon$  dimensions and imposing a UV cutoff  $\Lambda$ , yields

$$-\frac{6}{\pi^2 N_f} \mu^\epsilon \int_0^\Lambda \frac{dp_0}{p_0^{1+\epsilon}} = -\frac{6}{\pi^2 N_f \epsilon} \mu^\epsilon \Lambda^{-\epsilon} = -\frac{6}{\pi^2 N_f} \left( \frac{1}{\epsilon} + \ln \left( \frac{\mu}{\Lambda} \right) + \mathcal{O}(\epsilon) \right) \quad (\text{A.33})$$

Which gives the same answer for  $z$  as when the irrelevant Higgs terms were used to regulate the divergences in the self-energy.

### A.5 HIGGS FIELD RENORMALIZATION IN THE SU(2) GAUGE THEORY

For completeness, we compute the  $\log^2$  corrections in the critical SU(2) gauge theory to the Yukawa couplings at one-loop level, since these determine the renormalization of the Higgs fields. The calculations are nearly identical to those of the SO(5) order parameter.

The correction to the  $\Phi_1$  Yukawa coupling is given by the integral

$$\begin{aligned} & \frac{(\mu^z \sigma^b)(\mu^z \sigma^a)(\mu^z \sigma^b)}{N_f} \int \frac{d^3 p}{(2\pi)^3} \gamma^x \frac{\not{p} - \not{k}_1}{(p - k_1)^2} \gamma^x \frac{\not{p} - \not{k}_2}{(p - k_2)^2} \gamma^x \frac{1}{\Gamma_1(p) + K p_x^2} \\ & + \frac{(\mu^x \sigma^b)(\mu^z \sigma^a)(\mu^x \sigma^b)}{N_f} \int \frac{d^3 p}{(2\pi)^3} \gamma^y \frac{\not{p} - \not{k}_1}{(p - k_1)^2} \gamma^x \frac{\not{p} - \not{k}_2}{(p - k_2)^2} \gamma^y \frac{1}{\Gamma_2(p) + K p_y^2} \end{aligned} \quad (\text{A.34})$$

Evaluating the first term in the limit in Eq. 2.55, we set the external momenta to zero and use it as an IR cutoff  $k$ , which gives to  $\log^2$  order

$$\frac{(\mu^z \sigma^b)(\mu^z \sigma^a)(\mu^z \sigma^b)}{2\pi^2 N_f} \ln^2(Kk). \quad (\text{A.35})$$

This coefficient is identical to the SO(5) correction, as the two integrals are the same to leading order in  $k$ . The contribution is the same for the second term in Eq. (A.34), giving the final Yukawa correction

$$-\frac{\mu_z \sigma^a}{\pi^2 N_f} \ln^2(Kk). \quad (\text{A.36})$$

The correction to the  $\Phi_2$  Yukawa term is identical, as the two are related by a spatial rotation.

We now renormalize the  $\Phi_{1,2}$  fields so that the Yukawa coupling remains invariant, as in Ref. [199]. Hence, the Higgs fields are renormalized at  $\log^2$  order,  $\Phi_i = \sqrt{Z_\Phi} \Phi_{i,R}$ , with

corrections from  $Z_\psi$  and (A.36)

$$Z_\Phi = 1 + \frac{6}{\pi^2 N_f} \ln^2(K\mu) + \frac{2}{\pi^2 N_f} \ln^2(K\mu) = 1 + \frac{8}{\pi^2 N_f} \ln^2(K\mu) \quad (\text{A.37})$$

## A.6 EVALUATION OF TWO-LOOP SO(5) ORDER PARAMETER CORRECTIONS

In this appendix, we evaluate the  $\mathcal{O}(N_f^{-1})$  two-loop correction to the SO(5) order parameter, shown in the main text and displayed here in Fig. A.2 with internal momenta labeled. The diagram shown is one of four possible contributions - additional diagrams can be generated by either exchanging  $\Phi^1 \leftrightarrow \Phi^2$  or crossing the propagators of the Higgs bosons, but all give the same correction for zero external momenta. The main conclusion of this appendix is that this contribution is well-behaved upon setting the dangerously irrelevant operators to zero and only contributes standard logarithm divergences, which we argue in the main text and in Appendix A.2 give non-universal corrections to the order parameter scaling. Intuitively, this may be thought of as related to the fact that these two-loop diagrams require *both* types of Higgs  $\Phi_{1,2}$ , as they vanish trivially when both Higgs propagators are of the same type. As the  $\log^2$  divergences are connected to the rotational symmetry breaking in the  $\mathcal{O}(N_f)$  effective action for the Higgs propagators, it is natural - although still a non-trivial fact - that these two-loop diagrams which respect rotational symmetry only contribute single logarithm divergences.

This two-loop correction vanishes for the VBS order parameter, so we focus on the Néel order parameter, where the source vertex contributes a factor of  $\mu^y \sigma^a$ . We first evaluate the fermion loop integral,

$$\begin{aligned} & (-1) N_f \text{Tr} \sigma^b \sigma^c \mu^y \mu^x \mu^z \int \frac{d^3 p}{(2\pi)^3} \frac{\not{p}}{p^2} \gamma^x \frac{\not{p} + \not{q}}{(p+q)^2} \gamma^y \frac{\not{p}}{p^2} \\ &= -4N_f \delta_{bc} \text{Tr} [\gamma^\mu \gamma^x \gamma^\nu \gamma^y \gamma^\sigma] \int \frac{d^3 p}{(2\pi)^3} \frac{p_\mu (p+q)_\nu p_\sigma}{p^4 (p+q)^2} \\ &= -8i N_f \delta_{bc} (\delta^{\mu x} \epsilon^{y\nu\sigma} + \delta^{\nu y} \epsilon^{x\sigma\mu} + \delta^{\sigma y} \epsilon^{x\nu\mu} - \delta^{\nu\sigma} \delta^{\mu 0}) \int \frac{d^3 p}{(2\pi)^3} \frac{p_\mu (p+q)_\nu p_\sigma}{p^4 (p+q)^2}. \end{aligned} \quad (\text{A.38})$$

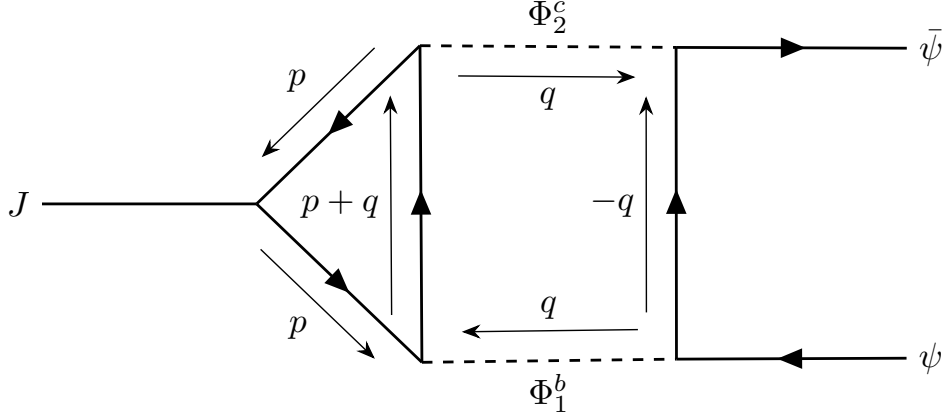


Figure A.2: The  $\mathcal{O}(N_f^{-1})$  two-loop correction to the SO(5) order parameter. We set all external momenta to zero. Shown is one of four possible diagrams - the other three can be obtained by either exchanging  $\Phi_1 \leftrightarrow \Phi_2$ , crossing the lines of the Higgs propagators, or both. All give the same contribution at zero external momenta.

The integral over  $p$  yields

$$\int \frac{d^3 p}{(2\pi)^3} \frac{p_\mu(p+q)_\nu p_\sigma}{p^4(p+q)^2} = \frac{1}{128} \frac{1}{|q|} \left[ 3\delta^{\mu\sigma} q_\nu - \delta^{\sigma\nu} q_\mu - \delta^{\mu\nu} q_\sigma + \frac{q_\mu q_\nu q_\sigma}{q^2} \right] \quad (\text{A.39})$$

and contracting with the tensors in Eq. (A.38) gives the final contribution of the fermion loop

$$\frac{iN_f}{2} \frac{q_0}{|q|} \delta_{bc}. \quad (\text{A.40})$$

We combine this with the remaining loop integral, setting the coefficient  $K$  of the irrelevant operators to zero, to give

$$\begin{aligned} & \frac{i}{2N_f} \delta_{bc} \mu^z \mu^x \sigma^b \sigma^c \int \frac{d^3 q}{(2\pi)^3} \frac{q_0}{|q|} \gamma^x \frac{(-q)}{q^2} \gamma^y \frac{16q^2}{(q_0^2 + q_x^2)(q_0^2 + q_y^2)} \\ &= -\frac{16\mu^y \sigma^a}{N_f} \int \frac{d^3 q}{(2\pi)^3} \frac{q_0^2}{|q|} \frac{1}{(q_0^2 + q_x^2)(q_0^2 + q_y^2)}. \end{aligned} \quad (\text{A.41})$$

Focusing on the integrand, we can compute this by converting to radial coordinates,

$$\begin{aligned} & \int \frac{dz d\theta r dr}{(2\pi)^3} \frac{z^2}{\sqrt{z^2 + r^2}} \frac{1}{(z^2 + r^2 \cos^2 \theta)(z^2 + r^2 \sin^2 \theta)} \\ &= \frac{1}{2\pi^2} \int dz dr \frac{|z|r}{(z^2 + r^2)(2z^2 + r^2)} \\ &= \frac{\ln 2}{4\pi^2} \int dz \frac{1}{|z|}. \end{aligned} \quad (\text{A.42})$$

Hence, this two-loop contribution only contributes a standard logarithm divergence, and is subleading in comparison to the one-loop Higgs corrections.

We also analyze the two-loop corrections to the  $\bar{\psi}\psi$  bilinear, whose symmetry properties correspond to the scalar spin chirality. This is motivated by the fact that  $\log^2$  terms in the  $\mathcal{O}(1/N_f)$  one-loop corrections exactly cancel the  $\log^2$  self-energy terms. Hence, if two-loop corrections only contributed standard logarithm divergences, then the scalar spin chirality would have a power law decay at  $\mathcal{O}(1/N_f)$ . In fact, the two-loop corrections involving two Higgs propagators vanish exactly. If the Higgs propagators are different, as was the case for the Néel corrections, then the trace over  $\mu$  in the fermion loop vanishes. If the Higgs propagators are the same, then the trace over  $\gamma$  vanishes, since

$$\text{Tr}[\gamma^\mu\gamma^x\gamma^\nu\gamma^x\gamma^\sigma]p_\mu(p+q)_\nu p_\sigma = \text{Tr}[\gamma^\mu\gamma^y\gamma^\nu\gamma^y\gamma^\sigma]p_\mu(p+q)_\nu p_\sigma = 0 \quad (\text{A.43})$$

### A.7 DERIVATION OF ONE-LOOP RENORMALIZATION GROUP EQUATIONS

In this appendix, we give a derivation of the renormalization group equations used in the main text. The one-loop contributions to the fermion self-energy  $\Sigma(k)$  are UV divergent, and hence require a UV cutoff  $\Lambda$ . The behavior of the self-energy upon integrating out high-energy modes is dictated by the logarithmic derivative with respect to the cutoff,  $\Lambda \frac{d}{d\Lambda} \Sigma(k)$ . The fact that our propagators are homogeneous functions of the three-momenta allow us to calculate this logarithmic derivative explicitly without reference to a specific cutoff. We assume that our regularized one-loop expression for the self-energy takes the form

$$\Sigma(k) = \int \frac{d^3 p}{(2\pi)^3} F(p+k) G(p) \mathcal{K}\left(\frac{p^2}{\Lambda^2}\right) \mathcal{K}\left(\frac{(k+p)^2}{\Lambda^2}\right) \quad (\text{A.44})$$

where  $F$  and  $G$  are homogeneous functions of the three-momenta with degree  $-1$  - we take  $F$  to be the fermion propagator, and  $G$  to be the boson propagator (either Higgs or gauge) along with the various vertex coefficients. The function  $\mathcal{K}(y)$  serves as a UV cutoff with the property that  $\mathcal{K}(0) = 1$  and  $\mathcal{K}(y)$  falls off rapidly for large  $y$ , i.e.,  $\mathcal{K}(y) = e^{-y}$ . Since we are

interested in the behavior at small momenta, we expand around  $k = 0$ ,

$$\Sigma(k) \approx k_\mu \int \frac{d^3 p}{(2\pi)^3} \left[ \frac{\partial F(p)}{\partial p_\mu} G(p) \mathcal{K}^2 \left( \frac{p^2}{\Lambda^2} \right) + F(p) G(p) \mathcal{K} \left( \frac{p^2}{\Lambda^2} \right) \frac{2p_\mu}{\Lambda^2} \mathcal{K}' \left( \frac{p^2}{\Lambda^2} \right) \right]. \quad (\text{A.45})$$

We then take the logarithmic derivative,

$$\begin{aligned} \Lambda \frac{d}{d\Lambda} \Sigma(k) &\approx k_\mu \int \frac{d^3 p}{(2\pi)^3} \left[ \left\{ -\frac{4p^2}{\Lambda^2} \frac{\partial F(p)}{\partial p_\mu} - 4F(p) \frac{p_\mu}{\Lambda^2} \right\} G(p) \mathcal{K} \left( \frac{p^2}{\Lambda^2} \right) \mathcal{K}' \left( \frac{p^2}{\Lambda^2} \right) \right. \\ &\quad \left. - 4 \frac{p^2 p_\mu}{\Lambda^4} F(p) G(p) \left\{ \mathcal{K} \left( \frac{p^2}{\Lambda^2} \right) \mathcal{K}'' \left( \frac{p^2}{\Lambda^2} \right) + \mathcal{K}'^2 \left( \frac{p^2}{\Lambda^2} \right) \right\} \right]. \end{aligned} \quad (\text{A.46})$$

We now convert to spherical coordinates,  $\vec{p} = y\Lambda(\cos\theta, \sin\theta\sin\phi, \sin\theta\cos\phi)$ , and use the homogeneity property of  $F$  and  $G$  to pull out factors of  $(y\Lambda)^{-1}$ .

$$\begin{aligned} \Lambda \frac{d}{d\Lambda} \Sigma(k) &\approx \frac{k_\mu}{8\pi^3} \int_0^\pi \sin\theta d\theta \int_0^{2\pi} d\phi \left[ \left\{ -4 \frac{\partial F(\hat{p})}{\partial p_\mu} - 4\hat{p}_\mu F(\hat{p}) \right\} G(\hat{p}) \int_0^\infty y dy \mathcal{K}(y^2) \mathcal{K}'(y^2) \right. \\ &\quad \left. - 4\hat{p}_\mu F(\hat{p}) G(\hat{p}) \int_0^\infty y^3 dy \{ \mathcal{K}(y^2) \mathcal{K}''(y^2) + \mathcal{K}'^2(y^2) \} \right]. \end{aligned} \quad (\text{A.47})$$

The integral over  $y$  can be done explicitly via integration by parts, which causes the dependence on the cutoff function  $\mathcal{K}$  to drop out. This leads to the expression cited in the main text

$$\Lambda \frac{d}{d\Lambda} \Sigma(k) = \frac{k_\lambda}{8\pi^3} \int_0^{2\pi} d\phi \int_0^\pi \sin\theta d\theta \frac{\partial F(\hat{p})}{\partial p_\lambda} G(\hat{p}). \quad (\text{A.48})$$

where  $\hat{p} \equiv (\cos\theta, \sin\theta\sin\phi, \sin\theta\cos\phi)$ .

Explicitly, we take, for the Higgs contribution to the self-energy, defining  $Q(p)$  as the fermion propagator,

$$\begin{aligned} F(p) &= (\mu^z \gamma^x + i\mu^x \gamma^y) \sigma^- Q(p) (\mu^z \gamma^x - i\mu^x \gamma^y) \sigma^+ \\ &\quad + (\mu^z \gamma^x - i\mu^x \gamma^y) \sigma^+ Q(p) (\mu^z \gamma^x + i\mu^x \gamma^y) \sigma^-, \\ G(p) &= \frac{1}{\Gamma(p)}. \end{aligned} \quad (\text{A.49})$$

For the gauge contribution,

$$\begin{aligned} F_{\mu\nu}(p) &= [\gamma^\mu + \Phi\mu^y\sigma^z(\delta_{\mu,x}\gamma^y + \delta_{\mu,y}\gamma^x)]Q(p)[\gamma^\nu + \Phi\mu^y\sigma^z(\delta_{\nu,x}\gamma^y + \delta_{\nu,y}\gamma^x)] , \\ G^{\mu\nu}(p) &= (\Pi^{-1}(p))^{\mu\nu} , \end{aligned} \quad (\text{A.50})$$

where the fermion self-energy now contains a summation over  $\mu, \nu$ . A similar approach can be used to regulate the one-loop vertex corrections, which take the form

$$\Xi_i = \int \frac{d^3 p}{(2\pi)^3} H_i(p) \mathcal{K}^3 \left( \frac{p^2}{\Lambda^2} \right) \quad (\text{A.51})$$

where  $H_i(p)$  is a homogeneous function of degree  $-3$ . Upon taking the logarithmic derivative,

$$\Lambda \frac{d}{d\Lambda} \Xi_i = -3 \int \frac{d^3 p}{(2\pi)^3} H_i(p) p^2 \mathcal{K}^2 \left( \frac{p^2}{\Lambda^2} \right) \mathcal{K}' \left( \frac{p^2}{\Lambda^2} \right) . \quad (\text{A.52})$$

Converting to spherical coordinates and integrating by parts, we get

$$\Lambda \frac{d}{d\Lambda} \Xi_i = \frac{1}{8\pi^3} \int_0^{2\pi} d\phi \int_0^\pi \sin \theta d\theta H_i(\hat{p}) . \quad (\text{A.53})$$

Explicitly, the Higgs correction is

$$\begin{aligned} H_i(p) &= Q(p)\mu^i Q(p)(\mu^z\gamma^x + i\mu^x\gamma^y)\sigma^- \frac{1}{\Gamma(p)}(\mu^z\gamma^x - i\mu^x\gamma^y)\sigma^+ \\ &\quad + Q(p)\mu^i Q(p)(\mu^z\gamma^x - i\mu^x\gamma^y)\sigma^+ \frac{1}{\Gamma(p)}(\mu^z\gamma^x + i\mu^x\gamma^y)\sigma^- , \end{aligned} \quad (\text{A.54})$$

and the gauge correction,

$$\begin{aligned} H_i(p) &= Q(p)\mu^i Q(p)[\gamma^\mu + \Phi\mu^y\sigma^z(\delta_{\mu,x}\gamma^y + \delta_{\mu,y}\gamma^x)] \\ &\quad \times (\Pi(p)^{-1})^{\mu\nu}[\gamma^\nu + \Phi\mu^y\sigma^z(\delta_{\nu,x}\gamma^y + \delta_{\nu,y}\gamma^x)] . \end{aligned} \quad (\text{A.55})$$

## A.8 ANISOTROPIC CORRELATION FUNCTIONS IN REAL SPACE

As shown in the main text, the momentum-space Néel correlator is given by

$$G_{\text{Néel}}(k) = \frac{1}{8(1 - \Phi^2)}(|k_+| + |k_-|) \quad (\text{A.56})$$

where we define  $|k_{\pm}| = \sqrt{k_0^2 + (k_x \pm \Phi k_y)^2 + (k_y \pm \Phi k_x)^2}$ . The Fourier transform of this function can be computed with the knowledge of the (suitably regularized) Fourier transform in three dimensions,  $|k| \rightarrow \frac{1}{r^x}$ . We take the Fourier transform

$$\int \frac{d^3k}{(2\pi)^3} e^{ik \cdot r} |k_{\pm}| \quad (A.57)$$

and perform a change of variables to shift the anisotropy to the spatial coordinates

$$\begin{aligned} \frac{1}{1 - \Phi^2} \int \frac{d^3k}{(2\pi)^3} e^{ik \cdot r_{\pm}} |k| \\ t_{\pm} = t \\ x_{\pm} = \frac{1}{1 - \Phi^2} (x \pm \Phi y) \\ y_{\pm} = \frac{1}{1 - \Phi^2} (y \pm \Phi x) \end{aligned} \quad (A.58)$$

which yields the real space correlator given in the main text.

To compute the Fourier transform of the VBS correlator, given perturbatively by

$$G_{\text{VBS}}(k) \sim |k| - \Phi^2 \left[ 2|k| + \frac{k_x^2 k_y^2 - k_0^2 k^2}{|k|^3} \right] + \mathcal{O}(\Phi^4), \quad (A.59)$$

we define the function

$$f(a_i, k_i) = \sqrt{a_0 k_0^2 + a_x k_x^2 + a_y k_y^2}. \quad (A.60)$$

The Fourier transform of this function can be calculated by a similar change of variables,

$$\int \frac{d^3k}{(2\pi)^3} f(a_i, k_i) \sim \frac{1}{\sqrt{a_0 a_x a_y}} \left( \frac{t^2}{a_0} + \frac{x^2}{a_x} + \frac{y^2}{a_y} \right)^{-2}. \quad (A.61)$$

The various terms in the  $\mathcal{O}(\Phi^2)$  corrections to the VBS correlator can be obtained by taking derivatives of  $f(a_i, k_i)$  with respect to  $a_i$  and setting  $a_i = 1$ . This allows us to calculate the real space VBS correlator and gives the result in the main text.

### A.9 PERTURBATIVE CORRECTIONS TO MONPOLE SCALING DIMENSION

In this appendix, we present a partial calculation of the  $\mathcal{O}(N_f)$  corrections to the scaling dimensions of a monopole at our deconfined critical point. As previously established [51], the  $\mathcal{O}(N_f)$  scaling dimension for isotropic QED<sub>3</sub> is  $\Delta = 1.06N_f$ . We present the scaling dimension using our convention, where QED<sub>3</sub> with  $N = 4$  Dirac fermions corresponds to  $N_f = 1$ . Although gauge and Higgs fluctuations give corrections to this value, these corrections are subleading in  $N_f$ , and the only  $\mathcal{O}(N_f)$  correction comes from taking the saddle-point solutions of the bosonic fields and calculating the shift in free energy arising from the anisotropic Dirac dispersion relation. We proceed perturbatively in the Dirac anisotropy parameter  $\Phi$  - this is necessary as the anisotropy will in principle modify the saddle-point monopole configuration of the gauge field. As we will see, to leading order in  $\Phi$ , the gauge field configuration corresponding to the isotropic Dirac monopole will be sufficient.

We start with the action for QED<sub>3</sub> with the allowed velocity anisotropy term, omitting the Higgs fields as they will not play any role in the calculation

$$S = i \int d^3r [\bar{\psi} \not{D} \psi + \Phi \bar{\psi} \mu^y (\gamma^x D_x - \gamma^y D_y)] \psi. \quad (\text{A.62})$$

We leave implicit the summation over the  $4N_f$  fermions. Note that this action is different than in the main text. This is because we follow the convention used in [187], where the gauge field is coupled in the usual way,  $D_\mu \equiv \partial_\mu - iA_\mu$ , and the microscopic SU(2) spin rotation symmetry is implemented explicitly by the  $\sigma^i$  matrices. We refrain from using this convention in the main calculation, as the coupling to the Higgs field is not easily expressible in this form and overall makes the calculation more complicated.

In the absence of a velocity anisotropy, the saddle-point configurations for the gauge field corresponding to  $n$  units of magnetic flux at the origin are given by

$$\overline{A}_n(r) = \frac{n}{2}(1 - \cos\theta) d\phi \quad (\text{A.63})$$

The non-zero anisotropy will affect these saddle-point solutions. The leading order corrections to these solutions are  $\mathcal{O}(\Phi^2)$ , as the  $\mathcal{O}(N_f)$  effective action for the gauge field upon integrating

out the fermions has only corrections of  $\mathcal{O}(\Phi^2)$  and higher. Hence, we write the saddle-point gauge field solution in the presence of a velocity anisotropy as  $A_n(r) \equiv \bar{A}_n(r) + \delta A_n$ , with  $\delta A_n \sim \mathcal{O}(\Phi^2)$ .

In order to calculate the scaling dimension of this monopole, we set  $r = e^\tau$  and perform a Weyl rescaling

$$\begin{aligned} g_{\mu\nu} &\rightarrow e^{-2\tau} g_{\mu\nu} \\ \bar{\psi}, \psi &\rightarrow e^{-\tau} \bar{\psi}, e^{-\tau} \psi \end{aligned} \quad (\text{A.64})$$

This rescaling maps the scaling dimension of the monopole operator to the free energy  $F = -\log Z$  of the system [314].

To leading order in  $N_f$ , we ignore gauge and Higgs fluctuations, and the action reduces down to one of free fermions with a background gauge field. For the isotropic case, this action can be put in a nearly-diagonal form with the aid of monopole harmonics [527] and their spinor generalization [51]. By expanding  $\psi$  in terms of these harmonics,

$$\psi(r) = \int \frac{d\omega}{2\pi} \left[ \sum_{\ell=n/2}^{\infty} \sum_{m=-\ell-1}^{\ell} \Psi_T^{\ell m}(\omega) T_{n,\ell m}(\theta, \phi) + \sum_{\ell=n/2}^{\infty} \sum_{m=-\ell}^{\ell} \Psi_S^{\ell m}(\omega) S_{n,\ell m}(\theta, \phi) \right] e^{-i\omega\tau} \quad (\text{A.65})$$

where  $T_{n,\ell m}$ ,  $S_{n,\ell m}$  are eigenvalues of the orbital angular momentum operator  $\vec{L}^2$  in the presence of a strength  $n$  monopole, with orbital angular momentum  $\ell$  and total angular momentum  $\ell + 1/2$  for  $T_{n,\ell m}$  and  $\ell - 1/2$  for  $S_{n,\ell m}$ . Explicit expressions for the spinor harmonics  $T_{n,\ell m}$  and  $S_{n,\ell m}$  may be found in [51]. The variables  $\Psi_T^{\ell m}$ ,  $\Psi_S^{\ell m}$  are anti-commuting coefficients.

Expanded in this form, the isotropic action with  $\Phi = 0$  can be written as

$$S_0 = \int \frac{d\omega}{2\pi} \sum_{\ell=n/2}^{\infty} \sum_{m=-\ell}^{\ell-1} \begin{pmatrix} \Psi_T^{(\ell-1)m}(\omega)^* & \Psi_S^{\ell m}(\omega)^* \end{pmatrix} \mathbf{N}_{n,\ell}(\omega + i\mathbf{M}_{n,\ell}) \begin{pmatrix} \Psi_T^{(\ell-1)m}(\omega) \\ \Psi_S^{\ell m}(\omega) \end{pmatrix} \quad (\text{A.66})$$

with

$$\begin{aligned} \mathbf{M}_{n,\ell} &= \begin{pmatrix} \ell \left(1 - \frac{n^2}{4\ell^2}\right) & -\frac{n}{2} \sqrt{1 - \frac{n^2}{4\ell^2}} \\ -\frac{n}{2} \sqrt{1 - \frac{n^2}{4\ell^2}} & \ell \left(1 - \frac{n^2}{4\ell^2}\right) \end{pmatrix}, \\ \mathbf{N}_{n,\ell} &= \begin{pmatrix} -\frac{n}{2\ell} & -\sqrt{1 - \frac{n^2}{4\ell^2}} \\ -\sqrt{1 - \frac{n^2}{4\ell^2}} & \frac{n}{2\ell} \end{pmatrix}. \end{aligned} \quad (\text{A.67})$$

The free energy is then given by

$$\log Z_0 = 4N_f \int \frac{d\omega}{2\pi} \sum_{\ell=n/2}^{\infty} \log \det(\mathbf{N}_{n,\ell}(\omega + i\mathbf{M}_{n,\ell})) . \quad (\text{A.68})$$

This expression can be evaluated via zeta function regularization, yielding the aforementioned scaling dimension of  $\Delta = 1.06N_f$ .

Corrections to the free energy as a consequence of a non-zero  $\Phi$  can be calculated perturbatively. Writing the action as  $S = S_0 + \delta S$ , with  $\delta S \sim \mathcal{O}(\Phi)$ , we have

$$\begin{aligned} \log Z &= \log \left[ \int \mathcal{D}\psi \mathcal{D}\bar{\psi} e^{-S} \right] = \log \left[ Z_0 + \int \mathcal{D}\psi \mathcal{D}\bar{\psi} e^{-S_0} \left( -\delta S + \frac{1}{2}\langle \delta S^2 \rangle + \dots \right) \right] \\ &= \log Z_0 - \langle \delta S \rangle + \frac{1}{2}\langle \delta S^2 \rangle + \dots , \end{aligned} \quad (\text{A.69})$$

where the expectation values are evaluated with the isotropic action. There are two components of  $\delta S$  that are  $\mathcal{O}(\Phi^2)$  or lower, as can be seen from Eq. (A.62). The first comes from the velocity anisotropy term  $\Phi \bar{\psi} \mu^y (\gamma^x \overline{D}_x - \gamma^y \overline{D}_y) \psi$ , where the bar indicates that the covariant derivative is defined with the isotropic monopole gauge configuration. The second component arises from  $\mathcal{O}(\Phi^2)$  corrections to the isotropic gauge configuration, which appear in the term  $\bar{\psi} \not{D} \psi$ . Only the first of these corrections gives  $\mathcal{O}(\Phi^2)$  contributions to the free energy; the corrections to the saddle-point gauge configuration  $\delta A_n$  couple to the conserved current  $J^\mu = \bar{\psi} \gamma^\mu \psi + \mathcal{O}(\Phi)$ , whose expectation value vanishes. Hence, the free energy to  $\mathcal{O}(\Phi^2)$  is given by

$$\begin{aligned} F &= \log Z_0 + 2\Phi^2 \text{Tr} \int d^3r d^3r' \langle \bar{\psi}(r)(\gamma^x(\overline{D}_x - \hat{x}) - \gamma^y(\overline{D}_y - \hat{y}))\psi(r) \\ &\quad \times \bar{\psi}(r')(\gamma^x(\overline{D}_x - \hat{x}) - \gamma^y(\overline{D}_y - \hat{y}))\psi(r') \rangle \end{aligned} \quad (\text{A.70})$$

The additional factors of  $\hat{x}, \hat{y}$  arise from the Weyl rescaling.

The calculation in Eq. (A.70) amounts to calculating the two-point function of the fermion bilinear  $\bar{\psi}(r)(\gamma^y(\overline{D}_x - \hat{x}) + \gamma^x(\overline{D}_y - \hat{y}))\psi(r)$ . To this end, we denote the matrix elements of

the operator  $(\gamma^y(\overline{D}_x - \hat{x}) + \gamma^x(\overline{D}_y - \hat{y}))$  in the spinor harmonic basis

$$B_{n,\ell m \ell' m'}(\omega) = \int d\Omega \begin{pmatrix} T_{n,\ell m}^\dagger(\theta, \phi) e^{i\omega\tau} \\ S_{n,\ell m}^\dagger(\theta, \phi) e^{i\omega\tau} \end{pmatrix} [\gamma^y(\overline{D}_x - \hat{x}) + \gamma^x(\overline{D}_y - \hat{y})] \times \begin{pmatrix} T_{n,\ell m}(\theta, \phi) e^{-i\omega\tau} & S_{n,\ell m}(\theta, \phi) e^{-i\omega\tau} \end{pmatrix} \quad (\text{A.71})$$

These functions are exactly calculable in terms of Wigner 3-j symbols, and are only non-zero for  $|\ell - \ell'|, |m - m'| \leq 2$ . In order to calculate these functions, we need the matrix elements

$$\begin{aligned} & \langle Y_{q,\ell m} | \hat{x} | Y_{q,\ell' m'} \rangle \\ & \langle Y_{q,\ell m} | \hat{y} | Y_{q,\ell' m'} \rangle \\ & \langle Y_{q,\ell m} | D_x^\perp | Y_{q,\ell' m'} \rangle \\ & \langle Y_{q,\ell m} | D_y^\perp | Y_{q,\ell' m'} \rangle \end{aligned} \quad (\text{A.72})$$

where  $Y_{q,\ell m}$  is the scalar monopole harmonic [527] in a background monopole of strength  $2q \equiv n$  and  $D_i^\perp$  is the angular component of the covariant derivative  $D_i$ ; the radial component is simply equal to  $\hat{i} \frac{\partial}{\partial \tau}$ . For this, we need the integral formula for three monopole harmonics

$$\begin{aligned} \int d\hat{n} Y_{q,\ell m} Y_{q',\ell' m'} Y_{q'',\ell'' m''} &= (-1)^{\ell+\ell'+\ell''} \sqrt{\frac{(2\ell+1)(2\ell'+1)(2\ell''+1)}{4\pi}} \\ &\times \begin{pmatrix} \ell & \ell' & \ell'' \\ q & q' & q'' \end{pmatrix} \begin{pmatrix} \ell & \ell' & \ell'' \\ m & m' & m'' \end{pmatrix} \end{aligned} \quad (\text{A.73})$$

The first two matrix elements can be easily computed with the identity

$$\begin{aligned}
 \hat{x} &= -\sqrt{\frac{4\pi}{6}} (Y_{0,l,1} - Y_{0,1,-1}) \\
 \hat{y} &= i\sqrt{\frac{4\pi}{6}} (Y_{0,l,1} + Y_{0,1,-1}) \\
 \langle Y_{q,\ell,m} | \hat{x} | Y_{q,\ell',m'} \rangle &= (-1)^{\ell+\ell'+q+m} \sqrt{\frac{(2\ell+1)(2\ell'+1)}{2}} \\
 &\quad \times \begin{pmatrix} \ell & 1 & \ell' \\ -q & 0 & q \end{pmatrix} \left[ \begin{pmatrix} \ell & 1 & \ell' \\ -m & 1 & m' \end{pmatrix} - \begin{pmatrix} \ell & 1 & \ell' \\ -m & -1 & m' \end{pmatrix} \right] \quad (\text{A.74}) \\
 \langle Y_{q,\ell,m} | \hat{y} | Y_{q,\ell',m'} \rangle &= -i(-1)^{\ell+\ell'+q+m} \sqrt{\frac{(2\ell+1)(2\ell'+1)}{2}} \\
 &\quad \times \begin{pmatrix} \ell & 1 & \ell' \\ -q & 0 & q \end{pmatrix} \left[ \begin{pmatrix} \ell & 1 & \ell' \\ -m & 1 & m' \end{pmatrix} + \begin{pmatrix} \ell & 1 & \ell' \\ -m & -1 & m' \end{pmatrix} \right]
 \end{aligned}$$

To calculate the last two matrix elements, we must utilize the raising and lowering angular momenta operators

$$zL_x = z(L_+ + L_-) = D_x^\perp - \hat{y} \frac{\partial}{\partial \phi} \quad (\text{A.75})$$

and similarly for  $D_y^\perp$ . This equation can be easily verified for the angular momenta operators without a monopole background, and we verify numerically that this formula correctly

generalizes to non-zero  $q$ . This leads to the formula

$$\begin{aligned}
 \langle Y_{q,\ell m} | D_x^\perp | Y_{q,\ell' m'} \rangle &= (-1)^{1+\ell+\ell'+q+m} \sqrt{\frac{(2\ell+1)(2\ell'+1)}{4}} \begin{pmatrix} \ell & 1 & \ell' \\ -q & 0 & q \end{pmatrix} \\
 &\times \left[ \sqrt{(\ell'-m')(\ell'+m'+1)} \begin{pmatrix} \ell & 1 & \ell' \\ -m & 0 & m'+1 \end{pmatrix} - \sqrt{(\ell'+m')(\ell'-m'+1)} \begin{pmatrix} \ell & 1 & \ell' \\ -m & 0 & m'-1 \end{pmatrix} \right] \\
 &- im' \langle Y_{q,\ell,m} | \hat{y} | Y_{q,\ell',m'} \rangle \\
 \langle Y_{q,\ell m} | D_y^\perp | Y_{q,\ell' m'} \rangle &= -i(-1)^{1+\ell+\ell'+q+m} \sqrt{\frac{(2\ell+1)(2\ell'+1)}{4}} \begin{pmatrix} \ell & 1 & \ell' \\ -q & 0 & q \end{pmatrix} \\
 &\times \left[ \sqrt{(\ell'-m')(\ell'+m'+1)} \begin{pmatrix} \ell & 1 & \ell' \\ -m & 0 & m'+1 \end{pmatrix} + \sqrt{(\ell'+m')(\ell'-m'+1)} \begin{pmatrix} \ell & 1 & \ell' \\ -m & 0 & m'-1 \end{pmatrix} \right] \\
 &- im' \langle Y_{q,\ell,m} | \hat{y} | Y_{q,\ell',m'} \rangle
 \end{aligned} \tag{A.76}$$

From these matrix elements, the components of  $B_{n,\ell m \ell' m'}$  can be assembled by expressing the spinor monopole harmonics in terms of the scalar harmonics.

Upon obtaining an expression for  $B$ , we have

$$\begin{aligned}
 F = \log Z_0 - 4\Phi^2 \sum_{\ell,\ell',m,m'} \int \frac{d\omega}{2\pi} \text{Tr} \left[ B_{n,\ell m \ell' m'}(\omega) \mathbf{N}_{n,\ell}(\omega + i\mathbf{M}_{n,\ell}) \right. \\
 \left. \times B_{n,\ell' m' \ell m}^\dagger(\omega) \mathbf{N}_{n,\ell'}(\omega - i\mathbf{M}_{n,\ell'}) \right]
 \end{aligned} \tag{A.77}$$

The minus sign outside the summation relative to Eq. A.70 arises from the fermion loop. What remains is a suitable procedure for regularizing the divergent expression in Eq. A.77 - as the functions  $B_{n,\ell m \ell' m'}$  are rather complicated summations of Wigner 3-j symbols, this is a non-trivial task and we leave this as an open question for future study.

# B

## Appendix to Chapter 3

### B.1 DERIVATION OF EFFECTIVE MODEL

For completeness, we summarize the derivation of our effective model, first calculated in [408].

Our starting point is the spin-1/2 Heisenberg antiferromagnet on the triangular lattice,

$$H = \sum_{ij} J_{ij} \vec{S}_i \cdot \vec{S}_j, \quad (\text{B.1})$$

with  $J_{ij}$  short-ranged antiferromagnetic interactions. In our derivation, we will take  $J_{ij} = J$  on nearest-neighbor sites, and 0 otherwise. We use a Schwinger boson representation, where the  $(2S + 1)$  states of a spin- $S$  representation of SU(2) can be represented in terms of bosonic operators  $s_{i\uparrow}, s_{i\downarrow}$ ,

$$|S, m\rangle = \frac{1}{\sqrt{(S+m)!(S-m)!}} \left(s_{i\uparrow}^\dagger\right)^{S+m} \left(s_{i\downarrow}^\dagger\right)^{S-m} |0\rangle \quad (\text{B.2})$$

where  $m = -S, \dots, S$  is the  $z$  component of the spin, and the vacuum  $|0\rangle$  contains no Schwinger bosons. Our physical Hilbert space is obtained by the restriction

$$s_{i\alpha}^\dagger s_i^\alpha = 2S \equiv n_s. \quad (\text{B.3})$$

The  $n_s \rightarrow \infty$  limit is classical and results in non-collinear antiferromagnetic order. In order to retain quantum fluctuations, we additionally generalize the  $\text{SU}(2)$  symmetry to  $\text{USp}(2M)$  and take the limit  $n_s, M \rightarrow \infty$  with  $\kappa = n_s/M$  fixed. The generalization to  $\text{USp}(2M)$  rather than  $\text{SU}(2M)$  is chosen to ensure the existence of a spin singlet state, given by

$$\mathcal{J}^{\alpha\beta} s_{i\alpha}^\dagger s_{j\beta}^\dagger |0\rangle, \quad (\text{B.4})$$

with  $\mathcal{J}^{\alpha\beta}$  a  $2M \times 2M$  matrix,

$$J = \begin{pmatrix} & & & 1 \\ & & -1 & & \\ & & & & 1 \\ & & & -1 & & \\ & & & & & \ddots \\ & & & & & \dots \end{pmatrix} \quad (\text{B.5})$$

and the  $\text{USp}(2M)$  group defined by the set of unitary matrices  $U$  that satisfy  $U^T \mathcal{J} U = \mathcal{J}$ .

Writing our Hamiltonian in Eq. B.1 in terms of Schwinger bosons,

$$H = - \sum_{i>j} \frac{J_{ij}}{2M} \left( \mathcal{J}^{\alpha\beta} s_{i\alpha}^\dagger s_{j\beta}^\dagger \right) \left( \mathcal{J}_{\gamma\delta} s_i^\gamma s_j^\delta \right) \quad (\text{B.6})$$

moving to a path integral representation, and performing a Hubbard-Stratonovich transfor-

mation to decouple the four-boson term, we obtain

$$\begin{aligned} Z &= \int \mathcal{D}\mathcal{Q} \mathcal{D}s \mathcal{D}\lambda \exp\left(-\int_0^\beta \mathcal{L} d\tau\right), \\ \mathcal{L} &= \sum_i \left[ s_{i\alpha}^\dagger \left( \frac{d}{d\tau} + i\lambda_i \right) s_i^\alpha - i\lambda_i n_s \right] \\ &\quad + \sum_{\langle ij \rangle} \left[ M \frac{J_{ij} |\mathcal{Q}_{ij}|^2}{2} - \frac{J_{ij} \mathcal{Q}_{ij}^*}{2} \mathcal{J}^{\alpha\beta} s_{i\alpha} s_{j\beta} + \text{h.c.} \right]. \end{aligned} \quad (\text{B.7})$$

This Lagrangian has U(1) gauge invariance, under which

$$\begin{aligned} s_{i\alpha}^\dagger &\rightarrow s_{i\alpha}^\dagger \exp(i\rho_i(\tau)), \\ \mathcal{Q}_{ij} &\rightarrow \mathcal{Q}_{ij} \exp(i\rho_i(\tau) - i\rho_j(\tau)), \\ \lambda_i &\rightarrow \lambda_i + \frac{\partial \rho_i}{\partial \tau}. \end{aligned} \quad (\text{B.8})$$

The saddle-point solutions  $\bar{\mathcal{Q}}, \bar{\lambda}$  of Eq. B.7 have been obtained previously [408]. The saddle-point values  $\bar{\mathcal{Q}}$  satisfy

$$\bar{\mathcal{Q}}_{ij} = \langle \mathcal{J}_{\alpha\beta} s_i^\alpha s_j^\beta \rangle, \quad (\text{B.9})$$

which imply anti-symmetry under exchange of  $i$  and  $j$ . These saddle-point solutions can be chosen to satisfy  $\mathcal{Q}_{i,i+\hat{e}_p} = \bar{\mathcal{Q}}$ ,  $i\lambda_i = \bar{\lambda}$ , where the unit vectors  $\hat{e}_p$

$$\hat{e}_1 = \left( \frac{1}{2}, \frac{\sqrt{3}}{2} \right)$$

$$\hat{e}_2 = \left( \frac{1}{2}, -\frac{\sqrt{3}}{2} \right) \quad (\text{B.10})$$

$$\hat{e}_3 = (-1, 0)$$

point between nearest neighbor sites. The anti-symmetry under exchange of  $i$  and  $j$  implies that the mean-field solution for  $\mathcal{Q}$  will break reflection symmetry; however, reflection symmetry can be restored by a gauge transformation. Of note are non-translationally-invariant saddle-point solutions for  $\mathcal{Q}$  [198], whose solutions  $\mathcal{Q}_{ij}^v$  relative to the translationally-invariant saddle-point correspond to a localized defect, along with a “branch cut” extended outwards

from the core, where  $\text{sgn}(\mathcal{Q}_{ij}^v) = -\text{sgn}(\overline{\mathcal{Q}}_{ij})$ . These saddle-point solutions are identified with gapped vison excitations in the corresponding  $\mathbb{Z}_2$  spin liquid, whose exchange statistics with the Schwinger bosons are mutual semions.

Taking these saddle-point solutions, the hopping term  $\mathcal{J}^{\alpha\beta} s_{i\alpha} s_{j\beta}$  can be diagonalized, leading to a continuum Lagrangian

$$\begin{aligned}\mathcal{L} = & x_\alpha^* \frac{\partial x_\alpha}{\partial \tau} + y_\alpha^* \frac{\partial z_\alpha}{\partial \tau} + z_\alpha^* \frac{\partial y_\alpha}{\partial \tau} + \left( \bar{\lambda} - 3\sqrt{3}J\overline{\mathcal{Q}}/2 \right) |z_\alpha|^2 \\ & + \left( \bar{\lambda} + 3\sqrt{3}J\overline{\mathcal{Q}}/2 \right) |y_\alpha|^2 + \bar{\lambda}|x_\alpha|^2 + \frac{3J\overline{\mathcal{Q}}}{2} \left( |\partial_x z_\alpha|^2 + |\partial_y z_\alpha|^2 \right) + \dots\end{aligned}\quad (\text{B.11})$$

where we have written our bosonic spinons  $s_{i\alpha}$  in terms of three variables  $x_\alpha, y_\alpha, z_\alpha$ , related by a unitary transformation to the three bosonic spinons on the three site of each unit cell. The bosonic spinon  $z_\alpha$  has the lowest mass, and hence the transition between the theory with antiferromagnetic long-range order ( $\langle \vec{S}_i \rangle \neq 0$ ) and the quantum-disordered phase is driven by the condensation of  $z_\alpha$ . The other spinon fields can be integrated out, yielding the effective Lagrangian

$$\begin{aligned}\mathcal{L} = & \frac{1}{\bar{\lambda} + 3\sqrt{3}J\overline{\mathcal{Q}}/2} |\partial_\tau z_\alpha|^2 + \frac{3J\overline{\mathcal{Q}}\sqrt{3}}{8} \left( |\partial_x z_\alpha|^2 + |\partial_y z_\alpha|^2 \right) \\ & + \left( \bar{\lambda} - 3\sqrt{3}J\overline{\mathcal{Q}}/2 \right) |z_\alpha|^2 + \dots\end{aligned}\quad (\text{B.12})$$

Provided the visons remain gapped, this theory describes a deconfined critical point separating a state with long-range antiferromagnetic order to an odd  $\mathbb{Z}_2$  spin liquid. One may additionally consider a possible vison condensation, where the vison Berry phase will lead to valence bond solid ordering. These two transitions can be captured in the partition function

$$\begin{aligned}\mathcal{Z} = & \sum_{s_{j,j+\hat{\mu}}=\pm 1} \prod_j \int dz_{j\alpha} \delta \left( \sum_\alpha |z_{j\alpha}^2| - 1 \right) \left[ \prod_j s_{j,j+\tau} \right]^{2S} \exp(-H[z_\alpha, s]) \\ H[z_\alpha, s] = & -\frac{J}{2} \sum_{\langle j,\mu \rangle} s_{j,j+\hat{\mu}} (z_{j,\alpha}^* z_{j+\hat{\mu},\alpha} + \text{c.c.}) - K \sum_{\Delta\Box} \prod_{\Delta\Box} s_{j,j+\hat{\mu}},\end{aligned}\quad (\text{B.13})$$

where we have introduced the  $\mathbb{Z}_2$  gauge field  $s_{ij}$  defined on the links of our lattice. The model is defined on a three-dimensional stacked triangular lattice, where we have discretized our temporal direction. For large  $J$ , fluctuations of  $z$  are suppressed and we recover Néel order. For small  $K$ , vison excitations proliferate and we obtain either a trivial phase (integer  $S$ )

or valence bond solid order (half-integer  $S$ ). Importantly, we must include a Berry phase term  $\prod_j s_{j,j+\tau}$ , which is non-trivial for half-integer spin. In particular, this Berry phase is an obstacle for using classical Monte Carlo methods to evaluate the partition function for half-integer spin, as the sign of each term in the partition function may be either positive or negative and hence prevents evaluation via probabilistic sampling. One of the results of this work is to derive a sign-free representation of Eq. 3.2 amenable to Monte Carlo studies.

## B.2 DETAILS OF NUMERICAL SIMULATIONS

Here, we provide additional information regarding Monte Carlo simulations of our effective model. A single Monte Carlo simulation consists of  $10^6$  sweeps, where a single sweep consists of  $L^3$  of each of the local and cluster updates described in the main text. The first 50% of sweeps are used to thermalize the system. All measurements are averaged over 100 runs with different random seeds. We use the Xoshiro256+ algorithm for generating random numbers. In order to reduce the computational bottleneck arising from repeated evaluations of the modified Bessel function  $I_p(x)$  present in our partition function, we pre-compute a lookup table of size  $10 \times 10^4$  for integer values of  $0 \leq p < 10$  and a discretized grid of size  $10^4$  of  $x$  values between 0 and the maximum possible value of  $x$ ,  $J/2$ . With this, the majority of the computation time is spent computing geometric information, such as finding nearest neighbor sites or the bonds surrounding a plaquette. A large amount of geometric data is relevant for our simulations as we work with sites, bonds, dual sites, and dual bonds; as a result, pre-computing all the required geometric data and storing it in memory leads to a large number of cache misses and is ultimately slower than computing the information each time.

## B.3 SURFACE WORM ALGORITHM

Details of the surface worm algorithm (SWA), first discussed in [106], are presented here.

The idea behind the SWA, as with worm algorithms more generally, is to generate large moves via probabilistically moving through unphysical configurations such that the final physical configuration obeys detailed balance with respect to the original one. Traditional worm algorithms are applied to systems where physical configurations correspond to some form of

closed loops, and the unphysical configurations that the algorithm moves through are ones with an open loop. For gauge-Higgs models, this simple application is not appropriate - the closed loops correspond to bosonic worldlines, and the presence of a gauge field means that worldlines of charged operators must form the boundary of a surface of gauge flux. Rather than growing a single current, the SWA grows a “ligament” corresponding to two parallel current loops bounded by flux. This process is illustrated in Fig B.1.

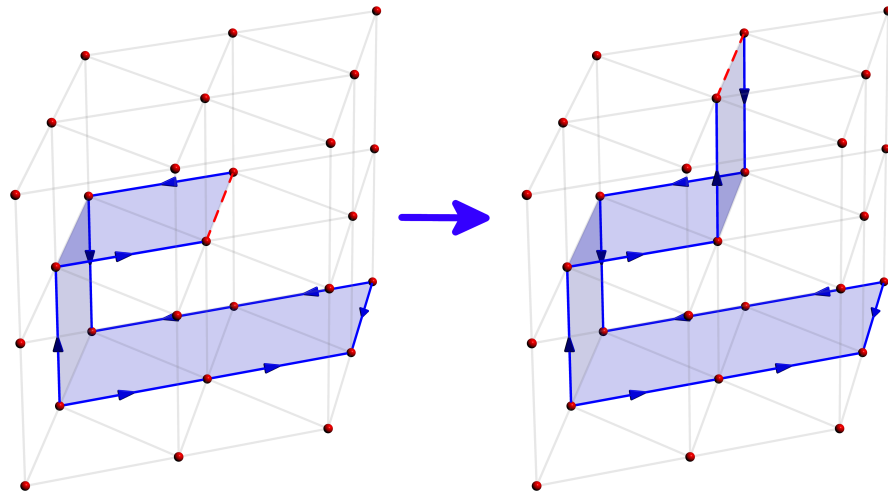


Figure B.1: We illustrate the growing of a “surface worm” using the SWA. At each step, the worm can either attempt to grow in a random direction or attempt to close the loop. Each move is accepted probabilistically according to the Metropolis algorithm. Note that this worm can move in all directions, not just the two-dimensional plane illustrated.

There is a geometric subtlety in implementing the SWA here, which arises from the non-cubic lattice structure. For a cubic lattice, all possible moves from a given bond are chosen with equal probability. For a stacked triangular lattice, there is a difference depending on whether the constraint-violating bond is a spatial and temporal bond - the former has 10 possible moves, whereas the latter has 18. In order to maintain detailed balance, the probability of picking a temporal bond while on a spatial one must equal the probability of picking a spatial bond while on a temporal one. To enforce this constraint, all 18 moves from a temporal bond are chosen with equal probability, and the moves from a spatial bond are chosen in a skewed manner such that the probability of moving to any of the four neighboring temporal bonds is  $4 \times \frac{1}{18}$ .

#### B.4 CLUSTER ALGORITHM FOR DUAL ISING MODEL

Here, we provide more details on the cluster updates we use for the dual Ising degrees of freedom. This style of updates was described in [320]. The update we use is a variant on the Wolff cluster update [524], a well-known cluster algorithm for efficiently generating global moves in Ising models. However, this algorithm becomes inefficient in the presence of frustration. As our dual Ising model only has frustration in the spatial bonds, we adapt the algorithm such that clusters are only grown along the frustration-free temporal bonds - a standard Wolff algorithm may still in principle be used and will lead to comparable convergence times when measured in terms of Monte Carlo steps, but will be significantly more computationally demanding than this more targeted cluster update.

We apply this algorithm to both single dual sites and pairs of dual sites - the latter is necessary as movement between low-energy configurations is accomplished by flipping neighboring pairs of spins. For a single site update, we pick a dual site  $\bar{j}$  at random and calculate the energy  $\Delta E_s$  incurred from the spatial bonds after flipping the Ising degree of freedom on that site. This site is then added to our cluster. We grow the cluster in the temporal direction, where growing a cluster in the  $\pm\tau$  direction is accepted with probability  $p = \min\{0, 1 - e^{-2K_d^\tau \sigma_j \sigma_{j\pm\tau}}\}$ . The energy from the spatial bonds of these spins are added to  $\Delta E_s$ . Once the cluster has finished growing, the entire cluster is flipped with probability  $\min\{0, e^{-\Delta E_s}\}$ . This illustrates the necessity for keeping the temporal coupling  $K_d^\tau$  relatively small, as a sufficiently large  $K_d^\tau$  will lead to clusters spanning the entire temporal direction and our model effectively reduces to that of a classical 2D Ising model.

For performing this update on a pair of neighboring dual sites  $\bar{j}, \bar{k}$ , we proceed in an identical fashion, growing of a cluster in the  $\pm\tau$  direction with probability  $p = \min\{0, 1 - e^{-2K_d^\tau (\sigma_j \sigma_{j\pm\tau} + \sigma_k \sigma_{k\pm\tau})}\}$ . The inclusion of these moves are important as  $\Delta E_s$  will generally be much smaller for these moves.

# C

## Appendix to Chapter 5

### C.1 PERTURBATIVE DERIVATION OF THE CONDITION FOR REALITY OF EIGENVALUES

Here we provide a formal derivation of the statement of Sec. 4.2 of the main text that the eigenvalues of any (almost) degenerate subspace of  $H_0$  in Eq. (4.2b) will remain real upon adiabatically turning on the non-Hermitian perturbation  $\epsilon V$ , if all states in the (almost) degenerate subspace have the same eigenvalue under the metric operator  $\eta$ . We will discuss two different perturbative expansions and prove that the above holds true to all orders. We will then discuss the approximate orthogonality of the associated eigenstates.

To this end, we will consider a pseudo-Hermitian Hamiltonian of the form of Eq. (4.2b),

$$H_\epsilon = H_0 + \epsilon V, \quad \epsilon \in \mathbb{R}, \tag{C.1}$$

and a metric operator  $\eta$ , such that  $[\eta, H_0] = 0$  for the Hermitian unperturbed part,  $H_0 = H_0^\dagger$ , and  $\eta V \eta^{-1} = V^\dagger$  for the perturbation.

We are interested in the behavior of the eigenvalues of a subset of (orthonormal) eigenstates,  $\{|\psi_i\rangle, i = 1, \dots, n\}$ , of  $H_0$ , which can be arbitrarily close or identical in energy but are well

separated from all other eigenvalues. We refer to the space spanned by  $\{|\psi_i\rangle, i = 1, \dots, n\}$  as the almost degenerate subspace.

To analyze how their eigenvalues,  $E_i(\epsilon)$ ,  $i = 1, 2, \dots, n$ , evolve when turning on  $\epsilon V$  in Eq. (C.1), we define the projectors  $P$  and  $Q$ ,

$$P = \sum_{i=1}^n |\psi_i\rangle \langle \psi_i|, \quad Q = \mathbb{1} - P,$$

to the almost degenerate subspace and its complement. We use that the exact eigenstates,  $|\Psi_i(\epsilon)\rangle$ , obeying

$$H_\epsilon |\Psi_i(\epsilon)\rangle = E_i(\epsilon) |\Psi_i(\epsilon)\rangle,$$

must also satisfy [62]

$$H_\epsilon^{\text{eff}}(E_i(\epsilon))P |\Psi_i(\epsilon)\rangle = E_i(\epsilon)P |\Psi_i(\epsilon)\rangle \quad (\text{C.2})$$

with the effective Hamiltonian

$$H_\epsilon^{\text{eff}}(E) = PH_\epsilon P + PH_\epsilon QG_\epsilon(E)QH_\epsilon P, \quad (\text{C.3})$$

$$G_\epsilon(E) = [E - QH_\epsilon Q]^{-1}. \quad (\text{C.4})$$

As follows from Eq. (C.2), the eigenvalues  $E_i(\epsilon)$ ,  $i = 1, 2, \dots, n$ , can be obtained by diagonalizing the effective Hamiltonian  $H_\epsilon^{\text{eff}}$  in the almost degenerate subspace. Of course, this is not straightforward to do as the effective Hamiltonian itself depends on these eigenvalues; however, the effective-Hamiltonian formulation is a good starting point to develop a perturbative expansion.

### C.1.1 EXPANSION IN $\epsilon$

Since we view the non-Hermitian part  $\epsilon V$  as a perturbation to  $H_0$  in our discussion in the main text, it is very natural to expand in  $\epsilon$ . Note that  $PH_0Q = 0$ , so the second term in the effective Hamiltonian (C.3) is  $\mathcal{O}(\epsilon^2)$ ,

$$H_\epsilon^{\text{eff}}(E) = PH_0P + \epsilon PVP + \epsilon^2 PVQG_\epsilon(E)QVP. \quad (\text{C.5})$$

Let us now assume that we can obtain  $E_i(\epsilon)$  via perturbative expansion in  $\epsilon$ . To keep the notation compact, let us define the operator  $T_N$  which performs a Taylor expansion on a function or operator up to and including order  $N$ , i.e.,  $T_N[f(x)] := \sum_{k=0}^N \frac{x^k}{k!} \frac{df}{dx}(0)$ . As follows from Eq. (C.5),  $T_1[E_i(\epsilon)]$ , for any  $i = 1, 2, \dots, n$ , is obtained by diagonalization of

$$h_{ij}^{(1)} := \langle \psi_i | (H_0 + \epsilon V) | \psi_j \rangle, \quad i, j = 1, 2, \dots, n. \quad (\text{C.6})$$

Since, by construction, all  $|\psi_i\rangle$  have the same eigenvalue under  $\eta$ , we conclude from Eq. (4.3) that  $h_{ij}^{(1)}$  is Hermitian and, thus,  $T_1[E_i(\epsilon)] \in \mathbb{R}$ . Higher orders,  $T_{N>1}[E_i(\epsilon)]$ , are obtained by iteratively diagonalizing

$$\begin{aligned} h_{ij}^{(N)} := & \langle \psi_i | (H_0 + \epsilon V \\ & + \epsilon^2 T_{N-2}[VQG_\epsilon(T_{N-2}[E_i(\epsilon)])QV]) | \psi_j \rangle. \end{aligned} \quad (\text{C.7})$$

First, note that  $Q$  commutes with  $\eta$  which implies that  $G_\epsilon(E)$  and, thus, also  $VQG_\epsilon(E)QV$  are pseudo-Hermitian if  $E \in \mathbb{R}$ . Since this holds for a continuous set of values of  $\epsilon$ , this property holds for each order in the Taylor expansion separately. As such, it also applies to  $T_{N-2}[VQG_\epsilon(E)QV]$  in Eq. (C.7). Due to  $T_1[E_i(\epsilon)] \in \mathbb{R}$ , iterative diagonalization of Eq. (C.7) will always yield real eigenvalues. Taken together we have shown that  $E_i(\epsilon)$ ,  $i = 1, 2, \dots, n$ , stay real to any order in  $\epsilon$ .

If the eigenstates are exactly degenerate for  $\epsilon = 0$ , the leading non-zero contribution to the energy splitting will determine whether the eigenvalues of  $H_\epsilon$  stay real or become complex. In most cases, the first order corrections, given by diagonalizing  $PH_\epsilon P$ , break the degeneracy. Since  $PH_\epsilon P$  is clearly Hermitian, our result is simple if the first order energy splitting is non-zero. In fact, a mathematical proof to first order in perturbation theory has been provided in Ref. [65]. However, topological degeneracies are often broken only at higher orders in perturbation theory, so a more general result is required.

If, however, the degeneracy is already broken for  $\epsilon = 0$ , our current perturbative approach cannot be used to understand whether the eigenvalues stay real or not: by construction, we assume that  $E_i(\epsilon)$  is an analytic function of  $\epsilon$  and therefore will never be able to reproduce the  $\epsilon$  dependence of real eigenvalues meeting and moving into the complex plane. For this

reason, we next present an alternative approach.

### C.1.2 EXPANSION IN ENERGY SEPARATION

The problem noted above that arises when the eigenstates of  $H_0$  are not exactly degenerate can be reconciled by performing an expansion in the energy gap between the almost degenerate subspace and the rest of spectrum. More formally, we generalize the effective Schrödinger equation (C.2) by introduction of a dimensionless parameter  $\lambda$ ,

$$H_{\epsilon,\lambda}^{\text{eff}}(E_{i\epsilon}(\lambda))P|\Psi_{i\epsilon}(\lambda)\rangle = E_{i\epsilon}(\lambda)P|\Psi_{i\epsilon}(\lambda)\rangle, \quad (\text{C.8})$$

where

$$H_{\epsilon,\lambda}^{\text{eff}}(E) = PH_\epsilon P + \lambda PH_\epsilon QG_\epsilon(E)QH_\epsilon P. \quad (\text{C.9})$$

We assume that we can expand  $E_{i\epsilon}(\lambda)$  in a power series of  $\lambda$ , but treat its  $\epsilon$ -dependence exactly, and show that it stays real to all orders in  $\lambda$ . Since  $\lambda$  multiplies  $G_\epsilon$  in Eq. (C.9), this expansion is controlled by the gap to the other states of the spectrum being large (compared to  $\epsilon V$ ). The argument proceeds similar to the one above: the zeroth order contribution,  $T_0[E_{i\epsilon}(\lambda)] = E_{i\epsilon}(0)$ , is obtained from diagonalization of Eq. (C.6) and as such real. One can compute  $T_N[E_{i\epsilon}(\lambda)]$  from  $T_{N-1}[E_{i\epsilon}(\lambda)]$  by iterative diagonalization of

$$\begin{aligned} h_{ij}^{(N)} &:= \\ \langle \psi_i | (H_\epsilon + \lambda T_{N-1}[H_\epsilon QG_\epsilon(T_{N-1}[E_{i\epsilon}(\lambda)])QH_\epsilon]) | \psi_j \rangle. \end{aligned}$$

With the same arguments as above, this implies that  $T_N[E_{i\epsilon}(\lambda)]$  will stay real for any  $N$ . Of course, the perturbative approach is expected to break down when the gap between the almost degenerate subspace and another part of the spectrum with different eigenvalue under  $\eta$  closes since  $G_\epsilon$  will develop a pole.

### C.1.3 APPROXIMATE ORTHOGONALITY

Above, we have argued that the effective Hamiltonians in Eqs. (C.3) and (C.9) will be Hermitian if the eigenvalues of  $\eta$  are identical in the almost degenerate subspace. This does not only

have consequences for the reality of the eigenvalues, but also for their mutual orthogonality.

To first order in  $\epsilon$  and zeroth order in  $\lambda$ , i.e., to leading order in the limit of a large gap to the excited states, the effective Hamiltonian is also independent of  $E$ . Therefore, the projections  $P |\Psi_i(\epsilon)\rangle$ ,  $i = 1, 2, \dots, n$ , are obtained as eigenstates of the same Hermitian Hamiltonian and, as such, orthogonal. Naturally, this does not mean that  $|\Psi_i(\epsilon)\rangle$  are orthogonal in the full Hilbert space; however, the differences between the full and the projected states,  $|\Psi_i(\epsilon)\rangle - P |\Psi_i(\epsilon)\rangle = Q |\Psi_i(\epsilon)\rangle$ , are also suppressed in the limit of large energetic separation to the rest of the spectrum since [62]

$$Q |\Psi_i(\epsilon)\rangle = \epsilon G_\epsilon(E_i(\epsilon)) Q V P |\Psi_i(\epsilon)\rangle, \quad (\text{C.10})$$

as stated in the main text.

## C.2 INTERPLAY BETWEEN X-CUBE FOLIATION AND METRIC OPERATORS

In the main paper, we noted that the ground states of the X-cube model all have the same eigenvalue under our choice of metric operator  $\eta$  in Eq. (4.5), provided all lengths are even. This is because  $\eta$  can be assembled by a collection of stabilizers. While  $\eta$  cannot be assembled by stabilizers on a system with odd lengths, it is known that the X-cube model exhibits *foliated fracton order* [450], which implies that an  $L \times L \times L$  X-cube model ground state can be enlarged to a ground state of an  $L \times L \times L + 1$  model by the attachment of an  $L \times L$  toric code ground state and the application of local unitary operators. If  $L$  is even, then the original X-cube ground states and the toric code ground states will all have the same eigenvalue under  $\eta$ . Because of this, one may suspect that the resulting  $L \times L \times L + 1$  ground states may also have the same eigenvalue under the appropriately enlarged  $\eta$ . However, as we will show, the process of attaching the two states and applying local unitary operators yields an  $L \times L \times L + 1$  state that is not an eigenstate of the enlarged  $\eta$ .

We first describe the process of adding an extra layer to the X-cube model, illustrated in Fig. C.1. We begin with an  $L \times L \times L$  X-cube ground state,  $|\psi_X\rangle$ , an  $L \times L$  toric code ground state,  $|\psi_{TC}\rangle$ , and a collection of  $L^2$  additional qubits initialized in the  $|0\rangle$  state,  $Z|0\rangle = |0\rangle$ . The statement of foliated fracton order is that an  $L \times L \times L + 1$  X-cube ground state,  $|\psi'_X\rangle$ ,

can be written as

$$|\psi'_X\rangle = S \left( |\psi_X\rangle \otimes |\psi_{TC}\rangle \otimes |0\rangle^{L^2} \right)$$

where  $S$  is a series of local unitary transformations, which in our case is given by a collection of CNOT gates [450].

This foliation allows us to deduce the behavior of  $\eta$  in Eq. (4.5) applied to  $|\psi'_X\rangle$  based on the action of  $S^\dagger \eta S$  on the three constituent states, assuming  $L$  is even. This behavior is dependent on the form of  $\eta$ . We first begin with an analysis of  $\eta_Z \equiv \prod_i Z_i$ . Carrying out the corresponding CNOT gate transformations, we see in Fig. C.2 that the action of  $S^\dagger \eta_Z S$  on the original X-cube ground state is not simply the product of all  $Z_i$  operators—some sites are missing in a way that cannot simply be compensated by a product of stabilizers; this means that  $|\psi_X\rangle \otimes |\psi_{TC}\rangle \otimes |0\rangle^{L^2}$  will generally not be an eigenstate of  $S^\dagger \eta_Z S$ . Carrying this through with  $\eta_X = \prod_i X_i$  and  $\eta_Y = \prod_i Y_i$  yields a similar result. In accordance with the analysis of the main text, we conclude that not every ground state of an even-by-even-by-odd X-cube model will be an eigenstate of  $\eta$ , as the foliation process complicates the behavior of the metric operator.

One can take this  $L \times L \times L + 1$  model and attach additional toric code layers in either of the two remaining directions, and an identical analysis implies that even-by-odd-by-odd and odd-by-odd-by-odd ground states will not all have the same eigenvalue under  $\eta$ . Of course, one can add another toric code layer to give an  $L \times L \times L + 2$  model, in which case the metric operator *does* decompose nicely into the metric operators on the constituent ground states.

### C.3 HAAH’S CUBIC CODES

In this section, we provide a more detailed account of Haah’s 17 cubic codes, and the behavior of their ground states under pseudo-Hermitian perturbations. Throughout, we assume periodic boundary conditions as before.

Haah’s 17 CSS cubic codes [174] are defined on a cubic lattice, with two Pauli spins on each vertex,  $i$ . There are two classes of stabilizers—one consisting solely of  $Z$  operators, and the other with  $X$  operators. The structure of these stabilizers is detailed in Fig. C.3 and

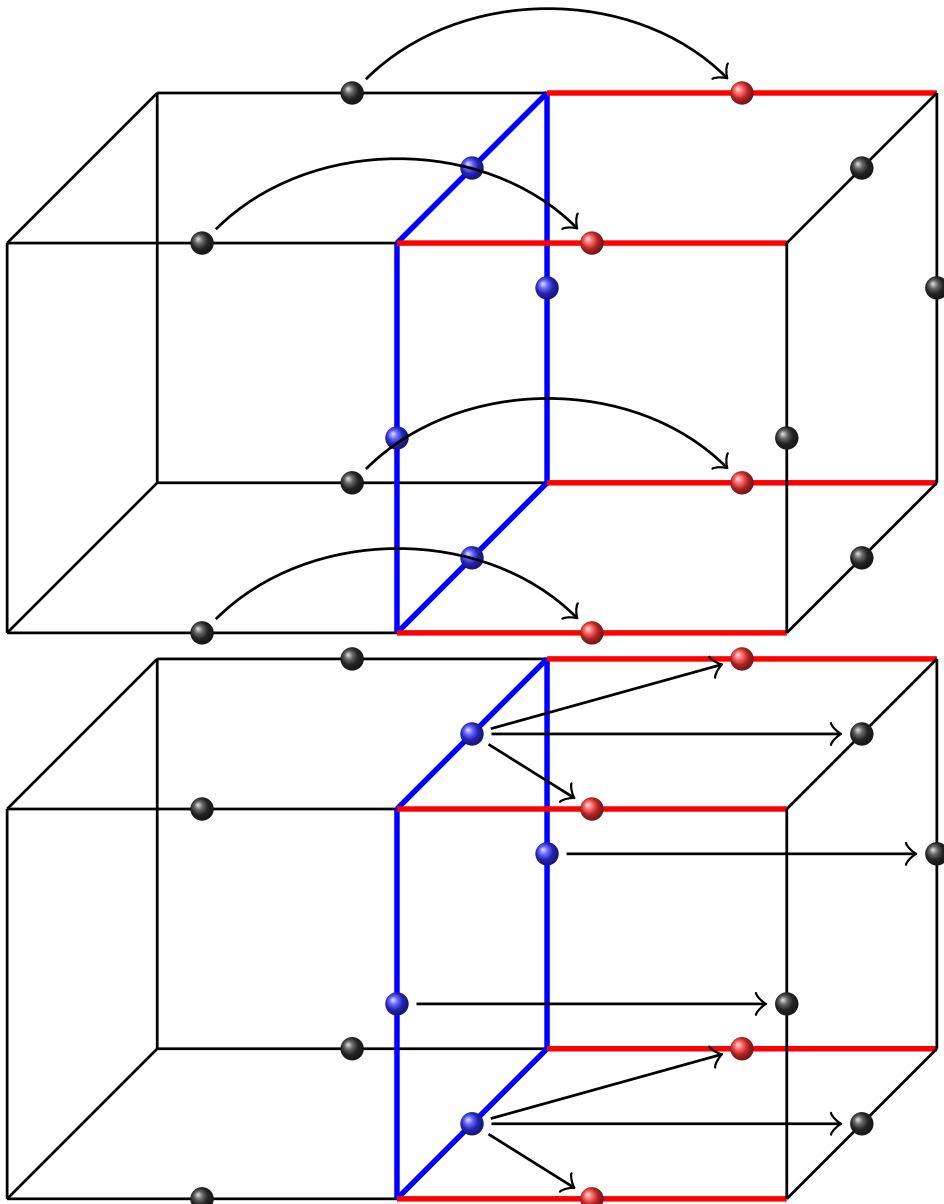


Figure C.1: The size of an X-cube model ground state can be increased along one axis by adding a layer of toric code (blue) and an additional set of qubits initialized in the  $|0\rangle$  state (red). A series of CNOT gates are applied to this tensor product of states to yield an enlarged X-cube model ground state. The application of the CNOT gates is shown above, with arrows pointing from the control to the target qubit. The CNOT gates are applied in two steps—the gates in the top diagram are used first, then the gates in the bottom diagram are applied.

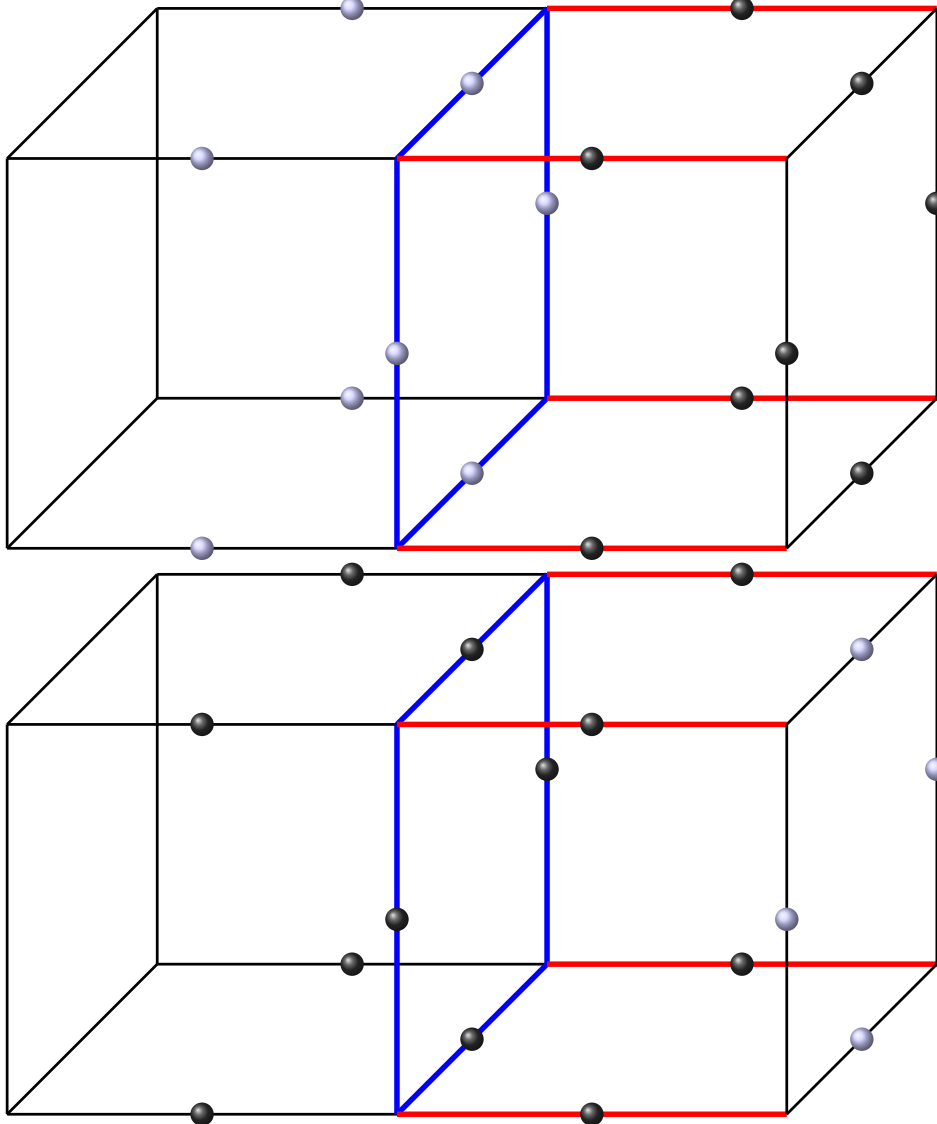


Figure C.2: The behavior of the metric operator  $\eta$  on an  $L \times L \times L + 1$  X-cube model ground state can be calculated by an effective operator,  $S^\dagger \eta S$ , acting on the exfoliated parts of the X-cube model. Here, we show the action of  $S^\dagger \eta_Z S$  (top) and  $S^\dagger \eta_X S$  (bottom), where the effective operator is the product of Z (X) operators on all the dark sites. The tensor product of the exfoliated parts of the X-cube ground state is not generally an eigenstate of the corresponding effective operators. The decomposition of  $\eta_Y$  is identical to that of  $\eta_X$ .

Table C.1. In the polynomial representation used in Sec. 4.5.1, the stabilizers take the general form  $Z(f, g)$  and  $X(\bar{g}, \bar{f})$  for polynomials  $f$  and  $g$ . As stated in the main text, these codes admit a large set of possible pseudo-Hermitian perturbations that leave the code subspace real: in analogy to Eq. (4.5), a very natural set of choices for the metric operator  $\eta$  is given by Eq. (4.14).

Since all the stabilizers in Haah’s cubic codes are mutually commuting, all ground states have the same eigenvalue under  $\eta$ , provided  $\eta$  can be assembled by stabilizers. For the toric code, the X-cube and checkerboard model discussed in the main text, it is straightforward both to find the combination of stabilizers that yield  $\eta$  on a lattice with an even number of sites in all directions, and to show that  $\eta$  cannot be made of stabilizers on any other lattice. For Haah’s codes, the more complex form of the stabilizers makes the analysis more demanding, but possible using the polynomial representation of stabilizers [302].

Using the same conventions as in Sec. 4.5.1, the metric operators in Eq. (4.14) can be written as

$$\begin{aligned} \eta &= Z(h, h), X(h, h), iX(h, h)Z(h, h), \\ h &= \sum_{j=1}^{L_x} \sum_{k=1}^{L_y} \sum_{\ell=1}^{L_z} x^{j-1} y^{k-1} z^{\ell-1}. \end{aligned} \tag{C.11}$$

We will first consider  $\eta = Z(h, h)$ . For stabilizers  $Z(f, g)$ , a choice of covering (i.e., a product of stabilizers at different points) can be specified by a *covering polynomial*  $k$ , with the covering given by  $Z(kf, kg)$ . For example, if  $k = 1 + x$ , then the covering  $Z(kf, kg)$  would consist of the product of two stabilizers—one at the origin, and one at  $(x, y, z) = (1, 0, 0)$ . Therefore, the question of whether  $\eta$  can be assembled from stabilizers is equivalent to the question of whether  $h = kf = kg$  for some polynomial  $k$ . Mathematically, this factorization takes place in the quotient ring  $P/I$ , where  $P$  is the ring of polynomials of three variables with coefficients over  $\mathbb{F}_2$ , and  $I$  is the ideal generated by  $x^{L_x} + 1$ ,  $y^{L_y} + 1$ , and  $z^{L_z} + 1$ . This quotienting procedure imposes the periodic boundary conditions of the model.

We calculate this factorization with the computer algebra system SageMath. Generically, this factorization procedure will yield two different coverings,  $h = k_f f = k_g g$ . To determine whether these two coverings are compatible, we calculate whether  $k_f + k_g$  can be separated

into two polynomials  $d_f + d_g$ , where  $d_f \in (I : f)$  and  $d_g \in (I : g)$ , where  $(I : f)$  is the *colon ideal*,  $(I : f) = \{p \in P : pf \in I\}$ . This is equivalent to checking whether  $k_f + k_g$  belongs to the ideal generated by  $(I : f) \cup (I : g)$ . If such a separation exists, then  $k_f + d_f = k_g + d_g \equiv k$ , and  $h = kf = kg$  in  $P/I$ . This covering may not be unique, as  $k + d_{fg}$  also works as a covering, where  $d_{fg} \in (I : f) \cap (I : g)$ ; however, for the purposes of understanding the behavior of non-Hermitian perturbations, we are only interested in the existence of such a covering. We note that this procedure should always be able to find a covering  $k$  if it exists, so if a decomposition  $k_f + k_g = d_f + d_g$  does not exist, it should imply the non-existence of a covering.

Once we have obtained the covering  $k$  for  $Z(h, h)$ , we immediately know that  $X(h, h)$  in Eq. (C.11) can be assembled from  $X$ -stabilizers with the covering  $\bar{k}$ , since  $X(\bar{k}\bar{g}, \bar{k}\bar{f}) = X(\bar{h}, \bar{h}) = X(h, h)$ .

This calculation is done in SageMath for system sizes  $L_x \times L_y \times L_z$  for  $1 \leq L_x, L_y, L_z \leq 19$ . Although the existence/non-existence of a covering follows no clear pattern for very small system sizes, we see regular behavior emerge once the system size is larger than  $3 \times 3 \times 3$ . Specifically, the existence/non-existence of a covering for a certain cubic code is only dependent on whether each length is even or odd and, if it is even, whether it is divisible by 4. This admits  $3^3 = 27$  different possible classes of system sizes—however, we find that some classes are equivalent in terms of which cubic codes have coverings on them. A full table of this behavior is shown in Table C.2. We note several trends. On an odd-by-odd-by-odd lattice, none of the 17 cubic codes have code subspaces that stay real under pseudo-Hermitian perturbations. If only a portion of the system lengths are odd, the reality of the code subspace depends on which dimensions have odd lengths, and whether the remaining lengths are divisible by 4. In contrast, if  $L_x$  and  $L_y$  are divisible by 4 and  $L_z$  is even, all the code subspaces stay real under pseudo-Hermitian perturbations. Overall, cubic code 17 is the most unstable to pseudo-Hermitian perturbations, in that its code subspaces will become complex for almost all system sizes. In contrast, cubic code 7 has the most stable code subspace. There are some groups of codes with the same sensitivity to system sizes. If we consider codes with the same behavior up to a lattice rotation, these groups are  $(11, 12, 14, 15)$ ,  $(5, 8, 10, 16)$ , and  $(2, 3, 6, 9)$ . It is interesting to note that, with the exception of cubic code 16, all codes within a group transform the same under entanglement renormalization [115]. Note

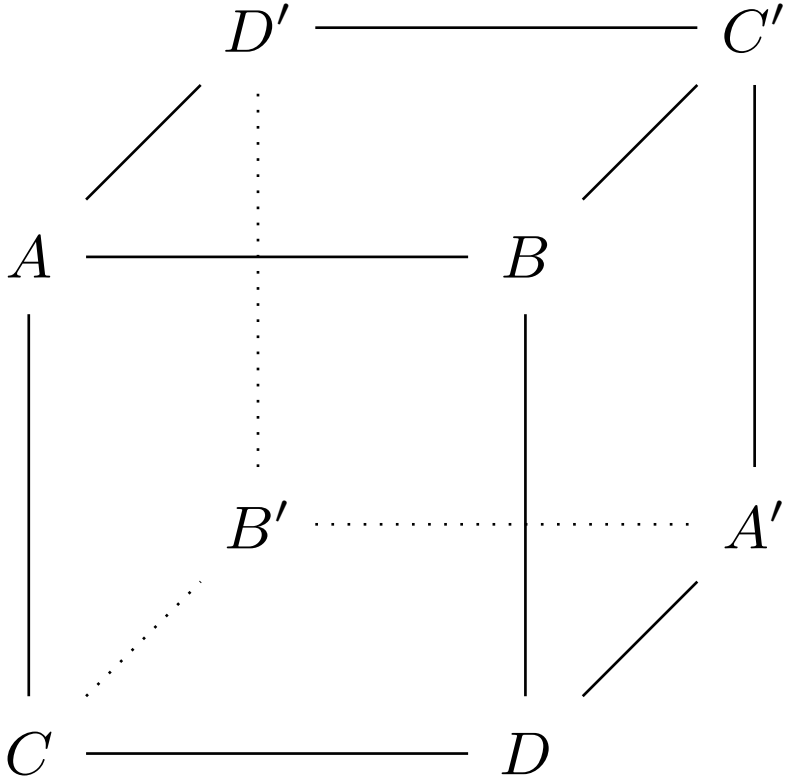


Figure C.3: The stabilizers of Haah’s cubic codes correspond to cube operators, with generically different operators on each vertex as labelled by  $A$ - $D$  and  $A'$ - $D'$ . The operators at each vertex for the 17 different cubic codes are given in Table C.1.

that cubic codes related by modular transformations [114]—specifically, cubic codes 5/9 and 15/16—may have different system size dependencies. This is because a stabilizer covering in one model will generically transform non-trivially under modular transformations. In other words, the existence of a stabilizer covering in one cubic code does not imply the existence of a stabilizer covering in another cubic code related to the original by a modular transformation.

While our results are purely numerical, an analytic verification of these trends for all system sizes is likely possible if one was to manually follow the factorization processes carried out in SageMath and show that their conclusions are only sensitive to the system sizes’ evenness/oddness and whether they are divisible by 4. We do not attempt this, as there are 459 separate cases that must be checked (27 possible system sizes for the 17 codes), and instead analyze the numerical results which show clear trends up to  $19 \times 19 \times 19$  lattices.

	$A$	$B$	$C$	$D$	$A'$	$B'$	$C'$	$D'$
1	$ZI$	$ZZ$	$IZ$	$ZI$	$IZ$	$II$	$ZI$	$IZ$
2	$IZ$	$ZZ$	$ZI$	$ZI$	$ZI$	$ZZ$	$IZ$	$ZI$
3	$IZ$	$ZZ$	$ZZ$	$ZI$	$ZZ$	$II$	$IZ$	$IZ$
4	$IZ$	$ZZ$	$ZI$	$ZI$	$IZ$	$II$	$IZ$	$ZI$
5	$ZI$	$ZZ$	$II$	$ZZ$	$ZI$	$II$	$IZ$	$IZ$
6	$ZI$	$II$	$ZI$	$ZZ$	$IZ$	$ZZ$	$II$	$IZ$
7	$ZI$	$ZZ$	$ZI$	$IZ$	$IZ$	$II$	$II$	$ZZ$
8	$ZI$	$ZI$	$IZ$	$ZZ$	$IZ$	$II$	$IZ$	$ZI$
9	$ZI$	$IZ$	$ZZ$	$ZZ$	$IZ$	$ZZ$	$II$	$IZ$
10	$ZI$	$IZ$	$ZI$	$ZZ$	$IZ$	$ZZ$	$ZI$	$ZI$
11	$ZI$	$ZZ$	$II$	$IZ$	$ZI$	$II$	$IZ$	$ZZ$
12	$ZI$	$IZ$	$ZZ$	$ZZ$	$ZI$	$II$	$II$	$IZ$
13	$ZI$	$ZZ$	$IZ$	$ZI$	$IZ$	$II$	$II$	$ZZ$
14	$ZI$	$IZ$	$ZZ$	$ZZ$	$IZ$	$II$	$ZZ$	$IZ$
15	$ZI$	$IZ$	$II$	$ZZ$	$IZ$	$ZZ$	$II$	$ZI$
16	$ZI$	$ZI$	$II$	$IZ$	$IZ$	$ZZ$	$II$	$ZZ$
17	$ZI$	$ZZ$	$IZ$	$ZI$	$IZ$	$ZI$	$ZI$	$ZZ$

Table C.1: The  $Z$  stabilizers for Haah's 17 CSS cubic codes, defined on the eight vertices of a cube, with vertices labeled according to Fig. C.3. The  $X$  stabilizers are obtained by exchanging  $A \leftrightarrow A'$ , and likewise for the other vertices, and by exchanging the two Pauli spins on each site.

System Size	$CC_1$	$CC_2$	$CC_3$	$CC_4$	$CC_5$	$CC_8$	$CC_7$	$CC_{11}$	$CC_{12}$	$CC_{14}$	$CC_{13}$	$CC_{17}$
$E \times E \times E$												
$E \times E \times e$	✓	✓	✓	✓	✓	✓	✓	✓	✓	✓	✓	✓
$e \times E \times E$												
$o \times E \times E$												
$E \times e \times E$												
$E \times e \times e$	✓	✓	✓	✓	✓	✓	✓	✓	✓	✓	✓	✗
$e \times e \times E$												
$e \times E \times E$												
$E \times o \times E$												
$e \times e \times e$	✓	✓	✓	✓	✓	✓	✓	✓	✗	✗	✗	✗
$E \times E \times o$	✓	✓	✓	✓	✓	✓	✗	✗	✗	✗	✓	✓
$e \times o \times E$												
$E \times o \times e$												
$e \times o \times e$	✗	✓	✓	✓	✓	✓	✓	✓	✗	✗	✗	✗
$e \times E \times o$												
$E \times e \times o$												
$e \times e \times o$												
$e \times o \times o$												
$E \times o \times o$	✗	✓	✗	✓	✓	✓	✗	✗	✗	✗	✗	✗
$o \times e \times E$												
$o \times E \times e$												
$o \times e \times e$	✗	✗	✓	✓	✓	✓	✓	✓	✗	✗	✗	✗
$o \times o \times E$												
$o \times o \times e$	✗	✗	✗	✗	✓	✓	✓	✗	✗	✗	✗	✗
$o \times E \times o$												
$o \times e \times o$												
$o \times o \times o$	✗	✗	✗	✗	✗	✗	✗	✗	✗	✗	✗	✗

Table C.2: The reality of the code subspace of Haah's cubic codes under pseudo-Hermitian perturbations are highly sensitive to the system size. The reality of the subspace depends on whether each dimension length is odd ( $o$ ), even and divisible by 4 ( $E$ ), or even and not divisible by 4 ( $e$ ). Shown are all 17 of Haah's cubic codes and the dependence of the code subspace stability on the system size. Codes with identical dependencies have been grouped together, and some have been redefined by a spatial rotation. The trends listed have been confirmed numerically to hold from system sizes  $3 \times 3 \times 3$  to  $19 \times 19 \times 19$ .

# D

## Appendix to Chapter 6

### D.1 CONSTRUCTION OF GAMMA MATRICES

In our main text, we outline two possible constructions of Gamma matrices in terms of physical degrees of freedom. There is much freedom in choosing this representation, with different representations making different aspects of the resulting dynamics simpler. An alternate choice is:

$$\begin{aligned}\Gamma^1 &= S^z \otimes S^y, & \Gamma^2 &= S^x \otimes \mathbb{1}, \\ \Gamma^3 &= S^z \otimes S^x, & \Gamma^4 &= S^y \otimes \mathbb{1}, \\ \Gamma^5 &= S^z \otimes S^z.\end{aligned}\tag{D.1}$$

The unitary dynamics of our model are governed by a Hamiltonian with terms  $\Gamma_j^1\Gamma_{j+\hat{x}}^2$  and  $\Gamma_j^3\Gamma_{j+\hat{y}}^4$ , which translate into three-spin interactions of the form  $S_{j,1}^z S_{j,2}^y S_{j+\hat{x},1}^x$  and  $S_{j,1}^z S_{j,2}^x S_{j+\hat{y},1}^y$ . The jump operator  $L_j = S_{j,1}^z S_{j,2}^z$  corresponds to a coordinated dephasing term, where the four energy levels of the pair of qubits are subjected to a stochastic noise which leaves fixed the energy difference between the  $|\uparrow\uparrow\rangle$  and  $|\downarrow\downarrow\rangle$  states, as well as the  $|\uparrow\downarrow\rangle$  and  $|\downarrow\uparrow\rangle$  states. We note an especially simple feature of this choice, which is the representation of the string-like operators discussed in the main text and whose expectation values decay less rapidly than

single-site operators. A string-like operator corresponding to a pair of  $d$  Majorana fermion excitations that lies along the  $x$ -direction is given by  $\Gamma_j^1 \Gamma_{j+\hat{x}}^{12} \Gamma_{j+2\hat{x}}^{12} \dots \Gamma_{j+n\hat{x}}^2$ , which in our representation corresponds to a string of  $S^y$  operators with an  $S^z$  and  $S^x$  operator on either end. Similar simplifications arise for strings in the  $\hat{y}$  directions, as well as strings corresponding to  $d'$  Majorana excitations.

## D.2 NON-VANISHING STEADY-STATE EXPECTATION VALUES

In the main text, we claim that any operator that has eigenvalue 1 under the superoperators  $U_{j,\alpha}$  and equal eigenvalues under  $W_{j,R}$  and  $W_{j,L}$  is a product of  $V_{j,\alpha}$  bond operators. One can readily verify that these operators satisfy the required constraints, but a more careful argument is required to show that these are the *only* operators with such a property. We do so by counting the dimension of the subspace (within the doubled Hilbert space) spanned by these operators. With a square lattice having  $2N$  bonds, there are naively  $2^{2N}$  orthogonal combination of bond operators; however, this double counts the true number of operators, as the product of all bond operators is  $\mathbb{1}$ . So, the subspace is  $2^N$  dimensional. The full dimension of our doubled Hilbert space is  $2^{4N}$ , and we have  $3N$  independent constraints - for each site  $j$ , we have  $U_{j,\hat{x}} = 1$ ,  $U_{j,\hat{y}} = 1$ , and  $W_{j,R} = \overline{W}_j$  (the constraint on  $W_{j,L}$  is automatically satisfied under these constraints). Each constraint halves the dimension of the allowed subspace, so we find a  $2^N$  dimensional Hilbert space, as desired.

## D.3 DIAGONALIZATION OF THE FREE FERMION LINDBLADIAN

In this appendix, we provide more detail on the diagonalization of the free fermion Lindbladian. For a general choice of gauge sector, we work with the Lindbladian written in terms of Majorana fermions, as in Eq. 5.14. This can be re-expressed in the form

$$i\mathcal{L} = \mathbf{d}^T \cdot \mathbf{A} \cdot \mathbf{d} - i\gamma N \quad (\text{D.2})$$

where  $\mathbf{d}$  is a  $2N$ -dimensional vector containing both  $d_{j,L}$  and  $d_{j,R}$  Majorana fermion operators. We follow the procedure described in [372] for obtaining the spectrum of this Lindbladian, which we summarize here. As  $\mathbf{A}$  is an antisymmetric matrix, its spectrum comes in

the form  $\{\beta_1, -\beta_1, \beta_2, -\beta_2 \dots \beta_N, -\beta_N\}$ , where we take  $\text{Im} \beta_\alpha \geq 0$ . One can construct  $N$  creation/annihilation operators  $b_\alpha, b'_\alpha$  that obey the canonical fermionic anti-commutation relations (with the caveat that  $b'_\alpha$  is in general not the Hermitian adjoint of  $b_\alpha$ ). With this, we can write

$$i\mathcal{L} = -2 \sum_{\alpha=1}^N \beta_\alpha b'_\alpha b_\alpha - \left( i\gamma N - \sum_{\alpha=1}^N \beta_\alpha \right) \quad (\text{D.3})$$

The term in parenthesis gives the dissipative strength of the state with weakest dissipation within this gauge sector. Note that this Majorana fermion representation obfuscates the constraint of gauge invariance, which is most easily enforced in terms of the complex fermions  $f_j^\dagger$ . As such, this representation is only useful in gauge sectors where pairing terms would appear if written in the  $f_j^\dagger$  basis, in which case a proper analysis of gauge invariance is equally difficult in either representation.

#### D.4 IDENTIFICATION OF SINGLE-SITE OPERATORS WITH FLUX CONFIGURATIONS

In the main text, we emphasize that the spectrum of our Lindbladian decomposes into an extensive number of symmetry sectors, each of which is specified by a gauge flux configuration. A Liouvillian gap for each sector can be defined, and one can identify operators - which we remind the reader should be thought of as *states* in this doubled Hilbert space - that are contained in these symmetry sectors, which the Liouvillian gap then defines an equilibration timescale for. Here, we catalog the flux configurations associated with the set of single-site operators.

A particular flux configuration is defined by the interlayer fluxes  $U_{j\alpha} = V_{j,\alpha} = V'_{j,\alpha,R} V'_{j,\alpha,L}$  as well as the intralayer fluxes  $W_{j,\alpha,R}, W_{j,\alpha,L}$ . As our Lindbladian spectrum is invariant under the transformation  $W_{j,\alpha,R} \leftrightarrow W_{j,\alpha,L}$ , we will only identify operators based on their eigenvalues under the combined flux  $W_{j,\alpha,R} W_{j,\alpha,L}$ . The eigenvalues of an operator under these fluxes is simply determined by whether the operators  $V'_{j,\alpha}$  and  $W_j$  commute or anti-commute with the operators. If we take as our basis of operators to be products of  $\Gamma$  matrices, every basis operator will either commute or anti-commute with  $V'_{j,\alpha}$  and  $W_j$ .

The operators  $\Gamma_k^5$  commutes with all plaquette operators  $W_j$ . It also commutes with all the bond operators  $V'_{j,\alpha}$  aside from the four bonds adjacent to site  $k$ . The flux configurations

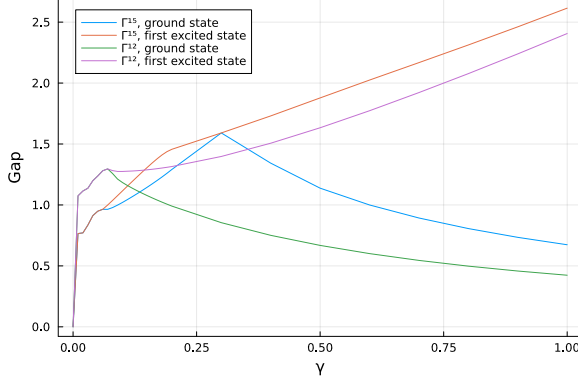


Figure D.1: We plot Liouvillian gaps for the gauge sectors associated with  $\Gamma^{15}$  and  $\Gamma^{12}$  operators, and demonstrate a sharp jump in the gap when the dissipation is turned on.

associated with this operator are given precisely by the interlayer gauge excitations studied in Section 5.3.3.

The operators  $\Gamma_k^\mu$ ,  $\mu = 1, 2, 3, 4$ , commute with all the bond operators  $V'_{j,\alpha}$  except for a single one adjacent to site  $k$  which anticommutes with it. Additionally, it commutes with all but two  $W_j$  operators - these two offending plaquette operators share a bond given by the anticommuting  $V'_{j,\alpha}$  operator. The flux configuration associated with these operators can be obtained starting from a steady-state gauge sector and flipping an intralayer gauge field on this bond and its spectrum is analyzed in Section 5.3.3.

The operators  $\Gamma_k^{\mu 5}$  have the same commutation relations with the plaquette operators as  $\Gamma_k^\mu$ , but differ with respect to the  $V'_{j,\alpha}$  operators; it now anticommutes with the three  $V'_{j,\alpha}$  bond operators connected to site  $k$  that aren't the bond shared by the flux operators. This flux configuration can be obtained from the intraylayer gauge excitation studied in Section 5.3.3 and flipping an additional interlayer gauge field  $\hat{v}_k$ .

Finally, we identify the operators  $\Gamma_k^{\mu\nu}$ , with  $\mu, \nu = 1, 2, 3, 4$  and  $\mu \neq \nu$ . For a given site  $k$ , there are  $\binom{4}{2} = 6$  different operators of this type. These operators will anticommute with two of the four  $V'_{j,\alpha}$  bond operators, and either two fluxes  $W_j$  that only share a corner at site  $k$  or all four fluxes connected to site  $k$ . These flux sectors are obtained by flipping *two* intralayer gauge fields connected to a site  $k$  - as expected, there are  $\binom{4}{2} = 6$  ways of doing this.

The Liouvillian gap of excitations corresponding to the  $\Gamma_k^\mu$  operators are shown in Fig. 5.6. We plot the Liouvillian gap of  $\Gamma_k^{\mu 5}$  and  $\Gamma_k^{\mu\nu}$  operators in Fig. D.1 and verify that similar

behavior occurs. This implies that our observation of the rapid equilibration of  $\Gamma_k^\mu$  operators holds *generically* for single-site operators, with the exception of  $\Gamma_k^5$  due to its interpretation as the bound state of two Majorana fermion excitations, or alternatively due to the fact that  $\Gamma_k^5$  are precisely the quantum jump operators describing the coupling to the environment.

# E

## Appendix to Chapter 1

### E.1 SPIN GLASS ANALYSIS

As described in the main text, the spectral function of the random  $t$ - $J$  model near half filling has a peak at low frequency, suggesting spin glass order. To establish this rigorously, one must show that the variance of the peak goes to zero in the thermodynamic limit while the integrated spectral weight remains non-zero, indicating delta function-like behavior. We isolate the low-frequency peak by subtracting off a background contribution, given by the large- $M$  solution of the SY model. We then fit the remaining low-frequency peak to the function

$$\chi''_{low}(\omega) = \omega C \exp\left[-\frac{\omega^2}{2\sigma^2}\right]. \quad (\text{E.1})$$

In Fig. E.1, we show the extrapolation of  $\Gamma$  to the thermodynamic limit for several values of doping up to  $p = 1/3$ . As expected of spin glass behavior,  $\Gamma$  vanishes in the thermodynamic limit. This is in contrast with the integrated spectral weight of Eq. E.1, which we show in the main text is non-zero in the the thermodynamic limit and corresponds to the Edwards-Anderson spin glass order parameter  $q$ .

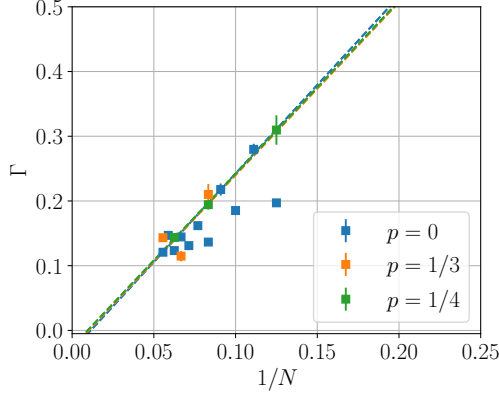


Figure E.1: At low dopings, the low-frequency peak in the spectral function can be isolated and fit to Eq. E.1. In the thermodynamic limit, we confirm that the variance  $\Gamma$  vanishes up to  $p = 1/3$ . Due to a prominent even/odd particle effect at half filling, we only extrapolate  $\Gamma$  at half-filling for even system sizes.

## E.2 THERMAL PURE QUANTUM STATES

The computation of thermodynamic quantities in the main text has been performed using thermal pure quantum states [469, 470] together with the Lanczos algorithm. This allowed us to reach system sizes beyond the reach of full exact diagonalization. This approach is closely related to the finite-temperature Lanczos method [215, 367]. We will now briefly explain the method. The trace of any operator  $H$  can be evaluated by taking random average values,

$$\text{Tr}(A) = D \overline{\langle r | A | r \rangle}, \quad (\text{E.2})$$

where  $|r\rangle$  is a normalized random vector,  $\langle r | r | r \rangle = 1$ , with normal distributed coefficients,  $\langle m | r | m | r \rangle \sim \mathcal{N}(0, 1)$ , and  $D$  denotes the dimension of the Hilbert space. Here,  $\{|m\rangle\}_{m=1,\dots,D}$  denotes an arbitrary orthonormal basis of the Hilbert space and  $\overline{\dots}$  denotes averaging over random realizations of  $|r\rangle$ . Hence, a thermal expectation value of an observable  $\mathcal{O}$  can be written as as,

$$\langle \mathcal{O} \rangle \frac{1}{Z} \text{Tr}(e^{-\beta H} \mathcal{O}) = \frac{\overline{\langle \beta | \beta \rangle \mathcal{O} | \beta \rangle}}{\overline{\langle \beta | \beta \rangle}}, \quad (\text{E.3})$$

where  $\mathcal{Z} = \text{Tr}(\text{e}^{-\beta H})$  denotes the partition function and we define the so-called *thermal pure quantum* (TPQ) state [469, 470] at inverse temperature  $\beta = 1/T$ ,

$$|\beta\rangle = \text{e}^{-\beta H/2} |r\rangle. \quad (\text{E.4})$$

This way, thermal expectation values can be evaluated efficiently using the Lanczos algorithm, whereas the exact computation of the trace of an exponential requires full diagonalization. In the main text we present data for the specific heat, internal energy and entropy, which are all computed from expectation values of powers of the Hamiltonian with TPQ states of the form  $\langle\beta| H^k |\beta\rangle$ . Using the Lanczos algorithm this quantity is efficiently approximated by,

$$\langle\beta|\beta\rangle H^k |\beta\rangle \approx e_1^\dagger \text{e}^{-\frac{\beta}{2} T_n} T_n^k \text{e}^{-\frac{\beta}{2} T_n} e_1, \quad (\text{E.5})$$

where  $e_1 = (1, 0, \dots, 0)^\dagger$  and  $T_n$  denotes the tridiagonal matrix of the Lanczos algorithm after  $n$  steps. The convergence is typically exponentially fast, such that results can be attained up to machine precision. For a more detailed description of the method we refer the reader to Ref. [518]. We notice in E.5, that once the Lanczos algorithm has been applied to compute the tridiagonal matrix, results can be derived at all temperatures simultaneously without rerunning the expensive Lanczos algorithm.

Instead of one single computation as done for evaluating a trace, using TPQ states requires us to perform random sampling with multiple vectors  $|r\rangle$  and compute error estimates. Since expectation values of the form E.3 are non-linear in  $|r\rangle$ , we perform jackknife resampling [126] of the data. Interestingly, larger system sizes typically require less random realizations  $|r\rangle$  to obtain comparable errorbars. Refs. [469, 470] give a mathematical proof, that for a constant free energy density, the variance of the estimate in E.3 is exponentially small in the system size. In the main text we typically average over  $R = 5$  random realizations of the TPQ states.

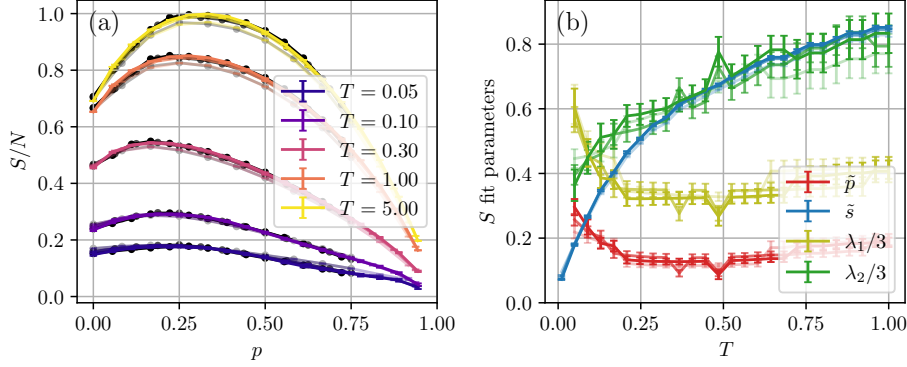


Figure E.2: (a) The thermal entropy  $S$  as a function of doping for various temperatures. Black dots show the ansatz Eq. E.6 at optimal fitting parameters. (b) Estimates of the parameters in Eq. E.6.  $\tilde{p}$  corresponds to the doping value with maximal entropy,  $\tilde{s}$  corresponds to the maximal entropy density.

### E.3 TEMPERATURE DEPENDENCE OF THE THERMAL ENTROPY

In the limit  $T \rightarrow \infty$  the thermal entropy  $S$  attains a maximum exactly at  $p = 1/3$  for  $N \rightarrow \infty$  in the canonical ensemble. The ansatz,

$$S/N = \begin{cases} -K |p - \tilde{p}|^{\lambda_1} + \tilde{s} & \text{for } p \leq \tilde{p} \\ -K |p - \tilde{p}|^{\lambda_2} + \tilde{s} & \text{for } p > \tilde{p} \end{cases}, \quad (\text{E.6})$$

is found to describe our entropy data with considerable precision. A comparison between the ansatz (black circles) and the ED data is shown in Fig. E.2(a). The parameters  $\tilde{p}$ ,  $\tilde{s}$ ,  $\lambda_1$ ,  $\lambda_2$ , and  $K$  are fitted for dopings  $p \in [0, 0.75]$  using the Levenberg-Marquardt algorithm [277, 306], from which we obtain an (error) estimate of the parameters, shown in Fig. E.2(e).

Our estimate of  $\tilde{p}$  is increasing when lowering the temperature below  $T = 0.25$ . At  $T = 0.05$  and  $N = 18$  we obtain an estimate,

$$\tilde{p} \approx 0.296 \pm 0.025 \quad [\text{from } S(T = 0.05)]. \quad (\text{E.7})$$

This value is consistent with the maximum of  $\gamma$ , observed in the main text. However, we find that both increasing the system size and lowering temperature increases our estimate of the critical doping  $\tilde{p}$  when estimated as above. At temperatures below  $T = 0.05$  estimates are

found to be unreliable due to sample fluctuations.

## E.4 SELF-AVERAGING, ELECTRON DISTRIBUTIONS, AND THE LUTTINGER THEOREM

### E.4.1 SELF-AVERAGING FROM THE CAVITY METHOD

In this section, we establish that, in the thermodynamic limit  $N \rightarrow \infty$ , some local observables have *self-averaging* properties in this fully connected random model. This means that, when considered for a given site, they converge with probability one to their average over samples. We also establish the connection to extended dynamical mean-field equations (EDMFT) that allow for a direct study of the model in the thermodynamic limit. We *do not* consider the spin-glass phase in this section.

For the sake of generality, we consider the finite- $U$  version of the model, the  $t$ - $J$  limit corresponding to  $U = \infty$ . The model is defined on a fully connected lattice of  $N$  sites by the Hamiltonian:

$$H = - \sum_{ij,\sigma=\uparrow,\downarrow} t_{ij} c_{i\sigma}^\dagger c_{j\sigma} + U \sum_i n_{i\uparrow} n_{i\downarrow} - \sum_{i < j} J_{ij} \vec{S}_i \cdot \vec{S}_j \quad (\text{E.8})$$

with:

$$t_{ij} = \frac{t}{\sqrt{N}} \varepsilon_{ij} , \quad J_{ij} = \frac{J}{\sqrt{N}} \eta_{ij} \quad (\text{E.9})$$

In these expressions,  $\varepsilon$  and  $\eta$  are random variables of zero mean and unit variance. The precise distribution is not important in the infinite-size (large- $N$ ) limit, as shown below.

Let us consider a fixed sample  $\{\varepsilon_{ij}, \eta_{ij}\}$ , and envision formally integrating over all sites except a single one (denoted by  $i = 1$ ). The lattice with the ‘cavity’ removed (consisting of that site and all connections through  $t_{1j}$  and  $J_{1j}$ ) is in this case just a fully connected lattice of  $N - 1$  sites. We follow the procedure in Ref. [154], Sec.III.A: in the large- $N$  limit, the effective action for site 1 obtained after integrating out all other d.o.f.s is:

$$\begin{aligned} S_{\text{eff}}[1] = & - \int \int_0^\beta d\tau d\tau' \sum_\sigma c_{1\sigma}^\dagger(\tau) (\delta(\tau - \tau')(-\partial_\tau + \mu) - \Delta_1(\tau - \tau')) c_{1\sigma}(\tau') + \\ & + U \int_0^\beta d\tau n_{1\uparrow} n_{1\downarrow} - \frac{1}{2} \int_0^\beta d\tau d\tau' Q_1(\tau - \tau') \vec{S}_1(\tau) \cdot \vec{S}_1(\tau'). \end{aligned} \quad (\text{E.10})$$

All higher order correlators are lower order in  $1/N$  (finite-size corrections). The dynamical mean-fields, i.e the hybridisation function  $\Delta_1$  and retarded spin-spin interaction  $Q_1$  are given by the cavity equations:

$$\Delta_1 = \frac{t^2}{N} \sum_{i,j \neq 1} \varepsilon_{1i} \varepsilon_{1j} G_{ij}^{[1]} , \quad Q_1 = \frac{J^2}{N} \sum_{i,j \neq 1} \eta_{1i} \eta_{1j} \chi_{ij}^{[1]} \quad (\text{E.11})$$

In this expression  $G_{ij}(\tau - \tau') \equiv -\langle T c_i^\dagger(\tau) c_j(\tau') \rangle$  and  $\chi_{ij} \equiv \langle \vec{S}_i \cdot \vec{S}_j \rangle / 3$  are the Green's function and spin-spin correlation function. The superscript  $G^{[1]}$  means that we are considering these quantities for the subsystem of  $N - 1$  spins remaining once the cavity (site 1 and its connections) has been created.

Let us analyze Eqs. (E.11) for the hybridisation function, separating diagonal and off-diagonal terms:

$$\Delta_1 = \frac{t^2}{N} \sum_{i=2}^N \varepsilon_{1i}^2 G_{ii}^{[1]} + \frac{t^2}{N} \sum_{i,j \neq 1; i \neq j} \varepsilon_{1i} \varepsilon_{1j} G_{ij}^{[1]} \quad (\text{E.12})$$

The key point is that  $G_{ij}^{[1]}$  do not depend on the random variables  $\varepsilon_{1i}$ . Taking the  $N \rightarrow \infty$  limit amounts to take a disorder average of these terms, and because of this independence, the average applies separately to  $\varepsilon_{1i}$  and  $G_{ii}^{[1]}$ . The second term ( $i \neq j$ ) averages out to zero, and the first one yields finally:

$$\Delta_1 = t^2 \lim_{N \rightarrow \infty} \overline{\sum_i G_{ii}} = t^2 \overline{G} , \quad (N \rightarrow \infty) \quad (\text{E.13})$$

In which the overline denotes an average over samples. We are assuming here that there is no ‘ergodicity breaking’ in the phase being considered: the average over sites is equivalent to an average over samples. Hence, the dynamical mean field  $\Delta$  does not depend on the specific site or on the specific sample, in the infinite size limit: it *self-averages*. A similar reasoning applies to  $Q$ . Finally the self-consistent equations read for infinite size (I am dropping the overlines and site index everywhere when there is no possible confusion):

$$\Delta(i\omega_n) = t^2 G(i\omega_n) , \quad Q(i\omega_n) = J^2 \chi(i\omega_n) \quad (\text{E.14})$$

in which the local ( $i = j$ ) correlators  $G$  and  $\chi$  have to be calculated with the effective action

(E.10) - that's the EDMFT construction.

For completeness, we recall that the (local) self-energy in the infinite-volume limit is given by the difference between the inverse of the interacting and non-interacting Green's functions, namely:

$$\Sigma(i\omega_n) = i\omega_n + \mu - \Delta(i\omega_n) - G^{-1}(i\omega_n) = i\omega_n + \mu - t^2 G - G^{-1} \quad (\text{E.15})$$

$\Delta$  and the local  $G_{ii}$  being self-averaging,  $\Sigma_{ii}$  also is.

Incidentally, for the non-interacting system ( $U = J = 0$ ),  $\Sigma = 0$  and the solution of the quadratic equation:  $z - t^2 G - G^{-1} = 0$  yields the non-interacting local Green's function ( $z \equiv i\omega_n + \mu$ , but the formula is valid for any  $z$  in the complex plane):

$$G_0(z) = \frac{1}{2t^2} \left[ z - \text{sign}[\text{Im}(z)] \sqrt{z^2 - 4t^2} \right] = \int d\varepsilon \frac{D_\infty(\varepsilon)}{z - \varepsilon} \quad (\text{E.16})$$

from which the (Wigner) semi-circular distribution immediately follows:

$$D_\infty(\varepsilon) \equiv -\frac{1}{\pi} \text{Im} G_0(\varepsilon + i0^+) = \frac{1}{2\pi t^2} \sqrt{4t^2 - \varepsilon^2}, \quad \varepsilon \in [-2t, +2t] \quad (\text{E.17})$$

#### E.4.2 GREEN'S FUNCTION AND ONE-PARTICLE ENERGY DISTRIBUTION

We can use the eigenstates of the one-particle non-interacting problem ( $U = J_{ij} = 0$ ) as a *basis set* to represent any single-particle correlation function of the interacting problem. These states are defined by, for a given sample  $t_{ij}$ :

$$\hat{t}|\lambda\rangle = \varepsilon_\lambda |\lambda\rangle, \quad \text{i.e. } \sum_j t_{ij} \langle j|\lambda\rangle = \varepsilon_\lambda \langle i|\lambda\rangle \quad (\text{E.18})$$

The Fock space of the many-body problem is constructed as the number occupancy states  $|\{n_\lambda\}\rangle$  and is a full basis for the many-body problem. The single-particle DOS of the non-interacting system reads:

$$D_{ij}(\varepsilon) = \frac{1}{N} \sum_\lambda \delta(\varepsilon - \varepsilon_\lambda) \langle i|\lambda\rangle \langle \lambda|j\rangle \quad (\text{E.19})$$

In the  $N \rightarrow \infty$  limit,  $D_{ii}$  converges (and self-averages) to the semi-circular DOS  $D_\infty$  defined above.

Consider now the interacting system, for a given sample  $t_{ij}, J_{ij}$  and finite  $N$ . We define the one-electron Green's function in the usual way  $G_{ij}(\tau - \tau') \equiv -\langle T c_i^\dagger(\tau) c_j(\tau') \rangle$ , but it can actually be viewed as a one-body operator  $\hat{G}$  that we can look at in any basis set, for example in the eigenstate basis:

$$G_{\lambda\lambda'}(i\omega_n) = \langle \lambda | \hat{G} | \lambda' \rangle = \sum_{ij} \langle \lambda | i \rangle G_{ij}(i\omega_n) \langle j | \lambda' \rangle \quad (\text{E.20})$$

Note that for a given sample and finite  $N$ , this is not diagonal in  $\lambda$ . Correspondingly, a self-energy  $\sigma_{ij}$  can be defined as (we are careful to use a different notation here, since this is for a given sample and finite  $N$ ):

$$\hat{G}^{-1} \equiv i\omega_n + \mu - \hat{t} - \hat{\sigma} \text{ , in site basis : } [G^{-1}]_{ij} = (i\omega_n + \mu) \delta_{ij} - t_{ij} - \sigma_{ij} \quad (\text{E.21})$$

Things get simpler in the infinite-volume limit. The off-diagonal components of the self-energy  $\sigma_{i \neq j}$  vanish, and the diagonal ones self-average and converge to the local self-energy defined above:  $\sigma_{ii} \rightarrow \Sigma$ . Hence, the expression of the Green's function becomes:

$$[G^{-1}]_{ij} = [i\omega_n + \mu - \Sigma(i\omega_n)] \delta_{ij} - t_{ij} \text{ , } (N \rightarrow \infty) \quad (\text{E.22})$$

Note that off-diagonal components of the Green's functions *do not self-average*. They are individually of typical order  $1/\sqrt{N}$ , but we have to take them into account when calculating the kinetic energy for example, since we sum over all bonds. Given (E.22), the Green's function for  $N = \infty$  now acquires a simple *diagonal* representation in the basis of eigenstates of  $\hat{t}$ :

$$G_{ij}(i\omega_n) = \sum_{\lambda} \langle i | \lambda \rangle \frac{1}{i\omega_n + \mu - \Sigma(i\omega_n) - \varepsilon_{\lambda}} \langle \lambda | j \rangle \quad (\text{E.23})$$

It is convenient to define the (sample independent) Green's function for a given energy  $\varepsilon$  in

the semi-circular ‘band’ as:

$$G(i\omega_n, \varepsilon) \equiv \frac{1}{i\omega_n + \mu - \Sigma(i\omega_n) - \varepsilon} \quad (\text{E.24})$$

which is the natural quantity we would routinely look at in the EDMFT framework. The connection between this and the Green’s function for a given sample, in the infinite size limit  $N = \infty$ , is given by:

$$G_{ij}(i\omega_n) = \int d\varepsilon D_{ij}(\varepsilon) G(i\omega_n, \varepsilon) , \quad (N = \infty) \quad (\text{E.25})$$

Let us now consider (for a given sample and any  $N$ ) the one-body distribution function:

$$N_\lambda = \langle \hat{n}_\lambda \rangle = \sum_{ij} \langle \lambda | i \rangle \sum_\sigma \langle c_{i\sigma}^\dagger c_{j\sigma} \rangle \langle j | \lambda \rangle \quad (\text{E.26})$$

In the non-interacting case, the ground-state is a Slater determinant of the  $\lambda$  states, and hence at  $T = 0$   $N_\lambda = 1$  for all filled states and 0 for empty states. We can more conveniently look at it by filtering in energy and define:

$$\mathcal{N}(\varepsilon) = \frac{1}{N} \sum_\lambda \delta(\varepsilon - \varepsilon_\lambda) N_\lambda = \frac{1}{N} \sum_\lambda \delta(\varepsilon - \varepsilon_\lambda) \sum_{ij\sigma} \langle \lambda | i \rangle \langle c_{i\sigma}^\dagger c_{j\sigma} \rangle \langle j | \lambda \rangle \quad (\text{E.27})$$

which can also be written:

$$\mathcal{N}(\varepsilon) = \sum_{ij\sigma} D_{ij}(\varepsilon) \langle c_{i\sigma}^\dagger c_{j\sigma} \rangle \quad (\text{E.28})$$

obeying (with  $n$  the electron density):

$$\int d\varepsilon \mathcal{N}(\varepsilon) = \frac{N_e}{N} = n \quad (\text{E.29})$$

We can also sample average and consider  $\overline{\mathcal{N}(\varepsilon)}$ .

Now we establish the connection, in the  $N = \infty$  limit, between this distribution function and what we would naturally calculate in the EDMFT context, which is the number distribution

function as a function of the single-particle energy:

$$N(\varepsilon) = 2G(\tau = 0^-, \varepsilon) = 2\frac{1}{\beta} \sum_n e^{i\omega_n 0^+} \frac{1}{i\omega_n + \mu - \Sigma(i\omega_n) - \varepsilon} \quad (\text{E.30})$$

The factor of 2 is for the sum over spin. We note that:

$$\int d\varepsilon D_\infty(\varepsilon) N(\varepsilon) = n \quad (\text{E.31})$$

Using (E.25), we obtain:

$$\overline{N(\varepsilon)} = \frac{1}{N} \sum_\lambda \delta(\varepsilon - \varepsilon_\lambda) N(\varepsilon_\lambda) = D_\infty(\varepsilon) N(\varepsilon) , \quad (N = \infty) \quad (\text{E.32})$$

#### E.4.3 LUTTINGER'S THEOREM.

In the (self-averaging) infinite volume limit, the Green's function  $G(\omega, \varepsilon)$  has a pole  $\omega(\varepsilon)$  given by the quasiparticle equation:

$$\omega + \mu - \text{Re}\Sigma(\omega + i0^+) = \varepsilon \quad (\text{E.33})$$

where we have assumed that at low  $\omega, T$  the imaginary part  $\text{Im}\Sigma(\omega + i0^+)$  is negligible. Hence the ‘Fermi surface’ (for a typical large sample) is located at:

$$\varepsilon_F = \mu - \text{Re}\Sigma(0) \quad (\text{E.34})$$

In the non-interacting system, the Fermi level  $\varepsilon_F$  is given by:

$$n = 2 \int_{-\infty}^{\varepsilon_F} d\varepsilon D(\varepsilon) \quad (\text{E.35})$$

Hence, for a fixed density, the Luttinger theorem (Fermi ‘surface’ unchanged by interactions) translates into the following requirement:

$$\mu(n) - \text{Re}\Sigma(0) = \varepsilon_F(n) \quad (\text{E.36})$$

In the Fermi liquid phase, this can be established following the usual proof based on the existence of a Luttinger-Ward functional.

# F

## Appendix to Chapter 4

### F.1 PATH INTEGRAL CALCULATION OF FLUCTUATIONS

In this Appendix, we review the procedure for calculating the fluctuations of observables in disordered systems using the path integral approach.

Calculating statistical quantities in disordered systems, such as averages and variances, is in general a non-trivial task. This arises from the fact that correlation functions such as  $G(\tau - \tau')$  for a given disorder realization  $J_{ijkl}$  (this notation is specific to an SYK model, which we will use without loss of generality) are given by functional integrals of the form

$$G(\tau - \tau') = \frac{1}{N} \frac{\int \mathcal{D}c^\dagger \mathcal{D}c \sum_i c_i^\dagger(\tau) c_i(\tau') e^{-S[c, c^\dagger, J_{ijkl}]}}{\int \mathcal{D}c^\dagger \mathcal{D}c e^{-S[c, c^\dagger, J_{ijkl}]}}. \quad (\text{F.1})$$

The mean of this quantity over an ensemble  $P(J_{ijkl})$  is given by integrating it over all realizations of  $J_{ijkl}$ . This averaging cannot simply be done, as Eq. F.1 is a ratio of two quantities. What can be done analytically is carry out the average of the numerator and denominator separately - this constitutes treating the random variables  $J_{ijkl}$  on the same footing as our physical variables  $c_i^\dagger, c_i$ . Treating the disorder average properly requires techniques such as the replica trick [123], which we will employ here. Supersymmetric techniques have also been

developed for dealing with these averages [124], which is the primary method used for calculating conductance fluctuations of free electrons and generally yields more reliable results than the replica approach, the latter of which requires a generally-uncontrolled analytical continuation of the number of replicas  $M \rightarrow 0$ . However, these supersymmetric techniques are not appropriate for including the effects of strong interactions. Recent advances have generalized these supersymmetry techniques to a particular variant of the SYK model [431], and an interesting direction for future research would be to see whether such an approach is applicable to our model or a variant thereof that would allow for more controlled calculations of transport fluctuations.

Here, we make explicit the setup we use to calculate fluctuations of quantities like  $G(i\omega)$ . What we are interested in is the covariance of the Green's function at different frequencies, such as  $\frac{1}{N^2} \sum_{ij} \left[ \overline{G_{ii}(i\omega)G_{jj}(i\epsilon)} - \overline{G_{ii}(i\omega)} \overline{G_{jj}(i\epsilon)} \right]$ . Using the replica trick, we can rewrite the product of Green's functions  $G(\tau_1 - \tau_2)G(\tau_3 - \tau_4)$  as a functional integral taken over two copies of fermionic variables,  $c_i^a, c_i^{\dagger a}, \tilde{c}_i^{a'}, \tilde{c}_i^{\dagger a'}$ , with  $i$  a site index and  $a, a'$  replica indices,

$$\lim_{M, M' \rightarrow 0} \frac{1}{N^2 MM'} \sum_{\substack{1 < a < M \\ 1 < a' < M'}} \int \sum_{i,j} c_i^{\dagger a}(\tau_1) c_i^a(\tau_2) \tilde{c}_j^{\dagger a'}(\tau_3) \tilde{c}_j^{a'}(\tau_4) e^{-\sum_a S[c_i^{\dagger a}, c_i^a, J_{ijkl}] - \sum_{a'} S[\tilde{c}_i^{\dagger a'}, \tilde{c}_i^{a'}, J_{ijkl}]} \quad (\text{F.2})$$

We can dispense of the independent replica summations and the distinction between  $c$  and  $\tilde{c}$  by combining them into an enlarged summation,

$$\lim_{M \rightarrow 0} \frac{1}{N^2 M^2} \sum_{\substack{1 < a, b < M \\ a \neq b}} \int \sum_{i,j} c_i^{\dagger a}(\tau_1) c_i^a(\tau_2) c_j^{\dagger b}(\tau_3) c_j^b(\tau_4) e^{-\sum_d S[c_i^{\dagger d}, c_i^d, J_{ijkl}]} \quad (\text{F.3})$$

The action  $S$  is a function of the random variables  $J_{ijkl}$ , and the disorder average is performed over the above quantity. Doing this induces interactions between the different replicas. Subtracting off the disconnected contribution,  $\overline{G(\tau_1 - \tau_2)} \overline{G(\tau_3 - \tau_4)}$  constitutes disregarding contributions that do not contain any interactions between the two replica indices. An analogous treatment of the off-diagonal covariance,  $\frac{1}{N^2} \sum_{ij} \left[ \overline{G_{ij}(i\omega)G_{ji}(i\epsilon)} - \overline{G_{ij}(i\omega)} \overline{G_{ji}(i\epsilon)} \right]$  leads to an expectation value of the form  $c_i^{\dagger a}(\tau_1) c_i^b(\tau_2) c_j^{\dagger b}(\tau_3) c_j^a(\tau_4)$ .

For our calculations, we will proceed perturbatively starting from the replica-symmetric saddle point. If we use this as our starting point, our propagators will remain replica-symmetric

to all orders in perturbation theory [19]. It has been shown that for free fermions, this approximation is sufficient for accurately recovering the leading-order contribution to the mean value of  $G(\tau_1 - \tau_2)$ , although  $N^{-1}$  corrections require replica-off-diagonal saddles [230]. For four-point functions like Eq. F.2, it is known that a replica-diagonal ansatz is insufficient for reproducing the full spectral correlations of random matrix theory [490] for small  $\mathcal{O}(N^{-1})$  energy differences, but can be recovered by considering off-diagonal saddle manifolds [230]. This discrepancy is not relevant for our analysis, as we will only be interested in spectral correlations over  $\mathcal{O}(T)$  energy differences.

## F.2 REPLICA OFF-DIAGONAL FLUCTUATIONS IN THE $(G, \Sigma)$ ACTION

The calculation of the Green's function covariances may be performed within the formalism of the  $(G, \Sigma)$  path integral, which we describe here. Although this perspective does not provide a direct computational advantage over the fermionic diagram approach in the main text - all non-trivial integrals are still present - it admits an explicit  $N^{-1}$  expansion, in contrast with the diagrammatic approach in the main text where the task of writing down all diagrams that contribute at a given order requires careful analysis of index summations. The approach here is more easily generalizable to the calculation of higher order moments, and also provides a more general framework for understanding which observables obey a straightforward crossover from SYK-like to Fermi liquid-like as a function of temperature and which ones have more subtle crossover behavior - the former are functions of only the saddle point solutions of the  $(G, \Sigma)$  path integral, whereas the latter are properties of fluctuations around the saddle point. Here, we rederive the off-diagonal Green's function covariance,  $\rho_o$ , using this formulation.

We begin with a derivation of the  $(G, \Sigma)$  path integral. Recall that our Hamiltonian is given by

$$H = \frac{1}{(2N)^{3/2}} \sum_{ij;kl=1}^N J_{ij;kl} c_i^\dagger c_j^\dagger c_k c_l + \frac{1}{N^{1/2}} \sum_{ij=1}^N t_{ij} c_i^\dagger c_j - \mu \sum_i c_i^\dagger c_i \quad (\text{F.4})$$

where  $J_{ij;kl}$  and  $t_{ij}$  are complex random numbers with zero mean and variances  $J^2$  and  $t^2$ ,

respectively. In path integral form, we have the partition function

$$\begin{aligned} \overline{Z[h]^M} &= \int \mathcal{D}J \mathcal{D}t \mathcal{D}c \mathcal{D}c^\dagger e^{-\sum_{a=1}^M S_a[J]} \\ S_a[J] &= \sum_{ij} \int d\tau c_i^{\dagger a}(\tau) \left[ (\partial_\tau - \mu) \delta_{ij} + \frac{t_{ij}}{N^{1/2}} \right] c_j^a(\tau) \\ &\quad + \frac{1}{(2N)^{3/2}} \sum_{ij;kl} \int d\tau J_{ij;kl} c_i^{\dagger a}(\tau) c_j^{\dagger a}(\tau) c_k^a(\tau) c_l^a(\tau) \end{aligned} \quad (\text{F.5})$$

Integrating over disorder, our path integral becomes

$$\begin{aligned} Z[h] &= \int \mathcal{D}c \mathcal{D}c^\dagger e^{-S} \\ S &= \sum_{a,i} \int d\tau c_i^{\dagger a}(\partial_\tau - \mu) c_i^a \\ &\quad - \sum_{a,b} \int d\tau_1 d\tau_2 \left[ \frac{NJ^2}{4} \left( \frac{1}{N} \sum_i c_i^{\dagger a}(\tau_1) c_i^b(\tau_2) \right)^2 \left( \frac{1}{N} \sum_i c_i^{\dagger b}(\tau_2) c_i^a(\tau_1) \right)^2 \right. \\ &\quad \left. - \frac{Nt^2}{2} \left( \frac{1}{N} \sum_i c_i^{\dagger a}(\tau_1) c_i^b(\tau_2) \right) \left( \frac{1}{N} \sum_i c_i^{\dagger b}(\tau_2) c_i^a(\tau_1) \right) \right] \end{aligned} \quad (\text{F.6})$$

We now insert the field

$$G^{ab}(\tau_1, \tau_2) \equiv \frac{1}{N} \sum_i c_i^{\dagger a}(\tau_1) c_i^b(\tau_2) \quad (\text{F.7})$$

where the equivalence is enforced with a Lagrange multiplier  $\Sigma^{ab}(\tau_1, \tau_2)$ . The  $c, c^\dagger$  fields can be integrated out to yield the action

$$\begin{aligned} \frac{S[G, \Sigma, h]}{N} &= -\ln \det(-\partial_\tau + \mu - \Sigma) - \sum_{a,b} \int d\tau_{1,2} \left( \Sigma^{ab}(\tau_1, \tau_2) G^{ba}(\tau_2, \tau_1) \right. \\ &\quad \left. + \frac{J^2}{4} \left( G^{ab}(\tau_1, \tau_2) G^{ba}(\tau_2, \tau_1) \right)^2 - \frac{t^2}{2} G^{ab}(\tau_1, \tau_2) G^{ba}(\tau_2, \tau_1) \right). \end{aligned} \quad (\text{F.8})$$

We take the replica-diagonal saddle point,  $G^{ab}(\tau_1, \tau_2) = \delta_{ab} G(\tau_1 - \tau_2)$  and likewise for  $\Sigma^{ab}$ . The replica-diagonal Schwinger-Dyson equations are given by Eq. 8.46 in the main text - as emphasized earlier, it is the solution to this set of equations that displays a crossover from SYK-like for  $T \gg E_{\text{coh}}$  to Fermi liquid-like for  $T \ll E_{\text{coh}}$ . This saddle-point solution does not contribute to the Green's function covariance; to obtain a non-zero value, we must consider fluctuations around it,  $G^{ab}(\tau_1, \tau_2) \equiv \delta_{ab} G(\tau_1 - \tau_2) + \delta G^{ab}(\tau_1, \tau_2)$ .

In this representation, our observables of interest are

$$\begin{aligned} g_o(\tau_{1,2,3,4}) &\equiv \frac{1}{N^2} \sum_{ij} \left[ \overline{G_{ij}(\tau_1 - \tau_2) G_{ji}(\tau_3 - \tau_4)} - \overline{G_{ij}(\tau_1 - \tau_2)} \overline{G_{ji}(\tau_3 - \tau_4)} \right] \\ &= \langle G^{ab}(\tau_1 - \tau_2) G^{ba}(\tau_3 - \tau_4) \rangle - \frac{1}{N} \langle G^{aa}(\tau_1 - \tau_2) G^{bb}(\tau_3 - \tau_4) \rangle \end{aligned} \quad (\text{F.9})$$

for  $a \neq b$ . Note the subleading correction in  $g_o$ , which arises from the  $i = j$  term in the disconnected contribution (the “standard” disconnected part of  $g_o$  vanishes due to the fact that  $\langle G^{ab} \rangle = 0$  for fluctuations around the replica-diagonal saddle point).

These replica off-diagonal observables vanish at the replica-diagonal saddle point. To find the leading order non-zero result, we expand the action around its saddle-point solution. The expansion of everything other than the determinant is rather straightforward. For evaluation of the determinant, we use Jacobi’s formula

$$\begin{aligned} \frac{1}{\det(-\partial_\tau + \mu - \Sigma)} \frac{\partial \det(-\partial_\tau + \mu - \Sigma)}{\partial \Sigma^{ab}(\tau_1, \tau_2)} &= -\text{Tr} \left[ (-\partial_\tau + \mu - \Sigma)^{-1} \frac{\partial \Sigma}{\partial \Sigma^{ab}(\tau_1, \tau_2)} \right] \\ &= - \left[ (-\partial_\tau + \mu - \Sigma)^{-1} \right]^{ba}(\tau_2, \tau_1) = -\delta_{ab} G(\tau_2 - \tau_1) \end{aligned} \quad (\text{F.10})$$

where in the final line we evaluate the expression at the replica-diagonal saddle point. To second order, we use

$$\begin{aligned} \frac{1}{\det(-\partial_\tau + \mu - \Sigma)} \frac{\partial^2 \det(-\partial_\tau + \mu - \Sigma)}{\partial \Sigma^{ab}(\tau_1, \tau_2) \partial \Sigma^{cd}(\tau_3, \tau_4)} \\ &= -\frac{1}{\det(-\partial_\tau + \mu - \Sigma)} \frac{\partial}{\partial \Sigma^{cd}(\tau_3, \tau_4)} \left[ \det(-\partial_\tau + \mu - \Sigma) \text{Tr} \left[ (-\partial_\tau + \mu - \Sigma)^{-1} \frac{\partial \Sigma}{\partial \Sigma^{ab}(\tau_1, \tau_2)} \right] \right] \\ &= \delta_{ab} \delta_{cd} G(\tau_2 - \tau_1) G(\tau_4 - \tau_3) - \text{Tr} \left[ \delta \Sigma^{ab} G \delta \Sigma^{ba} G \right] \end{aligned} \quad (\text{F.11})$$

This leads to the quadratic action

$$\begin{aligned}
 \frac{\delta S[\delta G, \delta \Sigma]}{N} = & \sum_{ab} \left[ \frac{1}{2} \text{Tr} [G \delta \Sigma^{ab} G \delta \Sigma^{ba}] \right. \\
 & - \int d\tau_1 d\tau_2 \delta G^{ab}(\tau_1, \tau_2) \left[ \delta \Sigma^{ba}(\tau_2, \tau_1) - \frac{t^2}{2} \delta G^{ba}(\tau_2, \tau_1) \right] \\
 & - \frac{J^2 \delta_{ab}}{2} \int d\tau_1 d\tau_2 \left( 2G(\tau_1, \tau_2)G(\tau_2, \tau_1)\delta G^{aa}(\tau_1, \tau_2)\delta G^{aa}(\tau_2, \tau_1) \right. \\
 & \left. \left. + G(\tau_1, \tau_2)^2 \delta G^{aa}(\tau_2, \tau_1)\delta G^{aa}(\tau_1, \tau_2) \right) \right]
 \end{aligned} \tag{F.12}$$

The trace notation in the first term is shorthand for four time integrals, i.e.  $\text{Tr}[G\Sigma] =$

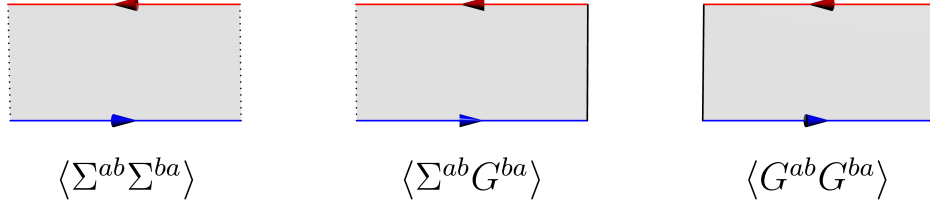


Figure F.1: We illustrate the propagators for use in a diagrammatic expansion in  $N^{-1}$  around the saddle point of the  $(G, \Sigma)$  action. The fields  $G$  and  $\Sigma$  are a function of two times and two replica indices, which necessitates the sheet-like representation above. The colors indicate different replica indices  $a, b$ , and solid (dotted) lines indicate a  $G$  ( $\Sigma$ ) field.

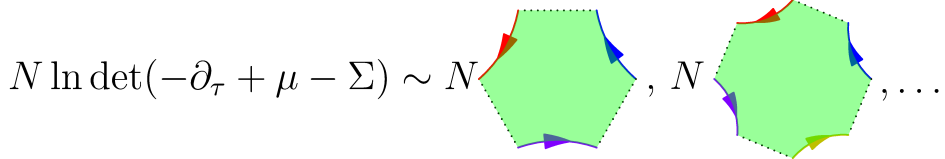


Figure F.2: Interactions arise in an expansion around the  $(G, \Sigma)$  saddle point from expanding the  $\ln \det(-\partial_\tau + \mu - \Sigma)$  term, which leads to arbitrary order sheets for which  $\Sigma$  propagators can be attached to

$\int d\tau_a d\tau_b G(\tau_a, \tau_b)\Sigma(\tau_b, \tau_a)$ . We can invert the quadratic action to obtain a propagator, which we can do separately for the replica diagonal and replica off-diagonal components. For the

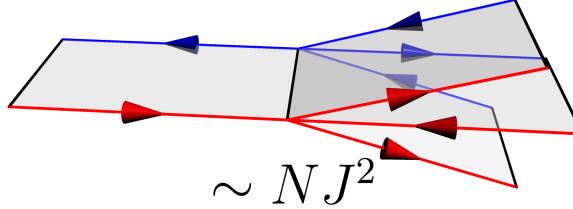


Figure F.3: Within a diagrammatic expansion around the  $(G, \Sigma)$  saddle point, the SYK interaction generates a vertex such that four  $G$  fields can be attached at a “seam.”

latter, we have

$$\begin{aligned}
 -\frac{2\delta S}{N} = & \int d\tau_{1,2,3,4} \begin{pmatrix} \delta G^{ab}(\tau_1, \tau_2) & \delta \Sigma^{ab}(\tau_1, \tau_2) \end{pmatrix} \begin{pmatrix} -t^2 \delta_{\tau_1, \tau_3} \delta_{\tau_2, \tau_4} & \delta_{\tau_1, \tau_3} \delta_{\tau_2, \tau_4} \\ \delta_{\tau_1, \tau_3} \delta_{\tau_2, \tau_4} & -G(\tau_1 - \tau_3)G(\tau_2 - \tau_4) \end{pmatrix} \\
 & \times \begin{pmatrix} \delta G^{ba}(\tau_4, \tau_3) \\ \delta \Sigma^{ba}(\tau_4, \tau_3) \end{pmatrix}
 \end{aligned} \tag{F.13}$$

The matrix must be inverted, which can most easily be done in Matsubara frequency space.

This leads to the result

$$\begin{aligned}
 \langle \delta G^{a \neq b}(\tau_1, \tau_2) \delta G^{b \neq a}(\tau_4, \tau_3) \rangle &= \frac{1}{N\beta^2} \sum_{i\omega_n, i\epsilon_n} e^{-i\omega_n(\tau_1 - \tau_3) - i\epsilon_n(\tau_4 - \tau_2)} \frac{G(i\omega_n)G(i\epsilon_n)}{1 - t^2 G(i\omega_n)G(i\epsilon_n)}, \\
 \langle \delta \Sigma^{a \neq b}(\tau_1, \tau_2) \delta G^{b \neq a}(\tau_4, \tau_3) \rangle &= \frac{1}{N\beta^2} \sum_{i\omega_n, i\epsilon_n} e^{-i\omega_n(\tau_1 - \tau_3) - i\epsilon_n(\tau_4 - \tau_2)} \frac{1}{1 - t^2 G(i\omega_n)G(i\epsilon_n)}, \\
 \langle \delta \Sigma^{a \neq b}(\tau_1, \tau_2) \delta \Sigma^{b \neq a}(\tau_4, \tau_3) \rangle &= \frac{1}{N\beta^2} \sum_{i\omega_n, i\epsilon_n} e^{-i\omega_n(\tau_1 - \tau_3) - i\epsilon_n(\tau_4 - \tau_2)} \frac{t^2}{1 - t^2 G(i\omega_n)G(i\epsilon_n)}.
 \end{aligned} \tag{F.14}$$

This gives the expected result for  $g_o$  in Eq. 8.21 of the main text once the trivial disconnected piece of  $g_o$  is subtracted off. Note that for  $t = 0$ , while  $\langle \delta G^{ab} \delta G^{ba} \rangle$  is non-zero, its contribution to  $g_o$  is subtracted off exactly by the disconnected piece. Hence, the leading order contribution to  $g_o$  when  $t = 0$  is given by the first correction to the  $G^{ab}$  propagator, illustrated in Fig. F.4. This corresponds to the fermionic Feynman diagram shown in the top of Fig. 8.3 in the main text.

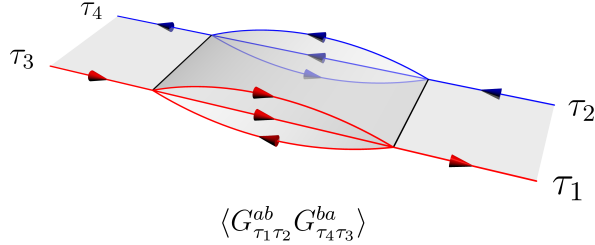


Figure F.4: We illustrate Feynman diagrams that contribute to the off-diagonal Green's function covariance in a pure SYK model. For a model that includes random hoppings, there exists a non-trivial contribution in the bare  $\delta G^{ab}\delta G^{ba}$  propagator; for a pure SYK model, this contribution is subtracted off exactly in the covariance and one must include the leading order correction to obtain a non-zero result.

### F.3 STATISTICS OF RATIO DISTRIBUTIONS

Here, we provide a summary of relevant results involving ratio distributions, which we utilize for calculating statistical properties of the thermopower.

We take  $X_1, X_2$  to be two correlated Gaussian random variables, with means  $\mu_{1,2}$ , variances  $\sigma_{1,2}^2$ , and correlation coefficient  $r$ . Our quantity of interest is the random variable  $Z \equiv X_1/X_2$ . The probability density function  $f(z)$  of  $Z$  can be obtained from the joint density  $g(x_1, x_2)$  of  $X_{1,2}$ ,

$$f(z) = \int_{-\infty}^{\infty} |y| g(zy, y) dy . \quad (\text{F.15})$$

This function along with the cumulative distribution function  $F(z) \equiv \int_{-\infty}^z f(x) dx$  are known [189]. However, much like the Cauchy distribution - which is a limiting case of a ratio distribution when the numerator and denominator have zero mean - the integrals  $\int_{-\infty}^{\infty} z^a f(z) dz$ ,  $\alpha \geq 1$  do not converge and the mean and variance are formally ill-defined.

One can make progress in the limit where  $|\sigma_2/\mu_2| \rightarrow 0$ ; or in other words, when the probability of the denominator in  $Z$  becoming negative is zero. This result can equivalently be derived from the assumption that  $X_2 > 0$  which implies  $F(z) \equiv P(x_1/x_2 < z) = P(x_1 - zx_2 < 0)$ . Note that for our physical quantity of interest, the denominator is given by the integral of the single particle density of states weighted by the derivative of the Fermi function, which is strictly positive. Therefore, such manipulations are actually justified exactly, although this fact becomes less apparent when we only consider the leading order moments and take the distribution to be Gaussian. Since the sum of two correlated Gaussians is also a Gaussian,

this gives the cumulative distribution function

$$F(z) = \Phi\left(\frac{\mu_2 z - \mu_1}{\sqrt{\sigma_1^2 - 2zr\sigma_1\sigma_2 + z^2\sigma_2^2}}\right) \quad (\text{F.16})$$

where  $\Phi(x)$  is the cumulative distribution function of a Gaussian random variable,  $\Phi(x) \equiv \int_{-\infty}^x \phi(y) dy$ ,  $\phi(x) \equiv \frac{1}{\sqrt{2\pi}} e^{-\frac{1}{2}x^2}$ .

For small fluctuations around the mean value,  $\bar{z} = \mu_1/\mu_2$ , we have

$$\Phi\left(\frac{\mu_2 z - \mu_1}{\sqrt{\sigma_1^2 - 2zr\sigma_1\sigma_2 + z^2\sigma_2^2}}\right) \approx \Phi\left(\frac{z - \bar{z}}{\bar{z}\sqrt{\frac{\sigma_1^2}{\mu_1^2} - \frac{2r\sigma_1\sigma_2}{\mu_1\mu_2} + \frac{\sigma_2^2}{\mu_2^2}}}\right) \quad (\text{F.17})$$

which yields the approximation to normality, with variance

$$\frac{\text{Var } z}{\bar{z}^2} \approx \frac{\sigma_1^2}{\mu_1^2} - \frac{2r\sigma_1\sigma_2}{\mu_1\mu_2} + \frac{\sigma_2^2}{\mu_2^2}. \quad (\text{F.18})$$

In the main text, we find several situations where the numerator and denominator are highly correlated such that  $r = 1 - \mathcal{O}(N^{-1})$ , where we use  $N$  as a stand-in for a generic large dimensionless parameter, which depending on the context may refer to either the actual system size or  $T/E_{\text{coh}}$ . To leading order in  $N^{-1}$ , we therefore have *perfect* correlation between the numerator and denominator, leading to

$$\frac{\text{Var } z}{\bar{z}^2} \approx \left(\frac{\sigma_1}{\mu_1} - \frac{\sigma_2}{\mu_2}\right)^2 + \mathcal{O}(N^{-1}). \quad (\text{F.19})$$

Working in the limit of perfect correlation means that we may think of  $X_1$  and  $X_2$  as arising from the same normal distribution  $X$ , i.e.  $X_1 = \sigma_1 X + \mu_1$  and  $X_2 = \sigma_2 X + \mu_2$ . The ratio distribution is still non-trivial even if both variables arise from the same probability distribution. However, it does imply a special limit  $\sigma_1/\mu_1 = \sigma_2/\mu_2$  where the distribution becomes trivial and the variance vanishes due to the numerator and denominator being directly proportional to each other. In this limit, the variance incurs an additional  $N^{-1}$  suppression due to the necessity of expanding out  $r$  to higher order. This prediction is confirmed by numerical simulation, see Fig. F.5. We take 10000 samples of the ratio distribution  $Z$  for

parameters  $\sigma_1^2 = 1.5$ ,  $\sigma_2^2 = 1$ ,  $\mu_y = 10$ ,  $r = 1 - 1/N$ , and variable  $\mu_x$ . We fit the power law scaling of the variance as a function of  $N$  for  $500 < N < 10000$  and plot the exponent while varying  $\mu_x$ . As expected, an anomalous suppression of the variance appears at the critical value where  $\sigma_1/\mu_1 = \sigma_2/\mu_2$ .

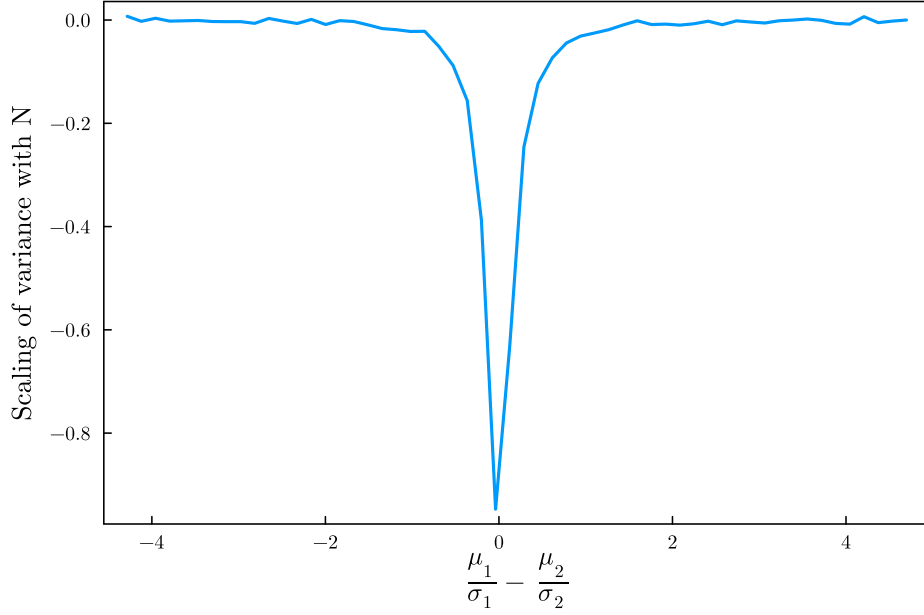


Figure F.5: By drawing from a ratio distribution, where the correlation coefficient between the numerator and denominator is given by  $1 - 1/N$ , we fit the variance to an  $N^\alpha$  form and plot the exponent  $\alpha$ . When the probability distributions are tuned such that  $\sigma_1/\mu_1 = \sigma_2/\mu_2$ , we obtain a  $N^{-1}$  suppression of the variance.

#### F.4 CONDUCTANCE FLUCTUATIONS FOR SINGLE-LEAD COUPLING

In the main text, we present results for conductance fluctuations for a model where we take our leads to be coupled to all sites with equal magnitude. To leading order in  $N^{-1}$ , fluctuations are controlled by the off-diagonal Green's function covariance  $\rho_o$ . If we instead choose to model our leads as only being coupled to a single site in the quantum dot, our results are modified as fluctuations are driven by the diagonal Green's function covariance  $\rho_d$ , which is generically suppressed relative to  $\rho_o$  by an additional factor of  $N^{-1}$ . Note that this contribution is still present in our model in the main text, but is ignored in virtue of this  $N^{-1}$  suppression. We present results for both  $\rho_o$  and  $\rho_d$  in the main text but focus on conductance fluctuations for

fully-connected leads. Here, we present results for conductance fluctuations that arise from  $\rho_d$ , which are subleading in  $N^{-1}$  for fully-connected leads but are the dominant contribution for leads coupled to a single site. We remind the reader that average conductance is insensitive to this choice and remains the same as in the main text.

For a free fermion model, we have the physical interpretation that  $\rho_d$  gives the covariance of the single-particle eigenvalues, the form of which is universal and well-known from random matrix theory. In particular, the variance of linear statistics such as the conductance is given by the Dyson-Mehta formula [121, 122], which yields the conductance variance

$$\text{Var } \sigma_{FF} = \left( \frac{e^2}{\hbar} \frac{\Gamma}{TN} \right)^2 \frac{3\zeta(3)}{\pi^4}. \quad (\text{F.20})$$

For a pure SYK model, our expression for  $\rho_d$  given in Eq. 8.40 yields

$$\text{Var } \sigma_{SYK} = \left( \frac{e^2 \Gamma}{\hbar} \right)^2 \frac{0.07}{N^4 JT}. \quad (\text{F.21})$$

We now consider the case with both SYK interactions and random hopping terms. For the low temperature Fermi liquid phase, we predict a scaling similar to the free fermion result in Eq. F.20, but with a renormalization which can be deduced on dimensional grounds to be

$$\text{Var } \sigma_{tSYK} \propto \left( \frac{\Gamma e^2}{\hbar TN} \frac{t}{J} \right)^2, \quad T \ll E_{\text{coh}}. \quad (\text{F.22})$$

For the SYK regime,  $T \gg E_{\text{coh}}$ , we find nearly identical to the case considered to the main text, due to the fact that in this regime,  $\rho_d(\omega, \epsilon) = N^{-1} \rho_o(\omega, \epsilon)$  to leading order in  $E_{\text{coh}}/T$ . Hence,

$$\text{Var } \sigma_{tSYK} = 2.02 \mathcal{E}^2 \left( \frac{\Gamma e^2}{\hbar NT} \frac{t}{J} \right)^2, \quad T \gg E_{\text{coh}}. \quad (\text{F.23})$$

Note that this is the same scaling as in the Fermi liquid regime, albeit with the crucial difference that the overall coefficient is proportional to the particle-hole asymmetry.

## References

- [1] Abrahams, E., Anderson, P. W., Licciardello, D. C., & Ramakrishnan, T. V. (1979). Scaling Theory of Localization: Absence of Quantum Diffusion in Two Dimensions. *Physical Review Letters*, 42(10), 673–676.
- [2] Abrahams, E. & Ramakrishnan, T. V. (1980). Scaling theory of localization and non-ohmic effects in two dimensions. *Journal of Non-Crystalline Solids*, 35–36, 15–20.
- [3] Affleck, I. & Marston, J. B. (1988a). Large-n limit of the heisenberg-hubbard model: Implications for high-T<sub>c</sub> superconductors. *Physical Review B*, 37(7), 3774–3777.
- [4] Affleck, I. & Marston, J. B. (1988b). Large-n limit of the heisenberg-hubbard model: Implications for high-T<sub>c</sub> superconductors. *Physical Review B*, 37(7), 3774–3777.
- [5] Alicea, J. (2008). Monopole quantum numbers in the staggered flux spin liquid. *Physical Review B*, 78(035126), 035126.
- [6] Alicki, R., Fannes, M., & Horodecki, M. (2009). On thermalization in Kitaev's 2D model. *Journal of Physics A: Mathematical and Theoretical*, 42(6), 065303.
- [7] Altinisik, S., Dizdarevic, D., & Main, J. (2019). Balanced gain and loss in spatially extended non-PT-symmetric multiwell potentials. *Physical Review A: Atomic, Molecular, and Optical Physics*, 100(6), 063639.
- [8] Altland, A. & Bagrets, D. (2018). Quantum ergodicity in the SYK model. *Nuclear Physics B*, 930, 45–68.
- [9] Altland, A., Bagrets, D., & Kamenev, A. (2019). Sachdev-ye-kitaev non-fermi-liquid correlations in nanoscopic quantum transport. *Physical Review Letters*, 123(22), 226801.
- [10] Al'tshuler, B. L. (1985). Fluctuations in the extrinsic conductivity of disordered conductors. *Soviet Journal of Experimental and Theoretical Physics Letters*, 41, 648.
- [11] Altshuler, B. L., Aronov, A. G., & Lee, P. A. (1980). Interaction effects in disordered fermi systems in two dimensions. *Physical Review Letters*, 44(19), 1288–1291.
- [12] Al'tshuler, B. L. & Shklovskii, B. I. (1986). Repulsion of energy levels and conductivity of small metal samples. *Soviet Journal of Experimental and Theoretical Physics*, 64, 127.
- [13] Amir, A., Hatano, N., & Nelson, D. R. (2016). Non-Hermitian localization in biological networks. *Physical Review E: Statistical Physics, Plasmas, Fluids, and Related Interdisciplinary Topics*, 93(4), 042310.
- [14] Anderson, L. E. (2022). Electrical and thermoelectric transport in mixed-dimensional graphitic mesoscopic systems. *Ph.D. thesis, Harvard University*.

- [15] Anderson, L. E., Laitinen, A., Zimmerman, A., Werkmeister, T., Shackleton, H., Kruchkov, A., Taniguchi, T., Watanabe, K., Sachdev, S., & Kim, P. (2023). Magneto-thermoelectric transport in graphene quantum dot with strong correlations. *to appear*.
- [16] Anderson, P. W. (1958). Absence of Diffusion in Certain Random Lattices. *Physical Review*, 109(5), 1492–1505.
- [17] Anderson, P. W. (1987). The Resonating Valence Bond State in La<sub>2</sub>CuO<sub>4</sub> and Superconductivity. *Science*, 235(4793), 1196–1198.
- [18] Anderson, P. W., Abrahams, E., & Ramakrishnan, T. V. (1979). Possible Explanation of Nonlinear Conductivity in Thin-Film Metal Wires. *Physical Review Letters*, 43(10), 718–720.
- [19] Aref'eva, I., Khramtsov, M., Tikhanovskaya, M., & Volovich, I. (2019). Replica-nondiagonal solutions in the SYK model. *Journal of High Energy Physics*, 2019(7), 113.
- [20] Arovas, D., Schrieffer, J. R., & Wilczek, F. (1984). Fractional Statistics and the Quantum Hall Effect. *Physical Review Letters*, 53(7), 722–723.
- [21] Arrachea, L. & Rozenberg, M. J. (2002). Infinite-range quantum random Heisenberg magnet. *Physical Review B*, 65(224430), 224430.
- [22] Ashida, Y., Furukawa, S., & Ueda, M. (2017). Parity-time-symmetric quantum critical phenomena. *Nature Communications*, 8(1), 15791.
- [23] Ashida, Y., Gong, Z., & Ueda, M. (2020). Non-hermitian physics. *arXiv e-prints*.
- [24] Assaad, F. F., Imada, M., & Scalapino, D. J. (1996). Quantum transition between an antiferromagnetic mott insulator and d<sub>x<sup>2</sup>-y<sup>2</sup></sub> superconductor in two dimensions. *Physical Review Letters*, 77(22), 4592–4595.
- [25] Babbush, R., Berry, D. W., & Neven, H. (2019). Quantum simulation of the sachdev-ye-kitaev model by asymmetric qubitization. *Physical Review A: Atomic, Molecular, and Optical Physics*, 99(4), 040301(R).
- [26] Bahari, B., Ndao, A., Vallini, F., El Amili, A., Fainman, Y., & Kanté, B. (2017). Non-reciprocal lasing in topological cavities of arbitrary geometries. *Science (New York, N.Y.)*, 358(6363), 636–640.
- [27] Bandres, M. A., Wittek, S., Harari, G., Parto, M., Ren, J., Segev, M., Christodoulides, D. N., & Khajavikhan, M. (2018). Topological insulator laser: Experiments. *Science (New York, N.Y.)*, 359(6381).
- [28] Bao, Y., Fan, R., Vishwanath, A., & Altman, E. (2023). Mixed-state topological order and the errorfield double formulation of decoherence-induced transitions.
- [29] Baranger, H. U. & Mello, P. A. (1994). Mesoscopic transport through chaotic cavities: A random S-matrix theory approach. *Physical Review Letters*, 73(1), 142–145.
- [30] Barlas, Y. & Yang, K. (2009). Non-Fermi-liquid behavior in neutral bilayer graphene. *Physical Review B*, 80(161408), 161408.

- [31] Barreiro, J. T., Müller, M., Schindler, P., Nigg, D., Monz, T., Chwalla, M., Hennrich, M., Roos, C. F., Zoller, P., & Blatt, R. (2011/02/01, 2011). An open-system quantum simulator with trapped ions. *Nature*, 470(7335), 486–491.
- [32] Becca, F. (2020). Talk at KITP, university of california, santa barbara, november 5. *Correlated Systems with Multicomponent Local Hilbert Spaces*.
- [33] Beenakker, C. W. J. (1997). Random-matrix theory of quantum transport. *Reviews of Modern Physics*, 69(3), 731–808.
- [34] Bender, C. M. (2007). Making sense of non-Hermitian hamiltonians. *Reports on Progress in Physics*, 70(6), 947–1018.
- [35] Bender, C. M. (2015). PT-symmetric quantum theory. *Journal of Physics: Conference Series*, 631, 012002.
- [36] Bender, C. M., Berntson, B. K., Parker, D., & Samuel, E. (2013a). Observation of PT phase transition in a simple mechanical system. *American Journal of Physics*, 81(3), 173–179.
- [37] Bender, C. M. & Boettcher, S. (1998). Real spectra in non-hermitian hamiltonians having PT symmetry. *Physical Review Letters*, 80(24), 5243–5246.
- [38] Bender, C. M., Boettcher, S., & Meisinger, P. N. (1999). PT-symmetric quantum mechanics. *Journal of Mathematical Physics*, 40(5), 2201–2229.
- [39] Bender, C. M., Brody, D. C., & Jones, H. F. (2003). Must a hamiltonian be hermitian? *American Journal of Physics*, 71(11), 1095–1102.
- [40] Bender, N., Factor, S., Bodyfelt, J. D., Ramezani, H., Christodoulides, D. N., Ellis, F. M., & Kottos, T. (2013b). Observation of asymmetric transport in structures with active nonlinearities. *Physical Review Letters*, 110(23), 234101.
- [41] Bergholtz, E. J., Budich, J. C., & Kunst, F. K. (2019). Exceptional topology of non-hermitian systems. *arXiv e-prints*, (arXiv:1912.10048), arXiv:1912.10048.
- [42] Bernu, B., Lecheminant, P., Lhuillier, C., & Pierre, L. (1994). Exact spectra, spin susceptibilities, and order parameter of the quantum Heisenberg antiferromagnet on the triangular lattice. *Physical Review B*, 50(14), 10048–10062.
- [43] Berthod, C., Giamarchi, T., Biermann, S., & Georges, A. (2006). Breakup of the fermi surface near the mott transition in low-dimensional systems. *Physical Review Letters*, 97(13), 136401.
- [44] Bittner, S., Dietz, B., Günther, U., Harney, H. L., Miski-Oglu, M., Richter, A., & Schäfer, F. (2012). PT symmetry and spontaneous symmetry breaking in a microwave billiard. *Physical Review Letters*, 108(2), 024101.
- [45] Bojesen, T. A. & Sudbø, A. (2013). Berry phases, current lattices, and suppression of phase transitions in a lattice gauge theory of quantum antiferromagnets. *Physical Review B*, 88(9), 094412.
- [46] Bonderson, P., Cheng, M., Patel, K., & Plamadeala, E. (2016). Topological enrichment of luttinger's theorem. *arXiv e-prints*.

- [47] Bonzom, V., Gurau, R., Riello, A., & Rivasseau, V. (2011). Critical behavior of colored tensor models in the large N limit. *Nuclear Physics B*, 853(1), 174–195.
- [48] Bordelon, M., Kenney, E., Hogan, T., Posthuma, L., Kavand, M., Lyu, Y., Sherwin, M., Brown, C., Graf, M. J., Balents, L., & Wilson, S. D. (2019). Field-tunable quantum disordered ground state in the triangular lattice antiferromagnet NaYbO<sub>2</sub>. *Nature Physics*, 15(10), 1058–1064.
- [49] Bordelon, M. M., Liu, C., Posthuma, L., Sarte, P. M., Butch, N. P., Pajerowski, D. M., Banerjee, A., Balents, L., & Wilson, S. D. (2020). Spin excitations in the frustrated triangular lattice antiferromagnet NaYbO<sub>2</sub>. *Physical Review B*, 101(224427), 224427.
- [50] Borgnia, D. S., Kruchkov, A. J., & Slager, R.-J. (2020). Non-hermitian boundary modes and topology. *Physical Review Letters*, 124(5), 056802.
- [51] Borokhov, V., Kapustin, A., & Wu, X. (2002). Topological disorder operators in three-dimensional conformal field theory. *Journal of High Energy Physics*, 2002(11), 049–049.
- [52] Boyack, R., Yerzhakov, H., & Maciejko, J. (2021). Quantum phase transitions in Dirac fermion systems. *European Physical Journal ST: Special Topics*, 230(4), 979–992.
- [53] Brandstetter, M., Liertzer, M., Deutsch, C., Klang, P., Schöberl, J., Türeci, H. E., Strasser, G., Unterrainer, K., & Rotter, S. (2014). Reversing the pump dependence of a laser at an exceptional point. *Nature Communications*, 5(1), 4034.
- [54] Bravyi, S., Leemhuis, B., & Terhal, B. M. (2011). Topological order in an exactly solvable 3D spin model. *Annals of Physics*, 326(4), 839–866.
- [55] Brézin, E. & Zee, A. (1994). Correlation functions in disordered systems. *Physical Review E*, 49(4), 2588–2596.
- [56] Brody, D. C. (2014). Biorthogonal quantum mechanics. *Journal of Physics A Mathematical General*, 47(035305), 035305.
- [57] Broholm, C., Cava, R. J., Kivelson, S. A., Nocera, D. G., Norman, M. R., & Senthil, T. (2020). Quantum spin liquids. *Science (New York, N.Y.)*, 367(6475), eaay0668.
- [58] Brown, B. J., Loss, D., Pachos, J. K., Self, C. N., & Wootton, J. R. (2016). Quantum memories at finite temperature. *Reviews of Modern Physics*, 88(4), 045005.
- [59] Brzezinska, M., Guan, Y., Yazyev, O. V., Sachdev, S., & Kruchkov, A. (2023). Engineering SYK interactions in disordered graphene flakes under realistic experimental conditions. *Physical Review Letters*, 131(3), 036503.
- [60] Buča, B. & Prosen, T. (2012). A note on symmetry reductions of the Lindblad equation: Transport in constrained open spin chains. *New Journal of Physics*, 14(7), 073007.
- [61] Budich, J. C., Carlström, J., Kunst, F. K., & Bergholtz, E. J. (2019). Symmetry-protected nodal phases in non-Hermitian systems. *Physical Review B*, 99(4), 041406(R).
- [62] Buth, C., Santra, R., & Cederbaum, L. S. (2004). Non-hermitian Rayleigh-Schrödinger perturbation theory. *Physical Review A: Atomic, Molecular, and Optical Physics*, 69(3), 032505.

- [63] Cai, Z. & Barthel, T. (2013). Algebraic versus Exponential Decoherence in Dissipative Many-Particle Systems. *Physical Review Letters*, 111(15), 150403.
- [64] Cai, Z. & Liu, J. (2018). Approximating quantum many-body wave functions using artificial neural networks. *Physical Review B*, 97(3), 035116.
- [65] Caliceti, E. (2004). Real spectra of PT-symmetric operators and perturbation theory. *Czechoslovak Journal of Physics*, 54(10), 1065–1068.
- [66] Camjayi, A. & Rozenberg, M. J. (2003). Quantum and thermal fluctuations in the SU(N) heisenberg spin-glass model near the quantum critical point. *Physical Review Letters*, 90(217202), 217202.
- [67] Can, O., Nica, E. M., & Franz, M. (2019). Charge transport in graphene-based mesoscopic realizations of Sachdev-Ye-Kitaev models. *Physical Review B*, 99(4), 045419.
- [68] Capriotti, L., Becca, F., Parola, A., & Sorella, S. (2001). Resonating valence bond wave functions for strongly frustrated spin systems. *Physical Review Letters*, 87(097201), 097201.
- [69] Capriotti, L., Trumper, A. E., & Sorella, S. (1999). Long-range néel order in the triangular heisenberg model. *Physical Review Letters*, 82(19), 3899–3902.
- [70] Carleo, G. & Troyer, M. (2017). Solving the Quantum Many-Body Problem with Artificial Neural Networks. *Science*, 355(6325), 602–606.
- [71] Carmichael, H. (1993). *An Open Systems Approach to Quantum Optics: Lectures Presented at the Université Libre de Bruxelles October 28 to November 4, 1991*, volume 18 of *Lecture Notes in Physics Monographs*. Berlin, Heidelberg: Springer.
- [72] Celardo, G. L. & Kaplan, L. (2009). Superradiance transition in one-dimensional nanostructures: An effective non-Hermitian Hamiltonian formalism. *Physical Review B*, 79(15), 155108.
- [73] Cha, P., Wentzell, N., Parcollet, O., Georges, A., & Kim, E.-A. (2020). Linear resistivity and Sachdev-Ye-Kitaev (SYK) spin liquid behavior in a quantum critical metal with spin-1/2 fermions. 117, 18341.
- [74] Chamon, C. (2005). Quantum glassiness in strongly correlated clean systems: An example of topological overprotection. *Physical Review Letters*, 94(4), 040402.
- [75] Chandra, P., Coleman, P., & Larkin, A. I. (1990). Ising transition in frustrated Heisenberg models. *Physical Review Letters*, 64(1), 88–91.
- [76] Chang, L., Jiang, X., Hua, S., Yang, C., Wen, J., Jiang, L., Li, G., Wang, G., & Xiao, M. (2014). Parity-time symmetry and variable optical isolation in active-passive-coupled microresonators. *Nature Photonics*, 8(7), 524–529.
- [77] Chatterjee, S. & Sachdev, S. (2016). Fractionalized Fermi liquid with bosonic chargons as a candidate for the pseudogap metal. *Physical Review B*, 94(205117), 205117.
- [78] Chen, A., Ilan, R., de Juan, F., Pikulin, D. I., & Franz, M. (2018). Quantum Holography in a Graphene Flake with an Irregular Boundary. *Physical Review Letters*, 121(3), 036403.

- [79] Chen, K., Huang, Y., Deng, Y., Kuklov, A. B., Prokof'ev, N. V., & Svistunov, B. V. (2013). Deconfined criticality flow in the heisenberg model with ring-exchange interactions. *Physical Review Letters*, 110(18), 185701.
- [80] Cheng, M., Zaletel, M., Barkeshli, M., Vishwanath, A., & Bonderson, P. (2016). Translational symmetry and microscopic constraints on symmetry-enriched topological phases: A view from the surface. *Physical Review X*, 6(4), 041068.
- [81] Chester, S. M. & Su, N. (2024). Bootstrapping deconfined quantum tricriticality. *Physical Review Letters*, 132(11), 111601.
- [82] Chew, A., Essin, A., & Alicea, J. (2017). Approximating the Sachdev-Ye-Kitaev model with Majorana wires. *Physical Review B*, 96(12), 121119(R).
- [83] Choi, Y., Kang, S., Lim, S., Kim, W., Kim, J.-R., Lee, J.-H., & An, K. (2010). Quasieigenstate coalescence in an atom-cavity quantum composite. *Physical Review Letters*, 104(15), 153601.
- [84] Chong, Y. D., Ge, L., & Stone, A. D. (2011). P T -Symmetry breaking and laser-absorber modes in optical scattering systems. *Physical Review Letters*, 106(9), 093902.
- [85] Chowdhury, D., Georges, A., Parcollet, O., & Sachdev, S. (2022). Sachdev-Ye-Kitaev models and beyond: Window into non-Fermi liquids. *Reviews of Modern Physics*, 94(3), 035004.
- [86] Christos, M., Haehl, F. M., & Sachdev, S. (2022). Spin liquid to spin glass crossover in the random quantum Heisenberg magnet. *Physical Review B*, 105(8), 085120.
- [87] Christos, M., Luo, Z.-X., Shackleton, H., Zhang, Y.-H., Scheurer, M. S., & Sachdev, S. (2023). A model of d-wave superconductivity, antiferromagnetism, and charge order on the square lattice. 120(21), e2302701120.
- [88] Christos, M. & Sachdev, S. (2024). Emergence of nodal Bogoliubov quasiparticles across the transition from the pseudogap metal to the d-wave superconductor. *npj Quantum Materials*, 9(4), 4.
- [89] Christos, M., Shackleton, H., Sachdev, S., & Luo, Z.-X. (2024). Deconfined quantum criticality of nodal \$d\$-wave superconductivity, N\'eel order and charge order on the square lattice at half-filling.
- [90] Chua, V., Yao, H., & Fiete, G. A. (2011). Exact chiral spin liquid with stable spin Fermi surface on the kagome lattice. *Physical Review B*, 83(18), 180412(R).
- [91] Coissard, A., Wander, D., Vignaud, H., Grushin, A. G., Repellin, C., Watanabe, K., Taniguchi, T., Gay, F., Winkelmann, C. B., Courtois, H., Sellier, H., & Sacépé, B. (2022). Imaging tunable quantum Hall broken-symmetry orders in graphene. *Nature*, 605(7908), 51–56.
- [92] Coletta, T., Picon, J.-D., Korshunov, S. E., & Mila, F. (2011). Phase diagram of the fully frustrated transverse-field Ising model on the honeycomb lattice. *Physical Review B*, 83(5), 054402.

- [93] Cookmeyer, T., Motruk, J., & Moore, J. E. (2021). Four-Spin Terms and the Origin of the Chiral Spin Liquid in Mott Insulators on the Triangular Lattice. *Physical Review Letters*, 127(8), 087201.
- [94] Costi, T. A. & Zlatić, V. (2010). Thermoelectric transport through strongly correlated quantum dots. *Physical Review B*, 81(23), 235127.
- [95] Cotler, J. S., Gur-Ari, G., Hanada, M., Polchinski, J., Saad, P., Shenker, S. H., Stanford, D., Streicher, A., & Tezuka, M. (2017). Black Holes and Random Matrices. *Journal of High Energy Physics*, 2017(5), 118.
- [96] Cunden, F. D., Facchi, P., & Vivo, P. (2015). Joint statistics of quantum transport in chaotic cavities. *Europhysics Letters*, 110(5), 50002.
- [97] Cunden, F. D. & Vivo, P. (2014). Universal Covariance Formula for Linear Statistics on Random Matrices. *Physical Review Letters*, 113(7), 070202.
- [98] Dagotto, E. & Moreo, A. (1989). Phase diagram of the frustrated spin-1/2 Heisenberg antiferromagnet in 2 dimensions. *Physical Review Letters*, 63(19), 2148–2151.
- [99] Dai, P.-L., Zhang, G., Xie, Y., Duan, C., Gao, Y., Zhu, Z., Feng, E., Tao, Z., Huang, C.-L., Cao, H., Podlesnyak, A., Granroth, G. E., Everett, M. S., Neufeld, J. C., Voneshen, D., Wang, S., Tan, G., Morosan, E., Wang, X., Lin, H.-Q., Shu, L., Chen, G., Guo, Y., Lu, X., & Dai, P. (2021). Spinon fermi surface spin liquid in a triangular lattice antiferromagnet NaYbSe<sub>2</sub>. *Physical Review X*, 11(021044), 021044.
- [100] Dai, X.-D., Song, F., & Wang, Z. (2023). Solvable BCS-Hubbard Lindbladians in arbitrary dimensions.
- [101] Daley, A. J. (2014). Quantum trajectories and open many-body quantum systems. *Advances in Physics*, 63(2), 77–149.
- [102] Danshita, I., Hanada, M., & Tezuka, M. (2017). Creating and probing the Sachdev-Ye-Kitaev model with ultracold gases: Towards experimental studies of quantum gravity. *Progress of Theoretical and Experimental Physics*, 2017(8), 083I01.
- [103] Dasgupta, C. & Halperin, B. I. (1981). Phase Transition in a Lattice Model of Superconductivity. *Physical Review Letters*, 47(21), 1556–1560.
- [104] de Leeuw, M., Paletta, C., & Pozsgay, B. (2021). Constructing Integrable Lindblad Superoperators. *Physical Review Letters*, 126(24), 240403.
- [105] de Vega, I. & Alonso, D. (2017). Dynamics of non-Markovian open quantum systems. *Reviews of Modern Physics*, 89(1), 015001.
- [106] Delgado Mercado, Y., Gattringer, C., & Schmidt, A. (2013). Dual Lattice Simulation of the Abelian Gauge-Higgs Model at Finite Density: An Exploratory Proof of Concept Study. *Physical Review Letters*, 111(14), 141601.
- [107] Dennis, E., Kitaev, A., Landahl, A., & Preskill, J. (2002). Topological quantum memory. *Journal of Mathematical Physics*, 43(9), 4452–4505.

- [108] Depenbrock, S., McCulloch, I. P., & Schollwöck, U. (2012). Nature of the Spin-Liquid Ground State of the  $S=1/2$  Heisenberg Model on the Kagome Lattice. *Physical Review Letters*, 109(6), 067201.
- [109] Diehl, S., Micheli, A., Kantian, A., Kraus, B., Büchler, H. P., & Zoller, P. (2008/11/01, 2008). Quantum states and phases in driven open quantum systems with cold atoms. *Nature Physics*, 4(11), 878–883.
- [110] Diehl, S., Rico, E., Baranov, M. A., & Zoller, P. (2011). Topology by Dissipation in Atomic Quantum Wires. *Nature Physics*, 7(12), 971–977.
- [111] Dietz, B., Harney, H. L., Kirillov, O. N., Miski-Oglu, M., Richter, A., & Schäfer, F. (2011). Exceptional points in a microwave billiard with time-reversal invariance violation. *Physical Review Letters*, 106(15), 150403.
- [112] Ding, L., Manuel, P., Bachus, S., Grußler, F., Gegenwart, P., Singleton, J., Johnson, R. D., Walker, H. C., Adroja, D. T., Hillier, A. D., & Tsirlin, A. A. (2019). Gapless spin-liquid state in the structurally disorder-free triangular antiferromagnet  $\text{NaYbO}_2$ . *Physical Review B*, 100(144432), 144432.
- [113] Doebner, H. D., Scherer, W., & Schroeck, F., Eds. (1993). *Classical and Quantum Systems: Foundations and Symmetries. Proceedings, 2nd International Wigner Symposium, Goslar, Germany, July 16-20, 1991*.
- [114] Dua, A., Kim, I. H., Cheng, M., & Williamson, D. J. (2019a). Sorting topological stabilizer models in three dimensions. *Physical Review B*, 100(15), 155137.
- [115] Dua, A., Sarkar, P., Williamson, D. J., & Cheng, M. (2019b). Bifurcating entanglement-renormalization group flows of fracton stabilizer models.
- [116] Dum, R., Parkins, A. S., Zoller, P., & Gardiner, C. W. (1992a). Monte Carlo simulation of master equations in quantum optics for vacuum, thermal, and squeezed reservoirs. *Physical Review A*, 46(7), 4382–4396.
- [117] Dum, R., Zoller, P., & Ritsch, H. (1992b). Monte Carlo simulation of the atomic master equation for spontaneous emission. *Physical Review A*, 45(7), 4879–4887.
- [118] Dumitrescu, P. T., Wentzell, N., Georges, A., & Parcollet, O. (2022). Planckian metal at a doping-induced quantum critical point. *Physical Review B*, 105(18), L180404.
- [119] Dupuis, É., Paranjape, M. B., & Witczak-Krempa, W. (2019). Transition from a dirac spin liquid to an antiferromagnet: Monopoles in a  $\text{QED}_3$ -Gross-Neveu theory. *Physical Review B*, 100(9), 094443.
- [120] Dupuis, É. & Witczak-Krempa, W. (2021). Monopole hierarchy in transitions out of a Dirac spin liquid. *Annals of Physics*, 435, 168496.
- [121] Dyson, F. J. (1972). A Class of Matrix Ensembles. *Journal of Mathematical Physics*, 13(1), 90–97.
- [122] Dyson, F. J. & Mehta, M. L. (1963). Statistical Theory of the Energy Levels of Complex Systems. IV. *Journal of Mathematical Physics*, 4(5), 701–712.

- [123] Edwards, S. F. & Anderson, P. W. (1975). Theory of spin glasses. *Journal of Physics F: Metal Physics*, 5(5), 965.
- [124] Efetov, K. (1983). Supersymmetry and theory of disordered metals. *Advances in Physics*, 32(1), 53–127.
- [125] Efetov, K. B. (1995). Temperature Effects in Quantum Dots in the Regime of Chaotic Dynamics. *Physical Review Letters*, 74(12), 2299–2302.
- [126] Efron, B. & Stein, C. (1981). The jackknife estimate of variance. *Annals of Statistics*, 9(3), 586.
- [127] Else, D. V. & Thorngren, R. (2020). Topological theory of Lieb-Schultz-Mattis theorems in quantum spin systems. *Physical Review B*, 101(22), 224437.
- [128] Endres, M. G. (2007). Method for simulating O(N) lattice models at finite density. *Physical Review D*, 75(6), 065012.
- [129] Esaki, K., Sato, M., Hasebe, K., & Kohmoto, M. (2011). Edge states and topological phases in non-Hermitian systems.
- [130] Esposito, F. P., Goodman, B., & Ma, M. (1987). Thermoelectric power fluctuations. *Physical Review B*, 36(8), 4507–4509.
- [131] Essin, A. M. & Hermele, M. (2013). Classifying fractionalization: Symmetry classification of gapped Z2 spin liquids in two dimensions. *Physical Review B*, 87(10), 104406.
- [132] Essin, A. M. & Hermele, M. (2014). Spectroscopic signatures of crystal momentum fractionalization. *Physical Review B*, 90(12), 121102.
- [133] Essler, F. H. L. & Piroli, L. (2020). Integrability of one-dimensional Lindbladians from operator-space fragmentation. *Physical Review E*, 102(6), 062210.
- [134] Fabrizio, M. (2023). Spin-liquid insulators can be landau's fermi liquids. 130(156702), 156702.
- [135] Fang, Y., Grissonnanche, G., Legros, A., Verret, S., Laliberte, F., Collignon, C., Ataei, A., Dion, M., Zhou, J., Graf, D., Lawler, M. J., Goddard, P., Taillefer, L., & Ramshaw, B. J. (2020). Fermi surface transformation at the pseudogap critical point of a cuprate superconductor. *arXiv e-prints*.
- [136] Fang, Y., Grissonnanche, G., Legros, A., Verret, S., Laliberte, F., Collignon, C., Ataei, A., Dion, M., Zhou, J., Graf, D., Lawler, M. J., Goddard, P., Taillefer, L., & Ramshaw, B. J. (2022). Fermi surface transformation at the pseudogap critical point of a cuprate superconductor. *Nature Physics*, 18, 558.
- [137] Feng, L., Wong, Z. J., Ma, R.-M., Wang, Y., & Zhang, X. (2014). Single-mode laser by parity-time symmetry breaking. *Science (New York, N.Y.)*, 346(6212), 972–5.
- [138] Feng, L., Xu, Y.-L., Fegadolli, W. S., Lu, M.-H., Oliveira, J. E. B., Almeida, V. R., Chen, Y.-F., & Scherer, A. (2013). Experimental demonstration of a unidirectional reflectionless parity-time metamaterial at optical frequencies. *Nature Materials*, 12(2), 108–113.

- [139] Ferrari, F. & Becca, F. (2018). Spectral signatures of fractionalization in the frustrated Heisenberg model on the square lattice. *Physical Review B*, 98(100405), 100405.
- [140] Ferrari, F. & Becca, F. (2020). Gapless spin liquid and valence-bond solid in the J<sub>1</sub>-J<sub>2</sub> Heisenberg model on the square lattice: Insights from singlet and triplet excitations. *Physical Review B*, 102(014417), 014417.
- [141] Finkelstein, A. M. (1983). Influence of Coulomb interaction on the properties of disordered metals. *Soviet Physics–JETP [translation of Zhurnal Eksperimentalnoi i Teoreticheskoi Fiziki]*, 57, 97.
- [142] Frachet, M., Vinograd, I., Zhou, R., Benhabib, S., Wu, S., Mayaffre, H., Krämer, S., Ramakrishna, S. K., Reyes, A. P., Debray, J., Kurosawa, T., Momono, N., Oda, M., Komiya, S., Ono, S., Horio, M., Chang, J., Proust, C., LeBoeuf, D., & Julien, M.-H. (2020). Hidden magnetism at the pseudogap critical point of a cuprate superconductor. *Nature Physics*, 16(10), 1064–1068.
- [143] Fradkin, E., Huse, D. A., Moessner, R., Oganesyan, V., & Sondhi, S. L. (2004). Bipartite rokhsar-kivelson points and cantor deconfinement. *Physical Review B*, 69(224415), 224415.
- [144] Frahm, K. (1995). Crossover of Magnetoconductance Autocorrelation for a Ballistic Chaotic Quantum Dot. *Europhysics Letters*, 30(8), 457.
- [145] Fratino, L., Sémond, P., Sordi, G., & Tremblay, A. M. S. (2016). An organizing principle for two-dimensional strongly correlated superconductivity. *Scientific Reports*, 6(22715), 22715.
- [146] Fu, L., Sachdev, S., & Xu, C. (2011). Geometric phases and competing orders in two dimensions. *Physical Review B*, 83(165123), 165123.
- [147] Gallagher, B. L., Galloway, T., Beton, P., Oxley, J. P., Beaumont, S. P., Thoms, S., & Wilkinson, C. D. W. (1990). Observation of universal thermopower fluctuations. *Physical Review Letters*, 64(17), 2058–2061.
- [148] Gao, T., Estrecho, E., Bliokh, K. Y., Liew, T. C. H., Fraser, M. D., Brodbeck, S., Kamp, M., Schneider, C., Höfling, S., Yamamoto, Y., Nori, F., Kivshar, Y. S., Truscott, A. G., Dall, R. G., & Ostrovskaya, E. A. (2015). Observation of non-Hermitian degeneracies in a chaotic exciton-polariton billiard. *Nature*, 526(7574), 554–558.
- [149] García-Álvarez, L., Egusquiza, I. L., Lamata, L., del Campo, A., Sonner, J., & Solano, E. (2017). Digital quantum simulation of minimal AdS/CFT. *Physical Review Letters*, 119(4), 040501.
- [150] Gauvin-Ndiaye, C., Tindall, J., Moreno, J. R., & Georges, A. (2023). Mott Transition and Volume Law Entanglement with Neural Quantum States.
- [151] Gazit, S., Assaad, F. F., Sachdev, S., Vishwanath, A., & Wang, C. (2018). Confinement transition of Z<sub>2</sub> gauge theories coupled to massless fermions: Emergent quantum chromodynamics and SO(5) symmetry. *Proceedings of the National Academy of Science*, 115(30), E6987–E6995.

- [152] Gel'fand, I. M. & Lidskii, V. B. (1955). On the structure of the regions of stability of linear canonical systems of differential equations with periodic coefficients. *Uspekhi Matematicheskikh Nauk*, 10(1), 3–40.
- [153] Gelfand, M. P., Singh, R. R. P., & Huse, D. A. (1989). Zero-temperature ordering in two-dimensional frustrated quantum Heisenberg antiferromagnets. *Physical Review B*, 40(16), 10801–10809.
- [154] Georges, A., Kotliar, G., Krauth, W., & Rozenberg, M. J. (1996). Dynamical mean-field theory of strongly correlated fermion systems and the limit of infinite dimensions. *Reviews of Modern Physics*, 68, 13–125.
- [155] Georges, A., Parcollet, O., & Sachdev, S. (2000). Mean field theory of a quantum heisenberg spin glass. *Physical Review Letters*, 85(4), 840–843.
- [156] Georges, A., Parcollet, O., & Sachdev, S. (2001). Quantum fluctuations of a nearly critical Heisenberg spin glass. *Physical Review B*, 63(134406), 134406.
- [157] Gidugu, J. & Arovas, D. P. (2023). A study of dissipative models based on Dirac matrices.
- [158] Gnezdilov, N. V., Hutasoit, J. A., & Beenakker, C. W. J. (2018). Low-high voltage duality in tunneling spectroscopy of the Sachdev-Ye-Kitaev model. *Physical Review B*, 98(8), 081413(R).
- [159] Godijn, S. F., Möller, S., Buhmann, H., Molenkamp, L. W., & van Langen, S. A. (1999). Thermopower of a Chaotic Quantum Dot. *Physical Review Letters*, 82(14), 2927–2930.
- [160] Goldin, G. A., Menikoff, R., & Sharp, D. H. (1980). Particle statistics from induced representations of a local current group. *Journal of Mathematical Physics*, 21(4), 650–664.
- [161] Goldstone, J. (1961). Field theories with « Superconductor » solutions. *Il Nuovo Cimento (1955-1965)*, 19(1), 154–164.
- [162] Gong, S., Zhu, W., & Sheng, D. N. (2021). Robust d-Wave superconductivity in the square-lattice t-J model. *Physical Review Letters*, 127(9), 097003.
- [163] Gong, Z., Ashida, Y., Kawabata, K., Takasan, K., Higashikawa, S., & Ueda, M. (2018). Topological phases of non-hermitian systems. *Physical Review X*, 8(3), 031079.
- [164] Gorbenko, V., Rychkov, S., & Zan, B. (2018a). Walking, weak first-order transitions, and complex CFTs. *JHEP*, 10, 108.
- [165] Gorbenko, V., Rychkov, S., & Zan, B. (2018b). Walking, weak first-order transitions, and complex CFTs II. Two-dimensional potts model at Q>4. *SciPost Physics*, 5(5), 050.
- [166] Gorini, V., Kossakowski, A., & Sudarshan, E. C. G. (1976). Completely positive dynamical semigroups of N-level systems. *Journal of Mathematical Physics*, 17(5), 821–825.
- [167] Gor'kov, L. P., Larkin, A. I., & Khmel'nitski?, D. E. (1996). Particle conductivity in a two-dimensional random potential. In *30 Years of the Landau Institute ? Selected Papers*, volume Volume 11 of *World Scientific Series in 20th Century Physics* (pp. 157–161). WORLD SCIENTIFIC.

- [168] Gu, Y., Kitaev, A., Sachdev, S., & Tarnopolsky, G. (2020). Notes on the complex Sachdev-Ye-Kitaev model. *Journal of High Energy Physics*, 2020(2), 157.
- [169] Guo, A., Salamo, G. J., Duchesne, D., Morandotti, R., Volatier-Ravat, M., Aimez, V., Siviloglou, G. A., & Christodoulides, D. N. (2009). Observation of P T -Symmetry breaking in complex optical potentials. *Physical Review Letters*, 103(9), 093902.
- [170] Guo, C.-X., Wang, X.-R., & Kou, S.-P. (2019). Topological order on non-Hermitian toric-code model with parity-time symmetry.
- [171] Guo, C.-X., Wang, X.-R., & Kou, S.-P. (2020a). Non-hermitian avalanche effect: Non-perturbative effect induced by local non-hermitian perturbation on a Z2 topological order.
- [172] Guo, H., Gu, Y., & Sachdev, S. (2020b). Linear in temperature resistivity in the limit of zero temperature from the time reparameterization soft mode. *Annals Phys.*, 418, 168202.
- [173] Gur-Ari, G., Mahajan, R., & Vaezi, A. (2018). Does the SYK model have a spin glass phase? *Journal of High Energy Physics*, 2018(11), 70.
- [174] Haah, J. (2011). Local stabilizer codes in three dimensions without string logical operators. *Physical Review A: Atomic, Molecular, and Optical Physics*, 83(4), 042330.
- [175] Haga, T., Nakagawa, M., Hamazaki, R., & Ueda, M. (2021). Liouvillian skin effect: Slowing down of relaxation processes without gap closing. *Physical Review Letters*, 127(7), 070402.
- [176] Halperin, B. I. (1984). Statistics of Quasiparticles and the Hierarchy of Fractional Quantized Hall States. *Physical Review Letters*, 52(18), 1583–1586.
- [177] Hanai, R. & Littlewood, P. B. (2019). Critical fluctuations at a many-body exceptional point. *arXiv e-prints*.
- [178] Hastings, M. B. (2004). Lieb-Schultz-Mattis in Higher Dimensions. *Physical Review B*, 69(10), 104431.
- [179] Hatano, N. & Nelson, D. R. (1996). Localization transitions in non-hermitian quantum mechanics. *Physical Review Letters*, 77(3), 570–573.
- [180] Hatano, N. & Nelson, D. R. (1997). Vortex pinning and non-Hermitian quantum mechanics. *Physical Review B*, 56(14), 8651–8673.
- [181] Haule, K., Rosch, A., Kroha, J., & Wölfle, P. (2002). Pseudogaps in an incoherent metal. *Physical Review Letters*, 89(236402), 236402.
- [182] He, Y.-C., Rong, J., & Su, N. (2021). Non-Wilson-Fisher kinks of O(N) numerical bootstrap: From the deconfined phase transition to a putative new family of CFTs. *SciPost Physics*, 10, 115.
- [183] He, Y.-C., Zaletel, M. P., Oshikawa, M., & Pollmann, F. (2017). Signatures of Dirac Cones in a DMRG Study of the Kagome Heisenberg Model. *Physical Review X*, 7(3), 031020.
- [184] Heiss, W. D. (2012). The physics of exceptional points. *Journal of Physics A Mathematical General*, 45(444016), 444016.

- [185] Helbig, T., Hofmann, T., Imhof, S., Abdelghany, M., Kiessling, T., Molenkamp, L. W., Lee, C. H., Szameit, A., Greiter, M., & Thomale, R. (2020). Generalized bulk-boundary correspondence in non-Hermitian topoelectrical circuits. *Nature Physics*.
- [186] Hermele, M. (2007). SU(2) gauge theory of the Hubbard model and application to the honeycomb lattice. *76*(035125), 035125.
- [187] Hermele, M., Senthil, T., & Fisher, M. P. A. (2005). Algebraic spin liquid as the mother of many competing orders. *Physical Review B*, *72*(104404), 104404.
- [188] Hertz, J. A. (1976). Quantum critical phenomena. *Physical Review B*, *14*(3), 1165–1184.
- [189] Hinkley, D. V. (1969). On the ratio of two correlated normal random variables. *Biometrika*, *56*(3), 635–639.
- [190] Hodaei, H., Miri, M.-A., Heinrich, M., Christodoulides, D. N., & Khajavikhan, M. (2014). Parity-time-symmetric microring lasers. *Science (New York, N.Y.)*, *346*(6212), 975–8.
- [191] Homeier, L., Bohrdt, A., Linsel, S., Demler, E., Halimeh, J. C., & Grusdt, F. (2023). Realistic scheme for quantum simulation of  $Z_2$  lattice gauge theories with dynamical matter in  $(2 + 1)$ D. *Communications Physics*, *6*(1), 1–10.
- [192] Honecker, A., Richter, J., Schnack, J., & Wietek, A. (2020). Loop-gas description of the localized-magnon states on the kagome lattice with open boundary conditions.
- [193] Hu, S., Zhu, W., Eggert, S., & He, Y.-C. (2019). Dirac Spin Liquid on the Spin-1/2 Triangular Heisenberg Antiferromagnet. *Physical Review Letters*, *123*(20), 207203.
- [194] Hu, W.-J., Becca, F., Parola, A., & Sorella, S. (2013). Direct evidence for a gapless  $Z_2$  spin liquid by frustrating Néel antiferromagnetism. *Physical Review B*, *88*(060402), 060402.
- [195] Hu, W.-J., Gong, S.-S., Zhu, W., & Sheng, D. N. (2015). Competing spin-liquid states in the spin-1/2 Heisenberg model on the triangular lattice. *Physical Review B*, *92*(14), 140403.
- [196] Hu, Y. C. & Hughes, T. L. (2011). Absence of topological insulator phases in non-Hermitian PT-symmetric Hamiltonians. *Physical Review B*, *84*(15), 153101.
- [197] Huh, Y., Punk, M., & Sachdev, S. (2011a). Vison states and confinement transitions of  $Z_2$  spin liquids on the kagome lattice. *Physical Review B*, *84*, 094419.
- [198] Huh, Y., Punk, M., & Sachdev, S. (2011b). Vison states and confinement transitions of  $Z_2$  spin liquids on the kagome lattice. *Physical Review B*, *84*, 094419.
- [199] Huh, Y. & Sachdev, S. (2008). Renormalization group theory of nematic ordering in d-wave superconductors. *Physical Review B*, *78*(064512), 064512.
- [200] Huse, D. A. & Elser, V. (1988). Simple variational wave functions for two-dimensional heisenberg spin-1/2 antiferromagnets. *Physical Review Letters*, *60*(24), 2531–2534.
- [201] Hwang, K. (2023). Mixed-State Quantum Spin Liquid in Kitaev Lindbladian: Dynamical Anyon Condensation.

- [202] Iida, S., Weidenmüller, H. A., & Zuk, J. A. (1990a). Statistical scattering theory, the supersymmetry method and universal conductance fluctuations. *Annals of Physics*, 200(2), 219–270.
- [203] Iida, S., Weidenmüller, H. A., & Zuk, J. A. (1990b). Wave propagation through disordered media and universal conductance fluctuations. *Physical Review Letters*, 64(5), 583–586.
- [204] Ioffe, L. B. & Larkin, A. I. (1988). Effective action of a two-dimensional antiferromagnet. *International Journal of Modern Physics B*, 02(02), 203–219.
- [205] Iqbal, Y., Becca, F., & Poilblanc, D. (2011). Projected wave function study of  $\mathbb{Z}_2$  spin liquids on the kagome lattice for the spin- $\frac{1}{2}$  quantum Heisenberg antiferromagnet. *Physical Review B*, 84(2), 020407.
- [206] Iqbal, Y., Becca, F., Sorella, S., & Poilblanc, D. (2013). Gapless spin-liquid phase in the kagome spin- $\frac{1}{2}$  Heisenberg antiferromagnet. *Physical Review B*, 87(6), 060405.
- [207] Iqbal, Y., Hu, W.-J., Thomale, R., Poilblanc, D., & Becca, F. (2016). Spin liquid nature in the Heisenberg  $J_1$ - $J_2$  triangular antiferromagnet. *Physical Review B*, 93(144411), 144411.
- [208] Iqbal, Y., Poilblanc, D., & Becca, F. (2014). Vanishing spin gap in a competing spin-liquid phase in the kagome Heisenberg antiferromagnet. *Physical Review B*, 89(2), 020407.
- [209] Iqbal, Y., Poilblanc, D., & Becca, F. (2015). Spin- $\frac{1}{2}$  Heisenberg  $\langle J \rangle - \langle J \rangle$  antiferromagnet on the kagome lattice. *Physical Review B*, 91(2), 020402.
- [210] Iskin, M. (2020). Non-hermitian BCS-BEC evolution with a complex scattering length. *arXiv e-prints*, (arXiv:2002.00653), arXiv:2002.00653.
- [211] Itou, T., Oyamada, A., Maegawa, S., Tamura, M., & Kato, R. (2008). Quantum spin liquid in the spin-1/2 triangular antiferromagnet  $\text{EtMe}_3\text{Sb}[\text{Pd}(\text{dmit})_2]_2$ . *Physical Review B*, 77(10), 104413.
- [212] Ivanov, D. A. & Senthil, T. (2002a). Projected wave functions for fractionalized phases of quantum spin systems. *Physical Review B*, 66(115111), 115111.
- [213] Ivanov, D. A. & Senthil, T. (2002b). Projected wave functions for fractionalized phases of quantum spin systems. *Phys. Rev. B*, 66(115111), 115111.
- [214] Jafferis, D., Zlokapa, A., Lykken, J. D., Kolchmeyer, D. K., Davis, S. I., Lauk, N., Neven, H., & Spiropulu, M. (2022). Traversable wormhole dynamics on a quantum processor. *Nature*, 612(7938), 51–55.
- [215] Jaklič, J. & Prelovšek, P. (1994). Lanczos method for the calculation of finite-temperature quantities in correlated systems. *Physical Review B*, 49(7), 5065–5068.
- [216] Jalabert, R. A., Pichard, J.-L., & Beenakker, C. W. J. (1994). Universal Quantum Signatures of Chaos in Ballistic Transport. *Europhysics Letters*, 27(4), 255.
- [217] Jalabert, R. A. & Sachdev, S. (1991). Spontaneous alignment of frustrated bonds in an anisotropic, three-dimensional Ising model. *Physical Review B*, 44(2), 686–690.

- [218] Jia, Y. & Verbaarschot, J. J. M. (2020). Spectral Fluctuations in the Sachdev-Ye-Kitaev Model. *Journal of High Energy Physics*, 2020(7), 193.
- [219] Jian, C.-M., Thomson, A., Rasmussen, A., Bi, Z., & Xu, C. (2018). Deconfined quantum critical point on the triangular lattice. *Physical Review B*, 97(19), 195115.
- [220] Jiang, H.-C. & Kivelson, S. A. (2021a). High temperature superconductivity in a lightly doped quantum spin liquid. *Physical Review Letters*, 127(9), 097002.
- [221] Jiang, H.-C. & Kivelson, S. A. (2021b). High temperature superconductivity in a lightly doped quantum spin liquid. *Physical Review Letters*, 127(097002), 097002.
- [222] Jiang, H.-C., Kivelson, S. A., & Lee, D.-H. (2023). Superconducting valence bond fluid in lightly doped eight-leg t-J cylinders. *Physical Review B*, 108(054505), 054505.
- [223] Jiang, H.-C., Wang, Z., & Balents, L. (2012a). Identifying topological order by entanglement entropy. *Nature Physics*, 8(12), 902–905.
- [224] Jiang, H.-C., Yao, H., & Balents, L. (2012b). Spin liquid ground state of the spin- $\frac{1}{2}$  square  $J_1-J_2$  Heisenberg model. *Physical Review B*, 86(2), 024424.
- [225] Jin, H.-K., Knolle, J., & Knap, M. (2022). Fractionalized Prethermalization in a Driven Quantum Spin Liquid.
- [226] Jing, H., Özdemir, S. K., Geng, Z., Zhang, J., Lü, X.-Y., Peng, B., Yang, L., & Nori, F. (2015). Optomechanically-induced transparency in parity-time-symmetric microresonators. *Scientific Reports*, 5(1), 9663.
- [227] José, J. V., Kadanoff, L. P., Kirkpatrick, S., & Nelson, D. R. (1977). Renormalization, vortices, and symmetry-breaking perturbations in the two-dimensional planar model. *Physical Review B*, 16(3), 1217–1241.
- [228] Joshi, D. G., Li, C., Tarnopolsky, G., Georges, A., & Sachdev, S. (2020). Deconfined critical point in a doped random quantum Heisenberg magnet. *Physical Review X*, 10(2), 021033.
- [229] Joy, A. P. & Rosch, A. (2022). Dynamics of visons and thermal hall effect in perturbed kitaev models. *Physical Review X*, 12(4), 041004.
- [230] Kamenev, A. & Mézard, M. (1999). Wigner-Dyson statistics from the replica method. *Journal of Physics A: Mathematical and General*, 32(24), 4373.
- [231] Kanega, M., Ikeda, T. N., & Sato, M. (2021). Linear and nonlinear optical responses in Kitaev spin liquids. 3(3), L032024.
- [232] Kaneko, R., Morita, S., & Imada, M. (2014). Gapless Spin-Liquid Phase in an Extended Spin 1/2 Triangular Heisenberg Model. *Journal of the Physical Society of Japan*, 83(9), 093707.
- [233] Kato, T. (1966). Perturbation theory for linear operators. *Springer-Verlag, Berlin-New York*.

- [234] Kaul, R. K. (2015). Spin nematics, valence-bond solids, and spin liquids in SO(N) quantum spin models on the triangular lattice. *Physical Review Letters*, 115(157202), 157202.
- [235] Kaul, R. K., Kim, Y. B., Sachdev, S., & Senthil, T. (2008). Algebraic charge liquids. *Nature Physics*, 4(1), 28–31.
- [236] Kaul, R. K., Kolezhuk, A., Levin, M., Sachdev, S., & Senthil, T. (2007). Hole dynamics in an antiferromagnet across a deconfined quantum critical point. *Physical Review B*, 75(235122), 235122.
- [237] Kawabata, K., Kulkarni, A., Li, J., Numasawa, T., & Ryu, S. (2023). Symmetry of open quantum systems: Classification of dissipative quantum chaos. *PRX Quantum*, 4(3), 030328.
- [238] Kawabata, K. & Ryu, S. (2020). Nonunitary scaling theory of non-hermitian localization. *arXiv e-prints*.
- [239] Kawabata, K. & Sato, M. (2020). Real spectra in non-Hermitian topological insulators. *arXiv e-prints*.
- [240] Kawabata, K., Shiozaki, K., Ueda, M., & Sato, M. (2018). Symmetry and topology in non-hermitian physics.
- [241] Kawabata, K., Sohal, R., & Ryu, S. (2024). Lieb-Schultz-Mattis Theorem in Open Quantum Systems. *Physical Review Letters*, 132(7), 070402.
- [242] Keimer, B., Kivelson, S. A., Norman, M. R., Uchida, S., & Zaanen, J. (2015). From quantum matter to high-temperature superconductivity in copper oxides. *Nature*, 518, 179.
- [243] Kessler, E. M. (2012). Generalized Schrieffer-Wolff formalism for dissipative systems. *Physical Review A*, 86(1), 012126.
- [244] Kitaev, A. (2003a). Fault tolerant quantum computation by anyons. *Annals Phys.*, 303, 2–30.
- [245] Kitaev, A. (2006). Anyons in an exactly solved model and beyond. *Annals of Physics*, 321(1), 2–111.
- [246] Kitaev, A. (2015a). A simple model of quantum holography, talk given at KITP program: Entanglement in Strongly-Correlated Quantum Matter. *USA April 2015*.
- [247] Kitaev, A. & Suh, S. J. (2018a). The soft mode in the Sachdev-Ye-Kitaev model and its gravity dual. *JHEP*, 05, 183.
- [248] Kitaev, A. & Suh, S. J. (2018b). The soft mode in the Sachdev-Ye-Kitaev model and its gravity dual. *Journal of High Energy Physics*, 2018(5), 183.
- [249] Kitaev, A. & Suh, S. J. (2019). Statistical mechanics of a two-dimensional black hole. *Journal of High Energy Physics*, 2019(5), 198.
- [250] Kitaev, A. Y. (2015b). Talks at KITP, university of california, santa barbara. *Entanglement in Strongly-Correlated Quantum Matter*.

- [251] Kitaev, A. Yu. (2003b). Fault-tolerant quantum computation by anyons. *Annals of Physics*, 303(1), 2–30.
- [252] Klaiman, S., Günther, U., & Moiseyev, N. (2008). Visualization of branch points in P T -Symmetric waveguides. *Physical Review Letters*, 101(8), 080402.
- [253] Klümper, A., Schadschneider, A., & Zittartz, J. (1993). Matrix-product-groundstates for one-dimensional spin-1 quantum antiferromagnets. *Europhysics Letters (EPL)*, 24(4), 293–297.
- [254] Kobrin, B., Yang, Z., Kahanamoku-Meyer, G. D., Olund, C. T., Moore, J. E., Stanford, D., & Yao, N. Y. (2021). Many-Body Chaos in the Sachdev-Ye-Kitaev Model. *Physical Review Letters*, 126(3), 030602.
- [255] Kogut, J. B. (1983). The lattice gauge theory approach to quantum chromodynamics. *Reviews of Modern Physics*, 55(3), 775–836.
- [256] Kosterlitz, J. M., Nelson, D. R., & Fisher, M. E. (1976). Bicritical and tetracritical points in anisotropic antiferromagnetic systems. *Physical Review B*, 13(1), 412–432.
- [257] Kotliar, G., Savrasov, S. Y., Haule, K., Oudovenko, V. S., Parcollet, O., & Marianetti, C. A. (2006). Electronic structure calculations with dynamical mean-field theory. *Reviews of Modern Physics*, 78(3), 865–951.
- [258] Kozii, V. & Fu, L. (2017). Non-hermitian topological theory of finite-lifetime quasiparticles: Prediction of bulk fermi arc due to exceptional point. *arXiv e-prints*.
- [259] Kraus, B., Büchler, H. P., Diehl, S., Kantian, A., Micheli, A., & Zoller, P. (2008). Preparation of entangled states by quantum Markov processes. *Physical Review A*, 78(4), 042307.
- [260] Krein, MG. (1950). A generalization of some investigations of linear differential equations with periodic coefficients. In *Doklady Akad. Nauk SSSR*, volume 73 (pp. 445–448).
- [261] Kruchkov, A., Patel, A. A., Kim, P., & Sachdev, S. (2020). Thermoelectric power of Sachdev-Ye-Kitaev islands: Probing Bekenstein-Hawking entropy in quantum matter experiments. *Physical Review B*, 101(20), 205148.
- [262] Kuklov, A. B., Matsumoto, M., Prokof'ev, N. V., Svistunov, B. V., & Troyer, M. (2008). Deconfined criticality: Generic first-order transition in the SU(2) symmetry case. *Physical Review Letters*, 101(5), 050405.
- [263] Kulkarni, A., Numasawa, T., & Ryu, S. (2022). Lindbladian dynamics of the Sachdev-Ye-Kitaev model. *Physical Review B*, 106(7), 075138.
- [264] Kunst, F. K., Edvardsson, E., Budich, J. C., & Bergholtz, E. J. (2018). Biorthogonal bulk-boundary correspondence in non-hermitian systems. *Physical Review Letters*, 121(2), 026808.
- [265] Landau, L. D. (1937). On the theory of phase transitions. *Zh. Eksp. Teor. Fiz.*, 7, 19–32.
- [266] Landau, L. D. (1956). The Theory of a Fermi Liquid. *Zh. Eksp. Teor. Fiz.*, 30(6), 1058.

- [267] Lang, N. & Büchler, H. P. (2015). Exploring quantum phases by driven dissipation. *Physical Review A: Atomic, Molecular, and Optical Physics*, 92(1), 012128.
- [268] Lee, G., McDonald, A., & Clerk, A. (2023a). Anomalously large relaxation times in dissipative lattice models beyond the non-Hermitian skin effect. *Physical Review B*, 108(6), 064311.
- [269] Lee, J. Y., Jian, C.-M., & Xu, C. (2023b). Quantum criticality under decoherence or weak measurement.
- [270] Lee, P. A., Nagaosa, N., & Wen, X.-G. (2006). Doping a Mott insulator: Physics of high-temperature superconductivity. *Reviews of Modern Physics*, 78(1), 17–85.
- [271] Lee, P. A. & Ramakrishnan, T. V. (1985). Disordered electronic systems. *Reviews of Modern Physics*, 57(2), 287–337.
- [272] Lee, P. A. & Stone, A. D. (1985). Universal Conductance Fluctuations in Metals. *Physical Review Letters*, 55(15), 1622–1625.
- [273] Lee, P. A., Stone, A. D., & Fukuyama, H. (1987). Universal conductance fluctuations in metals: Effects of finite temperature, interactions, and magnetic field. *Physical Review B*, 35(3), 1039–1070.
- [274] Lee, T. E. (2016). Anomalous edge state in a non-hermitian lattice. *Physical Review Letters*, 116(13), 133903.
- [275] Lee, T. E. & Chan, C.-K. (2014). Heralded magnetism in non-hermitian atomic systems. *Physical Review X*, 4(4), 041001.
- [276] Lee, T. E., Reiter, F., & Moiseyev, N. (2014). Entanglement and spin squeezing in non-hermitian phase transitions. *Physical Review Letters*, 113(25), 250401.
- [277] Levenberg, K. (1944). A method for the solution of certain non-linear problems in least squares. *Quarterly of Applied Mathematics*, 2(2), 164–168.
- [278] Leykam, D., Bliokh, K. Y., Huang, C., Chong, Y. D., & Nori, F. (2017). Edge modes, degeneracies, and topological numbers in non-hermitian systems. *Physical Review Letters*, 118(4), 040401.
- [279] Li, Y., Chen, G., Tong, W., Pi, L., Liu, J., Yang, Z., Wang, X., & Zhang, Q. (2015). Rare-earth triangular lattice spin liquid: A single-crystal study of YbMgGaO<sub>4</sub>. *Physical Review Letters*, 115(167203), 167203.
- [280] Li, Z.-X., Jian, S.-K., & Yao, H. (2019). Deconfined quantum criticality and emergent SO(5) symmetry in fermionic systems. *arXiv e-prints*, (arXiv:1904.10975), arXiv:1904.10975.
- [281] Liang, X., Liu, W.-Y., Lin, P.-Z., Guo, G.-C., Zhang, Y.-S., & He, L. (2018). Solving frustrated quantum many-particle models with convolutional neural networks. *Physical Review B*, 98(10), 104426.
- [282] Lieb, E., Schultz, T., & Mattis, D. (1961). Two soluble models of an antiferromagnetic chain. *Annals of Physics*, 16(3), 407–466.

- [283] Lieb, E. H. (1994). The Flux-Phase of the Half-Filled Band.
- [284] Lieu, S. (2018). Topological symmetry classes for non-Hermitian models and connections to the bosonic Bogoliubov–de Gennes equation. *Physical Review B*, 98(11), 115135.
- [285] Lieu, S. (2019). Non-Hermitian Majorana modes protect degenerate steady states. *Physical Review B*, 100(8), 085110.
- [286] Lieu, S., McGinley, M., & Cooper, N. R. (2020). Tenfold Way for Quadratic Lindbladians. *Physical Review Letters*, 124(4), 040401.
- [287] Lin, Z., Ramezani, H., Eichelkraut, T., Kottos, T., Cao, H., & Christodoulides, D. N. (2011). Unidirectional invisibility induced by P T -Symmetric periodic structures. *Physical Review Letters*, 106(21), 213901.
- [288] Lindblad, G. (1976). On the generators of quantum dynamical semigroups. *Communications in Mathematical Physics*, 48(2), 119–130.
- [289] Liu, T., He, J. J., Yoshida, T., Xiang, Z.-L., & Nori, F. (2020). Non-hermitian topological mott insulators in 1D fermionic superlattices. *arXiv e-prints*.
- [290] Liu, W.-Y., Gong, S.-S., Li, Y.-B., Poilblanc, D., Chen, W.-Q., & Gu, Z.-C. (2022a). Gapless quantum spin liquid and global phase diagram of the spin-1/2 J1-J2 square anti-ferromagnetic Heisenberg model. *Science Bulletin*, 67(10), 1034–1041.
- [291] Liu, W.-Y., Hasik, J., Gong, S.-S., Poilblanc, D., Chen, W.-Q., & Gu, Z.-C. (2022b). Emergence of gapless quantum spin liquid from deconfined quantum critical point. *Physical Review X*, 12(3), 031039.
- [292] Liu, W.-Y., Hasik, J., Gong, S.-S., Poilblanc, D., Chen, W.-Q., & Gu, Z.-C. (2022c). Emergence of gapless quantum spin liquid from deconfined quantum critical point. *Physical Review X*, 12(3), 031039.
- [293] Liu, Z.-P., Zhang, J., Özdemir, Ş. K., Peng, B., Jing, H., Lü, X.-Y., Li, C.-W., Yang, L., Nori, F., & Liu, Y.-x. (2016). Metrology with PT-Symmetric cavities: Enhanced sensitivity near the PT-Phase transition. *Physical Review Letters*, 117(11), 110802.
- [294] Longhi, S. (2019). Topological phase transition in non-Hermitian quasicrystals. *Physical Review Letters*, 122(23), 237601.
- [295] Lu, Y.-M., Ran, Y., & Lee, P. A. (2011).  $\mathbb{Z}_2$  spin liquids in the  $S=\frac{1}{2}$  Heisenberg model on the kagome lattice: A projective symmetry-group study of Schwinger fermion mean-field states. *Physical Review B*, 83(22), 224413.
- [296] Luitz, D. J. & Piazza, F. (2019). Exceptional points and the topology of quantum many-body spectra. *Physical Review Research*, 1(033051), 033051.
- [297] Luo, D. & Clark, B. K. (2019). Backflow Transformations via Neural Networks for Quantum Many-Body Wave Functions. *Physical Review Letters*, 122(22), 226401.
- [298] Luo, Z., You, Y.-Z., Li, J., Jian, C.-M., Lu, D., Xu, C., Zeng, B., & Laflamme, R. (2019). Quantum simulation of the non-fermi-liquid state of Sachdev-Ye-Kitaev model. *npj Quantum Information*, 5(1), 1–6.

- [299] Ma, H. & He, Y.-C. (2019). Shadow of complex fixed point: Approximate conformality of  $Q>4$  Potts model. *Physical Review B*, 99(19), 195130.
- [300] Ma, H., Lake, E., Chen, X., & Hermele, M. (2017). Fracton topological order via coupled layers. *Physical Review B*, 95(24), 245126.
- [301] Ma, R. & Wang, C. (2020). Theory of deconfined pseudocriticality. *Physical Review B*, 102(2), 020407.
- [302] MacWilliams, F. J. & Sloane, N. J. A. (1977). *The Theory of Error-Correcting Codes*, volume 16. Elsevier.
- [303] Maldacena, J. & Stanford, D. (2016a). Remarks on the Sachdev-Ye-Kitaev model. *Physical Review D*, 94(10), 106002.
- [304] Maldacena, J. & Stanford, D. (2016b). Remarks on the sachdev-ye-kitaev model. *Physical Review D: Particles and Fields*, 94(10), 106002.
- [305] Mandal, S. & Surendran, N. (2009). Exactly solvable Kitaev model in three dimensions. *Physical Review B*, 79(2), 024426.
- [306] Marquardt, D. W. (1963). An algorithm for least-squares estimation of nonlinear parameters. *Journal of the Society for Industrial and Applied Mathematics*, 11(2), 431–441.
- [307] Martinez Alvarez, V. M., Barrios Vargas, J. E., & Foa Torres, L. E. F. (2018). Non-Hermitian robust edge states in one dimension: Anomalous localization and eigenspace condensation at exceptional points. *Physical Review B*, 97(12), 121401(R).
- [308] Matsumoto, N., Kawabata, K., Ashida, Y., Furukawa, S., & Ueda, M. (2019). Continuous phase transition without gap closing in non-hermitian quantum many-body systems. *arXiv e-prints*.
- [309] McCann, E. & Lerner, I. V. (1996). Mesoscopic conductance fluctuations in dirty quantum dots with single channel leads. *Journal of Physics: Condensed Matter*, 8(36), 6719.
- [310] McGreevy, J. (2023). Generalized Symmetries in Condensed Matter. *Annual Review of Condensed Matter Physics*, 14(1), 57–82.
- [311] Medvedyeva, M. V., Essler, F. H. L., & Prosen, T. (2016). Exact Bethe Ansatz Spectrum of a Tight-Binding Chain with Dephasing Noise. *Physical Review Letters*, 117(13), 137202.
- [312] Medvedyeva, M. V. & Kehrein, S. (2014). Power-law approach to steady state in open lattices of noninteracting electrons. *Physical Review B*, 90(20), 205410.
- [313] Mei, J.-W., Kawasaki, S., Zheng, G.-Q., Weng, Z.-Y., & Wen, X.-G. (2012). Luttinger-volume violating Fermi liquid in the pseudogap phase of the cuprate superconductors. *Physical Review B*, 85(13), 134519.
- [314] Metlitski, M. A., Hermele, M., Senthil, T., & Fisher, M. P. A. (2008). Monopoles in  $\mathbb{CP}^{N-1}$  model via the state-operator correspondence. *Physical Review B*, 78(21), 214418.
- [315] Metlitski, M. A. & Thorngren, R. (2018). Intrinsic and emergent anomalies at deconfined critical points. *Physical Review B*, 98(8), 085140.

- [316] Michon, B., Girod, C., Badoux, S., Kačmarčík, J., Ma, Q., Dragomir, M., Dabkowska, H. A., Gaulin, B. D., Zhou, J. S., Pyon, S., Takayama, T., Takagi, H., Verret, S., Doiron-Leyraud, N., Marcenat, C., Taillefer, L., & Klein, T. (2019). Thermodynamic signatures of quantum criticality in cuprate superconductors. *Nature*, 567(7747), 218–222.
- [317] Millis, A. J. (1993). Effect of a nonzero temperature on quantum critical points in itinerant fermion systems. *Physical Review B*, 48(10), 7183–7196.
- [318] Misguich, G. & Mila, F. (2008a). Quantum dimer model on the triangular lattice: Semiclassical and variational approaches to vison dispersion and condensation. *Physical Review B*, 77(13), 134421.
- [319] Misguich, G. & Mila, F. (2008b). Quantum dimer model on the triangular lattice: Semiclassical and variational approaches to vison dispersion and condensation. *Physical Review B*, 77(134421), 134421.
- [320] Moessner, R. & Sondhi, S. L. (2001). Ising models of quantum frustration. *Physical Review B*, 63(22), 224401.
- [321] Moon, E. G. & Sachdev, S. (2011). Underdoped cuprates as fractionalized Fermi liquids: Transition to superconductivity. *Physical Review B*, 83(224508), 224508.
- [322] Moors, K., Zyuzin, A. A., Zyuzin, A. Y., Tiwari, R. P., & Schmidt, T. L. (2019). Disorder-driven exceptional lines and Fermi ribbons in tilted nodal-line semimetals. *Physical Review B*, 99(4), 041116(R).
- [323] Mori, T. & Shirai, T. (2020). Resolving a discrepancy between liouvillian gap and relaxation time in boundary-dissipated quantum many-body systems. *Physical Review Letters*, 125(23), 230604.
- [324] Mori, T. & Shirai, T. (2023). Symmetrized liouvillian gap in markovian open quantum systems. *Physical Review Letters*, 130(23), 230404.
- [325] Mostafazadeh, A. (2002a). Pseudo-Hermiticity versus PT-symmetry. II: A complete characterization of non-Hermitian Hamiltonians with a real spectrum. *Journal of Mathematical Physics*, 43(5), 2814–2816.
- [326] Mostafazadeh, A. (2002b). Pseudo-Hermiticity versus PT-symmetry III: Equivalence of pseudo-Hermiticity and the presence of antilinear symmetries. *Journal of Mathematical Physics*, 43(8), 3944–3951.
- [327] Mostafazadeh, A. (2002c). Pseudo-Hermiticity versus PT symmetry: The necessary condition for the reality of the spectrum of a non-Hermitian Hamiltonian. *Journal of Mathematical Physics*, 43(1), 205–214.
- [328] Motrunich, O. I. & Vishwanath, A. (2004). Emergent photons and transitions in the O(3) sigma model with hedgehog suppression. *Physical Review B*, 70(075104), 075104.
- [329] Mu, S., Lee, C. H., Li, L., & Gong, J. (2019). Emergent Fermi surface in a many-body non-Hermitian Fermionic chain. *arXiv e-prints*.
- [330] Murugan, A. & Vaikuntanathan, S. (2017). Topologically protected modes in non-equilibrium stochastic systems. *Nature Communications*, 8.

- [331] Naghiloo, M., Abbasi, M., Joglekar, Y. N., & Murch, K. W. (2019). Quantum state tomography across the exceptional point in a single dissipative qubit. *Nature Physics*, 15(12), 1232–1236.
- [332] Nahum, A. (2020). Note on Wess-Zumino-Witten models and quasiuniversality in 2+1 dimensions. *Physical Review B*, 102(20), 201116.
- [333] Nakagawa, M., Kawakami, N., & Ueda, M. (2018). Non-hermitian kondo effect in ultracold alkaline-earth atoms. *Physical Review Letters*, 121(20), 203001.
- [334] Nakagawa, M., Kawakami, N., & Ueda, M. (2021). Exact Liouvillian Spectrum of a One-Dimensional Dissipative Hubbard Model. *Physical Review Letters*, 126(11), 110404.
- [335] Nakane, K., Shimizu, A., & Ichinose, I. (2009). Phase structure of  $Z_2$  gauge theories for frustrated antiferromagnets in two dimensions. *Physical Review B*, 80(22), 224425.
- [336] Nambu, Y. (1960). Quasi-Particles and Gauge Invariance in the Theory of Superconductivity. *Physical Review*, 117(3), 648–663.
- [337] Nandkishore, R. & Levitov, L. (2010). Electron interactions in bilayer graphene: Marginal Fermi liquid and zero-bias anomaly. *Physical Review B*, 82(115431), 115431.
- [338] Nandkishore, R. M. & Hermele, M. (2019). Fractons. *Annual Review of Condensed Matter Physics*, 10, 295–313.
- [339] Nelson, D. R. & Shnerb, N. M. (1998). Non-Hermitian localization and population biology. *Physical Review E: Statistical Physics, Plasmas, Fluids, and Related Interdisciplinary Topics*, 58(2), 1383–1403.
- [340] Nikolaenko, A., Tikhonovskaya, M., Sachdev, S., & Zhang, Y.-H. (2021). Small to large Fermi surface transition in a single band model, using randomly coupled ancillas. *Physical Review B*, 103, 235138.
- [341] Nikolaenko, A., von Milczewski, J., Joshi, D. G., & Sachdev, S. (2023). Spin density wave, Fermi liquid, and fractionalized phases in a theory of antiferromagnetic metals using paramagnons and bosonic spinons. 108(045123), 045123.
- [342] Nomura, Y. & Imada, M. (2021). Dirac-type nodal spin liquid revealed by refined quantum many-body solver using neural-network wave function, correlation ratio, and level spectroscopy. *Physical Review X*, 11(3), 031034.
- [343] Nussinov, Z. & Ortiz, G. (2008). Autocorrelations and thermal fragility of anyonic loops in topologically quantum ordered systems. *Physical Review B*, 77(6), 064302.
- [344] Ogunnaike, O., Feldmeier, J., & Lee, J. Y. (2023). Unifying emergent hydrodynamics and lindbladian low-energy spectra across symmetries, constraints, and long-range interactions. *Physical Review Letters*, 131(22), 220403.
- [345] Oitmaa, J. (2020). Magnetic phases in the  $J_1$ - $J_2$  Heisenberg antiferromagnet on the triangular lattice. *Physical Review B*, 101(21), 214422.
- [346] Okugawa, R. & Yokoyama, T. (2019). Topological exceptional surfaces in non-Hermitian systems with parity-time and parity-particle-hole symmetries. *Physical Review B*, 99(4), 041202(R).

- [347] Okuma, N. & Sato, M. (2019). Topological phase transition driven by infinitesimal instability: Majorana fermions in non-hermitian spintronics. *Physical Review Letters*, 123(9), 097701.
- [348] Oliviero, V., Gilmutdinov, I., Vignolles, D., Benhabib, S., Bruyant, N., Forget, A., Colson, D., Atkinson, W. A., & Proust, C. (2024). Charge order near the antiferromagnetic quantum critical point in the trilayer high T<sub>c</sub> cuprate HgBa<sub>2</sub>Ca<sub>2</sub>Cu<sub>3</sub>O<sub>8+δ</sub>. *arXiv e-prints*.
- [349] Oshikawa, M. (2000). Topological approach to Luttinger's theorem and the Fermi surface of a Kondo lattice. *Physical Review Letters*, 84(15), 3370–3373.
- [350] P. W. Anderson (1987). The resonating valence bond state in La<sub>2</sub>CuO<sub>4</sub> and superconductivity. *Science (New York, N.Y.)*, 235(4793), 1196–1198.
- [351] Paddison, J. A. M., Daum, M., Dun, Z., Ehlers, G., Liu, Y., Stone, M. B., Zhou, H., & Mourigal, M. (2017). Continuous excitations of the triangular-lattice quantum spin liquid YbMgGaO<sub>4</sub>. *Nature Physics*, 13(2), 117–122.
- [352] Parcollet, O. & Georges, A. (1999a). Non-Fermi-liquid regime of a doped Mott insulator. *Physical Review B*, 59, 5341.
- [353] Parcollet, O. & Georges, A. (1999b). Non-Fermi-liquid regime of a doped Mott insulator. *Physical Review B*, 59(8), 5341–5360.
- [354] Parisi, G. (1980). A sequence of approximated solutions to the S-K model for spin glasses. *Journal of Physics A: Mathematical and General*, 13(4), L115.
- [355] Park, K. & Sachdev, S. (2002). Bond and Néel order and fractionalization in ground states of easy-plane antiferromagnets in two dimensions. *Physical Review B*, 65(220405), 220405.
- [356] Patel, A. A., Guo, H., Esterlis, I., & Sachdev, S. (2023). Universal theory of strange metals from spatially random interactions. *Science*, 381(6659), 790–793.
- [357] Patel, A. A., Lunts, P., & Sachdev, S. (2024). Localization of overdamped bosonic modes and transport in strange metals. *Proceedings of the National Academy of Sciences*, 121(14), e2402052121.
- [358] Pavlov, A. I. & Kiselev, M. N. (2021). Quantum thermal transport in the charged Sachdev-Ye-Kitaev model: Thermoelectric Coulomb blockade. *Physical Review B*, 103(20), L201107.
- [359] Peng, B., Özdemir, Ş. K., Lei, F., Monifi, F., Gianfreda, M., Long, G. L., Fan, S., Nori, F., Bender, C. M., & Yang, L. (2014a). Parity-time-symmetric whispering-gallery microcavities. *Nature Physics*, 10(5), 394–398.
- [360] Peng, B., Özdemir, Ş. K., Liertzer, M., Chen, W., Kramer, J., Yilmaz, H., Wiersig, J., Rotter, S., & Yang, L. (2016). Chiral modes and directional lasing at exceptional points. *Proceedings of the National Academy of Sciences of the United States of America*, 113(25), 6845–50.
- [361] Peng, B., Özdemir, Ş. K., Rotter, S., Yilmaz, H., Liertzer, M., Monifi, F., Bender, C. M., Nori, F., & Yang, L. (2014b). Loss-induced suppression and revival of lasing. *Science (New York, N.Y.)*, 346(6207), 328–32.

- [362] Peralta Gavensky, L., Sachdev, S., & Goldman, N. (2023). Connecting the many-body chern number to luttinger's theorem through středa's formula. *Physical Review Letters*, 131(236601), 236601.
- [363] Peskin, M. E. (1978). Mandelstam-'t Hooft duality in abelian lattice models. *Annals of Physics*, 113(1), 122–152.
- [364] Pidatella, A., Metavitsiadis, A., & Brenig, W. (2019). Heat transport in the anisotropic Kitaev spin liquid. *Physical Review B*, 99(7), 075141.
- [365] Pikulin, D. I. & Franz, M. (2017). Black Hole on a Chip: Proposal for a Physical Realization of the Sachdev-Ye-Kitaev model in a Solid-State System. *Physical Review X*, 7(3), 031006.
- [366] Podolsky, D. & Sachdev, S. (2012). Spectral functions of the Higgs mode near two-dimensional quantum critical points. *Physical Review B*, 86, 054508.
- [367] Prelovšek, P. & Bonča, J. (2013). Ground state and finite temperature lanczos methods. In *Strongly Correlated Systems: Numerical Methods* (pp. 1–30). Berlin, Heidelberg: Springer Berlin Heidelberg.
- [368] Pretko, M., Chen, X., & You, Y. (2020). Fracton phases of matter. *International Journal of Modern Physics A*, 35(2030003), 2030003.
- [369] Prigodin, V. N., Efetov, K. B., & Iida, S. (1993). Statistics of conductance fluctuations in quantum dots. *Physical Review Letters*, 71(8), 1230–1233.
- [370] Prokof'ev, N. & Svistunov, B. (2001). Worm Algorithms for Classical Statistical Models. *Physical Review Letters*, 87(16), 160601.
- [371] Prokof'ev, N. V., Svistunov, B. V., & Tupitsyn, I. S. (1998). “Worm” algorithm in quantum Monte Carlo simulations. *Physics Letters A*, 238(4), 253–257.
- [372] Prosen, T. (2008). Third quantization: A general method to solve master equations for quadratic open Fermi systems. *New Journal of Physics*, 10(4), 043026.
- [373] Qi, Y. & Fu, L. (2015). Detecting crystal symmetry fractionalization from the ground state: Application to  $\mathbb{Z}_2$  spin liquids on the kagome lattice. *Physical Review B*, 91(10), 100401.
- [374] Qi, Y. & Sachdev, S. (2010). Effective theory of Fermi pockets in fluctuating antiferromagnets. *Physical Review B*, 81(115129), 115129.
- [375] Qian, X. & Qin, M. (2023a). Absence of spin liquid phase in the  $J_1$ - $J_2$  heisenberg model on the square lattice.
- [376] Qian, X. & Qin, M. (2023b). Absence of spin liquid phase in the  $J_1$ - $J_2$  heisenberg model on the square lattice.
- [377] Raghu, S., Kivelson, S. A., & Scalapino, D. J. (2010). Superconductivity in the repulsive Hubbard model: An asymptotically exact weak-coupling solution. *Physical Review B*, 81(224505), 224505.

- [378] Ralko, A., Ferrero, M., Becca, F., Ivanov, D., & Mila, F. (2005). Zero-temperature properties of the quantum dimer model on the triangular lattice. *Physical Review B*, 71(22), 224109.
- [379] Ralko, A., Ferrero, M., Becca, F., Ivanov, D., & Mila, F. (2006). Dynamics of the quantum dimer model on the triangular lattice: Soft modes and local resonating valence-bond correlations. *Physical Review B*, 74(13), 134301.
- [380] Ramezani, H., Kottos, T., El-Ganainy, R., & Christodoulides, D. N. (2010). Unidirectional nonlinear PT -symmetric optical structures. *Physical Review A*, 82(4), 043803.
- [381] Ran, Y. (2007). *Spin Liquids, Exotic Phases and Phase Transitions*. PhD thesis, MIT Physics Department, Cambridge, MA.
- [382] Ran, Y., Hermele, M., Lee, P. A., & Wen, X.-G. (2007). Projected-Wave-Function Study of the Spin-\$1/2\$ Heisenberg Model on the Kagom\`e Lattice. *Physical Review Letters*, 98(11), 117205.
- [383] Ran, Y., Vishwanath, A., & Lee, D.-H. (2008). A direct transition between a Neel ordered Mott insulator and a  $d_{x^2-y^2}$  superconductor on the square lattice. *arXiv e-prints*, (arXiv:0806.2321), arXiv:0806.2321.
- [384] Ran, Y. & Wen, X.-G. (2006). Continuous quantum phase transitions beyond Landau's paradigm in a large-N spin model.
- [385] Ranjith, K. M., Dmytriieva, D., Khim, S., Sichelschmidt, J., Luther, S., Ehlers, D., Yasuoka, H., Wosnitza, J., Tsirlin, A. A., Kühne, H., & Baenitz, M. (2019a). Field-induced instability of the quantum spin liquid ground state in the  $J_{\text{eff}}=1/2$  triangular-lattice compound  $\text{NaYbO}_2$ . *Physical Review B*, 99(180401), 180401.
- [386] Ranjith, K. M., Luther, S., Reimann, T., Schmidt, B., Schlender, Ph., Sichelschmidt, J., Yasuoka, H., Strydom, A. M., Skourski, Y., Wosnitza, J., Kühne, H., Doert, Th., & Baenitz, M. (2019b). Anisotropic field-induced ordering in the triangular-lattice quantum spin liquid  $\text{NaYbSe}_2$ . *Physical Review B*, 100(224417), 224417.
- [387] Rantner, W. & Wen, X.-G. (2002). Spin correlations in the algebraic spin liquid: Implications for high- $T_c$  superconductors. *Physical Review B*, 66(144501), 144501.
- [388] Read, N. (1995). Landau theory of quantum spin glasses of rotors and Ising spins. *Physical Review B*, 52(1), 384–410.
- [389] Read, N. & Sachdev, S. (1989). Valence-bond and spin-Peierls ground states of low-dimensional quantum antiferromagnets. *Physical Review Letters*, 62(14), 1694–1697.
- [390] Read, N. & Sachdev, S. (1990). Spin-Peierls, valence-bond solid, and Néel ground states of low-dimensional quantum antiferromagnets. *Physical Review B*, 42(7), 4568–4589.
- [391] Read, N. & Sachdev, S. (1991a). Large-N expansion for frustrated quantum antiferromagnets. *Physical Review Letters*, 66(13), 1773–1776.
- [392] Read, N. & Sachdev, S. (1991b). Large-N expansion for frustrated quantum antiferromagnets. *Physical Review Letters*, 66(13), 1773–1776.

- [393] Regensburger, A., Bersch, C., Miri, M.-A., Onishchukov, G., Christodoulides, D. N., & Peschel, U. (2012). Parity-time synthetic photonic lattices. *Nature*, 488(7410), 167–171.
- [394] Reiter, F. & Sørensen, A. S. (2012). Effective operator formalism for open quantum systems. *Physical Review A*, 85(3), 032111.
- [395] Rende, R., Viteritti, L. L., Bardone, L., Becca, F., & Goldt, S. (2023). A simple linear algebra identity to optimize Large-Scale Neural Network Quantum States.
- [396] Robinson, N. J., Johnson, P. D., Rice, T. M., & Tsvelik, A. M. (2019). Anomalies in the pseudogap phase of the cuprates: Competing ground states and the role of umklapp scattering. *Reports on Progress in Physics*, 82(12), 126501.
- [397] Robledo Moreno, J., Carleo, G., Georges, A., & Stokes, J. (2022). Fermionic wave functions from neural-network constrained hidden states. *Proceedings of the National Academy of Sciences*, 119(32), e2122059119.
- [398] Roth, C., Szabó, A., & MacDonald, A. H. (2023). High-accuracy variational Monte Carlo for frustrated magnets with deep neural networks. *Physical Review B*, 108(5), 054410.
- [399] Rothe, H. J. (2012). *Lattice Gauge Theories*. World Scientific, 4 edition.
- [400] Rotter, I. (2009). A non-Hermitian Hamilton operator and the physics of open quantum systems. *Journal of Physics A: Mathematical and Theoretical*, 42(15), 153001.
- [401] Rubtsov, A. N., Savkin, V. V., & Lichtenstein, A. I. (2005). Continuous-time quantum Monte Carlo method for fermions. *Physical Review B*, 72(3), 035122.
- [402] Rui, W. B., Hirschmann, M. M., & Schnyder, A. P. (2019). PT-symmetric non-Hermitian dirac semimetals.
- [403] Rüter, C. E., Makris, K. G., El-Ganainy, R., Christodoulides, D. N., Segev, M., & Kip, D. (2010). Observation of parity-time symmetry in optics. *Nature Physics*, 6(3), 192–195.
- [404] Sá, L., Ribeiro, P., & Prosen, T. (2022). Lindbladian dissipation of strongly-correlated quantum matter. *Physical Review Research*, 4(2), L022068.
- [405] Sá, L., Ribeiro, P., & Prosen, T. (2023). Symmetry Classification of Many-Body Lindbladians: Tenfold Way and Beyond. *Physical Review X*, 13(3), 031019.
- [406] Saad, P., Shenker, S. H., & Stanford, D. (2019). A semiclassical ramp in SYK and in gravity.
- [407] Saadatmand, S. N. & McCulloch, I. P. (2016). Symmetry fractionalization in the topological phase of the spin-1/2 J<sub>1</sub>-J<sub>2</sub> triangular Heisenberg model. *Physical Review B*, 94(12), 121111.
- [408] Sachdev, S. (1992). Kagome- and triangular-lattice Heisenberg antiferromagnets: Ordering from quantum fluctuations and quantum-disordered ground states with unconfined bosonic spinons. *Physical Review B*, 45(21), 12377–12396.
- [409] Sachdev, S. (1994). Quantum phases of the Shraiman-Siggia model. *Physical Review B*, 49, 6770–6778.

- [410] Sachdev, S. (2010). Holographic metals and the fractionalized Fermi liquid. *Physical Review Letters*, 105, 151602.
- [411] Sachdev, S. (2019a). Topological order, emergent gauge fields, and Fermi surface reconstruction. 82(1), 014001.
- [412] Sachdev, S. (2019b). Topological order, emergent gauge fields, and Fermi surface reconstruction. *Reports on Progress in Physics*, 82(014001), 014001.
- [413] Sachdev, S. (2023). *Quantum Phases of Matter*. Cambridge, UK: Cambridge University Press.
- [414] Sachdev, S. & Park, K. (2002a). Ground states of quantum antiferromagnets in two dimensions. *Annals of Physics*, 298(1), 58–122.
- [415] Sachdev, S. & Park, K. (2002b). Ground states of quantum antiferromagnets in two dimensions. *Annals of Physics*, 298(1), 58–122.
- [416] Sachdev, S. & Read, N. (1991). Large N expansion for frustrated and doped quantum antiferromagnets. *International Journal of Modern Physics B*, 5(1-02), 219–249.
- [417] Sachdev, S., Read, N., & Oppermann, R. (1995). Quantum field theory of metallic spin glasses. *Physical Review B*, 52(14), 10286–10294.
- [418] Sachdev, S., Scammell, H. D., Scheurer, M. S., & Tarnopolsky, G. (2019). Gauge theory for the cuprates near optimal doping. *Physical Review B*, 99(5), 054516.
- [419] Sachdev, S. & Vojta, M. (1999). Translational symmetry breaking in two-dimensional antiferromagnets and superconductors. *J. Phys. Soc. Jpn* **69**, Supp. B, 1.
- [420] Sachdev, S. & Ye, J. (1993a). Gapless spin-fluid ground state in a random quantum Heisenberg magnet. *Physical Review Letters*, 70, 3339.
- [421] Sachdev, S. & Ye, J. (1993b). Gapless spin-fluid ground state in a random quantum Heisenberg magnet. *Physical Review Letters*, 70(21), 3339–3342.
- [422] Sakai, S., Motome, Y., & Imada, M. (2009). Evolution of electronic structure of doped mott insulators: Reconstruction of poles and zeros of green's function. *Physical Review Letters*, 102(5), 056404.
- [423] San-Jose, P., Cayao, J., Prada, E., & Aguado, R. (2016). Majorana bound states from exceptional points in non-topological superconductors. *Scientific Reports*, 6.
- [424] Sato, M., Hasebe, K., Esaki, K., & Kohmoto, M. (2011). Time-reversal symmetry in non-hermitian systems.
- [425] Sato, T., Wang, Z., Liu, Y., Hou, D., Hohenadler, M., Guo, W., & Assaad, F. F. (2023). Simulation of fermionic and bosonic critical points with emergent SO(5) symmetry. *Physical Review B*, 108(12), L121111.
- [426] Savary, L. & Balents, L. (2016a). Quantum spin liquids: A review. *Reports on Progress in Physics*, 80(1), 016502.

- [427] Savary, L. & Balents, L. (2016b). Quantum spin liquids: A review. *Reports on Progress in Physics*, 80(1), 016502.
- [428] Sayyad, S., Yu, J., Grushin, A. G., & Sieberer, L. M. (2021). Entanglement spectrum crossings reveal non-Hermitian dynamical topology. *3(3)*, 033022.
- [429] Scheie, A. O., Ghioldi, E. A., Xing, J., Paddison, J. A. M., Sherman, N. E., Dupont, M., Sanjeeewa, L. D., Lee, S., Woods, A. J., Abernathy, D., Pajerowski, D. M., Williams, T. J., Zhang, S.-S., Manuel, L. O., Trumper, A. E., Pemmaraju, C. D., Sefat, A. S., Parker, D. S., Devereaux, T. P., Movshovich, R., Moore, J. E., Batista, C. D., & Tennant, D. A. (2021). Witnessing quantum criticality and entanglement in the triangular antiferromagnet KYbSe<sub>2</sub>. *arXiv e-prints*, (arXiv:2109.11527), arXiv:2109.11527.
- [430] Schindler, J., Li, A., Zheng, M. C., Ellis, F. M., & Kottos, T. (2011). Experimental study of active LRC circuits with PT symmetries. *Physical Review A: Atomic, Molecular, and Optical Physics*, 84(4), 040101(R).
- [431] Sedrakyan, T. A. & Efetov, K. B. (2020). Supersymmetry method for interacting chaotic and disordered systems: The Sachdev-Ye-Kitaev model. *Physical Review B*, 102(7), 075146.
- [432] Self, C. N., Knolle, J., Iblisdir, S., & Pachos, J. K. (2019). Thermally induced metallic phase in a gapped quantum spin liquid: Monte Carlo study of the Kitaev model with parity projection. *Physical Review B*, 99(4), 045142.
- [433] Sengupta, A. M. & Georges, A. (1995). Non-Fermi-liquid behavior near a T=0 spin-glass transition. *Physical Review B*, 52(14), 10295–10302.
- [434] Senthil, T., Balents, L., Sachdev, S., Vishwanath, A., & Fisher, M. P. A. (2004a). Quantum criticality beyond the landau-ginzburg-wilson paradigm. *Physical Review B*, 70(144407), 144407.
- [435] Senthil, T. & Fisher, M. P. A. (2000). Z<sub>2</sub> gauge theory of electron fractionalization in strongly correlated systems. *Physical Review B*, 62, 7850.
- [436] Senthil, T. & Fisher, M. P. A. (2006). Competing orders, nonlinear sigma models, and topological terms in quantum magnets. *Physical Review B*, 74(064405), 064405.
- [437] Senthil, T. & Lee, P. A. (2005). Cuprates as doped U (1) spin liquids. *Physical Review B*, 71(174515), 174515.
- [438] Senthil, T., Sachdev, S., & Vojta, M. (2003). Fractionalized fermi liquids. *Physical Review Letters*, 90(216403), 216403.
- [439] Senthil, T., Vishwanath, A., Balents, L., Sachdev, S., & Fisher, M. P. A. (2004b). Deconfined quantum critical points. *Science (New York, N.Y.)*, 303, 1490–1494.
- [440] Senthil, T., Vojta, M., & Sachdev, S. (2004c). Weak magnetism and non-Fermi liquids near heavy-fermion critical points. *Physical Review B*, 69(035111), 035111.
- [441] Shackleton, H. & Sachdev, S. (2022). Anisotropic deconfined criticality in Dirac spin liquids. *JHEP*, 07, 141.
- [442] Shackleton, H., Thomson, A., & Sachdev, S. (2021). Deconfined criticality and a gapless Z<sub>2</sub> spin liquid in the square-lattice antiferromagnet. *Physical Review B*, 104(4), 045110.

- [443] Shao, H., Guo, W., & Sandvik, A. W. (2016). Quantum criticality with two length scales. *Science (New York, N.Y.)*, 352(6282), 213–216.
- [444] Shen, H., Zhen, B., & Fu, L. (2018). Topological band theory for non-hermitian hamiltonians. *Physical Review Letters*, 120(14), 146402.
- [445] Shen, Y., Li, Y.-D., Wo, H., Li, Y., Shen, S., Pan, B., Wang, Q., Walker, H. C., Steffens, P., Boehm, M., Hao, Y., Quintero-Castro, D. L., Harriger, L. W., Frontzek, M. D., Hao, L., Meng, S., Zhang, Q., Chen, G., & Zhao, J. (2016). Evidence for a spinon Fermi surface in a triangular-lattice quantum-spin-liquid candidate. *Nature*, 540(7634), 559–562.
- [446] Shi, Z. D., Else, D. V., Goldman, H., & Senthil, T. (2023). Loop current fluctuations and quantum critical transport. *SciPost Physics*, 14, 113.
- [447] Shibata, N. & Katsura, H. (2019). Dissipative spin chain as a non-Hermitian Kitaev ladder. *Physical Review B*, 99(17), 174303.
- [448] Shimizu, Y., Miyagawa, K., Kanoda, K., Maesato, M., & Saito, G. (2003). Spin liquid state in an organic mott insulator with a triangular lattice. *Physical Review Letters*, 91(107001), 107001.
- [449] Shimizu, Y., Miyagawa, K., Kanoda, K., Maesato, M., & Saito, G. (2006). Emergence of inhomogeneous moments from spin liquid in the triangular-lattice Mott insulator  $\kappa$ -(ET)<sub>2</sub>Cu<sub>2</sub>(CN)<sub>3</sub>. *Physical Review B*, 73(140407), 140407.
- [450] Shirley, W., Slagle, K., Wang, Z., & Chen, X. (2018). Fracton models on general three-dimensional manifolds. *Physical Review X*, 8(3), 031051.
- [451] Si, T. & Yu, Y. (2008). Anyonic Loops in Three Dimensional Spin liquid and Chiral Spin Liquid. *Nuclear Physics B*, 803(3), 428–449.
- [452] Sieberer, L. M., Buchhold, M., & Diehl, S. (2016). Keldysh field theory for driven open quantum systems. *Reports on Progress in Physics*, 79(096001), 096001.
- [453] Skolimowski, J. & Fabrizio, M. (2022). Luttinger’s theorem in the presence of Luttinger surfaces. *Physical Review B*, 106(4), 045109.
- [454] Slagle, K. & Kim, Y. B. (2017). Quantum field theory of X-cube fracton topological order and robust degeneracy from geometry. *Physical Review B*, 96(19), 195139.
- [455] Slagle, K. & Xu, C. (2014). Quantum phase transition between the Z<sub>2</sub> spin liquid and valence bond crystals on a triangular lattice. *Physical Review B*, 89(10), 104418.
- [456] Smith, J. L. & Si, Q. (2000). Spatial correlations in dynamical mean-field theory. *Physical Review B*, 61(8), 5184–5193.
- [457] Sommer, O. E., Piazza, F., & Luitz, D. J. (2021). Many-body hierarchy of dissipative timescales in a quantum computer. *Physical Review Research*, 3(2), 023190.
- [458] Song, X.-Y., He, Y.-C., Vishwanath, A., & Wang, C. (2018). From spinon band topology to the symmetry quantum numbers of monopoles in Dirac spin liquids. *arXiv e-prints*, (arXiv:1811.11182), arXiv:1811.11182.

- [459] Song, X.-Y., He, Y.-C., Vishwanath, A., & Wang, C. (2020a). From spinon band topology to the symmetry quantum numbers of monopoles in Dirac spin liquids. *Physical Review X*, 10(1), 011033.
- [460] Song, X.-Y., He, Y.-C., Vishwanath, A., & Wang, C. (2020b). From spinon band topology to the symmetry quantum numbers of monopoles in Dirac spin liquids. *Physical Review X*, 10(1), 011033.
- [461] Song, X.-Y., Jian, C.-M., & Balents, L. (2017). Strongly Correlated Metal Built from Sachdev-Ye-Kitaev Models. *Physical Review Letters*, 119(21), 216601.
- [462] Song, X.-Y., Wang, C., Vishwanath, A., & He, Y.-C. (2019a). Unifying description of competing orders in two dimensional quantum magnets. *Nature Commun.*, 10(1), 4254.
- [463] Song, X.-Y., Wang, C., Vishwanath, A., & He, Y.-C. (2019b). Unifying description of competing orders in two-dimensional quantum magnets. *Nature Communications*, 10(4254), 4254.
- [464] Sordi, G., Walsh, C., Sémon, P., & Tremblay, A. M. S. (2019). Specific heat maximum as a signature of Mott physics in the two-dimensional Hubbard model. *Physical Review B*, 100(121105), 121105(R).
- [465] Souza, L. d. S., dos Prazeres, L. F., & Iemini, F. (2023). Sufficient condition for gapless spin-boson Lindbladians, and its connection to dissipative time-crystals. *Physical Review Letters*, 130(18), 180401.
- [466] St-Jean, P., Goblot, V., Galopin, E., Lemaître, A., Ozawa, T., Le Gratiet, L., Sagnes, I., Bloch, J., & Amo, A. (2017). Lasing in topological edge states of a one-dimensional lattice. *Nature Photonics*, 11(10), 651–656.
- [467] Stanescu, T. D. & Kotliar, G. (2006). Fermi arcs and hidden zeros of the Green function in the pseudogap state. *Physical Review B*, 74(12), 125110.
- [468] Starchl, E. & Sieberer, L. M. (2023). Quantum quenches in driven-dissipative quadratic fermionic systems with parity-time symmetry. *arXiv e-prints*, (arXiv:2304.01836), arXiv:2304.01836.
- [469] Sugiura, S. & Shimizu, A. (2012). Thermal pure quantum states at finite temperature. *Physical Review Letters*, 108(24), 240401.
- [470] Sugiura, S. & Shimizu, A. (2013). Canonical thermal pure quantum state. *Physical Review Letters*, 111(1), 010401.
- [471] Sun, G.-Y., Wang, Y.-C., Fang, C., Qi, Y., Cheng, M., & Meng, Z. Y. (2018). Dynamical Signature of Symmetry Fractionalization in Frustrated Magnets. *Physical Review Letters*, 121(7), 077201.
- [472] Sun, Y., Tan, W., Li, H.-q., Li, J., & Chen, H. (2014). Experimental demonstration of a coherent perfect absorber with PT phase transition. *Physical Review Letters*, 112(14), 143903.
- [473] Szasz, A., Motruk, J., Zaletel, M. P., & Moore, J. E. (2020). Chiral Spin Liquid Phase of the Triangular Lattice Hubbard Model: A Density Matrix Renormalization Group Study. *Physical Review X*, 10(2), 021042.

- [474] Takahashi, J. & Sandvik, A. W. (2020). Valence-bond solids, vestigial order, and emergent SO(5) symmetry in a two-dimensional quantum magnet. *2*(3), 033459.
- [475] Takahashi, J., Shao, H., Zhao, B., Guo, W., & Sandvik, A. W. (2024). SO(5) quantum tri-criticality in two-dimensional quantum magnets. *to appear*.
- [476] Takasu, Y., Yagami, T., Ashida, Y., Hamazaki, R., Kuno, Y., & Takahashi, Y. (2020). PT-symmetric non-Hermitian quantum many-body system using ultracold atoms in an optical lattice with controlled dissipation. *arXiv e-prints*.
- [477] Tanaka, A. & Hu, X. (2005). Many-body spin berry phases emerging from the  $\pi$ -Flux state: Competition between antiferromagnetism and the valence-bond-solid state. *Physical Review Letters*, 95(036402), 036402.
- [478] Tarnopolsky, G., Li, C., Joshi, D. G., & Sachdev, S. (2020). Metal-insulator transition in a random Hubbard model. *Physical Review B*, 101(20), 205106.
- [479] Terhal, B. M. (2015). Quantum error correction for quantum memories. *Reviews of Modern Physics*, 87(2), 307–346.
- [480] Thomson, A. & Sachdev, S. (2018a). Fermionic spinon theory of square lattice spin liquids near the néel state. *Physical Review X*, 8(1), 011012.
- [481] Thomson, A. & Sachdev, S. (2018b). Fermionic spinon theory of square lattice spin liquids near the néel state. *Physical Review X*, 8(1), 011012.
- [482] Tikhanovskaya, M., Guo, H., Sachdev, S., & Tarnopolsky, G. (2020). Excitation spectra of quantum matter without quasiparticles I: Sachdev-Ye-Kitaev models. *arXiv e-prints*.
- [483] Tikhanovskaya, M., Guo, H., Sachdev, S., & Tarnopolsky, G. (2021). Excitation spectra of quantum matter without quasiparticles. II. Random t-J models. *Physical Review B*, 103(7), 075142.
- [484] Tikhanovskaya, M., Sachdev, S., & Samajdar, R. (2023). Equilibrium dynamics of infinite-range quantum spin glasses in a field.
- [485] Tocchio, L. F., Montorsi, A., & Becca, F. (2021). Hubbard model on triangular \$N\$-leg cylinders: Chiral and nonchiral spin liquids. *Physical Review Research*, 3(4), 043082.
- [486] Tzortzakakis, A. F., Makris, K. G., & Economou, E. N. (2020). Non-Hermitian disorder in two-dimensional optical lattices. *Physical Review B*, 101(1), 014202.
- [487] Uhrich, P., Bandyopadhyay, S., Sauerwein, N., Sonner, J., Brantut, J.-P., & Hauke, P. (2023). A cavity quantum electrodynamics implementation of the Sachdev–Ye–Kitaev model.
- [488] van Langen, S. A., Silvestrov, P. G., & Beenakker, C. W. J. (1998). Thermopower of single-channel disordered and chaotic conductors. *Superlattices and Microstructures*, 23(3), 691–698.
- [489] Verbaarschot, J. J. M., Weidenmüller, H. A., & Zirnbauer, M. R. (1985). Grassmann integration in stochastic quantum physics: The case of compound-nucleus scattering. *Physics Reports*, 129(6), 367–438.

- [490] Verbaarschot, J. J. M. & Zirnbauer, M. R. (1985). Critique of the replica trick. *Journal of Physics A: Mathematical and General*, 18(7), 1093.
- [491] Verresen, R., Thorngren, R., Jones, N. G., & Pollmann, F. (2021). Gapless topological phases and symmetry-enriched quantum criticality. *Physical Review X*, 11(4), 041059.
- [492] Verstraete, F. & Cirac, J. I. (2004). Renormalization algorithms for Quantum-Many Body Systems in two and higher dimensions.
- [493] Verstraete, F. & Cirac, J. I. (2006). Matrix product states represent ground states faithfully. *Physical Review B*, 73(9), 094423.
- [494] Vijay, S., Haah, J., & Fu, L. (2015). A new kind of topological quantum order: A dimensional hierarchy of quasiparticles built from stationary excitations. *Physical Review B*, 92(235136), 235136.
- [495] Vijay, S., Haah, J., & Fu, L. (2016). Fracton topological order, generalized lattice gauge theory, and duality. *Physical Review B*, 94(23), 235157.
- [496] Viteritti, L. L., Rende, R., & Becca, F. (2023). Transformer Variational Wave Functions for Frustrated Quantum Spin Systems. *Physical Review Letters*, 130(23), 236401.
- [497] Wagner, N., Crippa, L., Amaricci, A., Hansmann, P., Klett, M., König, E. J., Schäfer, T., Sante, D. D., Cano, J., Millis, A. J., Georges, A., & Sangiovanni, G. (2023). Mott insulators with boundary zeros. *Nature Communications*, 14(7531), 7531.
- [498] Walsh, C., Sémon, P., Poulin, D., Sordi, G., & Tremblay, A. M. S. (2019). Local entanglement entropy and mutual information across the mott transition in the two-dimensional hubbard model. *Physical Review Letters*, 122(067203), 067203.
- [499] Walsh, C., Sémon, P., Poulin, D., Sordi, G., & Tremblay, A.-M. S. (2020). Entanglement and classical correlations at the doping-driven mott transition in the two-dimensional hubbard model. *PRX Quantum*, 1(2), 020310.
- [500] Wang, C., Nahum, A., Metlitski, M. A., Xu, C., & Senthil, T. (2017a). Deconfined quantum critical points: Symmetries and dualities. *Physical Review X*, 7(3), 031051.
- [501] Wang, C., Nahum, A., Metlitski, M. A., Xu, C., & Senthil, T. (2017b). Deconfined quantum critical points: Symmetries and dualities. *Physical Review X*, 7(3), 031051.
- [502] Wang, F. & Vishwanath, A. (2006). Spin Liquid States on the Triangular and Kagome Lattices: A Projective Symmetry Group Analysis of Schwinger Boson States. *Physical Review B*, 74(17), 174423.
- [503] Wang, H., Bagrets, D., Chudnovskiy, A. L., & Kamenev, A. (2019). On the replica structure of Sachdev-Ye-Kitaev model. *Journal of High Energy Physics*, 2019(9), 57.
- [504] Wang, K., Piazza, F., & Luitz, D. J. (2020). Hierarchy of Relaxation Timescales in Local Random Liouvillians. *Physical Review Letters*, 124(10), 100604.
- [505] Wang, L. & Sandvik, A. W. (2018). Critical level crossings and gapless spin liquid in the square-lattice spin-1 /2 J<sub>1</sub>-J<sub>2</sub> heisenberg antiferromagnet. *Physical Review Letters*, 121(107202), 107202.

- [506] Wang, Z., Zaletel, M. P., Mong, R. S. K., & Assaad, F. F. (2021). Phases of the (2+1) dimensional SO(5) nonlinear sigma model with topological term. *Physical Review Letters*, 126(045701), 045701.
- [507] Wei, C. & Sedrakyan, T. A. (2021). Optical lattice platform for the Sachdev-Ye-Kitaev model. *Physical Review A*, 103(013323), 013323.
- [508] Weidemann, S., Kremer, M., Helbig, T., Hofmann, T., Stegmaier, A., Greiter, M., Thomale, R., & Szameit, A. (2020). Topological funneling of light. *Science (New York, N.Y.)*, 368(6488), 311–314.
- [509] Weimer, H., Müller, M., Lesanovsky, I., Zoller, P., & Büchler, H. P. (2010/05/01, 2010). A rydberg quantum simulator. *Nature Physics*, 6(5), 382–388.
- [510] Wen, X. G. (1991). Mean-field theory of spin-liquid states with finite energy gap and topological orders. *Physical Review B*, 44(6), 2664–2672.
- [511] Wen, X.-G. (2002). Quantum orders and symmetric spin liquids. *Physical Review B*, 65(165113), 165113.
- [512] Wen, X.-G. & Lee, P. A. (1996). Theory of underdoped cuprates. *Physical Review Letters*, 76(3), 503–506.
- [513] Wen, X.-G. & Lee, P. A. (1998). Theory of quasiparticles in the underdoped high-  $t_c$  superconducting state. *Physical Review Letters*, 80(10), 2193–2196.
- [514] White, S. R. (1992). Density matrix formulation for quantum renormalization groups. *Physical Review Letters*, 69(19), 2863–2866.
- [515] Whitsitt, S. & Sachdev, S. (2016). Transition from the  $Z_2$  spin liquid to antiferromagnetic order: Spectrum on the torus. *Physical Review B*, 94(085134), 085134.
- [516] Wiersig, J. (2014). Enhancing the sensitivity of frequency and energy splitting detection by using exceptional points: Application to microcavity sensors for single-particle detection. *Physical Review Letters*, 112(20), 203901.
- [517] Wietek, A., Capponi, S., & Läuchli, A. M. (2023). Quantum electrodynamics in 2+1 dimensions as the organizing principle of a triangular lattice antiferromagnet. *arXiv e-prints*, (arXiv:2303.01585), arXiv:2303.01585.
- [518] Wietek, A., Corboz, P., Wessel, S., Normand, B., Mila, F., & Honecker, A. (2019). Thermodynamic properties of the Shastry-Sutherland model throughout the dimer-product phase. *Physical Review Research*, 1(3), 033038.
- [519] Wietek, A. & Läuchli, A. M. (2018). Sublattice coding algorithm and distributed memory parallelization for large-scale exact diagonalizations of quantum many-body systems. *Physical Review E: Statistical Physics, Plasmas, Fluids, and Related Interdisciplinary Topics*, 98(3), 033309.
- [520] Wietek, A. & Läuchli, A. M. (2020). Valence bond solid and possible deconfined quantum criticality in an extended kagome lattice Heisenberg antiferromagnet. *Physical Review B*, 102(2), 020411.

- [521] Wigner, E. P. (1967). Random Matrices in Physics. *SIAM Review*, 9(1), 1–23.
- [522] Wilczek, F. (1982). Quantum Mechanics of Fractional-Spin Particles. *Physical Review Letters*, 49(14), 957–959.
- [523] Witten, E. (2016). An SYK-Like Model Without Disorder.
- [524] Wolff, U. (1989). Collective Monte Carlo Updating for Spin Systems. *Physical Review Letters*, 62(4), 361–364.
- [525] Wu, C., Arovas, D., & Hung, H.-H. (2009).  $\Gamma$ -Matrix generalization of the Kitaev model. *Physical Review B*, 79(13), 134427.
- [526] Wu, M., Peng, R., Liu, J., Zhao, Q., & Zhou, J. (2020). Direct observation of energy band attraction effect in non-Hermitian systems. *arXiv e-prints*, (arXiv:2004.14744), arXiv:2004.14744.
- [527] Wu, T. T. & Yang, C. N. (1976). Dirac monopole without strings: Monopole harmonics. *Nuclear Physics B*, 107(3), 365–380.
- [528] Xiao, L., Wang, K., Zhan, X., Bian, Z., Kawabata, K., Ueda, M., Yi, W., & Xue, P. (2019). Observation of critical phenomena in parity-time-symmetric quantum dynamics. *Physical Review Letters*, 123(23), 230401.
- [529] Xiao-Gang Wen (1995). Topological orders and edge excitations in fractional quantum Hall states. *Advances in Physics*, 44(5), 405–473.
- [530] Xiong, Y. (2018). Why does bulk boundary correspondence fail in some non-hermitian topological models. *Journal of Physics Communications*, 2(3), 035043.
- [531] Xu, C. & Sachdev, S. (2008). Square-lattice algebraic spin liquid with SO(5) symmetry. *Physical Review Letters*, 100(137201), 137201.
- [532] Xu, H., Mason, D., Jiang, L., & Harris, J. G. E. (2016). Topological energy transfer in an optomechanical system with exceptional points. *Nature*, 537(7618), 80–83.
- [533] Xu, K.-J., Guo, Q., Hashimoto, M., Li, Z.-X., Chen, S.-D., He, J., He, Y., Li, C., Berntsen, M. H., Rotundu, C. R., Lee, Y. S., Devoreaux, T. P., Rydh, A., Lu, D.-H., Lee, D.-H., Tjernberg, O., & Shen, Z.-X. (2023/12/01, 2023a). Bogoliubov quasiparticle on the gossamer Fermi surface in electron-doped cuprates. *Nature Physics*, 19(12), 1834–1840.
- [534] Xu, S., Bag, R., Sherman, N. E., Yadav, L., Kolesnikov, A. I., Podlesnyak, A. A., Moore, J. E., & Haravifard, S. (2023b). Realization of U(1) dirac quantum spin liquid in YbZn<sub>2</sub>GaO<sub>5</sub>.
- [535] Xu, X. Y. & Grover, T. (2021). Competing nodal d-Wave superconductivity and anti-ferromagnetism. *Physical Review Letters*, 126(21), 217002.
- [536] Xu, Z. & Chen, S. (2020). Topological Bose-Mott insulators in one-dimensional non-Hermitian superlattices. *arXiv e-prints*.
- [537] Yamamoto, K., Nakagawa, M., Adachi, K., Takasan, K., Ueda, M., & Kawakami, N. (2019). Theory of non-hermitian fermionic superfluidity with a complex-valued interaction. *Physical Review Letters*, 123(12), 123601.

- [538] Yamamoto, K., Nakagawa, M., Tsuji, N., Ueda, M., & Kawakami, N. (2021). Collective excitations and nonequilibrium phase transition in dissipative fermionic superfluids. *Physical Review Letters*, 127(5), 055301.
- [539] Yamashita, M., Nakata, N., Kasahara, Y., Sasaki, T., Yoneyama, N., Kobayashi, N., Fujimoto, S., Shibauchi, T., & Matsuda, Y. (2009). Thermal-transport measurements in a quantum spin-liquid state of the frustrated triangular magnet  $\kappa$ -(BEDT-TTF)<sub>2</sub>Cu<sub>2</sub>(CN)<sub>3</sub>. *Nature Physics*, 5(1), 44–47.
- [540] Yan, S., Huse, D. A., & White, S. R. (2011). Spin Liquid Ground State of the \$S=1/2\$ Kagome Heisenberg Model. *Science*, 332(6034), 1173–1176.
- [541] Yan, Z., Wang, Y.-C., Ma, N., Qi, Y., & Meng, Z. Y. (2021). Topological phase transition and single/multi anyon dynamics of Z<sub>2</sub> spin liquid. *npj Quantum Materials*, 6(39), 39.
- [542] Yang, J., Sandvik, A. W., & Wang, L. (2022). Quantum criticality and spin liquid phase in the Shastry-Sutherland model. *Physical Review B*, 105(6), L060409.
- [543] Yang, K., Morampudi, S. C., & Bergholtz, E. J. (2021). Exceptional Spin Liquids from Couplings to the Environment. *Physical Review Letters*, 126(7), 077201.
- [544] Yang, K.-Y., Rice, T. M., & Zhang, F.-C. (2006). Phenomenological theory of the pseudogap state. *Physical Review B*, 73(17), 174501.
- [545] Yang, S., Zhou, D. L., & Sun, C. P. (2007). Mosaic spin models with topological order. *Physical Review B*, 76(18), 180404(R).
- [546] Yao, H., Zhang, S.-C., & Kivelson, S. A. (2009). Algebraic Spin Liquid in an Exactly Solvable Spin Model. *Physical Review Letters*, 102(21), 217202.
- [547] Yao, S. & Wang, Z. (2018). Edge states and topological invariants of non-hermitian systems. *Physical Review Letters*, 121(8), 086803.
- [548] Ye, W., Guo, M., He, Y.-C., Wang, C., & Zou, L. (2022). Topological characterization of Lieb-Schultz-Mattis constraints and applications to symmetry-enriched quantum criticality. *SciPost Physics*, 13(3), 066.
- [549] Yoshida, B. (2013). Exotic topological order in fractal spin liquids. *Physical Review B*, 88(12), 125122.
- [550] Yoshida, T., Kudo, K., & Hatsugai, Y. (2019). Non-Hermitian fractional quantum Hall states. *Scientific Reports*, 9(1), 16895.
- [551] Yoshida, T., Peters, R., Kawakami, N., & Hatsugai, Y. (2020). Exceptional band touching for strongly correlated systems in equilibrium. *arXiv e-prints*, (arXiv:2002.11265), arXiv:2002.11265.
- [552] Young, A. F., Sanchez-Yamagishi, J. D., Hunt, B., Choi, S. H., Watanabe, K., Taniguchi, T., Ashoori, R. C., & Jarillo-Herrero, P. (2014). Tunable symmetry breaking and helical edge transport in a graphene quantum spin Hall state. *Nature*, 505(7484), 528–532.
- [553] Yuce, C. & Ramezani, H. (2019). Topological states in a non-Hermitian two-dimensional su-schrieffer-heeger model. *Physical Review A: Atomic, Molecular, and Optical Physics*, 100(3), 032102.

- [554] Zaletel, M., Lu, Y.-M., & Vishwanath, A. (2017). Measuring space-group symmetry fractionalization in Z\$<sub>2</sub>\$ spin liquids. *Physical Review B*, 96(19), 195164.
- [555] Zaletel, M. P. & Vishwanath, A. (2015). Constraints on topological order in Mott Insulators. *Physical Review Letters*, 114(7), 077201.
- [556] Zhang, D.-W., Chen, Y.-L., Zhang, G.-Q., Lang, L.-J., Li, Z., & Zhu, S.-L. (2020a). Skin superfluid, topological Mott insulators, and asymmetric dynamics in an interacting non-Hermitian Aubry-André-Harper model. *Physical Review B*, 101(23), 235150.
- [557] Zhang, D.-W., Tang, L.-Z., Lang, L.-J., Yan, H., & Zhu, S.-L. (2020b). Non-hermitian topological anderson insulators. *Science China Physics, Mechanics & Astronomy*, 63(6), 267062.
- [558] Zhang, F. C., Gros, C., Rice, T. M., & Shiba, H. (1988). A renormalised Hamiltonian approach for a resonant valence bond wavefunction. *Superconductor Science and Technology*, 1, 36.
- [559] Zhang, K. L., Yang, X. M., & Song, Z. (2019). Quantum transport in non-Hermitian impurity arrays. *Physical Review B*, 100(2), 024305.
- [560] Zhang, R., Qin, H., Xiao, J., & Liu, J. (2018). What breaks parity-time-symmetry? – pseudo-Hermiticity and resonance between positive- and negative-action modes. *arXiv e-prints*.
- [561] Zhang, Y.-H. & Sachdev, S. (2020a). Deconfined criticality and ghost Fermi surfaces at the onset of antiferromagnetism in a metal. *Physical Review B*, 102(155124), 155124.
- [562] Zhang, Y.-H. & Sachdev, S. (2020b). From the pseudogap metal to the Fermi liquid using ancilla qubits. *Physical Review Research*, 2, 23172.
- [563] Zhang, Y.-H. & Sachdev, S. (2020c). From the pseudogap metal to the Fermi liquid using ancilla qubits. *Physical Review Research*, 2(023172), 023172.
- [564] Zhang, Z., Li, J., Xie, M., Zhuo, W., Adroja, D. T., Baker, P. J., Perring, T. G., Zhang, A., Jin, F., Ji, J., Wang, X., Ma, J., & Zhang, Q. (2022). Low-energy spin dynamics of the quantum spin liquid candidate NaYbSe<sub>2</sub>. *Physical Review B*, 106(085115), 085115.
- [565] Zhang, Z., Ma, X., Li, J., Wang, G., Adroja, D. T., Perring, T. P., Liu, W., Jin, F., Ji, J., Wang, Y., Kamiya, Y., Wang, X., Ma, J., & Zhang, Q. (2021). Crystalline electric field excitations in the quantum spin liquid candidate NaYbSe<sub>2</sub>. *Physical Review B*, 103(035144), 035144.
- [566] Zhang, Z., Zhang, Y., Sheng, J., Yang, L., Miri, M.-A., Christodoulides, D. N., He, B., Zhang, Y., & Xiao, M. (2016). Observation of parity-time symmetry in optically induced atomic lattices. *Physical Review Letters*, 117(12), 123601.
- [567] Zhao, B., Takahashi, J., & Sandvik, A. W. (2020). Multicritical deconfined quantum criticality and lifshitz point of a helical valence-bond phase. 125(257204), 257204.
- [568] Zhou, B. & Zhang, Y.-H. (2023). Ancilla wavefunctions of Mott insulator and pseudogap metal through quantum teleportation.

- [569] Zhou, H. & Lee, J. Y. (2019). Periodic table for topological bands with non-Hermitian symmetries. *Physical Review B*, 99(23), 235112.
- [570] Zhou, H., Peng, C., Yoon, Y., Hsu, C. W., Nelson, K. A., Fu, L., Joannopoulos, J. D., Soljačić, M., & Zhen, B. (2018). Observation of bulk Fermi arc and polarization half charge from paired exceptional points. *Science (New York, N.Y.)*, 359(6379), 1009–1012.
- [571] Zhou, R., Vinograd, I., Hirata, M., Wu, T., Mayaffre, H., Krämer, S., Hardy, W. N., Liang, R., Bonn, D. A., Loew, T., Porras, J., Keimer, B., & Julien, M. H. (2024). Deconstructing the spin susceptibility of a cuprate superconductor. *arXiv e-prints*.
- [572] Zhou, S., Zelenayova, M., Hart, O., Chamon, C., & Castelnovo, C. (2022). Probing fractional statistics in quantum simulators of spin liquid Hamiltonians. *arXiv e-prints*.
- [573] Zhou, Y. & Wen, X.-G. (2003). Quantum Orders and Spin Liquids in Cs\$ \_2 \$CuCl\$ \_4 \$.
- [574] Zhou, Z., Hu, L., Zhu, W., & He, Y.-C. (2023). The SO(5) deconfined phase transition under the fuzzy sphere microscope: Approximate conformal symmetry, pseudo-criticality, and operator spectrum.
- [575] Zhu, Z. & White, S. R. (2015). Spin liquid phase of the S=1/2 J<sub>1</sub>-J<sub>2</sub> Heisenberg model on the triangular lattice. *Physical Review B*, 92(4), 041105.
- [576] Zinn-Justin, J. (2002). *Quantum Field Theory and Critical Phenomena*. International Series of Monographs on Physics. Clarendon Press.
- [577] Žnidarič, M. (2015). Relaxation times of dissipative many-body quantum systems. *Physical Review E*, 92(4), 042143.